Finanziato dall'Unione europea
NextGenerationEU
Ministero dell'Università e della Ricerca
Italiadomani
PIANO NAZIONALE DI RIPRESA E RESILIENZA
UNIVERSITÀ DEGLI STUDI DELL'AQUILA

UNIVERSITÀ DEGLI STUDI DELL'AQUILA
DIPARTIMENTO DI SCIENZE FISICHE E CHIMICHE

Dottorato di Ricerca in Scienze Fisiche e Chimiche

Curriculum Chimico

XXXVIII ciclo

Titolo della tesi

Soft Interactions and Hard Chemistry: Strategic Catalysis from the Molecular to the Industrial Scale

SSD CHEM-05/A

Dottorando

Alessio Carioscia

Coordinatore del corso

Prof. Massimiliano Aschi

Tutor

Prof. Armando Carlone

Dr. Fabio Pesciaioli

a.a. 2024/2025

A Sofia, Anna e Santino,

Questo traguardo è tanto mio quanto vostro.

"Home is behind, the world ahead
And there are many paths to tread
Through shadow, to the edge of night
Until the stars are all alight"

Pippin – Lord of The Rings

"If there were a little more goodness in the world,
and everyone saw each other as a brother,
there would be fewer worries and fewer sorrows,
and the world would be a much more beautiful place"
P. P.

"Chemistry is like cooking: just don't lick the spoon!"
Anonymous

Summary

Abstract 1

Chapter 1 – General Introduction 2

Catalysis as a Powerful tool in Modern Chemical Science and Technology 2

Organocatalysis: pushing the boundaries of enantioselective and sustainable chemistry 4

Covalent Organocatalysis 6

Asymmetric Aminocatalysis 6

Asymmetric NHC catalysis 9

Noncovalent Organocatalysis 12

Chiral Brønsted Acids and Bases 13

Phase Transfer Catalysts 21

Hydrogen bond donor catalysis 23

Halogen and chalcogen bond donor catalysis 27

Anion-binding catalysis 32

Chapter 2 - Nitrogen-Rich Carbon Dots as Effective Catalysts in the 1,4-Reduction of α,β-Unsaturated Aldehydes via Ion Pair Asymmetric Nano-Organocatalysis 38

Introduction 38

Carbon Dots: Versatile Nanoarchitectures for Catalysis and Beyond 38

Asymmetric hydrogenation of α,β-unsatured aldehydes via ACDC 41

Aim of the project 42

Results and Discussion 43

Design, synthesis, purification and characterization of Nitrogen-doped CDs 43

Rational optimization of the reaction conditions 45

Substrate Scope and Mechanistic Investigations 49

Conclusions 52

Experimental section 53

Instrumentation 53

Material and methods 53

Determination of enantiomeric purity 53

Determination of absolute configuration 54

Preparation of Carbon Dots and Characterisation of Superficial Amines 54
Experimental procedures 61
  General procedure for the nano-organocatalysed reactions 61
Synthesis of substrates 62
  General Procedure for the synthesis of ethyl (E)-3-phenylbut-2-enoate derivatives (**8a-h**) 62
  General Procedure for the synthesis of (E)-3-phenylbut-2-en-1-ol derivatives (**9a-h**) 63
  General Procedure for the synthesis of (E)-3-phenylbut-2-enal derivatives (**1a-h**) 64
  Synthesis of diethyl 2,6-dimethyl-1,4-dihydropyridine-3,5-dicarboxylate (**H1**) 64
  Synthesis of dibenzyl 2,6-dimethyl-1,4-dihydropyridine-3,5-dicarboxylate (**H2**) 65
  Synthesis of diethyl 2,6-diisopropyl-1,4-dihydropyridine-3,5-dicarboxylate (**H3**) 65
  Synthesis of diethyl 2-isopropyl-6-methyl-1,4-dihydropyridine-3,5-dicarboxylate (**H4**) 66
  Synthesis of dimethyl 2-isopropyl-6-methyl-1,4-dihydropyridine-3,5-dicarboxylate (**H5**) 66
Additional experiments 67
Characterization of compounds 73
  (*E*)-3-phenylbut-2-enal (**5a**) 73
  (E)-3-(4-methoxyphenyl)but-2-enal (**5b**) 73
  (E)-3-(p-tolyl)but-2-enal (**5c**) 74
  (E)-3-phenylpent-2-enal (**5d**) 74
  (E)-3-(4-nitrophenyl)but-2-enal (**5e**) 75
  (E)-3-(4-fluorophenyl)but-2-enal (**5f**) 75
  (E)-3-(4-chlorophenyl)but-2-enal (**5g**) 76
  (E)-3-(4-bromophenyl)but-2-enal (**5h**) 76
  (R)-3-phenylbutanal (**6a**) 77
  (R)-3-(4-methoxphenyl)butanal (**6b**) 77
  (R)-3-(p-tolyl)butanal (**6c**) 78
  (R)-3-phenylpentanal (**6d**) 78
  (R)-3-(4-nitrophenyl)butanal (**6e**) 79
  (R)-3-(4-fluorophenyl)butanal (**6f**) 79
  (R)-3-(4-chlorophenyl)butanal (**6g**) 80
  (R)-3-(4-bromophenyl)butanal (**6h**) 80
  (R)-3,7-dimethyloct-6-enal (**6i**) 81
  Diethyl 2-isopropyl-6-methyl-1,4-dihydropyridine-3,5-dicarboxylate (**H4**) 81
Chapter 3 – A Subtle Twist: Hantzsch Ester-Controlled Enantiodivergence Driven by Weak Non-Covalent Interactions 82

Introduction ***82***

Enantiodivergence: a powerful tool in asymmetric organocatalysis 82

Solvent-controlled inversion of enantioselectivity 83

Different achiral reagents or additives 91

Minimal catalysts modification 100

Other strategies to achieve enantiodivergence 111

Aim of the project ***114***

Results and discussion ***115***

Influence of the **HE** structure – experimental data 115

Influence of the **HE** structure – computational investigation 117

Conclusions ***122***

Experimental section ***123***

Instrumentations 123

Materials and methods 123

Determination of enantiomeric purity 124

Determination of absolute configuration 124

Synthesis and characterization of **HEs** 124

Synthesis of diethyl 2-ethyl-6-isopropyl-1,4-dihydropyridine-3,5-dicarboxylate (**HE-2**) 124

Synthesis of diethyl 2-ethyl-6-methyl-1,4-dihydropyridine-3,5-dicarboxylate (**HE-3**) 125

Analysis of Temperature dependence of the enantiomeric excess 126

Computational Details for MD simulations 126

Conformational analysis of Ion-Pair through Essential Dynamics 127

Calculation of relative free energies and enthalpies using MD data 129

Structural analysis of HE-X/IP adducts in the proR and proS regions. 132

Probability of formation of ternary complex 132

HPLC Traces 134

Compound **76a** 134

Compound **76b** 135

Chapter 4 – Strategies in Anion Binding Catalysis: From Carbazole Frameworks to Fluorinated Cyclohexanes **136**

General introduction ***136***

Design and Applications of Carbazole-Based Anion Receptors ***137***

Carbazole-based receptors for anions – an overview 139

1,8-diaminocarbazole platform 139

1,8-disulfonamide-carbazole platform 160

Indolo[2,3-α]carbazole platform 164

Miscellaneous carbazole platforms 168

Aim of the project 173

Results and discussion 175

Design of the family of catalysts 175

Synthesis of aldehydes **110a-e** 176

Synthesis of carbazole-triazole based receptors **106a-e** 177

Binding properties of compounds **106a-e**: molecular dynamics, fluorescence and NMR titrations 178

Application in anion-binding catalysis 190

Conclusions 196

Experimental section 197

Instrumentation 197

Material and methods 197

Experimental procedures 198

Characterizations 204

NMR titrations – experimental details 212

Fitting binding isotherms 212

Application of all-cis-fluorinated cyclohexanes in anion-binding catalysis 215

Synthesis and supramolecular properties of all-cis-fluorinated cyclohexanes – an overview 215

Aim of the project 217

Results and discussion 219

Design and synthesis and characterization of the catalyst 219

Catalysis explorative experiments 224

Conclusions 227

Experimental section 228

Materials and methods 228

Experimental procedures & characterization 229

Crystallographic data 230

Chapter 5 – From Lab Bench to Industry: Reinventing Tolterodine Synthesis via Prins Reaction 232

Introduction 232

Tolterodine: Mechanism of Action and Clinical Significance 232

Synthetic approaches to Tolterodine 234

Racemic Syntheses 234

Asymmetric Syntheses 240

Stereoselective vs Non-stereoselective synthesis of Tolterodine: a cost comparison 243

Aim of the project ***245***

Prins reaction 246

Results and discussion ***248***

Synthesis of 1,3-dioxane **49** 248

Hydrolysis of dioxane **49** 250

Prins reaction in acetic acid – batch conditions 252

Scale-Up and Final Conversion to Intermediate **24** (Fumarate Salt) 256

Prins reaction in acetic acid – continuous conditions 258

Conclusions ***269***

Experimental section ***270***

Instrumentations 270

Materials and methods 271

Experimental procedures 271

Synthesis of 4-phenyl-1,3-dioxane **49** 271

Synthesis of 1-Phenyl-1,3-propanediol (**23**) via acetal hydrolysis 271

Synthesis of 1,3-diacetoxy-1-phenylpropane (**50**) in batch conditions 272

Synthesis of 1-phenyl-1,3-propanediol (**23**) via hydrolysis of 1,3-diacetoxy-1-phenylpropane **50** 273

Synthesis of 3-(diisopropylamino)-1-phenylpropan-1-ol (**24**) 274

Synthesis of 3-(diisopropylamino)-1-phenylpropan-1-ol Fumarate (**24-Fumarate**) 275

General Flow procedure for the synthesis of 1,3-diacetoxy-1-phenylpropane (**50**) 276

Conclusions **278**

List of publications **280**

Conferences & Seminars attended **280**

Seminars ***280***

Conferences & Contributions ***281***

Aknowledgments **284**

Abstract

Catalysis represents a cornerstone for the advancement of human technology, offering invaluable tools to solve critical real-world problems such as climate change, energy consumption, and industrial productivity. While academia displays a profound interest in developing novel catalytic methodologies, the industrial world leverages these tools to establish economical, safe, and sustainable synthetic routes for producing highly valuable intermediates and final products. In the present work, both the fundamental academic and applied industrial perspectives on catalysis and technology are explored.

In the first part (**Chapter 2, 3, 4**), areas of fundamental academic interest are investigated, focusing on the development of novel catalytic systems driven by non-covalent interactions and the use of nanostructured materials. **Chapters 2** and **3** specifically detail the application of nitrogen-doped carbon dots (N**CDs**) in asymmetric organocatalysis, exploring their synergistic interplay with chiral counteranions (via ACDC) and the surprising impact of weak London dispersion forces on achieving complete enantiodivergence. **Chapter 4** further expands on non-covalent strategies by introducing new catalyst families for anion-binding catalysis, presenting novel scaffolds based on rigid 1,8-diaminocarbazole frameworks and rationally designed, facially polarized fluorinated cyclohexanes.

On the other hand, **Chapter 5** highlights how catalytic principles and modern technology, specifically continuous flow chemistry, can be leveraged to accelerate and intensify industrial "heavy chemistry," rendering it significantly more effective, economical, and sustainable. This is demonstrated through the development of a novel, safer, and more cost-effective synthesis of a key pharmaceutical intermediate for Tolterodine, which successfully eliminates hazardous reagents (like $NaBH_4$) and achieves higher purity via a process optimized in both batch and continuous flow regimes.

Chapter 1 – General Introduction

Catalysis as a Powerful tool in Modern Chemical Science and Technology

The present work is structured in two main sections. The first focuses on the development of novel approaches in supramolecular organocatalysis, with particular emphasis on the role of noncovalent interactions and nanostructured systems in promoting reactivity and selectivity (Chapter 2, 3, 4). The second part is dedicated to the industrial translation of chemical processes, addressing the challenges of process scaling and the application of advanced technologies for the implementation of efficient and sustainable catalytic systems on a larger scale (Chapter 5). Catalysis represents the common thread of the present work, serving as the conceptual and methodological foundation across its two main sections. For this reason, it is crucial to highlight the prominent role that catalysis has in chemistry and, more broadly, in modern technological advancement. As highlighted by Prof. Benjamin List, Nobel Laureate in Chemistry (2021), "Catalysis is not only a beautiful concept; it is a very important technology, too. Some would even state that it is the most important technology for humankind on this planet".[1]Catalysts operate by lowering the activation energy barrier of chemical transformations without undergoing permanent chemical change themselves (Figure 1), thereby enabling alternative and more efficient reaction pathways. As a result, catalytic systems significantly enhance reaction rates and render otherwise kinetically inaccessible transformations feasible under mild conditions.[2] Consequently, catalysis stands at the forefront of sustainable and green chemistry, aiming to reduce energy consumption, utilize environmentally benign reagents, and optimize material life cycles. As a cornerstone of modern chemical technology, catalysis contributes substantially to the global economy, accounting for an estimated one-third of global GDP,[3] and plays a central role in the production of over 80% of all industrial goods, from pharmaceuticals to fuels. Beyond its economic significance, catalysis is instrumental in addressing pressing global challenges such as climate change, energy conversion, and resource efficiency. It enables the development of clean energy technologies, carbon capture and utilization strategies, improved air and water quality,

---

[1] B. List, Asymmetric Organocatalysis, Nobel Prize Lecture, Stockholm, **2021**.

[2] R. van Santen, H. Niemantsverdriet, *Chemical Kinetics and Catalysis*, Springer New York, **1995**

[3] Z. Ma, F. Zaera, in *Encyclopedia of Inorganic Chemistry*, Wiley, **2005**.

and sustainable agricultural practices, often through more selective, energy-efficient processes that rely on renewable feedstocks.[4,5]

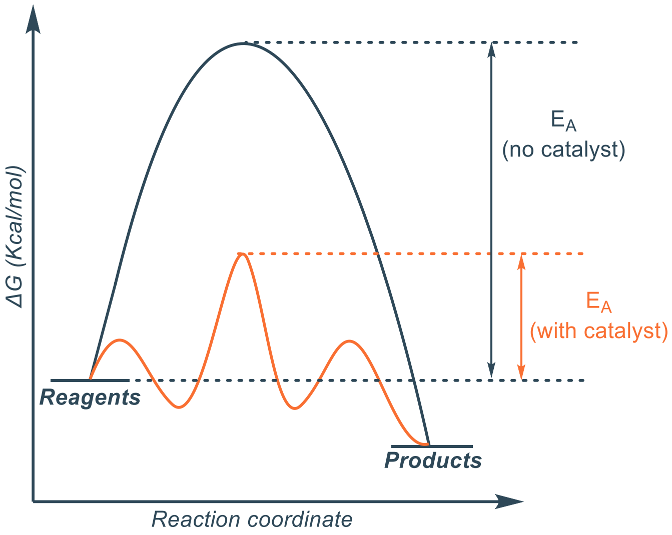

Figure 1 Mechanism of action of a catalyst. The catalyst provides an alternative reaction pathway with a lower activation energy by stabilizing different intermediates, thus increasing the rate of reaction.

Numerous industrial processes exemplify the critical importance of catalysis. For example, the Haber–Bosch process for ammonia synthesis, catalyzed by iron-based heterogeneous catalysts, is foundational for global fertilizer production. Although the formation of ammonia from nitrogen and hydrogen is thermodynamically favorable at low temperatures, the reaction proceeds extremely slowly under such conditions. The introduction of an effective catalyst, combined with optimized high-pressure and moderate temperature conditions, dramatically increases the reaction rate, thus making the process industrially viable.[6] Another prominent example regards the three-way catalytic converters in automotive exhaust systems. This technology utilizes platinum-group metal catalysts to convert NO_x, CO, and unburnt hydrocarbons into nitrogen, carbon dioxide, and water, significantly reducing urban air pollution.[7]

These examples underscore how the advancement of catalytic technologies has profoundly influenced the course of human development and holds the potential to address future global challenges. In this

---

[4] P. W. N. M. van Leeuwen, J. A. Moulijn, R. A. van Santen, *Catalysis - An Integrated Approach to Homogeneous, Heterogeneous and Industrial Catalysis*, Elsevier, **1993**.

[5] U. Hanefeld, L. Lefferts, Catalysis: *An Integrated Textbook for Students*, Wiley, **2018**.

[6] V. Kyriakou, I. Garagounis, A. Vourros, E. Vasileiou, M. Stoukides, *Joule* **2020**, *4*, 142–158.

[7] K. Kumar, N. Kumar, H. Singh, *Comprehensive Review of Three Way Catalytic Converter*, **2017**.

context, the development of efficient, robust, and sustainable catalytic systems remains a critical area of scientific research and innovation.

Organocatalysis: pushing the boundaries of enantioselective and sustainable chemistry

Traditionally, transition metal-based catalysts have dominated both academic research and industrial applications due to their high catalytic efficiency, broad substrate scope, and low required catalyst loadings. Moreover, homogeneous catalysis employing chiral ligands, such as phosphines or N-heterocyclic carbenes, has enabled highly enantioselective transformations, offering precise stereocontrol.[8] However, increasing environmental and economic pressures, such as the scarcity and toxicity of noble metals (e.g., Rh, Pd, Pt), have driven the development of more sustainable alternatives. In this scenario, Organocatalysis appears as a prominent catalytic platform to harness the power of small organic molecules to perform as efficient catalysts in chemical transformations.[9] When a chiral catalyst is employed, enantioselective transformations can be achieved, significantly enhancing the synthetic utility of this technique. The use of organic molecules as catalysts to perform metal-free reactions offer a plethora of advantages: these catalysts are generally non-toxic, readily available, stable, and often allow the reactions to be performed under mild conditions, even in the presence of water or air, which enhances reproducibility and operational simplicity.[10]

For these reasons, over the past 25 years, organocatalysis has emerged as a powerful and widely adopted catalytic strategy, gaining substantial traction in both academic research and industrial applications.[11,12] Its versatility has contributed significantly to the development of novel synthetic methodologies and has played a pivotal role in the execution of complex total syntheses.[13,14]

---

[8] J. F. Hartwig, *Organotransition Metal Chemistry: From Bonding to Catalysis*, University Science Books, **2009**.

[9] D. W. C. MacMillan, *Nature* **2008**, *455*, 304-308

[10] A. Berkessel, H. Gröger, *Asymmetric Organocatalysis: From Biomimetic Concepts to Applications in Asymmetric Synthesis*, Wiley, **2005**.

[11] A. Carlone, L. Bernardi, P. McCormack, T. Warr, S. Oruganti, C. J. Cobley, *Org. Process. Res. Dev.* **2021**, *25*, 2795-2805

[12] L. Bernardi, A. Carlone, F. Fini, in *Methodologies in Amine Synthesis: Challenges and Applications*, **2021**.

[13] B. Han, X.-H. He, Y.-Q. Liu, G. He, C. Peng, J.-L. Li, *Chem. Soc. Rev.* **2021**, *50*, 1522–1586.

[14] Y. Hayashi, *Acc. Chem. Res.* **2021**, *54*, 1385-1398

Furthermore, the integration of organocatalysis with other catalytic platforms, such as photoredox catalysis, transition metal catalysis, and electrocatalysis, has unlocked new reactivity paradigms.[15,16]

Owing to its metal-free nature, operational simplicity, and broad functional group tolerance, organocatalysis has become a cornerstone technology in the pursuit of sustainable, environmentally benign, and cost-effective chemical processes.[17,18] The significance of asymmetric organocatalysis was internationally recognized in 2021, when the Nobel Prize in Chemistry was awarded to Prof. Benjamin List and Prof. David MacMillan for their pioneering contributions to this field.

Most of the organocatalytic strategies can be classified depending on the nature of the interaction between the catalyst and the substrate(s). When the catalyst exploits its catalytic activity through the formation of covalent bonds with the reactive species, the process is referred to as covalent organocatalysis. In other cases, the catalyst can interact through noncovalent interactions; in this case, the process is classified as noncovalent organocatalysis. Each of these two broad categories can be further based on the specific activation mode. Covalent organocatalyst typically operates through the formation of reactive intermediates such as enamines, iminium ion and Breslow intermediates (from N-heterocyclic carbenes), each of them delivering a peculiar reactivity. Noncovalent organocatalysts are, on the other hand, classified according to the nature of the noncovalent interaction, such as ion pairing, hydrogen bond, halogen bond and chalcogen bond. A detailed classification of the most important activation mode in organocatalysis is depicted in Figure 2.

Figure 2. Classification of the most important activation mode in organocatalysis

---

[15] F. Pesciaioli, V. Nori, A. Sinibaldi, A. Carlone, in *Asymmetric Organocatalysis: New Strategies, Catalysts, and Opportunities: Volume 1-2*, **2022**

[16] A. Del Vecchio, A. Sinibaldi, V. Nori, G. Giorgianni, G. Di Carmine, F. Pesciaioli, *Chem. Eur. J.* **2022**, *28*, e202200818

[17] D. Krištofíková, V. Modrocká, M. Mečiarová, R. Šebesta, *ChemSusChem* **2020**, *13*, 2828–2858.

[18] T. Fulgheri, F. Della Penna, A. Baschieri, A. Carlone, *Curr. Opin. Green. Sustain. Chem.* **2020**, 25:100387

The following sections will provide an overview of the historical perspective, reactivity and typical mechanisms of enantioinduction, along with mechanistic insights and considerations on the relationship between structure of the catalyst and its activity.

Covalent Organocatalysis

Section outline *- This section provides an overview of covalent organocatalysis, detailing the key mechanistic paradigms - such as enamine, iminium, and NHC catalysis - and illustrating how structural modifications of the catalyst scaffold govern reactivity and stereoselectivity in asymmetric transformations.*

Covalent organocatalysis is generally divided into two main classes: aminocatalysis and N-heterocyclic carbene (NHC) catalysis, depending on the nature of the covalent intermediate formed with the substrate.

Asymmetric Aminocatalysis

The first report of an organocatalytic asymmetric activation came from Hajos, Parrish and coworkers, who pioneered the use of (S)-Proline to activate the triketone **1**, leveraging the formation of an enamine intermediate, which undergoes an asymmetric intramolecular aldol reaction, delivering bicycle **2** with 93% ee (Scheme 1).[19]

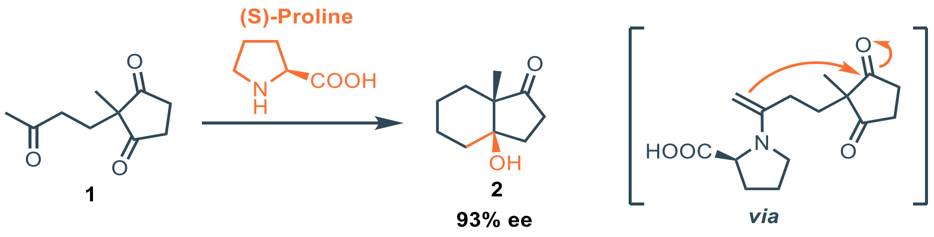

Scheme 1. First report of activation of a carbonyl compound *via* enamine

Although impactful, this distinctive activation mode of (S)-proline, and, more broadly, of secondary chiral amines, was not initially recognized as a novel catalytic paradigm until the early 2000s, even though other reports exploited the potential of chiral amines to perform enantioselective reactions

---

[19] Z. G. Hajos, D. R. Parrish, *J. Org. Chem.* **1974**, *39*, 1615–1621.

leveraging enamine activation.[20,21] At that time, pioneering studies by List and co-workers, as well as MacMillan and co-workers, independently demonstrated the catalytic activation of carbonyl compounds *via* enamine and iminium ion intermediates, respectively, using chiral secondary amines. List's work employed enantiopure (S)-proline to catalyze the enantioselective intermolecular aldol reaction between acetone **3** and substituted benzaldehydes **4** (Scheme 2a, left).[22] In this approach, the formation of an enamine raises the HOMO energy level of the enol form of acetone, enhancing its nucleophilicity and facilitating more effective overlap with the LUMO of the electrophile, delivering the aldol adduct **5** with good ee. This strategy is now widely referred to as HOMO-raising, which underpins enamine-based organocatalysis (Scheme 2a, right).

Conversely, MacMillan's approach involved the use of a chiral imidazolidinone catalyst to promote an enantioselective Diels–Alder reaction through iminium ion activation of the α,β-unsaturated aldehyde **6** (Scheme 2b, left).[23] In this case, formation of the iminium ion lowers the LUMO of the aldehyde, increasing its susceptibility to nucleophilic attack, an approach described as LUMO-lowering, characteristic of iminium-based catalysis (Scheme 2b, right). From a mechanistic perspective, enamine and iminium ion catalysis offer complementary reactivities, being two species always present in both the catalytic cycles. In general, when enamine activation occurs, α-functionalised carbonyl compounds are obtained. On the other hand, iminium-ion activation provides reactivity on β position of α,β-unsaturated carbonyl compounds. Thus, the use of bifunctional reagents with both a nucleophilic and electrophilic moiety can lead to tandem iminium-ion/enamine reactivity, as demonstrated for the enantioselective epoxidation and aziridination of α,β-unsaturated carbonyl compounds,[24,25] and for multicomponent reactions (MCRs) such as the Ender's cascade.[26]

---

[20] S. Danishefsky, P. Cain, *J. Am. Chem. Soc.* **1976**, *98*, 4975–4983.

[21] R. B. Woodward, E. Logusch, K. P. Nambiar, K. Sakan, D. E. Ward, B. W. Au-Yeung, P. Balaram, L. J. Browne, P. J. Card, C. H. Chen, *J. Am. Chem. Soc.* **1981**, *103*, 3210–3213.

[22] B. List, R. A. Lerner, C. F. Barbas, *J. am. chem. soc.* **2000**, *122*, 2395–2396.

[23] K. A. Ahrendt, C. J. Borths, D. W. C. MacMillan, *J. Am. Chem. Soc.* **2000**, *122*, 4243–4244.

[24] F. Pesciaioli, F. De Vincentiis, P. Galzerano, G. Bencivenni, G. Bartoli, A. Mazzanti, P. Melchiorre, *Angew. Chem. Int. Ed.* **2008**, *47*, 8703–8706.

[25] S. Lee, D. W. C. MacMillan, *Tetrahedron* **2006**, *62*, 11413–11424.

[26] D. Enders, M. R. M. Hüttl, C. Grondal, G. Raabe, *Nature* **2006**, *441*, 861–863.

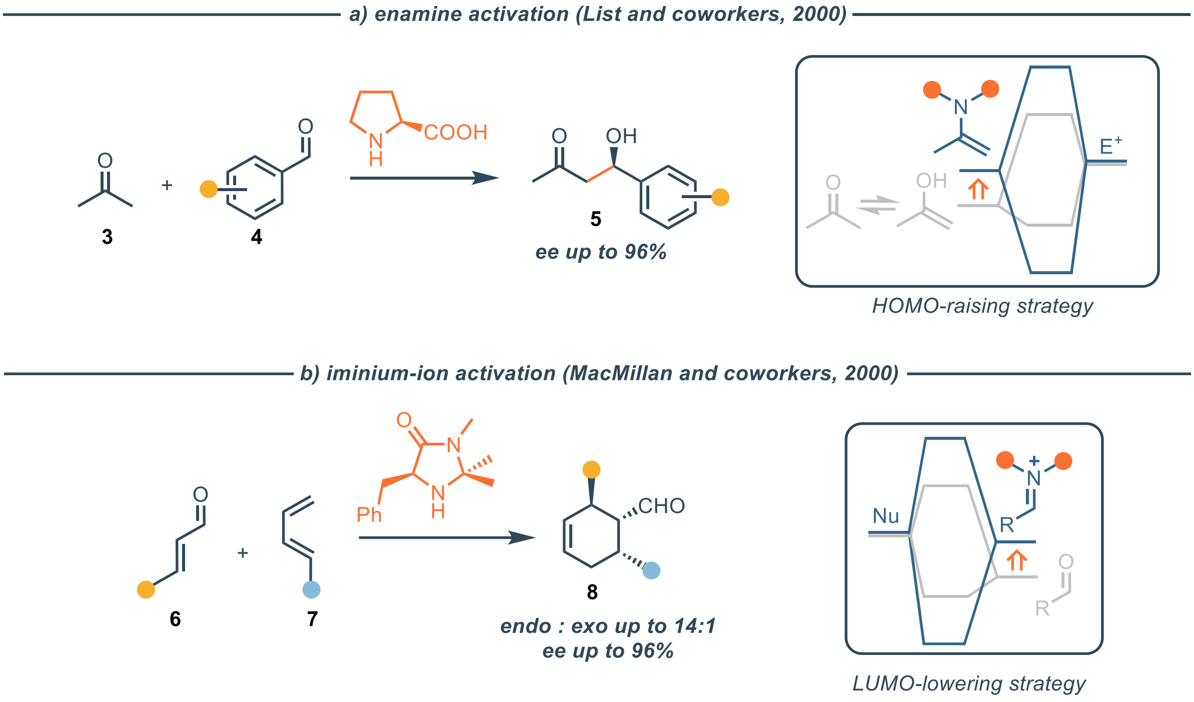

Scheme 2. a) Enamine activation of acetone to deliver the aldol adduct **5** b) Iminium-ion activation of compound 6 to deliver the Diels-Alder adduct **8**

After the two seminal works by List et. al. and MacMillan et. al., a plethora of different organocatalytic methodologies have been developed, giving rise to a real “Gold Rush”,[27] with the aim to fully explore the power of this new catalytic approach. For this purpose, several different catalysts have been developed. Notably, precise structural tailoring of these catalysts has led to distinct paradigms of stereocontrol. For instance, proline is known to induce enantioselectivity through a fine balanced combination of rigidity - provided by the pyrrolidine ring - and noncovalent interactions, mediated by the carboxylic acid moiety. The latter plays a crucial rose in stabilizing both the electrophile and the transition state via hydrogen bonding interactions.[28,29] The Zimmerman-Traxler model,[30] in which the enamine and the electrophile are in a six-membered chair-like arrangement minimizing 1,3-diaxial interactions and with a favorable orbital overlap, justifies the observed enantioselectivity (Figure 3a). On the other hand, imidazolidinone-based catalysts generally exert enantioinduction through face-selective shielding provided by the bulky substituent on the imidazolidinone framework, thus preventing the nucleophile/electrophile attack on one of the two faces of the iminium ion/enamine (Figure 3b).[31] A similar mechanism occurs when diarylprolinol silyl ethers are

---

[27] P. Melchiorre, M. Marigo, A. Carlone, G. Bartoli, *Angew. Chem. Int. Ed.* **2008**, *47*, 6138–6171

[28] S. Bahmanyar, K. N. Houk, H. J. Martin, B. List, *J. Am. Chem. Soc.* **2003**, *125*, 2475–2479.

[29] S. Bahmanyar, K. N. Houk, *J. Am. Chem. Soc.* **2001**, *123*, 12911–12912.

[30] H. E. Zimmerman, M. D. Traxler, *J. Am. Chem. Soc.* **1957**, *79*, 1920–1923.

[31] C. Allemann, R. Gordillo, F. R. Clemente, P. H. Y. Cheong, K. N. Houk, *Acc. Chem. Res.* **2004**, *37*, 558–569.

used as organocatalyst. This class of catalysts retains the pyrrolidine core but features a quaternary carbon equipped with two aromatic moieties and a silyl protected hydroxyl moiety.[32] The two aryl substituent finely tune steric and electronic properties of the catalyst, while the silyl PG is used to prevent the formation of hemiaminal species (Figure 3c).[33] Moreover, the steric profile and hydrophobicity of the silyl group significantly influence the solubility of the catalyst and its conformational behavior, ultimately affecting both reactivity and enantioselectivity. The selection of an appropriate silyl group - be it trimethyl silyl (TMS), tert-butyldimethylsilyl (TBDMS), or triisopropylsilyl (TIPS) - thus represents a strategic design element for optimizing catalyst performance across various transformations.[34,35] Notably, aminocatalysis has been synergistically merged with noncovalent catalysis employing bifunctional catalysts that can act with a hybrid mechanism, thus activating two or more reactive species at the same time (see Noncovalent Organocatalysis for a more detailed discussion).

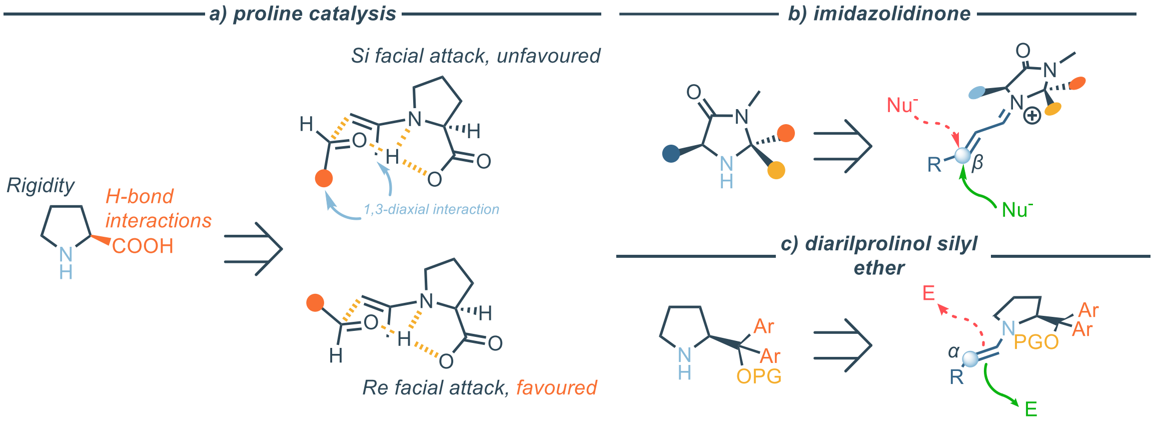

Figure 3. Typical stereocontrol modes in asymmetric aminocatalysis. a) Proline-based catalysis and a representative Zimmerman–Traxler transition state for the asymmetric aldol reaction [34]; b) General structure and stereocontrol mode of imidazolidinone catalysts; c) General structure and stereocontrol mode of diarylprolinol silyl ether catalysts

Asymmetric NHC catalysis

A complementary activation mode in covalent asymmetric organocatalysis regards the use of N-Heterocyclic Carbenes (NHCs). The core mechanism of this approach involves the generation *in situ*

---

[32] K. L. Jensen, G. Dickmeiss, H. Jiang, L. Albrecht, K. A. Jørgensen, *Acc. Chem. Res.* **2012**, *45*, 248–264.

[33] J. Franzén, M. Marigo, D. Fielenbach, T. C. Wabnitz, A. Kjærsgaard, K. A. Jørgensen, *J. Am. Chem. Soc.* **2005**, *127*, 18296–18304.

[34] Y. Hayashi, D. Okamura, T. Yamazaki, Y. Ameda, H. Gotoh, S. Tsuzuki, T. Uchimaru, D. Seebach, *Chem. Eur. J.* **2014**, *20*, 17077–17088

[35] M. H. Haindl, M. B. Schmid, K. Zeitler, R. M. Gschwind, *RSC Adv* **2012**, *2*, 5941–5943

of a nucleophilic carbene species, which can react with carbonyl compounds generating a key intermediate, generally referred to as Breslow intermediate, which serves as an acyl anion equivalent, providing effective umpolung of the carbonyl system, enabling unique reactivity mode (e.g. reaction with electrophiles).[36] The carbene is generated through deprotonation of an azolium salt, typically imidazolium or triazolium derivatives.[37] The earliest example of umpolung reactivity resembling modern NHC catalysis dates back to 1832, when Wöhler and Liebig reported the cyanide-catalyzed benzoin condensation of benzaldehyde.[38] In 1943, Ugai and co-workers discovered that the same transformation could be catalyzed by thiazole-based compounds such as thiamine (vitamin B_1), providing the first indication of carbene-like catalysis by heterocyclic systems.[39] This mechanistic insight was clarified in 1958 by Breslow and co-workers, who proposed that thiamine catalysis proceeds via formation of a reactive carbene intermediate, which subsequently generates the nucleophilic Breslow intermediate, a key species enabling the reversal of carbonyl polarity (Scheme 3).[40]

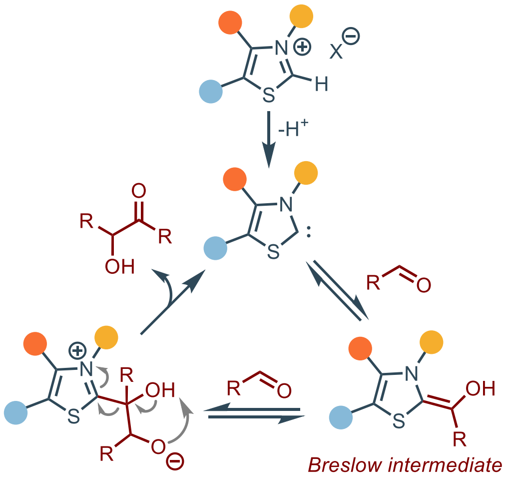

Scheme 3. NHC catalysis for benzoin condensation as proposed by Breslow et. al.

The origin of enantioselectivity in chiral N-heterocyclic carbene catalysis arises from the ability of the chiral environment surrounding the carbene center to differentiate between the two enantiotopic faces of the reacting intermediates or substrates during key bond-forming steps. This is primarily achieved through steric and, in some cases, secondary noncovalent interactions imparted by the chiral

---

[36] S. Chakraborty, S. Barik, A. T. Biju, *Chem. Soc. Rev.* **2024**, *54*, 1102–1124.

[37] D. Enders, O. Niemeier, A. Henseler, *Chem. Rev.* **2007**, *107*, 5606–5655.

[38] F. Wöhler, J. Liebig, *J. Ann. Pharm.* **1832**, *3*, 249–282.

[39] T. Ukai, R. Tanaka, T. Dokawa, *J. Pharm. Soc. Jpn.* **1943**, *63*.

[40] R. Breslow, *J. Am. Chem. Soc.*, **1958**, *80,* 3719–3726

substituents on the NHC framework. Seminal examples of asymmetric NHC catalysis involve the asymmetric benzoin condensation proposed by Enders et. al., using a triazolium-based carbene precursor (Scheme 4a),[41] and the intramolecular Stetter reaction, proposed by Rovis et. al., who employed a tetracyclic triazolium catalyst (Scheme 4b).[42] Notably, rigid chiral scaffolds, such as those based on bicyclic or cyclic backbones, tend to perform better than more flexible ones, as they more effectively enforce well-defined transition state geometries.[43] This rigidity ensures consistent delivery of the nucleophile/electrophile from the preferred face across a range of substrates. Moreover, bulky N-substituents (e.g., 2,6-diisopropylphenyl or mesityl groups) not only enhance carbene stability by suppressing dimerization, but also create chiral pockets that facilitate diastereofacial discrimination in enantioselective reactions.[44]

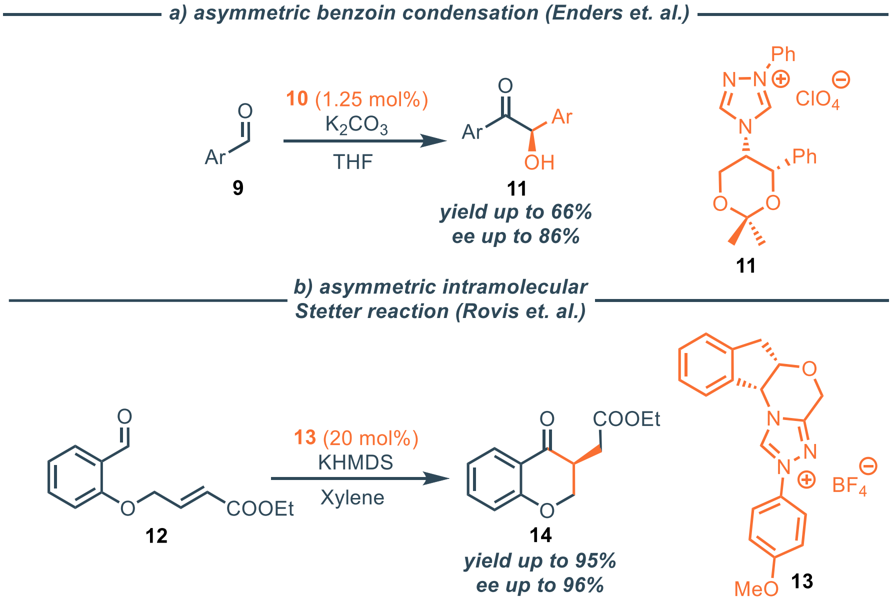

Scheme 4. Relevant examples of asymmetric NHC catalysis. a) Asymmetric benzoin condensation; b) Asymmetric intramolecular Stetter reaction

---

[41] D. Enders, K. Breuer, J. H. Teles, *Helv Chim Acta* **1996**, *79*, 1217–1221

[42] M. S. Kerr, J. R. De Alaniz, T. Rovis, *J. Am. Chem. Soc.* **2002**, *124*, 10298–10299

[43] Q. Liu, S. Perreault, T. Rovis, *J. Am. Chem. Soc.* **2008**, *130*, 14066–14067

[44] M. N. Hopkinson, C. Richter, M. Schedler, F. Glorius, *Nature* **2014**, *510*, 485–496

Noncovalent Organocatalysis

Section outline *- This section outlines noncovalent organocatalysis, covering key activation modes (hydrogen bonding, ion pairing, σ-hole interactions, and anion-binding catalysis) and their roles in neutral and ionic pathways. It summarizes major catalyst classes, from chiral Brønsted acids and bases to phase-transfer and hydrogen-bond donor systems, and notes how structural features influence reactivity, selectivity, and potential for cooperative activation.*

While enzymes sometimes employ covalent activation to catalyse transformations,[45] they more commonly rely on noncovalent interactions, such as hydrogen bonding, ion pairing, and π-stacking, to activate substrates and stabilize transition states.[46] Thus, taking inspiration from nature, synthetic chemists exploited this concept developing small molecules that act as catalyst without forming transient covalent intermediates, but rather relying on reversible and directional interactions, enabling precise molecular recognition and activation of substrates. As per the covalent organocatalysis, several and different activation modes are possible, each relying on specific noncovalent interactions tailored to achieve selective substrate activation. Before introducing a classification of noncovalent organocatalysts, it is important to acknowledge that the distinction between "ionic" and "neutral" activation modes is not strictly binary. Many catalytic systems rely on overlapping types of interactions or may shift between ion-paired and neutral pathways depending on the substrate, environment, or reaction mechanism.[47,48] Broadly speaking, noncovalent organocatalysts can be grouped according to the predominant noncovalent interactions they exploit. Catalysts that operate through ionic interactions include chiral Brønsted acids and bases and phase-transfer catalysts (PTCs), which stabilize or deliver charged species *via* ion pairing and electrostatic attraction.[49,50] In contrast, hydrogen bonding, halogen bonding, and chalcogen bonding are commonly harnessed in systems that proceed via neutral transition states, where directionality and reversibility of the interaction enable fine control over activation and selectivity.[51,52] In addition to

---

[45] J. Wagner, R. A. Lerner, C. F. Barbas, *Science,* **1995**, *270*, 1797–1800

[46] R. R. Knowles, E. N. Jacobsen, *Proc. Natl. Acad. Sci. USA* **2010**, *107*, 20678–20685

[47] A. M. F. Phillips, M. H. G. Prechtl, A. J. L. Pombeiro, *Catalysts* **2021**, *11*, 569

[48] C. C. J. Loh, *Nat. Rev. Chem.* **2021**, *5*, 792–815

[49] D. C. M. Albanese, M. Penso, *European J. Org. Chem.* **2023**, *26*, e202300224

[50] T. Akiyama, J. Itoh, K Fuchibe, *Adv. Synth. Catal.* **2006**, *348*, 999 – 1010

[51] S. J. Connon, *Chem. Eur. J.* **2006**, *12*, 5418–5427

[52] R. L. Sutar, S. M. Huber, *ACS Catal.* **2019**, *9*, 9622–9639

these broad classes, more focused strategies such as anion-binding catalysis [53] and cation-binding catalysis have emerged.[54] These approaches exploit tailored noncovalent interactions, typically hydrogen bonding or σ-hole interactions (e.g., halogen or chalcogen bonding for anions,[55] crown ethers or polyether motifs for cations)[56], to engage and modulate the reactivity of charged species. These systems often lie at the interface between ionic and neutral catalysis, highlighting the spectrum of noncovalent strategies beyond a simple ionic vs neutral dichotomy.

Chiral Brønsted Acids and Bases

Despite the long-standing familiarity with acid/base principles in organic chemistry, the ability to induce enantioselectivity through chiral Brønsted acids and bases has only been systematically explored since the early 2000s. These catalysts operate through mechanistic strategies that, in many respects, resembles those seen in covalent organocatalysis. For instance, chiral Brønsted acids can increase the electrophilicity of a substrate by protonating a Lewis basic site, effectively stabilizing the LUMO and facilitating nucleophilic addition (Figure 4a). Similarly, chiral bases enhance the reactivity of nucleophilic partners by abstracting a proton, thereby elevating the HOMO and enabling attack on an electrophile (Figure 4b).[57]

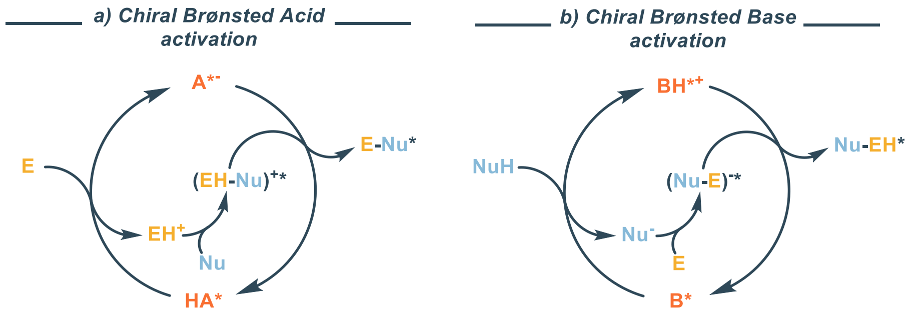

Figure 4. Activation mechanism of chiral Brønsted acids (a) and chiral Brønsted bases (b)

A particularly versatile approach is offered by bifunctional catalysts, which integrate both acidic and basic domains within a single chiral framework. These systems can engage two reaction partners simultaneously, stabilizing the transition state through cooperative, noncovalent interactions.[58]

---

[53] Z. Zhang, P. R. Schreiner, *Chem. Soc. Rev.*, **2009**,*38,* 1187-1198

[54] A. P. Jadhav, S. Y. Park, J. W. Lee, H. Yan, C. E. Song, *Acc. Chem. Res.* **2021**, *54*, 4319–4333

[55] S. Benz, A. I. Poblador-Bahamonde, N. Low-Ders, S. Matile, *Angew. Chem. Int. Ed.* **2018**, *130*, 5506–5510

[56] J. G. Jeong, Y. H. Oh, T. H. Park, S. S. Lee, D. W. Kim, S. Lee, *Nat. Commun.* **2025**, 16:1236

[57] J. Clayden, N. Greeves, S. Warren, *Organic Chemistry, 2nd edition*, Oxford University Press, Oxford, **2012.**

[58] C. S. Cucinotta, M. Kosa, P. Melchiorre, A. Cavalli, F. L. Gervasio, *Chem. Eur. J.*, **2009**, *15*, 7913 – 7921

The most extensively used scaffolds in chiral Brønsted acid catalysis are C_2-symmetric frameworks derived from 1,1'-Bi-2-naphthol (BINOL).[59] The early generations of these catalysts, mainly phosphoric acids, offered a balance between moderate acidity and configurational control. In addition to BINOL derivatives, 3,3′-diphenyl-2,2′-bi-1-naphthalol (VANOL), 2,2′-Diphenyl-(4-biphenanthrol) (VAPOL), 2,2',3,3'-tetrahydro-1,1'-spirobi[indene]-7,7'-diol (SPINOL) and (2,2-Dimethyl-1,3-dioxolane-4,5-diyl)bis(diphenylmethanol) (TADDOL) diols have been effectively phosphorylated, to deliver the corresponding phosphoric acids.[60] Different substitution patterns in position 3 and 3' allows for diverse structural modification, thereby modulating the steric hinderance and the enantioinducion. Notably, chiral phosphoric acids (CPAs) can be considered as bifunctional catalysts, since they feature both Brønsted acid and basic sites, possibly doing multiple interactions with both the reagents in the catalytic system. The general structure of the most common CPAs is reported in Figure 5.

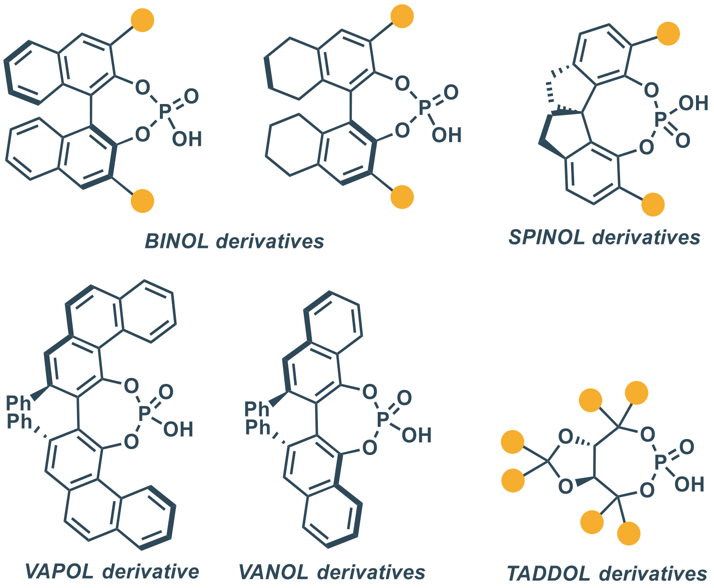

Figure 5. The different classes of CPAs

Seminal reports regarding the use of Chiral Brønsted acids for enantioselective catalysis date back to 2004, when the group of Akiyama demonstrated that BINOL-derived phosphoric acids could effectively promote enantioselective Mannich-type reactions. Akiyama's approach involved the addition of ketene silyl acetals to aldimines (Figure 5a), where the use of a phosphoric acid bearing para-nitrophenyl groups at the 3,3'-positions was key to achieving high levels of enantiocontrol, attributed not only to the increased acidity but also to favorable spatial interactions within the ion

---

[59] J. M. Brunel, *Chem. Rev.*, **2005**, 105, 857–897

[60] E. Cocco, A. Antenucci, A. Carlone, P, Manini, F. Pesciaioli, S. Dughera *ChemCatChem*, **2024**, e202400328

pair.[61] In parallel, Terada and colleagues focused on the reaction between N-Boc imines and acetylacetone, finding that sterically demanding 3,3'-substituents, such as β-naphthyl groups, were essential for inducing high enantioselectivity.[62] Despite targeting different nucleophiles, both studies converged on the insight that fine-tuning the substitution pattern of the CPA scaffold allows for modulation of both reactivity and selectivity, likely due to a combination of steric interactions and secondary noncovalent contact with the substrates. These findings laid the groundwork for the widespread adoption and further evolution of CPAs in asymmetric synthesis.

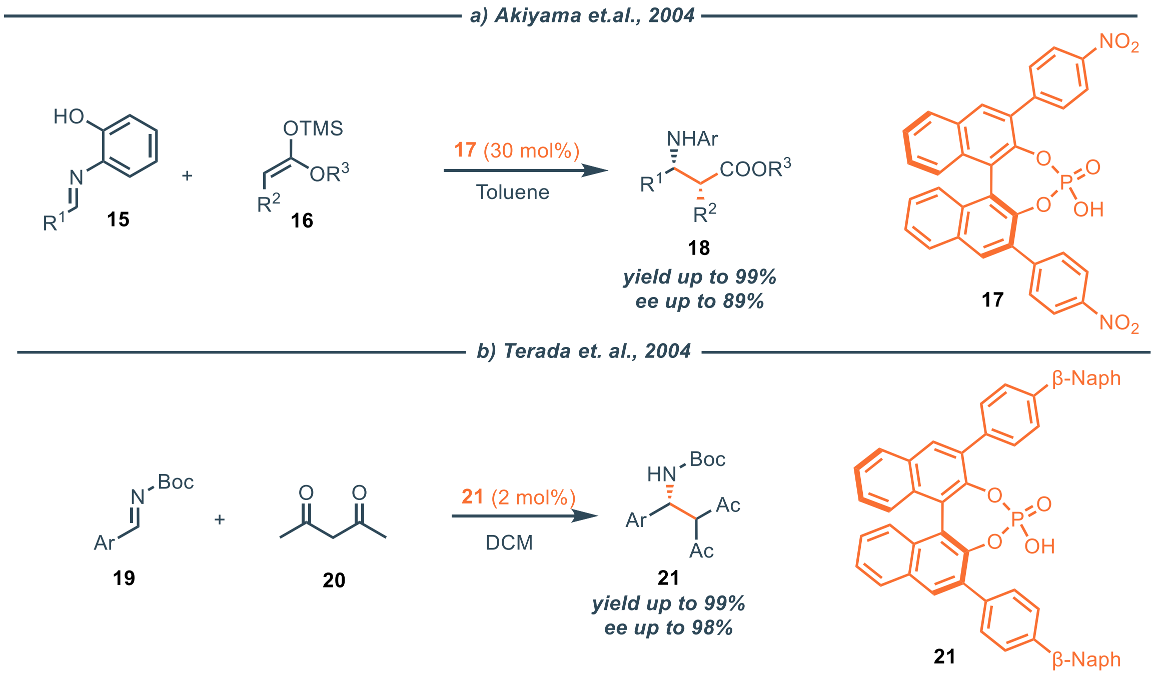

Scheme 5. Chiral Brønsted acid-catalysed Mannich reaction proposed by Akiyama (a) and Terada (b)

In recent years, enhanced acidity and broader reactivity profiles have been achieved through the development of structurally related derivatives such as disulfonimides (DSIs)[63], imidodiphosphates (IDPs)[64], iminoimidodiphosphates (iIDPs)[65] and imidodiphosphorimidates (IDPis)[66], which have opened new possibilities in Brønsted acids catalysis. While CPAs typically have pKa values between 12 and 14 (in MeCN), these newer catalyst families demonstrate markedly increased acidity pKa ≈ 10–11 for IDPs, 9 for iIDPs, 8–9 for DSIs, and as low as 2–4.5 for IDPis (measured in MeCN).[66] This increased acidity, together with the ability to act as Lewis acids and their increased steric

---

[61] T. Akiyama, J. Itoh, K. Yokota, K. Fuchibe, *Angew. Chem. Int. Ed.*, **2004**, *43*, 1566-1568

[62] D. Uraguchi, M. Terada, *J. Am. Chem. Soc.*, **2004**, *126*, 1356-5357

[63] P. Garcìa-Garcìa, F. Lay, P. Garcìa-Garcìa, C. Rabalakos, B. List, *Angew. Chem. Int. Ed.*, **2009**, *48*, 4363-4366

[64] I. Ĉorić, B. List, *Nature*, **2012**, *483*, 315-319

[65] L. Liu, P. S. J. Kaib, A. Tap, B. List, *J. Am. Chem. Soc.*, **2016**, *138*, 10822-10825

[66] L. Schreyer, R. Properzi, B. List, *Angew. Chem. Int. Ed.*, **2019**, *58*, 12761-12777

encumbrance, make them general catalysts to activate a broad scope of substrate with excellent levels of enantiocontrol.[67,68] The general structure of DSIs, IDPs, iIDPs and IDPis is reported in Figure 6.

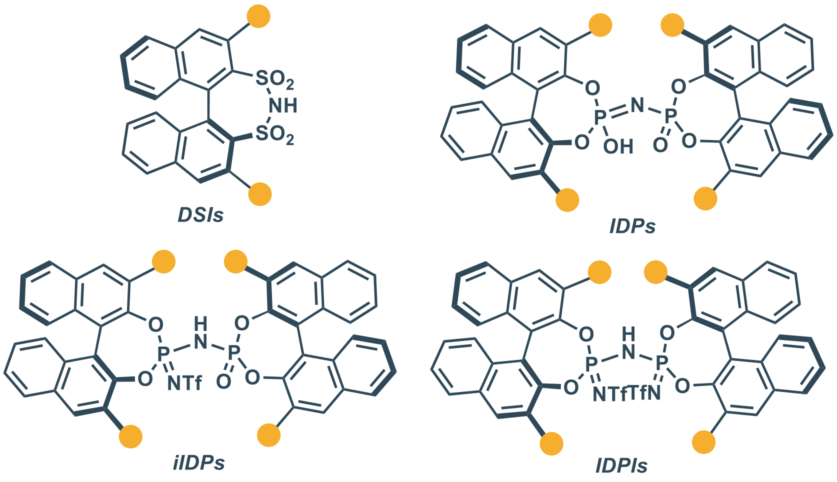

Figure 6. DSIs, IDPs, iIDPs and IDPIs general structures

From a mechanistic perspective, enantioselectivity in these systems arises from the generation of a chiral ion pair, in which a stereochemically defined counteranion, derived from the chiral Brønsted acid, is responsible for the enantioselective approach of the nucleophile on the activated electrophile, via generation of a chiral ionic pair and influencing the geometry of the reactive complex. This concept is central to what Benjamin List formally described in 2006 as Asymmetric Counteranion-Directed Catalysis (ACDC)[69], a term that includes catalytic processes where stereocontrol arises from the spatial arrangement induced by a chiral counteranion on a reactive, achiral or prochiral cation. While traditional enantioselective Brønsted acid catalysis is a straightforward illustration of this paradigma,[70] more intricate examples highlight the versatility of this principle.

Among these are catalytic salts in which an ammonium specie acts as the cationic catalytic unit, often engaging in iminium ion chemistry, while the associated chiral counterion dictates the stereochemical course of the transformation.[71] Such systems merge features of covalent organocatalysis with noncovalent asymmetric control, enabling precise induction of chirality across a broad spectrum of reactions. For example, salts formed between achiral secondary amines and chiral phosphoric acids were shown to catalyze the asymmetric transfer hydrogenation of enals via iminium ion activation,

---

[67] L. Alama, N. Frank, L. Brucher, J. Nienhaus, B. List, *ACS Catal.*, **2025**, *15*, 8297-8302

[68] N. Frank, M. Leutzsch, B. List, *J. Am. Chem. Soc.*, **2025**, *147*, 7932-7938

[69] M.Malahu, B.List, *Angew. Chem. Int. Ed.*, **2013**, *52*, 518-533

[70] M. Rueping, E. Sugiono, C. Azap, T. Theissmann, M. Bolte, *Org. Lett.*, **2005**, *7*, 3781-3783

[71] M.Malahu, B.List, *Isr. J. Chem.*, **2012**, *52*, 630-638

with the phosphate anion dictating the stereoselectivity of the hydride delivery (Scheme 6a).[72] A similar approach was used for the enantioselective hydrogenation of enones. In this case, the amine component is the tert-butyl ester of valine, which is itself chiral. Notably, experimental evidence revealed a pronounced match/mismatch effect between the stereochemistry of the amine and that of the chiral phosphate counterion, significantly influencing the enantioselectivity of the transformation (Scheme 6b).[73] The development of new strategies in ACDC catalysis mediated by iminium ion activation is the focus of one of the chapters of this thesis (*Chapter 2 and 3*).

a) asymmetric hydrogenation of enals via ACDC

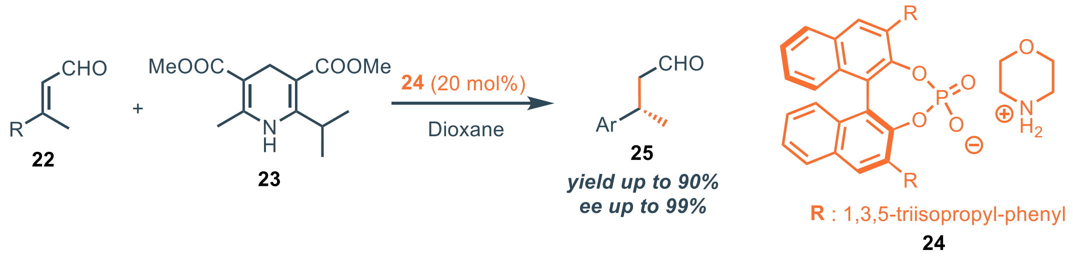

b) asymmetric hydrogenation of enones via ACDC

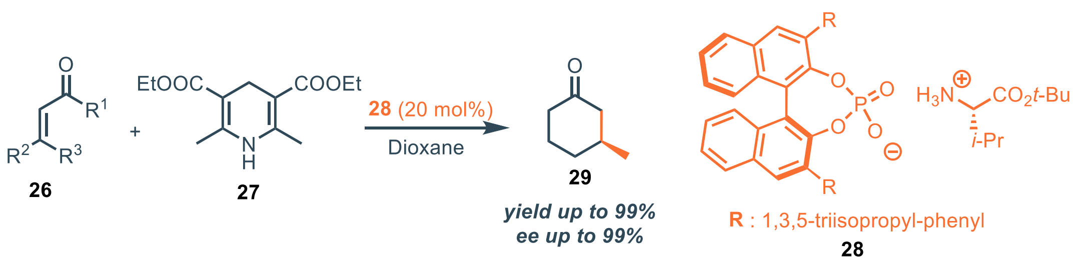

Scheme 6. Notable examples of ACDC catalysis for the asymmetric transfer hydrogenation of enals (a) and enones (b)

The ACDC strategy has also been successfully extended to transition metal (TM) catalysis. Traditionally, in metal-catalyzed processes, the counterion is often viewed as an inert or non-influential component. However, it has been convincingly demonstrated that chiral counteranions can impart significant enantioselectivity, even without forming covalent bonds to the substrate. Instead, they exert their influence through the formation of tight ion pairs with cationic metal intermediates, subtly guiding the spatial approach of the reacting species.[74] Importantly, the steric and electronic features of the chiral counteranion can be finely tuned to optimize both reactivity and enantioselectivity. A seminal example of this concept was reported by the Toste group, who showed that a cationic Au(I) complex, in combination with a chiral BINOL-derived phosphate anion,

---

[72] S. Mayer, B. List, *Angew. Chem. Int. Ed.*, **2006**, *45*, 4193-4195

[73] N. J. A. Martin, B. List, *J. Am. Chem. Soc.*, **2006**, *128*, 13368-13369

[74] S. Mukherjee, B. List, *J. Am. Chem. Soc.*, **2007**, *129*, 11336-11337

effectively catalyzed the enantioselective cyclization of allenols, achieving high levels of stereocontrol (Scheme 7).[75]

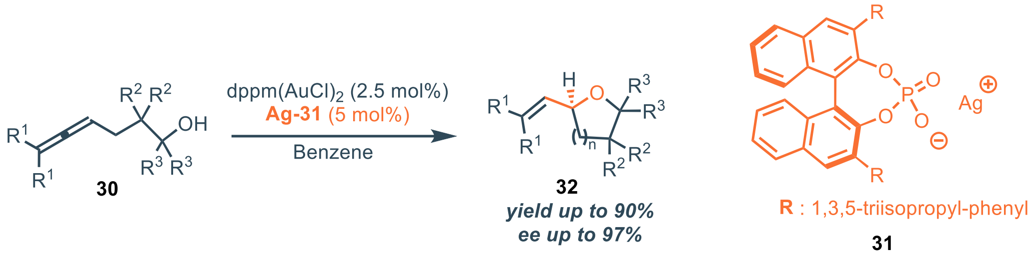

Scheme 7. Enantioselective Au(I)-catalysed cyclization of allenoles using an ACDC approach

Anion-binding catalysis also falls under the ACDC umbrella. Here, an anionic functional group of the substrate interacts through directional, noncovalent forces - such as hydrogen bonding or more recently, halogen and chalcogen bonding - with a chiral framework, via the formation of a defined supramolecular complex. This noncovalent association organizes the reactive ion pair in a defined chiral environment, thereby inducing enantioselectivity without requiring covalent modification of the catalyst or direct proton transfer.[76] Although the catalyst does not generate the ion pair through protonation, the stereochemical outcome is governed by the spatial arrangement imposed on the anion, which is tightly bound within the chiral framework (Figure 7).[69] A detailed discussion on anion binding catalysis will be provided in the next section.

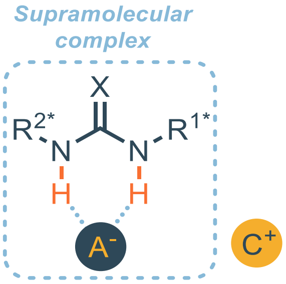

Figure 7. The supramolecular complex formed between the anion and the chiral receptor can be considered as the chiral counteranion of the cationic counterpart (ACDC). A hydrogen bonding donor is displayed for clarity.

Chiral Brønsted bases, on the other hand, offer a complementary strategy. In fact, in this case the mechanism of action involves deprotonation of a relatively acidic pro-nucleophile, and the enantioinduction arises from the chiral environment of the base, which governs the facial selectivity of this addition. While the concept of Brønsted bases is classical, the use of chiral bases to impart

---

[75] G. L. Hamilton, E. J. Kang, M. Mba, F. D. Toste, *Science*, **2007**, *317*, 496-499

[76] L-M. Entgelmeier, O-G. Mancheno, *Synthesis*, **2022**, *54*, 3907-3927

stereochemical information emerged significantly in the early 2000s, providing access to numerous highly enantioselective C–C and C–X bond-forming reactions. One of the earliest and most influential examples of asymmetric Brønsted base catalysis was reported by Corey and coworkers,[77] building upon the foundational studies of Chinchilla[78] and Lipton.[79] In this work, a chiral C_2-symmetric guanidine catalyst was developed and successfully applied to the asymmetric Strecker reaction, achieving excellent enantioselectivities. (Scheme 8). The catalytic cycle proceeds via deprotonation of hydrogen cyanide (HCN) by the chiral guanidine base, generating the nucleophilic cyanide anion. This cyanide species then attacks the electrophilic imine, which is simultaneously activated through hydrogen bonding with the conjugate acid of the guanidine catalyst. This dual activation mechanism ensures effective enantioinduction by precisely orienting the imine and directing the nucleophilic addition.

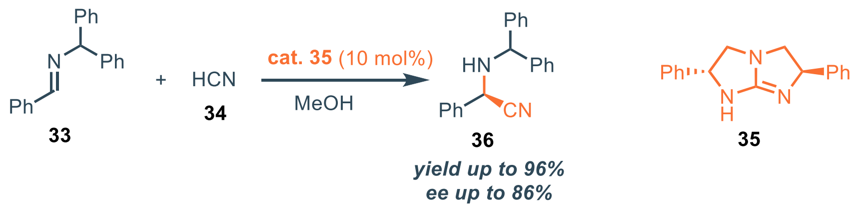

Scheme 8. Chiral guanidine-catalysed asymmetric Strecker reaction

Initially, monofunctional chiral bases such as guanidines and amidines played a central role, directly engaging the pro-nucleophile without additional interaction with the electrophile. These catalysts are often efficient when dealing with highly reactive electrophiles but may struggle to deliver high selectivity when both reacting partners require spatial orientation.[80] As understanding of catalytic stereocontrol advanced, attention shifted towards bifunctional Brønsted base catalysts, which integrate a basic site (e.g., guanidine, amine) with a complementary hydrogen-bond donor motif (e.g., thiourea, squaramide). This architectural evolution allows for dual activation of the reaction partners, deprotonating the nucleophile while simultaneously stabilizing the electrophile, thus promoting reactivity and selectivity in a cooperative fashion.[81]

---

[77] E. J. Corey, M. J. Grogan, *Org. Lett.*, **1999**, *1*, 157-160

[78] R. Chinchilla, C. Najera, P. Sanchez-Agullo, *Tetr. Asymm.*, **1994**, *5*, 1393-1402

[79] M. S. Iyer, K. M. Gigstad, N. D. Namdev, M. Lipton, *J. Am. Chem. Soc.*, **1996**, *118*, 4910-4911

[80] M. Freund, S. Schenker, A. Zamfir, S. B. Tsogoeva, *Curr. Org. Chem.*, **2011**, *15*, 2282-2310

[81] A. Sinibaldi, V. Nori, A. Baschieri, F. Fini, A. Arcadi, A. Carlone, *Catalyst*, **2019**, *9*, 928

A particularly notable class of bifunctional Brønsted base catalysts is based on cinchona alkaloid derivatives.[82] These natural-product-inspired frameworks combine a quinuclidine nitrogen, capable of deprotonating nucleophiles, with a proximal hydroxyl group that engages electrophiles through hydrogen bonding. Furthermore, the steric and electronic environment of the catalyst can be finely tuned via substitution on the quinuclidine scaffold.[83] (Figure 8, left) This built-in bifunctionality has enabled their successful application in a variety of asymmetric reactions, including Michael additions and Mannich-type processes. Beyond their role in Brønsted base catalysis, cinchona alkaloids have also been widely applied in asymmetric phase-transfer catalysis (PTC), a topic explored in the next section. Other notable examples of bifunctional catalysts include Takemoto-type catalysts,[84] which incorporate thiourea or squaramide units adjacent to 1,2-cyclohexyldiamine moiety. This has been exploited in asymmetric Michael additions of nitroalkanes to α,β-unsaturated ketones, where the thiourea unit coordinates the electrophile while the base deprotonates the nucleophile, bringing both reactants into proximity in a chiral environment (Figure 8, right).[85]

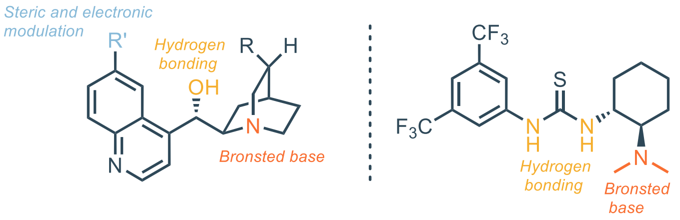

Figure 8. Structural features of bifunctional organocatalysts. left: Chinconine as representative example of Chincona-related catalysts; right: Takemoto's catalyst

Importantly, the synergy between the basic site and the hydrogen-bonding donor is not merely additive but results in a highly cooperative catalytic system.[85]

Catalyst design in Brønsted base catalysis focuses on achieving a fine balance between basicity, structural rigidity, and complementary noncovalent interactions. Basicity is essential to enable the deprotonation of relatively inert pronucleophiles. For instance, chiral ureate-based superbases, reported more recently, can activate challenging substrates such as α-thioacetamides. These catalysts exploit an N,N′-dialkylurea scaffold, deprotonated to the corresponding ureate, which displays strong basicity and can deliver both high reactivity and excellent enantioselectivity.[86]

---

[82] T. Marcelli, H. Hiemstra, *Synthesis*, **2010**, *8*, 1229-1279

[83] K. Kacprzak, J. Gawronski, *Synthesis*, **2001**, *7*, 961-98

[84] T. Okino, Y. Hoashi, Y. Takemoto, *J. Am. Chem. Soc.*, **2003**, *125*, 12672-12673

[85] R. Miyaji, Y. Wada, A. Matsumoto, K. Asane, S. Matsubara, *Beilstein J. Org. Chem.* **2017,** *13,* 1518–1523

[86] A. Kondoh, S. Ishikawa, M. Terada, *J. Am. Chem. Soc.*, **2020**, *142*, 3724–3728

Phase Transfer Catalysts

Phase-transfer catalysis (PTC) is a powerful strategy for promoting reactions between reagents located in immiscible phases, typically an aqueous and an organic layer. The catalyst, often a quaternary ammonium or phosphonium salt, acts as a shuttle, transporting ionic species (usually anions) from the aqueous phase into the organic phase where the reaction occurs.[87] Since water is used as cosolvent, PTC is generally addressed as a green alternative to most common catalytic methods, resulting in its widespread use in large scale synthesis and industry.[88,89] In asymmetric PTC, a chiral cation is used to create a chiral environment around the transferred anion, enabling enantioselective transformations.[90] The most typical mechanistic pathway involves generation of an ion pair between the chiral cation and the nucleophilic anion, usually generated through deprotonation from a base at the organic/aqueous interface. The chiral environment of the ion pair governs the facial selectivity of the attack on an electrophile, resulting in enantioinduction. The strength and geometry of this ion pair, as well as the ability to maintain it in the organic phase, are crucial to achieving high enantioselectivity. After the reaction, the quaternary ammonium salt is regenerated and returns to the interface, ready to participate in another catalytic cycle (Figure 9).[91]

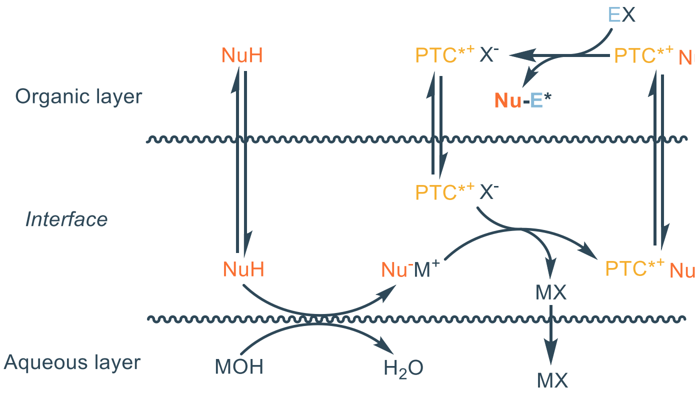

Figure 9. Typical mechanism for asymmetric PTC

Asymmetric phase-transfer catalysis began to gain traction in the 1980s and 1990s, with pivotal contributions from O'Donnell and co-workers, who pioneered the use of cinchona-based quaternary ammonium salts to promote the enantioselective alkylation of glycine Schiff base derivatives for the

---

[87] C. M. Starks, *J. Am. Chem. Soc.*, **1971**, *93*, 195

[88] J. Tan, N. Yasuda, *Org. Proc. Res. Dev.*, **2015**, *19*, 1731-1746

[89] K. Maruoka, *Org. Proc. Res. Dev.*, **2008**, *12*, 679-697

[90] T. Hashimoto, K. Maruoka, *Chem. Rev.*, **2007**, *107*, 5656-5682

[91] T. Ooi, K. Maruoka, *Angew. Chem. Int. Ed.*, **2007**, *46*, 4222-426

enantioselective synthesis of α-amino acids (Scheme 9a).[92] Subsequently, Lygo and colleagues advanced this methodology by introducing structurally refined catalysts that delivered improved levels of enantioselectivity and broader applicability across diverse substrates (Scheme 9b).[93] Although the initial breakthroughs in asymmetric PTC were achieved using cinchona-derived frameworks, the field has since expanded to include a variety of privileged scaffolds. These include binaphthyl-based architectures,[94] pentadinium, (bis)guanidinium,[95] and tartaric acid-derived structures,[96] each offering distinct steric and electronic characteristics for tuning enantioselectivity (Figure 10).[49] Furthermore, the incorporation of hydrogen bond donor motifs, such as ureas and thioureas, has enabled the development of bifunctional PTCs. These designs enhance substrate preorganization and transition state stabilization through secondary interactions, thereby improving both reactivity and selectivity.[97]

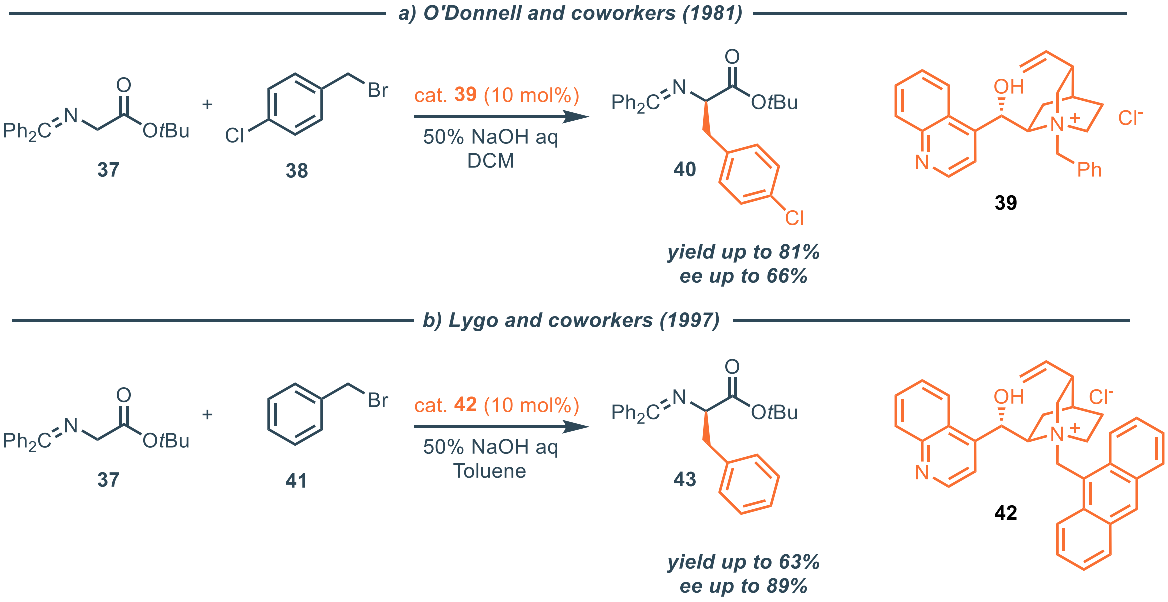

Figure 9. Asymmetric PTC using chincona-based catalysts proposed by O'Donnell (a) and Lygo (b)

---

[92] M. J. O'Donnell, W. D. Bennett, S. Wu, *J. Am. Chem. Soc.*, **1981**, *111*, 2353-2355

[93] B. Lygo, P. G. Wainwright, *Tetrahedron Lett.*, **1997**, *38*, 8595

[94] T. Ooi, M. Kameda, K. Maruoka, *J. Am. Chem. Soc.*, **1999**, *121*, 6519-6520

[95] L. Zomg, C.-H. Tan, *Acc. Chem. Res.*, **2017**, *40*, 842-856

[96] T. Ohshima, T. Shibuguchi, Y. Fukata, M. Shibasaki, *Tetrahedron Lett.*, **2004**, *60*, 7743-7754

[97] H. Wang, *Catalyst*, **2019**, *9*, 244

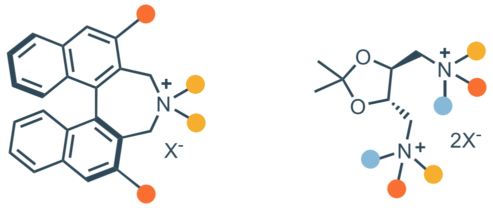

Binaphtyl based PTCs *Tartaric acid based PTCs*

Bisguanidinium based PTCs *Pentadinium based PTCs*

Figure 10. Most common frameworks for asymmetric PTC

Hydrogen bond donor catalysis

Noncovalent catalysis exploits reversible, directional interactions to organize reactants and stabilize transition states without forming covalent bonds with the substrates. Among the most impactful of these interactions in asymmetric catalysis are hydrogen bonding (HB). HB catalysis typically involves (thio)urea or squaramide motifs that interact with electron-rich sites on electrophilic substrate(s) (carbonyl oxygens or nitro groups) and organize the transition state with a LUMO-lowering of the electrophile. This activation mode frequently mimics enzymatic binding pockets, enabling highly selective substrate orientation. Hydrogen bonding interactions are a unifying element across several covalent and noncovalent catalytic approaches. These systems typically incorporate hydrogen bond donor groups within a chiral scaffold to enable simultaneous activation of both nucleophile and electrophile. Most of these catalysts possess rigid backbones (e.g., 1,2-cyclohexanediamines, BINOLs, 1,2-ethylenediamines) that preorganize the hydrogen-bonding units in well-defined spatial arrangements. The acidity of the NH groups, often enhanced by electron-withdrawing substituents, along with steric features introduced by bulky aryl substituents, modulates both reactivity and selectivity. Moreover, multifunctionality of the catalysts allow for achieving dual activations mode and to expand the scope of the possible transformations.

Thioureas are the most privileged scaffolds for HBD catalysis.[51] Their utility has been extensively studied, particularly in the context of supramolecular anion recognition and co-crystal formation.[98,99] Compared to their non-sulfurated analogues (ureas), thioureas feature several advantages, such as

---

[98] M. C. Etter, T. W. Panunto, *J. Am. Chem. Soc.*, **1988**, *110*, 5896-5897

[99] S. Kundu, T. K. Egboluche, A. Hossain, *Acc. Chem. Res.*, **2023**, *56*, 1320-1329

their generally higher solubility, easier preparation and higher acidity; these features collectively enhance their hydrogen-bond donating capability.[100] Early non-enantioselective applications of (thio)ureas by Curran and Schreiner demonstrated their ability to catalyze pericyclic reactions such as the Claisen rearrangement and Diels–Alder cycloadditions.[101,102] Interestingly, the presence of electron withdrawing substituents on the aromatic thioureas significantly accelerate the reaction rate, indicating that the pKa of the NHs is an important parameter that can correlate with the catalytic power of the HBD. The first enantioselective reaction catalyzed by a thiourea was reported by Jacobsen and coworkers, who developed a chiral thiourea catalyst for the asymmetric Strecker-type hydrocyanation of N-benzyl imines, where the acidic NHs activates the electrophile interacting with the lone pair of the imine (Scheme 10a).[103] Catalyst **44** proved to have wide applicability, since different nucleophiles (e.g. phosphonate, silyl ketene acetals, acrylate derivatives)[104,105] could be reactive within the same catalytic system. Rational modification of the thiourea scaffold enabled its application to related transformations, such as Mannich and nitro-Mannich reactions involving N-protected imines, affording excellent enantioselectivity (Scheme 10b).[106] In this case, the presence of the N-acetamido group is crucial to achieve high catalyst performance.

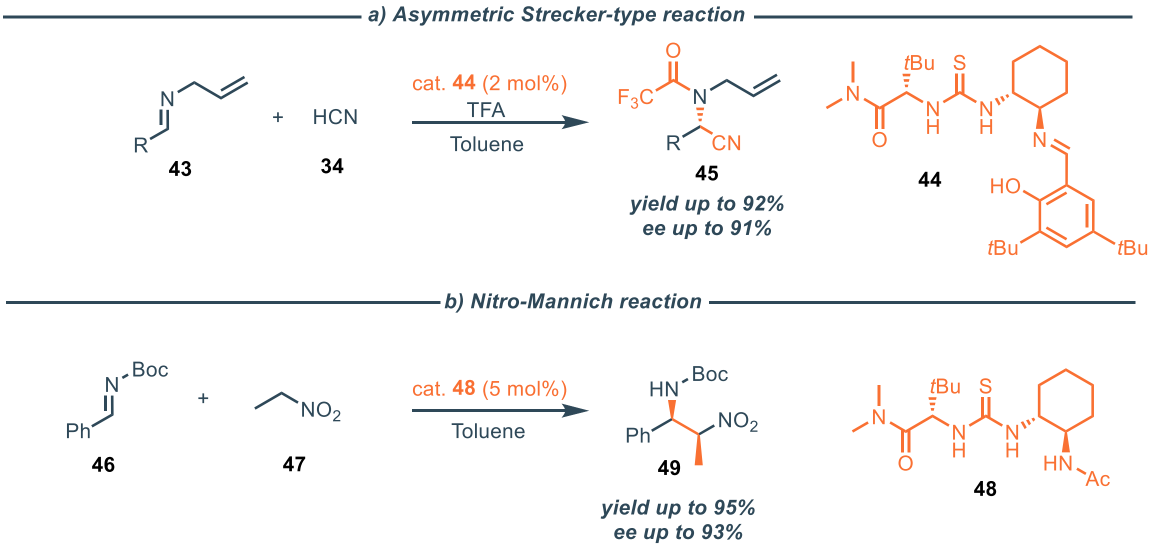

Scheme 10. Seminal examples of enantioselective thiourea-catalysed reactions

---

[100] G. Jakab, C. Tancon, Z. Zhang, K. M. Lippert, P. R. Schreiner, *Org. Lett.*, **2012**, *14*, 1724-1727

[101] D. P. Curran, L. H. Kuo, *J. Org. Chem.*, **1994**, *59*, 3259-3261

[102] A. Wittkopp, P. R. Schreiner, *Chem. Eur. J.*, **2003**, *9*, 407-414

[103] M. S. Sigman, E. N. Jacobsen, *J. Am. Chem. Soc.*, **1998**, *120*, 4901-4902

[104] G. D. Joly, E. N. Jacobsen, *J. Am. Chem. Soc.*, **2004**, *126*, 4102

[105] A. G. Wenzel, E. N. Jacobsen, *J. Am. Chem. Soc.*, **2002**, *124*, 12964

[106] T. P. Yoon, E. N. Jacobsen, *Angew. Chem. Int. Ed.*, **2004**, *44*, 466-468

Moreover, chiral thioureas have been effectively employed in the activation on N-acyl iminium ions in the acyl Pictet-Spengler reaction.[107] These systems fall within the broader paradigm of anion-binding catalysis, which will be elaborated upon in the next section.

The incorporation of thiourea motifs into bifunctional catalysts allowed to activate multiple reaction partners with different pathways at the same time. Specifically, Takemoto reported that catalyst **51** (see *Chiral Brønsted Acids and Bases* section, Figure 8 right) could be employed in the asymmetric Michael reaction of malonates to nitroolefines (Scheme 11a). The catalyst interacts with the nitro group of the electrophile, while its Bronsted basic site activates the malonate, bringing the two reactants in close proximity and efficiently delivering the stereochemical information.[84] The same catalyst was later on employed for the Michael addition of malononitrile to α,β-unsatured imides [108] and for the nitro-Mannich reaction of nitromethane on N-phosphinoylimines.[109] Later on, the thiourea framework have been integrated into the epiquinine structure, promoting the addition of nitromethane to chalchones following a similar mechanistic paradigma.[110] Furthermore, bis-thiourea catalysts, capable of engaging both reaction partners through cooperative H-bonding, were shown to effectively mediate the Baylis-Hillman reaction between cyclohexenone and aromatic aldehydes, delivering the products in high yields and enantioselectivities (Scheme 11b).[111]

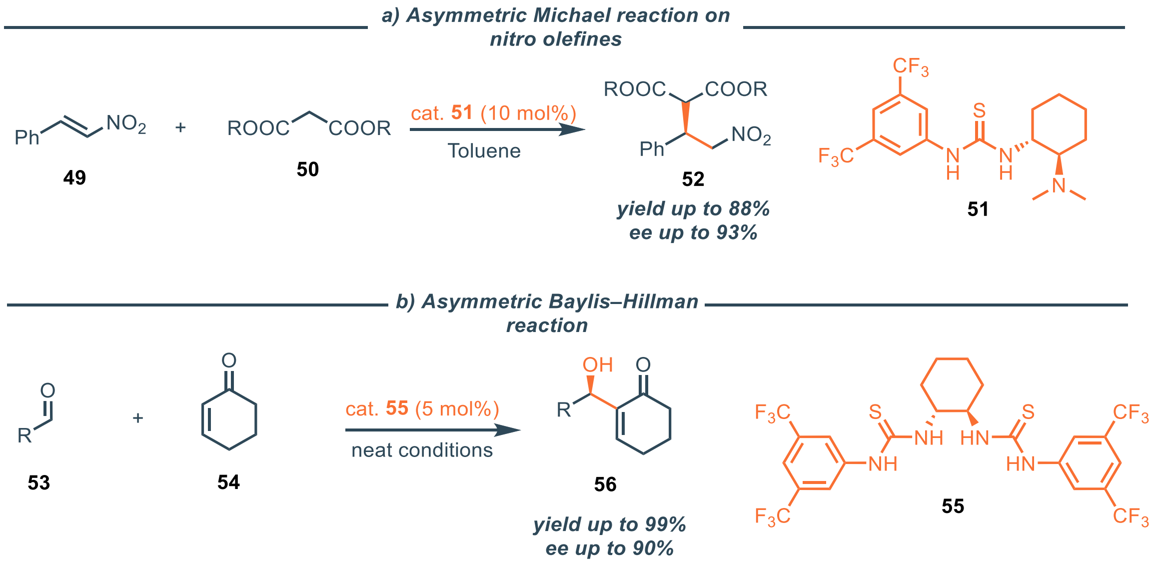

---

[107] M.S. Taylor, E. N. Jacobsen, *J. Am. Chem. Soc.*, **2004**, *126*, 10558-10559

[108] Y. Hoashi, T. Okino, Y. Takemoto, *Angew. Chem. Int. Ed.*, **2005**, *44*, 4032-4035

[109] T. Okino, S. Nakamura, T. Furukawa, Y. Takemoto, *Org. Lett.*, **2004**, *6*, 625-627

[110] B. Vakulya, S. Varga, A. Csampai, T. Soos, *Org. Lett.*, **2005**, *7*, 1967-1969

[111] Y. Sohtome, A. Tanatani, Y. Hashimoto, K. Nagasawa, *Tetrahedron Lett.*, **2004**, *45*, 5589-5592

Scheme 11. Representative examples of bifunctional thiourea catalysts able to activate multiple reaction partners

Given the success of thioureas, further advancements have led to the development of squaramides, structurally related motifs that offer enhanced acidity, planarity, and rigidity.[112] These features translate into stronger and more directional hydrogen bonds, enabling superior control over substrate orientation and transition state stabilization. Derived from squaric acid, squaramides incorporate two acidic NH groups and a rigid, electron-deficient cyclobutene-1,2-dione core that facilitates strong, directional bidentate hydrogen bonding.[113] The planar and pseudoaromatic nature of the scaffold enhances both the acidity of the NH protons and the conformational rigidity of the catalyst, contributing to high stereochemical control in a broad range of transformations.[114] A critical advantage of squaramides over thioureas lies in their enhanced hydrogen-bond donating ability. This is supported by indicator overlap experiments showing higher NH acidity, as well as by structural differences: the increased spacing (~0.6 Å) between the two NH donors in squaramides allows more efficient dual substrate binding and transition state organization.[115]

The first reported example of enantioselective catalysis by a squaramide was disclosed in 2008 by Rawal and coworkers, who demonstrated the squaramide-catalyzed Michael addition of a 1,3-diketone to β-nitrostyrene. In this seminal study, the squaramide catalyst, which integrates a chinconine motif, exhibited excellent levels of reactivity and enantioselectivity, marking a turning point in HBD catalysis by surpassing previously established thiourea systems for the high modularity and versatility of the synthesis of the catalyst (Scheme 12a).[116] Mechanicistically, the catalyst operates analogously to Takemoto's catalyst **51**. Subsequently, a similar catalytic system was employed for the asymmetric addition of diphenyl phosphites to nitroalkenes, to deliver β-nitrophosphonates with high enantioinduction (Scheme 12b).[117] A notable extension of the squaramide framework was reported by Rawal in 2017, who developed chiral thiosquaramides, squaramide analogues bearing one or two thiocarbonyl groups. These catalysts exhibit enhanced acidity (pKa 4–5 units lower than oxosquaramides), improved solubility, and stronger hydrogen-bonding capacity. Applied to the

---

[112] E. A. Popova, Y. A. Pronina, A. V. Davtian, G. D. Nepochatyi, M. L. Petrov, V. M. Boitsov, A. V. Stepakov, *Russ. J. Gen. Chem.*, **2022**, *92*, 287-347

[113] P. Chauhan, S. Mahajan, U. Kaya, D. Hack, D. Enders, *Adv. Synth. Catal.*, **2015**, *357*, 253-281

[114] M. Renio, M. R. Ventura, *Org. Biomol. Chem.*, **2025,** *23***,** 7521-7537

[115] Y. Qian, G. Ma, A. Lv, H.-L. Zhu, J. Zhao, V. H. Rawal, *Chem. Commun.*, **2010**, *46*, 3004-3006

[116] J. P. Malerich, K. Hagihara, V. H. Rawal, *J. Am. Chem. Soc.*, **2008**, *130*, 14416-14417

[117] Y. Zhu, J. P. Malerich, V. H. Rawal, *Angew. Chem. Int. Ed.*, **2010**, *49*, 153-156

Michael addition of barbituric acid derivatives to β-nitrostyrenes, they delivered excellent yields and enantioselectivities (up to 97% ee) even at very low loadings (0.05 mol%) under mild conditions (Scheme 12c).[118]

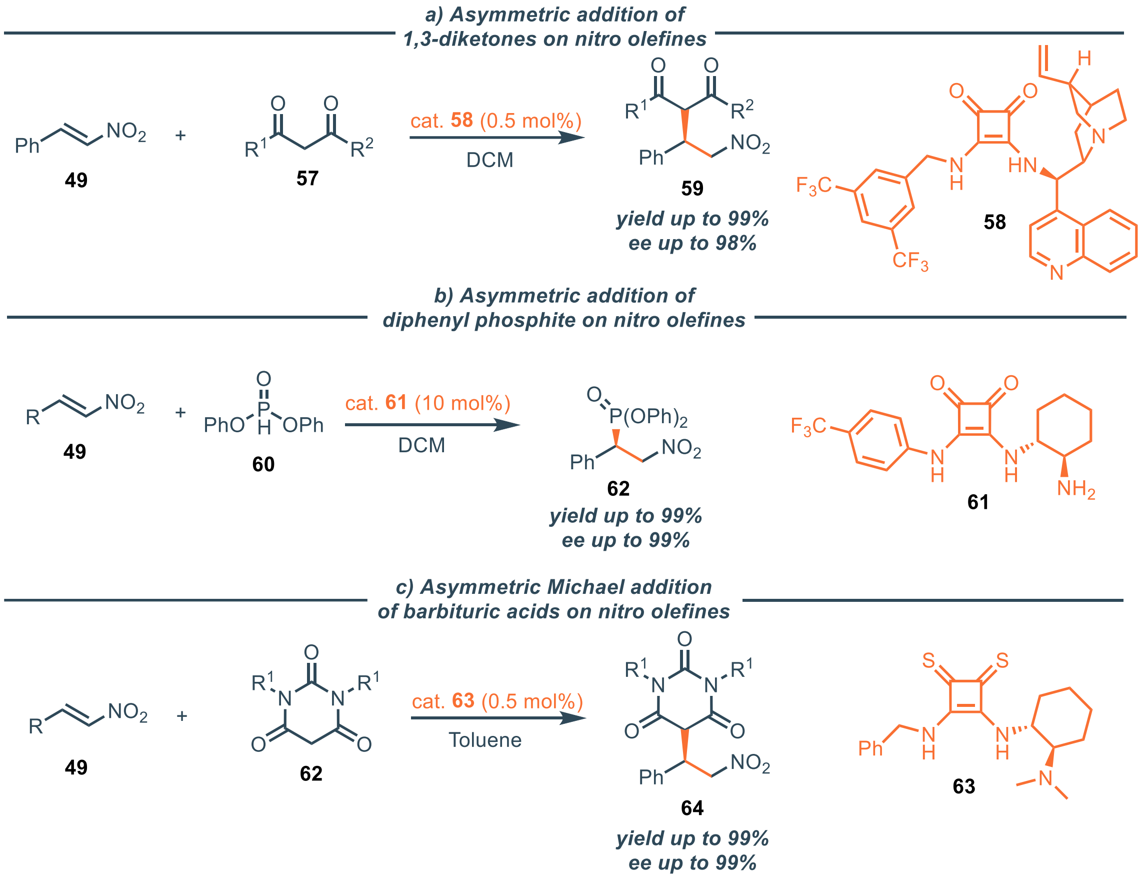

Scheme 12. Seminal examples of squaramides and thiosquaramides in asymmetric organocatalysis

Halogen and chalcogen bond donor catalysis

Halogen bond (XB) and chalcogen bond (ChB) belong to the class of σ-hole interactions, characterized by a region of positive electrostatic potential along the extension of a covalent bond.[119] This electron-deficient area, despite being associated with highly electronegative atoms such as halogens (F, Cl, Br, I) and chalcogens (S, Se, Te), allows these atoms to act as electrophilic sites capable of interacting with electron-rich Lewis bases.[120] The strength of these interactions increases with the polarizability of the atom (I > Br > Cl > F for halogens; Te > Se > S for chalcogens), and their

---

[118] M. Rombola, C. S. Sumaria, T. D. Montgomery, V. H. Rawal, *J. Am. Chem. Soc.*, **2017**, *139*, 5297–5300

[119] G. Cavallo, P. Metrangolo, R. Milani, T. Pilati, A. Priimagi, G. Resnati, G. Terraneo, *Chem. Rev.*, **2016**, *116*, 2478-2601

[120] D. Bulfield, S. M. Huber, *Chem. Eur. J.*, **2016**, *22*, 14434-14450

pronounced directionality (often approaching 180°) makes them highly attractive interactions for a plethora of different applications (Figure 11)

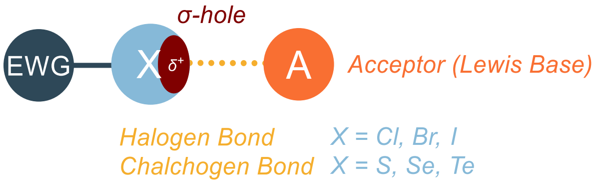

Figure 11. Schematic representation of XB and ChB

As a matter of facts, XB and ChB have found extensive applications in supramolecular chemistry and crystal engineering, where their high directionality enables the rational design of complex molecular architectures.[121] These interactions have also been harnessed in materials science, including the development of conductive and magnetic materials, organic light-emitting diodes (OLEDs), and self-assembled nanostructures.[122] Moreover, they play a role in biological systems, contributing to protein-ligand recognition, enzyme activity, and macromolecular conformational stability.[123] Despite their widespread utility in these domains, their application in catalysis remains comparatively underexplored, particularly when contrasted with the more established hydrogen bond donor catalysis.[52]

In catalysis, XBs and ChBs serve as Lewis acidic sites that can activate substrates or stabilize intermediates, thereby enhancing reaction rates and enabling new reactivity.[124] A critical aspect of establishing XB/ChB catalysis has been to rigorously rule out other competing activation modes, particularly hidden Brønsted acid catalysis or radical pathways, a challenge that early studies often addressed. [52] The application of ChB donors in organocatalysis will not be further addressed in this thesis; instead, the following section will focus on halogen bonding.[125]

The first proposals of XB involvement in catalysis emerged in 2008, when Bolm and co-workers were among the first to propose the involvement of halogen bonding in the reduction of quinoline derivatives using perfluoroalkyl iodides.[126] However, these early studies faced ambiguity regarding the

---

[121] P. Metrangolo, G. Resnati, *Chem. Eur. J.*, **2001**, *7*, 2511-2519

[122] P. Metrangolo, G. Resnati, *Halogen Bonding II*, Springer, **2015**

[123] G. Sekar, V. V. Nair, J. Zhu, *Chem. Soc. Rev.*, **2024**, *53*, 586-605

[124] R. L. Sutar in *Halogen Bonding in Solution* (Ed. S. Huber), Wiley, **2021**, pp. 269-305

[125] For detailed reviews, see: G. Gao, D. Xie, P.-P. Zhou, *Asian J. Org. Chem.*, **2025**, *14*, e202500098; K. T. Mahmudov, M. N. Kopylovich, M. F. C. Guedes da Silva, A. J. L. Pombeiro, *Dalton Trans.*, **2017**, *46*, 10121; Y. A. Cheng, Y.-Y. Yeung in Nonnitrogenous Organocatalysis (Ed. A.M. Harned), Taylor & Francis, pp.91-118

[126] A. Bruckmann, M. A. Pena, C. Bolm, *Synlett*, **2008**, *2008*, 900-902

actual catalytic species. A pivotal contribution came in 2011 from Huber and co-workers, who rigorously demonstrated the operation of non-transient halogen bonding in organic halide activation, particularly studying the Ritter-type solvolysis of benzhydril bromide. The catalyst, operating with a halide abstraction mechanism, proved to effectively accelerate the reaction rate with halogen bonding interactions (Scheme 13a).[127] In this case, the use of stoichiometric amounts of catalysts was required, due to catalyst inhibition, where the halogen-bond donor binds too strongly to the liberated halide anion, preventing further substrate activation. To prevent this, often silyl enol ethers are used as nucleophile, which can abstract the halide from the non-covalent adduct, thus restoring the free catalyst. This concept was employed in the halide abstraction reaction on 1-chloroisochromane as a substrate, performed with a silyl enol ether (Scheme 13b).[128] Similar systems were then employed by the same group for the activation of carbonyl moiety turning out in catalysis of Diels-Alder reaction,[129] as well as Michael addition[130] and Nazarov cyclization.[131]

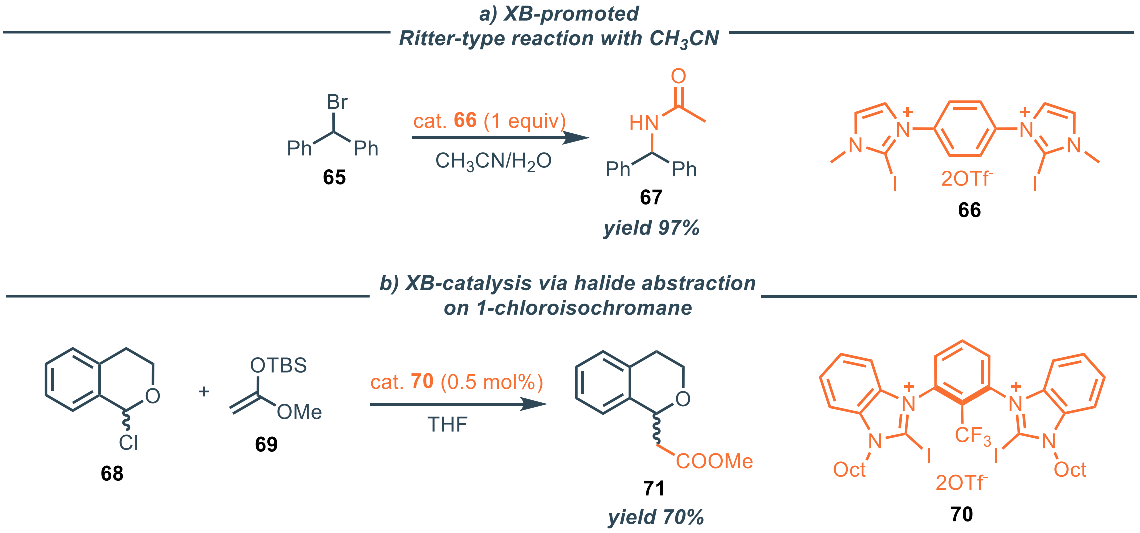

Scheme 13. Seminal examples of XB donors in organocatalysis

Catalysts typically employ halogens (especially iodine) directly bonded to carbon atoms, often with strong electron-withdrawing groups (e.g., perfluoroaryl) or cationic structures (e.g., imidazolium, triazolium salts) to enhance the electrophilicity of the halogen. Cationic and multidentate XB donors

---

[127] S. M. Walter, F. Kniep, E. Herdtweck, S. M. Huber, *Angew. Chem. Int. Ed.*, **2011**, *50*, 7187-7191

[128] F. Kniep, S. H. Jungbauer, Q. Zhang, S. M. Walter, S. Schindler, I. Schnapperelle, E. Herdtweck, S. M. Huber, *Angew. Chem. Int. Ed.*, **2013**, *52*, 1-6

[129] S. H. Jungbauer, S. M. Walter, S. Schindler, L. Rout, F. Kniep, S. M. Huber, *Chem. Commun.*, **2014**, *50*, 6281-6284

[130] J.-P. Gliese, S. H. Jungbauer, S. M. Huber, *Chem. Commun.*, **2017**, *53*, 12052-12055

[131] A. Dreger, P. Wonner, E. Engelage, S. M. Walter, S. M. Huber, *Chem. Commun.*, **2019**, *55*, 8262-8265

are generally more potent due to their stronger binding affinities and ability to form more rigid adducts with substrates. The nature of the counteranion can significantly influence the Lewis acidity of the halogen-bond donor. Generally, less coordinating or less Lewis basic counteranions (e.g., tetrafluoroborate (BF_4^-) or bis(trifluoromethanesulfonyl)imide (NTf_2^-)) tend to facilitate a stronger interaction between the catalyst and the substrate's halogen, thereby enhancing catalytic activity and reaction yields.

Despite notable advances in XB catalysis, its application in asymmetric organocatalysis remained elusive for a long time. The primary challenge in developing enantioselective XB catalysis lies in the highly directional nature of the interaction (~180°) between the halogen's σ-hole and the substrate, combined with the large size of the halogen (typically iodine). These structural constraints lead to a substantial spatial gap between the catalyst's chiral environment and the bound substrate, limiting effective chiral induction.

Early reports that proposed enantioselective transformations involving XB often relied on dual-function catalysts bearing hydrogen-bond donors or Brønsted basic sites. In such systems, it was difficult to determine whether the observed stereocontrol originated from halogen bonding or another interaction mode.[132,133] The first systems relying exclusively on halogen bonding for asymmetric induction yielded only modest results. In 2020, Huber and co-workers reported a chiral bidentate bis-iodoimidazolium XB donor that promoted a Mukaiyama aldol reaction with up to 33% enantiomeric excess.[134] Around the same time, García Mancheño's group introduced a chiral tetrakis-iodotriazole catalyst that produced similarly low enantioselectivity in a Reissert-type reaction.[135] Recent developments have significantly improved the efficacy of asymmetric XB catalysis. Huber and coworkers designed a second-generation family of modifiable bidentate iodine(I)-based catalysts that achieved up to 98% ee in the Mukaiyama aldol reaction across a broad range of substrates. Control experiments with non-iodinated analogues confirmed the central role of XB in both activation and stereocontrol (Scheme 14a).[136]

---

[132] L. Zong, X. Ban, C. W. Kee, C.-H. Tan, *Angew. Chem. Int. Ed.* **2014**, *126*, 12043-12047

[133] T. Arai, T. Suzuki, T. Inoue, S. Kuwano, *Synlett*, **2016**, *28*, 122-127

[134] R. L. Sutar, E. Engelage, R. Stoll, S. M. Huber, *Angew. Chem. Int. Ed.*, **2020**, *59*, 6808

[135] F. Ostler, D. G. Piekarski, T. Danelzik, M. S. Taylor, O. García Mancheño, *Chem. Eur. J.* **2021**, *27*, 2315

[136] J. Wolf, M. P. Mohanan, R. Robidas, R. L. Sutar, E. Engelage, C. Y. Legault, S. M. Huber, *Angew. Chem. Int. Ed.*, **2025**, *64*, e202506476

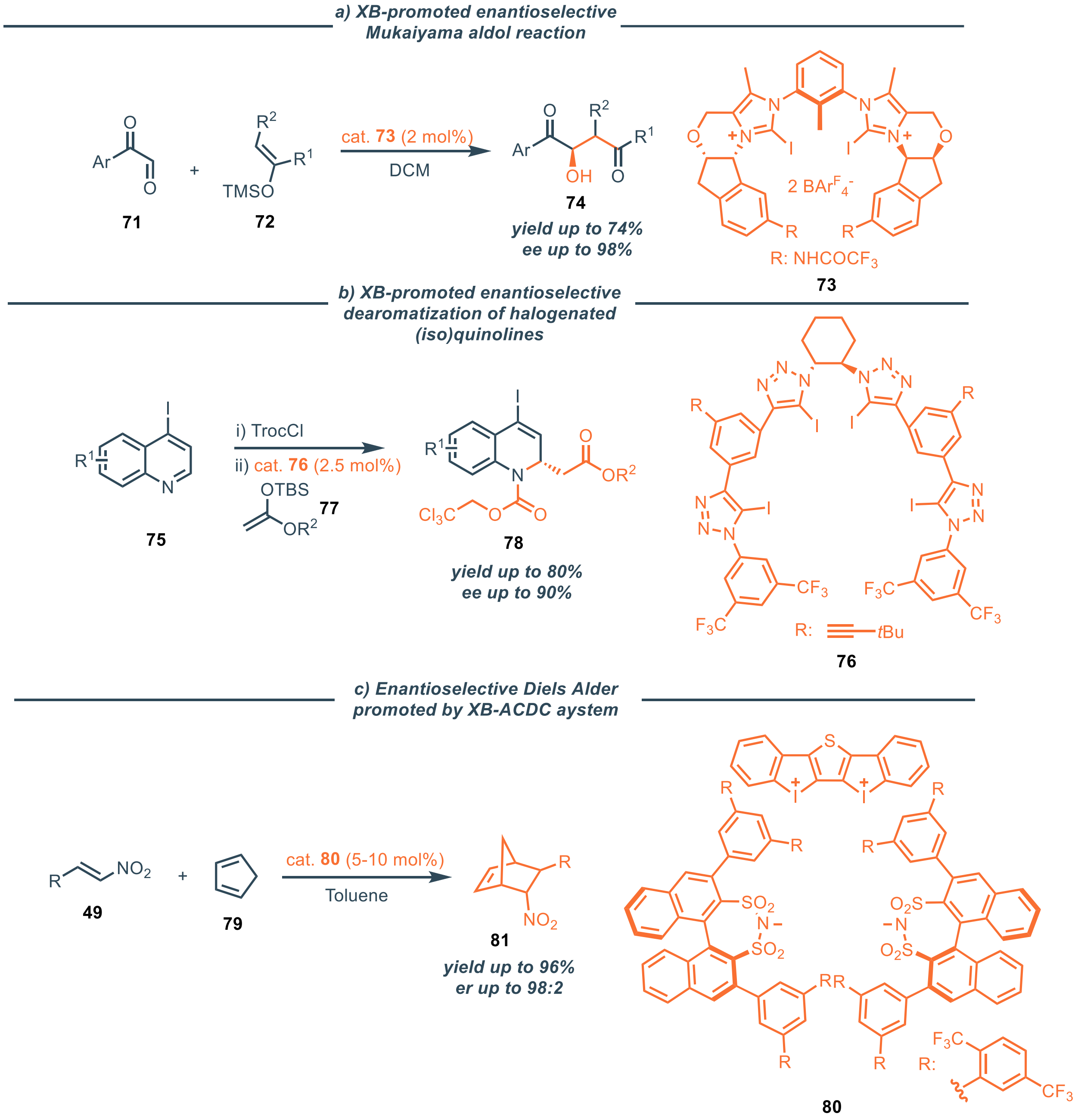
a) XB-promoted enantioselective Mukaiyama aldol reaction

b) XB-promoted enantioselective dearomatization of halogenated (iso)quinolines

c) Enantioselective Diels Alder promoted by XB-ACDC aystem

Scheme 14. Recent advances in asymmetric XB organocatalysis

In a parallel effort, García Mancheño's group devised a novel strategy involving substrates equipped with additional halogens capable of simultaneously acting as Lewis bases and σ-hole donors. This configuration enabled multiple, synergistic halogen-halogen contacts between the substrate and the catalyst, resulting in up to 90% ee in the dearomatization of halogen-substituted (iso)quinolines (Scheme 14b).[137] A breakthrough in the field was the integration of XB with asymmetric counteranion-directed catalysis (ACDC). List, Huber and coworkers developed the first highly enantioselective XB-

---

[137] A. C. Keuper, K. Fengler, F. Ostler, T. Danelzik, D. G. Pekarski, O. G. Mancheño, *Angew. Chem. Int. Ed.*, **2023**, *62*, e202304781

ACDC system using a strong bidentate iodine(III)-based halogen bond donor in combination with chiral disulfonimide counteranions. This strategy enabled a Diels–Alder reaction between cyclopentadiene and trans-β-nitrostyrene with up to 98:2 e.r. (Scheme 14c).[138]

Anion-binding catalysis

Anion-binding catalysis (ABC) is a significant branch of non-covalent organocatalysis that activates substrates through non-covalent interactions (NCIs) with neutral or negatively charged electron pairs.[139] This strategy takes inspiration from nature, where such interactions play central roles in enzymatic catalysis, ensuring precise substrate recognition, activation, and stereocontrol. Within organocatalysis, In ABC, small organic molecules are designed to bind anions, forming supramolecular complexes that stabilize transition states and guide stereoselectivity.[140]

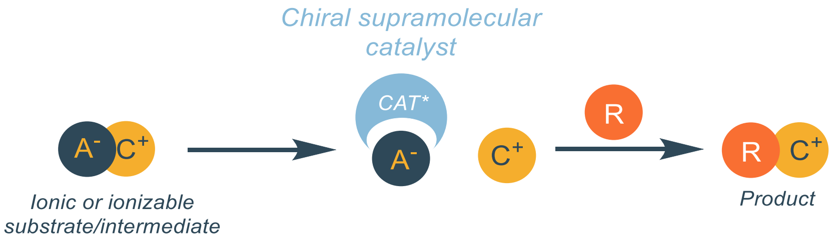

Figure 12. Graphical representation of anion-binding catalysis

Enantioselective ABC can be seen as an extension of the concept of ACDC (Asymmetric Counteranion Directed Catalysis), since the supramolecular complex formed between anion and catalyst is, in fact, a chiral counteranion of the cationic reactive specie (See *Chiral Brønsted Acids and Bases* section).

ABC activation can occur through multiple mechanistic pathways.[141] In addition reactions, the catalyst often binds an anionic nucleophile or to a developing negative charge on an electrophile. A representative example is the acid-free acetalization of aldehydes, where the catalyst stabilizes the developing oxyanion through dual hydrogen bonding.[142] In addition to this, bifunctional catalysts can simultaneously activate both the reaction partners (Figure 13a).[84] Other mechanisms follow S_N1-type pathways. Here, the catalyst binds the leaving group anion, thereby facilitating nucleophilic attack on

---

[138] D. L. Reinkard, A. Iniutina, S. Reese, T. Shaw, C. Merten, B. List, S. M. Huber, *J. Am. Chem. Soc.*, **2025**, *147*, 8107-8112

[139] S. Beckendorf, S. Asmus, O. G. Mancheño, *ChemCatChem*, **2012**, *4*, 926-936

[140] D. Seidel, *Synlett*, **2014**, *25*, 783-794

[141] L.-M. Entgelmeier, O. G. Mancheño, *Synthesis*, **2022**, *54*, 3907-3927

[142] M. Kotke, P. R. Schreiner, *Tetrahedron*, **2006**, *62*, 434-439

the resultant carbocation. This mechanism can occur both in an inter- and intramolecular fashion (Figure 13b).[143,144] Even more intricate are cooperative systems involving a Brønsted acid additive, which protonates the substrate and enables the catalyst to bind the resulting counterion within a structured chiral environment (Figure 13c).[107] Alternatively, ABC can proceed through enhancement of Lewis acidity, where the catalyst interacts with a Lewis basic site to increase the electrophilicity of a reaction partner (Figure 13d).[145] Ultimately, in phase-transfer systems, the catalyst binds an anion like fluoride, forming a soluble ion pair in an organic phase that facilitates nucleophilic substitution, as often seen in asymmetric fluorinations (Figure 13e).[146]

The conceptual underpinnings of ABC stem from early supramolecular studies in the 1980s and 1990s. Work by Simmons, Wilcox, and Hamilton investigated the use of (thio)urea motifs for anion binding through hydrogen bonding, while Etter's crystallographic studies revealed enhanced binding in electron-deficient ureas.[147] Although foundational, these studies were primarily limited to recognition rather than catalysis Schreiner played a central role in advancing the field, particularly through his late 1990s work demonstrating the ability of electron-deficient thioureas to activate substrates.

---

[143] S. E. Reisman, A. G. Doyle, E. N. Jacobsen, *J. Am. Chem. Soc.*, **2008**, *130*, 7198-7199

[144] D. A. Kutateladze, D. A. Strassfeld, E. N. Jacobsen, *J. Am. Chem. Soc.*, **2020**, *142*, 6951-6956

[145] S. M. Banik, A. Levina, A. M. Hyde, E. N. Jacobsen, *Science*, **2017**, *358*, 761-764

[146] G. Pupo, A. C. Vicini, D. M. H. Ascough, F. Ibba, K. E. Christensen, A. L. Thompson, J. M. Brown, R. S. Paton, V. Gouverneur, *J. Am. Chem. Soc.*, **2019**, *141*, 2878-2883

[147] F. Dressler, P. R. Schreiner in *Anion-Binding Catalysis* (Ed. O. G. Mancheño), Wiley, **2021**, pp. 1-64

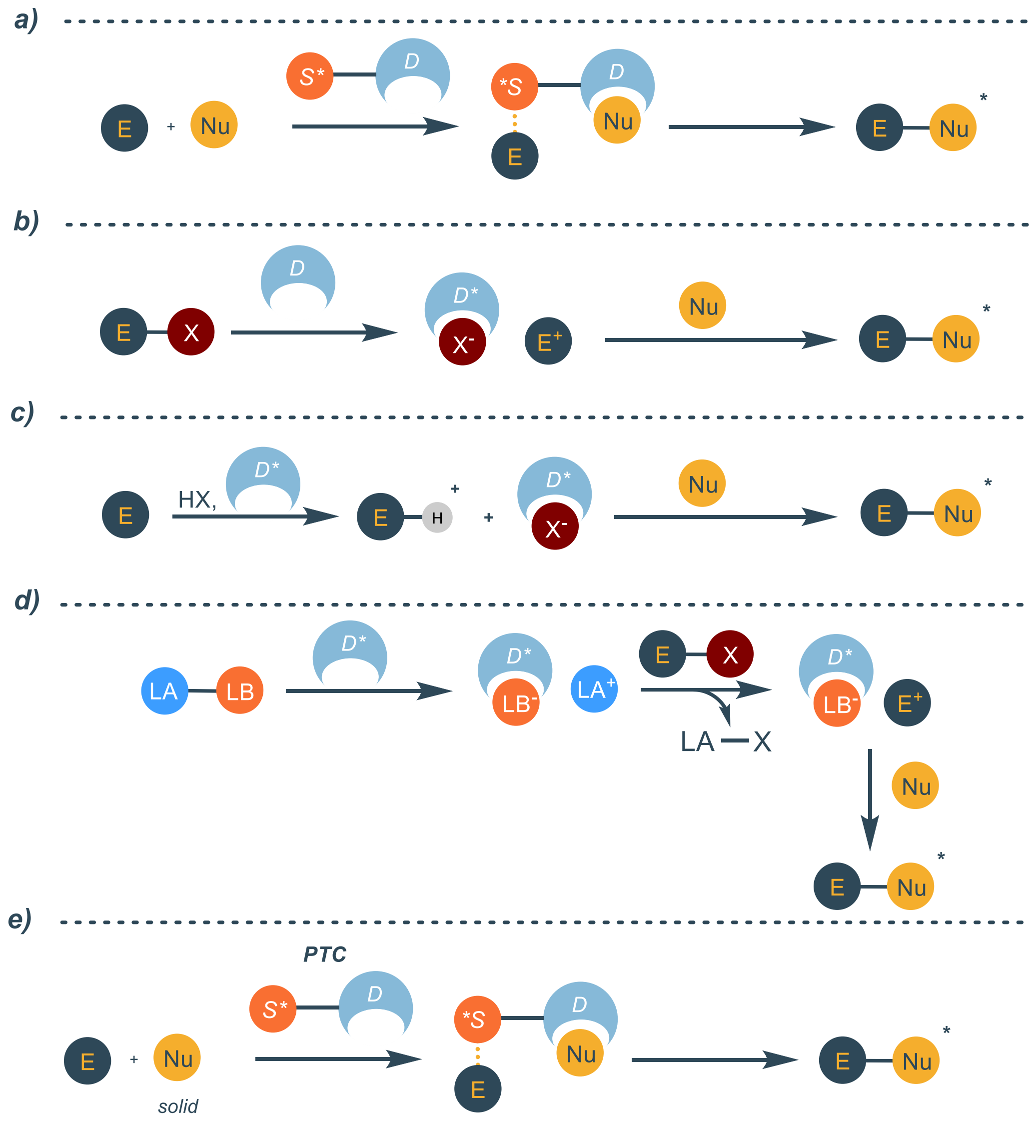

Figure 13. Possible activation modes in ABC

His 2006 study on the acid-free acetalization of carbonyl compounds provided a clear and influential example of the potential of anion-binding catalysis.[141] This reaction showcased how dual hydrogen bonding could stabilize an oxyanionic transition state (Scheme 15).

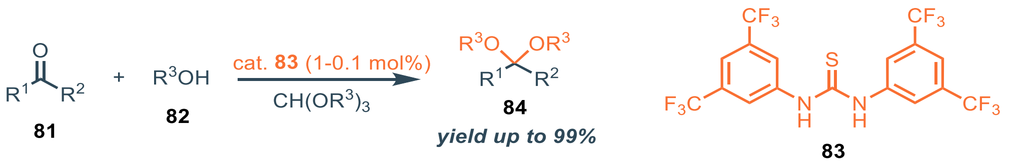

Scheme 15. Acid-free acetalization of carbonyl compounds promoted by thiourea catalyst

The concept was further validated by related applications such as THP protection, which demonstrated exceptional catalytic efficiency and high turnover frequencies.[148] Other developments

---

[148] M. Kotke, P. R. Schreiner, *Synthesis*, **2007**, *5*, 779-790

by Takemoto, Jacobsen and Rawal introduced bifunctional thiourea and squaramide catalysts for asymmetric Michael additions and related processes (see *Hydrogen bond donor catalysis* section).

The efficiency of anion-binding catalysis is deeply influenced by the molecular scaffold of the catalyst, which dictates both binding strength and selectivity. While (thio)ureas and squaramides remain archetypal and widely studied systems, especially for their NH-based hydrogen bond donor capabilities (see *Hydrogen bond donor catalysis section*), recent years have witnessed the emergence of several alternative and increasingly sophisticated frameworks. 1,2,3-Triazoles and their triazolium derivatives represent one such family.[149] Originally regarded as unconventional due to their use of polarized C–H bonds for anion recognition, they have since demonstrated notable binding capabilities. Triazolium cations, in particular, increase C–H acidity, enhancing anion affinity.[150] Bistriazoles bearing 3,5-bis(trifluoromethyl)phenyl substituents have shown a distinct preference for small halide ions, such as chloride, due to their compact binding pockets.[151] Moreover, their ability to adopt helical conformations upon anion binding has been linked to improved enantioselectivity.[152] Silanediols and phosphoramides offer another compelling scaffold. Silanediols, with their $Si(OH)_2$ functionality, can form strong hydrogen bonds with diverse substrates, including carbonyls and anions.[153] Their application in enantioselective acyl-Mannich reactions underscores their utility. Phosphoramides, especially thiophosphoramides and cyclophosphazanes, provide multidentate hydrogen bonding and show enhanced binding to tetrahedral anions, surpassing conventional (thio)ureas in binding efficiency.[154] Beyond traditional hydrogen bonding, non-covalent interactions based on σ-hole bonding, such as halogen and chalcogen bonding, have become viable tools for ABC. Halogen bonding has been the most extensively explored, particularly using perfluorinated aryl systems for halide abstraction. Chalcogen bonding is gaining traction, despite stability concerns with some donors (see *Halogen and chalcogen bond donor catalysis* section). The most common motifs for the construction of catalysts in anion-binding catalysis are depicted in Figure 14.

---

[149] K. Ohmatsu, T. Ooi in *Anion-Binding Catalysis* (Ed. O. G. Mancheño), Wiley, **2021**, pp. 221-242

[150] A. Kumar, P. S. Pandey, *Org. Lett.*, **2008**, *10*, 165-168

[151] L. Schiffer, M. Stinglhamer, K. Kaur, O. G. Mancheño, *Beilstein J. Org. Chem.*, **2021**, *17*, 2270-2286

[152] M. Zurro, S. Asmus, J. Bamberg, S. Beckendorf, O. G. Mancheño, *Chem. Eur. J.* **2016**, *22*, 3785-3793

[153] A. G. Schafer, J. M. Wieting, T. J. Fischer, A. E. Mattson, *Angew. Chem. Int. Ed.*, **2013**, *52*, 11321-11324

[154] A. Leveille, A. Mattson in *Anion-Binding Catalysis* (Ed. O. G. Mancheño), Wiley, **2021**, pp. 201-218

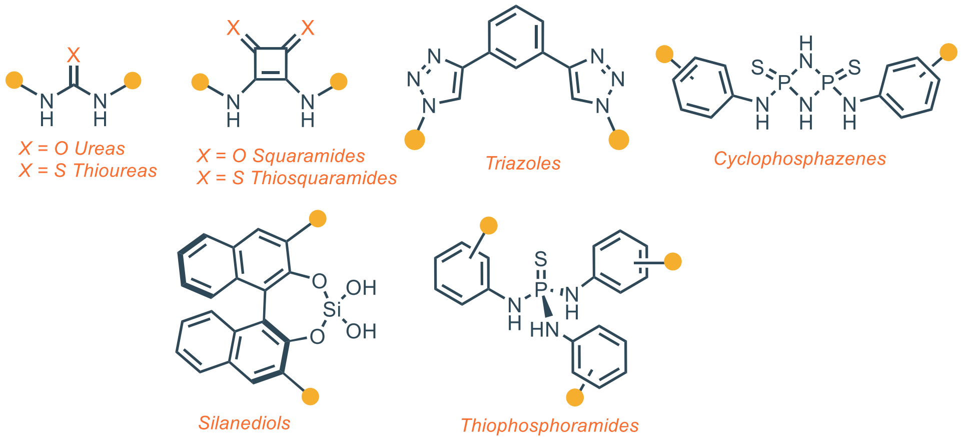

Figure 14. Most common HBD for anion binding catalysis

The design of effective ABC catalysts necessitates a deep understanding of how structure influences activity and selectivity. One of the most critical parameters is the electron deficiency of the hydrogen bond donor unit. Incorporating electron-withdrawing substituents, such as CF_3 groups, into the aryl backbone enhances the acidity of NH protons and improves their ability to participate in strong, directional hydrogen bonds. The thiourea motif equipped with two 3,5-bis(trifluoromethyl)phenyl rings, is recognized as a privileged scaffold with exceptional performance.[141] Conformational rigidity also contributes significantly: rigid catalysts provide a preorganized binding environment, minimizing entropic penalties and enhancing catalytic efficiency. This has been demonstrated in systems such as halogen bond donors and helical triazoles, where structural preorganization correlates with improved outcomes. Moreover, tailoring the geometry of the binding pocket to fit specific anions enhances selectivity.

The combination of anion-binding catalysis with other activation strategies, such as aminocatalysis or Brønsted/Lewis acid catalysis, has broadened the range of achievable transformations. In one example, dual ABC/aminocatalysis has been applied to the conjugate addition of oxindoles to enals, where the amine unit activates the α,β-unsaturated aldehyde through LUMO-lowering, while the thiourea component coordinates the enol form of the oxindole (Scheme 16a) Kinetic resolution of amines has also been achieved using chiral thioureas in combination with 4-Dimethylaminopyridine (DMAP) and an acylating agent. After DMAP undergoes acylation, a non-chiral ion pair is formed. This ion pair interacts with the thiourea to generate a chiral complex capable of selectively binding one enantiomer of the racemic amine, enabling efficient resolution (Scheme 16b).

a) Enantioselective addition of oxindoles to enals

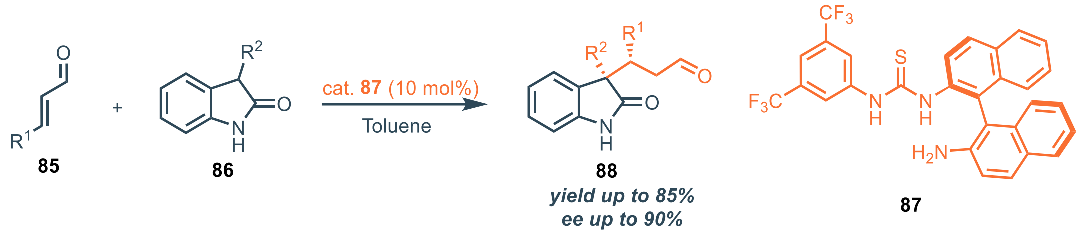

b) KR of racemic benzylic amines

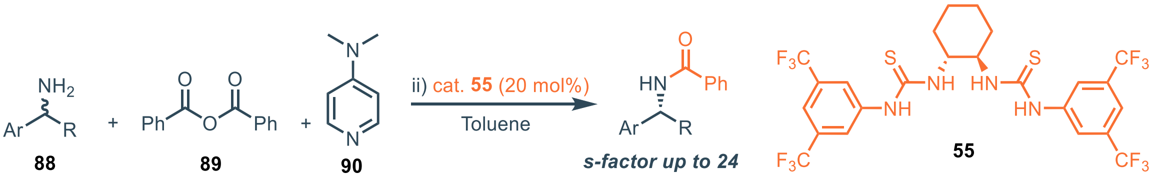

Scheme 16. Recent advances in ABC

ABC has also been integrated with metal catalysis. Hybrid systems, featuring ligands like ZhaoPhos that couple metal coordination sites with anion-binding domains, have proven effective in asymmetric hydrogenation, hydroformylation, and Pd-catalyzed allylic substitutions. In these cases, the anion-binding motif serves to orient and activate the substrate through ion-pairing.[155,156] Finally, anion–π catalysis has emerged as a powerful alternative, utilizing electron-deficient aromatic surfaces to stabilize anionic intermediates and transition states. From Kemp eliminations to epoxide openings and Michael additions, these systems leverage quadrupole moments to induce selectivity. Chiral π-acidic surfaces have extended this concept to enantioselective transformations, underscoring the versatility and future potential of ABC.[157]

The development of novel strategies in ABC is the focus of one of the chapters of this thesis (Chapter 4).

---

[155] Q. Zhao, S. Li, K. Huang, R. Wang, X. Zhang, *Org. Lett.*, **2013**, *15*, 4014-4017

[156] T. Smejkal, B. Breit, *Angew. Chem. Int. Ed.*, **2008**, *47*, 311-315

[157] C. Wang, F. N. Miros, J. Mareda, N. Sakai, S. Maile, *Angew. Chem. Int. Ed.*, **2016**, *55*, 14422-14426

Chapter 2 - Nitrogen-Rich Carbon Dots as Effective Catalysts in the 1,4-Reduction of α,β-Unsaturated Aldehydes via Ion Pair Asymmetric Nano-Organocatalysis

This chapter is based on the publication: A. Carioscia, E. Cocco, M. E. Casacchia, G. Gentile, M. Mamone, G. Giorgianni, E. Incerto, M. Prato, F. Pesciaioli, G. Filippini, A. Carlone, *ACS Catal.* **2024**, *14*, 13429–13438

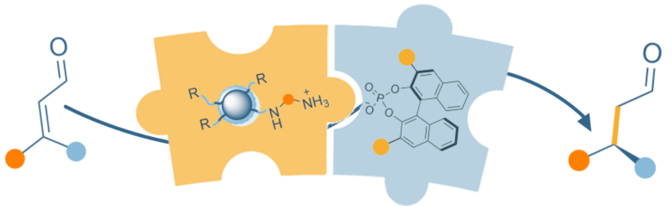

- **Easy preparation of the achiral CDs**
- **Nanostructured chiral salt**
- **Chirality on the counterion facilitates optimization of enantioinduction**

Chapter outline *– In this chapter, the development of novel strategies for Asymmetric ion-pair nano-organocatalysis is disclosed. Nitrogen-doped Carbon Dots (***NCDs***) have been successfully used for the development of a novel nanostructured catalyst, which features a chiral phosphonate as enantioinducing element. This proof of concept was applied to the enantioselctive 1,4-reduction of α,β-unsaturated aldehydes, with high yields and enantiomeric excesses.*

Introduction

Carbon Dots: Versatile Nanoarchitectures for Catalysis and Beyond

Carbon Dots (**CDs**) form a versatile and fast-growing class of carbon-based fluorescent nanomaterials. They are typically composed of quasi-spherical nanoparticles with diameters of 10 nm or less, and their physical and chemical behaviour is largely dictated by the precursor materials and reaction conditions used in their preparation.[1] These factors determine both the type and density of the functional groups on the particle surface, most often carboxylic acids, alcohols, and amines, which, in turn, influence solubility, biocompatibility, and environmental safety, and other physical

---

[1] C. Rosso, G. Filippini, M. Prato *ACS Catal.* **2020**, *10*, 15, 8090–8105

and chemical properties.[2] One of the reasons **CDs** have attracted so much attention in recent years is that they can be produced quickly, on a large scale, from low-cost and readily available starting materials.[3]

Broadly speaking, there are two main synthetic routes for the preparation of this new class of materials: *top-down* and *bottom-up*. In the top-down approach, bulk carbon structures such as graphite or carbon nanotubes are broken down into nanoparticles. This can be done through methods like chemical or electrochemical oxidation, arc discharge, laser ablation, acid exfoliation, or ultrasonic processing. While these techniques can produce high-quality dots, they are generally less practical for large-scale applications because they require long reaction times and expensive feedstocks.[1] The bottom-up approach works in the opposite direction, building **CDs** from smaller molecules. This is typically achieved by carbonization, pyrolysis, or hydrothermal treatment of organic precursors, or sometimes through the incomplete combustion of biomass.[4] Bottom-up methods are usually cheaper, greener, and operationally simpler than their top-down counterparts, and they tend to produce particles with well-defined shapes and sizes. An additional advantage is that it is straightforward to incorporate heteroatoms—such as oxygen, nitrogen, sulfur, phosphorus, or boron—into the **CD** structure by choosing appropriate dopant-rich starting materials, for example amino acids, amines, thiols, phosphonates, or borates.[1] Such doping allows the properties of **CDs** to be tuned for specific applications. In fact, thanks to their combination of tunable surface chemistry, high surface-to-volume ratio, and robust optical behaviour, **CDs** have found use in a wide range of areas:

- *Biomedicine*: Their fluorescence, water solubility, and good cell permeability make them useful in cellular and tissue bioimaging, biosensing (for glucose, metal ions, phosphates, nucleic acids), and drug delivery systems where drug tracking is needed.[5]
- *Optoelectronics*: They are being explored in dye-sensitized solar cells (DSCs), organic solar cells (OSCs), and light-emitting diodes (LEDs) as environmentally friendly luminescent components.[4]

---

[2] F. Arcudi, L. Đorđević, M. Prato *Acc. Chem. Res.* **2019**, *52*, 2070–2079

[3] M. Bortolami, I. I. Bogles, C. Bombelli, F. Pandolfi, M. Feroci, F. Vetica *Molecules* **2022**, *27*, 5150-5166

[4] Y. Wang, A. Hu *J. Mater. Chem. C.* **2014**, *2*, 6921–6939

[5] A. Sharma; J. Das *J. Nanobiotechnology* **2019**, *17*, 92-116

- *Catalysis*: TiO_2-derived **CDs** have been applied in photoelectrochemical hydrogen evolution (HER), while nitrogen-doped **CDs** show strong activity in oxygen reduction (ORR).[4]

- *Biosensing*: **CDs** can act as responsive probes, with their fluorescence intensity changing upon interaction with target analytes, enabling the detection of DNA, phosphates, nitrites, glucose, biothiols, and metal ions such as Fe^{3+}, Cu^{2+}, Ag^{+}, and Hg^{2+}.[4]

Given their diversity, **CDs** are sometimes grouped into categories according to nanostructure:

- *Graphene Quantum Dots (**GQDs**)*: 2D nanoparticles made of one or a few graphene layers, often obtained by exfoliating graphite.

- *Carbon Quantum Dots (**CQDs**)*: Quasi-spherical particles with crystalline cores, usually prepared by heating suitable precursors above 300 °C.

- *Carbon Nanodots (**CNDs**)*: Quasi-spherical, amorphous particles formed at lower temperatures, without quantum confinement effects but with excited states resembling those of small molecules.

- *Polymer-like Dots (**PDs**)*: Aggregates or cross-linked networks derived from polymers or monomers.

In practice, because their atomic structure and excited-state behaviour are difficult to pin down, “carbon dots” is used as a catch-all term for any quasi-spherical carbon nanoparticles whose properties lie between **CNDs** and **CQDs**.[1]

From a chemical standpoint, the surface composition of **CDs**, especially the number and type of terminal functional groups, plays a decisive role in determining their reactivity, solvation, and redox behaviour. While their precise structure is often unknown, owing to the complexity of their formation and the limits of current analytical techniques, several methods are used to study them. In particular, to analyse the core, Transmission Electron Microscopy (TEM) and Raman spectroscopy can differentiate between crystalline **CQDs** and amorphous **CNDs**;[2] Atomic Force Microscopy (AFM), Dynamic Light Scattering (DLS), and TEM, on the other hand, can measure particle size,[2] and UV–Vis absorption and photoluminescence spectroscopy reveal electronic transitions such as π–π^* and n–π^*.[1] For surface functional groups, amines can be identified by X-Ray Photoelectron Spectroscopy (XPS) and quantified using the Kaiser test or NMR after derivatisation, while carboxyl and hydroxyl groups are detectable by FT-IR spectroscopy and measurable by titration.[6] Finally, Thermogravimetric Analysis (TGA) can provide an estimate of the density of surface groups and their thermal stability.[1]

Several examples illustrate the catalytic capabilities of amine-rich **CDs**. Vetica and co-workers have reported their use in enantioselective aldol reactions (Scheme 1a),[7] while Prato's group has applied them to the racemic 1,4-addition of nucleophiles (Scheme 1b).[6] Building on these findings, the present work focuses on a new class of **CDs** functionalised with primary amines, namely Nitrogen-Doped Carbon Dots (**NCDs**). These materials combine the non-toxicity and handling ease of **CDs** with the catalytic efficiency of molecular amines. Here, they are used in Asymmetric Counteranion-Directed Catalysis (ACDC) for the first time, in combination with CPAs, for the enantioselective 1,4-reduction of α,β-unsaturated aldehydes.

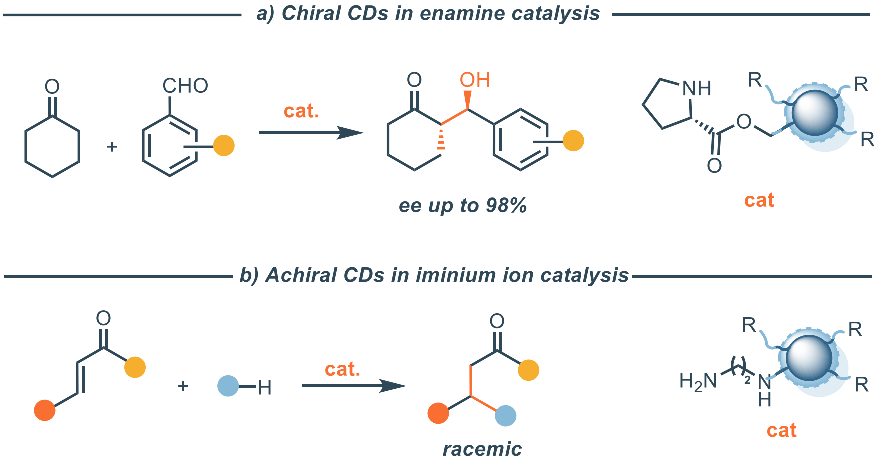

Scheme 1. **CDs** in organocatalysis – state of the art

Asymmetric hydrogenation of α,β-unsatured aldehydes via ACDC

Asymmetric Counteranion Directed Catalysis (ACDC) has emerged as a powerful strategy for achieving asymmetric synthesis in a wide array of reactions.[8] In ACDC, the catalytic species is formed by an ionic pair where the steric information is dictated by the chiral counteranion (See *Chiral Bronsted Acids and Bases* section, Chapter 1). The seminal example of ACDC catalysis is the Hantzsch ester-mediated asymmetric hydrogenation of α,β-unsatured aldehydes (Scheme 2).[9] In this system,

---

[6] G. Filippini, F. Amato, C. Rosso, G. Ragazzon, A. Vega-Penaloza, X. Companyo, L. Dell'Amico, M. Bonchio, M. Prato *Chem* **2020,** *6*,3022–3037

[7] M. Bortolami, D. Rocco, B. Simonis, M. Feroci, F. Vetica *Synth. Commun.* **2023**, *53*, 1647– 1663

[8] M.Malahu, B.List, *Angew. Chem. Int. Ed.*, **2013**, *52*, 518-533

[9] S. Mayer, B. List, *Angew. Chem. Int. Ed.*, **2006**, *45*, 4193-4195

the ionic catalyst is composed by a cationic achiral morpholinium moiety, responsible for the formation of an iminium ion, and an anionic counteranion, a chiral phosphate based on a BINOL scaffold, which is responsible for the asymmetric induction. Specifically, after the iminium ion is formed from the aldehyde and morpholine, it interacts with the chiral phosphate to create a chiral-ion pair intermediate. Consequently, the interaction between this chiral intermediate and the dihydropyridine can only occur on the non-shielded face, leading to an enantioenriched product.

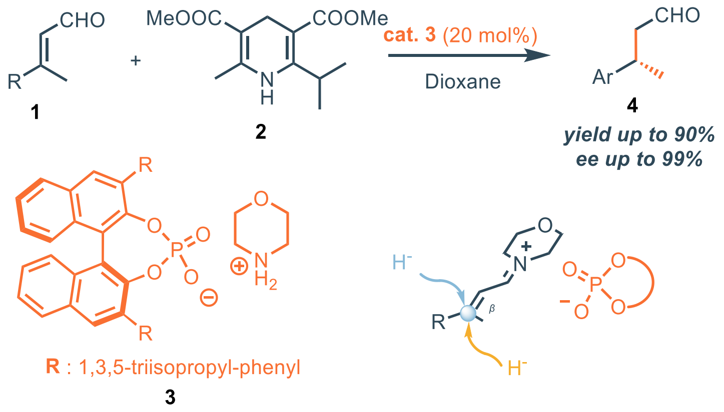

Scheme 2. Hantzsch ester-mediated asymmetric hydrogenation of α,β-unsatured aldehydes under ACDC paradigma proposed by List and coworkers

It is worth noting that the chiral iminium ion intermediate (primarily E-isomer) exists in equilibrium with its Z-conformer via dienamine formation, which could potentially lead to a lower enantiomeric excess. However, it has been demonstrated that, assuming hydride transfer is the rate-determining step, the nucleophilic attack of the hydride on the E-isomer is faster than on the Z-isomer, thus yielding the desired product with high ee. This approach to the enantioselective 1,4-reduction of α,β-unsaturated aldehydes has proven to be robust and efficient, capable of catalyzing the reduction of both aromatic and aliphatic aldehydes, such as citral.

Aim of the project

This investigation focused on the development of a novel strategy in asymmetric nano-organocatalysis by exploring the largely uncharted territory of enantioselective iminium ion catalysis mediated by **NCDs**. The central aim of this work was to conceptualize and successfully implement the first application of Asymmetric Counteranion-Directed Catalysis (ACDC) utilizing a nanostructured catalytic platform. The core of this approach lies in a paradigm shift from traditional methods that rely on intrinsically chiral nanocatalysts. Instead, this study pioneered a system wherein catalytically active, yet achiral, **NCDs** were paired with a discrete, enantiopure chiral counteranion to govern the stereochemical outcome of the reaction. Specifically, the catalytic salt was formed *in situ* between the primary amine functionalities on the **CD** surface and a chiral Brønsted acid, (S)-TRIP, which served as the sole source of chirality. The viability of this concept was demonstrated using the enantioselective transfer hydrogenation of various α,β-unsaturated aldehydes with a Hantzsch ester as the terminal reductant. This catalytic system proved to be highly reactive, operating with a catalyst loading of just 5 mol% and delivering yields up to 88% and enantiomeric excesses (ee) up to 84% (Scheme 3).[10]

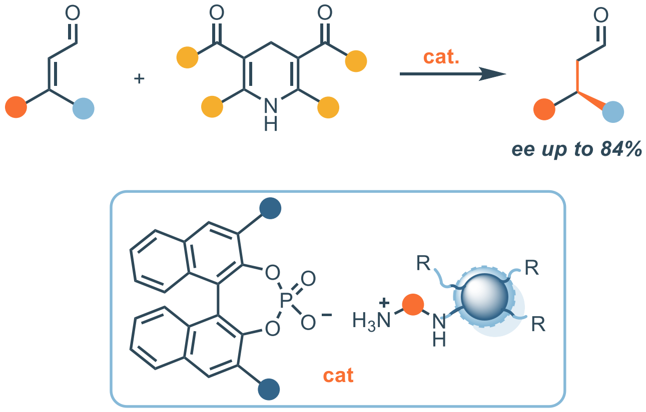

Scheme 3. **NCDs** in asymmetric aminocatalysis *via* ACDC

Results and Discussion

Design, synthesis, purification and characterization of Nitrogen-doped CDs

The **NCDs** were prepared from L-Arginine and various primary alkyl amines as starting materials, following a previously reported procedure.[11] Specifically, 1,4-diaminobutane and 1,2-diaminoethane were used for the synthesis of **CDs3** and **CDs4**, respectively, while the chiral diamines (R,R)-1,2-cyclohexanediamine and (S,S)-1,2-cyclohexanediamine were employed for the preparation of the chiral nanoparticles **CDs1** and **CDs2**. The synthesis began with the hydrothermal treatment of molecular precursors at 240 °C for 180 seconds, followed by filtration to remove large carbon particles and insoluble organic compounds. Subsequently, dialysis against water was performed to eliminate

---

[10] A. Carioscia, E. Cocco, M. E. Casacchia, G. Gentile, M. Mamone, G. Giorgianni, E. Incerto, M. Prato, F. Pesciaioli, G. Filippini, A. Carlone, *ACS Catal.* **2024**, *14*, 13429–13438

[11] *a)* L. Đordevic, F. Arcudi, A. D'Urso, M. Cacioppo, N. Micali, T. Bürgi, R. Purrello, M. Prato, *Nat. Commun.* **2018**, *9*, 3442; *b)* L. Đordevic, F. Arcudi, M. Prato, *Nat. Protoc.* **2019**, *14*, 2931–2953

soluble molecular species. Finally, the purified **CDs** were obtained as yellowish solid materials through freeze-drying (Figure 1a).[12]

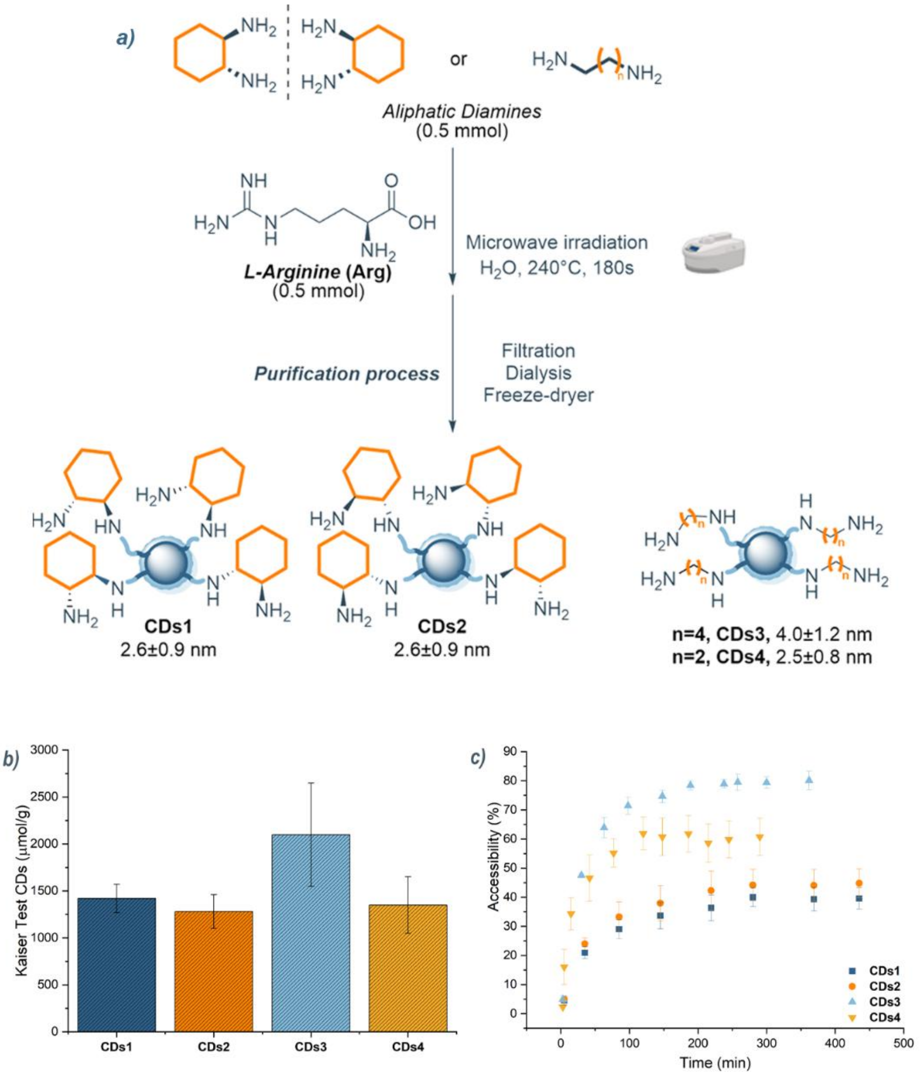

Figure 1. Synthesis, purification and characterization of Nitrogen-doped **CDs**

To enable the application of these **CDs** in aminocatalysis, it was essential to determine the density of amine moieties on their surface. A Kaiser Test (KT) was conducted for this quantification. In this analysis, ninhydrin reacts with aliphatic primary amines on the nanomaterial surface to generate Ruhemann's purple dye, which can be identified and measured by UV-vis spectroscopy.[13] All tested **CDs** showed a positive result for the presence of primary amines on their surface, indicated by the characteristic purple color. Both **CDs1** and **CDs2** exhibited a comparable number of amines,

---

[12] G. Gentile, M. Mamone, C. Rosso, F. Amato, C. Lanfrit, G. Filippini, M. Prato, *ChemSusChem* **2023**, *16*, e202202399

[13] a) E. Kaiser, R. L. Colescott, C. D. Bossinger, P. I. Cook, *Anal. Biochem.* **1970**, *34*, 595–598; b) M. Garrido, L. Gualandi, S. Di Noja, G. Filippini, S. Bosi, M. Prato, *Chem. Commun.* **2020**, *56*, 12698–12716

measured at 1420±150 µmol/g and 1280±180 µmol/g, respectively. Interestingly, **CDs3** had a higher amine content at 2100±550 µmol/g, while **CDs4** contained approximately 1350±300 µmol/g of primary amino groups (Figure 1b). The fact that the Kaiser test was conducted at high temperatures (120 °C) ensured the complete reaction of all amine moieties with ninhydrin. Additionally, a time-dependent Kaiser Test performed at room temperature allowed for the determination of the reactivity of primary aliphatic amines, with the time-dependent accessibility reported as a percentage of the value measured at 120 °C. Consistent with previous data, **CDs3** showed the highest accessibility value (80±5%), whereas **CDs4** (61±6%), **CDs1** (40±4%), and **CDs2** (45±5%) had lower values (Figure 1c).

Rational optimization of the reaction conditions

The optimization for the enantioselective 1,4-reduction of the model aldehyde **5a** consisted in the separate evaluation of several parameters, such as the type of **CDs**, the structure of **HE**, the evaluation of several **CPAs**, as well as temperature and solvent screenings. All the variables that were optimized are displayed in Figure 2, while the results of the optimization studies are summarized in Table 1. A preliminary screening using dihydropyridine **H1** (the simplest Hantzsch' ester), (S)-TRIP **CPA 1** (20 mol%), and **CDs3** (20 mol%) in toluene (c = 0.1 M) provided encouraging results after 24 hours. While almost complete conversions were observed, the initial yields (47%) and enantiomeric excesses (56%) were modest, indicating room for improvement.

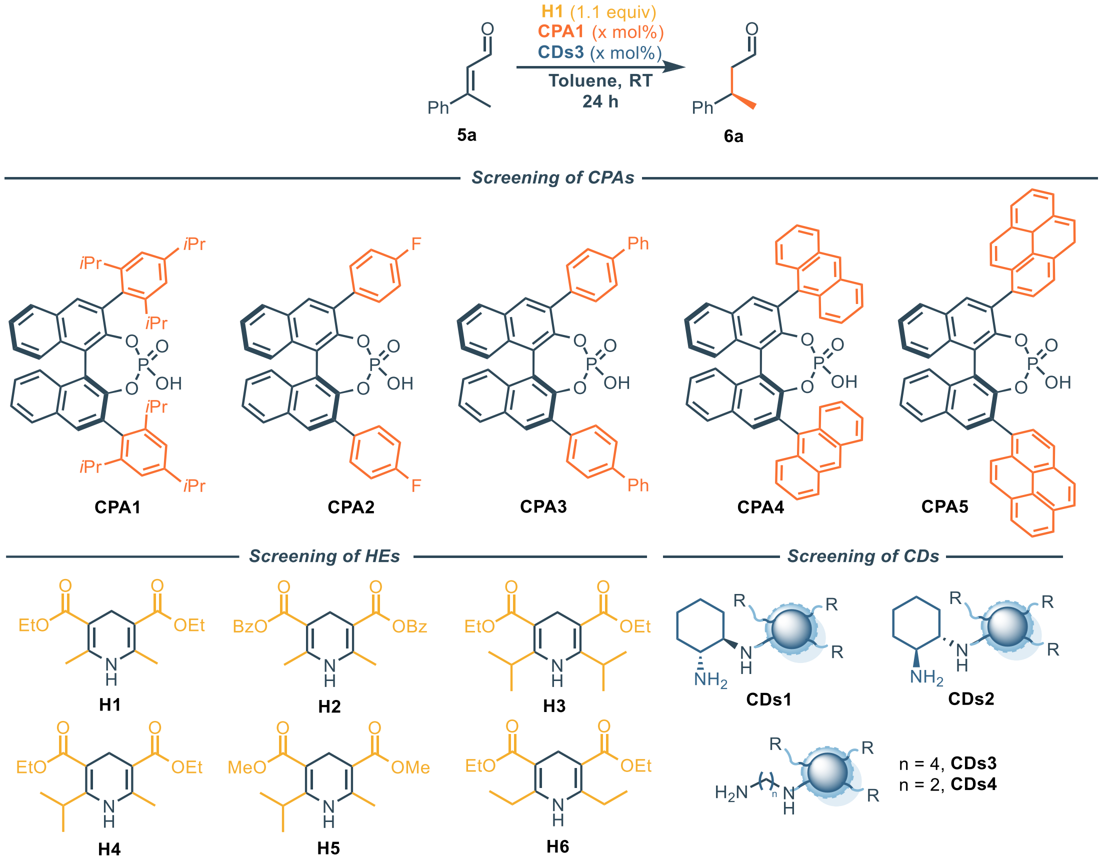

Figure 2. Model reaction and structure of the reagents screened

The optimization process began with a screening of different **CD** types (Entries 1-4, Table 1). KT analysis provides the density of amine groups on the **CDs**, defined as μmol of primary amines per g of CDs (μmol/g); thus the catalyst loading is evaluated as the equivalents of amines with respect to the substrate **5a**. **CDs3** proved to be the optimal choice, which was consistent with its higher accessibility of surface amino groups. Notably, using the opposite enantiomer of the nanocatalyst (**CDs1** and **CDs2**) had no observable effect on the stereoinduction of the reaction (entries 1-2). This contrasts with previous reports of homogeneous ACDC employing chiral primary amines, where a match/mismatch effect could significantly impact the ee.[14] Once the most efficient **CDs** type was identified, various **CPAs** were screened. (S)-TRIP (**CPA 1)** was confirmed as the most effective, while other CPAs, despite achieving almost total conversion, yielded only mediocre results in terms of yield and ee (entries 5-8, for further details see *Experimental Section*). Among the different solvents tested, toluene emerged as the best option, as a nonpolar solvent which probably favours the formation of a tight ion pair (entries 9-12, for further details see *Experimental Section*). Reasonably, A more stable, tighter ion pair creates a more rigid and defined chiral pocket around the reactive center, forcing

---

[14] N. J. A. Martin, B. List, *J. Am. Chem. Soc.*, **2006**, *128*, 13368-13369

incoming substrates to approach from a specific direction, thus enhancing enantioselectivity (See Chapter 1). Finally, a screening of different Hantzsch esters was performed. Increased steric hindrance at C-3 and C-5 (dihydropyridine **H2**) led to a reduced reaction rate and significant loss of stereoinduction (entry 13). Conversely, the presence of two bulky isopropyl substituents at C-2 and C-6 (dihydropyridine **H3**) resulted in a complete loss of reactivity (entry 14). A remarkable balance was achieved with the non-symmetric dihydropyridine **H4**, which exhibited a significant positive effect on enantioinduction (entry 15). Further modifications to the ester moiety (**H5**) did not lead to any improvements in ee (entry 16). Interestingly, the presence of two ethyl moieties at C-2 and C-6 (dihydropyridine **H6**, entry 17) led to an inversion in the enantioselectivity of the reaction. This unexpected inversion effect has been subsequently investigated and is indeed the main topic of the following chapter (*Chapter 3*).

A consistent observation was the discrepancy between the conversion and the yield of the reaction. This can be explained by aza-Michael additions of free amino groups on the surface of the **CDs** to the formed iminium ion, resulting in a loss of product, even though analysis of the recovered **CDs** did not yield conclusive information. The starting unsaturated aldehyde **5a** may also react with other functional groups present, although in lower abundance, on the surface of **CDs**, such as alcohol moieties. Another possible explanation could involve deterioration of the product; however, no variation in yield was observed over time, thus rendering this hypothesis less likely. Control experiments, however, yielded results that support the notion that **CDs** contribute, at least in part, to the observed yield decrease. It should be emphasised that this phenomenon is probably the outcome of multiple concurrent factors, the precise contribution of which remains to be fully elucidated. For instance, when the reaction was performed in the absence of dihydropyridine (entry 18), a conversion of 74% was observed with less than 5% yield. This outcome corroborated the result obtained in entry 14, where compound **5a** was consumed without reacting with dihydropyridine **H3**. A similar behavior was noted when the reaction was conducted in the absence of the **CPA** (entry 19). Moreover, entry 20 demonstrated that the formation of the iminium ion intermediate is crucial for transmitting chiral information: performing the reaction without **CDs** resulted in almost complete conversion and high yield, but a racemic product was isolated, indicating that in the absence of **CDs**, the reaction proceeds *via* Brønsted-acid catalysis. Additionally, **5a** was fully recovered in the absence of both **CDs** and **CPA** (entry 21), suggesting that retention of the reagent on the **CDs** could be the major side reaction.

Table 1. Optimization of the reaction conditions: selected experiments [a]

Entry	Deviation with respect to the starting conditions	Conv (%) [b]	Yield (%) [c]	ee (%) [d]
1	**CDs1** instead of **CDs3**	98	12	33
2	**CDs2** instead of **CDs3**	94	33	35
3	---	99	47	56
4	**CDs4** instead of **CDs3**	99	25	55
5	**CPA2** instead of **CPA1**	83	16	9
6	**CPA3** instead of **CPA1**	90	30	12
7	**CPA4** instead of **CPA1**	95	28	8
8	**CPA5** instead of **CPA1**	92	25	rac
9	$CHCl_3$ instead of toluene	99	41	54
10	Dioxane instead of toluene	92	47	30
11	EtOAc instead of toluene	99	27	37
12	THF instead of toluene	93	21	48
13	**H2** instead of **H1**	82	48	8
14	**H3** instead of **H1**	82	<5	---
15	**H4** instead of **H1**	99	59	78
16	**H5** instead of **H1**	99	66	70
17	**H6** instead of **H1**	>95	48	-55
18	No Hantzsch ester	74	<5	---
19	No **CPA**	43	<5	---
20	No **CDs**	90	62	rac
21	No **CDs**, no **CPA**	5	<5	---
22	**H4** instead of **H1**, 10 °C	99	70	78
23	**H4** instead of **H1**, -20 °C	99	74	83
24[e]	**H4** instead of **H1**, -20 °C, 5 mol% **CPA** and **CDs**	92	86[f]	82
25	**H4** instead of **H1**, -20 °C, 5 mol% **CPA**, 5 mol% benzylamine	84	41	81
26	**H4** instead of **H1**, -20 °C, 5 mol% **CPA**, 5 mol% butylamine	86	40	81

[a]Under the starting conditions, the reactions were performed with **5a** (14.6 mg, 0.1 mmol, 1 equiv), **CDs3** (9.6 mg, 0.02 mmol, 0.2 equiv), **CPA1** (15 mg, 0.02 mmol, 0.2 equiv), and **H1** (27.9 mg, 0.11 mmol, 1.1 equiv) in

toluene (1 mL, 0.1 M) for 24 h at RT. [b] Conversion of **5a**, determined by ^{1}H NMR using triphenylmethane as an internal standard. [c] Determined by ^{1}H NMR using triphenylmethane as an internal standard. [d] Determined by chiral HPLC analysis. [e] Reaction performed on a 0.25 mmol scale. [f] Isolated yield.

Lowering the reaction temperature allowed for better control over reactivity, leading to increased yield and ee (entries 22 and 23). Furthermore, reducing the catalyst loading did not negatively impact reactivity but instead increased the reaction yield (entry 24). To further prove the system's efficiency, the reaction was tested with primary molecular amines (benzylamine and butylamine, Entries 25 and 26) that mimic the moieties on the **CD** surface. While the ee values were similar, the yield drastically dropped, showcasing the superior efficiency of using the employed **CDs**. Interestingly, these findings indicate that **CDs3** exhibits a higher turnover number (TON) than comparable molecular catalytic systems, thereby achieving greater overall productivity. The observation that nanostructures can outperform their molecular counterparts is particularly noteworthy. Speculatively, this enhanced reactivity could be attributed to the presence of diverse polar hydrogen-bonding functional groups on the surface of **CDs3** (e.g., amines, carboxylic acids, alcohols), which may further activate the reaction intermediates, or alternatively to the contribution of London dispersion forces.[15]

Substrate Scope and Mechanistic Investigations

With the optimized conditions (entry 24, Table 1) in hand, the generality of the reaction was explored (Figure 3). The reaction performed well with aromatic substrates bearing both electron-donor substituents (**6a-d**) and electron-withdrawing groups (**6e-h**). A good result was also obtained when the steric hindrance on the reacting carbon was increased (**6d**). Moreover, an interesting behavior arose when the pure Z isomer of **5a** was used: the Z isomer of **5a** did not react to provide **6a**, suggesting it is less reactive and its isomerization does not occur under these conditions, unlike previous reports at higher temperatures. However, the system was not efficient in reducing aliphatic substrates, as demonstrated by the dramatically lower ee obtained when citral (1:1 E/Z mixture) **5i** was used, despite achieving a yield comparable to aromatic substrates.

---

[15] a) G. Lu, R. Y. Liu, Y. Yang, C. Fang, D. S. Labrecht, S. L. Buchwald, P. Liu, *J. Am. Chem. Soc.*, **2017**, *139*, 16548-16555; b) L. Rummel, P. R. Schreiner, *Angew. Chem. Int. Ed.*, **63**, e202316364; c) F. Mocci, L. de Villiers Engelbrecht, C. Olla, A. Cappai, M. F. Casula, C. Melis, L. Stagi, A. Laaksonen, C. M. Carbonaro, *Chem. Rev.*, **2022**, *122*, 13709-13799

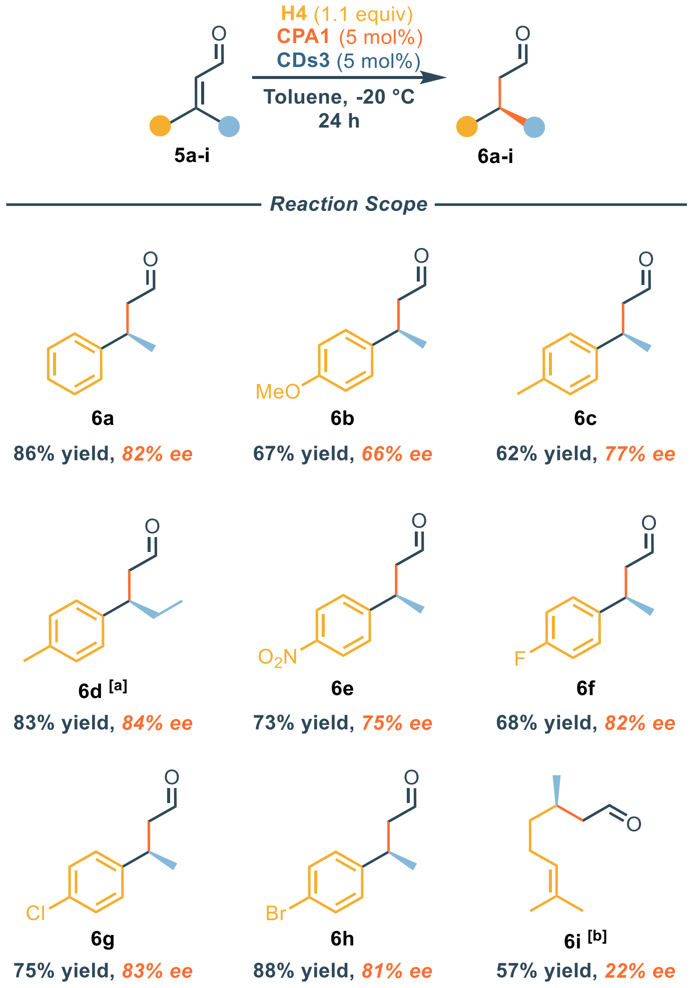

Figure 3. Scope of the reaction. Reactions performed with **5** (0.25 mmol, 1 equiv.), **CDs3** (0.0125 mmol, 0.05 equiv.), **CPA1** (0.0125 mmol, 0.05 equiv.), **H4** (0.275 mmol, 1.1 equiv.) in toluene (2.5 mL, 0.1 M) for 24 hours at -20 °C. Yields of isolated compounds are reported. Enantiomeric excess (ee) determined by chiral HPLC analysis. [a] **5d** was produced as an inseparable E/Z mixture (4:1) and used as such; isolated yield corrected with respect to E content. [b] **5i** used as 1:1 E/Z mixture; reaction carried out on a 0.5 mmol scale.

To confirm the formation of the iminium ion intermediate on **CDs** and the reliability of this approach, ^{19}F-nuclear magnetic resonance (NMR) spectroscopy was utilized (**Figure 4**). Using the fluorinated aldehyde **5f** as a probe enabled the display of ^{19}F-NMR signals that could be attributed to the *in situ* formation of covalent fluorinated intermediates. The chemical shifts of the iminium ions were identified by comparing them with iminium ions formed by reaction with dibenzylamine and butylamine (**Ia** and **Ib**, respectively). Remarkably, the formation of iminium ions on **CDs3** (**I-CDs3**) showed broad signals between -108.0 and -107.7 ppm, like **Ia** and **Ib**, thereby confirming the formation of various iminium ions on the surface of **CDs3**.

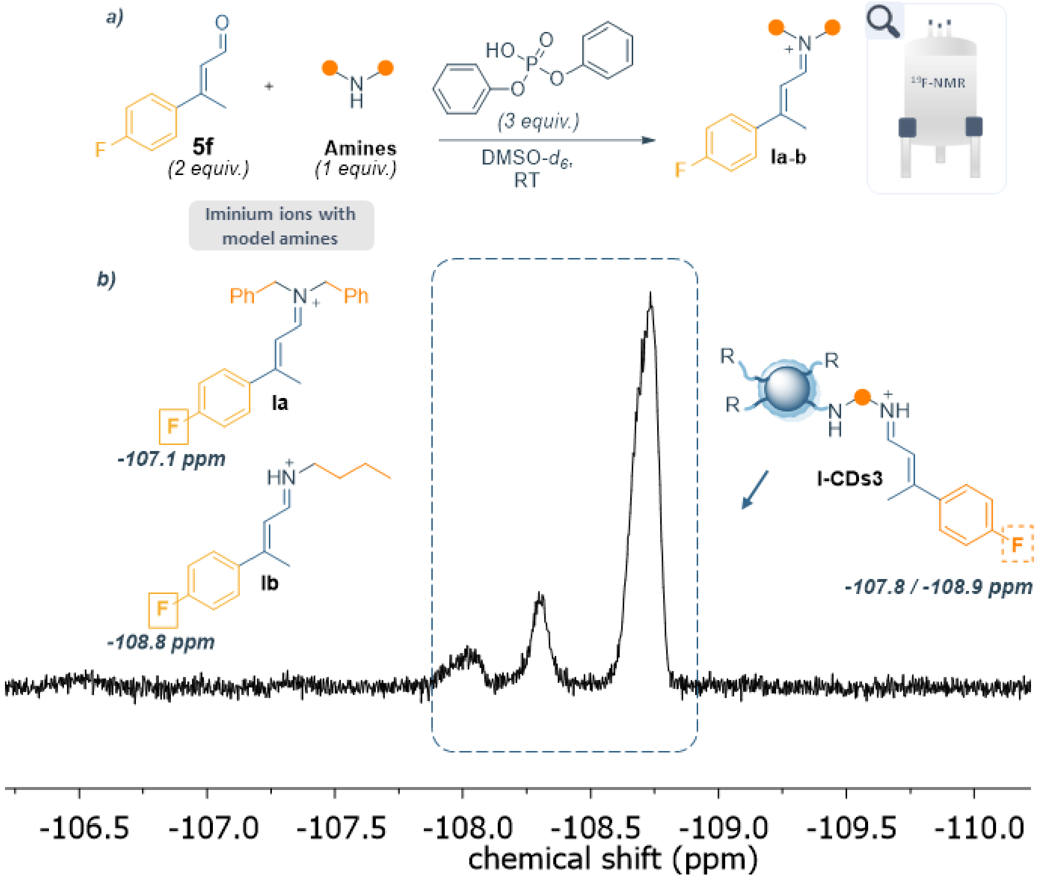

Figure 4. (a) Reaction scheme for the formation of iminium ion intermediates with model amines and compound 1f; (b) 19F NMR spectrum of **CDs3** and 1f in DMSO-d_6 to detect the superficial iminium ion formation.

Based on the outcomes from reaction optimization, control experiments, and substrate scope, a proposed mechanism is outlined in Figure 5. Once the catalytic species **I-CDs** is formed (from the amine-doped **CDs** and the corresponding **CPA**), it reacts with the α,β-unsaturated aldehyde **5**, forming the iminium ion intermediate which then creates an ionic couple (**II-CDs**) with the chiral phosphate. At this stage, the phosphate can direct the approach of the dihydropyridine through hydrogen bonding, leading to the transition state (TS-**CDs**). In this specific coordination of both the iminium ion and the dihydropyridine to the phosphate allows for the enantioselective hydride transfer, releasing the chiral neutral enamine intermediate **II-CDs**. The enamine intermediate is subsequently hydrolyzed, and the **CDs** are regenerated, ready to reform the catalytic species **I-CDs** with the regenerated **CPA**.

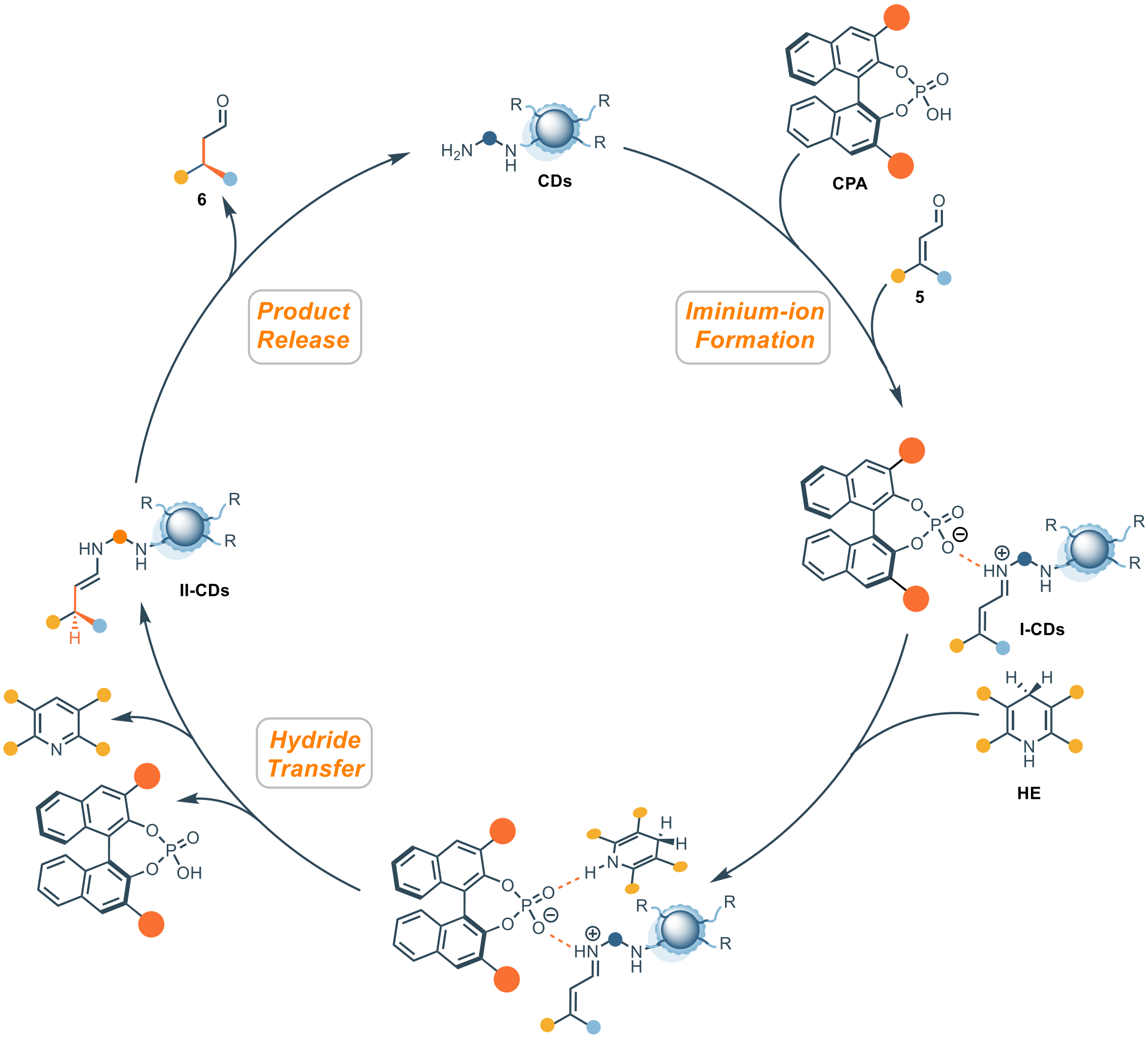

Figure 5. Proposed mechanism

Conclusions

This study reports, for the first time, an example of asymmetric iminium ion nano-organocatalysis achieved through ACDC. The innovative aspect of the work does not primarily reside in surpassing the performance of well-established privileged organocatalysts, but rather in demonstrating the potential of carbon dots (**CDs**) as asymmetric nanocatalysts and in highlighting their growing significance as organocatalysts within materials science. Research in this area remains scarce, and, to our knowledge, no prior examples exist where a **CDs**-based LUMO-lowering activation of carbonyl compounds has been accomplished by pairing an achiral nanocatalyst with a chiral, enantiopure counterion serving as the stereocontrolling element. This approach streamlines the selection of the chiral component. A systematic investigation of reaction conditions, various **CPAs**, and different Hantzsch esters led to optimized parameters that proved reliable across multiple substrates, consistently affording high enantioselectivity. Among the carbon dots evaluated, **CDs3** delivered the best results, a performance attributed to the greater accessibility of amino functionalities on its surface. In direct comparison, simple primary amines such as benzylamine and butylamine generated product **6a** in only moderate yields (up to 41%) despite providing good enantioselectivity, whereas **CDs3** exhibited markedly higher catalytic activity in the same transformation. The presence of the iminium ion intermediate on the **CDs** surface was verified through ^{19}F NMR experiments. Future efforts within our group are focused on extending this carbon-dot-mediated LUMO-lowering activation via ACDC to other synthetically relevant transformations.

Experimental section

Instrumentation

Nuclear magnetic resonance analyses (^{1}H-,^{19}F- and ^{13}C-NMR spectra) were acquired using a Bruker Advance III 400 MHz spectrophotometer. Chemical shifts (δ) are reported in ppm relative to residual solvent signals for ^{1}H- and ^{13}C-NMR (^{1}H-NMR: 7.26 ppm for $CDCl_3$; ^{13}C-NMR: 77.16 ppm for $CDCl_3$). Both ^{13}C-NMR and ^{19}F-NMR spectra were acquired with ^{1}H broadband decoupled mode. Coupling constants are given in Hz. ^{1}H-NMR yields were measured by analysing the reaction mixture using *t*riphenylmethane as internal standard. Chromatographic purifications of compounds **5a-h**, **6a-h**, **7a-h**, **8a-h**, **9a-h** and the dihydropyridines were performed using automated Biotage® Isolera LS Systems.

Material and methods

CPAs were purchased from BLDPharm, compounds **21a-i** were purchased from Merck and used as received unless otherwise stated. Silica Gel 60A (35-70 µm), HPLC solvents and analytical grade solvents were purchased from Merck. Compounds **5a-h**, **6a-h**, **7a-h**, **8a-h**, **9a-h** and the dihydropyridines were prepared as shown below. The Carbon Dots loading has been evaluated by KT analysis at 120 °C.

Determination of enantiomeric purity

Chiral HPLC analyses were acquired using an Agilent 1220 Infinity II liquid chromatographer equipped with Phenomenex columns (100 × 4.6 mm): Lux 3 µm i-Cellulose 1, Lux 3 µm i-Cellulose 2, Lux 3 µm i-Cellulose 3, and Lux 3µm-Amylose 2. HPLC analyses of 10a-h were performed on the corresponding alcohols obtained by reduction of the aldehydes using NaBH4 in methanol. HPLC analysis of 10i was performed on the compound obtained via reductive amination with benzylamine followed by tosylation of the secondary amine (N-benzyl-N-(3,7-dimethyloct-6-en-1-yl)-4-methylbenzenesulfonamide). HPLC traces were compared to racemic samples prepared using diphenyl phosphate (CAS Number: 838-85-7) and piperidine as catalysts, in toluene at 50 °C for 2 h. Optical rotations were measured on a ZUZI 412 Digital Polarimeter (tube length: 100 mm).

Determination of absolute configuration

The absolute configurations of the optically active compounds **6a-b** were determined on the basis of the measured optical rotations that were compared with literature values. All other absolute configurations were assigned by analogy based on a uniform reaction mechanism and the uniform elution order observed in the HPLC chromatograms.

Preparation of Carbon Dots and Characterisation of Superficial Amines

CDs1-4 synthesis: Arg (87.0 mg, 0.5 mmol, 1 equiv.), Milli-Q water (100.0 mL), along with one of the alkyl diamines (0.5 mmol, 1 equiv.), were introduced in a sealable microwave reaction vessel and heated in a microwave reactor (200 W) at 240 °C for 180 seconds. After this, the color of the reaction mixture turns from transparent to brown. The solution was then diluted with water and filtered through a 0.1 μm PTFE microporous membrane. The crude obtained was dialyzed against Milli-Q water through a dialysis membrane (0.5-1 kDa Cut-Off) Float-A-Lyzer® for 48 hours. After the **CDs** were lyophilized from their aqueous solution, they were obtained as a yellow foamy solid. Due to high hygroscopicity, the samples were stored in a desiccator. Scheme 4 summarizes the synthetic workflow.

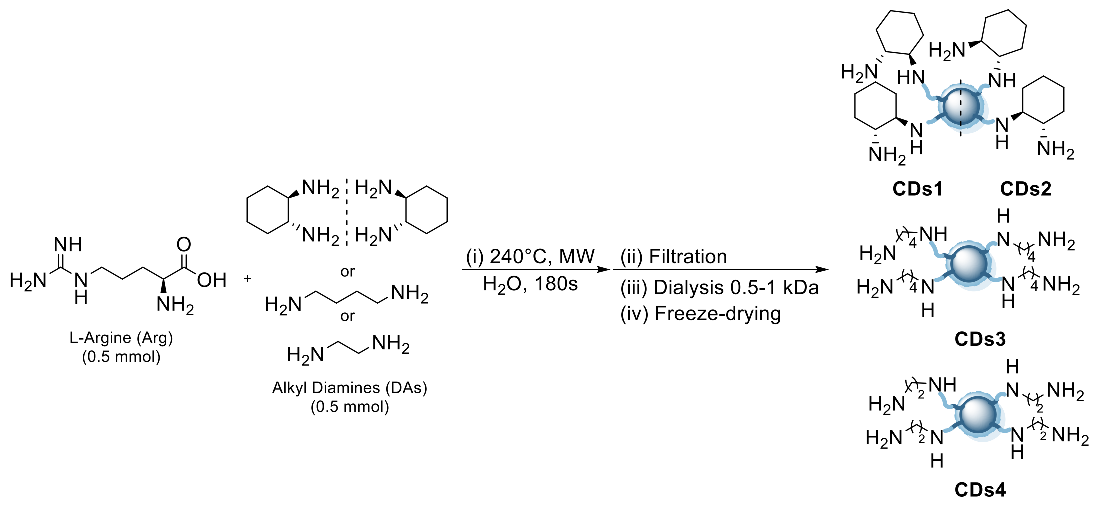

Scheme 4. Synthesis of the **CDs**.

CDs1 were synthesized according to a reported procedure.[12]

L-Arginine (87.0 mg, 0.5 mmol, 1 equiv.), (R,R)-1,2-cyclohexanediamine (57.0 mg, 1 equiv.) and Milli-Q water (100.0 mL) were irradiated into a microwave reactor (200 W) at 240 °C for 180 seconds. The aqueous solution of **CDs1** was lyophilized resulting in a yellow solid (**CDs1**: 21.3 mg, 15% mass yield). Analytical data in accordance with literature report.

CDs2 were synthesized according to a reported procedure.[12]

L-Arginine (87.0 mg, 0.5 mmol, 1 equiv.), (S,S)-1,2-cyclohexanediamine (57.0 mg, 1 equiv.) and Milli-Q water (100.0 mL) were irradiated into a microwave reactor (200 W) at 240 °C for 180 seconds. The aqueous solution of **CDs2** was lyophilized resulting in a yellow solid (**CDs2**: 20.8 mg, 14% mass yield). Analytical data in accordance with literature report.

CDs3 were prepared by following the literature.[13] L-Arginine (87.0 mg, 0.5 mmol, 1 equiv.), 1,4-Diaminobutane (BDA) (50 mL, 0.5 mmol, 1 equiv.) and Milli-Q water (100.0 mL) were irradiated into a microwave reactor (200 W) at 240 °C for 180 seconds. The aqueous solution of **CDs3** was lyophilized resulting in a yellow solid (**CDs3**: 15.6 mg, 17% mass yield). Analytical data in accordance with literature report.

CDs4 were prepared accordingly to the literature.[11] L-Arginine (87.0 mg, 0.5 mmol, 1 equiv.), 1,2-Diaminoethane (EDA) (32 mL, 0.5 mmol, 1 equiv.) and Milli-Q water (100.0 mL) were irradiated into a microwave reactor (200 W) at 240 °C for 180 seconds. The

aqueous solution of **CDs4** was lyophilized resulting in a yellow solid (**CDs4**: 29.4 mg, 25% mass yield). Analytical data in accordance with literature report.

Kaiser test Procedure: Kaiser tests (KTs) were performed according to a modified protocol by employing a commercially available kit provided by Merck.[16] Generally, a test tube was filled with 1 mg of **CDs**. Next, 100 mL of a KCN solution in pyridine/water (Sol B), 75 mL of a ninhydrin solution in ethanol (Sol C), and 75 mL of a phenolic solution in ethanol (Sol A) were added. A rapid formation of the purple pigment is observed. The tube was sealed and the so obtained mixture was heated at 120 °C for 10 minutes. The resulting solution was diluted with ethanol in water (60% v/v, 1:18 dilution) and its absorption spectrum was recorded. For reference, a blank solution was also executed. At least three separate analyses were carried out for every sample. Primary amines on the carbon dots surface were thus quantified from the absorbance value recorded at 570 nm, considering a molar absorption coefficient for the ninhydrin derivative of 15000 M^{-1} cm^{-1} (Ruhemann's purple). Equation S1 was used to determine the KT value.

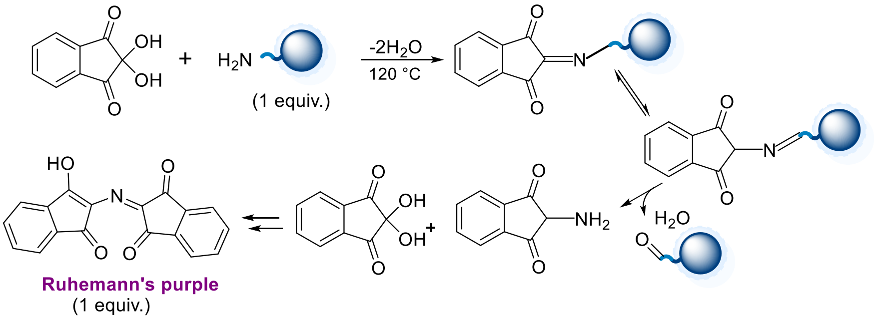

Scheme 5: Schematization of Kaiser test molecular mechanism.

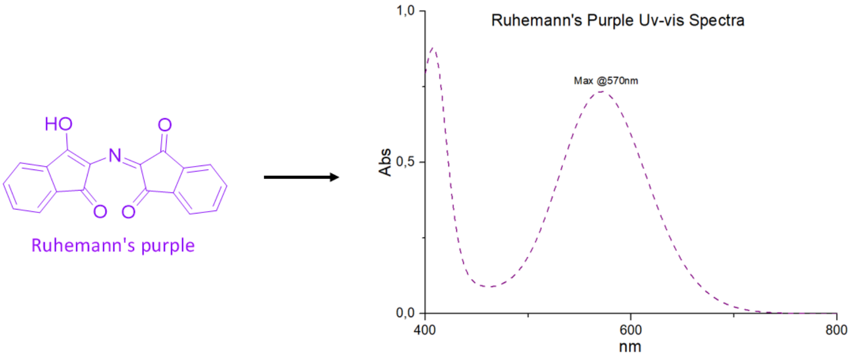

Scheme 6: Visible spectra of Ruhemann's purple dye.

---

[16] D. Iannazzo, A. Piperno, A. Ferlazzo, A. Pistone, C. Milone, M. Lanza, F. Cimino, A. Speciale, D. Trombetta, A. Saija, S. Galvagno, *Org. Biomol. Chem.* **2012**, *10*, 1025-1031

$$KT\ ({}^{\mu mol}/_{g}) = \frac{[Abs@570nm \times dil \times 10^6]}{\varepsilon \times Weight\ (mg)}$$

Equation 1: Calculation of primary amines on **CDs1**-**4**.

Room temperature Kaiser test Procedure (Accessibility %): In the accessibility experiments, the reaction mixture was kept at room temperature (25 °C) throughout the experiment. Therefore, to a known of **CDs** (about 1 mg), the Kaiser test solutions (Sol A, B and C) were added as previously described. An aliquot (20 mL) was collected, diluted, and analyzed. The experiment was repeated in triplicate for each **CDs** material. Equation **2** was used to determine the accessibility values.

$$Accessibility\ (\%) = \frac{KT\ (r.t)}{KT\ (120\ °C)} \times\ dil\ \times\ 100$$

Equation 2: Determination of the accessibility of the examined amines into the corresponding ninhydrin derivative.

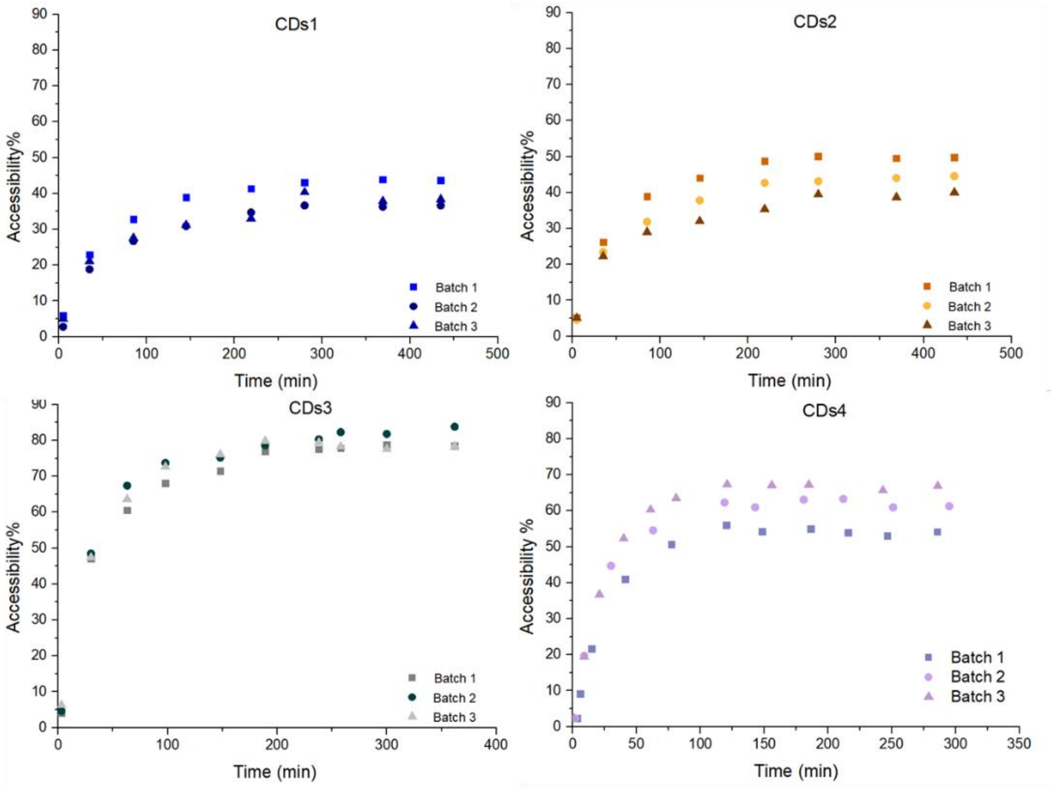

Figure 6: Time-dependent Kaiser test performed at 25°C for **CDs1**-**4**.

^{1}H and ^{19}F-NMR studies: First, the formation and stability of the iminium ions **Ia**-**b** derived from different representative amines (namely dibenzylamine and butylamine) have been studied with the fluorine aldehyde (**5f**) in DMSO-d$_6$. Then, the formation of iminium ions **I-CDs3** on the surface of the **CDs3** using the aldehyde **5f** have been performed**.** Therefore, the amine was added in a vial containing aldehyde in DMSO-d_6. After five minutes, the achiral phosphoric acid (3 equiv.) was added to the solution and immediately analysed through ^{1}H- and ^{19}F-NMR. ^{19}F-NMR (**Figure 7**) and ^{1}H-NMR (**Figure 8**) spectra have been used to characterize the so-formed iminium ion derivatives.

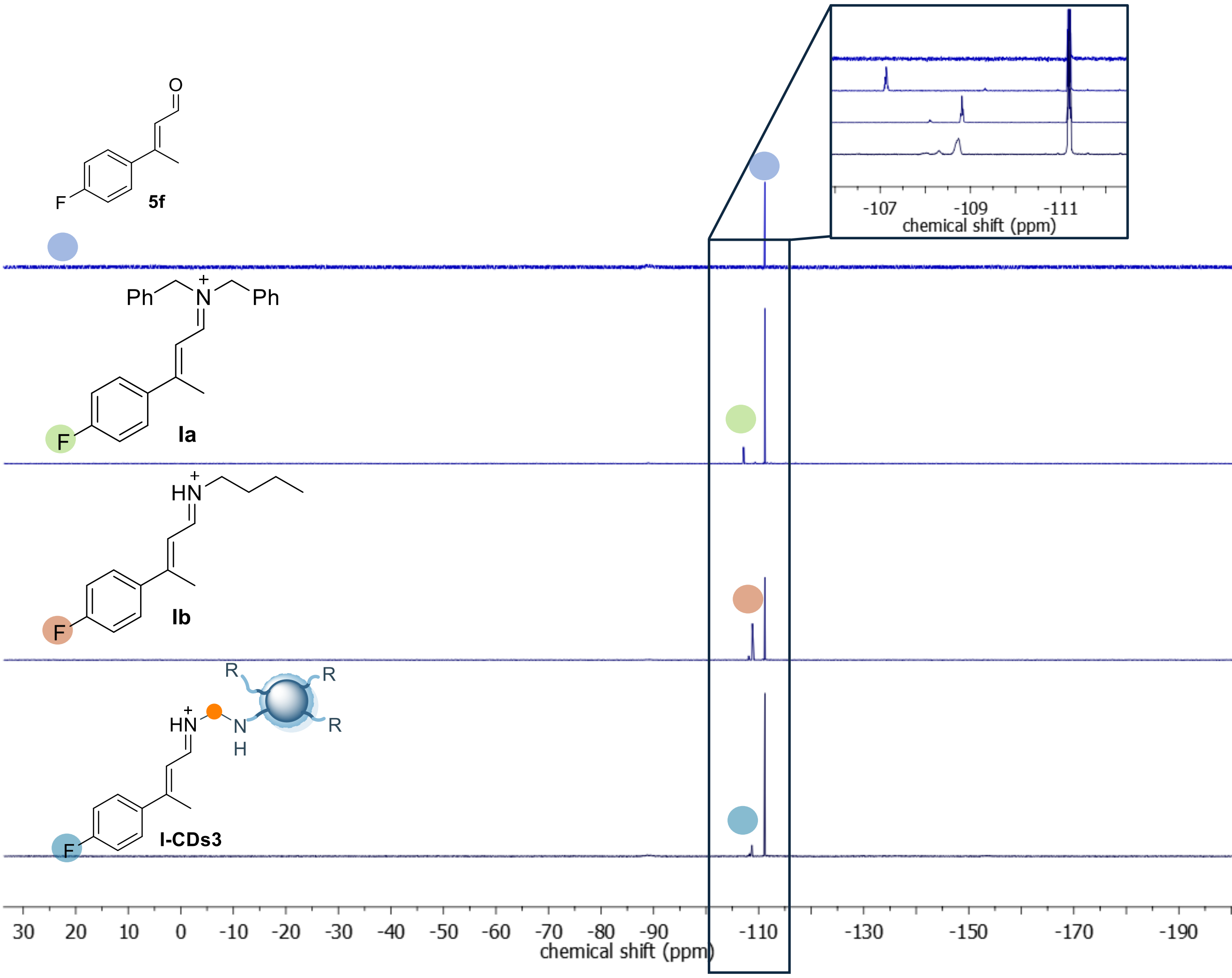

Figure 7: ^{19}F-NMR spectra of the *in-situ* formation of the iminium ions **Ia**-**b** and **I-CDs3** derived from aldehyde (**5f**) and respectively dibenzylamine, butylamine or **CDs3** in DMSO-d_6. Comparison between ^{19}F-NMR spectra of **1f**, and iminium ions **Ia**-**b** and **I-CDs3**.

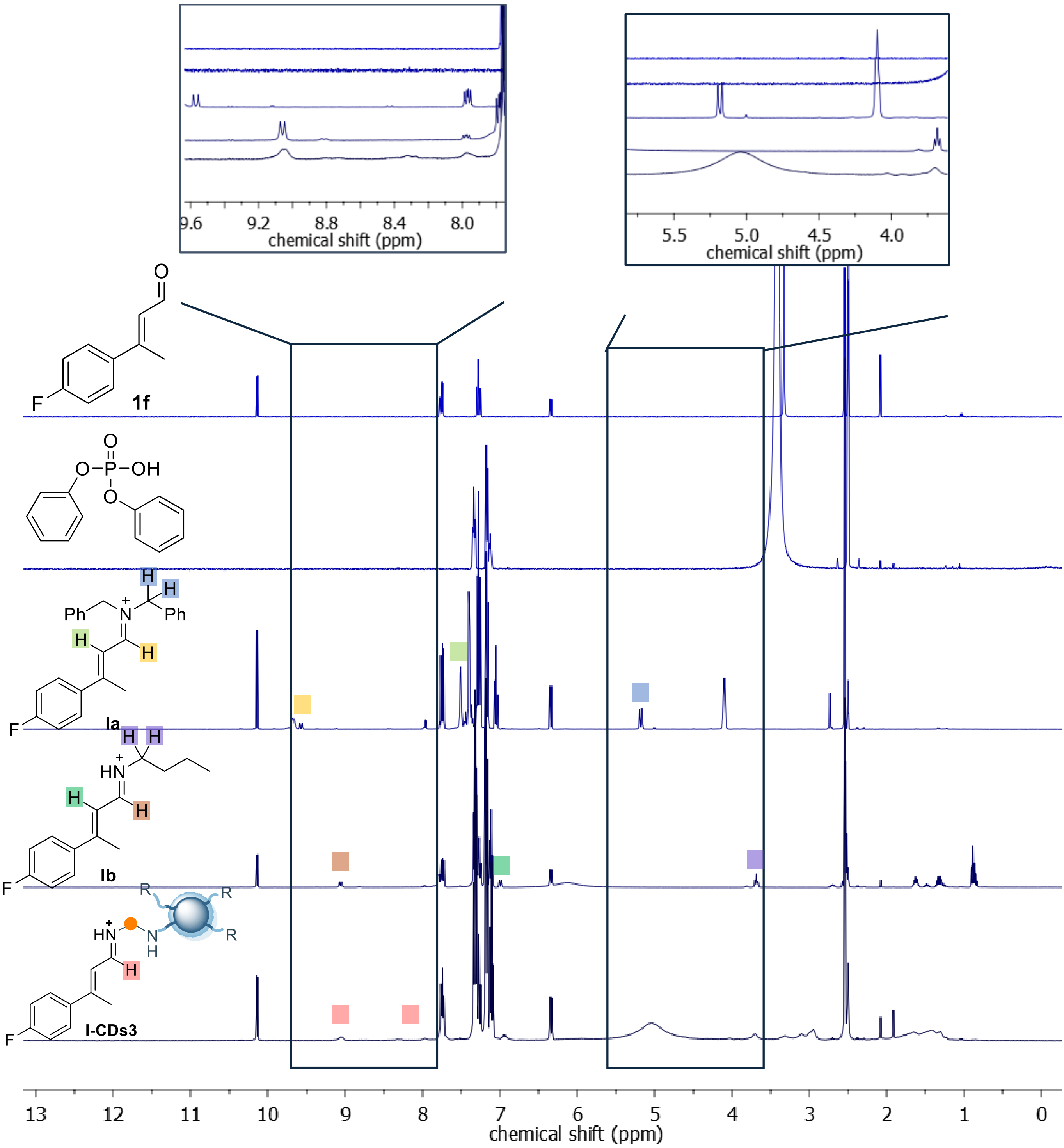

Figure 8: ^{1}H-NMR spectra of the in-situ formation of the iminium ions **Ia-b** and **I-CDs3** derived from aldehyde (**5f**) and respectively dibenzylamine, butylamine or **CDs3** in DMSO-d_6. Comparison between ^{1}H-NMR spectra of **5f**, and iminium ions **Ia-b** and **I-CDs3**.

Experimental procedures

General procedure for the nano-organocatalysed reactions

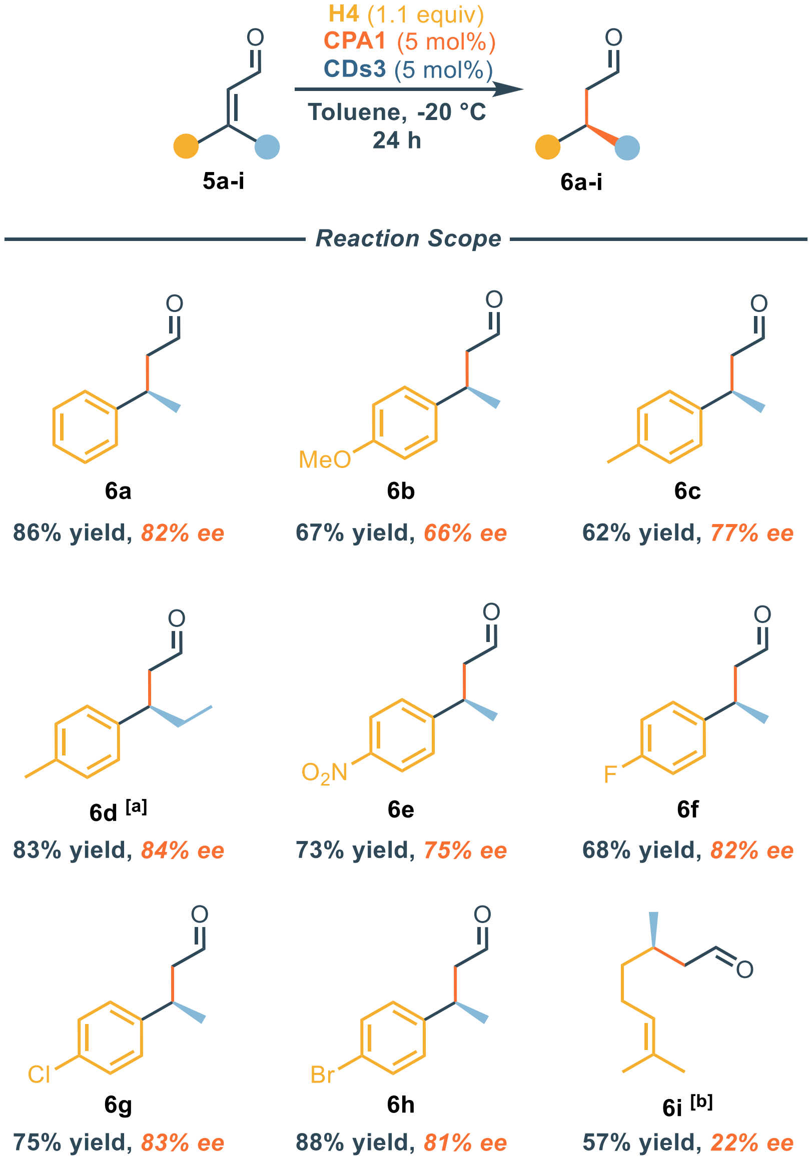

CDs (loading based on KT analysis at 120°C) were suspended in the solvent. Then the **CPA** was added, and the suspension was left to stir for 10 min. Then, the aldehyde was added, and the mixture was left to stir for 10 min. The Hantzsch's ester was added afterwards, and the suspension was left to stir until the completion of reaction, monitored through TLC analysis. The reaction was quenched with a saturated solution of NH_4Cl, the phases were separated, and the aqueous phase was extracted with DCM (3x5 mL). The organic phases were combined, dried over $MgSO_4$, filtered, and concentrated *in vacuo*. Purification over silica gel afforded the pure product.

Synthesis of substrates

General Procedure for the synthesis of ethyl (E)-3-phenylbut-2-enoate derivatives (8a-h)[17]

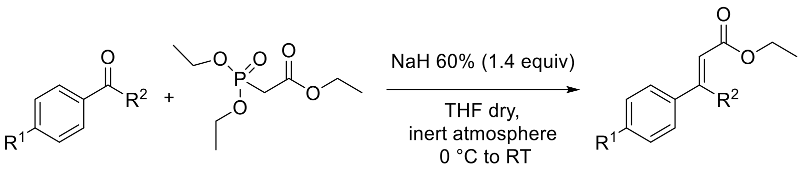

7a-h

8a-h

R^1=H, R^2=CH_3 **8a**
R^1=OMe, R^2=CH_3 **8b**
R^1=Me, R^2=CH_3 **8c**
R^1=H, R^2=CH_2CH_3 **8d**
R^1=NO_2, R^2=CH_3 **8e**
R^1=F, R^2=CH_3 **8f**
R^1=Cl, R^2=CH_3 **8g**
R^1=Br, R^2=CH_3 **8h**

NaH 60% dispersion in mineral oil (1.4 equiv.) was dissolved in anhydrous THF (0.2 M) at RT under inert atmosphere. The solution was then cooled down to 0°C and triethyl phosphonoacetate (1.5 equiv.) was added dropwise. The reaction was left to stir for 30 min ad 0 °C, and subsequently compound **7a**-**h** (1 equiv.) was slowly added. The reaction was then warmed up to room temperature and left to stir for 48-72 hours. After this time, the reaction was cooled down to 0 °C and quenched with a saturated solution of ammonium chloride, the phases were separated, and the water phase was extracted with ethyl acetate. The organic phases were then combined, washed with brine, dried over $MgSO_4$, filtered, and concentrated in vacuo. Purification over silica gel eluting in Petroleum/Ethyl Acetate 98:2 afforded the pure product.

---

[17] Y. Kanazawa, Y. Tscuchiya, K. Kobayashi, T. Shiomi, J. Itoh, M. Kikuchi, Y. Yamamoto, K. Nishiyama, *Chem. Eur. J.*, **2006**, *12*, 63-71

General Procedure for the synthesis of (E)-3-phenylbut-2-en-1-ol derivatives (9a-h)[18]

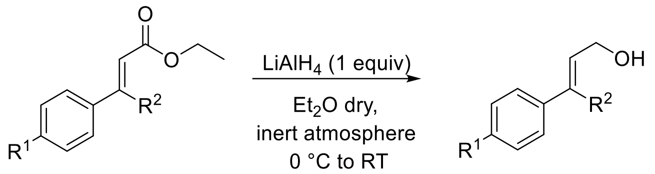

8a-h **9a-h**

R^1=H, R^2=CH_3 **9a**
R^1=OMe, R^2=CH_3 **9b**
R^1=Me, R^2=CH_3 **9c**
R^1=H, R^2=CH_2CH_3 **9d**
R^1=NO_2, R^2=CH_3 **9e**
R^1=F, R^2=CH_3 **9f**
R^1=Cl, R^2=CH_3 **9g**
R^1=Br, R^2=CH_3 **9h**

Compound **8a-h** (1 equiv.) was dissolved in anhydrous diethyl ether (0.8 M) under inert atmosphere. The solution was cooled down at 0 °C and a 1M solution of $LiAlH_4$ in diethyl ether (1 equiv.) was added dropwise. The reaction was allowed to warm to RT and left to stir at this temperature until completion (monitored through TLC analysis, Petroleum Ether/Ethyl Acetate 9:1, roughly 10 minutes). The reaction mixture was quenched with a saturated solution of $NaHCO_3$, the two phases were separated, and the aqueous phase was extracted with diethyl ether. The organic phases were combined, washed with brine, dried over $MgSO_4$, filtered, and concentrated in vacuo. The product was used with no further purifications. (Exception for **8d**: the reaction was conducted at -20 °C to avoid the reduction of the nitro group, the final product was purified over silica gel eluting in Petroleum Ether/Ethyl Acetate 9:1).

---

[18] X. Liu, J.-M. Pons, V. Monnier, L. Charles, A. Quintard, C. Bressy, *Eur J. Org. Chem.* **2022**, e202101475

General Procedure for the synthesis of (E)-3-phenylbut-2-enal derivatives (1a-h)[19]

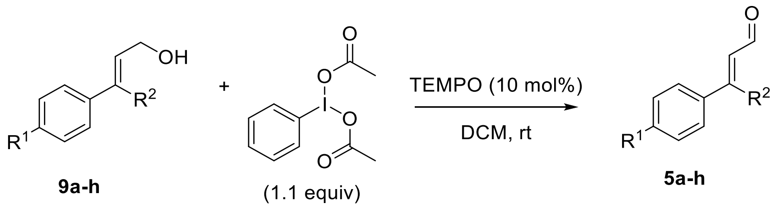

R^1=H, R^2=CH_3 **5a**
R^1=OMe, R^2=CH_3 **5b**
R^1=Me, R^2=CH_3 **5c**
R^1=H, R^2=CH_2CH_3 **5d**
R^1=NO_2, R^2=CH_3 **5e**
R^1=F, R^2=CH_3 **5f**
R^1=Cl, R^2=CH_3 **5g**
R^1=Br, R^2=CH_3 **5h**

Diacetoxyiodo(benzene)(BIAB) (1.1 equiv.) and compound **9a-h** (1 equiv.) were dissolved in DCM (0.5 M) and ((2,2,6,6-Tetramethylpiperidin-1-yl)oxyl) (TEMPO) (10 mol%) was then added. The reaction was stirred at RT until completion (monitored through TLC analysis, Petroleum Ether/Ethyl Acetate 8:2, roughly 2 hours). The mixture was diluted with dichloromethane and washed with a saturated solution of sodium thiosulfate. The two phases were separated and the aqueous phase was extracted with dichloromethane. The organic phases were then combined, washed with a saturated solution of sodium bicarbonate and then with brine, dried over $MgSO_4$, filtered, and concentrated in vacuo. Purification over silica gel eluting in Petroleum Ether/Ethyl Acetate 100:0 to 9:1 afforded the pure product.

Synthesis of diethyl 2,6-dimethyl-1,4-dihydropyridine-3,5-dicarboxylate (H1)[20]

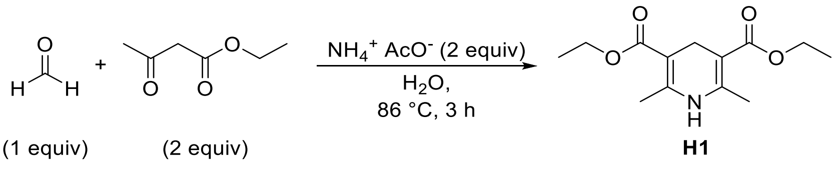

Formaldehyde solution in water 37% (2.44 g, 30.1 mmol), ethyl acetoacetate (15.2 mL, 120 mmol) and ammonium acetate (4.64 g, 60.2 mmol) were dissolved in water (55 mL). The reaction mixture was warmed at 86 °C and vigorously stirred for 3 h. The mixture was filtered and washed with water

---

[19] R. De Mico, L. Margarita, A. Parlanti, G. Vescovi, A. Piancatelli, *J. Org. Chem.*, **1997**, *62*, 6974-6977

[20] E. Tatunashvili, B. Chan, P. E. Nashar, C. S. P. McErlan, *Org. Biomol. Chem.* **2020**, *18*, 1812-1819

and cold diethyl ether. The solid was dried under vacuum to afford the Hantzsch ester **H1**. The product was used with no further purifications. Analytical data in accordance with literature reports.

Synthesis of dibenzyl 2,6-dimethyl-1,4-dihydropyridine-3,5-dicarboxylate (H2)[20]

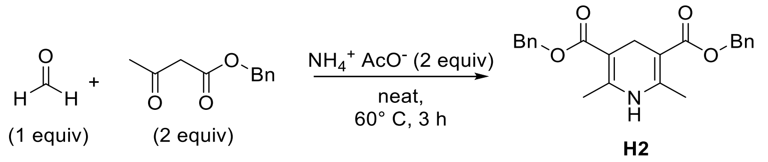

Formaldehyde solution in water 37% (0.97 mL, 13 mmol), benzyl acetoacetate (4.5 mL, 26 mmol), ammonium acetate (1.5 g, 19.5 mmol) were mixed, and the reaction was warmed at 60°C and vigorously stirred for 3 h. A yellow precipitate was formed. The suspension was filtered, and the yellow solid washed with water and then dried to afford the desired Hantszch ester **H2**. The product was used with no further purifications. Analytical data in accordance with literature reports.

Synthesis of diethyl 2,6-diisopropyl-1,4-dihydropyridine-3,5-dicarboxylate (H3) [20]

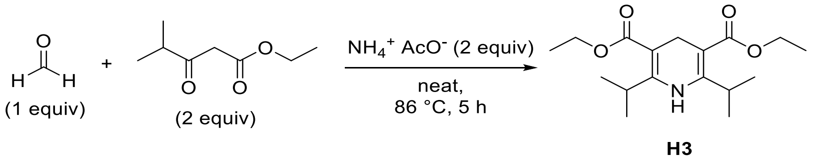

Formaldehyde solution in water 37% (746 mg, 9.2 mmol), ethyl 4,4-dimethylacetoacetate (3 g, 18.4 mmol) and ammonium acetate (1.48 g, 18.4 mmol) were mixed, and the reaction was warmed at 60 °C and vigorously stirred for 5 h. The mixture was extracted with DCM, the organic phases were combined, dryed over $MgSO_4$, filtered and concentrated in vacuo. Purification over silica gel eluting from pure Petroleum Ether to Petroleum Ether/Ethyl Acetate 8:2 afforded the pure product. Analytical data in accordance with literature reports.

Synthesis of diethyl 2-isopropyl-6-methyl-1,4-dihydropyridine-3,5-dicarboxylate (H4)

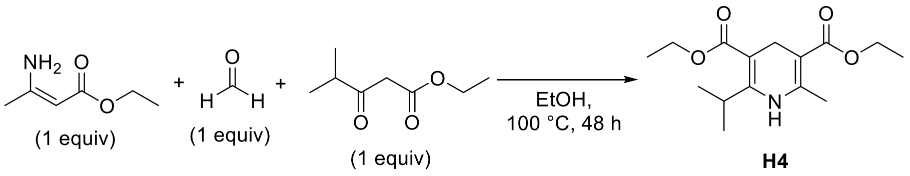

2.25 g (17.4 mmol) of ethyl 3-amino butanoate was dissolved in 120 mL of absolute ethanol under inert atmosphere. Then formaldehyde solution in water 37% (523 mg, 17.4 mmol) and ethyl isobutyrylacetate (2.81 mL, 17.4 mmol) were added. The solution was then heated to 100 °C until completion (48 h, monitored by ^{1}H-NMR analysis). The solvent was removed in vacuo and the crude was purified over silica gel eluting from pure Petroleum Ether to Petroleum Ether/Ethyl Acetate 95:5.

Synthesis of dimethyl 2-isopropyl-6-methyl-1,4-dihydropyridine-3,5-dicarboxylate (H5)[21]

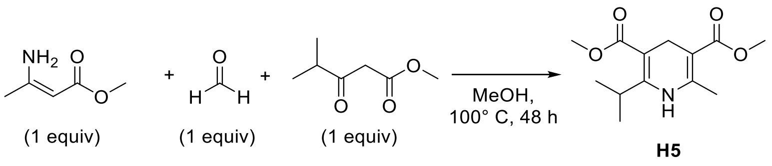

1.1g (9.55 mmol) of methyl 3-amino butanoate was dissolved in 100 mL of methanol under inert atmosphere. Then formaldehyde solution in water 37% (1.38 g, 9.55 mmol) and methyl isobutyrylacetate (287 mg, 9.55 mmol) were added. The solution was then heated to 60 °C until completion (48 h, monitored by ^{1}H-NMR analysis). The mixture was cooled down and the solvent evaporated under vacuum. The crude was purified over silica gel eluting in Petroleum Ether/Ethyl Acetate 8:2. Analytical data in accordance with literature reports.

---

[21] a) M. van Rhee, J. Jiang, N. Melman, M. E. Olah, G. L. Stiles, K. A. Jacobson, *J. Med. Chem.*, **1996**, *39*, 2980-2989; b) B. List, S. Mayer, N. Martin, X. Wang (Evonik Industries AG) US 2009/0030216 A1, **2009**

Additional experiments

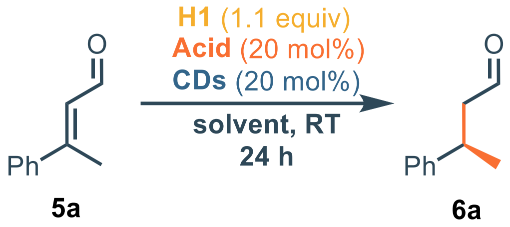

Table 2: Additional Control Experiments

Entry	Solvent	Acid	CDs	Conv. (%)	NMR yield (%)	ee (%)
1	Toluene	**CPA1**	-	84	64	rac.
2	Toluene	-	-	---	---	---
3	Toluene	-	**CDs3**	---	---	---
4	Mesytilene/ Pentane 1:1	**CPA1**	-	89	64	rac.
5	Toluene	DPPA[a]	-	37	16	rac.
6	Toluene	**CPA1**	-	90	62	rac.

[a]: abbreviation for diphenyl phosphate

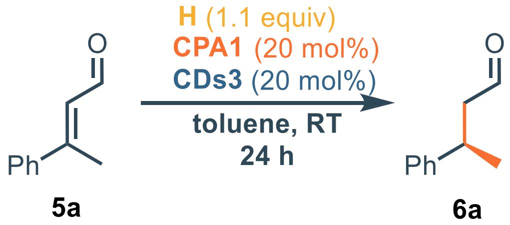

Table 3: Additional Experiments

Entry	HE	Temp. (°C)	Conv. (%)	NMR yield (%)	ee (%)
1	**H1**	25	99	47	56
2[a]	**H1**	25	96	53	26

4[b]	**H1**	25	74	---	---
5[c]	**H1**	25	99	32	58
6[d]	**H1**	25	99	53	57
7[e]	**H1**	10	63	25	70
8[f]	**H1**	10	42	7	---
9	**H1**	25	99	45	58
10	**H4**	10	99	70	79
11[g]	**H4**	-40	83	50	80
12	**H4**	-40	53	34	65

[a]: 0.2 equiv. of HCl in dioxane were added in the reaction mixture; [b]: performed in absence of Hantzsch's ester; [c]: 2 equivalents of **H1** used; [d]: **CDs/CPA** ratio different from 1:1, 8.5 mg (instead of 9.5 mg) of **CDs** Type 2 used for 15 mg of (*S*)-TRIP; [e]: concentration of the system 0.05 M; [f]: concentration of the system 0.15 M; [g]: Toluene dry.

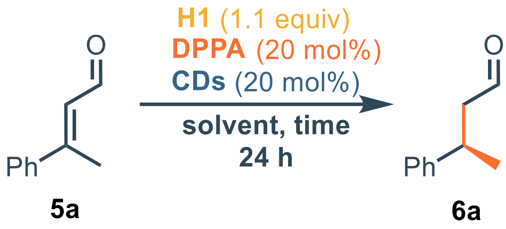

Table 4: Additional Experiments using DPPA as Phosphoric Acid

Entry[a]	Solvent	CDs	Time (h)	Temp. (°C)	Conv. (%)	NMR yield (%)
1[b]	DCM	**CDs4**	48	RT to 40	93	15
2[b]	Dioxane	**CDs4**	48	RT to 50	---	5
3[b]	Toluene	**CDs4**	48	RT to 50	94	13
4	$CHCl_3$	**CDs4**	48	RT to 40	85	10
5	Toluene	**CDs4**	48	50	>95	35

6	Toluene	**CDs4**	48	50	90	18
7	Toluene	**CDs4**	48	50	>95	37
8	Toluene	**CDs4**	6	50	80	16
9	Toluene	**CDs4**	12	50	85	23
10	Toluene	**CDs4**	18	50	85	34
11	Toluene	**CDs4**	24	50	98	35
12	Toluene	**CDs4**	24	50	83	19
13	Toluene	**CDs4**	48	50	>95	30
14	Benzene-d_6	**CDs4**	24	50	59	10
15	Benzene-d_6	**CDs4**	48	50	>95	12
16[c]	Toluene	**CDs4**	48	50	92	8
17	Toluene	**CDs3**	24	50	64	20
18	Toluene	**CDs3**	48	50	>95	30

[a]: Internal standard: trimethoxybenzene (0.1 mmol); [b]: work-up: plug on silica gel; [c]: 1 equiv. of DPPA

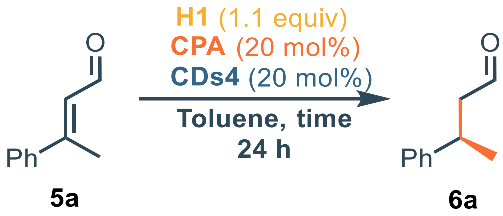

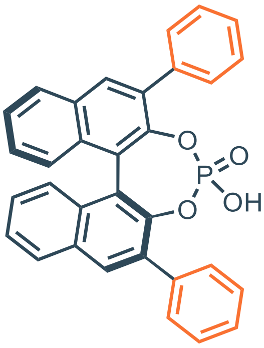

CPA6

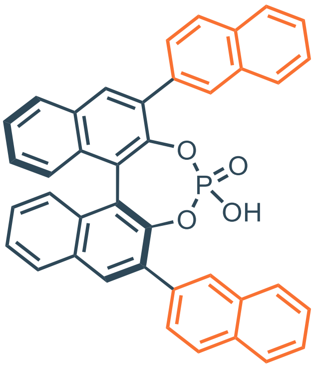

CPA7

Table 5: Additional Experiments of CPAs screening

Entry	CPA	Time (h)	Temp. (°C)	Conv. (%)	NMR yield (%)	ee (%)
1	**CPA6**	24	25	77	21	6
2	**CPA7**	24	25	71	36	3

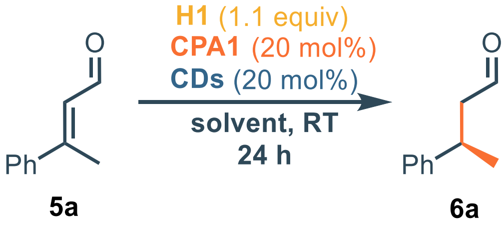

Table 6: Additional Solvent Screening Experiments

Entry	Solvent	CDs	Time (h)	Temp. (°C)	Conv. (%)	NMR yield (%)	ee (%)
1	Mesytilene	**CDs1**	48	30	>95	69	4
2	Toluene	**CDs3**	48	50	>95	43	36
3[a]	Toluene	**CDs3**	48	50	>95	30	50

4	MTBE	**CDs3**	36	30	>95	53	20
5	CHCl$_3$	**CDs3**	24	25	98	41	52
6	Dioxane	**CDs3**	24	25	92	47	30
7	1,3-Dichlorobenzene	**CDs3**	48	25	>95	55	37
8	1,3-dichlorobenzene-Hexane 1:1	**CDs3**	48	25	>95	45	28
9	Toluene	**CDs3**	48	30	>95	35	37
10	Mesytilene/ pentane 1:2	**CDs3**	24	25	95	47	29
11	Mesytilene/Pentane 2:1	**CDs3**	24	25	95	54	9
12	Mesytilene/ Pentane 1:3	**CDs3**	24	25	95	52	2
13	Mesytilene	**CDs3**	24	25	92	68	20
14	Mesytilene/ Pentane 1:1	**CDs3**	24	25	95	51	rac
15	Toluene	**CDs3**	24	25	96	60	40
16	MTBE	**CDs3**	24	25	99	43	18
17	CHCl$_3$	**CDs3**	16	25	97	33	52
18	CHCl$_3$	**CDs3**	6	25	81	39	46
19	Anisole	**CDs3**	24	25	95	40	54

[a]: addition *in situ* of NaBH$_4$

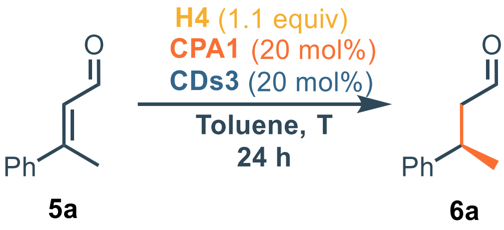

Table S1: Additional Screening Experiments

Entry	Acid	CDs	Time (h)	Temp. (°C)	Conv. (%)	NMR yield (%)	ee (%)
1	**CPA1**	**CDs3**	18	-40	92	72	82
2	**CPA1**	**CDs3**	24	-40	96	74	83
3[a]	**CPA1**	**CDs3**	24	-40	82	50	80
4[a]	**CPA1**	**CDs3**	24	-20	91	78	81
5[b]	**CPA1**	**CDs3**	24	-20	99	72	79
6[c]	**CPA1**	**CDs3**	24	-20	99	57	79
7[d]	**CPA1**	**CDs3**	24	-20	96	72	80
8	**CPA1** **2.5 mol%**	**CDs3** **2.5 mol%**	24	-20	23	11	76

[a]: Reaction performed in dry toluene; [b]: 100 mg of MS 4 Å were added to the reaction mixture; [c]: 100 mg of MS 13X were added to the reaction mixture; [d]: 100 mg of MS 5 Å were added to the reaction mixture.

Characterization of compounds

(*E*)-3-phenylbut-2-enal (5a)

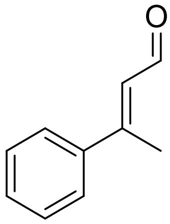

Synthesized in accordance *with general procedure for (E)-3-phenylbut-2-enal derivatives* using BIAB (2.54 g, 7.64 mmol), TEMPO (109 mg, 0.69 mmol) and (*E*)-3-phenylbut-2-en-1-ol 5a (1.03, 6.95 mmol) dissolved in 7.5 mL of DCM. Chromatography on silica gel (Petroleum Ether/Ethyl Acetate 100:0 to 90:10). The desired product was obtained as a yellowish oil (606 mg, 4.15 mmol, yield = 60 %).

^{1}H-NMR (400 MHz, $CDCl_3$, 303 K) δ 9.48 (d, J = 8.2 Hz, 1H), 7.49 - 7.37 (m, 2H), 7.35 - 7.26 (m, 2H), 6.14 (dt, *J* = 8.2, 1.4 Hz, 1H), 2.32 (d, *J* = 1.4 Hz, 3H). ^{13}C-NMR (101 MHz, $CDCl_3$, 303 K) δ 193.6, 162.2, 138.6, 129.3, 129.3, 128.5, 128.5, 26.6. Analytical data in accordance with literature reports.[22]

(E)-3-(4-methoxyphenyl)but-2-enal (5b)

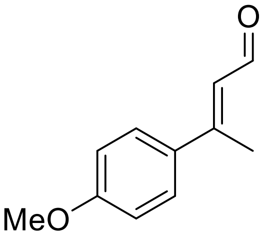

Synthesized in accordance with *general procedure for (E)-3-phenylbut-2-enal derivatives* using BIAB (451 mg, 1.4 mmol), TEMPO (20.7 mg, 0.13 mmol) and (*E*)-3-(4-methoxyphenyl)but-2-en-1-ol 5b (226 mg, 1.27 mmol) dissolved in 2 mL of DCM. Chromatography on silica gel (Petroleum Ether/Ethyl Acetate 100:0 to 90:10). The desired product was obtained as a waxy yellow solid (148 mg, 0.842 mmol, yield = 66 %). ^{1}H-NMR (400 MHz, $CDCl_3$) δ 10.15 (d, *J* = 7.9 Hz, 1H), 7.54 (d, *J* = 9.0 Hz, 2H), 6.93 (d, *J* = 8.9 Hz, 2H), 6.39 (d, *J* = 9.2 Hz, 1H), 3.85 (s, 3H), 2.54 (s, 3H). ^{13}C-NMR (101 MHz, $CDCl_3$, 303 K) δ 191.4, 161.5, 157.1, 132.5, 127.9, 125.7, 114.2, 55.5, 16.2. Analytical data in accordance with literature reports.[23]

---

[22] Q. Yan, D. Kong, W. Zhao, G. Zi, G. Hou, *J. Org. Chem.* **2016**, *81*, 2070-2077

[23] G. Griesbeck, M. Brautigam, M. Kleczka, A. Raabe, *Molecules*, **2017**, *22*, 119

(E)-3-(p-tolyl)but-2-enal (5c)

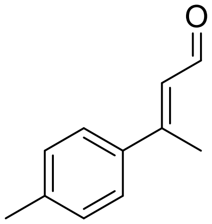

Synthesized in accordance with *general procedure for (E)-3-phenylbut-2-enal derivatives* using BIAB (632 mg, 1.95 mmol), TEMPO (29 mg, 0.19 mmol) and (*E*)-3-(p-tolyl)but-2-en-1-ol 5c (289 mg, 1.78 mmol) dissolved in 2 mL of DCM. Chromatography on silica gel (Petroleum Ether/Ethyl Acetate 100:0 to 90:10). The desired product was obtained as a yellow oil (209 mg, 1.3 mmol, yield = 73 %).

^{1}H-NMR (400 MHz, $CDCl_3$, 303 K) δ 10.17 (d, J = 7.9 Hz, 1H), 7.46 (d, J = 8.3 Hz, 2H), 7.22 (d, J = 8.2 Hz, 2H), 2.56 (s, 3H), 2.39 (s, 3H). ^{13}C-NMR (101 MHz, $CDCl_3$, 303 K) δ 191.4, 157.7, 140.7, 137.7, 129.6, 126.7, 126.4, 21.4, 16.4. Analytical data in accordance with literature reports.[24]

(E)-3-phenylpent-2-enal (5d)

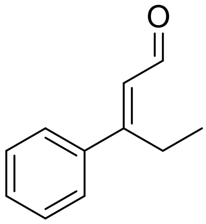

Synthesized in accordance with *general procedure for (E)-3-phenylbut-2-enal derivatives* using BIAB (707 mg, 2.13 mmol), TEMPO (30.2 mg, 0.194 mmol) and (*E*)-3-phenylpent-2-en-1-ol 5d (314 mg, 1.94 mmol) dissolved in 10 mL of DCM. Chromatography on silica gel (Petroleum Ether/Ethyl Acetate 100:0 to 90:10). The desired product was obtained as an inseparable mixture *E/Z* 4:1, as an orange oil (200 mg, 1.25 mmol, yield = 64 %). Major isomer (*E*): ^{1}H-NMR (400 MHz, $CDCl_3$, 303 K) δ 10.01 (d, J = 8.0 Hz, 1H), 7.34 - 7.24 (m, 5H), 6.11 (d, J = 7.9 Hz, 1H), 2.97 - 2.86 (m, 2H), 1.03 (d, J = 15.1 Hz, 3H). ^{13}C-NMR (101 MHz, $CDCl_3$, 303 K) δ 190.2, 163.84 138.8, 129.2, 128.2, 126.2, 125.9, 22.6, 14.3. Analytical data in accordance with literature reports.[25]

---

[24] K. Ren, B. Hu, M. Zhao, Y. Tu, X. Xie, Z. Zhang, *J. Org. Chem.*, **2014**, *79*, 2170-2177

[25] L. Naesborg, V. Corti, L. A. Leth, P. H. Poulsen, K. A. Jørgensen, *Angew. Chem. Int. Ed.* **2018**, *57*, 1606-1610

(E)-3-(4-nitrophenyl)but-2-enal (5e)

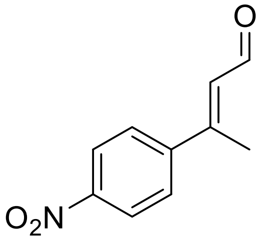

Synthesized in accordance with *general procedure for (E)-3-phenylbut-2-enal derivatives* using BIAB (345 mg, 1.07 mmol), TEMPO (15.2 mg, 0.097 mmol) and (*E*)-3-(4-nitrophenyl)but-2-en-1-ol 5e (188 mg, 0.97 mmol) dissolved in 2 mL of DCM. Chromatography on silica gel (Petroleum Ether/Ethyl Acetate 100:0 to 90:10). The desired product was obtained as a yellow solid (125 mg, 0.65 mmol, yield = 67 %). ^{1}H-NMR (400 MHz, $CDCl_3$, 303 K) δ 10.21 (d, *J* = 7.5 Hz, 1H), 8.28 (d, *J* = 9.0 Hz, 2H), 7.68 (d, *J* = 9.2 Hz, 2H), 6.40 (d, *J* = 8.9 Hz, 1H), 2.61 (d, *J* = 1.4 Hz, 3H). ^{13}C-NMR (101 MHz, $CDCl_3$, 303 K) δ 190.8, 154.6, 148.5, 147.2, 129.5, 127.4, 124.1, 16.7. Analytical data in accordance with literature report.[26]

(E)-3-(4-fluorophenyl)but-2-enal (5f)

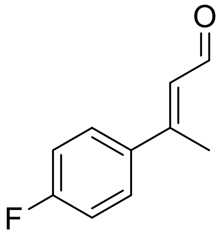

Synthesized in accordance with *general procedure for (E)-3-phenylbut-2-enal derivatives* using BIAB (4.64 g, 14.40 mmol), TEMPO (187 mg, 1.20 mmol) and 3-(4-fluorophenyl)but-2-en-1-ol 5f (2 g, 12 mmol) dissolved in 24 mL of DCM. Chromatography on silica gel (Petroleum Ether/Ethyl Acetate 100:0 to 90:10). The desired product was obtained a pale yellow solid (1.05 g, 6.39 mmol, yield = 53 %). ^{1}H-NMR (400 MHz, $CDCl_3$, 303 K) δ 10.17 (d, *J* = 7.8 Hz, 1H), 7.54 (dd, *J* = 8.9, 5.3 Hz, 2H), 7.10 (t, *J* = 8.7 Hz, 2H), 6.35 (dd, *J* = 7.7, 1.3 Hz, 1H), 2.56 (d, *J* = 1.4 Hz, 3H). ^{13}C-NMR (101 MHz, $CDCl_3$, 303 K) δ 191.1, 165.1, 162.6, 156.3, 136.6, 128.3, 128.3, 127.1, 127.1, 115.9, 115.7, 16.5. ^{19}F NMR (376 MHz, $CDCl_3$, 303 K) δ -110.50. Analytical data in accordance with literature report.[27]

---

[26] T. K. Johansen, C. V. Gomez, J. R. Bak, R. L. Davis, K. A. Jørgensen, *Chem. Eur. J.* **2013**, *19*, 16518-16522

[27] Y. Li, C. Barlose, J. Jørgensen, B. D. Carlsen, K. A. Jørgensen, *Chem. Eur. J.* **2017**, *23*, 38-41

(E)-3-(4-chlorophenyl)but-2-enal (5g)

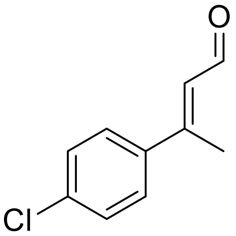

Synthesized in accordance with *general procedure for (E)-3-phenylbut-2-enal derivatives* using BIAB (2.1 g, 6.38 mmol), TEMPO (90.7 mg, 0.58 mmol) and (*E*)-3-(4-clorophenyl)but-2-en-1-ol 5g (1.06 g, 5.8 mmol) dissolved in 6 mL of DCM. Chromatography on silica gel (Petroleum Ether/Ethyl Acetate 100:0 to 90:10). The desired product was obtained as a yellowish solid (643 mg, 3.56 mmol, yield = 61 %). ^{1}H-NMR (400 MHz, $CDCl_3$, 303 K) δ 10.17 (d, J = 7.8 Hz, 1H), 7.48 (d, J = 8.8 Hz, 2H), 7.39 (d, J = 8.8 Hz, 2H), 6.36 (d, J = 7.8 Hz, 1H), 2.55 (d, J = 1.4 Hz, 3H). ^{13}C-NMR (101 MHz, $CDCl_3$, 303 K) δ 191.2, 156.1, 139.0, 136.3, 129.1, 127.7, 127.5, 16.4. Analytical data in accordance with literature report.[27]

(E)-3-(4-bromophenyl)but-2-enal (5h)

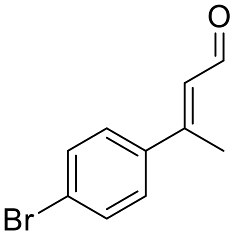

Synthesized in accordance with *general procedure for (E)-3-phenylbut-2-enal derivatives* using BIAB (1.77 g, 4.84 mmol), TEMPO (75.7 mg, 0.48 mmol) and (*E*)-3-(4-bromophenyl)but-2-en-1-ol 5h (1.10 g, 4.84 mmol) dissolved in 5 mL of DCM. Chromatography on silica gel (Petroleum Ether/Ethyl Acetate 100:0 to 90:10). The desired product was obtained as a yellow solid (820 mg, 3.64 mmol, yield = 75 %). ^{1}H-NMR (400 MHz, $CDCl_3$, 303 K) δ 10.17 (d, J = 7.7 Hz, 1H), 7.55 (d, J = 8.8 Hz, 2H), 7.41 (d, J = 8.7 Hz, 2H), 6.36 (d, J = 7.7 Hz, 1H), 2.54 (s, 3H). ^{13}C-NMR (101 MHz, $CDCl_3$, 303 K) δ 191.2, 156.2, 139.6, 132.1, 130.0, 127.9, 127.6, 124.6, 16.4. Analytical data in accordance with literature report.[26]

(R)-3-phenylbutanal (6a)

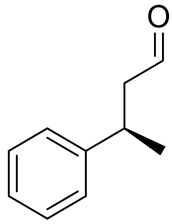

Synthesized in accordance with General Procedure for nano-organocatalysed reaction using (E)-3-phenylbut-2-enal 1a (0.25 mmol, 14.6 mg), Hantzsch's ester H4 (0.11 mmol, 30.9 mg), **CDs-3** (0.05 eq, loading 2100 µmol/g, 5.95 mg), (S)-TRIP (5 mol%, 3.76 mg) dissolved in 2.5 mL of toluene. Chromatography on silica gel (Petroleum ether/DCM 3:2) The desired product was obtained as a colourless oil (31 mg, 0.209 mmol, yield = 84 %). ^{1}H-NMR (400 MHz, $CDCl_3$, 303 K) δ 9.71 (t, J = 2.1 Hz, 1H), 7.35 - 7.27 (m, 1H), 7.22 (d, J = 7.8 Hz, 2H), 3.37 (h, J = 7.0 Hz, 1H), 2.82 - 2.60 (m, 2H), 1.33 (d, J = 7.0 Hz, 4H). ^{13}C-NMR (101 MHz, $CDCl_3$, 303 K) δ 201.9, 145.6, 128.8, 126.9, 126.7, 51.8, 34.4, 22.3. HPLC (Lux 3 µm-Cellulose 1, Hexane/i-Propanol 95:5, flow: 0.5 mL/min, λ =210 nm), tminor: 10.8 min; tmajor: 9.5 min. $[\alpha]_D^{25}$ = - 27.37 (c=0.0019 g/mL, CHCl3). Analytical data in accordance with literature report.[28]

(R)-3-(4-methoxphenyl)butanal (6b)

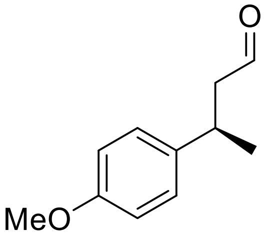

Synthesized in accordance with *General Procedure for nano-organocatalysed reaction* using (*E*)-3-(4-methoxyphenyl)but-2-enal 1b (0.25 mmol, 44.1 mg), Hantzsch's ester H4 (0.275 mmol, 86.9 mg), **CDs-3** (0.05 eq, loading 2100 µmol/g, 5.95 mg), (S)-TRIP (5 mol%, 9.41 mg) dissolved in 2.5 mL of toluene. Chromatography on silica gel (Petroleum Ether/Ethyl Acetate 95:5). The desired product was obtained as a yellowish oil (30 mg, 0.168 mmol, yield = 67 %). ^{1}H-NMR (400 MHz, $CDCl_3$,303 K) δ 9.70 (t, *J* = 2.1 Hz, 1H), 7.14 (d, *J* = 8.5 Hz, 2H), 6.85 (d, *J* = 8.8 Hz, 2H), 3.32 (m, 1H), 2.77 - 2.57 (m, 2H), 1.30 (d, J = 7.0 Hz, 3H). ^{13}C-NMR (101 MHz, $CDCl_3$, 303 K) δ 202.1, 158.4, 137.7, 127.9, 114.2, 55.4, 52.1, 33.7, 22.5. HPLC (Lux 3 µm-Amylose 2, Hexane/*i*-Propanol 98:2, flow: 0.3 mL/min, λ =225 nm), t_{minor}: 55.7 min; t_{major}: 48.7 min. $[\alpha]_D^{25}$=-27.84 (*c*=0.0027 g/mL, $CHCl_3$). Analytical data in accordance with literature report.[29]

---

[28] Y. Zhou, J. S. Bandar, R. Y. Liu, S. L. Buchwald, *J. Am. Chem. Soc.*, **2018**, *140*, 606-609

[29] C. You, S. Li, X. Li, J. Lan, Y. Yang, L. W. Chung, H. Lv, X. Zhang, *J Am Chcem Soc*, **2018**, *140*, 4977-4981

(R)-3-(p-tolyl)butanal (6c)

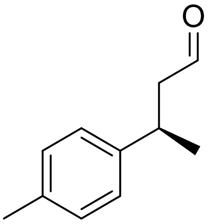

Synthesized in accordance with *General Procedure for nano-organocatalysed reaction* using (*E*)-3-(p-tolyl)but-2-enal 1c (0.25 mmol, 40.1 mg), Hantzsch's ester H4 (0.275 mmol, 86.9 mg), **CDs-3** (0.05 eq, loading 2100 µmol/g, 5.95 mg), (S)-TRIP (5 mol%, 9.41 mg) dissolved in 2.5 mL of toluene. Chromatography on silica gel (Petroleum ether/DCM 3:2). The desired product was obtained as a colourless oil (25 mg, 0.154 mmol, yield = 62 %). ^{1}H-NMR (400 MHz, $CDCl_3$, 303 K) δ 9.70 (s, 1H), 7.11 (s, 4H), 3.33 (q, J = 7.0 Hz, 1H), 2.79 - 2.58 (m, 2H), 2.32 (s, 3H), 1.30 (d, J = 7.0 Hz, 3H). ^{13}C-NMR (101 MHz, $CDCl_3$, 303 K) δ 202.2, 142.6, 136.2, 129.5, 126.8, 51.9, 34.1, 22.4, 21.1. HPLC (Lux 3 µm-Cellulose 3, Hexane/*i*-Propanol 95:5, flow: 0.5 mL/min, λ =210 nm), t_{minor}: 8.3 min; t_{major}: 9.1 min. $[\alpha]_D^{25}$ = +34.09 (*c*=0.0008 g/mL, $CHCl_3$). Interestingly, the direction of the optical rotation is opposite to the other compounds; this entry was repeated twice to confirm the measurement of the optical rotation. Analytical data in accordance with literature report.[29]

(R)-3-phenylpentanal (6d)

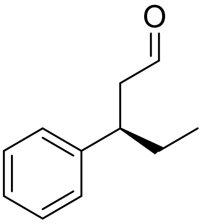

Synthesized in accordance with *General Procedure for nano-organocatalysed reaction* using (*E*)-3-phenylpent-2-enal 1d (0.25 mmol, 40.1 mg), Hantzsch's ester H4 (0.275 mmol, 86.9 mg), **CDs-3** (0.05 eq, loading 2100 µmol/g, 5.95 mg), (S)-TRIP (5 mol%, 9.41 mg) dissolved in 2.5 mL of toluene. Chromatography on silica gel (Petroleum ether/DCM 3:2). The desired product was obtained as a colourless oil (26.5 mg, 0.166 mmol, yield = 66 %). ^{1}H-NMR (400 MHz, $CDCl_3$, 303 K) δ 9.67 (t, J = 2.1 Hz, 1H), 7.35 - 7.26 (m, 2H), 7.26 - 7.11 (m, 2H), 3.14 - 2.96 (m, 1H), 2.72 (dd, J = 7.3, 2.1 Hz, 2H), 1.80 - 1.56 (m, 2H), 0.82 (t, J = 7.3 Hz, 3H). ^{13}C-NMR (101 MHz, CDC13) δ 190.2, 163.8, 138.8, 129.2, 128.8, 126.2, 125.9, 22.6, 14.3. HPLC (Lux 3 µm-Cellulose 3, Hexane/*i*-Propanol 95:5, flow: 0.5 mL/min, λ =210 nm), t_{minor}: 20.8 min; t_{major}: 17.0 min. $[\alpha]_D^{25}$ =-23.31 (*c*=0.0016 g/mL, $CHCl_3$). Analytical data in accordance with literature report.[30]

---

[30] S. Afewerki, B. Reistein, K. Pirrtila, L. Deiana, P. Dziedzic, I. Ibrahem, A. Cordova, *Chem. Eur. J.*, **2011**, *17*, 8784-8788

(R)-3-(4-nitrophenyl)butanal (6e)

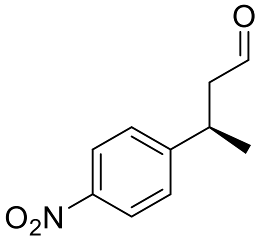

Synthesized in accordance with *General Procedure for nano-organocatalysed reaction* using (*E*)-3-(4-nitrophenyl)but-2-enal 1e (0.25 mmol, 47.8 mg), Hantzsch's ester H4 (0.275 mmol, 86.9 mg), **CDs-3** (0.05 eq, loading 2100 μmol/g, 5.95 mg), (S)-TRIP (5 mol%, 9.41 mg) dissolved in 2.5 mL of toluene. Chromatography on silica gel (Petroleum Ether/Ethyl Acetate 95:5). The desired product was obtained as a pale yellowish oil (35 mg, 0.181 mmol, yield = 73 %). ^{1}H-NMR (400 MHz, $CDCl_3$, 303 K) δ 9.73 (t, J = 1.5 Hz, 1H), 8.18 (d, J = 8.9 Hz, 2H), 7.39 (d, J = 8.5 Hz, 2H), 3.50 (m, 1H), 2.87 - 2.70 (m, 2H), 1.35 (d, J = 6.9 Hz, 3H). ^{13}C-NMR (101 MHz, $CDCl_3$, 303 K) δ 200.1, 153.2, 146.7, 127.7, 124.0, 51.3, 33.9, 21.8. HPLC (Lux 3 μm-Cellulose 2, Hexane/*i*-Propanol 95:5, flow: 0.5 mL/min, λ =250 nm), t_{minor}: 27.0 min; t_{major}: 31.4 min. $[\alpha]_D^{25}$ =+20.80 (*c*=0.0025 g/mL, $CHCl_3$). Interestingly, the direction of the optical rotation is opposite to the other compounds; this entry was repeated twice to confirm the measurement of the optical rotation. Analytical data in accordance with literature report.[31]

(R)-3-(4-fluorophenyl)butanal (6f)

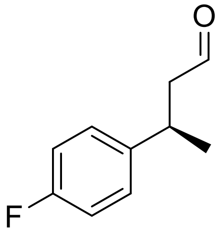

Synthesized in accordance with *General Procedure for nano-organocatalysed reaction* using (E)-3-(4-fluorophenyl)but-2-enal 1f (0.25 mmol, 47.8 mg), Hantzsch's ester H4 (0.275 mmol, 86.9 mg), **CDs-3** (0.05 equiv, loading 2100 μmol/g, 5.95 mg), (S)-TRIP (5 mol%, 9.41 mg) dissolved in 2.5 mL of toluene. Chromatography on silica gel (Petroleum ether/DCM 3:2). The desired product was obtained as a colourless oil (35 mg, 0.181 mmol, yield = 73 %). ^{1}H-NMR (400 MHz, $CDCl_3$, 303 K) δ 9.70 (t, J = 1.9 Hz, 1H), 7.23 - 7.13 (m, 2H), 7.04 - 6.93 (m, 2H), 3.36 (m, 1H), 2.78 - 2.58 (m, 2H), 1.30 (d, J = 7.0 Hz, 3H). ^{13}C-NMR (101 MHz, $CDCl_3$, 303 K) δ 201.6, 162.8, 160.4, 141.3, 128.4, 115.5, 52.0, 33.7, 22.4. ^{19}F-NMR (376 MHz, $CDCl_3$, 303 K) δ -116.64. HPLC (Lux 3 μm-Cellulose 3, Hexane/*i*-Propanol 98:2, flow: 0.5 mL/min, λ =210 nm), t_{minor}: 11.9 min; t_{major}: 13.2 min. $[\alpha]_D^{25}$ =-22.41 (*c*=0.0012 g/mL, $CHCl_3$). Analytical data in accordance with literature report.[32]

---

[31] T. Ru, G. Liang, L. Zhang, Y. Ning, F. Chen, *ChemCatChem*, **2021**, *13*, 5073-5077

[32] Y. Zhang, S. Torker, M. Sigrist, N. Bregovic, P. Dydio, *J. Am. Chem. Soc.*, **2020**, *142*, 18251-18265

(R)-3-(4-chlorophenyl)butanal (6g)

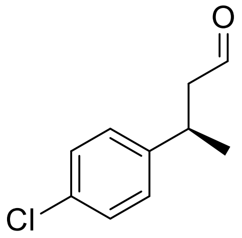

Synthesized in accordance with *General Procedure for nano-organocatalysed reaction* using (*E*)-3-(4-chlorophenyl)but-2-enal 1g (0.25 mmol, 45.2 mg), Hantzsch's ester H4 (0.275 mmol, 86.9 mg), **CDs-3** (0.05 equiv, loading 2100 μmol/g, 5.95 mg), (S)-TRIP (5 mol%, 9.41 mg) dissolved in 2.5 mL of toluene. Chromatography on silica gel (Petroleum ether/DCM 3:2). The desired product was obtained as a colourless oil (34.2 mg, 0.187 mmol, yield = 75 %). ^{1}H-NMR (400 MHz, $CDCl_3$, 303 K) δ 9.71 (t, J = 1.9 Hz, 1H), 7.33 - 7.24 (m, 2H), 7.21 - 7.11 (m, 2H), 3.35 (h, J = 7.0 Hz, 1H), 2.79 - 2.60 (m, 2H), 1.30 (d, J = 7.0 Hz, 4H). ^{13}C-NMR (101 MHz, $CDCl_3$, 303 K) δ 201.3, 144.1, 132.3, 128.9, 128.3, 51.8, 33.8, 22.2. HPLC (Lux 3 μm-Cellulose 2, Hexane/*i*-Propanol 99:1, flow: 0.5 mL/min, λ =210 nm), t_{minor}: 11.6 min; t_{major}: 13.3 min. $[\alpha]_D^{25}$ =-41.48 (*c*=0.0031 g/mL, $CHCl_3$). Analytical data in accordance with literature report.[28]

(R)-3-(4-bromophenyl)butanal (6h)

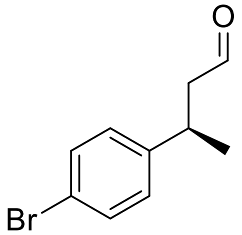

Synthesized in accordance with *General Procedure for nano-organocatalysed reaction* using (*E*)-3-(4-bromophenyl)but-2-enal 1h (0.25 mmol, 56.3 mg), Hantzsch's ester H4 (0.275 mmol, 86.9 mg), **CDs-3** (0.05 equiv, loading 2100 μmol/g, 5.95 mg), (S)-TRIP (5 mol%, 9.41 mg) dissolved in 2.5 mL of toluene. Chromatography on silica gel (Petroleum ether/DCM 3:2). The desired product was obtained as a colourless oil (50.2 mg, 0.221 mmol, yield = 88 %). ^{1}H-NMR (400 MHz, $CDCl_3$, 303 K) δ 9.70 (s, 1H), 7.43 (d, *J* = 8.3 Hz, 2H), 7.10 (d, *J* = 8.4 Hz, 2H), 3.33 (m, 1H), 2.78 - 2.53 (m, 2H), 1.29 (d, *J* = 7.0 Hz, 3H). ^{13}C-NMR (101 MHz, $CDCl_3$, 303 K) δ 201.3, 144.5, 131.9, 128.7, 120.4, 51.7, 33.9, 22.2. HPLC (Lux 3 μm-Cellulose 2, Hexane/*i*-Propanol 95:5, flow: 0.5 mL/min, λ =210 nm), t_{minor}: 14.1 min; t_{major}: 16.4 min. $[\alpha]_D^{25}$=-12.73 (*c*=0.0022 g/mL, $CHCl_3$). Analytical data in accordance with literature report.[29]

(R)-3,7-dimethyloct-6-enal (6i)

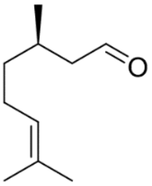

Synthesized in accordance with *General Procedure for nano-organocatalysed reaction* using (E)-3,7-dimethylocta-2,6-dienal (0.5 mmol, 76.1 mg), Hantzsch's ester H4 (0.55 mmol, 155 mg), **CDs-3** (0.05 equiv, loading 2100 µmol/g, 11.9 mg), (S)-TRIP (5 mol%, 18.8 mg) dissolved in 5 mL of toluene. Chromatography on silica gel (Petroleum ether/DCM 9:1). The desired product was obtained as a colourless oil (44 mg, 0.285 mmol, yield = 57 %). ^{1}H NMR ($CDCl_3$, 400 MHz, 303 K) δ: 9.74 (t, *J*= 4 Hz, 1H), 5.10-5.05 (m, 1H), 2.39 (ddd, *J* = 16.1, 5.6, 2.1 Hz , 1H), 2.22 (ddd, *J*= 15.9, 7.9, 2.6 Hz , 1H), 2.11-1.92 (m, 3H), 1.67 (s, 3H), 1.59 (s, 3H), 1.40-1.22 (m, 2H), 0.96 (d, *J* = 8 Hz, 3 H). ^{13}C NMR (CDCl3, 101 MHz, 303 K) δ: 203.04, 131.87, 124.18, 51.13, 37.08, 27.93, 25.80, 25.53, 19.99, 17.77.HPLC (Lux 3 µm-Cellulose 1, Hexane/*i*-Propanol 95:5, flow: 0.5 mL/min, λ =210 nm), t_{minor}: 10.99 min; t_{major}: 10.19 min. $[\alpha]_D^{25}$ =+10.43 (*c*=0.0023 g/mL, $CHCl_3$).

Diethyl 2-isopropyl-6-methyl-1,4-dihydropyridine-3,5-dicarboxylate (H4)

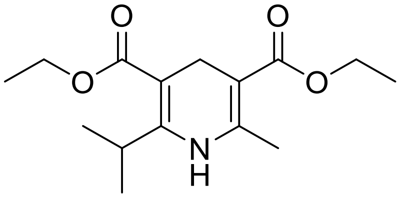

Synthesized in accordance with *synthesis of diethyl 2-isopropyl-6-methyl-1,4-dihydropyridine-3,5-dicarboxylate* procedure using 2.5 g (19.4 mmol) of ethyl 3-amino butanoate, paraformaldehyde solution in water 37% (581 mg, 19.4 mmol), and ethyl isobutyrylacetate (3.12 mL, 19.4 mmol) dissolved in 190 mL of absolute ethanol. The desired product was obtained as a yellow oil (2.75 g, 9.77 mmol, yield = 50 %). ^{1}H-NMR (400 MHz, $CDCl_3$, 303 K) *δ* 4.14 (m, 4H), 4.10 - 4.02 (m, 1H), 3.25 (s, 2H), 2.19 (s, 3H), 1.26 (t, *J* = 7.1 Hz, 6H), 1.07 (d, *J* = 7.0 Hz, 6H). ^{13}C-NMR (101 MHz, $CDCl_3$, 303 K) *δ* 168.1, 167.8, 153.2, 145.2, 99.2, 98.2, 59.7, 59.7, 27.2, 25.2, 20.2, 19.3, 14.6, 14.5.

Chapter 3 – A Subtle Twist: Hantzsch Ester-Controlled Enantiodivergence Driven by Weak Non-Covalent Interactions

The entire chapter has been submitted for publication in two different papers: D. Iapadre, A. Carioscia, F. Pesciaioli, A. Carlone, *paper submitted;* E. Cocco, A. Carioscia, F. Pesciaioli, M. Prato, G. Filippini, M. Aschi, A. Carlone, *Paper submitted*

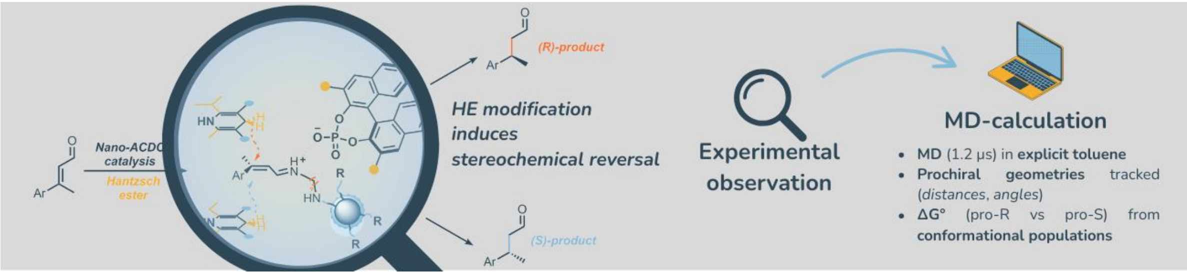

***Chapter outline** – In this chapter, a unique case of enantiodivergence controlled by an achiral reagent in asymmetric organocatalysis is disclosed. The study focuses on the 1,4-transfer hydrogenation of α,β-unsaturated aldehydes, employing a catalytic system of Nitrogen-Doped Carbon Dots (**NCDs**) and a Chiral Phosphoric Acid (CPA). This work demonstrates how a minimal structural modification to the Hantzsch ester hydride source, switching from dimethyl to diethyl substituents, completely reverses the reaction's stereochemical outcome from the (R)- to the (S)-enantiomer. The phenomenon is rationalized through a synergistic experimental and computational approach.*

Introduction

Enantiodivergence: a powerful tool in asymmetric organocatalysis

Enantiodivergence is a powerful concept in asymmetric catalysis that enables access to both enantiomers of a chiral product from a single enantiomer of a chiral catalyst.[1] Because nature is inherently homochiral, obtaining the opposite catalyst enantiomer is often challenging or impractical.[2] Enantiodivergent catalysis overcomes this limitation by inverting enantioselectivity through controlled modifications of reaction parameters, such as solvent, temperature, additives, or substrate design, without altering the catalyst's absolute configuration.[3] This strategy is especially valuable in pharmaceutical and bioorganic chemistry, where enantiomers of a bioactive molecule can

---

[1] T. Tanaka, M. Hayashi, *Synthesis*, **2008**, *21*, 3361–3376

[2] Q. Sallembien, L. Bouteiller, J. Crassous, M. Raynal, *Chem. Soc. Rev.*, **2022**, *51*, 3436-3476

[3] I. Beletskaya, C. Nájera, M. Yus, *Chem. Rev.* **2018**, *118*, 5080–5200

exhibit markedly different or even antagonistic biological activities. Asymmetric organocatalysis,[4] with its broad diversity of catalyst architectures and activation modes,[5] already provides a highly versatile platform for stereoselective synthesis, both in total synthesis and in industry.[6] Its potential is further enhanced when designed for enantiodivergence, enabling access to both enantiomers of a target molecule while retaining the sustainability, cost-effectiveness, and high selectivity characteristic of organocatalysis. The significance of enantiodivergent catalysis has been recognized in comprehensive reviews covering both metal- and organocatalyzed systems,[1,3,7] as well as in discussions of switchable catalysts capable of delivering opposite stereochemical outcomes under controlled conditions.[8] However, despite the growing number of enantiodivergent transformations, no recent (post-2018) review has focused exclusively on organocatalytic approaches. This chapter aims to address that gap by providing a focused, critical overview of enantiodivergent reactions in asymmetric organocatalysis from 2018 to the present. Each section will examine a different inversion strategy—such as solvent change, addition of achiral additives, variation of an achiral reagent, or minimal modifications to catalyst structure—highlighting milestone studies alongside innovative, recent methodologies that enable the enantiodivergent construction of complex structural motifs. Mechanistic insights into the structural and environmental factors that drive enantioselectivity inversion will be emphasized, with the aim of guiding the rational design of future organocatalysts and reaction conditions.

Solvent-controlled inversion of enantioselectivity

Solvent choice is a key determinant of both reaction outcome and enantioselectivity in asymmetric catalysis. These effects arise from the ability of solvents of different polarity to differentially organize substrates and catalysts within the transition state, thereby modifying the network of noncovalent interactions that govern stereochemical control. In noncovalent organocatalysis, where high enantioinduction depends on the formation of a well-defined chiral complex, such solvent-dependent organization can profoundly alter the stereochemical course of the reaction. In this context, the role

---

[4] a) B. List, R. A. Lerner, C. F. Barbas, *J. Am. Chem. Soc.*, **2000**, *122*, 2395–2396; b) K. A. Ahrendt, C. J. Borths, D. W. C. MacMillan, *J. Am. Chem. Soc.* **2000**, *122*, 4243–4244

[5] P. Melchiorre, M. Marigo, A. Carlone, G. Bartoli, *Angew. Chem. Int. Ed.*, **2008**, *47*, 6138-6171

[6] a) G. Giorgianni, L. Bernardi, F. Fini, F. Pesciaioli, F. Secci, A. Carlone, *Catalyst*, **2022**, *12*, 912; b) Y. Hayashi, *Acc. Chem. Res.* **2021**, *54*, 1385–1398

[7] a) Y. H. Kim, *Acc. Chem. Res.* **2001**, *34*, 955–962; b) M. Bartók, *Chem. Rev.* **2010**, *110*, 1663–1705

[8] G. Romanazzi, L. Degennaro, P. Mastrorilli, R. Luisi, *ACS Catal.*, **2017**, *7*, 4100–4114

of the solvent in the inversion of enantioselectivity in organocatalysis has been deeply studied. For instance, it is reported that the activity of several organocatalysts is deeply influenced by the solvent polarity, both in Mannich-type, aldol, (sulfa)Michael and chlorocyclization reactions.[9] Such solvent effects often reflect a shift in the thermodynamic nature of the stereodetermining transition state. In polar protic solvents, enantioselectivity is often enthalpically controlled: strong solvent–substrate or solvent–catalyst hydrogen bonding can selectively stabilize one transition state over the other, lowering its activation enthalpy ($\Delta H^{\ddagger}$). In contrast, apolar or weakly interacting solvents often lead to entropic control, where the favored pathway is determined by differences in conformational flexibility or pre-organization, thus minimizing entropic cost ($\Delta S^{\ddagger}$) in one pathway over another. The different control of the reaction, enthalpic or entropic depending on the solvent, can be significant enough to reverse the sense of stereoinduction. This effect can be analyzed through a detailed kinetic analysis based on the Eyring Equation (1), which is equivalent to another form of the same equation (2), whereas $\Delta\Delta S^{\ddagger}_{S\text{–}R}$ and $\Delta\Delta H^{\ddagger}_{S\text{–}R}$ denote the differential activation entropy and enthalpy values associated with the transition states leading to the S- and R- enantiomeric products.[10]

$$ln\left(\frac{k_S}{k_R}\right) = -\frac{\Delta\Delta H^{\ddagger}_{S-R}}{RT} + \frac{\Delta\Delta S^{\ddagger}_{S-R}}{R} \quad (1)$$

$$\Delta\Delta G^{\ddagger}_{S-R} = \Delta\Delta H^{\ddagger}_{S-R} - T\Delta\Delta S^{\ddagger}_{S-R} \quad (2)$$

From the value of the Gibbs free energy difference between the transition states leading to the two enantiomers ($\Delta\Delta G^{\ddagger}_{S\text{–}R}$), it is possible to determine the preferred stereochemical pathway: when $\Delta\Delta G^{\ddagger}_{S\text{–}R} > 0$, the pro-R transition state is favored; conversely, when $\Delta\Delta G^{\ddagger}_{S\text{–}R} < 0$, the reaction preferentially proceeds through the pro-S transition state. By plotting the natural logarithm of the ratio between the formation rates of the R and S enantiomers, $\ln(k_S/k_R)$, against the inverse of the absolute temperature (1/T), a linear relationship is obtained according to the Eyring equation. From this linear fit, the enthalpic ($\Delta\Delta H^{\ddagger}_{S\text{–}R}$) and entropic ($\Delta\Delta S^{\ddagger}_{S\text{–}R}$) contributions to enantioselectivity can be extracted: the slope corresponds to $-\Delta\Delta H^{\ddagger}_{S\text{–}R}/R$, and the y-intercept to $\Delta\Delta S^{\ddagger}_{S\text{–}R}/R$. In the case of enantiodivergent reactions, different solvents or conditions typically lead to plots with distinct slopes and intercepts, reflecting a switch in the dominant stereocontrolling factor — from enthalpic to

---

[9] a) Y. Sotohome, S. Tanaka, K. Takada, T. Yamaguchi, K. Nagasawa, *Angew. Chem. Int. Ed.*, **2010**, *122*, 9440-9443; b) F. C. Wu, C. S. Da, Z. X. Du, Q. P. Guo, W. P. Li, L. Yi, Y. N. Jia, X. Ma, *J. Org. Chem.*, **2009**, *74*, 4812-4818; c) Y. Sohtome, L. Nagasawa, *Chem. Commun.*, **2012**, *48*, 7777-7789; d) A. Garzan, A. Jaganathan, N. S. Marzijarani, R. Yousefi, D. C. Whitehead, J. E. Jackson, B. Borhan, *Chem. Eur. J.*, **2013**, *19*, 9015-9021;

[10] G. Cainelli, P Galletti, D. Giacomini, *Chem. Soc. Rev.*, **2009**, *38*, 990-1001; b) H. Eyring, *J Chem Phys*, **1935**, *3*, 63-71

entropic, or vice versa. For example, in 2010 Nagasawa and coworkers reported the enantioselective Mannich-type reaction between aldimines and diketones catalysed by bis-thiourea catalyst **3**.[9a] The authors reported that the enantiomeric outcome of the reaction could be reversed depending on the solvent polarity (Scheme 1a). Specifically, in nonpolar solvents such as toluene, the (S)-enantiomer of 4 was preferentially formed, while in polar aprotic solvents like acetonitrile, the (R)-enantiomer became dominant. Eyring plot analysis and extraction of the $\Delta\Delta H^{\ddagger}_{S\text{–}R}$, $\Delta\Delta S^{\ddagger}_{S\text{–}R}$ and $\Delta\Delta G^{\ddagger}_{S\text{–}R}$ parameters revealed that both enthalpic and entropic factors contribute to stereoselection. However, in toluene, the pro-S transition state was predominantly influenced by entropic effects, whereas in MeCN, the enantioselectivity favouring the pro-R pathway was primarily driven by enthalpic control (Scheme 1b).

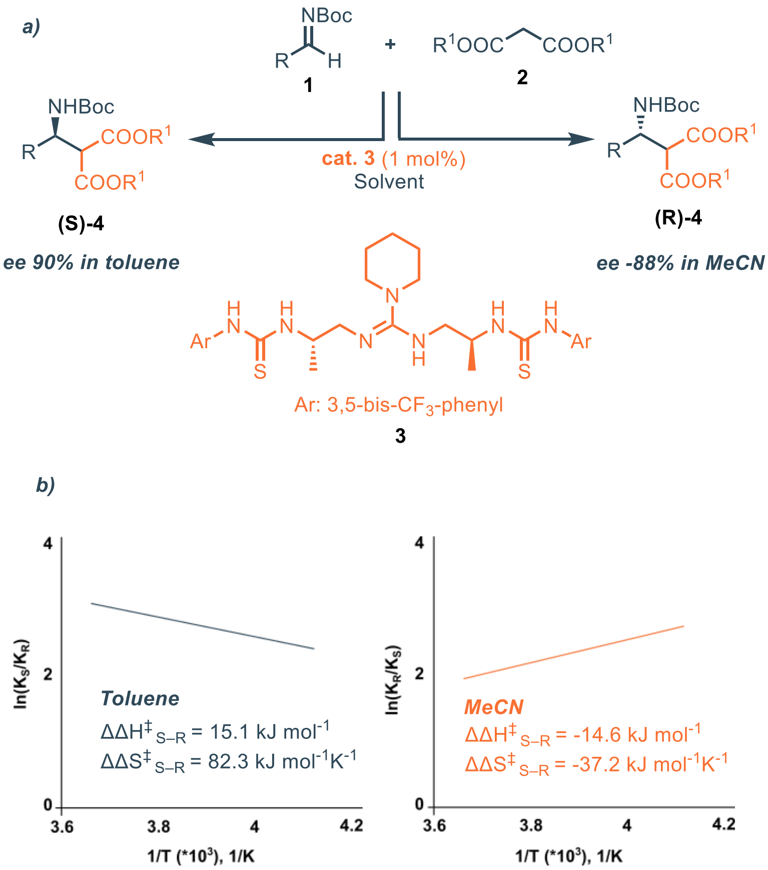

Scheme 1. a) enantiodivergent Mannich-type reaction of aldimines (**1**) with malonates (**2**) catalysed by **3**; b) Eyring plot for the reaction in toluene (blue line) and in acetonitrile (orange line) adapted from ref

The effect of the solvent can also be rationalized using DFT computational calculations by evaluating the relative stabilities of competing transition state (TS) structures in solvents of different polarity. Typically, nonpolar solvents tend to favor transition states stabilized by intramolecular noncovalent interactions (e.g., hydrogen bonding), which are less disrupted in such media. In contrast, polar solvents preferentially stabilize polar transition states via solvation, thereby altering the spatial arrangement of the reactants in the TS and possibly leading to opposite enantioselectivities. In this regard, Chinchilla, Gómez-Bengoa and coworkers reported that catalyst **7** could catalyse the enantioselective addition of α-branched aldehydes to maleimides.[11] Notably, the stereochemical outcome of this reaction was strongly dictated by the solvent. While $CHCl_3$ provides the desired **(S)-8** in 86% ee, a mixture of DMF/H_2O 2:1 delivered the opposite **(R)-8** enantiomer in –84% ee (Scheme 2a). The authors explained this solvent-dependent reversal of enantioselectivity mainly through DFT calculations. They modeled the intermediate enamine and identified two energetically favorable conformations (A and B). For conformation A, where the two NHs are in an anti relative orientation, the transition state TS-AR, where the enamine attacks the Si-face of the maleimide, was found to be highly polar and had the lowest activation barrier in water ($\Delta G^{\ddagger} \approx 14.8$ kcal/mol), leading to the (R)-enantiomer. In contrast, for conformation B, where the two NHs are oriented in a syn fashion, the corresponding transition state TS-BS was less polar and more stabilized in chloroform ($\Delta G^{\ddagger} \approx 16.0$ kcal/mol), due to reduced charge separation and favorable internal noncovalent interactions, thus favoring the (S)-enantiomer (Scheme 2b). Later on, the same group demonstrated that a similar catalyst could perform the same reaction retaining the enantiodivergent mechanism, albeit with a higher enantiomeric induction.[12]

---

[11] J. Flores-Ferrandiz, B. Fiser, E. Gomez-Bengoa, R. Chinchilla, *Eur J. Org. Chem.*, **2015**, *2015*, 1218-1225

[12] P. Vizcaino-Milla, J. M. Sansano, C. Najera, B. Fiser, E. Gomez-Bengoa, *Synthesis*, **2015**, *47*, 2199-2206

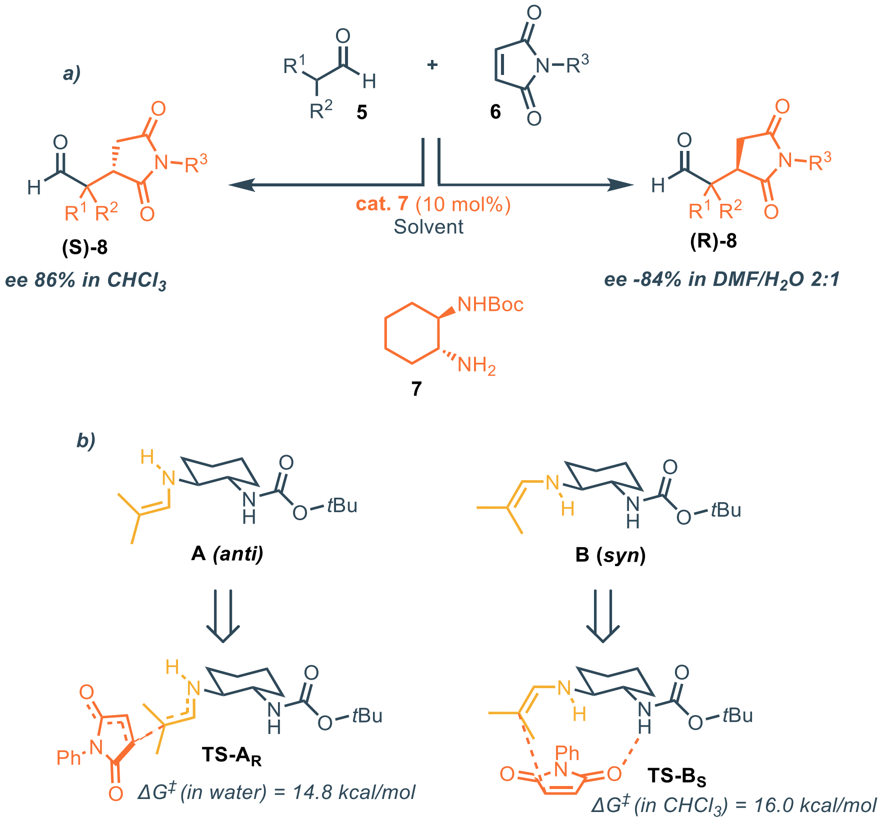

Scheme 2. a) enantiodivergent addition of aldehydes (**5**) to succinimmides (**6**) catalysed by **7**; b) Conformations of catalysts **7** and relative calculated TS structures

It becomes evident that the two analysis methods (experimental kinetic analysis based on Eyring equation vs DFT calculations) provide different, although complementary informations. While Eyring's analysis delivers global thermodynamic insights without showing any structure or geometries of the TS, DFT calculations predicts the ΔG‡ and practically shows how the reactants are arranged in the TS but relies on simplified models which are sensitive to the level of theory and to the solvatation model. Depending on the specific case, one of the two strategies are effective to study the enantiomeric outcome of an enantiodivergent transformation. A clear example of this is found in the enantiodivergent chlorocyclization of unsaturated carbamates 9 catalyzed by $(DHQD)_2PHAL$ catalyst **10**, as described by Borhan and coworkers (Scheme 3a).[9d] In this system, a solvent-induced inversion of enantioselectivity is observed: the reaction proceeds with high selectivity toward the **(R)-11** enantiomer in nonpolar solvents such as $CHCl_3$/hexanes, whereas polar protic solvents like n-propanol favor the (S)-enantiomer **(S)-11**. Crucially, the authors report the presence of inflection points in the Eyring plots, indicating that different transition states become dominant at different temperature regimes. This behavior implies a mechanistic switch, likely involving competing pathways with different sensitivities to enthalpic and entropic contributions. Under these conditions, kinetic analysis becomes a particularly powerful tool, as it can detect these mechanistic shifts by analyzing how the enantiomeric ratio varies with temperature. For instance, in $CHCl_3$/hexanes, the selectivity increases with temperature, suggesting that entropic factors dominate and favor a more disordered, possibly less structured transition state. Although both $\Delta\Delta H^‡$ and $\Delta\Delta S^‡$ remain positive across the temperature range, the entropic contribution to $\Delta\Delta G^‡$ ($T\cdot\Delta\Delta S^‡$) becomes smaller at lower temperatures, reducing the overall free energy difference between the competing transition states. As a result, the enantioselectivity in favor of the (R)-product diminishes. In contrast, in n-propanol, the selectivity decreases with increasing temperature, pointing to a transition state stabilized by specific enthalpic interactions (e.g., hydrogen bonding) at lower temperatures (Scheme 3b). These divergent trends are difficult to capture accurately with DFT alone, due to the complexity of modeling explicit solute–solvent and conformational effects across a wide temperature range.

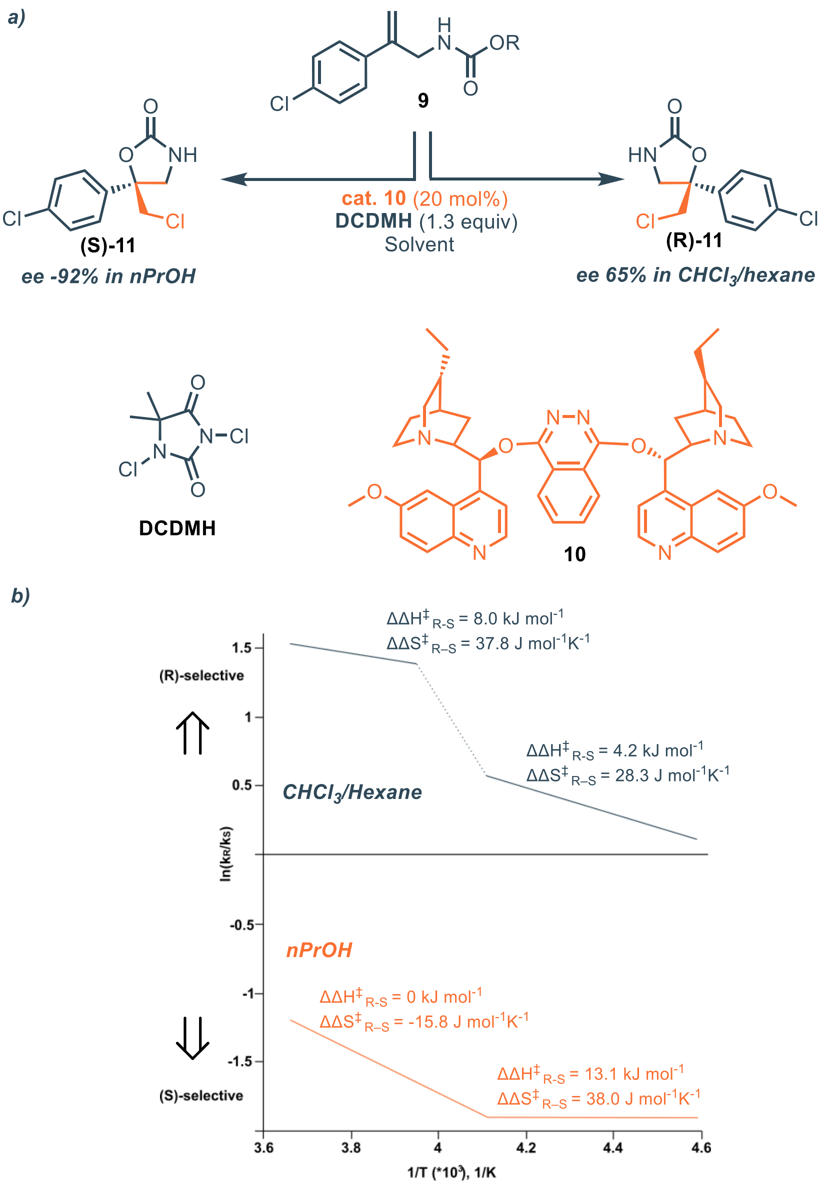

Scheme 3. enantiodivergent chlorocyclization of unsatured carbamates **9** catalysed by **10**; b) Eyring plot for the reaction in $CHCl_3$/hexane (blue line) and in n-propanol (orange line) adapted from ref

DFT calculations and Eyring kinetic analysis were jointly employed to elucidate the solvent effect in the enantiodivergent Friedel–Crafts reaction between sulfonyl indoles (**12**) and 1-naphthols (**13**), catalyzed by the quinine–urea bifunctional catalyst **14** (Scheme 4a).[13] As demonstrated, the solvent polarity plays a crucial role in controlling the enantioselectivity. While non-polar solvents (e.g., toluene, *m*-xylene, CHCl$_3$) afford the **(S)-15** adduct with good to excellent enantioselectivity (up to 97% ee in toluene), polar aprotic solvents such as 1,2-dichloroethane (1,2-DCE) give the (R)-enantiomer (–74% ee). The Eyring plots of ln(k_S/k_R) versus 1/T were constructed to extract the differential activation parameters ($\Delta\Delta H^{\ddagger}$ and $\Delta\Delta S^{\ddagger}$) based on the Eyring equation (Eq. 1). These plots revealed that in non-polar solvents, the enantioselection is entropy-driven, whereas in polar solvents, the selectivity is predominantly enthalpy-controlled (Scheme 4b). This mechanistic divergence is supported by DFT-calculated transition states: In toluene, the TS leading to the (S)-enantiomer (*Si*-face attack) was found to be more stable by ~3.1 kJ/mol, whereas in 1,2-DCE the (R)-selective TS (*Re*-face attack) was marginally favoured (ΔG ≈ –0.3 kJ/mol). Structurally, the transition states differ in their hydrogen-bonding geometry: the (S)-selective TS in toluene shows longer, weaker H-bonds, consistent with a more flexible, entropy-driven transition state, while the (R)-selective TS in 1,2-DCE features shorter, stronger H-bonds, indicative of a more rigid, enthalpy-controlled pathway. These energetic and geometric differences align well with the experimental enantioselectivities observed under each solvent condition.

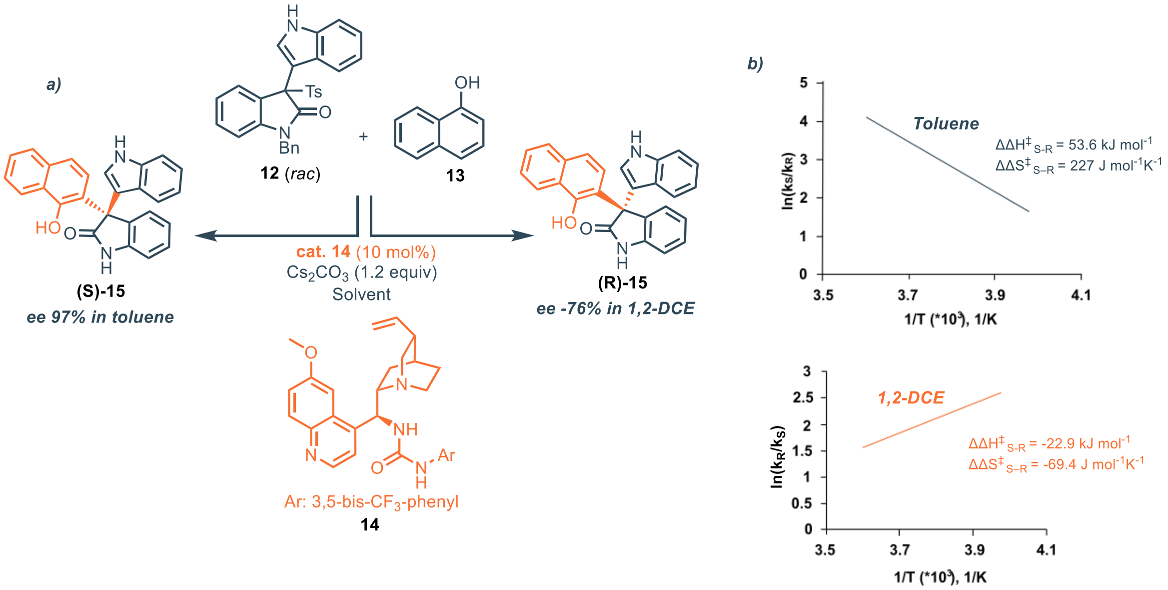

Scheme 4 a) enantiodivergent Friedel-Craft reaction of sulfonyl indole **12** with 1-naphtole **13** catalysed by **14**; b) Eyring plot for the reaction in toluene (blue line) and in 1,2-dichloroethane (orange line) adapted from ref

---

[13] C. H. Chang, N. Sathishkumar, Y. T. Liao, H. T. Chen, J. L. Han, *Adv. Synth. Catal.*, **2020**, *362*, 903-912

Recently, Hayashi and co-workers reported the enantiodivergent synthesis of Hajos–Parrish ketone (HPK) analogs via a domino Michael–Henry reaction catalyzed by diarylprolinol organocatalyst **18** (Scheme 5).[14] A key finding was that the amount of water in the solvent mixture dictates a complete inversion of all five contiguous stereocenters. When the reaction was carried out in dioxane with 3 equivalents of water (conditions A), compound **(–)-19** was obtained with excellent enantioselectivity. In contrast, performing the reaction in MeCN with 30 equivalents of water (conditions B, step 1) furnished the diastereomer **19'** as the kinetic product, again with excellent enantiocontrol. Subsequent treatment with 10 mol% DMAP (conditions B, step 2) induced epimerization at C6 of **19'**, affording **(+)-19** in high yield and enantioselectivity. The origin of this enantioselectivity reversal lies in the face selectivity of the nitrostyrene during the initial Michael addition, which establishes the configuration at C5 and thereby controls the subsequent stereochemical cascade. Under conditions A, the enamine reacts with the *Re*-face of nitrostyrene to give **(–)-19**, whereas under conditions B (step 1), the *Si*-face attack predominates, leading to **19'**. Thus, **(–)-19** is the kinetic product under conditions A, while **19'** is the kinetic product under conditions B. Epimerization of **19'** at C6 under basic conditions (step 2) converts it into the thermodynamically more stable **(+)-19**

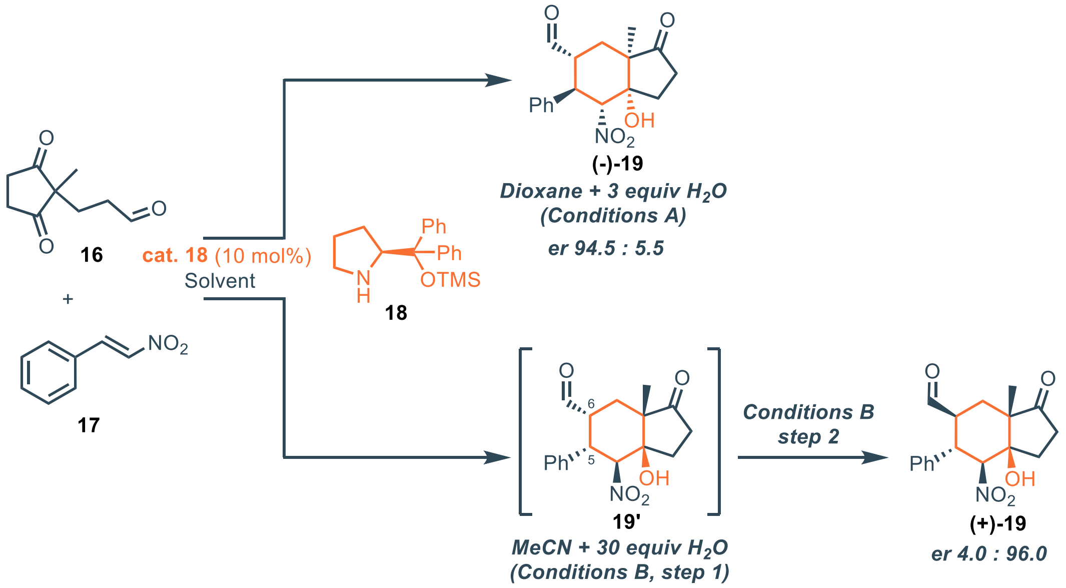

Scheme 5. Enantiodivergent Michael-Henry domino reaction for the construction of Hajos-Parrish ketones

---

[14] Y. Hayashi, Q. Xu, S. Koshino, *Chem. Eur. J.*, **2025**, *31*, e202403580

Different achiral reagents or additives

Authors often encounter enantiodivergence unexpectedly, when subtle modifications to an achiral reagent induce a switch in enantioselectivity. In many cases, the optimization of reaction conditions reveals that both enantiomers of a product can be obtained using the same enantiomer of a chiral catalyst under otherwise identical conditions, simply by employing a different source of achiral chemical input. Such an approach is particularly attractive when only one enantiomer of a catalyst or starting material is available. Similarly, the addition of achiral additives can also promote enantiodivergence in chiral products. Acids, bases, or other additives can influence the transition state by shaping noncovalent interactions (e.g., hydrogen bonding) or by modulating steric and electronic effects.

As extensively discussed in the comprehensive review by Beletskaya et al.,[3] in 2016 Akiyama reported the enantiodivergent synthesis of axially chiral molecules by dynamic kinetic resolution (DKR) using CPAs.[15] Axially chiral scaffolds are highly relevant in synthesis, as they often serve as chiral ligands for both metal- and organocatalysts. In Akiyama's study, reductive amination under DKR conditions with CPAs proceeded with excellent enantioselectivity, enabling access to both enantiomers of biaryl compounds by simply varying the substitution pattern of hydroxyaniline derivatives.

More recently, analogous enantiodivergent strategies for the synthesis of axially chiral molecules have attracted growing interest. Approaches based on different achiral reagents or additives now provide convenient access to both R and S atropisomers. For example, in 2021, Y. Hayashi and coworkers described the enantiodivergent one-pot synthesis of chiral biaryls using the Hayashi–Jørgensen catalyst (Scheme 6).[16] Their method relies on a Michael/aldol domino sequence that converts central into axial chirality, offering an efficient and versatile route to axially chiral frameworks. In this system, enantiodivergence is induced by the judicious choice of halogenated reagents combined with specific achiral additives.

---

[15] K. Mori, T. Itakura, T. Akiyama, *Angew. Chem. Int. Ed.*, **2016**, *128*, 11814-11818

[16] S. Koshino, T. Taniguchi, K. Monde, E. Kwon, Y. Hayashi, *Chem. Eur. J.*, **2021**, *27*, 15786-15794

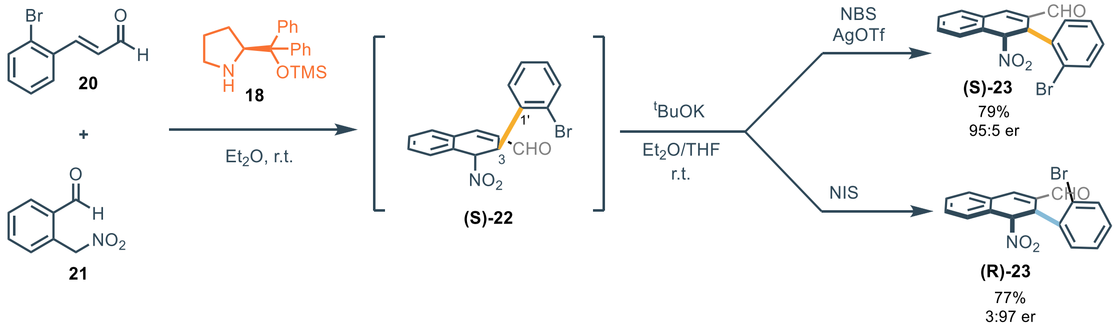

Scheme 6. One-pot organocatalyzed enantiodivergent synthesis of axially chiral biaryl compound **23**.

Prolinol **18** catalyzes the Michael/aldol domino reaction between **20** and **21** through a dual activation mode: via iminium ion formation and via the enamine pathway. The resulting compound **23** is obtained as both R and S isomers in good yields and with excellent diastereo- and enantioselectivities. The conversion of the central chiral intermediate **(S)-22** into the axially chiral product **23** proceeds through a three-step sequence: (i) nitronate generation in the presence of t-BuOK; (ii) halogenation of the nitronate with N-halosuccinimide (NXS); and (iii) aromatization through HX elimination. Notably, all these steps can be performed in a one-pot fashion.

Mechanistic investigations revealed that enantiodivergence in this transformation is closely linked to the stability of the halogenated intermediate and to the acid–base properties of the additives employed. To probe this effect, intermediates **24a** and **24b** were prepared using NBS and NIS, respectively. Both were isolated as single diastereoisomers, sharing the same C3–C1′ bond configuration. However, **24a** proved more stable and less reactive than **24b**, which readily decomposes at room temperature. After halogenation (step ii), potassium succinimide is generated as a weak base. Under these conditions, **24b** undergoes smooth conversion to **(R)-23**, whereas **24a** remains unreactive (Table 1, entries 1–2). The transformation of **24a** into **(R)-23** requires the presence of stronger bases (entries 3–4). Conversely, both **24a** and **24b** afford the opposite enantiomer **(S)-23** when Ag salts such as AgOTf are used as additives (entries 5–6).

Table 1. The reactivity of **24a** and **24b** in the presence of different additives.

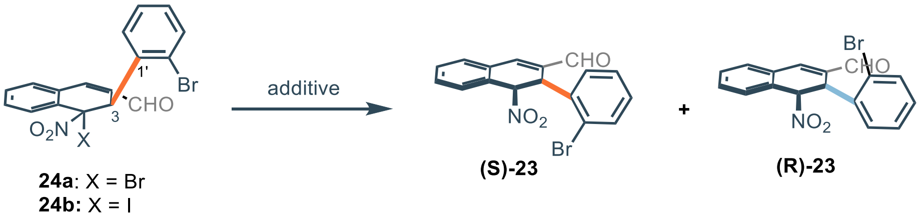

(S)-23 **(R)-23**

24a: X = Br
24b: X = I

Entry	Intermediate	Additive	(S)-23 : R-(23)
1	24b	K-succinimide	2:98
2	24a	K-succinimide	n.d.
3	24a	t-BuOK	>1:99
4	24a	Et_3N	>1:99
5	24a	AgOTf	97:3
6	24b	AgOTf	96:4

Two main aspects can be underlined from the results in Table 1. First, the more stable intermediate **24a** is significantly less reactive than **24b**; as a consequence, a weak base such as K-succinimide is ineffective under the reaction conditions. Second, the **(R)-23** enantiomer is favored under basic conditions, whereas the **(S)-23** enantiomer predominates under "acidic" conditions. Since entry 5 provided the best enantioselectivity for Method A, NBS was chosen as the halogen source. Conversely, NIS was selected for Method B because no external base is required when **24b** is formed as the intermediate. The proposed mechanism for these two distinct pathways is further supported by the strong agreement between DFT calculations and experimental data (Scheme 7).

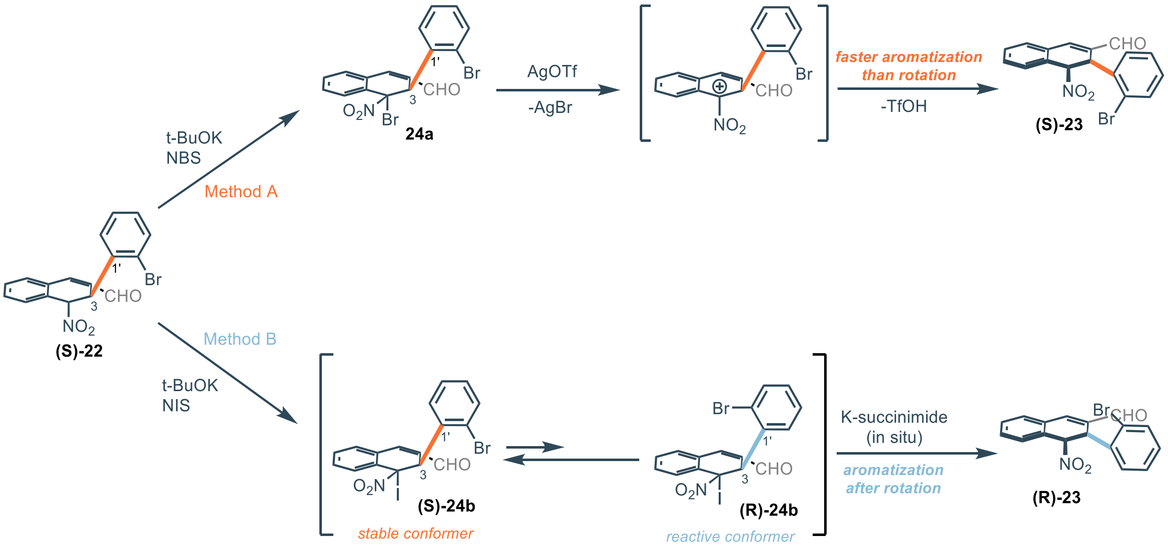

Scheme 7. Proposed mechanism for enantiodivergent synthesis of **23**

In Method A, treatment of **24b** with AgOTf generates a cationic intermediate that is highly reactive due to the presence of the adjacent NO_2 group. Under these conditions, deprotonation occurs rapidly before rotation around the C3–C1′ bond, leading to the formation of **(S)-23**. In Method B, by contrast, no highly reactive cationic intermediate is produced; as a result, rotation around the C3–C1′ bond takes place, giving rise to **(R)-23**, which is thermodynamically disfavored. In this pathway, the elimination step is mediated by the in situ generated K-succinimide. Notably, deprotonation at the C3 position is favored in **(R)-24b**, owing to reduced steric hindrance, ultimately affording the desired product as the opposite enantiomer **(R)-23**.

As mentioned above, enantiodivergence can also be induced by switching the activation mode of the transition state through modification of the achiral reagent. A clear example is the organocatalyzed synthesis of **(S)-27** and **(R)-27**, which becomes possible by simply changing the fluorinating source.[17] In the presence of an acid co-catalyst, chiral primary–tertiary diamines serve as efficient organocatalysts for the asymmetric fluorination of α-branched aldehydes (Scheme 8a). In this system, the primary amine engages in enamine catalysis with the aldehyde substrate, predominantly forming the E-enamine intermediate. Interestingly, the use of compound **25** or **26** directs the reaction toward opposite enantiomers, depending on whether hydrogen-bonding interactions or electrostatic repulsion dominate in the transition state. However, the extent of this enantiodivergence is strongly solvent-dependent, further highlighting the interplay between reagent, additive, and reaction medium.

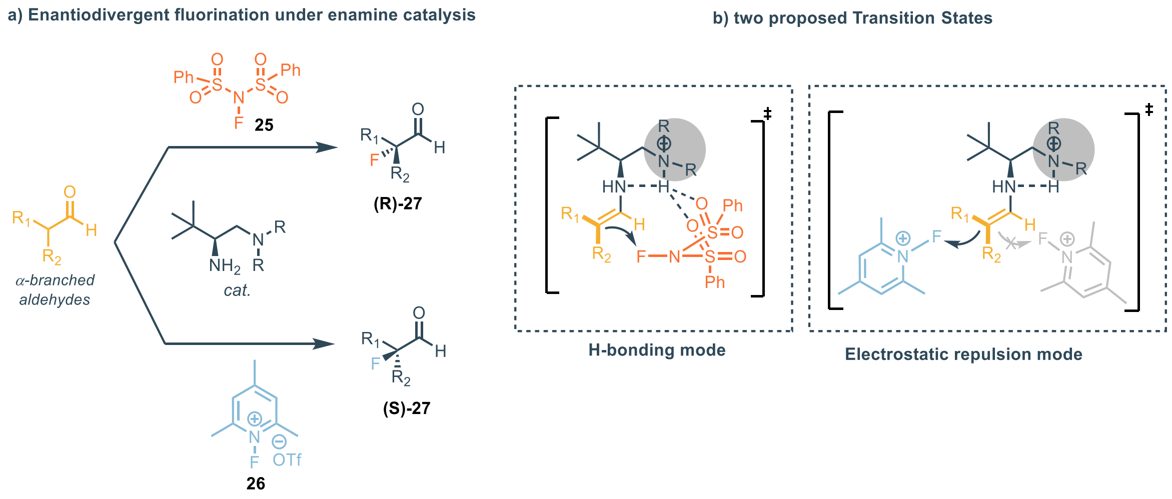

---

[17] L. Cui, Y. You, X. Mi, S. Luo, *J. Org. Chem.*, **2018**, *83*, 4250-4265

Scheme 8. a) organocatalyzed fluorination of α-branched aldehydes, an example of reagent-controlled enantiodivergent synthesis; b) proposed transition states related to hydrogen-bonding mode (*Re*-facial attack) and electrostatic repulsion mode (*Si*-facial attack).

The authors demonstrated that the R-selective pathway is favored when the neutral fluorinating reagent **25** is employed in aprotic, low-polarity solvents. For example, in $CHCl_3$, **(R)-27** was obtained in 86% yield and 85% ee, whereas in MeOH the enantioselectivity dropped sharply. This outcome is consistent with the hydrogen-bonding activation mode (Scheme 8b), since low-polarity solvents such as $CHCl_3$ minimize competing interactions and solvent effects. By contrast, the cationic fluorinating reagent **26** promoted the S-selective pathway in polar, protic solvents. In DMF, **(S)-27** was produced in 82% yield and –85% ee, while in $CHCl_3$ the same reagent afforded **(R)-27** with only modest enantioselectivity. The authors attributed this behavior to an electrostatic repulsion mode (Scheme 8b), in which polar solvents enhance charge-associated interactions, thus favoring the S-selective pathway. Selectivity could be further tuned by minor modifications of the catalyst structure. Bulkier substituents on the tertiary amine, such as an isopropyl group, reinforced the electrostatic repulsion mode by introducing steric hindrance, thereby improving the enantioselectivity. These studies represent clear examples of how a combination of achiral stimuli, reagents, additives, and solvents, can induce opposite stereochemical outcomes using a single enantiomer of a chiral catalyst.

More recently, the enantiodivergent synthesis of inherently chiral eight-membered lactones has been achieved through a carbene-catalyzed, base-controlled strategy.[18] In this transformation, different lactones were prepared, and it was demonstrated that one of the enantiomeric forms exhibits notable antimicrobial and antibacterial activity in the agricultural field. The key step involves the intramolecular cyclization of triaryl aldehyde **28** under basic conditions (Scheme 9). The reaction proceeds in excellent yields and with high enantioselectivity, and, quite remarkably, achiral bases themselves are responsible for inducing enantiodivergence. The best results were obtained using NaOAc and DBU as bases. The robustness of this methodology is underscored by its broad substrate scope: both electron-donating and electron-withdrawing substituents, as well as different substitution patterns on the triaryl aldehyde aromatic rings, are well tolerated. In most cases, both enantiomers of the product could be accessed in high yield and excellent enantioselectivity.

---

[18] L. Wei, Y. Chen, Q. Zhou, Z. Wei, T. Tu, S. Ren, Y. R. Chi, X. Zhang, X. Yang, *J. Am. Chem. Soc.*, **2025**, *147*, 30747-30756

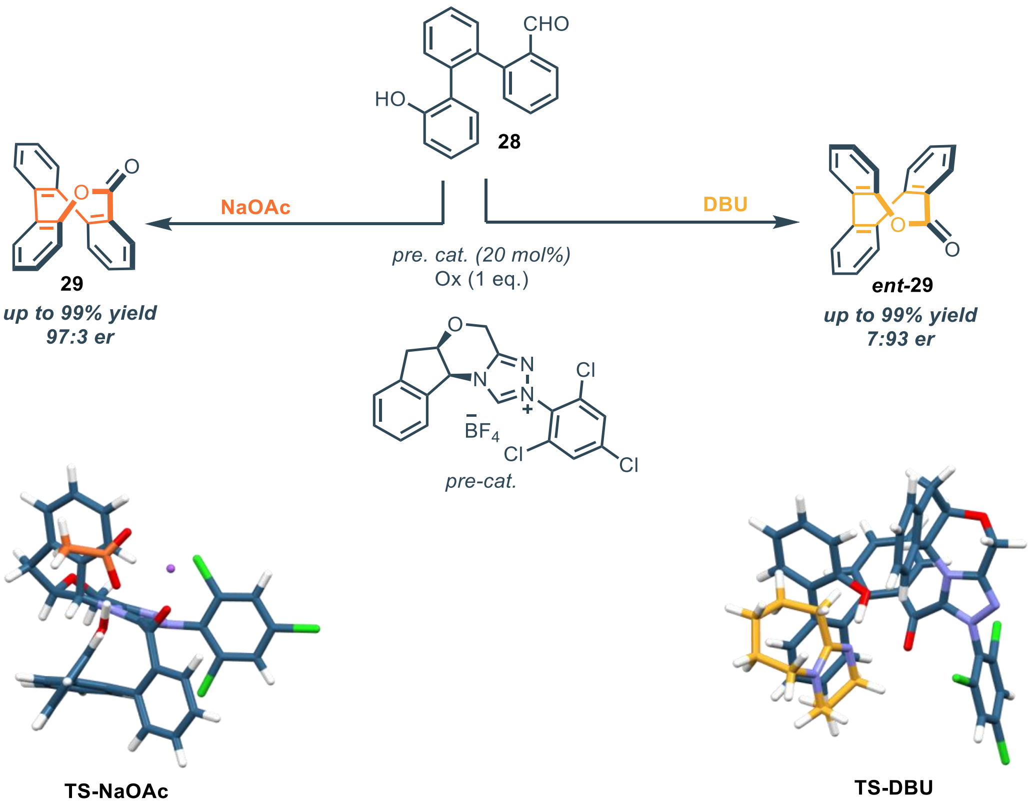

Scheme 9. Enantiodivergent carbene-catalyzed intramolecular cyclization of triaryl aldehydes to access inherently chiral lactones. The enantioselective switch is under base control.

DFT calculations were carried out to elucidate the base-controlled enantiodivergent mechanism. The results showed that different bases establish distinct interactions with the acyl azolium intermediate during the cyclization step. Initially, the carbene catalyst is generated in situ and reacts with **28** to form the acyl azolium intermediate. The lowest-energy conformers are those in which the hydroxyl group is positioned close to the carbonyl carbon of the acyl azolium. Rotation around the C–C axial bond occurs with a relatively low barrier, enabling facile interconversion between conformations.

The transition states (TSs) are strongly influenced by the mode in which the base deprotonates the hydroxyl group of substrate **28**. In particular, the oxygen of the phenoxide group can interact with the carbonyl of the acyl azolium, resulting in opposite ring closures. Noncovalent interactions and distortion energies are thus identified as the key driving forces behind enantiodivergence. For both NaOAc and DBU, two possible TS structures were considered; in each case, the lower-energy pathway corresponded to the experimentally observed major enantiomer, in excellent agreement with the measured er values (Scheme 9). Notably, the pathway associated with the lower barrier is stabilized by a higher degree of noncovalent interactions, which ultimately dictates the opposite stereochemical outcome of the ring closure.

Recently, the enantiodivergent synthesis of chiral sulfinimidate esters has been reported through a reagent-regulated organocatalytic strategy.[19] The process involves a tandem chlorination–nucleophilic substitution of sulfenamide in the presence of ethanol as the nucleophile (Scheme 10). The reaction is catalyzed by the chiral pentanidium **31**, which engages with sulfenamide **30** under basic conditions to generate a reactive ion pair.

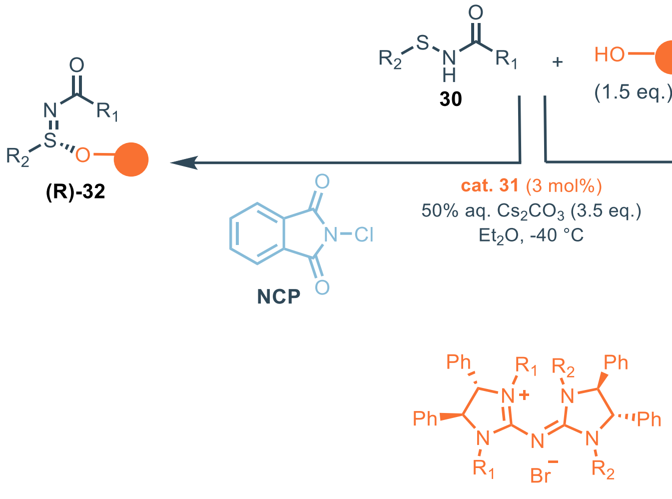

Scheme 10. General procedure for the reagent-controlled enantiodivergent synthesis of sulfinimidate **32** catalysed by PN catalyst.

N-Chlorophthalimide (NCP) and trichloroisocyanuric acid (TCCA) were employed as chlorinating reagents, leading respectively to the R- and S-enantiomers of the target sulfinimidate ester. With TCCA, the transformation is remarkably fast, completing in only 5 minutes, whereas reactions with NCP require up to 24 hours. The slower kinetics in the latter case are consistent with the formation of a stable intermediate. Indeed, ^{19}F NMR monitoring revealed the appearance of a new signal at the beginning of the reaction, which gradually disappeared as the reaction progressed. Although most of the starting material **30** was consumed within 9 hours, the concentration of product **32** continued to increase over time until the intermediate was completely consumed.

The authors proposed an enantiodivergent pathway in which the tandem chlorination–nucleophilic substitution sequence proceeds under strict reagent control (Scheme 11). With TCCA, the highly reactive intermediate **(R)-Int-1** undergoes a rapid nucleophilic attack by the alcohol, leading to inversion of configuration and affording **(S)-32**. This accounts for the very short reaction time observed. By contrast, when NCP is used, **(R)-Int-1** first reacts with the in situ generated phthalimide

---

[19] W. L. Cui, L. Zhang, C. Liu, J. Su, H. R. Zhang, R. Ma, D. Jian, W. Xiang, X. Ye, X. Zhang, *J. Am. Chem. Soc.*, **2025**, *147*, 19986-19995

anion, producing a second intermediate, **(S)-Int-2**. This species is significantly less reactive toward nucleophilic attack by the alcohol, thereby explaining the slower overall kinetics. Ultimately, (S)-Int-2 reacts with the alcohol to afford **(R)-32**, again through inversion of configuration.

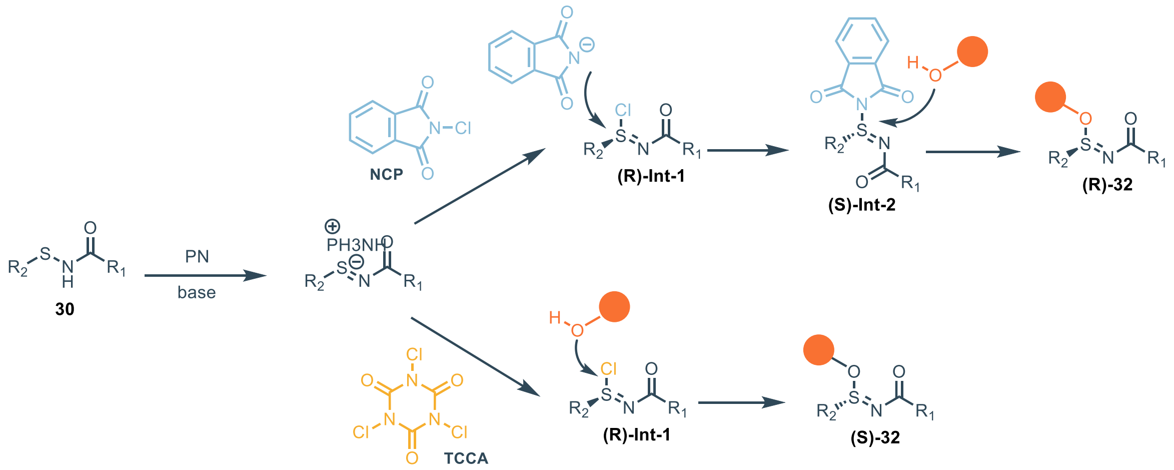

Scheme 11. Proposed mechanism for the reagent-controlled enantiodivergent synthesis of sulfinimidates.

In 2021, Chen, Yang and co-workers demonstrated the critical role of additives in the stereoselective organocatalytic [4+2]-annulation between isatylidenes **33** and 2-cyclopentenone **34**.[20] They developed a synthetic strategy that enables access to both enantiomers of the spirooxindole–norcamphor scaffold **35** by simply varying the additive: $CaCl_2$ in DMF favors one enantiomer, whereas H_2O in DCM directs the reaction toward the opposite enantiomer (Scheme 12).

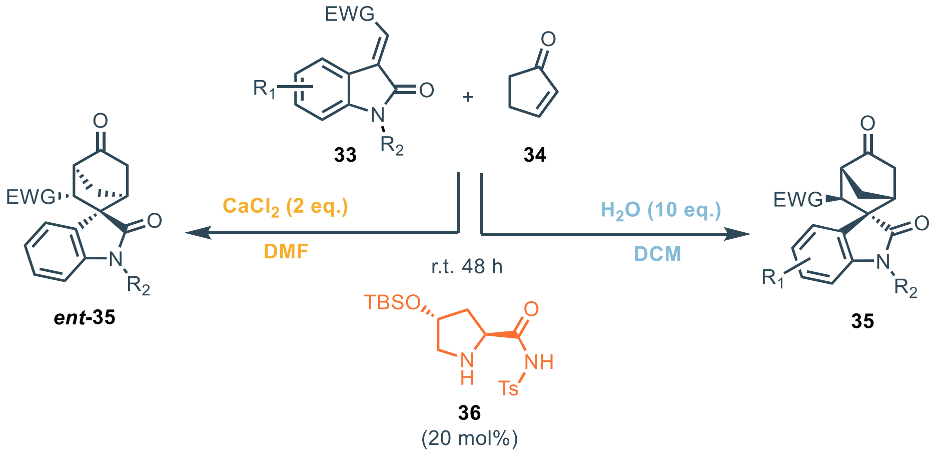

Scheme 12. Diastereo- and enantioselective organocatalytic [4+2]-annulation for the synthesis of spirooxindole-norcamphor scaffold. Enantiodivergence is induced by the presence of $CaCl_2$ in DMF.

The prolinosulfonamide catalyst **36** efficiently promotes the [4+2]-annulation reaction, affording both enantiomers of the product in high yield and with excellent diastereo- and enantioselectivity. In one case, the best results were obtained by adding 10 equivalents of H_2O in DCM (Table 2, entry 1).

---

[20] J. Wang, X. Z. Zheng, J. A. Xiao, K. Chen, H. Y. Xiang, X. Q. Chen, H. Yang, *Org. Lett.*, **2021**, *23*, 963-968

Conversely, the addition of $CaCl_2$ under otherwise identical conditions led to a sharp decrease in enantioselectivity (Table 2, entry 2), indicating that $CaCl_2$ promotes formation of the opposite enantiomer, ent-**35**. Indeed, when DMF was used as solvent in combination with $CaCl_2$, a complete reversal of enantioselectivity was achieved (Table 2, entries 3–4).

Mechanistically, prolinosulfonamide **36** activates both reaction partners: the pyrrolidine unit of **36** condenses with 2-cyclopentenone **34** to generate the corresponding chiral dienamine, while isatylidene **33** can be engaged through hydrogen-bonding interactions with the sulfonamide N–H group. This dual activation mode, combined with the effect of the additive, accounts for the observed enantiodivergence.

Table 2. Optimization of reaction conditions.

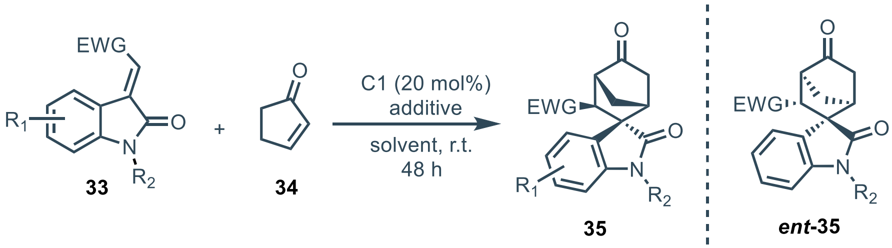

Entry	Solvent	Additive	Yield %	ee%
1	DCM	H_2O (10 eq.)	91	93 (35)
2	DCM	$CaCl_2$ (2 eq.)	15	0
3	DMF	$CaCl_2$ (2 eq.)	92	-59 (*ent*-35)
4	DMF	$CaCl_2$, K_2CO_3	94	-98 (*ent*-35)

The authors proposed that the Michael addition between the dienamine intermediate and compound **33** constitutes the selectivity-determining step. In the absence of $CaCl_2$, hydrogen-bonding interactions guide the addition of the dienamine intermediate to the C=C double bond of **33**, affording **35**. In contrast, $CaCl_2$ profoundly alters the transition state by coordinating with both the sulfonyl group of catalyst **36** and the carbonyl group of oxindole **33**. This coordination stabilizes an alternative transition state (TS1′), thereby reversing the enantioselectivity and leading to ent-**35** (Scheme 12).

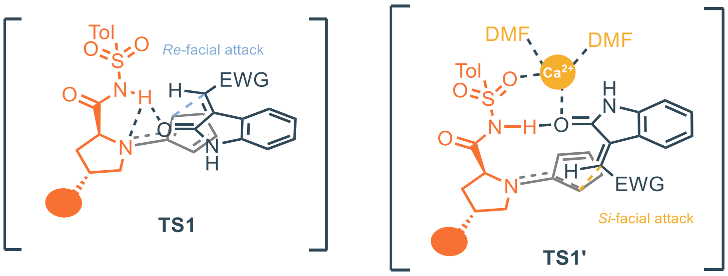

Scheme 12. Proposed transition states TS1 and TS1' in the presence or absence of $CaCl_2$ and DMF.

Minimal catalysts modification

Another strategy to achieve enantiodivergent organocatalysis is to introduce peripheral modifications to the catalyst structure without changing its inherent stereochemistry. While the stereochemical outcome of a reaction is usually governed by the diastereomeric transition state complex and therefore by the chirality of the catalyst, secondary noncovalent interactions often play a decisive role. Subtle alterations of these interactions can shift the balance of stereocontrol, ultimately leading to a reversal of enantioselectivity.

A prominent example in this regard comes from Huang and coworkers, who reported in 2021 the enantiodivergent NHC-catalyzed [4+2] cycloaddition of aldimines with activated ketones (Scheme 13a).[21] The reaction proceeds via formation of an aza-Breslow intermediate (**I**) between the NHC and the aldimine **36**, which, upon oxidation, yields intermediate **II**. Subsequent deprotonation generates a 1,4-dipolar species (**III**), which engages in a [4+2] cycloaddition with trifluoromethyl ketones, furnishing chiral heterocycles with quaternary carbon centers **38**. During the reaction optimization, the author noticed that subtle modification in the structure of the NHC dramatically affected the sense of enantioinduction. Catalyst **39b**, bearing bulky isopropyl groups on the aryl substituent, afforded the (S)-enantiomer in 93:7 enantiomeric ratio. In contrast, catalyst **39a**, which differs from **39b** only by having chlorine atoms instead of isopropyl groups on the aryl ring, completely reversed the enantioselectivity to 6:94 er (favoring the *R*-enantiomer) when used in conjunction with Schreiner's thiourea **40** as a non-chiral co-catalyst (Scheme 13b). This peculiar effect was studied via DFT analysis, revealing that the observed enantioselectivity is governed by non-covalent C–H···F hydrogen bond interactions between the NHC-substrate complex and the trifluoromethyl ketone. For catalyst **39b**, two stabilizing C–H···F interactions in the transition state favored the formation of the S-enantiomer. However, introduction of chlorine atoms in catalyst **39a** disrupted these interactions, leading to an inversion of the favored transition state geometry and thus enantioselectivity. The presence of the thiourea co-catalyst further stabilized the altered transition state through additional hydrogen bonding, amplifying the selectivity reversal. Notably, since the enantioselectivity reversal is driven by the weakening of C–H···F hydrogen bonds in the stereodetermining transition state, this

---

[21] G. Wang, Q. C. Zhang, C. Wei, Y. Zhang, L. Zhang, J. Huang, D. Wei, Z. Fu, W. Huang, *Angew. Chem. Int. Ed.*, **2021**, *60*, 7913-1919

divergence effect is strictly dependent on the presence of a CF_3 group in the electrophilic partner. When the substrate lacks a trifluoromethyl substituent, such as in reactions involving isatin derivatives, the non-covalent interactions that control enantioselectivity are no longer operative. As a result, no inversion of enantioinduction is observed, and the reaction proceeds with the inherent selectivity of the parent NHC catalyst.

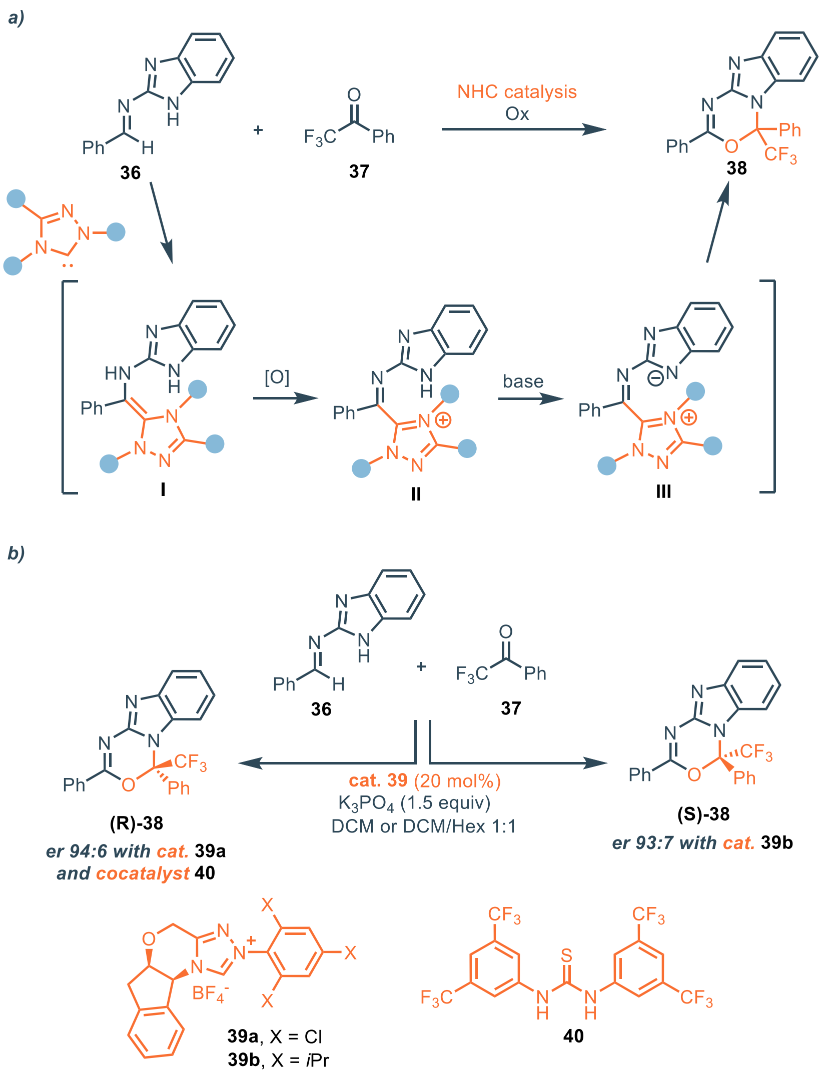

Scheme 13. a) Enantioselective NHC catalysed [4+2] cycloaddition of aldimines with trifluoromethyl ketones; b) Minimal modifications of the NHC precursor enable enantiodivergence

Another relevant example of this concept is the enantiodivergent Michael reaction between aldehydes (**42**) and C-alkynyl ketimines (**41**) proposed by Shao and coworkers.[22] In this case, chiral secondary amines catalysts were precisely engineered to achieve an enantiodivergent access to chiral propargylamines bearing quaternary stereocenters. In particular, the substitution pattern of the catalyst strongly influences the enantiomeric outcome. When a catalyst featuring a bulky i-Bu group

---

[22] J. Dai, Z. Wang, Y. Deng, L. Zhu, F. Peng, Y. Lan, Z. Shao, *Nat. Commun.*, **2019**, *10*, 5182

on the secondary amine was used (**43a**), the product **(S,R)-44** was formed with excellent diastereo- and enantiocontrol. On the other hand, catalyst **43b**, bearing a smaller N-Me group, could catalyse the same transformation delivering the opposite enantiomer **(R,S)-44**, also with high diastereo- and enantioselectivity. (Scheme 14a) The generality of these two enantiodivergent catalysts was demonstrated applying the same catalytic systems to a broad range of Mannich-type reactions involving structurally diverse substrates. DFT calculations were employed to clarify the origin of the enantiodivergence. The resulting data revealed that the enamines derived from **43a** and **43b** feature distinct conformational preferences. For **En-43a** the s-syn is energetically favored (by ~9 kcal/mol), while for **En-43b**, the s-anti conformation is preferred (13 kcal/mol). This is majorly due to different profiles of steric repulsion exerted by the N-substituents within the catalyst structure (Scheme 43b). This way, with catalyst xa the *Si* face of the enamine reacts with the *Re* face of the imine, delivering a 9-membered cycle TS(**43a**-S,R) with a chair-boat arrangement, while catalyst **43b** allows the reaction of the Re face of the enamine with the Si face of the imine, with a chair-chair arrangement of the transition state TS(4**3b**-R,S). (Scheme 14c)

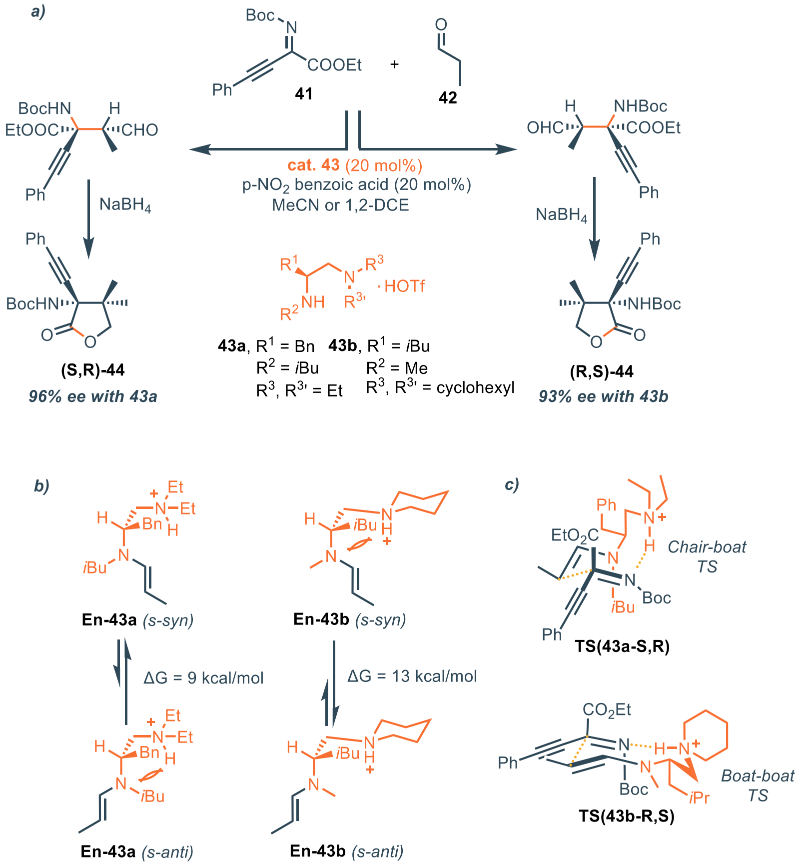

Scheme 14. a) enantiodivergent Michael addition on C-alkynyl ketimines; b) preferred conformation of the different enamines; c) Most stable TS structures delivering opposite enantiomers with the catalysts **43a** and **43b**

Interlocking the catalyst has emerged as an effective strategy to control, and even reverse, the sense of enantioselectivity in asymmetric catalysis. In 2019, Berna and coworkers reported that the mechanical interlocking of a prolinamide–fumaramide organocatalyst **48** significantly altered the stereochemical outcome of the Michael addition of ketones (**45**) to β-nitrostyrene **46** (Scheme 15a).[23] The catalyst is composed of a prolinamide moiety, responsible for enamine activation of the ketone, and a fumaramide scaffold which enables hydrogen bonding and, in the interlocked form, positions the macrocycle along the catalytic axis. When tested in the reaction between acetone and β-nitrostyrene, the non-interlocked catalyst **48** afforded the (S)-enantiomer of the product with an enantiomeric ratio of 72:28. In contrast, its interlocked analogue **49** reversed the sense of enantioinduction, yielding the (R)-enantiomer in 27:73 ratio. To understand the origin of this enantiodivergence, DFT calculations were performed on simplified enamine intermediates derived from both catalysts. In the case of the non-interlocked catalyst **48**, DFT calculations showed that both transition states, leading to the (S)- and (R)-enantiomers (respectively, $\mathbf{TS_{48,Si}}$ and $\mathbf{TS_{48,Re}}$), exhibit hydrogen bonding between the amide NH group of the catalyst and the nitro group of β-nitrostyrene, with H···O distances of 1.99 Å. The transition state leading to the (S)-product is favored by 7.0 kJ/mol, due to a more favorable spatial orientation between the enamine and the aromatic ring of the nitrostyrene, which allows for reduced steric interactions and an efficient Bürgi–Dunitz-type approach.[24] In the interlocked (rotaxane) catalyst **49**, hydrogen bonding with the nitrostyrene is observed only in the transition state leading to the (R)-enantiomer ($\mathbf{TS_{49,Re}}$). In this case, the hydrogen bond originates from the macrocycle's NH group, with an H···O distance of 1.92 Å and is accompanied by a favorable alignment of the reacting partners. This stabilizes the transition state relative to the alternative (pro-S) pathway ($\mathbf{TS_{49,Si}}$), which lacks such interaction, resulting in a 7.3 kJ/mol preference for the (R)-enantiomer (Scheme 15b).

---

[23] A. Martinez-Cuezva, M. Marin-Luna, D. A. Alonso, D. Ros-Niguez, M. Alajain, J. Berna, *Org. Lett.*, **2019**, *21*, 5192-5196

[24] H. B. Buergi, J. D. Dunitz, *Acc. Chem. Res.*, **1983**, *16*, 153-161

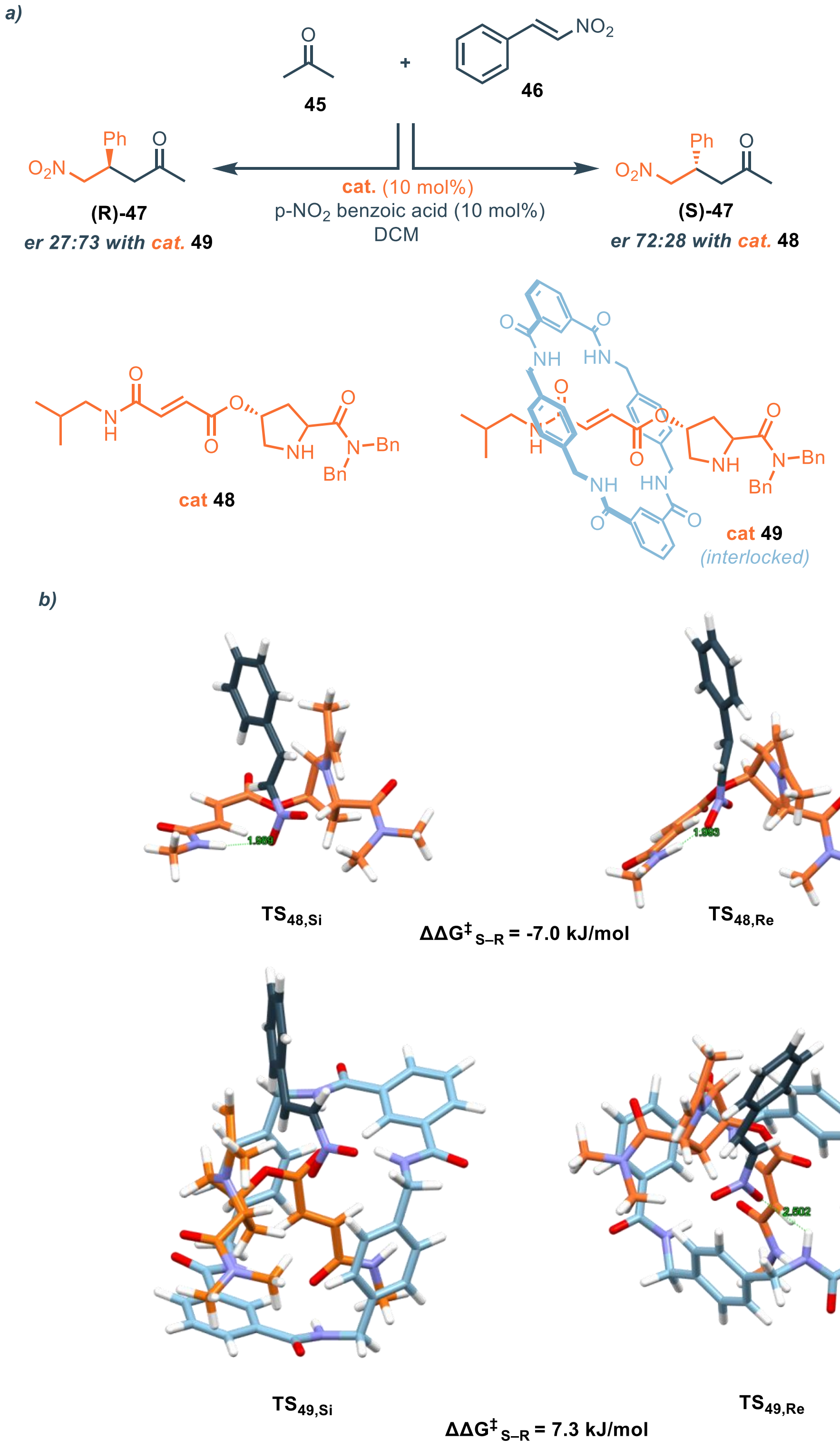

Scheme 15. a) Interlocked and non-interlocked catalysts **48** and **49** allows for the enantiodivergent Michael addition on nitro olefines; b) Most stable TS for the attack on the Si- and Re-face of nitrostyrene with catalysts **48** and **49**

In 2021, Wang and co-workers reported a highly enantiodivergent method for the synthesis of axially chiral biaryl compounds through DKR. In this strategy, dipeptide–phosphonium salts catalyze the reaction between phosphine oxides and 1,1′-biaryl-2,2′-diols or amino alcohols, affording axially chiral organophosphorus derivatives.[25] The approach was inspired by the Atherton–Todd reaction, a well-established method for the synthesis of organophosphorus compounds, which proceeds via in situ halogenation of phosphine oxides **50** under basic conditions.[26] The resulting phosphoryl chloride **51** is highly reactive and readily undergoes nucleophilic attack by alcohols and amines (Scheme 16a).

In the presence of phosphonium salts, intermediate **51** can evolve to generate a phosphorus anhydride **52**. Enantiodivergence is triggered by the nature of the phosphonium salts: substituents and counterions on the salt, while maintaining the same inherent stereochemistry, determine whether intermediate **51** or **52** is preferentially captured under the DKR regime. As a consequence, the system selectively channels the reaction into either an R-selective or an S-selective phosphorylation pathway (Scheme 16b).

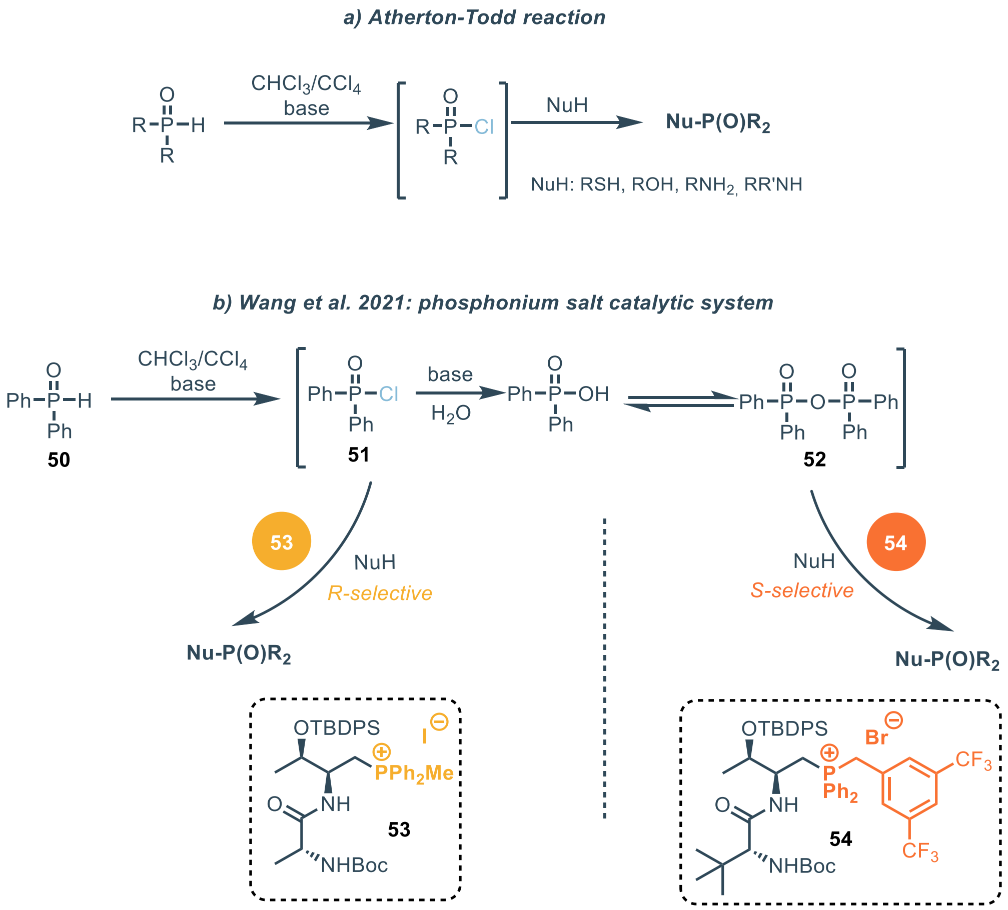

Scheme 16. a) a schematic representation of Atherton-Todd reaction for the synthesis of organophosphorus compound under basic conditions; b) catalytic process developed by Wang et al. inspired by the AT-reaction. Two P-species **51** and **52** are formed as intermediate. Single chiral phosphonium salts can differentiate between **51** and **52** leading to R or S-selective pathway.

---

[25] S. Fang, J. P. Tan, J. Pan, H. Zhang, Y. Chen, X. Ren, T. Wang, *Angew. Chem. Int. Ed.*, **2021**, *60*, 14921-14930

[26] F. R. Atherton, A. R. Todd, *J Chem Soc*, **1947**, 674-678

Dipeptides **53** and **54** efficiently catalyze the phosphorylation of 1,1′-biaryl-2,2′-diols (**rac-55**) and amino alcohols under DKR conditions, affording the desired products with excellent enantioselectivity (up to 99% ee). In CCl_4, catalyst **53** delivers the R-isomer, while **54** favors the S-isomer. In both cases, the unreacted starting material **55** was recovered in highly enantioenriched form. The broad substrate scope highlights the robustness of the protocol and its scalability, with reactions successfully performed on gram scale.

The origin of enantiodivergence stems from the different catalytic behaviors of the dipeptide–phosphonium salts. Catalyst **53** promotes a slow conversion of intermediate **51** into **52** (Scheme 17a). As a result, phosphorylation mainly occurs directly between **51** and the (R)-enantiomer of racemic **55**, producing **(R)-56** and leaving behind unreacted **(S)-55** (Scheme 17b). Conversely, in the presence of **54**, the conversion of **51** into **52** is rapid (Scheme 17a). In this scenario, **52** becomes the principal reactive P-species, and phosphorylation proceeds preferentially with **(S)-55**, yielding **(S)-56** (Scheme 17c).

Control experiments provided further mechanistic insights. When **51** was used directly as the substrate with catalyst **53**, the process remained R-selective, affording **(R)-56** with 99% ee. In contrast, using **52** with **53** led to the opposite enantiomer **(S)-56**, but with low selectivity. As expected, the situation was reversed for catalyst **54**: in the presence of **52**, **(S)-56** was formed with 99% ee, whereas reactions with **51** gave only modest selectivity. Additional tests with optically pure **55** confirmed these match/mismatch effects: catalyst **53** matched well with **(R)-55**, rapidly converting it into **(S)-55**, while **54** matched with **(S)-55**, affording **(R)-55**.

These observations suggest that enantioselectivity is governed by hydrogen-bonding interactions between the amide and carbamate moieties of the catalyst and the reactive phosphorus species. Transition-state models were proposed based not on computational studies, but on ^{1}H NMR titration experiments performed with catalysts **53** and **54** in the presence of **51** or **52**. For **54**, downfield shifts of the amide, carbamate, and benzylic protons were observed in the presence of **52**, consistent with the formation of three hydrogen-bonding interactions (Scheme 17b). In contrast, catalyst **53**, lacking the benzylic position, engages only its amide and carbamate groups in hydrogen bonding with **51** (Scheme 17c).

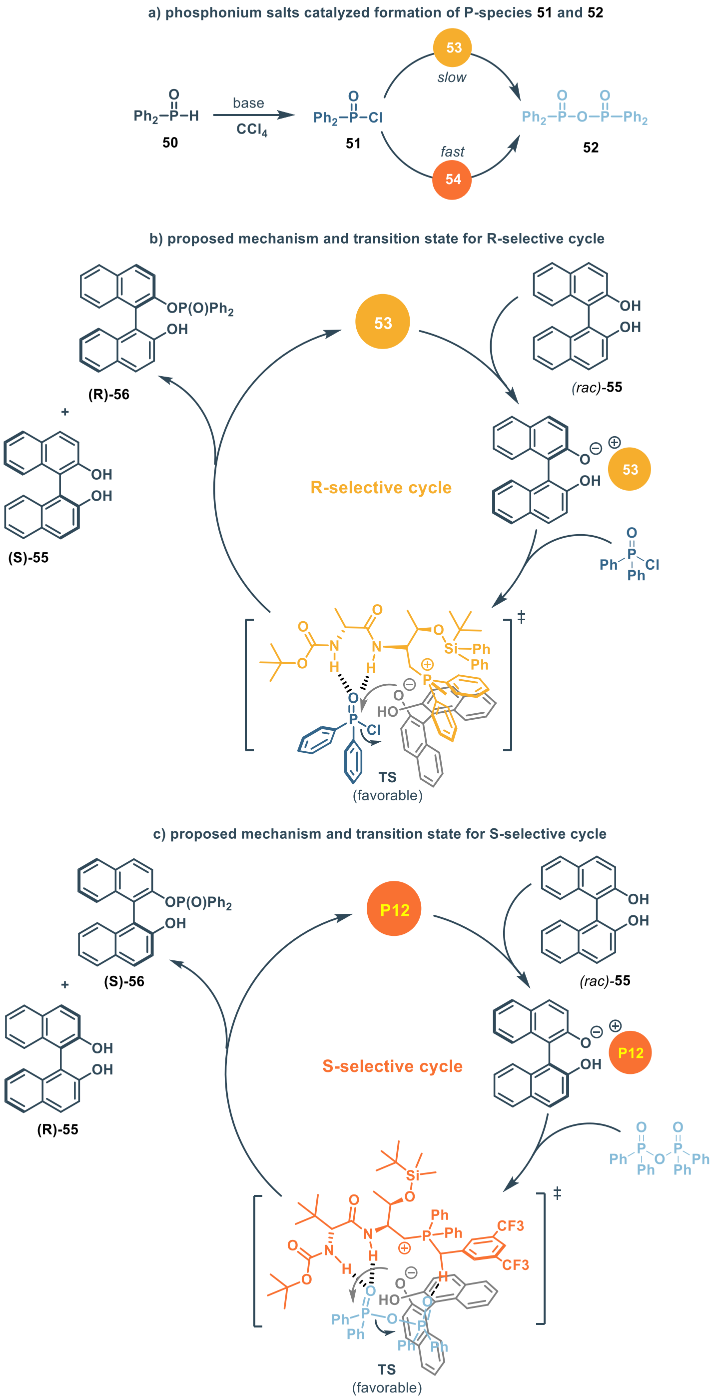

Scheme 17. Proposed mechanism for catalytic formation of P-species in the presence of **53** or **54** (a) and proposed enantiodivergent phosphorylation mechanism (b and c).

Phosphonium salt-based organocatalysts have been successfully employed in the enantiodivergent Michael addition of malonates (**58**) to α,β-unsaturated amides (**57**).[27] Notably, mono- and dipeptidic phosphonium catalysts enable a reversal of enantioselectivity in this transformation. When a phenylalanine-derived catalyst (**60**) was used, the corresponding (R)-configured product was obtained in good yield and with satisfactory enantioinduction. In contrast, the use of a dipeptidic

---

[27] G. Fang, H. Wang, C. Zheng, L. Pan, G. Zhao, *Org. Biomol. Chem.*, **2021**, *19*, 6334–6340

phosphonium catalyst (**61**) led to the formation of the (S)-enantiomer with excellent enantioselectivity (Scheme 18a). This switch in stereochemical outcome is attributed to the distinct hydrogen-bonding networks established by the two catalyst types. Importantly, the phenylalanine-based catalyst **60** showed reduced enantioselectivity with aliphatic Michael acceptors, presumably due to steric hindrance affecting the approach of the nucleophile. Conversely, the ditopic dipeptidic catalyst **61** maintained high levels of enantioinduction across a broader substrate scope. Mechanistic investigations and control experiments support a model in which each catalyst organizes the transition state to favour nucleophilic attack on opposite prochiral faces of the electrophile. In the case of the monopeptidic catalyst, the urea moiety engages in hydrogen bonding with the carbonyl of the Michael acceptor, while the phosphonium center electrostatically interacts with the malonate nucleophile, thereby favoring attack on the *Si*-face. The presence of bulky aliphatic groups in the Michael acceptor likely disrupts this transition state, leading to diminished selectivity. On the other hand, the dipeptidic catalyst, through a different three-dimensional arrangement and hydrogen-bonding network, orients the reactants such that attack occurs on the *Re*-face, thus yielding the opposite enantiomer with consistently high enantioselectivity (Scheme 18b).

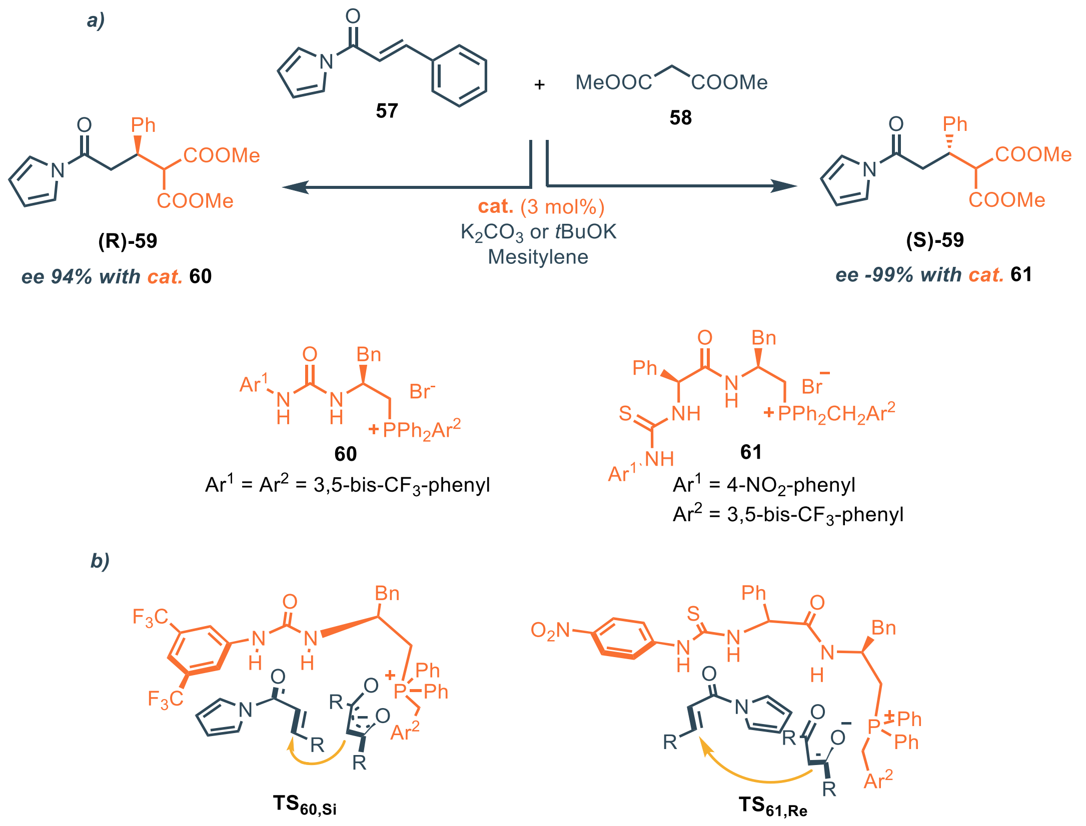

Scheme 18. a) Enantiodivergent Michael addition of malonates to α,β-unsaturated amides; b) Proposed TS for catalyst **60** (*Si*-attack) and **61** (*Re*-attack)

Bromolactonization of olefinic acids provides another example of enantiodivergence induced by minimal modifications of a single chiral catalyst. Yeung and co-workers reported the enantiodivergent bromolactonization of compound **62** using N-bromosuccinimide (NBS) as the brominating agent.[28] The reaction, catalyzed by a pair of quinine-derived regioisomeric catalysts, was performed at –60 °C under an inert atmosphere and in the absence of light (Scheme 19a). Enantioselectivity is inverted simply by changing the position of a methoxy substituent on the aryl amide moiety of the quinine-derived benzamide catalyst. Both catalysts delivered the desired product in good yield and with high enantiomeric excess.

Structural studies and DFT calculations on **62a** and **62b** were carried out to rationalize their distinct catalytic behaviors. NOE correlations indicated that both catalysts adopt an anti-open conformation (Scheme 19b). Nevertheless, subtle differences were detected between the two geometries. In the case of **62a**, a strong intramolecular hydrogen bond is established between the amide N–H and the ortho-OMe group of the 2,3,4-trimethoxyphenyl moiety. In contrast, for **62b**, the analogous intramolecular interaction with the ortho-OMe of the 2,4,6-trimethoxyphenyl group is weakened by steric hindrance.

These noncovalent interactions appear to be key in determining enantiodivergence. For catalyst **62a**, the intramolecular hydrogen bond restricts the orientation of the aryl amide, preventing its N–H from engaging in the catalytic process. In this scenario, the 2,3,4-trimethoxybenzamide acts primarily as a steric shield. Conversely, in catalyst **62b**, the amide N–H remains available to coordinate NBS, allowing both the amide and the quinuclidine groups to exert stereocontrol (Scheme 19c).

The crucial role of hydrogen bonding was further confirmed by experiments with N-methylated benzamide analogues, which delivered the desired product **63** with dramatically reduced enantioselectivity in both cases. Moreover, the phenomenon of chiral reversal was lost, as both catalysts afforded the same enantiomer, **(R)-63**.

---

[28] Y. C. Chan, X. Wang, Y. P. Lam, J. Wong, Y. L. S. Tse, Y. Y. Yeung, *J. Am. Chem. Soc.*, **2021**, *143*, 12745-12754

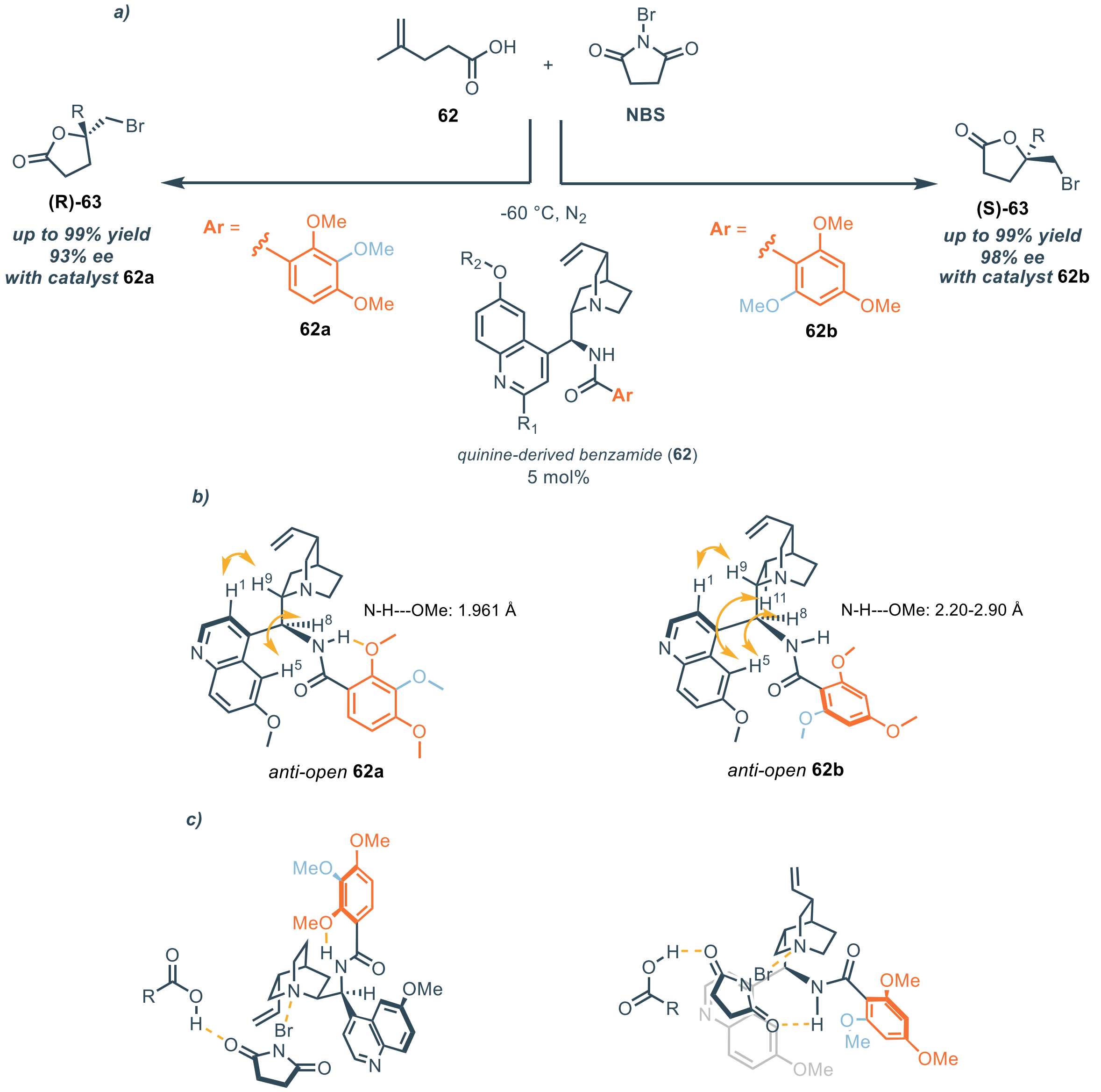

Scheme 19. a) Enantiodivergent Bromolactonization of olefinic acids catalyzed by a pair of quinide-derived benzamide; b) anti-open conformation of the two catalysts deduced by NOE studies; c) different coordination between catalysts and substrates.

Zhang, Luo and co-workers recently reported an enantiodivergent oxa-Diels–Alder reaction catalyzed by a single chiral phosphate.[29] Trifluoropyruvates (**64**) reacted smoothly with simple dienes (**65**) to afford chiral dihydropyrans **66** as either the R- or S-enantiomer, depending solely on the counterion: sodium versus proton (Scheme 20a). Among different chiral phosphate salts tested, the chiral sodium phosphate **67a** provided the best balance of yield and selectivity. Strikingly, when the corresponding free phosphoric acid analogue **67b** was used, the sense of chiral induction was completely reversed, despite the identical catalyst configuration.

---

[29] C. Yang, S. Hu, T. Li, L. Zhang, S. Luo, *ACS Catal.*, **2024**, *14*, 14195-14205

To probe the origin of this enantiodivergence, DFT calculations were performed, considering both concerted and stepwise pathways for the oxa-Diels–Alder reaction with ethyl trifluoropyruvate. The results revealed that stereoselectivity is governed primarily by weak noncovalent interactions, such as π-interactions and dispersion forces (Scheme 20b). For catalyst **67a**, chirality inversion arises from sodium cation–π interactions with the aryl ring, which induce a distortion from C_2 symmetry and generate an asymmetric chiral pocket. This assembly directs the substrates such that the diene attacks the trifluoropyruvate via the Si-face.

By contrast, catalyst **67b** is significantly less reactive, requiring harsher conditions (–60 °C instead of –40 °C, 24 h instead of 12 h, and 10 mol% catalyst loading instead of 1 mol%). In this case, stereocontrol originates from two bidentate hydrogen-bonding interactions: a strong O–H···O hydrogen bond with the trifluoropyruvate, and weaker C–H···O interactions with the diene. This cooperative binding favors Re-facial selectivity and thereby reverses the enantiomeric outcome.

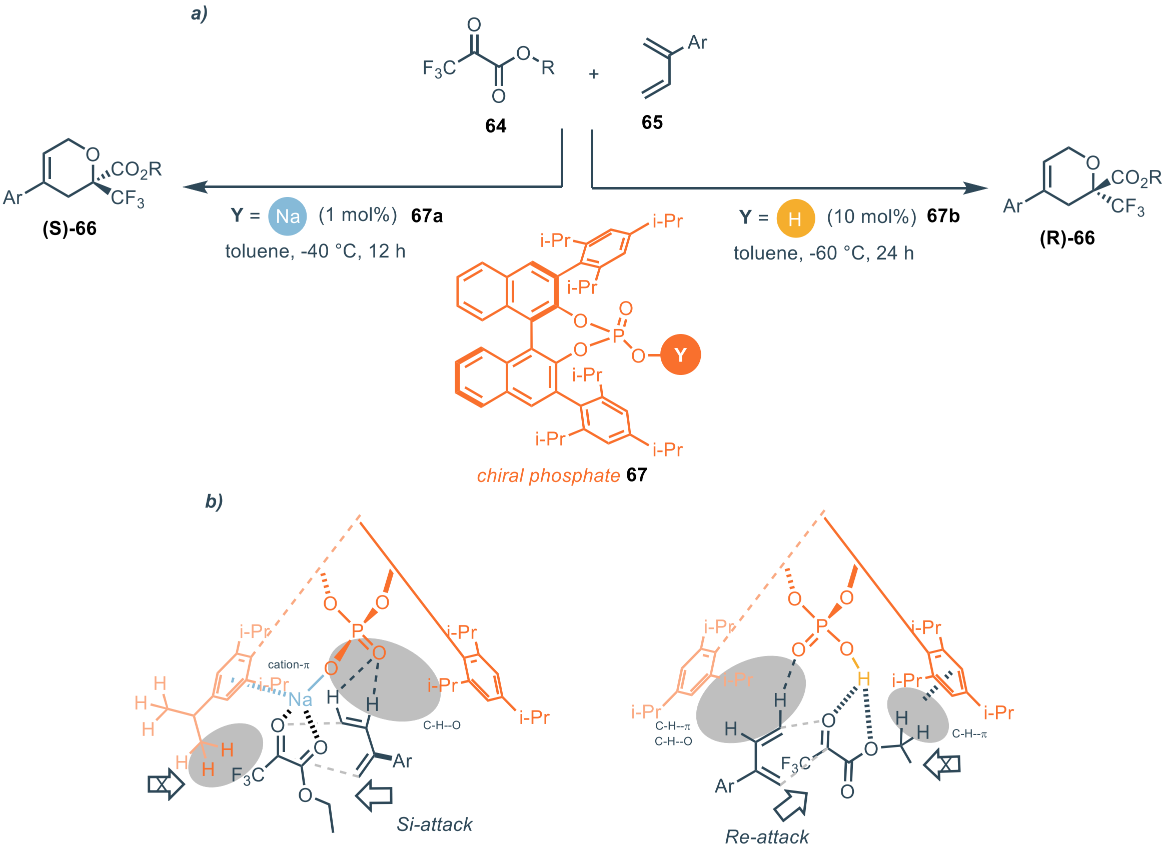

Scheme 20. a) Enantiodivergent oxa-Diels-Alder between trifluoropyruvate and simple dienes; b) proposed stereoselective models which explain the origin of enantiodivergent process when counter ion is switched from sodium to proton

Other strategies to achieve enantiodivergence

It is widely recognized that minimal modifications to the substrate can lead to dramatic differences in the enantiomeric outcome of a reaction. However, enantioselectivity reversal caused by small structural changes in the catalyst has been comparatively underexplored. In this context, in 2022, Chen and co-workers reported the CPA-catalyzed asymmetric allylation of β-alkenyl allylic boronates **68** with aldehydes **69** to afford enantioenriched homoallylic alcohols **71** (Scheme 20a).[30] Interestingly, the authors observed that subtle changes in the substrate structure had a profound impact on the sense of asymmetric induction. When the allylic boronate bears a vinyl group (i.e., β-vinyl-substituted allylic boronate, R = H, compound **68a**), the reaction proceeds with high enantioselectivity, yielding the (*R*)-configured alcohol **(R)-71**. In contrast, when the β-position is substituted with a 2-propenyl group (β-2-propenyl-substituted allylic boronate, R = Me, compound **68b**), the opposite enantiomer, (S)-configured alcohol **(S)-71**, is obtained, despite using the same chiral catalyst. To rationalize this unusual enantiodivergence, the authors performed DFT calculations to analyze the favored transition states for each substrate. In the case of **68a**, the preferred transition state (**TS$_{\mathbf{68a,Re}}$**) involves a re-face attack on the aldehyde, stabilized by a C–H···π interaction between the vinyl group of the substrate and the 9-anthracenyl substituent of the catalyst. However, when using **68b**, the additional methyl group disrupts the geometry required for this stabilizing interaction. As a result, C–H···π interactions are no longer significant. Instead, the methyl group introduces steric repulsion in the catalyst pocket, destabilizing the transition state that would lead to the (R)-product. The favored transition state for this substrate (TS-$_{\mathbf{68b,Si}}$) thus involves a *Si*-face attack on the aldehyde, benefiting instead from a reinforcing C–H···O=P hydrogen bond with the phosphoryl oxygen of the catalyst (Scheme 20b). This subtle change in non-covalent interactions accounts for the observed inversion of stereochemical outcome.

---

[30] S. Gao, M. Duan, L. R. Andreola, P. Yu, S. E. Wheeler, K. N. Houk, M. Chen, *Angew. Chem. Int. Ed.*, **2022**, *61*, e202208908

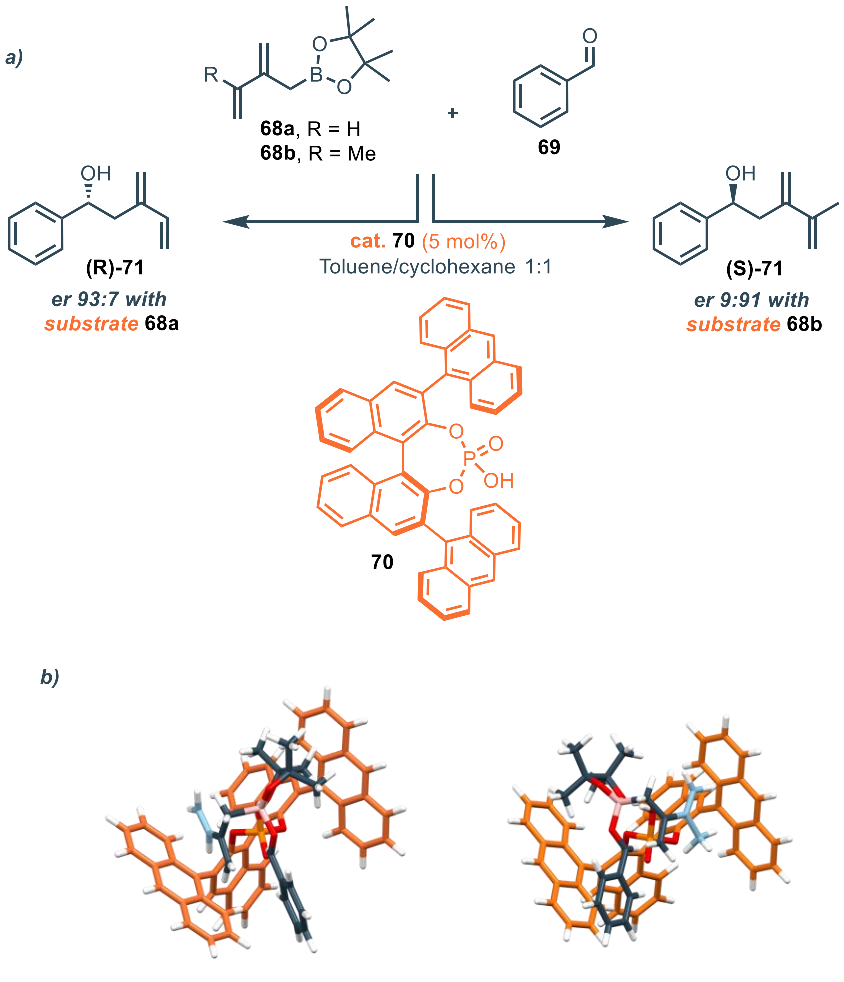

$TS_{68a,Re}$ $TS_{68b,Si}$

Scheme 20. a) Enantiodivergent allylation of β-alkenyl allylic boronates with benzaldehyde; b) Transition state for the two substrates **68a** and **68b**

In some cases, the order of addition can induce enantiodivergence, without any changing in the reaction component. This is incredibly advantageous because no synthetic modification is required both for reagents and catalyst. Asano, Matsubara at al. reported in 2013 an unexpected enantiodivergent [3+2] cyclization catalyzed by chinchona derivatives. Enantiodivergence mainly depends on the catalyst addition.[31] **(R)-72** is obtained in modest yield when isocyanate **71** reacts first with γ-hydroxy-α,β-unsaturated carbonyl compound **74** and then catalyst **73** is added (Scheme 21, procedure A). On the other hand, when **73** and isocyanate **71** are mixed first and compound **74** is added in a second moment, desired product is obtained as **(S)-72** in good yield (Scheme 20, procedure B). Enantiomeric excess is modest in both cases (74% ee) however, Asano and Matsubara's work

---

[31] Y. Fukata, K. Asano, S. Matsubara, *J. Am. Chem. Soc.*, **2013**, *135*, 12160-12163

represents one of the first examples of reversal enantioselectivity which requires no change in reaction components.

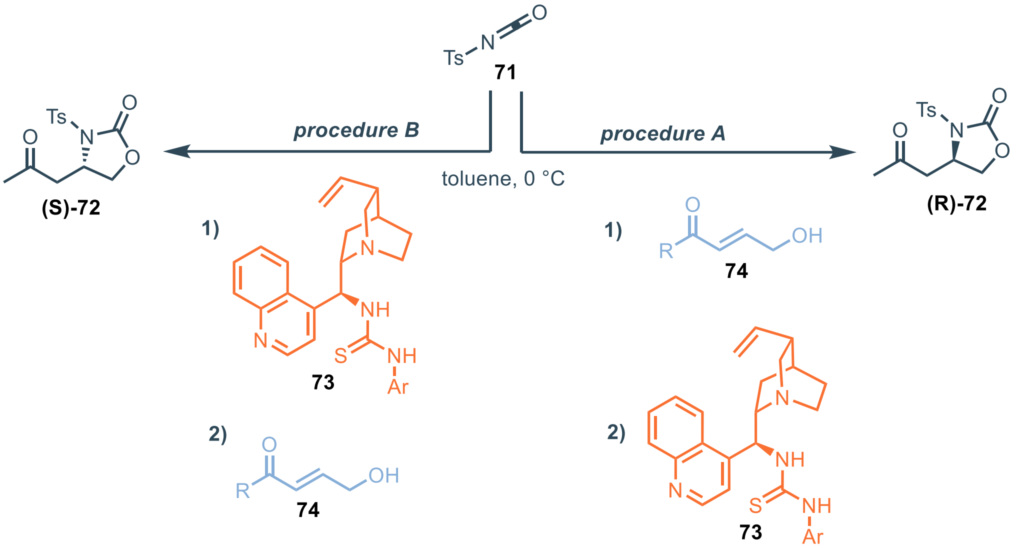

Scheme 20. Enantiodivergent procedure for the organocatalytic synthesis of 2-oxazolidinones by simply changing the order of substrates and catalyst.

Aim of the project

During our ongoing interest in asymmetric organocatalysis and its application and understanding, we recently reported the asymmetric transfer hydrogenation of α,β-unsaturated aldehydes *via* iminium ion organocatalysis using Nitrogen-Doped Carbon Dots (**NCDs**) as nano-organocatalysts within a counteranion-directed catalysis (ACDC) paradigma (See *Chapter 2*).[32] The **NCDs**, prepared from arginine (**Arg**), which constitutes the carbon-rich core, and a diamine (1,2- or 1,4-ethylenediamine, respectively **Put** and **EDA**), proved to be effective catalysts in this reaction, outperforming molecular amines. We noted then that the reaction is sensitive to the substitution pattern of the Hantzsch ester (**HE**) hydride source, a feature not typically observed with such prominence in reactions catalysed by **CPAs**. Building on this initial observation, in the present work, we uncover and investigate the underlying reasons for a remarkable reversal in the sense of asymmetric induction, triggered by minimal structural modifications to the substitution pattern on **HEs**. Crucially, this stereochemical switch occurs despite utilizing a **CPA** of a fixed handedness (Figure 1). To rationalize this counterintuitive observation, we present a synergistic experimental and computational investigation that elucidates the mechanistic underpinnings of this phenomenon. Our findings reveal a complex

---

[32] A. Carioscia, E. Cocco, M. E. Casacchia, G. Gentile, M. Mamone, G. Giorgianni, E. Incerto, M. Prato, F. Pesciaioli, G. Filippini, A. Carlone, *ACS Catal.* **2024**, *14*, 13429–13438

tripartite interplay between the **NCDs**, **CPA**, and **HE**, which collectively play an important role in the stereochemical outcome of the transformation.

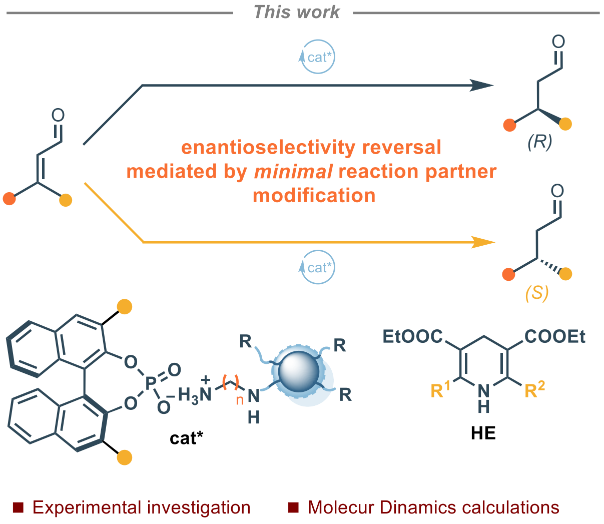

Figure 1. Minimal variation of substitution pattern on **HEs** enables enantioselectivity switch supported by computational studies

Results and discussion

Influence of the HE structure – experimental data

Given the strong influence of the substitution pattern of the **HE** in terms of yield and enantioinduction exhibited in our previous work,[32] we evaluated a series of 2,6-alkyl-substituted **HEs** under our reported standard conditions (Table 3). Replacing one of the two alkyl substituents on **HE-1** with an ethyl group (**HE-2** and **HE-3**) significantly decreased the performance, both in terms of yield and enantioinduction (entries 1-3). Strikingly, the symmetrical diethyl analogue **HE-4** displayed inversion in enantioselectivity, favouring the formation of the (*S*)-enantiomer (entry 4). Intrigued by this effect, we sought to determine whether a similar outcome could be observed when using molecular amines instead of the **NCDs**. Interestingly, the inversion was only evident in cases where a nanostructured iminium ion was involved, while it did not occur when molecular amines were employed (entries 5 and 6), suggesting that the phenomenon likely stems from a steric interplay among the **NCDs**, the **HE** and the **CPA** in the transition state. Temperature variations affected the enantioselectivity but did not alter the direction of the inversion (entries 7 and 8), thus ruling out entropic contributions as the primary cause. Finally, the use of the electron-deficient substrate **1b** in combination with **HE-4** again led to the prevalence of (*S*)-enantiomer (entry 9). Instead, applying either **HE-1** as the hydride donor or piperidine as the amine restored the original (*R*)-selectivity (entries 10 and 11), in line with our previous findings. These results collectively exclude substrate-dependent effects and underscore that the inversion arises from the unique combination of **NCDs**, **CPA**, and **HE**, that give rise to a chiral supramolecular assembly governing the sense of the chiral induction. Moreover, the same inversion effect is observed when **NCDs** prepared with 1,2-ethylenediamine (**CDs-2**) are used instead of those based on 1,4-butylenediamine (**CDs-1**), although the yield is lower, consistent with the higher number of surface-accessible amines in **CDs-1** (entries 12 and 13).[32]

Table 3: Influence of the **HE** and amine catalyst - selected experiments.[a]

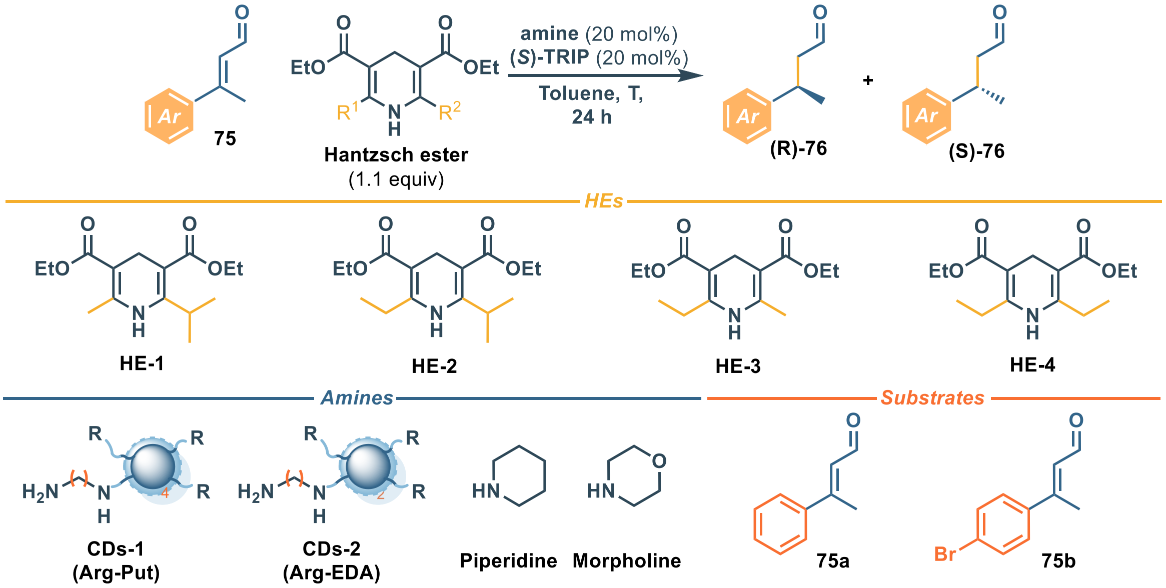

Entry	HE	Amine	Substrate	T(°C)	Conv.(%)[b]	Yield (%)[c]	er[d] (R:S)
1	**HE-1**	**CDs-1**	**75a**	25	>95	59	89:11
2	**HE-2**	**CDs-1**	**75a**	25	>95	27	60.5:39.5
3	**HE-3**	**CDs-1**	**75a**	25	>95	28	57.5:42.5
4	**HE-4**	**CDs-1**	**75a**	25	>95	48	22.5:77.5
5	**HE-4**	Piperidine	**75a**	25	61	19	68.5:31.5
6	**HE-4**	Morpholine	**75a**	25	>95	27	59:41
7	**HE-4**	**CDs-1**	**75a**	-20	90	36	24:76
8	**HE-4**	**CDs-1**	**75a**	50	>95	29	32:68
9	**HE-4**	**CDs-1**	**75b**	25	94	56	21.5:78.5
10	**HE-1**	**CDs-1**	**75b**	25	>95	51	87.5:12.5
11	**HE-4**	Piperidine	**75b**	25	70	18	58:42
12	**HE-1**	**CDs-2**	**75a**	25	>95	50	88:12

13	**HE-4**	**CDs-2**	**75a**	25	>95	35	28:72

[a] Reactions were performed with **1** (0.1 mmol, 1 equiv.), amine (0.02 mmol, 0.2 equiv.), (*S*)-TRIP (0.02 mmol, 0.2 equiv.), and **HE** (0.11 mmol, 1.1 equiv.) in toluene (1 mL, 0.1 M) for 24 h at the selected temperature. [b] Conversion of **1**, determined by ^{1}H NMR using triphenylmethane as an internal standard. [c] Determined by ^{1}H NMR using triphenylmethane as an internal standard. [d] Determined by chiral HPLC analysis. Arg: L-Arginine; Put: 1,4-butylenediamine (or putrescine); EDA: 1,2-ethylene-diamine.

Influence of the HE structure – computational investigation

To rationalize our experimental findings and elucidate the role of weak noncovalent forces in the observed enantioselectivity reversal, we undertook a dedicated computational study. It is well-established that, in solution, the magnitude of interactions like London dispersion forces is comparable to the available thermal energy. This creates a highly dynamic system with a vast ensemble of accessible conformations, rendering static computational models that focus on a single minimum-energy structure insufficient. A comprehensive understanding therefore requires a preliminary dynamic approach. We employed semi-classical Molecular Dynamics (MD) simulations, as this method allows for an exhaustive sampling of the conformational landscape in an explicit solvent. By using a sufficiently reliable force field, MD simulations can accurately map the supramolecular pre-organization of the reactants, which we posit is crucial for the stereochemical outcome. Our central aim was to investigate how subtle structural changes alter the conformational repertoire of the catalytic system. To this end, we directly compared MD simulations of **CPA**, **HE**, and **NCDs** in toluene, seeking to highlight differences that would explain the enantioselectivity switch. This investigation is corroborated and complements a concurrent report from the List group that highlighted the critical role of dispersion forces in a related transformation.[33] However, our computational strategy diverges from previous models and represents, to the best of our knowledge, a novel approach for rationalizing stereochemical outcomes in this catalytic system as it focuses on rationalizing the stereochemical outcome by analyzing the network of preceding equilibria. The complex network of interactions can be rationalized into three primary pathways (**Figure 2**): (i) direct coordination of the **CPA** to the iminium ion (**Im**) formed between the **NCD** and the unsatured aldehyde **75**, (ii) **CPA** activation of the **HE** via H-bonding, or (iii) formation of a ternary complex where the **CPA** bridges both reaction partners. While the hydride transfer is the chemically decisive

---

[33] W. Leinung, B. Mitschke, M. Leutzsch, V. N. Wakchaure, R. Maji, B. List, *J. Am. Chem. Soc.* **2025**, *147*, 14500–14508

step, understanding the preferred mode of the chiral supramolecular assembly of the reactants within this network is pivotal for explaining the final stereochemical result.

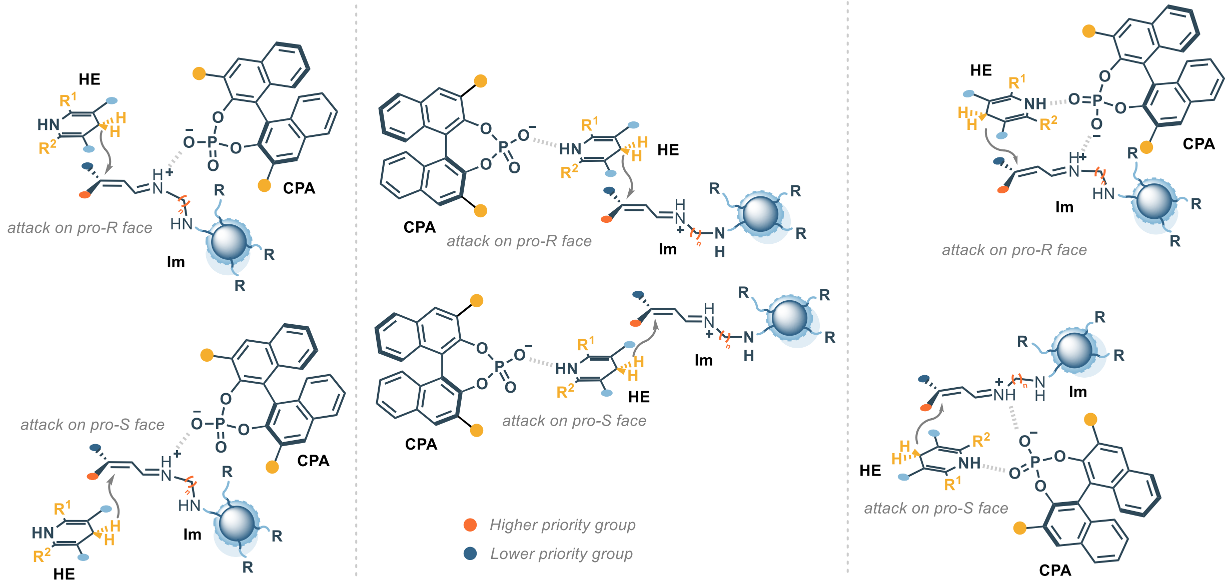

Figure 2 Possible interaction approaches of the reactants in the transition state.

To ensure the physical consistency of our analysis, we carefully established a robust computational model. The **NCD** was represented by a C60 fullerene-like framework bearing a covalently linked iminium ion (**Im**) (Arg-Put, according to **CDs-1**). While smaller than the experimental **NCDs**, there is enough confidence that this model effectively and qualitatively mimics the steric environment imposed by the nanostructure. The simulations feature the cationic iminium ion as a tight ion pair (**IP**) with the deprotonated **CPA**, alongside the Hantzsch ester (either **HE-1** or **HE-4**). The system was described using a modified Gromos force field,[34] as obtained from the Automated Topology Builder (ATB)[35] upon readapting the atomic charges for reproducing the **Im**-**CPA** and **Im**-**HE** interaction energies as obtained from Density Functional Theory calculations in vacuum. A key strength of our study is its comparative nature; by focusing on the differences between the systems containing **HE-1** and **HE-4**, any potential systematic errors in the force field are minimized. Three MD simulations were produced, i.e.: one for the **IP**, one for the **IP** with **HE-1**, and the last one for **IP** with **HE-4**. The species were inserted in a cubic box of 42.8 nm^3 volume with explicit toluene molecules and simulated at 298 K for a total of 1.2 µs. To probe the pre-organization, we monitored key geometric parameters throughout the trajectories (Figure 3): (i) the **Im**-**CPA** distance, i.e. the **IP** intra-partners distance, (ii)

---

[34] N. Schmid, A. P. Eichenberger, A. Choutko, S. Riniker, M. Winger, A. E. Mark, W. F. van Gunsteren, *Eur Biophys J* **2011**, *40*, 843–856

[35] A. K. Malde, L. Zuo, M. Breeze, M. Stroet, D. Poger, P. C. Nair, C. Oostenbrink, A. E. Mark, *J Chem Theory Comput* **2011**, *7*, 4026–4037

the distance between the prochiral iminium-ion carbon-atom and the **HE** hydrogen atom potentially leaving as hydride ion and, (iii) the corresponding approaching enantioselective angle (**Φ**).

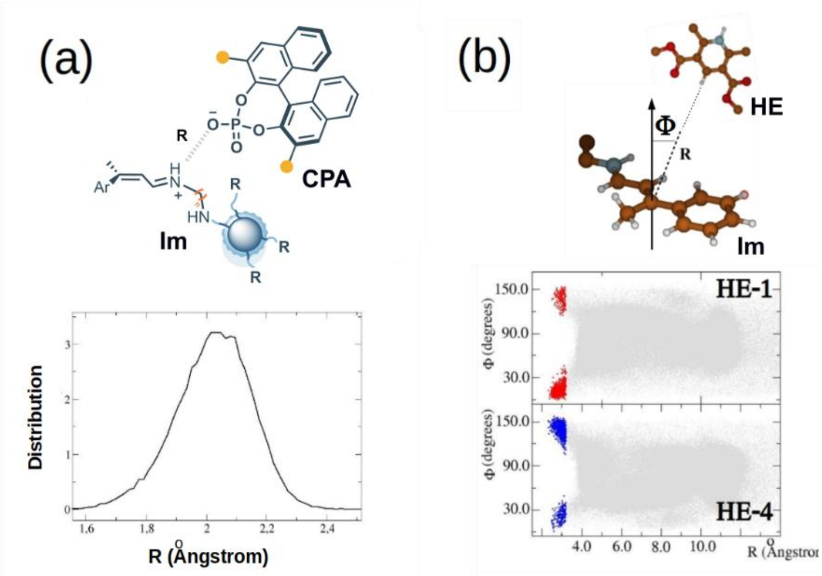

Figure 3 a) Top: schematic view of the intra-ion-pair minimal distance; bottom; distribution of the intra-ion-pair minimal distances monitored along the simulation with **HE-1**. The same distribution obtained along the simulation with **HE-4** (virtually identical) is not reported for clarity. b) Top: schematic view of the distance-angle prochiral variables monitored along the simulation. Bottom: projection on the R-F plane of all the values sampled along the two simulations. The regions considered as diagnostic for the formation of the reactive complex are highlighted in red (upper part) and blue (lower part).

The distance between the **NCD** and **CPA** catalyst remains short and remarkably constant, indicating a very stable and tightly bound species ion pair (Figure 3a), although it experiences a great number of quasi-degenerate conformations, excluding the hypothesis of pre-organization depicted in Figure 2, middle. Moreover, no significant contact is observed between the **CPA** and the **HE**, excluding the hypothesis of the three-point complex (Figure 2, right. See also SI). It is important to underline that, in order to take into account the possibility of finding stable conformations resembling **HE** bound to **CPA** or the three point contact model (see Figure 2, central and right panels), the simulation was initiated with the **HE** close to **CPA** - nevertheless, all these possible combinations did not appear as significant. Instead, the simulations confirm that the reaction proceeds *via* the approach of the neutral **HE** to the pre-formed, ion-paired iminium substrate (Figure 2, left). The crucial stereodetermining step is the formation of diastereomeric pre-reactive complexes. As shown in Figure 3b, the trajectories reveal significant populations of both pro-*R* and pro-*S* complexes, where the **HE** is poised for hydride transfer to either face of the iminium ion. Quantifying the relative stability of these complexes is therefore key to understanding the origin of the enantioselectivity (Figure 5).

The simulations successfully replicate the experimentally observed reversal in enantioselectivity, with the two systems undergoing a significantly different pro-chiral preorganization of the reactants. The calculated free energy difference (ΔG°) for a pro-R -> pro-S thermodynamic reveals a distinct preference for the pro-*R* complex with **HE-1** (ΔG° = +4 kJ mol^{-1}); conversely, **HE-4**, favours the pro-*S* complex (ΔG° = -4 kJ mol^{-1}), explaining the switch to the (*S*)-product (Figures 4 and 5).

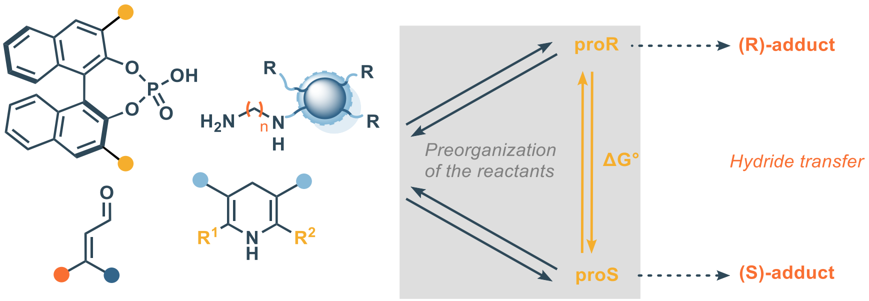

Figure 4. ΔG° represents the energy difference between the two prochiral supramolecular assemblies before the irreversible hydride transfer step.

A thermodynamic analysis indicates that this stereochemical preference is enthalpically controlled. In both cases, the favoured diastereomeric complex is the one with the lower internal energy, strongly suggesting that attractive London dispersion forces (the only forces 'active' in semi-classical MD simulations) dictate the pro-chiral preorganization. This finding is in excellent agreement with the conclusions by List and coworkers, recently reported using a rather different approach.[43] Interestingly, the minor, less-stable pro-chiral species is consistently the one that is entropically favoured.

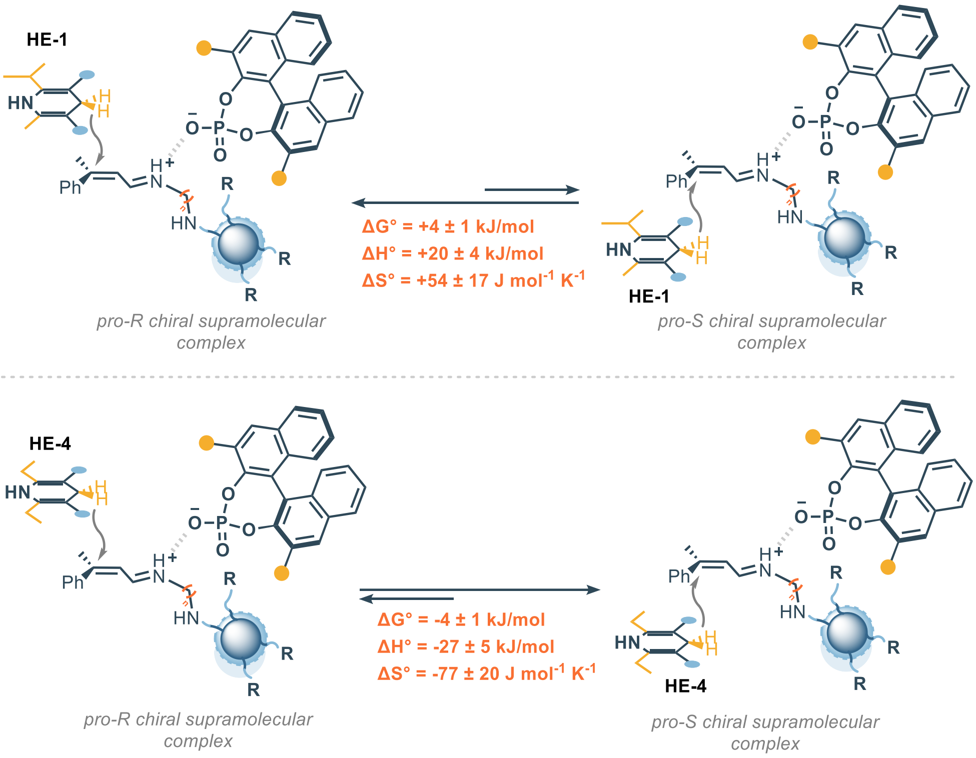

Figure 5. Energy differences between the two pro-R and pro-S prochiral complexes with **HE-1** and **HE-4;** pro-R -> pro-S thermodynamics as obtained from the data in **Figure 3b** (see Experimental Section for additional details). The associated uncertainty for the first two entries is defined as a standard error evaluated considering three subportions of the whole trajectories. The errors for the reaction entropy are calculated as the sum of the errors associated to free energy and enthalpy.

Deeper analysis of the trajectories revealed that these less stable complexes exhibit significantly greater structural fluctuations, corresponding to a higher conformational entropy, i.e. the pro-S in the case of **HE-1** and the pro-R in the case of **HE-4** (Figure 6). This complete thermodynamic picture - an enthalpically-driven process opposed by entropy - is further corroborated by our experimental data, which shows a slight erosion of enantioselectivity at elevated temperatures (see Experimental Section). Interestingly, if we assume that hydride transfer exhibited the same activation barrier, the standard free energy difference of 4 kJ/mol emerged by our calculations would produce an enantiomer ratio of 83:17, of the same order of magnitude as those found experimentally.

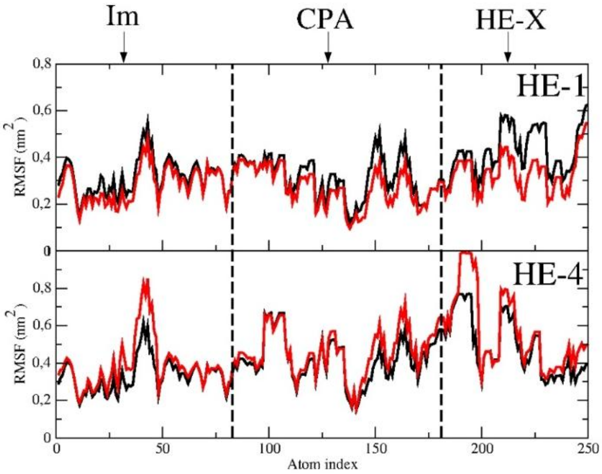

Figure 6. Root mean square fluctuations (RMSF) of the **Im**-**CPA**-**HE** moieties as obtained by collecting the MD frames in which the system is found in the diagnostic regions shown in Figure 3b for the pro-R complex (red) and pro-S complex (black). RMSF is a quantitative evaluation of the internal mobility of the species: the greater the value of the fluctuation, the greater the internal mobility (i.e. excluding rototranslations) of the system under examination.

Conclusions

In summary, this work sheds light on the fascinating and often elusive phenomenon of enantioselectivity reversal in asymmetric catalysis. We have demonstrated that subtle modifications to **HE** substituents can remarkably flip the enantiomeric outcome of asymmetric transfer hydrogenation reactions catalysed by **NCDs** within an ACDC framework, all without altering the catalyst's inherent handedness. To the best of our knowledge, this is a unique result of enantioswitching modulated by minimal modification of the hydride transfer agent. A comprehensive investigation, uniquely combining experimental evidence with extensive semi-classical Molecular Dynamics (MD) simulations, reveals that this unexpected enantiodivergence is driven by the intricate interplay of **NCDs**, **CPA**, and the **HE**. A very detailed and computationally demanding series of MD simulations, carried out on a model system in toluene at room temperature, has shown that an important role in the observed enantioswitching is played by the preliminary prochiral organization of the reactants, prodrome to the final chemical act, i.e., the hydride transfer. Collectively, our computational results (see Figure 3) show that the only the first scenario (Figure 2, left) is actually possible in our experimental conditions, i.e. the **CPA** systematically binds to the iminium ion, promoting an enantioselective reduction of the adduct formed between the aldehyde and the **CDs.** Notably, the relative stability of these prochiral complexes, and hence the driving force for such a preliminary step, has a predominantly energetic nature. In fact, the most stable complexes turn out to be those characterized by a lower internal energy and lower entropy. This finding reinforces recent results that attribute a key role to dispersion forces in asymmetric transfer hydrogenation catalysis.[33] While the reported current computational results primarily focus on the crucial pre-catalytic events and do not include the final hydride transfer step, they provide invaluable insights into the vast conformational repertoire of the system. This comprehensive analysis, which is challenging for traditional electronic structure theory calculations, underscores the unique power of MD simulations in unravelling the subtle drivers of stereochemical outcomes. Ultimately, this study offers a clear and compelling rationalization for the observed enantioselectivity reversal, demonstrating how weak dispersion forces and their fluctuations, comparable to thermal energy in liquid conditions, govern the conformational preorganization of the reactants. Our findings underscore the importance of understanding these early, non-covalent interactions in shaping the stereochemical path. This work paves the way for future studies utilizing advanced computational strategies to achieve an efficient interplay between semi-classical MD simulations and electronic structure theory calculations, providing the necessary insight for the rational design of highly controlled and versatile asymmetric reactions.

Experimental section

Instrumentations

Nuclear magnetic resonance analyses (^{1}H- and ^{13}C-NMR spectra) were acquired using a Bruker Advance III 400 MHz spectrophotometer and a Magritek 60 MHz spectrophotometer. Chemical shifts (δ) are reported in ppm relative to residual solvent signals for ^{1}H- and ^{13}C-NMR (1H-NMR: 7.26 ppm for $CDCl_3$; ^{13}C-NMR: 77.16 ppm for $CDCl_3$). ^{13}C-NMR spectra were acquired with ^{1}H broadband decoupled mode. Coupling constants are given in Hz. ^{1}H-NMR yields were measured by analysing the reaction mixture using Triphenylmethane as internal standard. Chromatographic purifications of compounds **75a-b**, **76a-b**, **HE-1** and **HE-4** were performed using automated Biotage® Isolera LS Systems.

Materials and methods

CPAs were purchased from BLDPharm. Silica Gel 60A (35-70 μm), HPLC solvents and analytical grade solvents were purchased from Merck. The Carbon Dots and compounds **75a-b**, **76a-b**, **HE-1** and **HE-4** were prepared according to the literature, and their characterization matches with the values reported.[32,36] The enantioselective reduction of α,β-unsaturated aldehydes was performed according to the literature.[32]

Determination of enantiomeric purity

Chiral HPLC analyses were acquired using an Agilent 1220 Infinity II liquid chromatographer equipped with Phenomenex columns (100 × 4.6 mm): Lux 3 µm i-Cellulose 1, Lux 3 µm i-Cellulose 2, Lux 3 µm i-Cellulose 3, and Lux 3µm-Amylose 2. HPLC analyses of 2a-b were performed on the corresponding alcohols obtained by reduction of the aldehydes using $NaBH_4$ in methanol. HPLC traces were compared to racemic samples prepared using diphenyl phosphate (CAS Number: 838-85-7) and piperidine as catalysts, in toluene at 50 °C for 2 h. Optical rotations were measured on a ZUZI 412 Digital Polarimeter (tube length: 100 mm).

Determination of absolute configuration

The absolute configurations of the optically active compounds 2a-b were determined based on the measured optical rotations that were compared with literature values.[31] All other absolute configurations were assigned by analogy based on a uniform reaction mechanism and the uniform elution order observed in the HPLC chromatograms.

Synthesis and characterization of HEs

Synthesis of diethyl 2-ethyl-6-isopropyl-1,4-dihydropyridine-3,5-dicarboxylate (HE-2)

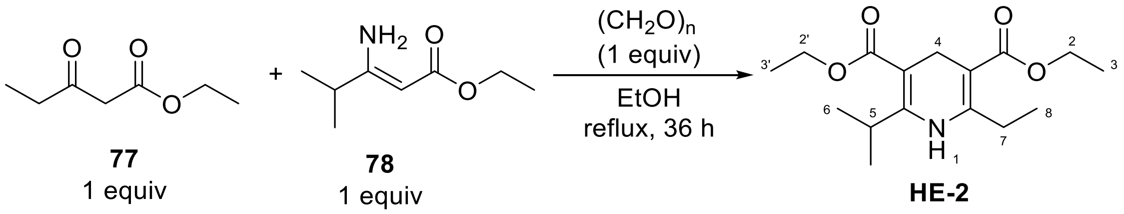

From a modification of a reported procedure,[37] to a two-necked round-bottom flask equipped with air condenser and under nitrogen, ethyl (Z)-3-amino-4-methylpent-2-enoate **78** (7.02 mmol, 1.1 g) was dissolved in absolute ethanol (100 mL), followed by paraformaldehyde (7.02 mmol, 211 mg) and ethyl propionilacetate **77** (7.02 mmol, 1.01 g). The solution was heated to 100 °C and monitored through NMR After 36 h, the reaction mixture was concentrated *in vacuo* and the product was

---

[36] H. T. Abdel-Mohsen, J. Conrad, U. Beifuss, *Green Chem* **2012**, *14*, 2686–2690

[37] A. M. van Rhee, J. Jiang, N. Melman, M. E. Olah, G. L. Stiles, K. A. Jacobson, *Med Chem* **1996**, *39*, 2980–2989

purified via chromatography (hexane to hexane/EtOAc 9:1, slow gradient) to afford 850 mg of HE-2 with 41% yield.

^{1}H NMR (400 MHz, CDCl$_3$) δ 5.40 (s, 1H, H-1), 4.25 – 3.99 (m, 5H, H-2,2’,5), 3.26 (s, 2H, H-4), 2.63 (q, J = 7.5 Hz, 2H, H-7), 1.28 (t, J = 7.1, 6H, H-3), 1.27 (t, J = 7.1, 6H, H-3’), 1.15 (t, J = 7.6 Hz, 3H, H-8), 1.10 (d, J = 7.1 Hz, 6H, H-6).

^{13}C NMR (101 MHz, CDCl$_3$) δ 167.8, 167.7, 153.5, 150.7, 98.3, 98.0, 59.8, 59.8, 27.3, 26.0, 25.1, 20.3, 14.6. 14.6, 12.7.

Synthesis of diethyl 2-ethyl-6-methyl-1,4-dihydropyridine-3,5-dicarboxylate (HE-3)

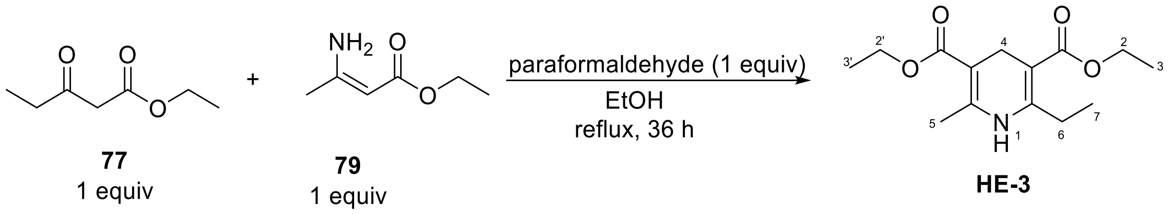

From a modification of a reported procedure,[37] to a two-necked round-bottom flask equipped with air condenser and under nitrogen, ethyl (Z)-3-aminobut-2-enoate 5 (7.02 mmol, 0.907 g) was dissolved in absolute ethanol (100 mL), followed by paraformaldehyde (7.02 mmol, 211 mg) and ethyl propionilacetate 3 (7.02 mmol, 1.01 g). The solution was heated to 100 °C and monitored through NMR After 36 h, the reaction mixture was concentrated in vacuo and the product was purified via chromatography (hexane to hexane/EtOAc 9:1, slow gradient) to afford 800 mg of HE-3 with 43% yield.

^{1}H NMR (400 MHz, CDCl$_3$) δ 5.27 (s, 1H, H-1), 4.16 (d, J = 7.1, 1.3 Hz, 2H, H-2), 4.15 (d, J = 7.1Hz, 2H, H-2’), 3.26 (s, 2H, H-4), 2.58 (q, J = 7.5 Hz, 2H, H-6), 2.19 (s, 3H, H-5), 1.27 (t, J = 7.1Hz, 3H, H-3), 1.26 (t, J = 7.1Hz, 3H, H-3’), 1.14 (t, J = 7.5 Hz, 3H, H-7).

^{13}C NMR (101 MHz, CDCl$_3$) δ 168.2, 167.8, 150.5, 145.2, 99.5, 98.8, 59.8, 59.8, 25.9, 25.0, 19.3, 14.6, 14.5, 12.7.

Analysis of Temperature dependence of the enantiomeric excess

In order to see the effect of the temperature on the enantiomeric ratio of the reaction, six experiments at different temperatures were performed, using the dihydropyridine **H1**. The results are reported on the Table S1. Even though not dramatically it is possible to appreciate a sharp effect of the temperature on the relative S/R concentration.

Table S1. Collection of the experimental data as a function of the temperature

Entry	T (K)	e.r. (R:S)	[S]/[R]
1	323.15	87.5:12.5	0,14
2	298.15	89.0:11.0	0,12
3	283.15	89.0:11.0	0,12
4	273.15	90.5:9.5	0,10
5	253.15	91.0:9.0	0,10
6	233.15	91.5:8.5	0,09

Given the standard thermodynamics relation $\frac{\partial \Delta G}{\partial T} = -\Delta S$ it is possible to attribute this behaviour to the fact that the enantiomer produced in lower yield is possibly the one characterized by a higher (absolute and/or activation) entropy.

Computational Details for MD simulations

All the MD simulations were carried out using the Gromacs program, version 5.0.4 [38] following the standard common protocol below described. An initial energy minimization of the whole box was first carried out. The system was then gradually heated from 50 K to the temperature of interest (300 K) using short (200 ps) MD simulations. The simulation was propagated for the productive run of 120 ms for both systems (i.e. with **HE-1** and with **HE-4**) in the NVT (constant number of molecules, volume and temperature) ensemble using the Velocity rescaling algorithm for keeping the temperature constant.[39]

The isobaric conditions in the NVT simulations were mimicked using a methodology recently proposed by our laboratory and based on the adjustment of the box-size of the solute-solvent system,

---

[38] D. van der Spoel, E. Lindahl, B. Hess, G. Groenhof, A. E. Mark, H. J. C. Berendsen, *J. Comput. Chem.* **2005**, *26*, 1701–1718

[39] G. Bussi, D. Donadio, M. Parrinello, *J. Chem. Phys.* **2007**, *126*, 014101

in order to reproduce the (average) pressure previously obtained by simulating the same number of solvent molecules at the same temperature and at the density of the liquid toluene (i.e. the solvent) at 1.0 bar. The LINCS algorithm was used to constrain all bond lengths.[40] Long range electrostatics was computed by the Particle Mesh Ewald method [41] with 34 wave vectors in each

dimension and a 4th order cubic interpolation. In all the simulations the adapted Gromos force-field (see main text and next paragraph) was used for the solutes and the solvent, respectively.

Conformational analysis of Ion-Pair through Essential Dynamics

The conformational repertoire of a system made up of a large number of atoms and characterized by an enormous number of conformational states is an extremely difficult aspect to analyse. The major problem is linked to the difficulty of non arbitrarily identifying a limited number of conformational coordinates (for example the dihedral angles of the Ramachandran plot). For this purpose it is possible to use the essential dynamics (see A Amadei, A B Linssen, H J Berendsen, Essential dynamics of proteins. 1993 Dec;17(4):412-25. doi: 10.1002/prot.340170408 for more details).

Brefly.

(i) run the MD simulation; (ii) Align the trajectory of the system of interest (in the present case the Ion-Pair, IP) to a reference structure to remove the roto-translations from the analysis of the fluctuations; (iii) Extract the IP atomic positions; (iv) construct the atomic covariance matrix of the positional fluctuations $C_{ij} = \langle (x_i - \langle x_i \rangle) \rangle \langle (x_j - \langle x_j \rangle) \rangle$; (v) diagonalize the covariance matrix; (vi) sort the eigenvectors by the eigenvalues (from the largest to the lowest) (vi) project, at each MD frame, the cartesian coordinates onto a reduced number (typically two) of eigenvectors termed as *Essential Eigenvectors*. This last step produces a map (typically 1D or 2D) of probability providing the distribution of the conformational states most sampled along the trajectory.

In the Figure S5 we report (inset a) the spectra of the eigenvalues from the diagonalization of the covariance in three different cases. The **IP** without the ester (black), and **IP** with **HE-1** (blue) and **HE-4** (red).

---

[40] B. Hess, H. Bekker, H. J. C. Berendsen, J. G. E. M. Fraaije, *J. Comput. Chem.* **1997**, *18*, 1463–1472

[41] 51. T. Darden, D. York, L. Pedersen, *J. Chem. Phys.* **1993**, *98*, 10089–10092

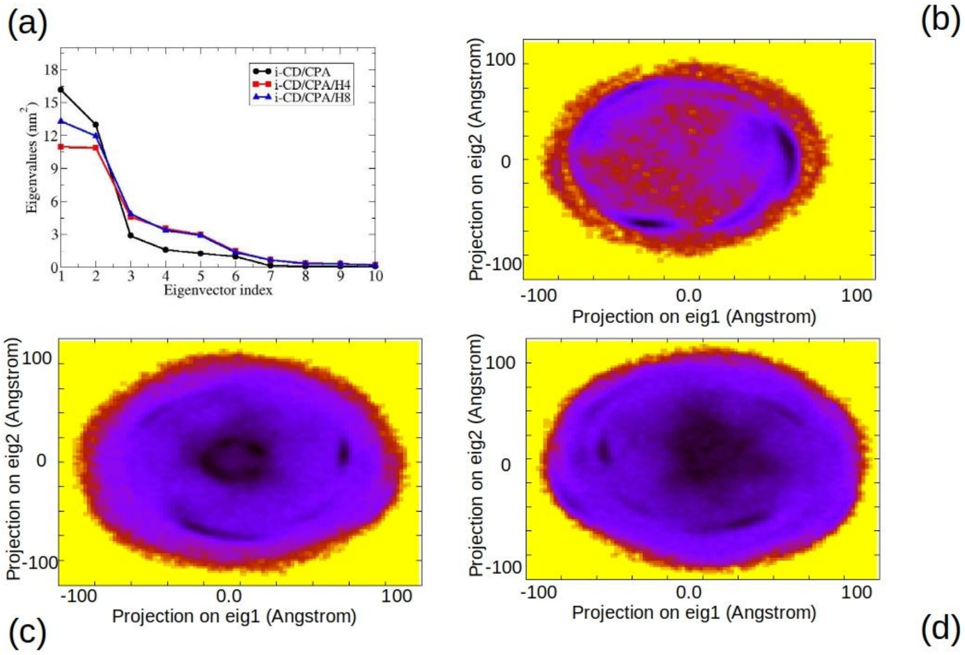

Figure S5. (a) Spectra of the eigevalues from the diagonalization of the covariance matrix for IP, IP with HE-1 and IP with HE-4. In the other insets are reported the projections of the IP trajectories on the corresponding plane formed by the first two eigenvectors reported in (a) in the absence (b) and in the presence of HE-1 (c) and HE-4 (d).

From the projections on the eigenvectors 1 and 2 (the x and y axis of the Figures) it is clear the **IP**, although never separated (see main text) spans a huge conformational space. For example, in the Figure S6 we have extracted, from the conformational plane in S1(b) three representative **IP** structures.

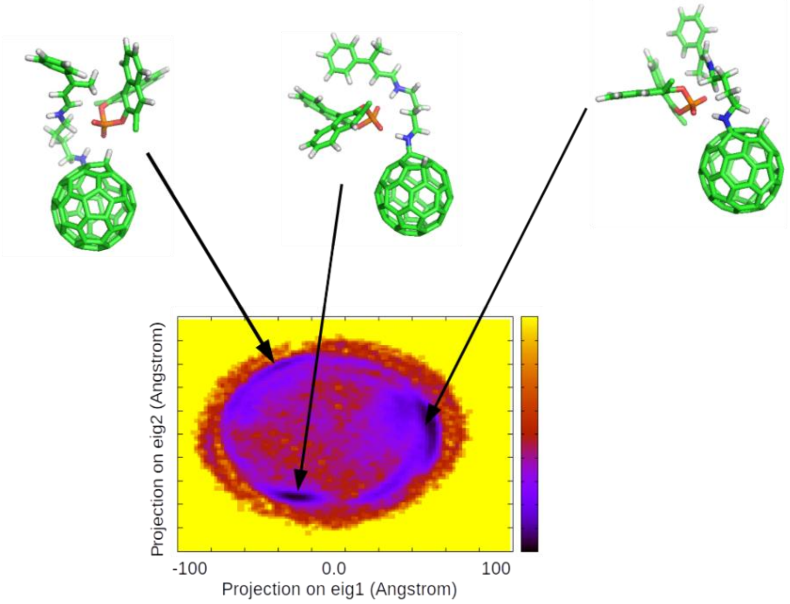

Figure S6. IP representative structures extracted from the MD simulation of IP in toluene.

Our results show that the two partners, although linked, form a highly dynamic complex undergoing continuous relative movements. As a consequence, at least in principle, all these structures should be taken into account for modelling the process under study.

Calculation of relative free energies and enthalpies using MD data

The calculation of the relative free energy between two states e.g. the two proR and proS complexes in the present study, can be calculated along a MD simulation carried out in the NVT ensemble through the following equation

$$\Delta F_{proR\rightarrow proS} \simeq -k_B T ln \frac{P_{proS}}{P_{proS}} \qquad \text{equation S1}$$

$k_B$is the Boltzmann constant;$\Delta F_{proR\rightarrow proS}$represents the Helmholtz free energy difference between the two states (note: the simulation is carried out in the isothermal-isocoric conditions),P_{proR}andP_{proS}indicate the probability for the formation of the state proR and proS complexes. These two latter quantities were evaluated, in the present study, using the results reported in the Figure S7 (see also the main text) using the below equation.

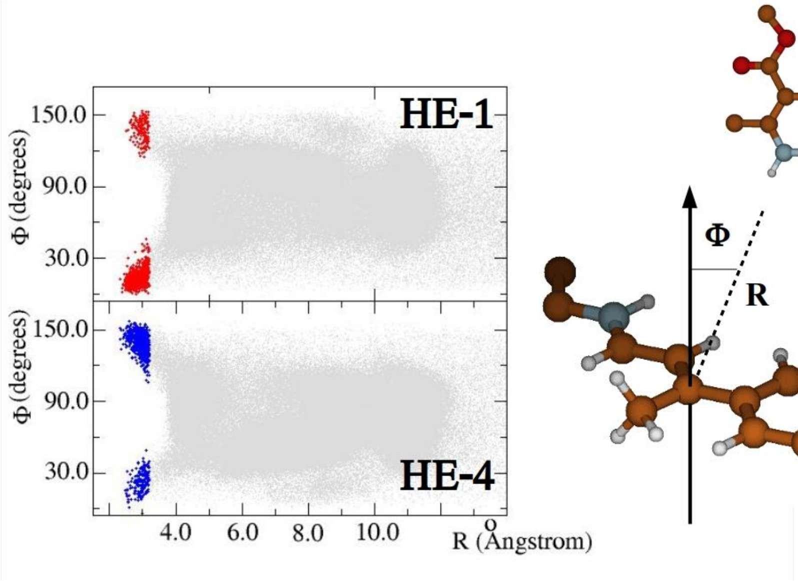

Figure S7 Distribution of the values of the distance between the N-H moiety and the prochiral carbon-atom of iminium ion and the corresponding angle (see also Figure) spanned along the MD trajectories

$$\frac{P_{proR}}{P_{proS}} = \frac{N_{points\Phi<90°,R<3.5Å}}{N_{points,\Phi>90°,R<3.5Å}} \qquad \text{equation S2}$$

where $N_{points\Phi<90°,R<3.5Å}$ and $N_{points\Phi>90°,R<3.5Å}$ is the number of frames falling in the two regions highlighted in the previous Figure termed as proR-region and proS-region.

Subsequently by using the total energies of the whole system evaluated along the trajectory, and reported in the Figure S8.

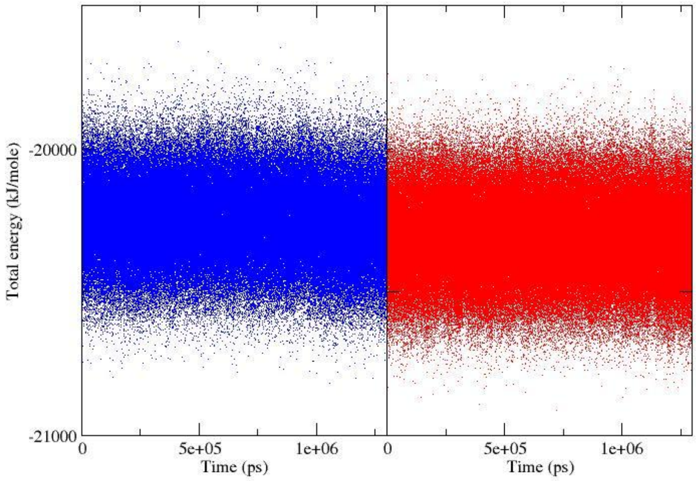

Figure S8 Total energies spanned along the simulations with HE-4 (blue) and HE-1 (red)

By collecting only those values corresponding to the states falling into the proR-region and proS-region (termed as $E_{i\in proS}$ and $E_{i\in proR}$) as schematically shown in Figure S9

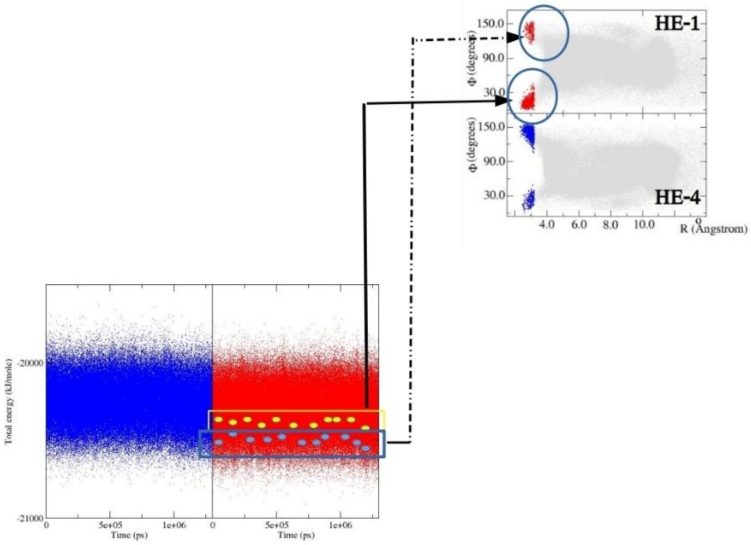

Figure S9 Schematic representation of the extraction of the energies of the whole system falling within the proR-region and proS-region already defined in the Figure S7 and in the main text.

We calculated the $\Delta U_{proR\rightarrow proS}$ using the equation S3

$$\Delta U_{proR\rightarrow proS} = \frac{\sum_{i=1}^{N_{pointsproS}} E_{i\in proS}}{N_{pointsproS}} - \frac{\sum_{i=1}^{N_{pointsproR}} E_{i\in proR}}{N_{pointsproR}} \qquad \text{equation S3}$$

Since we could safely assume that in both the cases $P\left(V_{proS} - V_{proR}\right) \simeq 0$ we can finally assess that

$\Delta F_{proR\rightarrow proS} \simeq \Delta G°_{proR\rightarrow proS}$ and $\Delta U_{proR\rightarrow proS} \simeq \Delta H°_{proR\rightarrow proS}$ as reported in the main text.

To justify the previous equalities it is important to further remark that

(i) in the calculation of $\Delta F_{proR\rightarrow proS}$ we also assumed as negligible the contribution of quantum vibration and semiclassical rotations, i.e. $-k_B T ln \frac{Q_{vib,proS} Q_{rot,proS}}{Q_{vib,proR} Q_{rot,proR}} \simeq 0$;

(ii) the above procedure was repeated dividing the trajectory in three subportions (assuming them as statistically uncorrelated) and evaluating the standard error reported in the main text.

Structural analysis of HE-X/IP adducts in the proR and proS regions.

In this section we describe the analysis carried out in order to conformationally characterize the adducts between HE-X and the IP necessary for the hydride transfer.

For this purpose, similarly to the previous step we extracted the MD frames falling in the proR and proS regions. Using these frames we carried out the Essential Dynamics analysis and we projected the proR and proS complexes on the plane formed by the first two eigenvectors.

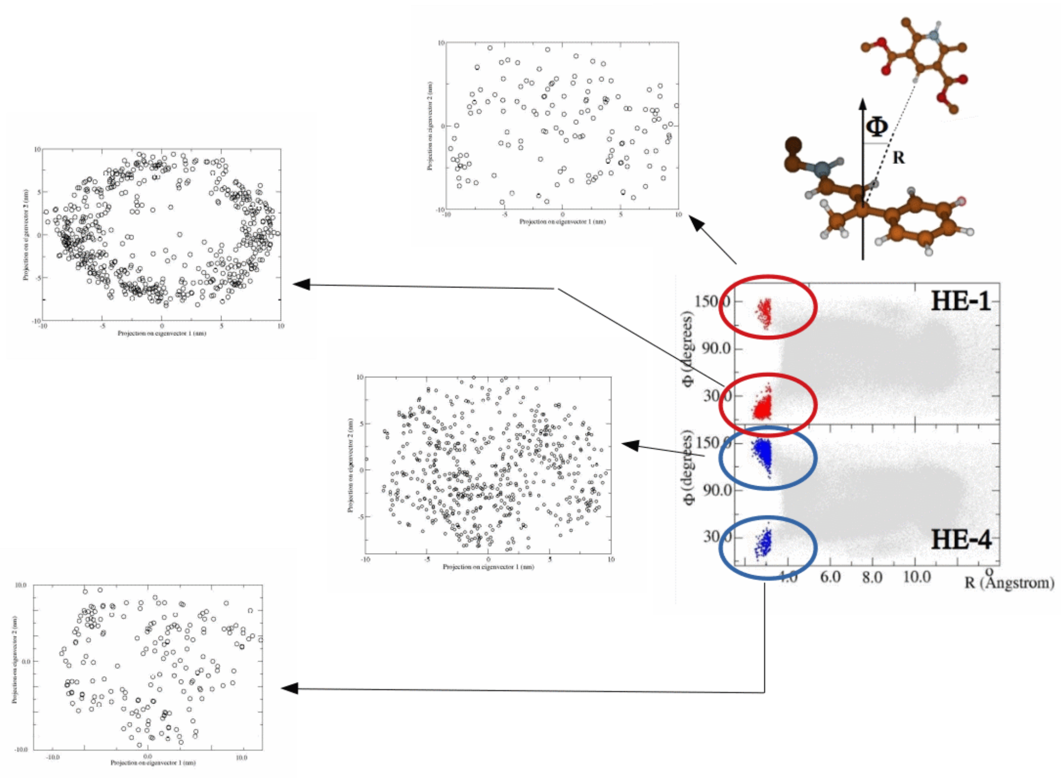

Figure S10 Projections of the proR and proS cartesian coordinates onto the corresponding essential planes from Essential Dynamics analysis.

The result, reported in the Figure S10, were utilized for calculating the Root Mean Square Fluctuations reported in the main text aimed at explaining the entropy difference between the proR and proS complexes in the two simulations.

Probability of formation of ternary complex

In this section we report the analysis, performed along the MD simulation, of the probability of formation of H-bond between the **HE** and **CPE**.

In the Figure S11 below reported, we have reported the distribution of the above distance (also highlighted with a red circle in the corresponding inset)

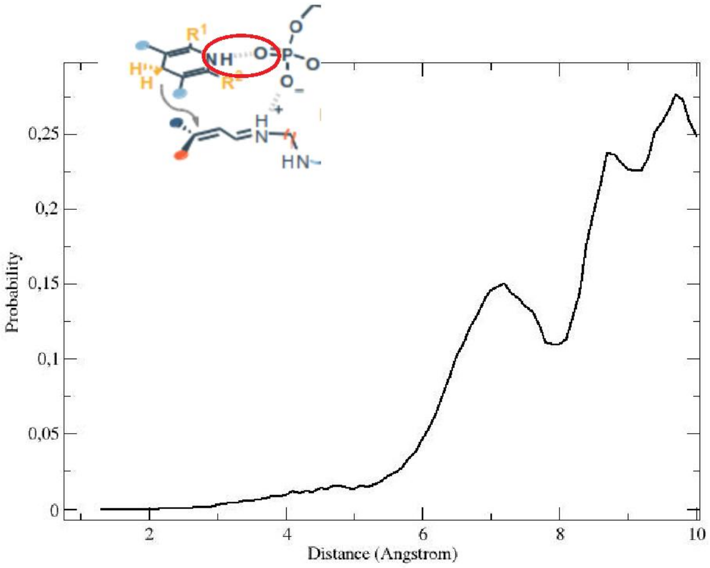

Figure S11 Distribution of the NH-CPA minimum distance monitored along the MD simulations. The two simulations produced a very similar results.

The result reported in the Figure clearly indicates that the probability of formation of a H-bond as the one schematically shown in the inset of Figure S11, is lower than 1% hence indicating the formation of ternary complex (see Figure 2 of the main text) as a highly unlikely event.

HPLC Traces

Compound 76a

Lux 3 μm-Cellulose 1, Hexane/i-Propanol 95:5, flow 0.5 mL/min, λ= 210 nm

Racemate

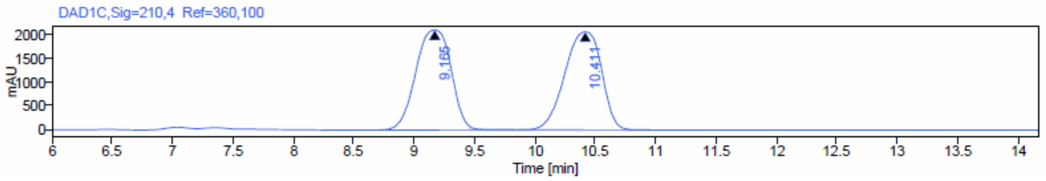

Peak	RT [min]	Type	Width [min]	Area mAU	Height	Area %
1	9.165	MM m	0.33	43036.37	2120.05	49.41
2	10.411	MM m	0.34	44067.78	2080.59	50.59

Entry 1

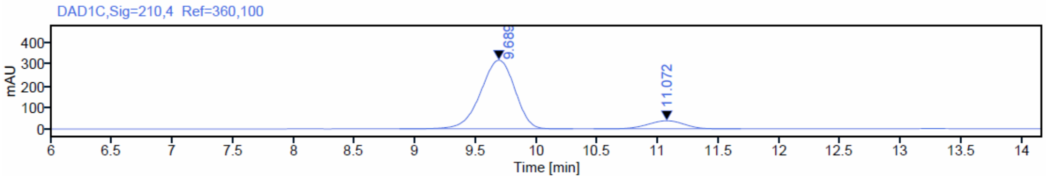

Peak	RT [min]	Type	Width [min]	Area mAU	Height	Area %
1	9.689	MM m	0.31	6325.44	322.10	88.94
2	11.072	MM m	0.33	786.80	37.85	11.06

Entry 4

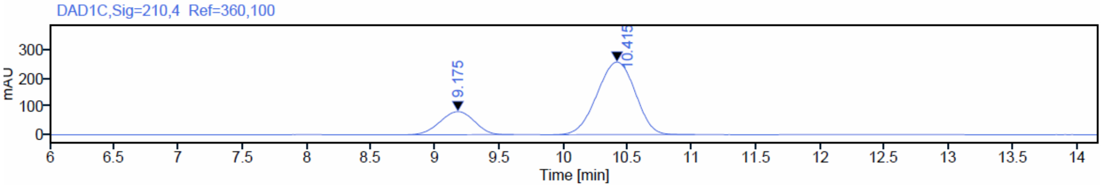

Peak	RT [min]	Type	Width [min]	Area mAU	Height	Area %
1	9.175	MM m	0.29	1533.42	82.56	22.19
2	10.415	MM m	0.33	5376.05	260.06	77.81

Compound 76b

Lux 3 µm-Cellulose 2, Hexane/i-Propanol 98:2, flow 0.5 mL/min, λ= 210 nm

Racemate

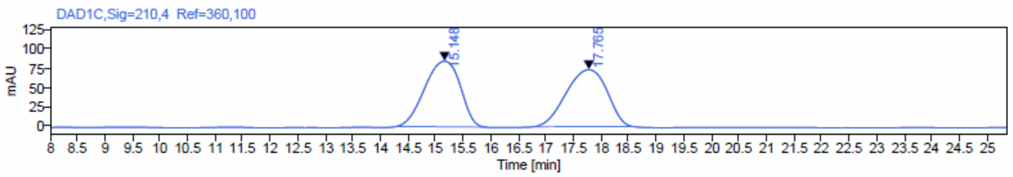

Peak	RT [min]	Type	Width [min]	Area mAU	Height	Area %
1	15.148	MM m	0.73	3796.21	84.43	50.05
2	17.765	MM m	0.85	3789.00	73.25	49.95

Entry 9

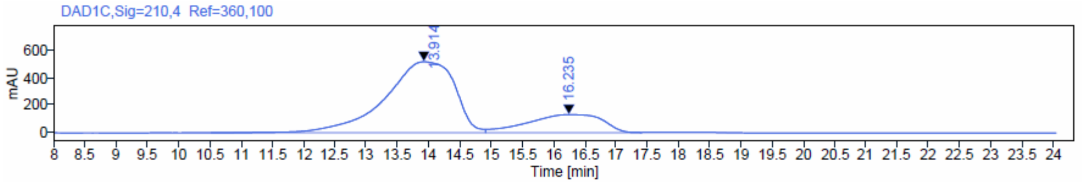

Peak	RT [min]	Type	Width [min]	Area mAU	Height	Area %
1	13.914	MM m	1.18	40253.38	519.15	78.61
2	16.235	MM m	1.08	10954.78	131.57	21.39

Entry 10

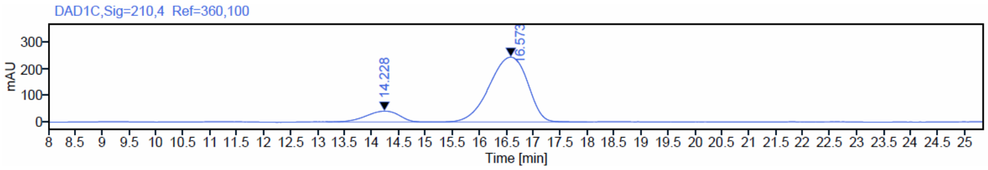

Peak	RT [min]	Type	Width [min]	Area mAU	Height	Area %
1	14.228	MM m	0.51	1719.93	40.60	12.42
2	16.573	MM m	0.79	12129.36	244.95	87.58

Chapter 4 – Strategies in Anion Binding Catalysis: From Carbazole Frameworks to Fluorinated Cyclohexanes

The introduction of the first part of this chapter is based on the publication: A. Carioscia, D. Iapadre, E. Incerto, J. Di Pietro, L. Giansanti, F. Pesciaioli, A. Carlone, *Chem Eur J.* **2025**, *31*, e202500126

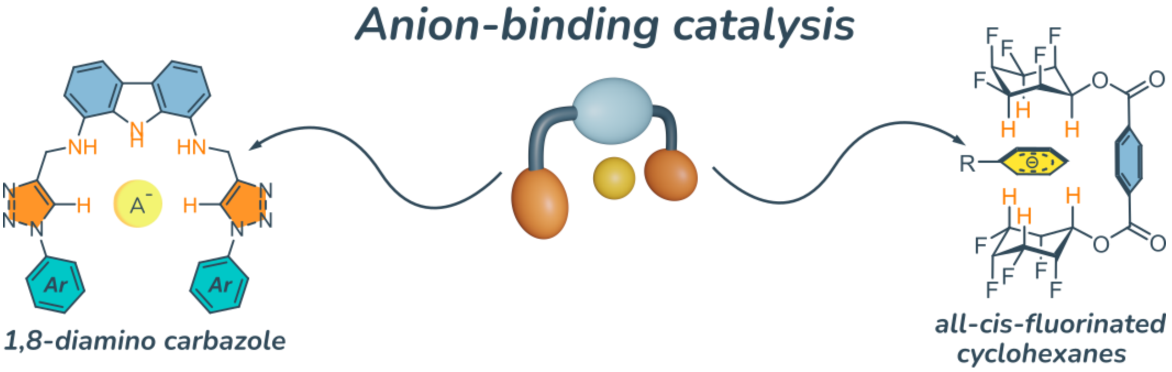

*Chapter outline – In this chapter, two novel scaffolds for anion-binding catalysis are introduced. The first section details 1,8-diaminocarbazole derivatives used for the first time as catalysts in an N-tritylation reaction, establishing a clear structure-activity relationship with catalyst **106c** showing optimal performance (83% yield). The second, exploratory part provides the first proof-of-concept for catalysis using all-cis-fluorinated cyclohexanes, demonstrating rate acceleration in an* S_NAr *reaction. Both studies validate these distinct frameworks as promising platforms for non-covalent catalysis.*

General introduction

Non-covalent catalysis, and in particular anion binding catalysis, represents one of the most dynamic and rapidly evolving areas in contemporary organic chemistry. The selective recognition and binding of anions by tailored molecular receptors provides powerful tools to modulate reactivity and control selectivity in catalytic transformations. This chapter presents two conceptually related research lines, both focused on the development of functional systems capable of engaging anions in catalytically relevant environments.

The first section is devoted to the development and investigation of carbazole-based receptors, which offer a promising scaffold due to their high anion affinity, rigid structural features, and synthetic versatility. These systems have been extensively studied for their role in promoting catalytic processes via anion binding. The section begins with a literature review adapted from a published article, followed by a detailed discussion of the experimental results and mechanistic aspects explored during the research.

The second section describes a complementary and exploratory project conducted within the research group of Prof. Max von Delius at the University of Ulm (Germany). This study focused on the application of all-cis fluorinated cyclohexanes as alternative molecular frameworks for anion binding catalysis. Although the outcomes are preliminary and limited in scope, the work lays the foundation for future investigations by showcasing a structurally distinct approach to anion recognition.

Despite clear differences in molecular design and experimental progress, both approaches aim at achieving selective and effective anion binding in catalytic systems. Their inclusion within the same chapter enables a comparative perspective and underlines key design strategies relevant to the broader field of non-covalent catalysis.

Design and Applications of Carbazole-Based Anion Receptors

The strategic engineering of molecular receptors for selective guest binding plays a pivotal role in advancing the field of supramolecular chemistry. Molecular recognition lies at the heart of numerous practical applications, including ion detection,[1] molecular diagnostics,[2] drug delivery,[3] and catalysis.[4] In recent years, significant attention has been devoted to designing host systems capable of forming strong and selective non-covalent interactions with small guest molecules, particularly anions.

A wide variety of molecular frameworks have been employed for this purpose—ranging from (thio)ureas[4] to squaramides,[5] triazoles,[6] imidazoles,[7] and other scaffolds such as pyrroles,[8] triphenylenes,[9] and steroids.[10] Among these, carbazole has emerged as a particularly attractive and multifunctional unit for building synthetic receptors. The appeal of carbazole lies in its structural and electronic features (Figure 1): its planar, rigid, and conjugated aromatic core facilitates

---

[1] I.V. Kolesnichenko, E.V. Anslyn, *Chem. Soc. Rev.* **2017**, *46*, 2385

[2] J. Chen, R.J. Hooley, W. Zhong, *Bioconjug. Chem.* **2022**, *33*, 2245

[3] B. R. Peterson, *Org. Biomol. Chem.* **2005**, *3*, 3607

[4] Z. Zhang, P.R. Schreiner, *Chem. Soc. Rev.* **2009**, *38*, 1187

[5] L.A. Marchetti, L.K. Kumawat, N. Mao, J.C. Stephens, R.B.P. Elmes, *Chem* **2019**, *5*, 1398

[6] B. Schulze, U.S. Schubert, *Chem. Soc. Rev.* **2014**, *43*, 2252

[7] Y. Hu, S. Long, H. Fu, Y. She, Z. Xu, J. Yoon, *Chem. Soc. Rev.* **2021**, *50*, 589

[8] G.I. Vargas-Zúñiga, J.L. Sessler, *Coord. Chem. Rev.* **2017**, *345*, 281

[9] Sonet, B. Bibal, *Tetrahedron Lett.* **2019**, *60*, 872

[10] A.P. Davis, *Coord. Chem. Rev.* **2006**, *250*, 2939

preorganization,[11] essential for binding efficiency, while its NH group serves as a robust hydrogen bond donor.[12]

In addition to its binding capacity, the carbazole moiety is intrinsically photophysically active. It functions as both a chromophore[13] and fluorophore,[14] which enables the design of optical sensors and probes. These properties change upon guest recognition, often resulting in distinct fluorescence quenching or enhancement effects. Such responsiveness has led to the successful application of carbazole-based systems in fluorescent imaging and sensing technologies.

Furthermore, the synthetic versatility of carbazole allows for diverse functionalization. Substituents can be introduced at the 1,8-positions or on the aromatic periphery to introduce additional non-covalent interaction sites—such as urea, thiourea, amide, sulfonamide, or halogen bond acceptors—enhancing the receptor's affinity and selectivity. These modular modifications also enable fine-tuning of the receptor's solubility, shape, and conformational behavior.

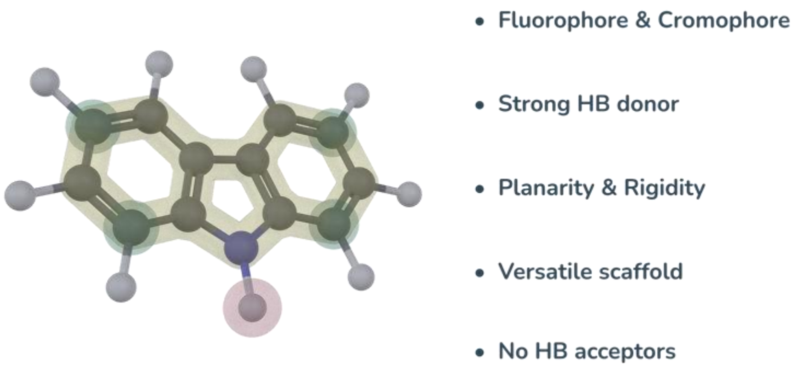

Figure 1: Carbazole scaffold and its properties.

While prior reviews have focused on selected examples of carbazole-containing receptors,[15] a broader and more unified perspective on their design strategies and performance is lacking. This chapter aims to fill that gap by offering a comprehensive overview of recent advances in the field. We will examine the design principles, structural variations, and guest-binding behaviors of carbazole-based receptors.

---

[11] K. Goto, in *Compr. Supramol. Chem. II* (Ed: J.L. Atwood), Elsevier, Oxford **2017**, pp. 61–71

[12] J. Jurczak, M.J. Chmielewski, P. Dydio, D. Lichosyt, F. Ulatowski, T. Zieliński, *Pure Appl. Chem.* **2011**, *83*, 1543

[13] M.J. Chmielewski, M. Charon, J. Jurczak, *Org. Lett.* **2004**, *6*, 3501

[14] K. Maslowska-Jarzyna, M.L. Korczak, J.A. Wagner, M.J. Chmielewski, *Molecules* **2021**, *26*, 3205

[15] a) A. Cholewiak, P. Stepniak, J. Jurczak, *Synthesis* **2018**, *50*, 4555; b) A. Cholewiak, P. Stepniak, J. Jurczak, *Synthesis* **2018**, *50*, 4555; c) N. Busschaert, C. Caltagirone, W. Van Rossom, P.A. Gale, *Chem. Rev.* **2015**, *115*, 8038; d) F. A. Mohammed, T. Xiao, L. Wang, R.B. P. Elmes, *Chem. Commun.* **2024**, *60*, 11812

Particular emphasis will be placed on how modifications of the carbazole core influence binding strength and selectivity, as well as how these systems operate in different media—including biologically relevant and aqueous environments.

The chapter will explore receptors designed for anion recognition, highlighting key applications such as environmental sensing and membrane transport. Although carbazole-derived hosts have been effectively used to target neutral, biologically relevant molecules, including carbohydrates and heterocycles like xanthines, those examples extend beyond the purpose of this chapter, and will not be thoroughly analysed. Nevertheless, collectively, these discussions will illustrate the versatility of the carbazole scaffold as a dynamic and functional platform for supramolecular receptor engineering.

Carbazole-based receptors for anions – an overview

Anions possess a prominent role in several biological processes. In particular, the chloride anion has been extensively studied as guest for synthetic receptors for its biological relevance in the regulation of transmembrane flux.[16] The disruption of ion channels is related to several diseases, namely channelopathies,[17] such as cystic fibrosis, epilepsy and dysfunction of the vestibular system. The development of synthetic carriers for biologically relevant anions is therefore interesting for therapeutical applications.[18] Furthermore, other anions, such as nitrate, sulfate and phosphate, have been recognized as pollutants both in soil and water.[19] Therefore, the development of host-guest systems for the binding of these anions is crucial.

1,8-diaminocarbazole platform

In 2004, Jurczak and coworkers reported the first synthetic receptor for anions based on a 1,8-diamino-3,6-dichlorocarbazole scaffold **I** (Figure 1). The significance of this work lies in the demonstration of the versatility of this scaffold, paving the way for the development of a new family of anion receptors. The authors show the higher affinity of the receptors **2** and **4** for polyatomic anions (e.g. dihydrogen phosphate and acetate) compared with chloride, since the cleft appears to be too wide to locate the small and monoatomic Cl^-.[13] The synthetic protocol involves the dichlorination of

---

[16] C.M. Armstrong, *Proc. Natl. Acad. Sci.* **2003**, *100*, 6257

[17] a) J.-B. Kim, *Korean J. Pediatr.* **2014**, *57*, 1; b) F.M. Ashcroft, in *Ion Channels Dis.*, Academic Press **1999**, pp. 1–2

[18] X. Wu, E.N.W. Howe, P.A. Gale, *Acc. Chem. Res.* **2018**, *51*, 1870

[19] a) A. Gizaw, F. Zewge, A. Kumar, A. Mekonnen, M. Tesfaye, *AQUA - Water Infrastruct. Ecosyst. Soc.* **2021**, *70*, 921 ; b) H. Wang, Q. Zhang, *Int. J. Environ. Res. Public. Health* **2019**, *16*, 1914

carbazole at positions 3 and 6, followed by nitration at positions 1 and 8 using absolute nitric acid. A catalytic hydrogenation step then enables the preparation of 1,8-diamino-3,6-dichlorocarbazole. There are some challenges related to the synthesis of these platforms. Generally, harsh conditions are required for the nitration of the 1,8-diaminocarbazole precursor and limitations are still present for the substitution of positions 3 and 6 of the carbazole skeleton. Substitutions in these positions are used to modulate carbazole properties like binding affinity, solubility or fluorescence response. T-Butyl groups are commonly used, which may additionally improve the solubility of desired receptor. Nevertheless, synthetic problems occur since t-butyl groups are introduced in the first step and can undergo partial cleavage during the following steps. After the short synthesis of the dehalogenated 1,8-diaminocarbazole developed by Chmielewski,[20] several groups reported the synthesis of mono- and bis-amido and imino carbazoles based receptors (Figure 2).[14,21] Most of the receptors shown in Figure 1, whose association constants with various anions are shown in Table 1, demonstrate a pronounced affinity for oxoanions in DMSO-d_6 + 0.5% H_2O (in particular for carboxylates and dihydrogen phosphate). The reduced binding affinity of halide anions (e.g., Cl^-) compared to oxoanions can be attributed to the lower basicity of chloride and its neither hard nor soft character compared to the oxoanions under study. Additionally, a structural mismatch between the receptor and the chloride anion hinders effective interactions with the receptor's proton sites.[13]

The functionalization of positions 3 and 6 on the carbazole ring with electron-withdrawing groups generally increases the binding affinities because the NH can act as stronger hydrogen bond donor. Notably, a significant difference between the 1:1 association constants is observed comparing receptor **1** ($K_A = 5.73 \times 10^2$ M^{-1} for benzoate; $K_A = 1.66 \times 10^3$ M^{-1} for dihydrogen phosphate) with its chlorinated analogue **2** ($K_A = 1.79 \times 10^3$ M^{-1} for benzoate; $K_A = 6.98 \times 10^3$ M^{-1} for dihydrogen phosphate).[21d] A similar trend is evident when receptor **8** ($K_A = 4.43 \times 10^3$ M^{-1} for benzoate; K_A = 1.10

---

[20] M.J. Chmielewski, *Synthesis* **2010**, *2010*, 3067

[21] a) M. L. Korczak, K. Maslowska-Jarzyna, M. J. Chmielewski, *RSC Adv.* **2024**, *14*, 29883; b) X. Shang, X. Li, J. Han, S. Jia, J. Zhang, X. Xu, *Inorg. Chem. Commun.* **2012**, *16*, 37; c) D.E. Gross, V. Mikkilineni, V.M. Lynch, J.L. Sessler, *Supramol. Chem.* **2010**, *22*, 135; d) K.M. Bąk, K. Chabuda, H. Montes, R. Quesada, M.J. Chmielewski, *Org. Biomol. Chem.* **2018**, *16*, 5188; e) M. Šekutor, S. Opačak, M. Alešković, K. Mlinarić-Majerski, *Croat. Chem. Acta* **2015**, *88*, 405; f) T.D. Thangadurai, N.J. Singh, I.-C. Hwang, J.W. Lee, R.P. Chandran, K.S. Kim, *J. Org. Chem.* **2007**, *72*, 5461; g) S.K. Lee, Y. Han, Y. Choi, J. Kang, *J. Incl. Phenom. Macrocycl. Chem.* **2012**, *74*, 177; h) X. Shu, Y. Xu, L. Liu, Y. Fan, X. Zhuang, C. Huang, S. Chen, C. Zheng, Y. Jin, C. Xia, *Polyhedron* **2022**, *214*, 115641; i) K.M. Bąk, M.J. Chmielewski, *Chem. Commun.* **2014**, *50*, 1305; j) K.M. Bąk, K. Masłowska, M.J. Chmielewski, *Org. Biomol. Chem.* **2017**, *15*, 5968; k) K. Maslowska-Jarzyna, M.L. Korczak, M.J. Chmielewski, *Front. Chem.* **2021**, *9*

$\times 10^4$ M^{-1} for dihydrogen phosphate) is compared to its chlorinated counterpart **9** ($K_A = 2.18 \times 10^4$ M^{-1} for benzoate; $K_A = 9.68 \times 10^4$ M^{-1} for dihydrogen phosphate) and when receptor **10** ($K_A = 4.65 \times 10^3$ M^{-1} for benzoate; $K_A = 1.02 \times 10^4$ M^{-1} for dihydrogen phosphate) is compared with receptor **11** ($K_A = 2.90 \times 10^4$ M^{-1} for benzoate; $K_A = 8.32 \times 10^4$ M^{-1} for dihydrogen phosphate).[21d] The highest affinity for dihydrogen phosphate with respect to benzoate could be ascribed to an higher structural complementarity with the host. It was observed that the non-substituted receptor **10** exhibited an excellent fluorescent response compared to **11** even though the latter is able to discriminate different anions. Chmielewski and coworkers, in 2021, investigated receptors with strongly electron-withdrawing groups at the 3,6 positions of the carbazole ring (**12** and **13**).[14]

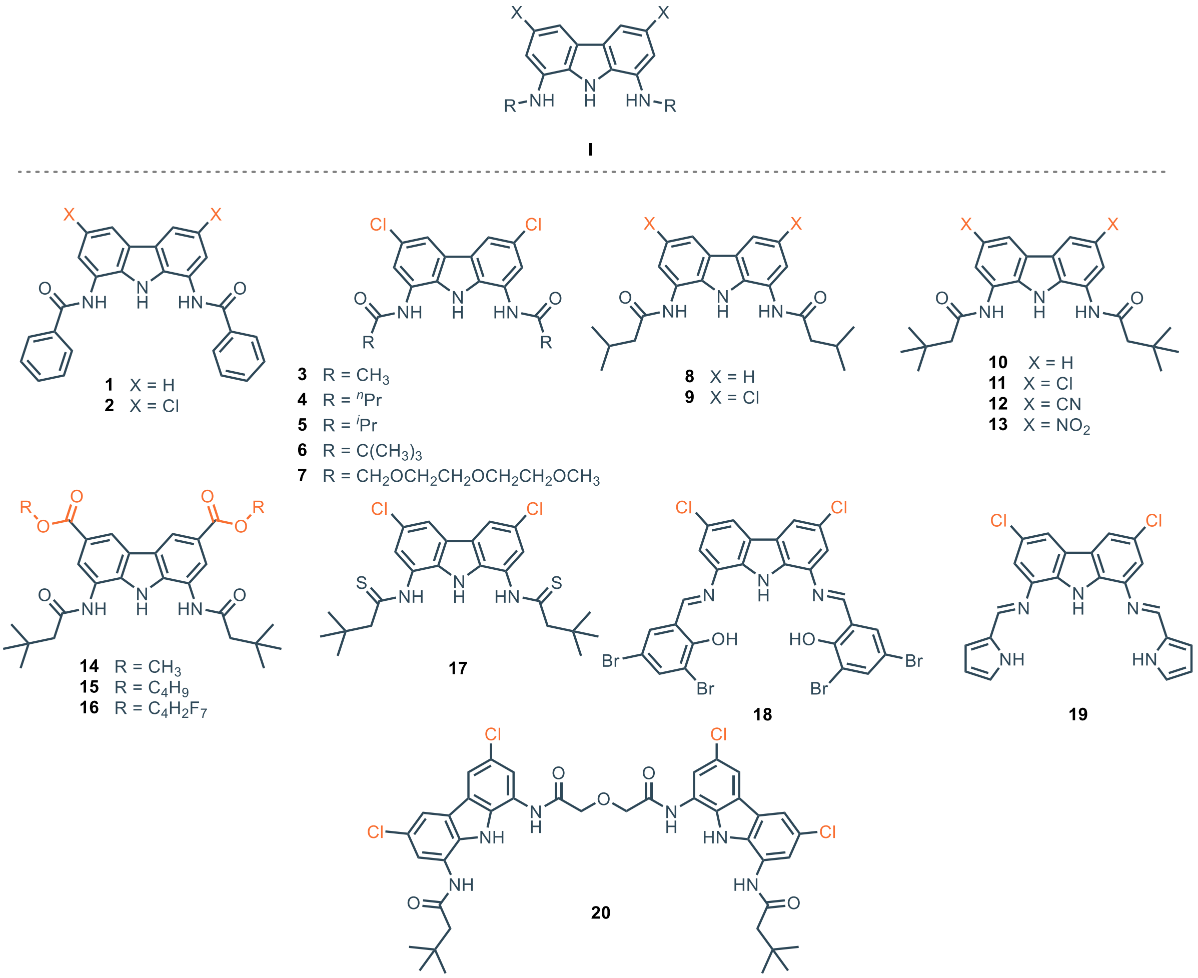

Figure 2: 1,8-diamino-3,6-dichlorocarbazole scaffold, mono- and bis-amido and imino-carbazoles receptors.

The binding strength is linearly dependent on the electron withdrawing character of the substituents and is influenced by proton transfer from carbazole to the basic anion, suggesting an increase in the acidity of carbazole NH resulting from the introduction of strongly electron-withdrawing groups. In 2024 the same group explored functionalization at the 3,6 positions with ester groups containing various alkoxy substituents (**14**, **15** and **16**).[21a] Their findings revealed a high binding affinity with dihydrogen phosphate and benzoate. In addition, they demonstrated the deprotonation of receptor 12 in the presence of acetate and sulfate, while no deprotonation was observed with benzoate, in contrast with the behavior exhibited by receptors **12** and **13**.[21a] This phenomenon can be attributed to the higher electron-withdrawing nature of -CN and -NO_2 groups in receptors **12** and **13** compared to the esters groups present in receptors **14**, **15** and **16**. Overall, the alkoxy groups of these ester functionalized receptors have a minimal impact on binding affinity.[21a] Later, compound **13** was employed as a chloride transporter across the lipid bilayer, functioning as a Cl^-/NO_3^- exchanger. Interestingly, its activity was found to be strongly influenced by pH, with the highest transport rate observed at acidic pH, while significantly decreasing at neutral pH.[22] This behavior is due to the electrostatic repulsion between the carbazole anion and the negative charged guest. The pH dependence was then exploited for the development of a dual-stimuli responsive anion transporter (**ONB-13**) based on the structure of 13 and appended with the light-cleavable o-nitrobenzyl group (ONB). (Figure 3) This carrier is inactive in its native form, and it requires two orthogonal stimuli - light and acidic pH - to achieve maximum activity.

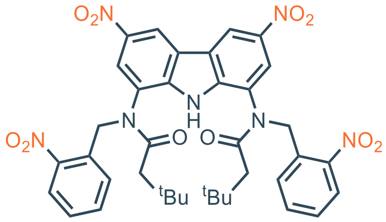

ONB-13

Figure 3. procarrier **ONB-13** which requires both light and acidic pH to become active.

Structural variations of amide R groups, whether aromatic or aliphatic, also impact anion binding affinities. Interestingly, receptors with aliphatic groups show stronger binding compared to their aromatic counterparts, despite the additional hydrogen bonds between ortho CH protons of the phenyl ring (of the receptors **1** and **2**) and the anion. This discrepancy may result from the higher energetic cost associated with disrupting intramolecular hydrogen bonds in aromatic substituents upon the anion binding.[21d] Comparing the activity of receptors with aliphatic substituents (**3**, **4**, **5**, **6**, **9** and **11**), it becomes evident that the binding affinity for anions is predominantly affected by subtle structural variations within the aliphatic chain.[21d] For instance, the introduction of methyl groups at the β carbon (e.g. receptor **9**, $K_A = 2.18 \times 10^4\ M^{-1}$ for benzoate) enhances binding affinity compared

---

[22] K. Maslowska-Jarzyna, M.L. Korczak, M.J. Chmielewski, *Front. Chem.* **2021**, *9*

to receptor **4** (e.g. $K_A = 1.60 \times 10^4$ M^{-1} for benzoate), while the addition of a methyl group at the α carbon (e.g. receptor **6**, $K_A = 2.01 \times 10^3$ M^{-1} for benzoate) decreases the binding affinity compared to receptor **5** (e.g. $K_A = 1.31 \times 10^4$ M^{-1} for benzoate).[21d] Nevertheless, the addition of a methyl group at the α position enhances the solubility of the receptor in organic solvents. This is likely attributed to the increased steric bulk, which not only hinders anion binding but also interferes with receptor-receptor interactions.[21d] The fact that enhanced steric bulk introduced with t-butyl groups at positions 3 and 6 on the carbazole ring increases hydrophobicity and steric hindrance, which in turn improves solubility in organic solvents, may explain the popularity of scaffolds derivatized in these positions. On the other hand, receptors with short linear alkyl chains at positions 3 and 6, such as n-butyl groups, are rarely used, likely because they do not offer advantages in terms of solubility or binding. t-Butyl groups have the same effect at position 2 and 5. In particular, n-hexyl groups confer a higher solubility compared to the t-butyl ones.[23]

Thioamide receptors, such as receptor **17**, demonstrate lower binding affinities compared to their amide analogues. This decreased affinity can likely be attributed to the larger size of the sulfur atom relative to oxygen, which induces twisted geometry, thus influencing the interaction with anions.[24] Nevertheless, the thioamide groups show higher solubility than the amide analogues, which suffer from poor solubility. For these reasons, **17** is a very efficient anionophore for the transport of chloride, oxoanions (e.g. carboxylates and organic phosphates) and non-steroidal anti-inflammatory drugs (NSAIDs) like aspirin across lipid membranes.[25] Diamide and dithioamide-carbazole receptors **11**, **12**, **13** and **17** also act as active transporters of bicarbonate anion across lipid membrane.[26] In 2022, exploiting a direct detection method based on an europium complex assay,[27] the effective transport mechanism of bicarbonate across a lipid membrane was established, determining that two different processes of transport occur in the presence of **11**–**13** and **17**: one is the indirect transport caused by the spontaneous diffusion of CO_2, coupled with pH equilibration via H^+Cl^- symport by receptors **11**–**13** and **17**; the other is the direct bicarbonate anion transport by these receptors via HCO_3^-/Cl^- antiport. These two processes, as expected, are remarkably dependent on receptor concentration, but

---

[23] T. Kader, G. Jin, M. Pletzer, D. Ma, J. Fröhlich, J. Chen, P. Kautny, *Org. Electron.* **2021**, *96*, 106215

[24] R. Pomorski, M. García-Valverde, R. Quesada, M. J. Chmielewski, *RSC Adv.* **2021**, *11*, 12249

[25] K.M. Bąk, B. van Kolck, K. Maslowska-Jarzyna, P. Papadopoulou, A. Kros, M.J. Chmielewski, *Chem. Commun.* **2020**, *56*, 4910

[26] K. Maslowska-Jarzyna, A. Cataldo, A. Marszalik, I. Ignatikova, S.J. Butler, R. Stachowiak, M.J. Chmielewski, H. Valkenier, *Org. Biomol. Chem.* **2022**, *20*, 7658

[27] S. J. Butler, *Chem. Commun.* **2015**, *51*, 10879

they are assumed to be independent of each other. **11** does not show active transport of HCO_3^- anions; on the other hand, the presence of electron-withdrawing groups on 12 and 13 enhances the transporter activity. The best performance is displayed by dithioamide **17** which confirms to be a potent anionophore for oxoanions. Diamide **11**–**13** and dithioamide **17** also showed antimicrobial activity in accordance with their efficiency as anion transporter.[26] The dithioamide receptor **17** was also effectively employed in the transport of amino acids (AAs) across lipid bilayers. Imine carbazole-based receptor **18** additionally employs phenolic protons for binding interactions and exhibits a high binding affinity in DMSO for dihydrogen phosphate ($K_A = 2.13 \times 10^4$ M^{-1}) and acetate ($K_A = 1.79 \times 10^4$ M^{-1}).[21b] Notably, fluoride is bound effectively ($K_A = 1.08 \times 10^4$ M^{-1}), unlike other halide anions.

Table 1: Association constants (M^{-1}) for compounds **1**-**20** towards anionic guests. Unless specified, the titrations are performed *via* UV-visible in DMSO + 0.5% H_2O.

Receptor	**K_A (CH_3COO^-)**	**K_A ($PhCOO^-$)**	**K_A ($H_2PO_4^-$)**	**K_A (F^-)**	**K_A (Cl^-)**	**K_A (Br^-)**	**K_A (SO_4^{-2})**
1	-	5.73×10^2	1.66×10^3	-	<10[b]	-	-
2	-	1.79×10^3	6.98×10^3	-	14[b]	-	-
3	-	7.55×10^3	1.21×10^5	-	75[b]	-	-
4	-	1.60×10^4	9.62×10^4	-	109[b]	-	-
5	-	1.31×10^4	1.21×10^5	-	131[b]	-	-
6	-	2.01×10^3	4.71×10^3	-	56[b]	-	-
7[a]	-	-	-	-	-	-	10^4
8	-	4.43×10^3	1.10×10^4	-	42[b]	-	-
9	-	2.18×10^4	9.68×10^4	-	123[b]	-	-
10	-	4.65×10^3	1.02×10^4	-	48[b]	-	-
11	-	2.90×10^4	8.32×10^4	-	159[b]	-	-
12[b]	-	deprot	2.51×10^5	-	309	-	-
13[b]	-	deprot	deprot	-	347	-	-
14	deprot	2.14×10^4	8.71×10^4	-	123[b]	-	deprot.
15	-	1.58×10^4	5.25×10^4	-	-	-	-
16	-	1.02×10^4	1.32×10^5	-	-	-	-
17[b]	-	-	-	-	67	-	-

18[c]	1.79×10^4	-	2.13×10^4	1.08×10^4	n.d	-	-
19[d]	2.24×10^4	-	6.17×10^4	-	2.57×10^3	3.16×10^3	-
20	-	6.02×10^4	2.19×10^5	-	758 [b]	-	[e]

[a] Measured *via* ^{1}H NMR titrations in DMSO-d_6 + 10% H_2O. [b] Measured *via* ^{1}H NMR titrations in DMSO-d_6 + 0.5% H_2O. [c] Measured in DMSO. [d] Measured in acetonitrile. [e] Too high to be measured. n.d. = The association constant could not be determined

The greater affinity for dihydrogen phosphate compared to acetate can be attributed to the tetrahedral conformation, which facilitates a more favorable interaction with the receptor. This is likely due to a better structural complementarity between the anion and the receptor, resulting in an increased number of interactions.[21b] The imine carbazole-based receptor **19** also comprises pyrrolic protons that can assist in the binding process. This receptor shows a strong binding affinity in acetonitrile for various anions, including dihydrogen phosphate ($K_A = 6.17 \times 10^4$ M^{-1}), acetate ($K_A = 2.24 \times 10^4$ M^{-1}), chloride ($K_A = 2.57 \times 10^3$ M^{-1}), and bromide ($K_A = 3.16 \times 10^3$ M^{-1}).[21e] The interaction is stronger with the first two anions (dihydrogen phosphate and acetate), consistent with their higher basicity. However, despite acetate being more basic, dihydrogen phosphate is bound more efficiently. This can be attributed to the ability of dihydrogen phosphate groups to interact with the lone pairs of the imine nitrogens. Specifically, the acidic protons of this guest act as hydrogen bond donors to the imine nitrogens of the receptor.[21e]

Receptors **11** and **7** form robust and orthogonal 2:1 complexes with SO_4^{2-} in DMSO-d_6 + 10% H_2O, even in the presence of a large amount of water (10%).[21i] This orthogonal assembly pattern was later utilized for the construction of catenanes as shown in Figure 6a.[28] In case of receptor **2**, in the 2:1 complex with sulfate, the formation of orthogonal complexes does not occur. Instead, the two receptor molecules adopt a biplanar arrangement, driven by the establishment of π–π stacking interactions due to the presence of aromatic groups.[21i] The dicarbazole receptor **20** exhibits selectivity for the sulfate anion, demonstrating high association constants in both 1:1 and 1:2 complex stoichiometries.[21j] Indeed, in both instances, the association constants could not be determined due to the exceptionally high affinity. Specifically, upon the addition of one mole of sulfate, receptor **20** binds the anion with both carbazole moieties. However, in presence of excess sulfate, the two

---

[28] K. M. Bąk, B. Trzaskowski, M. J. Chmielewski, *Chem. Sci.* **2024**, *15*, 1796

carbazole units bind two different sulfate anions, rather than sharing the same one. Figure 4 depicts the structural features of the complex under examination.[21j]

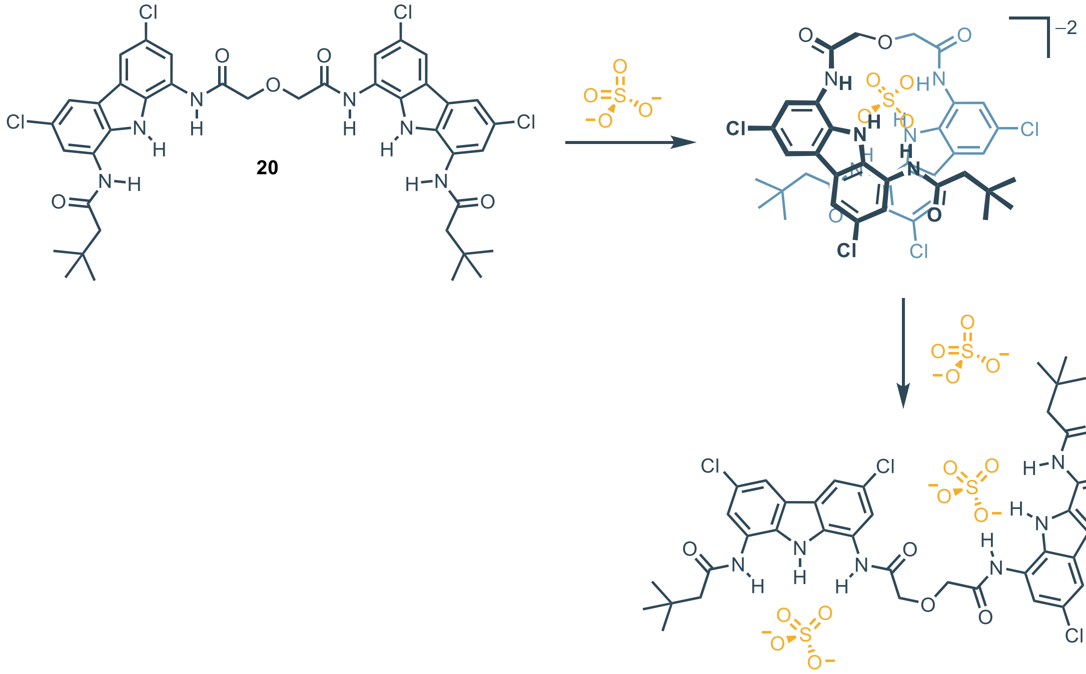

Figure 4: Structural features of the complex **20** with sulfate ion.

Designing an alternative method for the treatment of TcO_4^- in nuclear water waste, amidic and aminic carbazole scaffolds have also been inserted in the synthesis of receptors able to extract ReO_4^- and TcO_4^- from acidic aqueous solution.[21h] The method developed consists of a liquid-liquid extraction in which the organic phase is filled with diamide and diamino carbazole-based receptors equipped with tertiary amines as appendages (Figure 5). These receptors can extract ReO_4^-/TcO_4^- from acidic solutions of HNO_3 at various pH. Among all the receptors tested, **24** seems to display the best activity in comparison with the amide-based ones **21–23**. Amide-based receptors **21–23** show an intramolecular hydrogen bond, formed between carbazole NH and C=O groups, that brings to anti-preorganization because of the occlusion of the cavity intended for the anion. Moreover, due to intramolecular H-bonding, the two amide NH sites point out on different planes, hence their resulting interactions with the anion are less efficient.

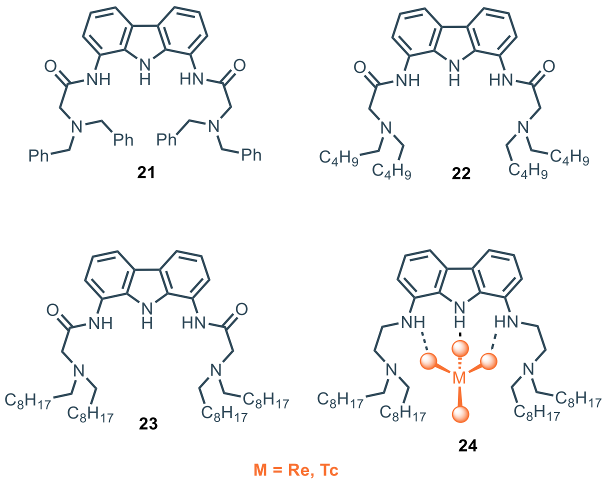

Figure 5. Amido and amino carbazole-based receptors for the extraction of ReO$_4^-$/TcO$_4^-$.

In 2023, Chmielewski and coworkers developed a charge-neutral [2]catenane **25** (Figure 6a) based on a 1,8-diamidocarbazole architecture via a sulfate-templated Ring Closing Metathesis (RCM) (Figure 6b),[28] starting from the observation that simple diamidocarbazole **11** exhibits strong affinity towards sulfate in a 2:1 (receptor:anion) stoichiometry, where the two ligands are arranged in an orthogonal fashion.[21i] The [2]catenane **25** showed excellent affinity for SO_4^{2-} in DMSO-d$_6$/H$_2$O 9:1 ($K_A = 7.76 \times 10^5$ M^{-1} via NMR). Furthermore, the 1:1 association constant of [2]catenane **25** towards dihydrogen phosphate and benzoate are 95 and 3400 times lower respectively, indicating outstanding selectivity. Compound **25** binds sulfate with one order of magnitude higher than simple diamidocarbazole **11**, and 2.5 times than bis(carbazole) receptor **20**. Notably, the macrocyclic compound **Macr-27** (obtained as a side product in the RCM reaction) and the acyclic precursor **27** have an association constant respectively 20 and 10 times lower than the catenane. The 1:1 complex (namely contracted co-conformation) and the 1:2 complex (namely expanded co-conformation) can be easily switched through acid-base triggering, as previously demonstrated for compound **11** (Figure 7).[29] Upon the addition of 1 equiv. of triflic acid to a 2 mM solution of [2]catenane and tetrabutylammonium sulfate (TBA$_2$SO$_4$) (2 equiv.) in DMSO-d$_6$, protonation of 1 equiv. of sulfate occurs, shifting the conformation from the expanded to the contracted one. The addition of 1 equiv. of tetrabutylammonium hydroxide (TBAOH) allows for the opposite conformation change. This co-conformation cycle can be repeated up to 8 times.

---

[29] K. M. Bąk, M. J. Chmielewski, *Eur. J. Org. Chem.* **2015**, *2015*, 4077

1,8-diaminocarbazoles have also been effectively conjugated with urea- and thiourea- motifs, which are known to be privileged hydrogen bonding donor moieties for their peculiar properties. In fact, the introduction of additional acidic NH protons that could synergistically interact with the guest is thought to increase the binding affinity. Additionally, the urea linker allows for the introduction of different diaminocarbazole moieties, exploiting the formation of macrocyclic compounds, thus defining shape-persistent cavities that could further assist in the binding process.[30] In 2021, Gale and coworkers reported a series of carbazole-based bis-ureas and thioureas, with the most relevant, compounds **29**–**34**, shown in Figure 8a.[31] This family of compounds displayed moderate affinity towards Cl^-, with the highest values reported for compounds bearing an aromatic moiety with EWG groups. Moreover, the urea-derivative compounds **29**–**30** showed a much higher association constant than their thiourea counterparts **31**–**32** (K_A = 100–300 M^{-1} vs K_A = 60–120 M^{-1} in DMSO-d_6 + 0.5% H_2O). This difference is probably due to the distortion of planarity induced by the steric hindrance of the sulfur atom. Interestingly, the titration for the thiourea derivatives revealed that a 1:2 (receptor:anion) stoichiometry is observed for high concentration of Cl^- (Figure 8b). The moderate affinity toward Cl^- has been rationalized considering the large cavity of the 1,8-diaminocarbazole scaffold, in accordance with other reports. It becomes clear that bigger, polyatomic anions are the favourite anionic guests for receptors based on the 1,8-diaminocarbazole scaffold. Nevertheless, both the urea and the thiourea derivatives **33** and **34** proved to bind Cl^- better than their amide counterpart **1** (K_A = 122 M^{-1} for **33** vs K_A = 67 M^{-1} for **34** vs K_A < 1 M^{-1} for **1**). This is probably due to the higher number of hydrogen bonding donors when the (thio)urea moieties are present, even though the spatial orientation of these groups is also important.

---

[30] R. Cao, R. B. Rossdeutcher, Y. Zhong, Y. Shen, D. P. Miller, T. A. Sobiech, X. Wu, L. S. Buitrago, K. Ramcharan, M. I. Gutay, M. F. Figueira, P. Luthra, E. Zurek, T. Szyperski, B. Button, Z. Shao, B. Gong, *Nat. Chem.* **2023**, *15*, 1559

[31] P. Wang, X. Wu, P. A. Gale, *Supramol. Chem.* **2021**, *33*, 143

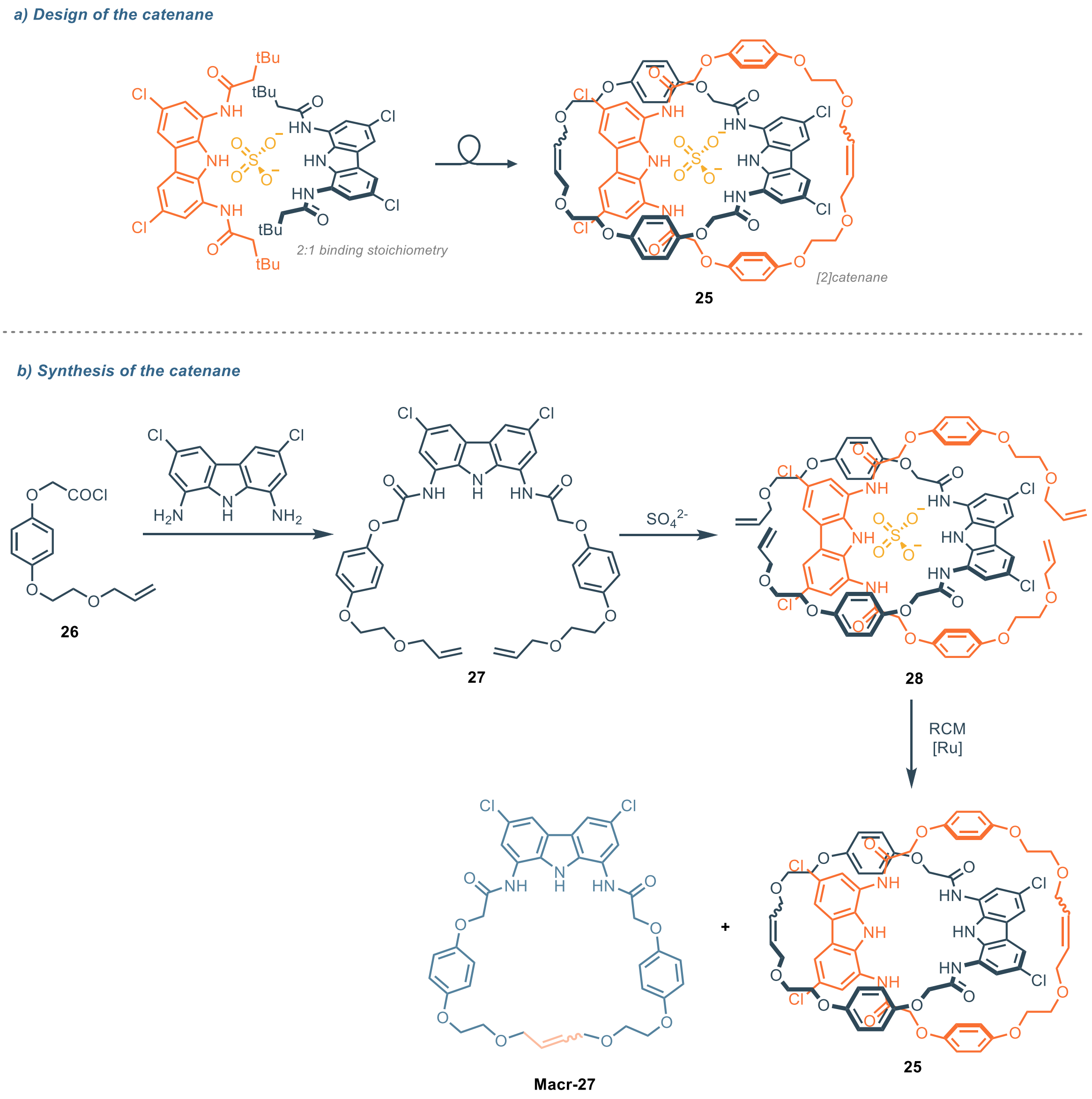

Figure 6. a) Design of [2]catenane exhibiting strong affinity and selectivity for sulfatein DMSO-d_6 + 10% H_2O; b) Synthesis of the [2]catenane *via* sulfatetempated RCM

The effort directed towards the development of receptors that feature a ditopic design is highlighted by the work of Molina and coworkers, where the ditopic 1,8-diaminocarbazole-based synthetic receptors **34** and **35** were synthesized and characterized (Figure 9a).[32] These receptors feature two diaminocarbazole scaffolds appended with fluorogenic pyrenyl and chromogenic p-nitrophenyl aromatic moieties; urea linkers are used to construct the molecular architectures. The eight well-oriented NH groups define a cavity which is optimal for the detection of hydrogenopyrophosphate with high affinity and selectivity both in CD_3CN and in competitive mixtures CD_3CN/H_2O.

---

[32] G. Sanchez, A. Espinosa, D. Curiel, A. Tarraga, P. Molina, *J. Org. Chem.* **2013**, *78*, 9725

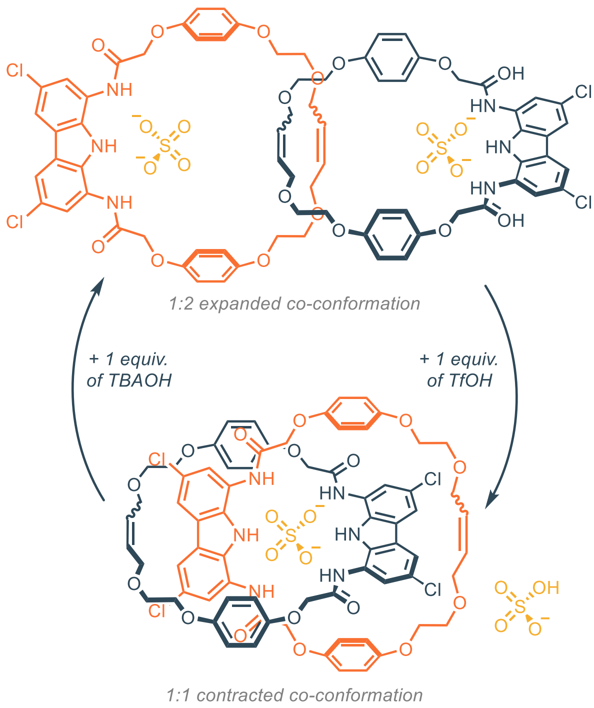

Figure 7. The co-conformation cycle for the [2]catenane triggered by acidic and basic conditions. Adapted from ref [28]

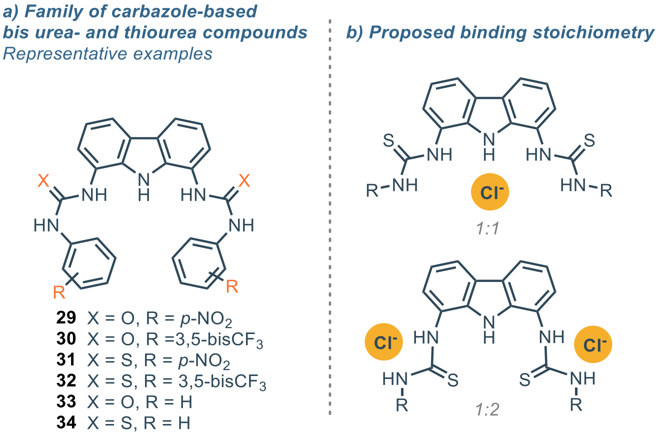

Figure 8. a) Family of urea and thiourea derivatives; b) Different binding stoichiometries

Here, a ditopic design seems to be optimal for the recognition of the large binuclear pyrophosphate, highlighting again the close relationship between the cavity size of the receptor and its corresponding optimal guest. Interestingly, the pyrenyl derivative **36** exhibits a large excimer emission band (λ = 496 nm) and two sharp bands (λ = 394 nm and 416 nm), consistent with the presence of a pyrene. The ratio between the excimer intensity and the monomer intensity (i.e. IE/IM) stays constant at different concentrations (10^{-7} M to 10^{-5} M), indicating that the excimer formation happens in an intramolecular fashion. This is probably due to a π-stacking interaction between the two pyrenyl groups (closed conformation A) or between a pyrenyl group and a carbazole moiety (closed conformation B). Interestingly, upon the addition of hydrogenopyrophosphate, the excimer band disappears, while the monomer band tends to increase. This behavior suggests that the inclusion of the anion inside the cavity inhibits intramolecular interaction, with preference for the corresponding open form which accommodates the guest (Figure 9b). From **35** or **36** it is possible the generation of self-assembled monolayers (SAM) bis(carbazolyl)urea **37** on gold surface.[33] **37** is a highly selective receptor and robust sensing probe for the surface plasmon resonance (SPR).[34] Indeed, **37** shows high affinity for hydrogen pyrophosphate anion, $HP_2O_7^{3-}$ in buffered aqueous solution under physiological conditions (Figure 9c). SPR consists of a thin metal surface appropriately modified with a SAM bearing a molecular probe selective towards a particular species, having the advantage of operating in aqueous media.[35] The high selectivity towards $HP_2O_7^{3-}$ makes receptor **37** an optimal sensor in the described systems. Interestingly, two different situations occur during the anion recognition in the operative conditions. At low anion concentration ($HP_2O_7^{3-}$ in the order of 10^{-10} to 10^{-7} M), the most accessible receptors molecules only interact with the anions at the interface of the SAM. In this case, the association constant for $HP_2O_7^{3-}$ is 4.95×10^3 M^{-1}. On the other hand, at higher concentration ($HP_2O_7^{3-}$ in the order of 10^{-6} to 10^{-4} M) the association constant is higher ($K_A = 4.39 \times 10^5$ M^{-1}) because in this case also the most buried receptors molecules at the interface can complex the anion. Furthermore, **37** proves to be selective towards $HP_2O_7^{3-}$ in the presence of different anions, even phosphate and trivalent anions which display similar features with $HP_2O_7^{3-}$. More recent SAMs of bis(amido)carbazole were developed by Chmielewski and coworkers for sulfate detection via vibrational spectroscopy techniques like surface infrared and Raman spectroscopy.[36] SAM-**38**–**40** are obtained from their analogue receptors **2** and **11** which showed high affinity and selectivity towards SO_4^{2-}. Sulfate affinity in acetonitrile depends on the substituents on the amide moieties. The affinity increases in the order: **38** < **40** < **39**. Nevertheless, no receptor-anion interaction is detected in water for the latter SAMs receptors probably because the desolvation free energy required for the sulfate to be dehydrated and its competition with water for the binding site (absent in acetonitrile).

---

[33] G. Sánchez, D. Curiel, W. Tatkiewcz, I. Ratera, A. Tárraga, J. Veciana, P. Molina, *Chem. Sci.* **2014**, *5*, 2328

[34] R. Bakhtiar, *J. Chem. Educ.* **2013**, *90*, 203

[35] J. Homola, M. Piliarik, in *Surface Plasmon Resonance Sensors* (Ed: J. Homola), Springer, Berlin, Heidelberg 2006, pp. 45–67

[36] P. Piotrowski, J. Bukowska, B. Pałys, R. Pomorski, M. J. Chmielewski, *Sens. Actuators, B: Chem.* **2019**, *283*, 172

a) Ditopic urea-based diaminocarbazoles

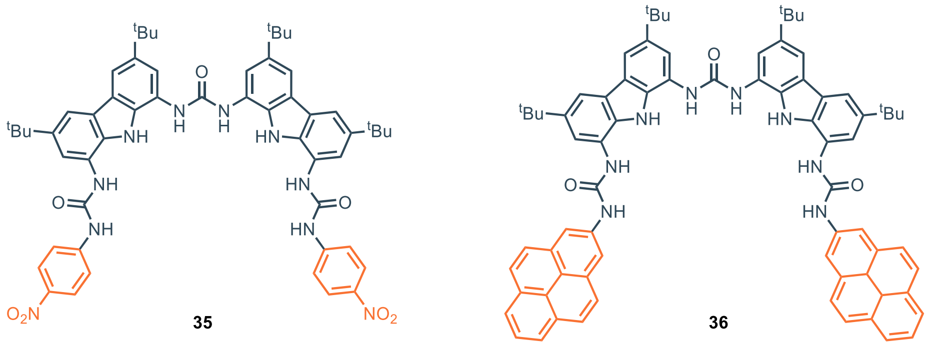

b) Open and closed conformations of 36

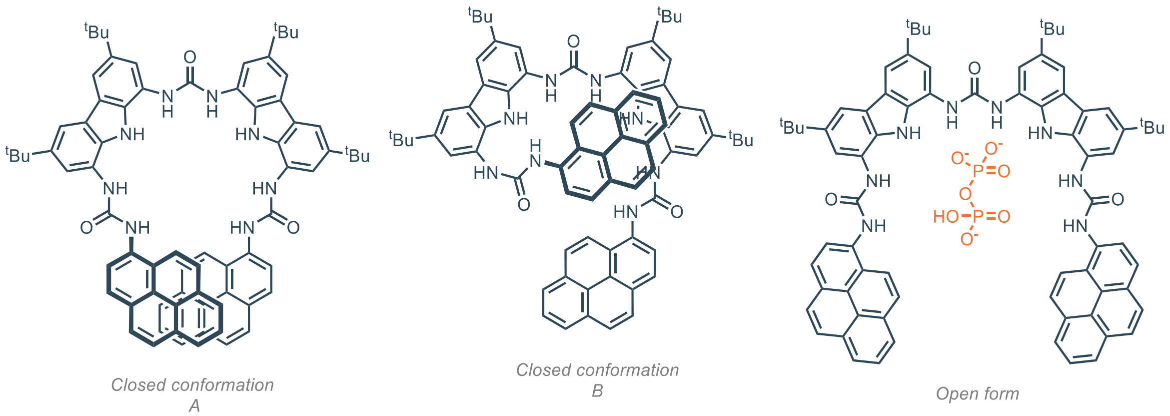

c) SAM bis(carbazoyl)urea receptor on gold

d) SAM bis(amido)carbazole receptors on gold

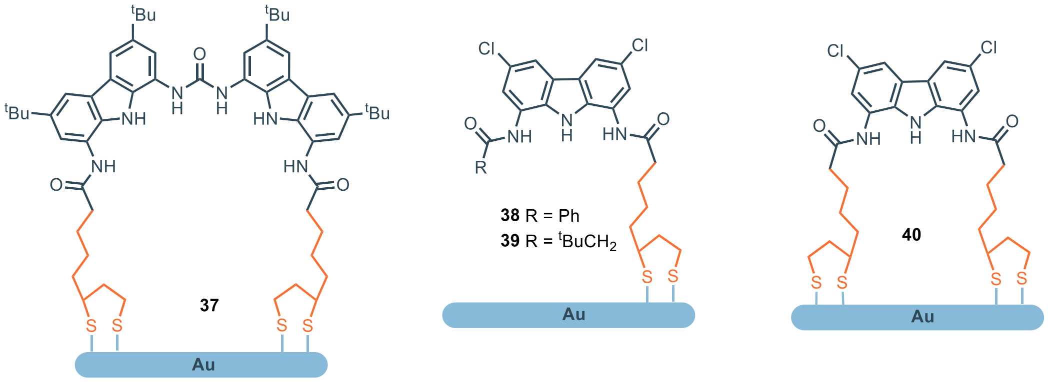

Figure 9. a) Ditopic urea-based diaminocarbazoles; b) different conformations of receptor **36;** c) SAM bis(carbazoyl)urea-based receptors receptor for $HP_2O_7^{3}$ developed by Molina and coworkers; d) SAMs receptors for SO_4^{2-} developed by Chmielewski and coworkers.

Following the same general structure, in 2017 Leito and coworkers studied several hosts based on different hydrogen bonding scaffolds as anion receptors for binding the glyphosate dianion Gly^{2-} (Figure 10).[37] Among all the different receptors studied, the bis(carbazolyl)urea derivatives **41** and **42** proved to be the most effective. In fact, in DMSO-d_6 + 0.5% H_2O, compound K_A exhibits a KA of 6.3 × 10^4 M^{-1}, while compound **42** has a constant too high to be measured. With the aim to test the

---

[37] S. A. Kadam, K. Haav, L. Toom, A. Pung, C. Mayeux, I. Leito, *Eur. J. Org. Chem.* **2017**, *2017*, 1396

receptors in more competitive assays, the titration was repeated with 5% and 10% of water content. Compound **42** outperformed compound **41** both with 5% water ($K_A = 3.16 \times 10^6$ M^{-1} for **42** vs $K_A = 10^3$ M^{-1} for **41**) and with 10% water ($K_A = 3.16 \times 10^5$ M^{-1} for **42** vs $K_A = 10^3$ M^{-1} for **41**). Interestingly, **42** decreases its binding strength of 1 order of magnitude when going from 5% to 10% water, while compound **41** displays no change in its binding affinity in the same conditions. The optimized geometry for compound **42** indicates that the presence of the two naphthyl rings promotes a spiral-like orientation of the NH groups around the phosphonate moiety of the glyphosate triggering the tautomerization of the acidic proton on the PO_3H^- to the NH group; in this conformation, the binding process between the receptor and Gly^{2-} occurs exclusively at the phosphonate. The binding data for compounds **29**–**36** and **40**–**42** are summarized in Table 2.

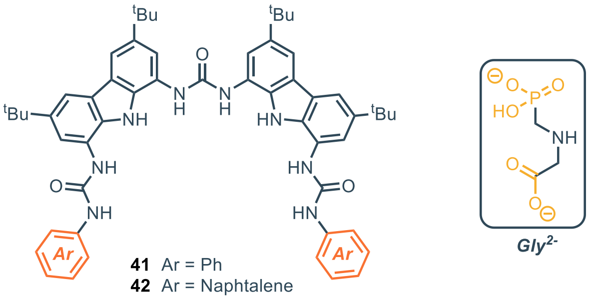

41 Ar = Ph
42 Ar = Naphtalene

Figure 10. Ditopic receptors for binding of glyphosate.

The bis-carbazolyl urea scaffold has also been employed in the design of macrocycles with different ring sizes (Figure 11). Kim and coworkers reported the cyclo-bis-(urea-3,6-dichlorocarbazole) **43** which exhibit good affinity for oxoanions, like acetate and dihydrogen phosphate ($K_{1:1} = 1.5 \times 10^3$ M^{-1} and $K_{1:2} = 1.5 \times 10^5$ M^{-1} for acetate; $K_{1:1} = 1.4 \times 10^3$ M^{-1} and $K_{1:2} = 1.8 \times 10^5$ M^{-1} for dihydrogen phosphate).[38] Interestingly, X-ray and computational analysis revealed that the binding occurs outside the cavity in a 1:2 fashion, with each anion interacting with the NH groups of one urea moiety. This explains the higher $K_{1:2}$ with respect to $K_{1:1}$ for the anions tested.

---

[38] N. Ahmed, V. Suresh, B. Shirinfar, I. Geronimo, A. Bist, I.-C. Hwang, K. S. Kim, *Org. Biomol. Chem.* **2012**, *10*, 2094

Table 2. Association constants (M^{-1}) for compounds **29-36** and **41-42** towards anionic guests. Unless specified, the titrations are performed *via* NMR in DMSO-d_6 + 0.5% H_2O

Receptor	$K_A(Cl^-)$	K_A ($HP_2O_7^{3-}$)	$K_A(Gly^{2-})$
29	100	-	-
30	300	-	-
31	60	-	-
32	120	-	-
33	122	-	-
34	67	-	-
35	-	3.16×10^6 [a],[b]	-
36	-	10^7 [a],[c]	-
41	-	-	6.31×10^4 [c]
42	-	-	[c],[d]

[a] Measured in CH_3CN. [b] Measured *via* UV/Vis absorption titrations. [c] Measured *via* fluorescence titration. [d] Association constant too high to be measured

Aiming to study the influence of the dimension of the cavity in the binding affinity, Leito and coworkers developed a series of carbazole-based macrocycles **45–56** with different ring sizes, together with the derivative **57**, which exhibits a macrocyclic structure featuring 12 hydrogen bonding donor moieties, and the corresponding open-chain analogue **58**.[39] Computational modelling of these receptors versus various carboxylate anions showed that for the small macrocycles **45–47** preferential intramolecular hydrogen bonding is present. In fact, those macrocycles are too small to accommodate an anion inside their cavity. This was confirmed by the evaluation of their binding properties. A general trend was observed, where the association constant towards several tetrabutylammonium (TBA) salts of carboxylic acids was observed to be proportional with the ring size of the macrocycle, until it reaches a plateau for the receptors **49–51** (-CH_2- : 7–9). A further increase in the methylene linker length has a negative effect on the binding affinity, which slowly decreases because the higher flexibility reduces the preorganization of the host.

The open-chain analogue **58** also competes well with other cyclic structures. In this case, macrocyclic structures did not prove to be significantly superior to more flexible open-chain structures. Surprisingly, the rigid macrocycle **57**, which features 12 hydrogen bonding donors, performed much

---

[39] A. Rüütel, V. Yrjänä, S. A. Kadam, I. Saar, M. Ilisson, A. Darnell, K. Haav, T. Haljasorg, L. Toom, J. Bobacka, I. Leito, *Beilstein J. Org. Chem.* **2020**, *16*, 1901

worse than other methylene-bridged macrocycles (**44**–**56**). Although the authors do not provide an explanation for this phenomenon, it is important to consider that the general paradigm "higher rigidity leads to better binding" is not always true. Instead, binding strength strongly depends on the geometry of the cavity and the specific guest analyzed. In this case, the computed lowest-energy conformations clearly indicate that the cavity is too large to accommodate small carboxylates. As a result, depending on the guest, the interaction involves only 4 to 7 of the 12 potentially available hydrogen-bonds available. It is therefore crucial to carefully tailor the receptor based on the desired guest, in order to maximize the structural match. The same group, in 2022, reported the synthesis and binding characterization of compounds **59**–**64** as carboxylate-binding receptors.[40] These molecules feature unusual connection motifs, such as imines and ether bridges. All the receptors were tested toward a set of carboxylate anions (acetate, benzoate, sorbate, formate and lactate) and the general trend is in line with the observation that the higher basicity of the anion correlates with higher binding strength.[41] The cyclic imine-derivative **59** proved to be the most powerful toward recognition for most of the anions. In particular, compound **59** strongly binds acetate in DMSO-d_6 + 0.5% H_2O ($K_A = 1.1 \times 10^5\ M^{-1}$), while its acyclic counterpart **60** has an affinity for the same anion 2.4 fold weaker in the same conditions. Computational analysis revealed that this difference is due to the presence of a rigid cavity in receptor **59**, which allows for the participation of a pyrrole NH group in the binding complex, which is not participating in the host-guest complexation for the acyclic **60**. In this case, the insertion of rigidifying elements proved to be an efficient strategy to construct shape-persistent receptors with higher binding affinities. Furthermore, the binding data of **58** and **60** are similar across all tested anions, suggesting that the addition of a pyrrolic hydrogen bond (**60**) compensates for the loss of the amide group (**58**). The association constants for the ether-bridged compounds **61** and **62** proved to be similar with each other and to compound **47**, with the highest affinity for sorbate ($K_A = 4.67 \times 10^4\ M^{-1}$ and $K_A = 2.95 \times 10^4\ M^{-1}$ respectively). In these cases, intramolecular hydrogen bonding occurs, partially deactivating them in terms of binding. Finally, among the two acyclic derivatives **63** and **64**, the smaller **63** showed higher association constants towards all the anions tested. In fact, the bigger **64** interacts with the anion only on "one side" of the receptor, resulting in several intramolecular interactions, which make the receptor less prone to engage in the binding process.

---

[40] S. Kheirjou, A. Rüütel, A. Darnell, T. Haljasorg, I. Leito, *Org. Biomol. Chem.* **2022**, *20*, 2121

[41] S. A. Kadam, K. Martin, K. Haav, L. Toom, C. Mayeux, A. Pung, P. A. Gale, J. R. Hiscock, S. J. Brooks, I. L. Kirby, N. Busschaert, I. Leito, *Chem. – Eur. J.* **2015**, *21*, 5145

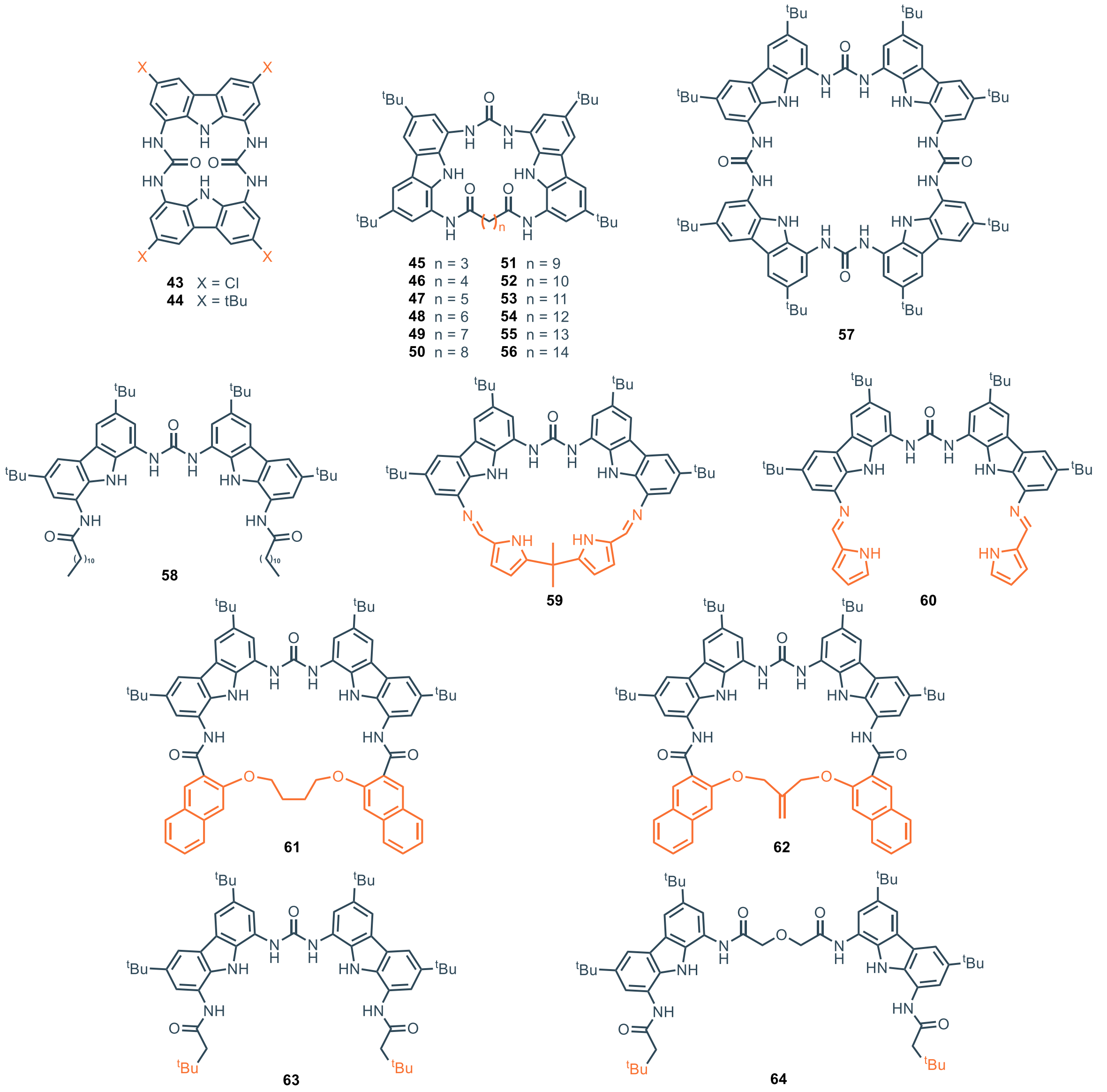

Figure 11. Cyclic and acyclic bis-carbazolyl urea derivatives for binding of carboxylates.

This supports the data obtained for the series of compounds **44**–**56**, where increasing the cavity size led to a decrease in the binding affinity. From a broader perspective, although high association affinities are achieved, receptors for carboxylates generally exhibit limited selectivity, as binding occurs exclusively at the carboxylate moiety, which remains identical across different guests.[42] The association constants for compounds **44**–**64** are summarized in Table 3. In 2020, Joliffe and coworkers reported the synthesis of the tetrathiourea macrocyclic carbazole receptors **65** and **66**, to investigate the cooperative effect of the two diaminocarbazole moieties in the binding of dicarboxylate anions (Figure 12).[43] The two compounds show comparable binding affinities for a series of linear and flexible

---

[42] A. Rüütel, S. Tshepelevitsh, I. Leito, *J. Org. Chem.* **2022**, *87*, 14186

[43] S. N. Berry, L. Qin, W. Lewis, K. A. Jolliffe, *Chem. Sci.* **2020**, *11*, 7015

dicarboxylates (with the highest association constant for adipate, namely **Adi**). This suggests that, despite the different pore sizes of the two receptors, the macrocycles feature a certain degree of flexibility, which allows for their structural adaptation to flexible guests. When rigid dicarboxylate guests (e.g. terephthalate, namely **Ter**, and trans,trans-muconate, namely **ttM**) are used, the difference in association constants between the two receptors becomes more pronounced: receptor **65** binds **Ter** and **ttM** with affinities that are three and two times higher, respectively, than those of receptor **66** in DMSO/H_2O 9:1 (measured via UV/Vis titrations). This can be ascribed to the effects of geometry match and mismatch, which become more pronounced as the rigidity of the guest increases.

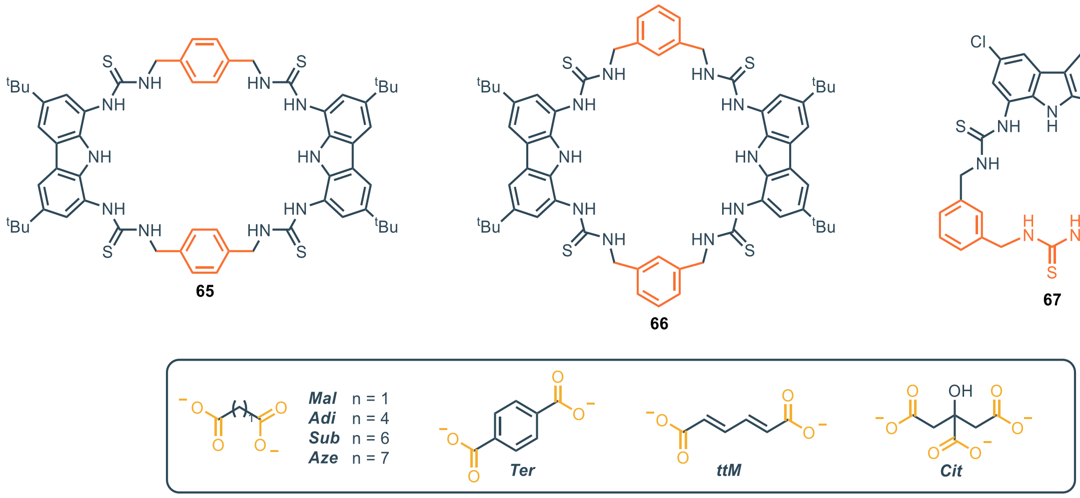

Figure 12. Mono and ditopic thiourea-based macrocyles for binding of dicarboxylates.

In addition, Double Mutant Cycle Analysis (DMC) provided insights into the chelate cooperativity in the binding process.[44] The binding process between a ditopic guest and a ditopic host involves an initial binding event at one end of the complex (defined by the constant $K_{(\mathrm{ini})}$), followed by a second binding event (characterized by $K_{(\mathrm{intra})}$), that leads to the 1:1 complex. The association constant $K_{(\mathrm{intra})}$ determines the chelate cooperativity. $K_{(\mathrm{intra})} > 1$ ($\log(K_{(\mathrm{intra})}) > 0$) reflects positive cooperativity, with the preferred formation of the 1:1 complex; $K_{(\mathrm{intra})} < 1$ ($\log(K_{(\mathrm{intra})}) < 0$) indicates negative cooperativity, where the second binding event is less favored, leading to the preferential formation of high-order oligomeric species.[45]

Table 3. Association constants (M^{-1}) for compounds **44-64** towards carboxylate guests. Unless specified, the titrations are performed *via* NMR in DMSO-d_6 + 0.5% H_2O

---

[44] A. Camara-Campos, D. Musumeci, C. A. Hunter, S. Turega, *J. Am. Chem. Soc.* **2009**, *131*, 18518

[45] C. A. Hunter, H. L. Anderson, *Angew. Chem., Int. Ed.* **2009**, *48*, 7488

Receptor	**K_A (acetate)**	**K_A (pivalate)**	**K_A (sorbate)**	**K_A (benzoate)**	**K_A (formate)**	**K_A (lactate)**
44	2.14×10^{3}	3.39×10^{3}	-	1.58×10^{4}	6.46×10^{3}	1.94×10^{3}
45	3.16×10^{3}	4.90×10^{3}	-	851	478	251
46	2.95×10^{4}	2.51×10^{4}	-	4.90×10^{3}	3.01×10^{3}	977
47	10^{5}	8.51×10^{4}	-	1.48×10^{4}	1.15×10^{4}	2.29×10^{3}
48	1.48×10^{5}	7.94×10^{4}	-	2.95×10^{4}	3.24×10^{4}	2.95×10^{3}
49	4.90×10^{5}	4.37×10^{5}	-	8.12×10^{4}	6.31×10^{4}	1.10×10^{4}
50	2.19×10^{5}	1.70×10^{5}	-	4.37×10^{4}	4.27×10^{4}	4.17×10^{3}
51	4.90×10^{5}	6.60×10^{5}	-	8.91×10^{4}	3.89×10^{4}	1.17×10^{4}
52	2.29×10^{5}	1.62×10^{5}	-	3.80×10^{4}	1.51×10^{4}	4.90×10^{3}
53	1.51×10^{5}	2.69×10^{5}	-	4.17×10^{4}	10^{4}	6.03×10^{3}
54	10^{5}	2.51×10^{5}	-	2.57×10^{4}	7.24×10^{3}	4.17×10^{3}
55	9.33×10^{4}	2.75×10^{5}	-	$2.14 \times 10^{4}\ \mathrm{M}^{-1}$	3.80×10^{3}	5.75×10^{3}
56	9.33×10^{4}	3.02×10^{5}	-	2.10×10^{4}	5.89×10^{3}	3.55×10^{3}
57	2.00×10^{3}	2.88×10^{3} [a]	-	724	457	478 [a]
58	6.61×10^{4}	1.45×10^{5}	-	1.58×10^{4}	6.46×10^{3}	1.95×10^{3}
59	1.15×10^{5}	-	7.41×10^{4}	1.66×10^{4}	1.91×10^{4}	5.37×10^{3}
60	4.47×10^{4}	-	3.16×10^{4}	1.17×10^{4}	5.01×10^{3}	2.34×10^{3}
61	1.29×10^{4}	-	2.95×10^{4}	7.41×10^{3}	1.32×10^{3}	661
62	1.86×10^{4}	-	4.67×10^{4}	7.41×10^{3}	1.86×10^{3}	550
63	7.08×10^{4}	-	8.71×10^{4}	2.04×10^{4}	5.89×10^{3}	3.80×10^{3}
64	3.39×10^{3}	-	4.68×10^{3}	1.10×10^{3}	661	355

[a] Measured *via* UV/Vis absorption titrations.

The authors observe that for small (malonate, namely **Mal**) and large (suberate, namely **Sub** and azepate, namely **Aze**) dicarboxylate anions, a negative chelate cooperative effect occurs, indicating preferred oligomerization. On the other hand, the medium-sized flexible dicarboxylate (Adi) and rigid dicarboxylate (**Ter** and **ttM**) showed moderate to strong positive cooperativity. This data reflects the differences in the association constant of the receptors varying the anion.

X-ray analysis shows that the cavity of receptor 65 is too wide to accommodate Mal cooperatively; the malonate forms a 2:2 complex, where two molecules of 65 are held together by hydrogen bonding interactions forming a sandwich-like complex (Figure 13a). On the other hand, the X-ray structure of 65 with Aze shows that the anion does not completely fit in the cavity, with the alkyl chain remaining outside of the cavity (Figure 13b). Adi represents a striking balance in terms of dimension, since it is perfectly encapsulated in the macrocycle itself (Figure 13c). This evidence fully supports both its higher association constant and its positive chelate cooperativity. A few years later, the same group reported macrocycle 67, which does not feature a ditopic design. Compound 67 displays an intense and selective fluorescence response toward citrate (Cit), and it was applied as a fluorescence turn-on sensor for detection of citrate in living cells.[46]

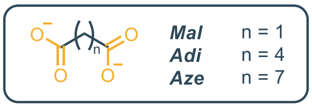

a) Receptor 65 + Mal

b) Receptor 65 + Aze

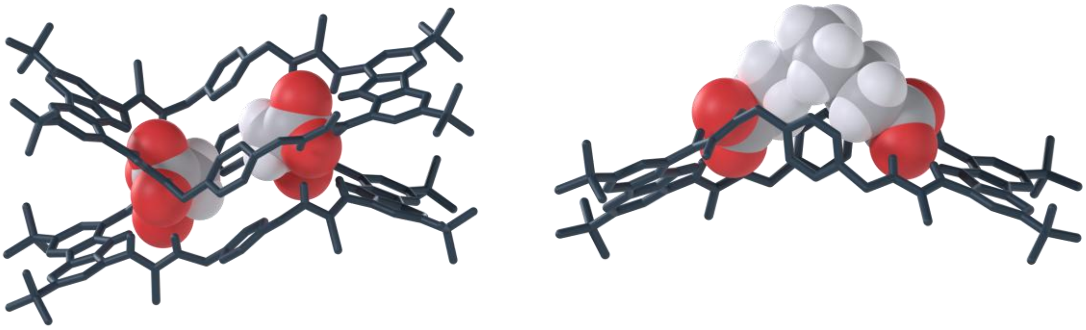

c) Receptor 65 + Adi

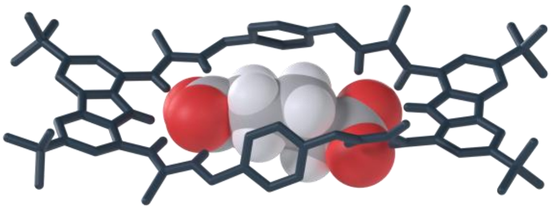

Figure 13. X-ray structure of the 65·Mal complex (a), 65·Aze complex (b) and 65·Adi complex (c). Adapted from ref [43]

---

[46] S. M. Butler, M. Hountondji, S. N. Berry, J. Tan, L. Macia, K. A. Jolliffe, *Org. Biomol. Chem.* **2023**, *21*, 8548.

1,8-disulfonamide-carbazole platform

A different family of carbazole receptors is based on the 1,8-disulfonamide-carbazole scaffold **II**, featuring the heterocyclic core functionalized with sulfonamide moieties in positions 1 and 8 (Figure 14). The synthetic protocol generally involves the introduction of *tert*-butyl groups at positions 3 and 6 of carbazole, followed by sulfonation at positions 1 and 8. The reaction with PCl_5 provides the 1,8-disulfonylchloride precursor, which furnishes 1,8-disulfonamide-carbazole-based receptors upon reaction with the desired amines.[47] One important example of receptors based on this scaffold was developed by Alcazar and co-workers.[47]As shown in Figure 14, receptor **68** displays three NH donor sites, two from the sulfonamide moiety and one from the carbazole skeleton. Receptor **68** can bind halides with high affinity, especially chloride, which is bound with an association constant of 7.9×10^6 M^{-1} in $CDCl_3$. This anion tends to form weak supramolecular interactions and, in general, is challenging to selectively bind in the presence of other anions in solution. Despite these characteristics, chloride plays a crucial role in biological systems because it is the only inorganic anion involved in transmembrane gradients in cells.[48] As a comparison with amide, urea or thiourea receptors **1**, **2** (Figure 2) and **30** (Figure 8), the substantial difference with 1,8-disulfonamide-carbazole is that the NH sites, beyond the carbazole-NH ones, are not directly linked to the carbazole backbone but to the SO_2 moieties. In 1,8-disulfonamide-carbazole receptors, sulfonamide-NH sites are not fixed in a rigid position; hence they exhibit greater mobility and adaptability toward anions. As an example, receptor **2** binds chloride asymmetrically when this anion is positioned in the carbazole cleft; NH_{amid_e}-Cl^- bond lengths are about 2.94 Å and 2.60 Å in Et_2O, and the strongest interaction occurs with the NH of the carbazole.[13] On the other hand, crystal structures of **68** reveal the existence of two symmetrical H-bonds between sulfonamide-NHs and chloride. The more flexible sulfonamide NH groups can establish a closer interaction with the anion, while the carbazole NH seems too distant to be involved in binding.[47]

This aspect likely contributes to the higher affinity of **65** towards chloride in DMSO, combined with:

- the presence of *tert*-butyl substituents on the carbazole scaffold, which help the receptor adopt a favorable conformation;

---

[47] Á. L. F. de Arriba, M. G. Turiel, L. Simón, F. Sanz, J. F. Boyero, F. M. Muñiz, J. R. Morán, V. Alcázar, *Org. Biomol. Chem.* **2011**, *9*, 8321

[48] K. Dabrowa, F. Ulatowski, D. Lichosyt, J. Jurczak, *Org. Biomol. Chem.* **2017**, *15*, 5927

- the presence of strong electron-withdrawing groups like 3,5-bis(trifluoromethyl) groups.[49]

A comparison between urea, thiourea and sulfonamide-based receptors in terms of binding affinity can be performed considering the affinity of **30**, **32** and **68** toward chloride in DMSO. Each receptor bears 3,5-bis(trifluoromethyl) substituents on the aryl appendages, and the affinity increases in the order: thiourea-**32** < sulfonamide-**68** < urea-**30** (see Table 2 and Table 4).

More recently, a series of carbazole sulfonamide-based macrocycles were prepared by Bao and colleagues.[50] Compounds **69** and **70** are constituted by the 1,8-disulfonamide-carbazole platform and a 1,3-xylyl or 2,6-lutidinyl linker (Figure 14). High affinity is shown toward different anions. In particular, **69** displays strong and selective binding toward fluoride, with association constants up to 5×10^4 M^{-1} in acetonitrile. Nevertheless, the affinity is dramatically lower in polar solvents; e.g., in DMSO it shows a $K_A = 147$ M^{-1}. This behavior can be ascribed to strong interaction of the polar solvent with both the guest and the host binding site.

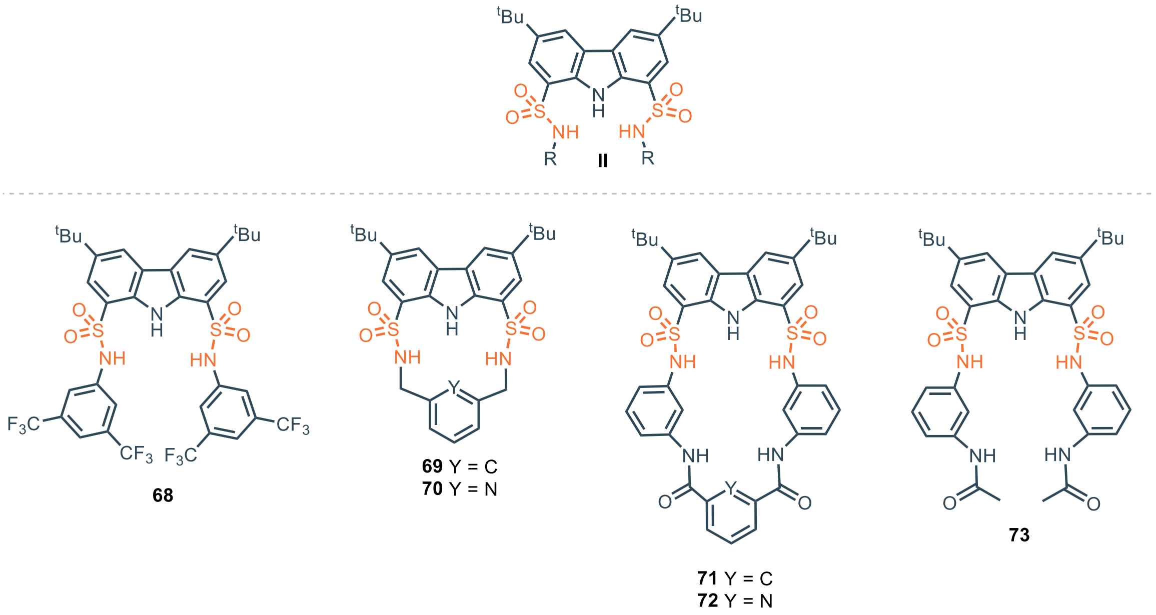

Figure 14 1,8-disulfonamide-carbazole as acyclic and cyclic anion binding receptors.

To overcome this issue, receptors **71**–**73** were designed with additional NH donor groups in the structure to maximize affinity toward anions in strongly polar media.[51] Receptors **71** and **72** are among the first examples of carbazole bis-sulfonamide-bis-amide macrocycles developed for anion recognition, and they are particularly sensitive toward F^-, CH_3COO^-, $PhCOO^-$ and $H_2PO_4^-$.

---

[49] K. M. Lippert, K. Hof, D. Gerbig, D. Ley, H. Hausmann, S. Guenther, P. R. Schreiner, *Eur. J. Org. Chem.* **2012**, *2012*, 5919

[50] N. Luo, J. Li, T. Sun, S. Wan, P. Li, N. Wu, Y. Yan, X. Bao, *RSC Adv.* **2021**, *11*, 10203

[51] N. Luo, J. Li, L. Yuan, N. Wu, X. Bao, *Tetrahedron* **2022**, *115*, 132795

Macrocycles **71** and **72** were compared with the acyclic analogue **73** to evaluate the macrocyclic effect. As expected, the affinity toward anions drastically drops in receptor **73**. Nevertheless, **71** and **72** showed a unique behavior toward chloride, highlighted by a pronounced downfield shift of amide NH groups, while no changes are detected for carbazole and sulfonamide NH moieties by ^{1}H-NMR analysis. On the other hand, chemical shift changes of carbazole and sulfonamide protons occur when CH_3COO^-, $PhCOO^-$, F^- and $H_2PO_4^-$ are present. This observation suggests that receptor **71** has two distinct binding sites: one pocket constituted by carbazole and sulfonamide NHs that binds CH_3COO^-, $PhCOO^-$, F^- and $H_2PO_4^-$ (Figure 15a); the other one constituted by two amide NH sites and three directed aromatic CH protons, which can accommodate Cl^- (Figure 15b). Regarding **72**, due to the replacement of a hydrogen donor site in the amide pocket with a nitrogen atom in the aromatic ring, chloride interacts much more with the carbazole/sulfonamide pocket (Figure 15d). In the case of F^-, CH_3COO^-, $PhCOO^-$ and $H_2PO_4^-$, the proposed model also shows involvement of aromatic CH interactions (Figure 15c). In 2023, Bao and colleagues presented a novel carbazole-1,8-disulfonamide cryptand-like receptor for anion recognition.[52] Cryptand **74** comprises three 1,8-disulfonamide-carbazole units held together by two tris(2-aminoethyl)amine (TREN) moieties as linkers. Compound **74** is synthesized in a straightforward manner through a one-step [2+3] condensation (Figure 16). The binding affinity was measured toward different monovalent anions, including AcO^-, $H_2PO_4^-$, F^- and Cl^-. Cryptand **74** exhibits strong binding principally toward AcO^-, F^- and $H_2PO_4^-$ even in polar solvents like DMSO, with association constants up to 8×10^3 M^{-1} for the 1:1 complex. The limited influence of solvent polarity on the association constants is a consequence of the reduced solvation shells in the binding cavity of these hosts. Specifically, **74** shows a clear preference for AcO^- with a KA of 5.1×10^4 M^{-1} in a less polar solvent like CH_3CN, assuming that all the available NHs bind the acetate anion both in DMSO and CH_3CN. The association constants for compounds **68**–**74** are summarized in Table 4.

---

[52] J. Li, L. Yuan, Q. Yang, N. Zhang, T. Sun, X. Bao, *J. Org. Chem.* **2023**, *88*, 14753

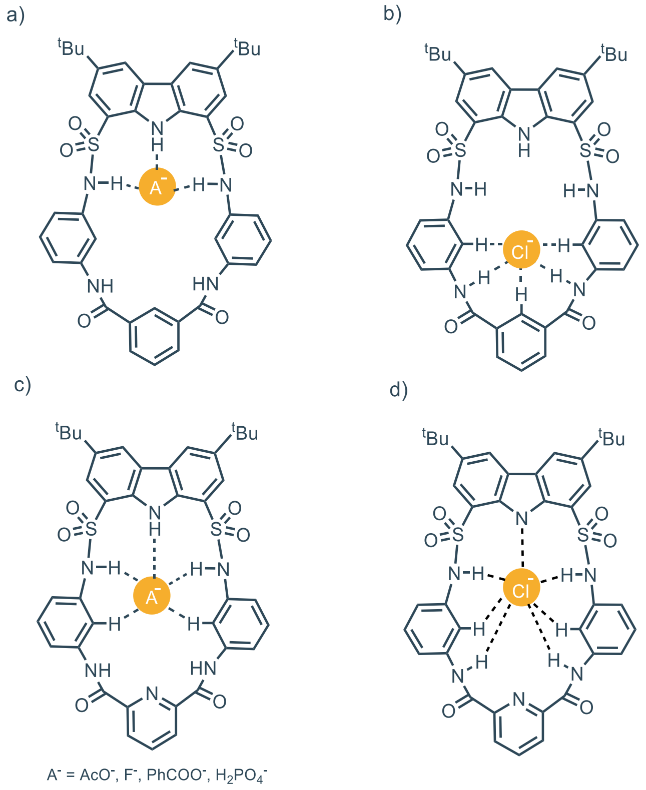

Figure 15 (a) receptor **71** involved in the binding of different anion A⁻; (b) receptor **71** involved in the binding of chloride; (c) receptor **72** involved in the binding of different anion A⁻; (d) receptor **72** involved in the binding of chloride. Adapted from ref [51]

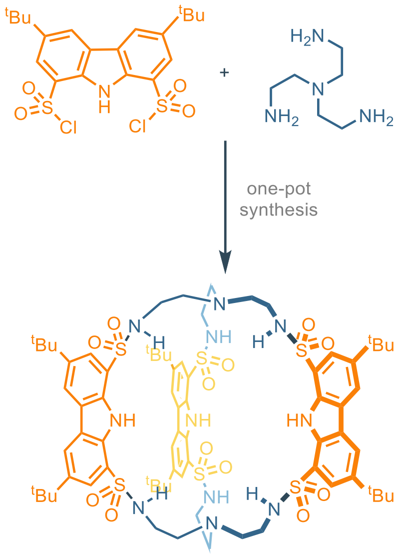

74

Figure 16. Three unit-carbazole cryptand developed by Bao et al. Adapted from ref [52]

Table 4. Association constants (M^{-1}) for compounds **68-74** towards different guests. Unless specified, the titrations are performed *via* NMR.

Receptor	$K_A(AcO^-)$	$K_A(BzO^-)$	K_A (Cl^-)	K_A (F^-)	$K_A(Br^-)$	K_A ($H_2PO_4^-$)
68 [a]	[b]	-	7.9×10^6 [c] 210 (DMSO-d_6)	2.2×10^4	1.1×10^6 [d] 25 (DMSO-d_6)	b
69 [e]	279	1.01×10^3	91	5.09×10^4 [f]	24	4.92×10^3
70 [e]	940	2.01×10^3	355	1.29×10^4	<10	2.43×10^3
71 [g]	7.30×10^3	6.80×10^3	30	1.53×10^4 [f]	n.d.	611
72 [g]	1.00×10^4	6.80×10^3	165	1.09×10^4 [f]	n.d.	688
73 [g]	2.70×10^3	2.40×10^3	17	1.08×10^4 [f]	n.d.	218
74 [e]	5.10×10^4	-	5.90×10^3	1.61×10^4	2.90×10^3	2.75×10^4

[a] In $CDCl_3$. [b] Data could not be fitted to a 1 : 1 or 1 : 2 binding stoichiometry. [c] Measured *via* competitive fluorescence titration with bromide. [d] Measured *via* fluorescence. [e] In CD_3CN. [f] Determined *via* UV-vis titration experiments. [g] In DMSO-d_6.

Indolo[2,3-α]carbazole platform

Starting from the mid-2000s, indolocarbazole has been used as a platform for anion recognition, displaying strong binding affinity and selectivity.[53] Indolocarbazoles are a family of different isomers characterized by a pentacyclic ring system of fused indole and carbazole moieties. In particular, the indolo[2,3-α]carbazole isomer is a suitable platform for the development of synthetic anion receptors, even though the synthesis of 1,10-substituted indolocarbazoles is still limited. The double Fischer indole synthesis from pre-functionalized precursors represents the general synthetic route to access the indolo[2,3-α]carbazole scaffold; however, this strategy fails when strong electron-withdrawing groups are introduced. For this reason, unlike carbazoles, 1,10-diamino-indolocarbazoles have never been reported, due to the difficulty in accessing the corresponding 1,10-dinitro-indolocarbazole precursor. The skeleton of indolo[2,3-α]carbazole features characteristics analogous to carbazole, such as high preorganization and rigidity. Nevertheless, the indolocarbazole scaffold provides an additional well-oriented NH group that acts as a hydrogen bond donor site for the recognition of anions (Figure 17).

---

[53] a) K.-J. Chang, D. Moon, M. S. Lah, K.-S. Jeong, *Angew. Chem., Int. Ed.* **2005**, *44*, 7926; b) J. Ju, M. Park, J. Suk, M. S. Lah, K.-S. Jeong, *Chem. Commun.* **2008**, 3546; c) P. A. Gale, *Chem. Commun.* **2008**, *2008*, 4525

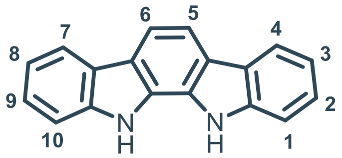

Figure 17. Numbered scaffold of indolo[2,3-α]carbazole.

The Beer group made a pioneering contribution in this field using indolo[2,3-α]carbazole as an axle in templated rotaxane formation in the presence of different anions (Figure 18). Rotaxane **76** is obtained between indolocarbazole and compound **75** in the presence of SO_4^{2-} anion in CH_3CN.[54] Different relevant works were conducted by the same group in this regard during the following years.[55]

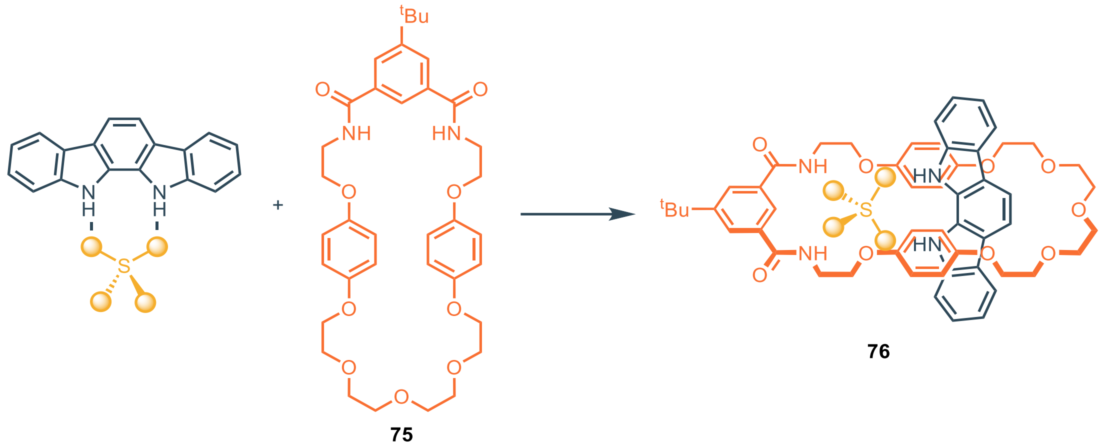

Figure 18. Sulfate anion templating of rotaxane **76** in the presence of indolo[2,3-α]carbazole. Adapted from ref [54]

Despite the possibility of isolating some indolocarbazole isomers from natural sources, the double Fischer indolisation is generally used as the synthetic route for their preparation.[56] The arch-shaped cavity makes indolo[2,3-α]carbazole optimal for binding "Y-shaped" anions like carboxylates. Indeed, unsubstituted indolo[2,3-α]carbazole (Figure 17) binds benzoate with an association constant of $K_A = 1 \times 10^5\ M^{-1}$ in acetonitrile. In this context, Molina and co-workers developed different 1,10-disubstituted indolo[2,3-α]carbazoles that are sensitive to "Y-shaped" anions.[56] In detail, Figure 19 shows receptor **77**, which binds strongly to benzoate with an association constant higher than $K_A = 10^7\ M^{-1}$ via NMR in acetonitrile (Table 5), thanks to the presence of two additional OH donor sites.

---

[54] M. J. Chmielewski, L. Zhao, A. Brown, D. Curiel, M. R. Sambrook, A. L. Thompson, S. M. Santos, V. Felix, J. J. Davis, P. D. Beer, *Chem. Commun.* **2008**, *2008*, 3154

[55] a) L. Zhao, J. J. Davis, K. M. Mullen, M. J. Chmielewski, R. M. J. Jacobs, A. Brown, P. D. Beer, *Langmuir* **2009**, *25*, 2935; b) A. Brown, K. M. Mullen, J. Ryu, M. J. Chmielewski, S. M. Santos, V. Felix, A. L. Thompson, J. E. Warren, S. I. Pascu, P. D. Beer, *J. Am. Chem. Soc.* **2009**, *131*, 4937; A. Brown, T. Lang, K. M. Mullen, P. D. Beer, *Org. Biomol. Chem.* **2017**, *15*, 4587

[56] G. Sánchez, D. Curiel, A. Tárraga, P. Molina, *Sensors* **2014**, *14*, 14038

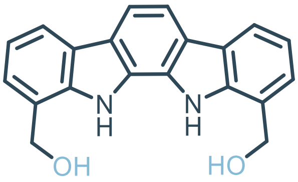

77

Figure 19. Di(hydroxymethyl)indolocarbazole synthetized by Molina and co-workers.

A comprehensive and extended review about the origin, synthesis, properties and applications of indolocarbazole has been recently published;[57] hence, herein only recent developments in this field will be discussed. The indolo[2,3-α]carbazole scaffold shows significant impact as a building block for the rational construction of synthetic helical foldamers. The helical conformation of proteins and enzymes provides the formation of a cavity that offers hydrogen bonding sites for the interaction and accommodation of guests. In this regard, it is a great challenge to design and construct synthetic foldamers that can mimic the behavior of biological receptors.

In 2008, Jeong and colleagues presented synthetic water-soluble foldamers based on indolo[2,3-α]carbazole units tied together by ethynyl linkers. These foldamers can bind halides thanks to the formation, upon folding, of tubular cavities.[58] During the following years, Jeong developed foldamers with related structures by inserting a heteroaromatic spacer that acts as a fulcrum and various appendages.[59] The authors demonstrated that it is possible to tune the binding affinity of synthetic foldamers by intra-receptor π-stacking interactions provided by aryl appendages.[60]

These foldamers consist of two indolo[2,3-α]carbazole units equipped with different appendages. The two units are tied together by ethynyl linkers separated by a pyridine, which acts as a fulcrum (Figure 20a). Receptors **78** and **79**, without any aryl appendages, exhibit association constants three orders of magnitude lower than receptors equipped with aryl substituents ($K_{A\ 78} = 32\ M^{-1}$, $K_{A\ 79} = 36\ M^{-1}$, $K_{A\ 82} = 1.17 \times 10^4\ M^{-1}$) in DMSO. The helical folding allows face-to-face π-stacking interactions between the aryl appendages and the indolocarbazole backbone. These intra-receptor interactions do not directly involve the guest but increase binding affinity by stabilizing the overall folded structure. In the case of electron-withdrawing groups on the aryl appendages, receptors **81** and **82** adopt a completely folded conformation, leading to 1:1 complexes with chloride anions (Figure 20b). On the

---

[57] T. Janosik, A. Rannug, U. Rannug, N. Wahlström, J. Slätt, J. Bergman, *Chem. Rev.* **2018**, *118*, 9058

[58] J. Suk, K.-S. Jeong, *J. Am. Chem. Soc.* **2008**, *130*, 11868

[59] a) J. Kim, H. Juwarker, X. Liu, M. S. Lah, K.-S. Jeong, *Chem. Commun.* **2010**, *46*, 764; b) J. Suk, V. R. Naidu, X. Liu, M. S. Lah, K.-S. Jeong, *J. Am. Chem. Soc.* **2011**, *133*, 13938

[60] S. B. Seo, S. Lee, H.-G. Jeon, K.-S. Jeong, *Angew. Chem., Int. Ed.* **2020**, *59*, 10441

other hand, electron-donating groups on the aryl appendages lead to a completely different scenario. Specifically, receptors **83** and **84** adopt extended conformations, and X-ray structures show 1:2 complexes, i.e., one chloride anion bound per indolocarbazole unit (Figure 20c). This is consistent with intra-receptor π-stacking interactions, which are favored by electron-withdrawing substituents due to attractive electrostatic effects. The larger trigonal planar nitrate anion maximizes hydrogen bonding interactions in the helical conformation, forming 1:1 complexes with foldamers regardless of the nature of the aryl substituent (Figure 20d). The same group recently developed related foldamers featuring a 1,8-naphthyridine moiety as the fulcrum between indolocarbazole units. This structural modification creates a wider cavity through helical folding, allowing for the binding of carbohydrate derivatives, as described in Section 3. The association constants for compounds **77–84** are summarized in Table 5.

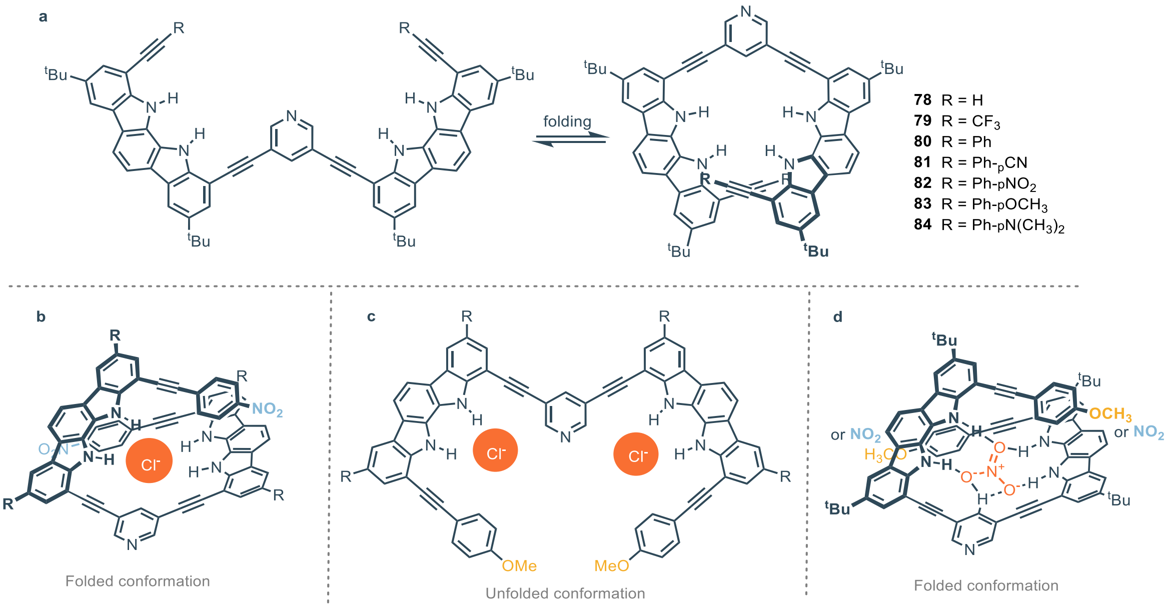

Figure 20. Foldamers based on indolo[2,3-α]carbazolo (a) and related conformations based on electron-withdrawing or electron-donating aryl-appendages in the presence of chloride or nitrate anions (b, c, d). Adapted from ref [58]

Table 5. Association constants (M^{-1}) for compounds **77-84.** The titrations are performed *via* NMR in DMSO-d_6 + 0.5% H_2O towards chloride and in DMSO-d_6 + 10% CD_2Cl_2 towards nitrate.

Receptor	K_A (Cl^-)	K_A(NO_3^-)	K_A(BzO^-)
77	-	-	$>10^7$ [a]
78	32	26	-
79	36	30	-
80	216	141	-
81	5.84×10^3	1.30×10^4	-
82	1.17×10^4	2.30×10^4	-
83	$K_1 = 68$, $K_2 = 16$	78	-
84	$K_1 = 31$, $K_2 = 9$	31	-

[a] in acetonitrile *via* fluorescence analysis.

Miscellaneous carbazole platforms

This section will address the binding properties and potential applications of miscellaneous carbazole-based receptors. Notably, most receptors depicted in Figure 21 lack similarities in functional group composition, unlike the receptors discussed in the previous paragraphs, which were grouped based on their common characteristics related to a specific functional group. Receptors **85**, **86**, **87**, and **88** have been extensively studied by Menéndez and coworkers due to their enhanced fluorescence properties compared to carbazole.[61] These receptors have been explored as potential fluorescent sensors in acetone for various anions, including F^-, Cl^-, Br^-, CN^-, AcO^-, and OH^-. Among them, receptor **86** exhibited the highest sensitivity with notable selectivity toward the halides F^- ($K_A = 9.64 \times 10^4$ M^{-1}) and Cl^- ($K_A = 1.55 \times 10^5$ M^{-1}). This sensitivity can be attributed to the spherical geometry of these anions. In fact, F^- and Cl^- exhibit a higher efficiency in displacing solvent molecules. This displacement facilitates direct interaction of the anions with the receptor, leading to a significant increase in fluorescence intensity. This can also be attributed to the fact that F^- and Cl^- induce a more rigid conformation in the carbazole structure, enhancing its fluorescence properties.[61]

---

[61] V. González-Ruiz, Á. Cores, M. M. Caja, V. Sridharan, M. Villacampa, M. A. Martín, A. I. Olives, J. C. Menéndez, *Biosensors* **2022**, *12*, 175

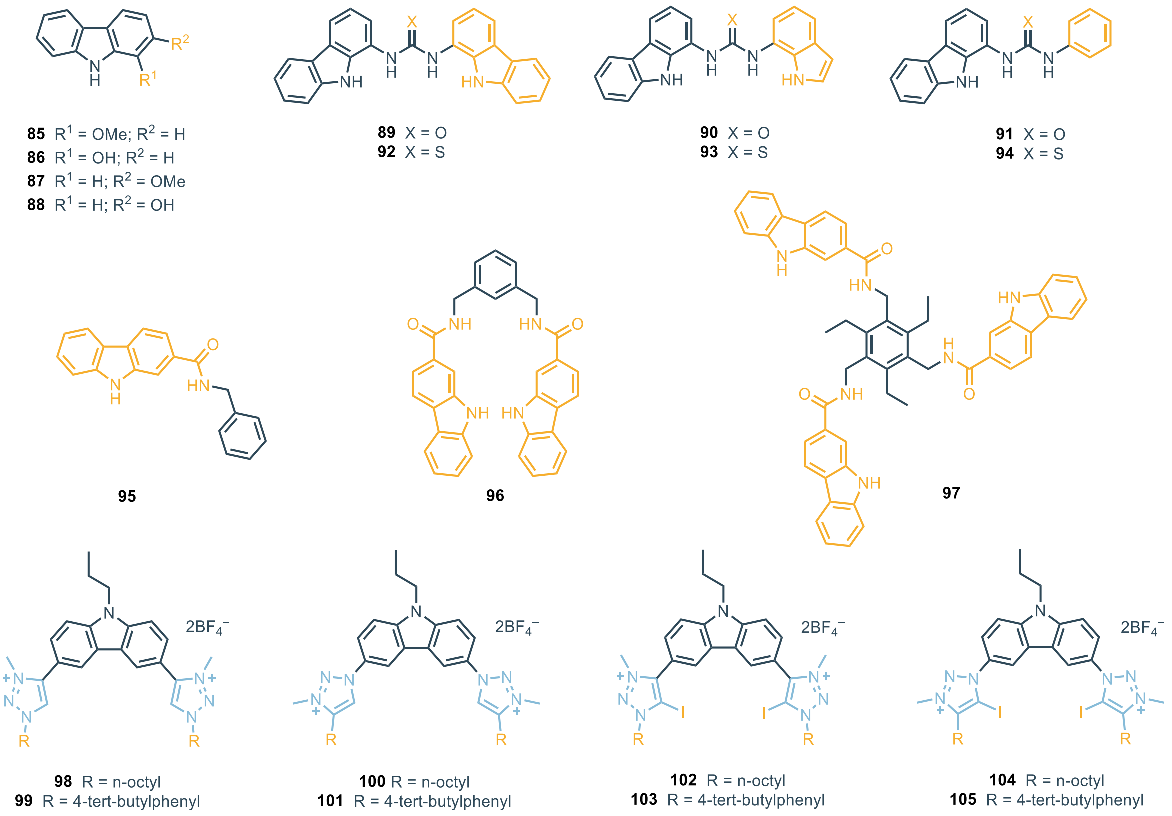

Figure 21. Miscellaneous carbazole-based receptors.

Urea-based receptors **89–91** exhibit a preferential binding affinity for oxoanions in DMSO-d_6 + 0.5% H_2O. Notably, all three receptors demonstrate significant affinity towards acetate and bicarbonate with $K_A > 10^4$ M^{-1}.[62] The corresponding thiourea-based receptors **92–94** unexpectedly display a reduced binding affinity (e.g., $K_A > 10^3$ M^{-1} for acetate), despite the increased acidity of the thiourea group relative to the urea group. This behavior could be attributed to conformational effects, as the larger size of sulfur compared to oxygen may induce a "twisted" geometry. Table 6 shows the association constants for receptors **89–94**.

---

[62] J. R. Hiscock, P. A. Gale, C. Caltagirone, M. B. Hursthouse, M. E. Light, *Supramol. Chem.* **2010**, *22*, 647

Table 6: Association constants (M^{-1}) for receptors **89-94**. The titrations are performed *via* NMR in DMSO-d_6 + 0.5% H_2O.

Receptor	K_A (CH_3COO^-)	K_A ($PhCOO^-$)	K_A ($H_2PO_4^-$)	K_A (Cl^-)	K_A(HCO_3^-)
89	$>10^4$	5.67×10^3	n.d.	102	$>10^4$
90	$>10^4$	5.88×10^3	n.d.	139	$>10^4$
91	$>10^4$	3.42×10^3	6.14×10^3	85	$>10^4$
92	223	658	687	15	n.d.
93	1.80×10^3	675	1.34×10^3	17	n.d.
94	1.78×10^3	870	n.d.	23	n.d.

n.d. = the association constant could not be determined

Receptors **95**, **96**, and **97** were synthesized and studied as ligands for a series of anions. Association constant studies were conducted for acetate, $H_2PO_4^-$ and $HP_2O_7^{3-}$.[63] It was observed that, in general, receptor 95 exhibits weaker binding to anions in DMSO-d_6 compared to **96** and **97**. Indeed, receptor **96** demonstrates a notable association constant toward $HP_2O_7^{3-}$ (KA > 10^3 M^{-1}), whereas receptor **97** displays such a high affinity for $HP_2O_7^{3-}$ that its association constant could not be determined in DMSO-d_6. Only the addition of 5% water to DMSO-d_6, creating a more competitive environment for anion binding, allowed the calculation of the association constant for receptor 97 with $HP_2O_7^{3-}$ (K_A = 145 M^{-1}). Table 7 shows the association constants for receptors **95–97**.

Table 7: Association constants (M^{-1}) for receptors **95-97**. The titrations are performed *via* NMR in DMSO-d_6.[104]

Receptor	K_A (CH_3COO^-)	K_A($H_2PO_4^-$)	K_A($P_2O_74^-$)
95	55	14	n.d.
96	65	20	$>10^4$
97	165	440	n.d.

n.d. = The association constant could not be determined

Carbazole-based cationic receptors featuring N-alkylated and disubstituted triazolium groups (**98–105**) have been investigated for their anion-binding properties in CD_3CN.[64] Binding affinities were evaluated toward halide anions and selected oxoanions, such as nitrate and sulfate. Generally, no significant difference in binding efficiency was observed between receptors with a carbazole–

---

[63] D. Curiel, G. Sánchez, C. R. de Arellano, A. Tárraga, P. Molina, *Org. Biomol. Chem.* **2012**, *10*, 1896

[64] B. R. Mullaney, B. E. Partridge, P. D. Beer, *Chem. Eur. J.* **2015**, *21*, 1660

triazolium linkage of the C–C type (**98**, **99**, **102**, **103**) and those with a C–N linkage (**100**, **101**, **104**, **105**). However, differences in anion-binding behavior became more pronounced when comparing receptors with alkyl versus aromatic pendants. Receptors with aromatic substituents (**99**, **101**, **103**, **105**) exhibited stronger anion-binding affinities than those with alkyl substituents (**98**, **100**, **102**, **104**). Substantial differences in halide binding were observed between receptors functionalized with iodine (**102**, **103**, **104**, **105**) and those without iodine functionalization (**98**, **99**, **100**, **101**). Iodine-functionalized receptors, also referred to as XB receptors, demonstrated enhanced halide ion interactions through halogen bonding, in contrast to the HB receptors, which rely solely on hydrogen bonding. Regarding sulfate binding, receptors **99** and **101** (bearing aromatic substituents and lacking iodine functionalization) exhibited the strongest affinities, even in competitive solvent mixtures such as DMSO-d_6 with 10% D_2O. This behavior is primarily driven by the Coulombic attraction between the dicationic receptor and the dianionic guest. In this context, to exploit the efficiency of XB-type receptors toward chloride and bromide, coupled with an isophthalamide-based macrocycle, rotaxane **108** was synthesized. The synthesis was achieved via Grubbs olefin metathesis of **107** in combination with the XB bis-iodotriazolium carbazole axle component **106** (Figure 22). Following purification, the rotaxane was subjected to anion exchange with aqueous NH_4PF_6, affording **108**·$2PF_6$. The anion-binding properties of rotaxane **108**·$2PF_6$ were examined using ^{1}H-NMR in a 45:45:10 mixture of $CDCl_3/CD_3OD/D_2O$. The results demonstrated a pronounced affinity for halides, in particular for bromide ions, over oxoanions. Notably, this behavior differs from that of simpler aryl-based XB receptors (**103** and **105**), which exhibit a higher binding affinity for chloride ions. Table 8 shows the association constants for receptors **98**–**105**.

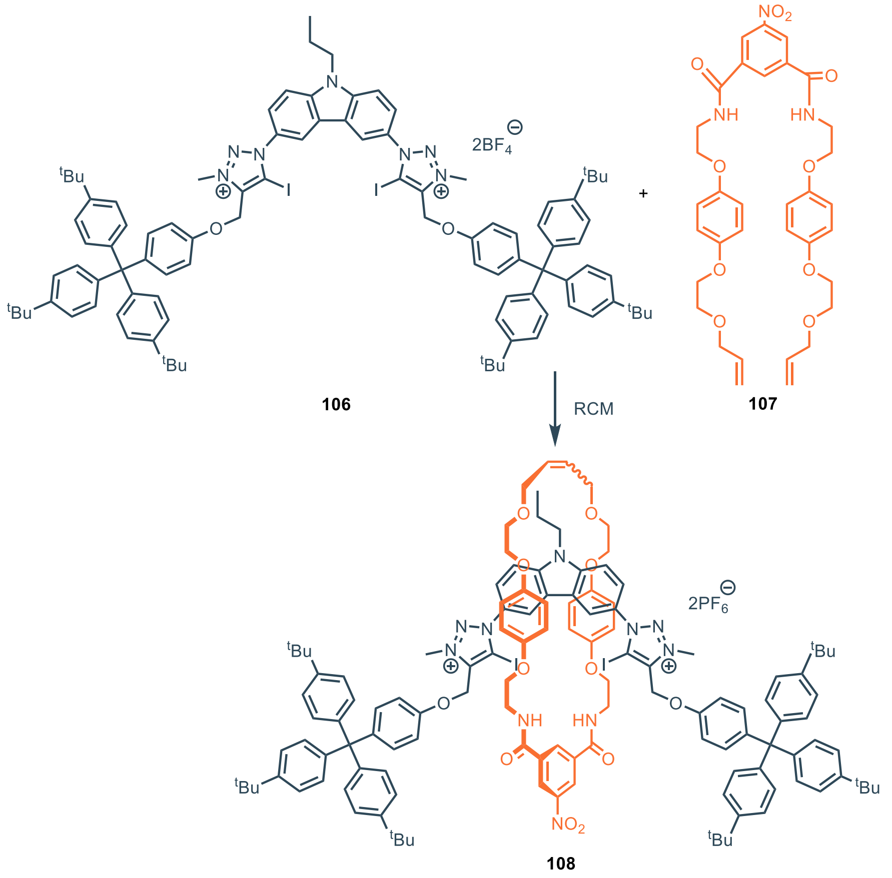

Figure 22: Synthesis of rotaxane **108**·2PF$_6$ *via* RCM.

Table 8: Association constants (M^{-1}) for receptors **98-105**. The titrations are performed *via* NMR in DMSO-d$_6$.

Receptor	K_A (Cl$^-$)	K_A(Br$^-$)	K_A(I$^-$)	K_A (NO$_3^-$)	K_A (SO$_4^{-2}$)[b]
98	141	200	161	121	341
99	430	337	214	295	1.54×10^3
100	214	274	233	244	282
101	240	287	310	213	1.03×10^3
102	217[a]	567	99	-	348
103	332[a]	893	254	-	493
104	341[a]	367	99	-	363
105	303[a]	900	222	-	652

[a] Titrations conducted in 10% D$_2$O/DMSO-d$_6$. [b]. Titration conducted in 10% D$_2$O/DMSO-d$_6$. n.d. = the association constant could not be determined

In summary, this Chapter highlights the most relevant advances in carbazole-based receptors as versatile, modular and efficient hosts for the recognition of anions. The structural tunability of the carbazole allows the introduction of several moieties, such as (thio)ureas, imines and sulfonamides, which could further assist the binding process *via* synergistic noncovalent interactions (*e.g.* hydrogen bonding, hydrophobic interactions). Further expansion of the rigid and planar skeleton leads to indolocarbazoles, which have been used as building blocks for the preparation of synthetic foldamers capable of binding anions and carbohydrates. Observing the binding properties, carbazole-based receptors typically show greater affinity for polyatomic oxoanions, although exceptions exist (*i.e.* 1,8-disulfonamide-carbazole derivatives). Modifying the carbazole scaffold with different frameworks may help create receptors with varied cavity sizes, potentially enhancing their ability to bind smaller anions, such as chloride, which typically show lower binding affinities. Moreover, it would be interesting to more widely explore the introduction of non-covalent interactions other than hydrogen-bonding moieties, to improve the selectivity towards specific guest, in particular in the case of organic anions. While the planarity of carbazole provides an appealing framework for constructing synthetic receptors, it also presents challenges, mostly the generally low solubility of these compounds. This aspect limits their applications in different fields as well as the study of their properties. Although some strategies have been employed to mitigate this issue (*e.g.* introduction of alkyl chains or ^{t}butyl groups), more effort is desirable to face this complication. Additionally, the synthesis of these platforms remains challenging. Obtaining 1,8-diaminocarbazole requires harsh nitration conditions, and functionalization at positions 3 and 6 remains limited, despite its role in tuning key properties. Additionally, the synthesis of 1,10-substituted indolocarbazoles is hindered by the failure of the double Fischer indole route with strong electron-withdrawing groups, making 1,10-diamino-indolocarbazoles inaccessible due to the difficulty of preparing the 1,10-dinitro precursor. Furthermore, while carbazole-based receptors have been extensively studied as sensors and transmembrane transporters, their application as supramolecular catalysts remain largely unexplored.

Aim of the project

Hydrogen bond donor (HBD) catalysis has emerged over the past two decades as a powerful strategy for promoting chemical transformations through favorable noncovalent secondary interactions between the catalyst and substrate(s). Typically, these interactions involve partially acidic hydrogen atoms from bi- or multidentate HBDs engaging with charged or polarized substrates. Additional noncovalent interactions, such as π–π stacking, can also play a synergistic role in substrate binding, further enhancing catalytic performance. Certain HBDs are particularly effective at binding the anionic counterparts of ionic (or ionizable) substrates, thereby stabilizing them and accelerating reaction progress—a strategy broadly referred to as anion-binding catalysis (Figure 23a, see *Chapter 1*).

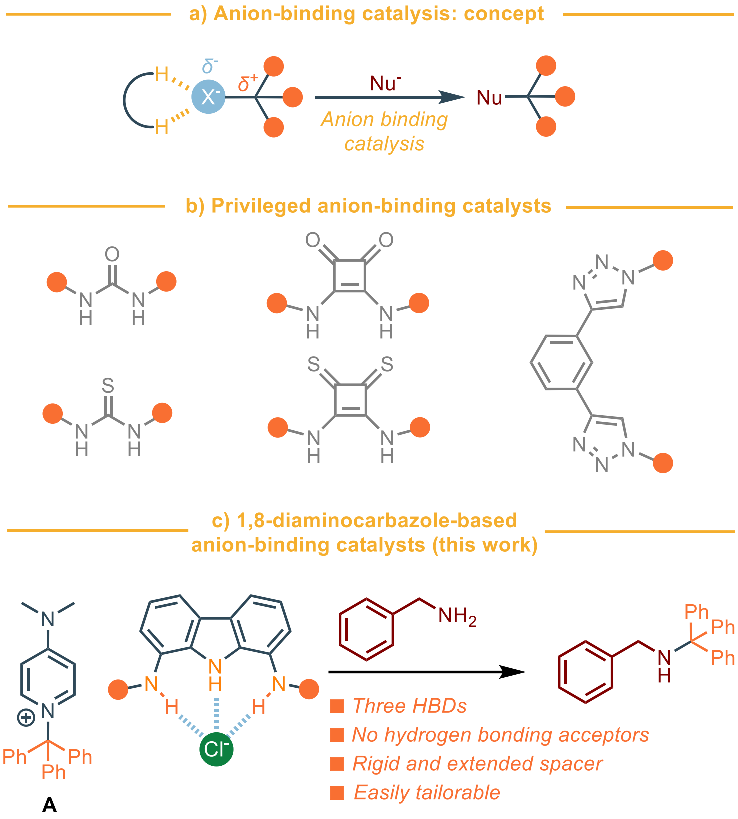

Figure 23. a) Concept of anion-binding catalysis; b) Most common HBD catalysts; c) New family of 1,8-diaminocarbazole-based anion-binding catalysts.

This approach has attracted considerable attention, with various HBD catalysts reported to date, including (thio)ureas, squaramides, and both neutral and charged triazole-based systems (Figure 23b). Despite the success of these scaffolds, some challenges related to their structural features still need to be addressed:

- Many of these catalysts also contain hydrogen bond acceptor sites, which can lead to self-association and the formation of off-cycle intermediates that diminish catalytic efficiency;
- (thio)ureas and squaramides typically rely on only two HBD units for binding, whereas incorporating an additional acidic NH group within the core structure could enhance binding capabilities;
- the (thio)urea and squaramide frameworks act as relatively small linkers (with NH–NH distances ranging from ~2.2 to 3.4 Å), whereas a more rigid and spatially extended building block could enable simultaneous interactions with multiple reaction partners, potentially improving selectivity and activity.

Following these features, we identified 1,8-diaminocarbazole as an extended and rigid aromatic platform which features 3 HBDs with no hydrogen bond acceptor sites. Moreover, the two NH_2 groups in 1,8 positions can be easily tailored, making 1,8-diaminocarbazole an ideal and highly tunable scaffold to be employed in molecular recognition studies, as demonstrated by its widespread use in the development of host-guest system for the recognition of anions, carbohydrates, xanthines and amino acids. Nevertheless, its application in HBD catalysis has not been reported by far. Herein, we report the rational development of a new family of 1,8-diaminocarbazole-based anion-binding molecules (Figure 23c) which were employed as anion-binding catalysts in the model N-tritylation reaction of benzylamine, which occurs via chloride-binding from the ionic precursor of the trityl cation **A**.

Results and discussion

Design of the family of catalysts

As illustrated in Figure 24, the core structure of the receptors relies on:

- the 1,8-diaminocarbazole scaffold, which provides three N–H donor sites;
- two 1,4-disubstituted-1,2,3-triazole units, well-established anion-binding motifs designed to further support the binding process and, consequently, the catalytic activity;
- two terminal chains incorporating both aromatic and aliphatic fragments.

The retrosynthetic analysis features a key disconnection between the carbazole core and the triazole unit. A major advantage of the developed synthetic route for this family of carbazole–triazole anion receptors is its convergent nature. Specifically, the target receptors **106a-e** can be obtained by condensation of 1,8-diaminocarbazole **I** with triazole-based aldehydes **II**, which are readily accessible via Copper(I)-catalyzed Azide-Alkyne Cycloaddition (CuAAC).

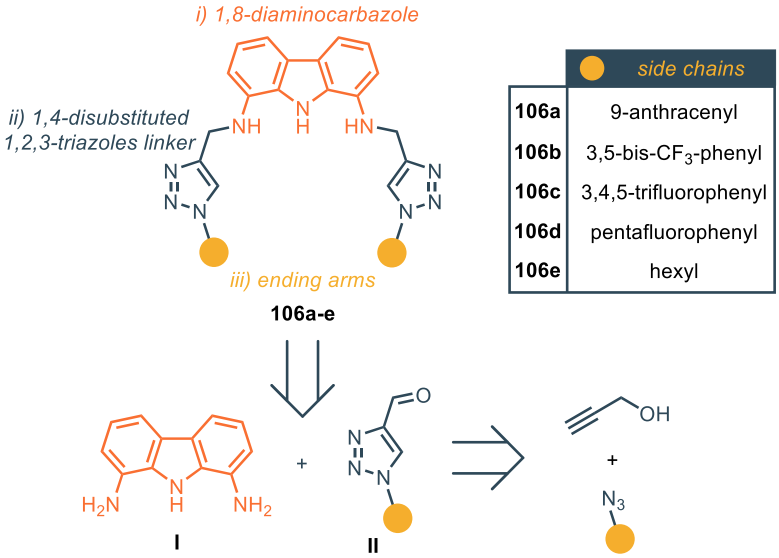

	● side chains
106a	9-anthracenyl
106b	3,5-bis-CF_3-phenyl
106c	3,4,5-trifluorophenyl
106d	pentafluorophenyl
106e	hexyl

Figure 24. Family of catalysts and disconnection approach

Each of these catalysts, which differ in the nature of the terminal arm, was designed to introduce specific features. The anthracene derivative (**106a**) is expected to display a higher degree of preorganization through intramolecular π–π stacking. Compounds **106b–d** incorporate electron-withdrawing substituents on the terminal arms, which are known to enhance proton acidity and thereby strengthen anion-binding ability. In contrast, the aliphatic derivative (**106e**) was designed to improve catalyst solubility and potentially increase the strength of the interaction with the anion.

Synthesis of aldehydes 110a-e

As depicted in Scheme 1, the synthesis of azides **108a–e** was achieved through three distinct strategies. For compound **110a**, bearing a 9-anthracenyl substituent, a Cu-mediated Chan–Lam-type coupling starting from 9-anthracenyl boronic acid (**107a**) afforded the corresponding azide in quantitative yield using catalytic amounts of $CuSO_4$.[65] In the case of electron-deficient aromatic substrates (**108b–d**), diazotization of the corresponding anilines (**107b-d**)proved to be the most effective route,[66] since aromatic boronic acids bearing electron-withdrawing groups are prone to protodeboronation.[67] For the aliphatic derivative **108e**, nucleophilic substitution of 1-bromohexane (**107e**) with sodium azide successfully delivered the desired product. Subsequent CuAAC reactions between azides **108a–e** and propargyl alcohol furnished the corresponding triazole alcohols **109a–e** in almost quantitative yields.

---

[65] C-Z. Tao, X. Cui, J. Li, A. X. Liu, L. Liu, Q. X. Guo, *Tetrahedron Lett.* **2007**, *48*, 3525–3529

[66] M. Zurro, S. Asmus, S. Beckendorf, C. Muck-Lichtenfeld, O. G. Mancheno, *J. Am. Chem. Soc.* **2014**, *136*, 13999–14002

[67] D. Hall (Ed.), *Boronic Acids: Preparation and Applications in Organic Synthesis, Medicine and Materials*, 2nd ed., Wiley-VCH, Weinheim, 2011, Vols. 1–2, pp. 1–133

Finally, oxidation of these alcohols under Piancatelli's conditions,[68] employing Diacetoxyiodo(benzene) (BIAB) and TEMPO, afforded the corresponding aldehydes **110a–e** in excellent yields.

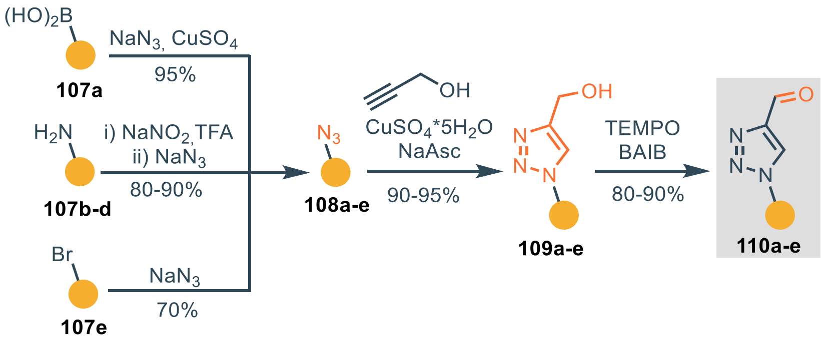

Scheme 1. Synthesis of triazole aldehydes **110a-e**

Synthesis of carbazole-triazole based receptors 106a-e

The last step of the synthetic sequence was carefully optimized for each compound (Scheme 2). For compound **106a** and **106c**, attempts of direct reductive amination resulting in poor yield, with precipitation of the insoluble and unreactive corresponding imines. Direct reduction of the isolated imines with different hydride sources ($NaBH_4$, $NaCNBH_3$, $Na(OAc)_3BH$) in commonly employed standard conditions only led to degradation of the SM. The low solubility of these imines, even in highly competitive environments, is likely the cause for their scarce reactivity and due to the high degree of conjugation of these molecules, together with intramolecular π-stacking. Hence, we hypothesized that the reaction would benefit from the use of an additive which could increase the solubility of the imines preventing these interactions. For instance, we gladly found that the addition of 2 equivalents of fluorobenzene in the reaction mixture dramatically increased the reactivity, leading to the formation of the desired compounds **106a** and **106c** in almost quantitatively yields. On the other hand, for compound **106b**, **106d** and **106e**, every attempt of isolating the corresponding imines resulted in their hydrolysis and recovery of the unaltered starting materials. For this reason, a one-pot reductive amination was developed using milder reductive agents. This protocol proved to be effective, delivering the desired products with satisfactory yields.

---

[68] G. Piancatelli, F. Leonelli, *Org. Synth.* 2**006**, *83*, 18

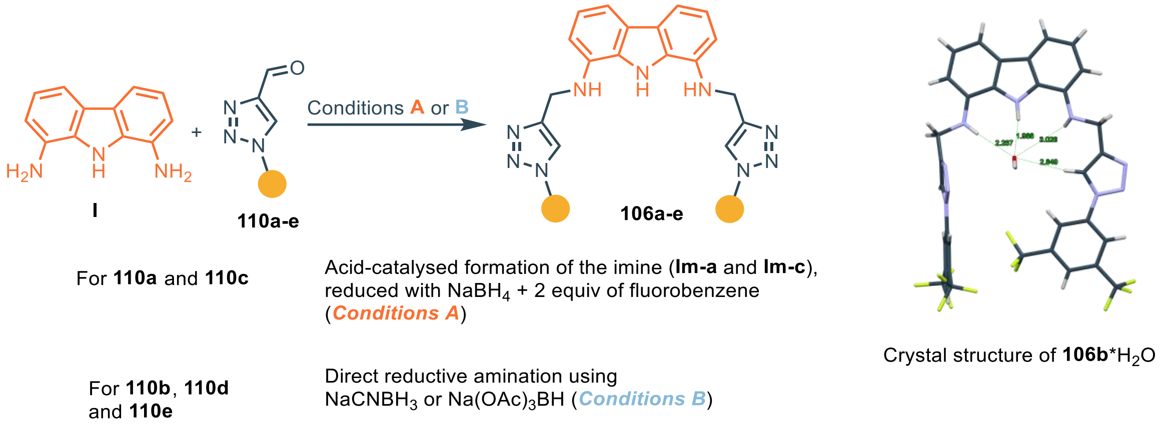

Scheme 2. Synthesis of final compounds **106a-e**

Binding properties of compounds 106a-e: molecular dynamics, fluorescence and NMR titrations

Aiming to use compounds **106a**-e in anion binding catalysis via chloride abstraction, we focused our attention on the characterization of the binding properties of compounds **106a**-e towards Cl^-. In the first place, molecular dynamics calculations were conducted, in collaboration with Prof. Massimiliano Aschi (University of L'Aquila). Through computational calculations, the interaction between each receptor and the chloride anion was evaluated in a model simulating the solvent (DMSO), in order to determine the theoretical association constants (Ka) for the formation of the 1:1 complex.

The calculations provided the following association constant values:

- **106c:** 55 M^{-1}
- **106a:** 24 M^{-1}
- **106b:** 5 M^{-1}
- **106d:** 4 M^{-1}
- **106e:** 4 M^{-1}

A clear affinity trend emerges from this data: **106c** > **106a** > **106b** > **106d** ≈ **106e**

Although the calculated absolute values differ from those that will be determined experimentally, this qualitative trend provides an important predictive basis. The computational results suggest that receptor **106c**, featuring the 3,4,5-trifluorophenyl group, possesses the highest intrinsic affinity for chloride. Conversely, receptors **106d** (pentafluorophenyl) and **106e** (hexyl) show a negligible calculated interaction. This theoretical hierarchy was then used as a reference for the validation and interpretation of the subsequent experimental binding studies.

The characterization of the binding properties of the family of catalysts developed was then experimentally evaluated. In collaboration with Prof. Giansanti (University of L'Aquila) the anion binding properties of **106a**-**e** towards chloride (as tetrabutylammonium salt) have been qualitatively investigated by fluorescence analyses in DMSO. DMSO was selected as the solvent owing to its high solubilizing ability, particularly important for **106a**, which exhibits limited solubility in most common organic solvents. However, it should be noted that DMSO is also a strong hydrogen-bond acceptor and, as such, generally suppresses anion binding when compared to less competitive media. Consequently, the observation of a fluorescence turn-on response under these conditions is indicative of an appreciable intrinsic affinity of the receptors for chloride. The use of tetrabutylammonium chloride as the chloride source further minimizes possible ion-pairing artifacts, while its negligible absorbance at the excitation/emission wavelengths employed excludes significant inner-filter or reabsorption effects under the low-absorbance conditions adopted in this study. The fluorescence emission intensities of the aromatic pendant groups (excitation at approximately 370 nm) do not show any changes following the addition of Cl^-, whereas only the emission intensity of the carbazole moiety (excitation at 290 nm) showed changes after the addition of Cl^-. In particular, in every case an increase of the fluorescence respons upon addition of the guest is observed. It is worth noting that minor baseline artifacts (negative intensity) resulted from the background subtraction process for the stacked spectra of compounds **106a-d**. While these titration experiments serve a purely qualitative purpose, aiming to monitor spectral changes rather than to derive thermodynamic binding parameters, and the current deviations do not impact the conclusions drawn, the measurements are nonetheless being repeated. This ensures the highest scientific consistency and eliminates these instrumental artifacts from the final dataset. The stack fluorescence spectra for the receptors are reported in Figures 25-29.

The analyses provide interesting insights, as the following trends have emerged:

- Receptors **106a** and **106b** behave similarly upon addition of TBACl: the fluorescence signal never reaches saturation (even after adding 35 equivalents of TBACl), indicating the presence of an interaction, but a weak one;

- Receptor **106c** behaves differently from all the others: after the addition of 5 equivalents of TBACl, the fluorescence intensity reaches saturation. This suggests a stronger interaction compared to the others, as fluorescence saturation indicates that all the binding sites of the receptor are occupied (and thus saturated) after "just" 5 equivalents of TBACl;

- Receptors **106d** and **106e** show similar behavior: they appear to be "unaffected" by the addition of TBACl. The fluorescence intensity remains completely unchanged throughout the titration, indicating no interaction between the receptor and Cl⁻.

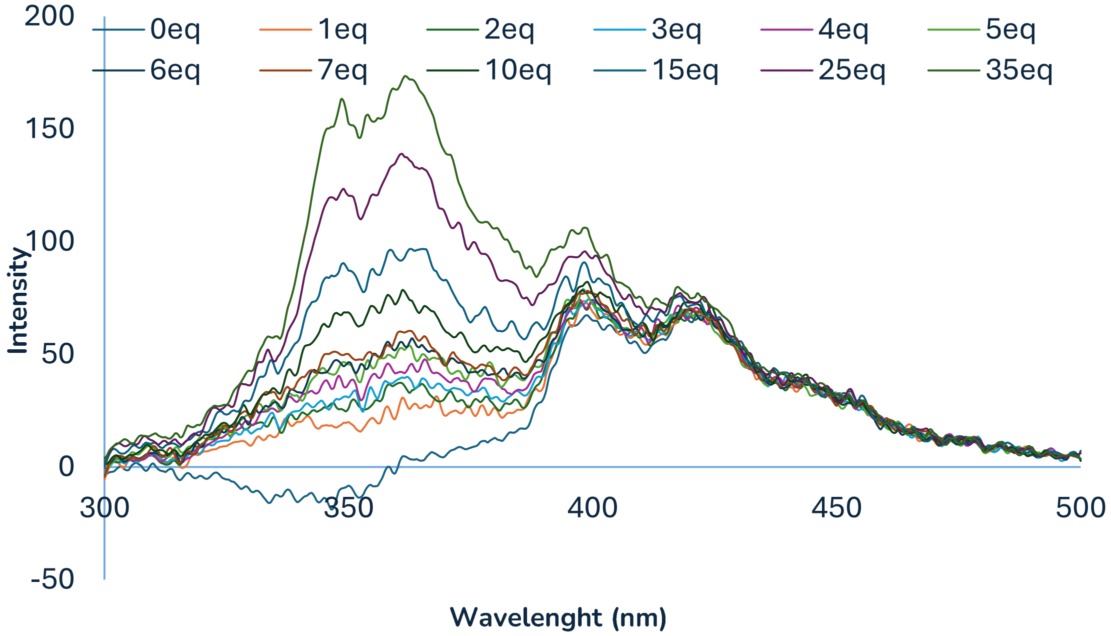

Figure 25. Fluorescence analysis of receptor **106a** (6.25×10^{-6} M) with TBACl (2.5×10^{-3} M) in DMSO at 298 K (exc: 290 nm).

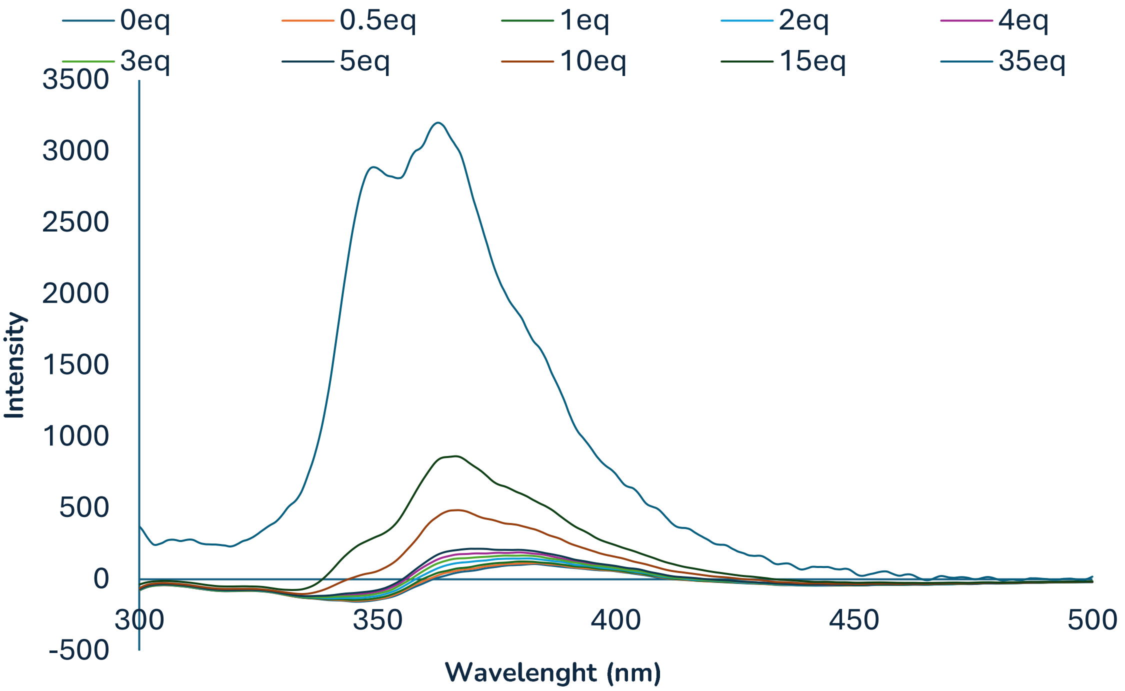

Figure 26. Fluorescence analysis of receptor **106b** (10^{-4} M) with TBACl (2.5×10^{-3} M) in DMSO at 298 K (exc: 290 nm).

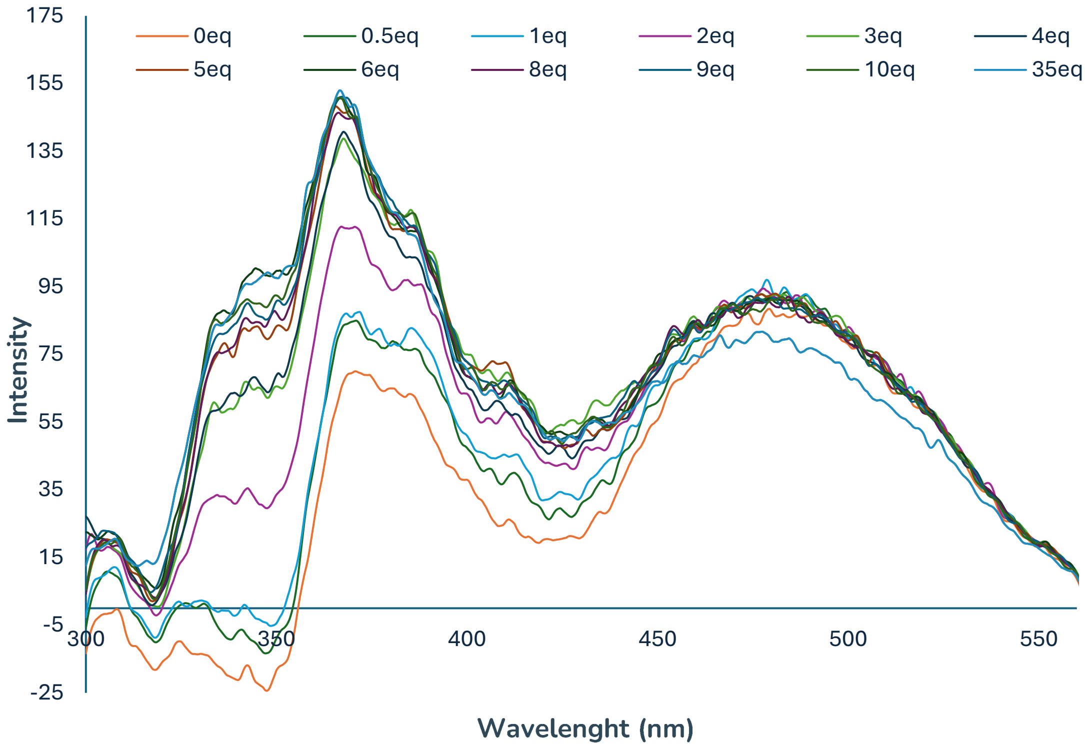

Figure 27. Fluorescence analysis of receptor **106c** (2×10^{-5} M) with TBACl (2.5×10^{-3} M) in DMSO at 298 K (exc: 290 nm).

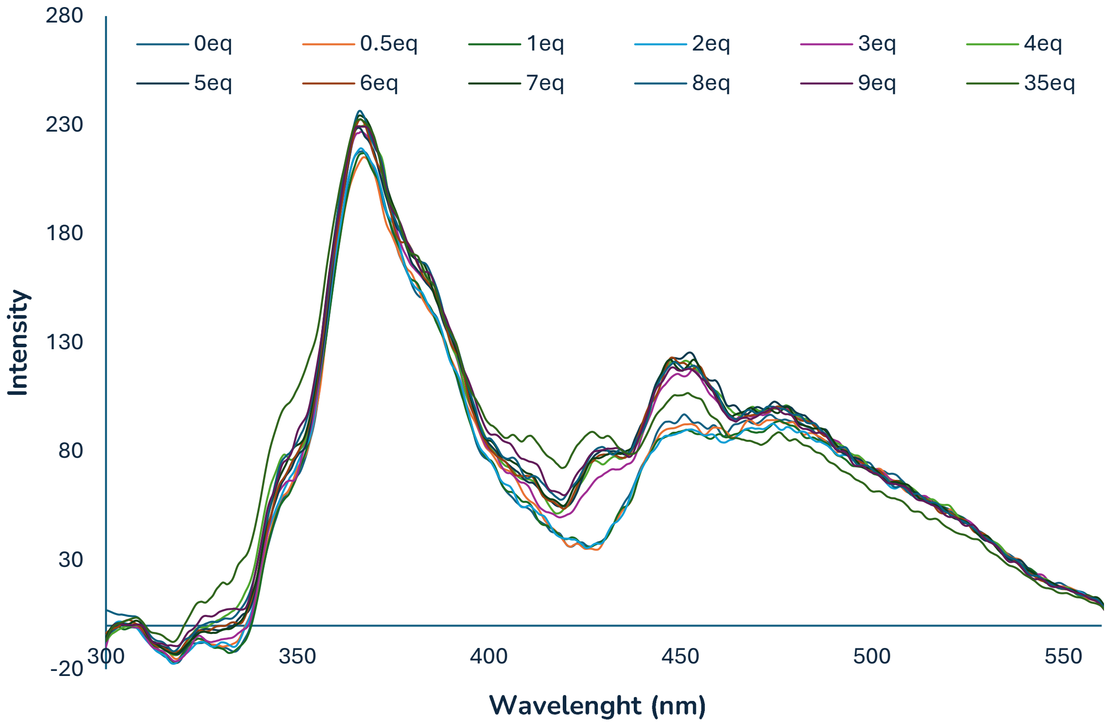

Figure 28. Fluorescence analysis of receptor **106d** (2 x 10^{-5} M) with TBACl (2.5 x 10^{-3} M) in DMSO at 298 K (exc: 290 nm).

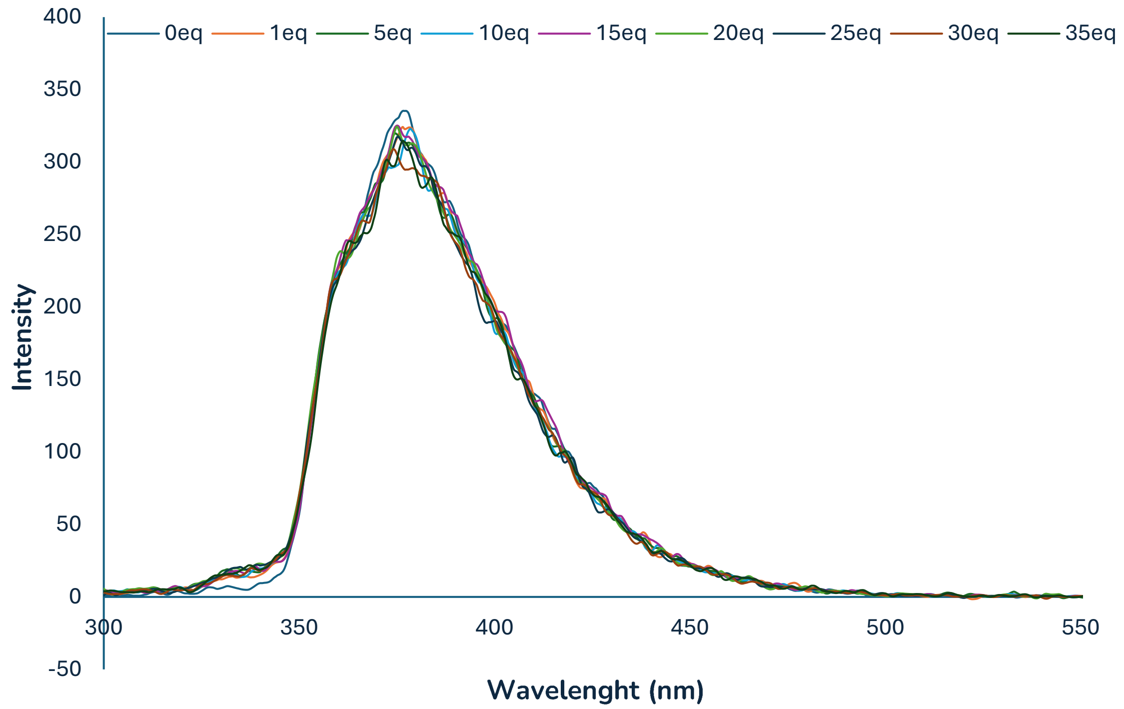

Figure 29. Fluorescence analysis of receptor **106e** (2.5 x 10^{-6} M) with TBACl (2.5 x 10^{-3} M) in DMSO at 298 K (exc: 290 nm).

In summary, the fluorimetric analyses suggest the following qualitative trend in interaction strength:

106c > **106a** ≈ **106b** > **106d** ≈ **106e**

In contrast, UV-Vis analyses revealed no significant changes in absorption upon addition of TBACl.

We therefore proceeded to a quantitative evaluation of the binding association constants (K_a) of compounds **106a–e** toward chloride by means of ^{1}H NMR titrations in DMSO-d_6/0.5% H_2O. Upon incremental addition of chloride to solutions of the receptors, a slight downfield shift of the carbazole NH signal was observed in all cases. The magnitude of this shift (Δδ, ppm) followed the order **106b** > **106c** > **106a** > **106d** > **106e**. This deshielding effect is consistent with the formation of hydrogen bonds between the carbazole NH and the chloride anion, supported by a secondary, weaker interaction involving the triazole C–H. The stacked ^{1}H NMR titration plots for the five receptors are shown in Figures 30–34.

The association constants were determined by fitting the titration data with a 1:1 binding model using the Bindfit software,[69] considering the chemical shift variations of both the carbazole NH and the triazole CH resonances. The calculated values are summarized in Table 3. The adoption of a simple 1:1 model is justified by the structural features of the receptors, which present a single carbazole NH as the main hydrogen-bond donor site, supported by the weaker contribution of the triazole CH. More complex binding models (e.g., 1:2 or 2:1) did not provide a better fit, further supporting the appropriateness of the 1:1 description.

The obtained association constants follow the order **106c > 106a > 106b > 106d > 106e** (Table 9), which is fully consistent with the qualitative trends deduced from the fluorescence studies. In particular, the relatively higher affinity of **106b** confirms their stronger interaction with chloride, as already suggested by the significant fluorescence response observed during the preliminary screening. Conversely, the negligible binding displayed by **106d** and **106e** is reflected in the very low association constants, in line with their lack of spectroscopic response in both fluorescence and UV-Vis analyses.

This agreement between qualitative (fluorescence) and quantitative (^{1}H NMR) data provides robust evidence of the binding behavior of the receptor series and highlights how subtle structural variations can dramatically affect their chloride-binding ability.

Table 9: Association constants (M^{-1}) for compounds **106a-e.** The titrations are performed *via* NMR in DMSO-d_6 + 0.5% H_2O towards chloride

---

[69] a) D. Brynn Hibbert, P. Thordarson, *Chem. Commun.* **2016**, *52*, 12792-12805; b) P. Thordarson, *Chem. Soc. Rev.*, **2011**, *40*, 1305-1323

Receptor	K_{ass} (M^{-1})
106a	38
106b	33
106c	125
106d	25
106e	19

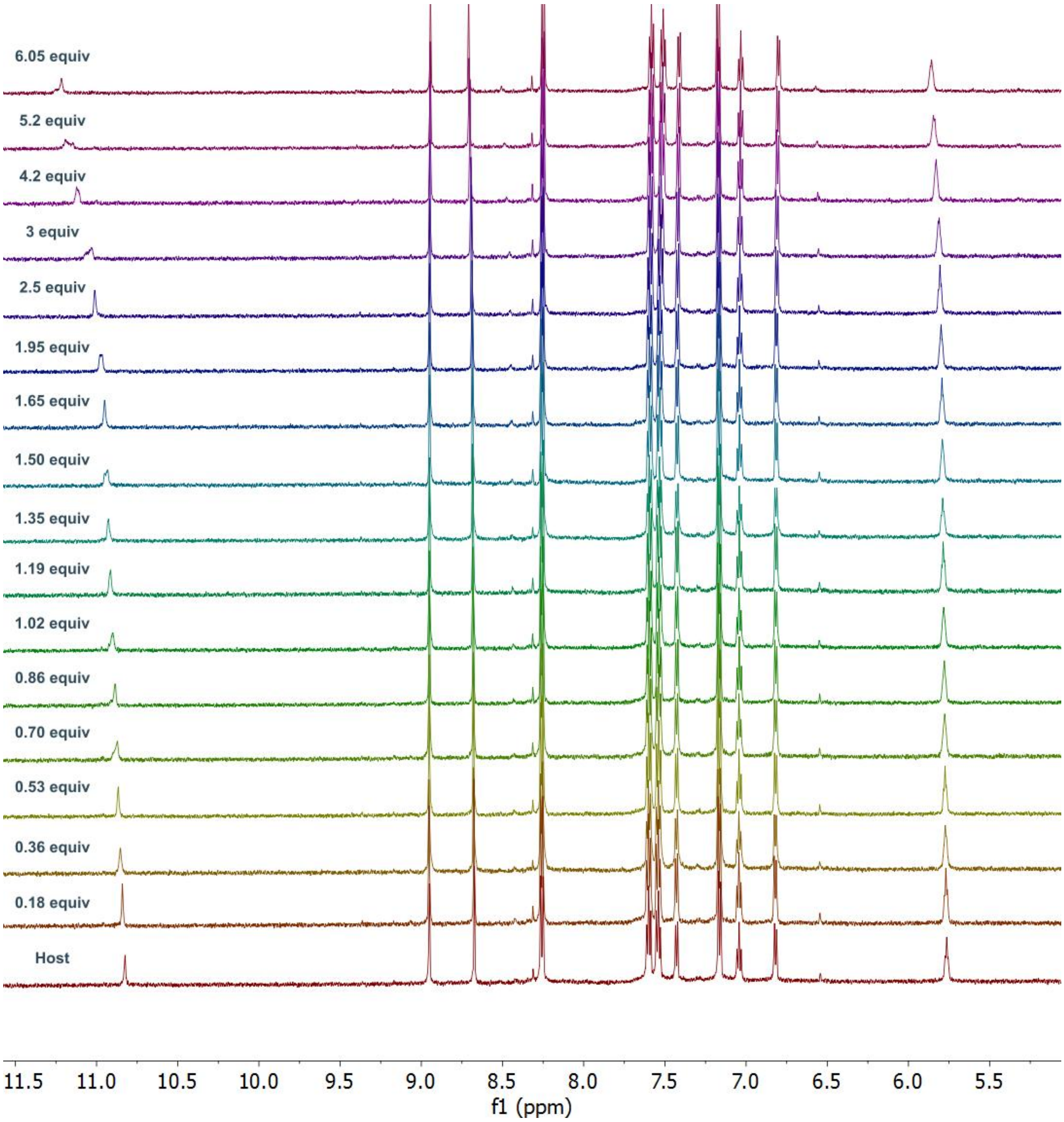

Figure 30: Stack plot for the titration of **106a** (0.001 M) with TBACl (0.015 M) in DMSO-d_6/0.5 % H_2O at 298 K.

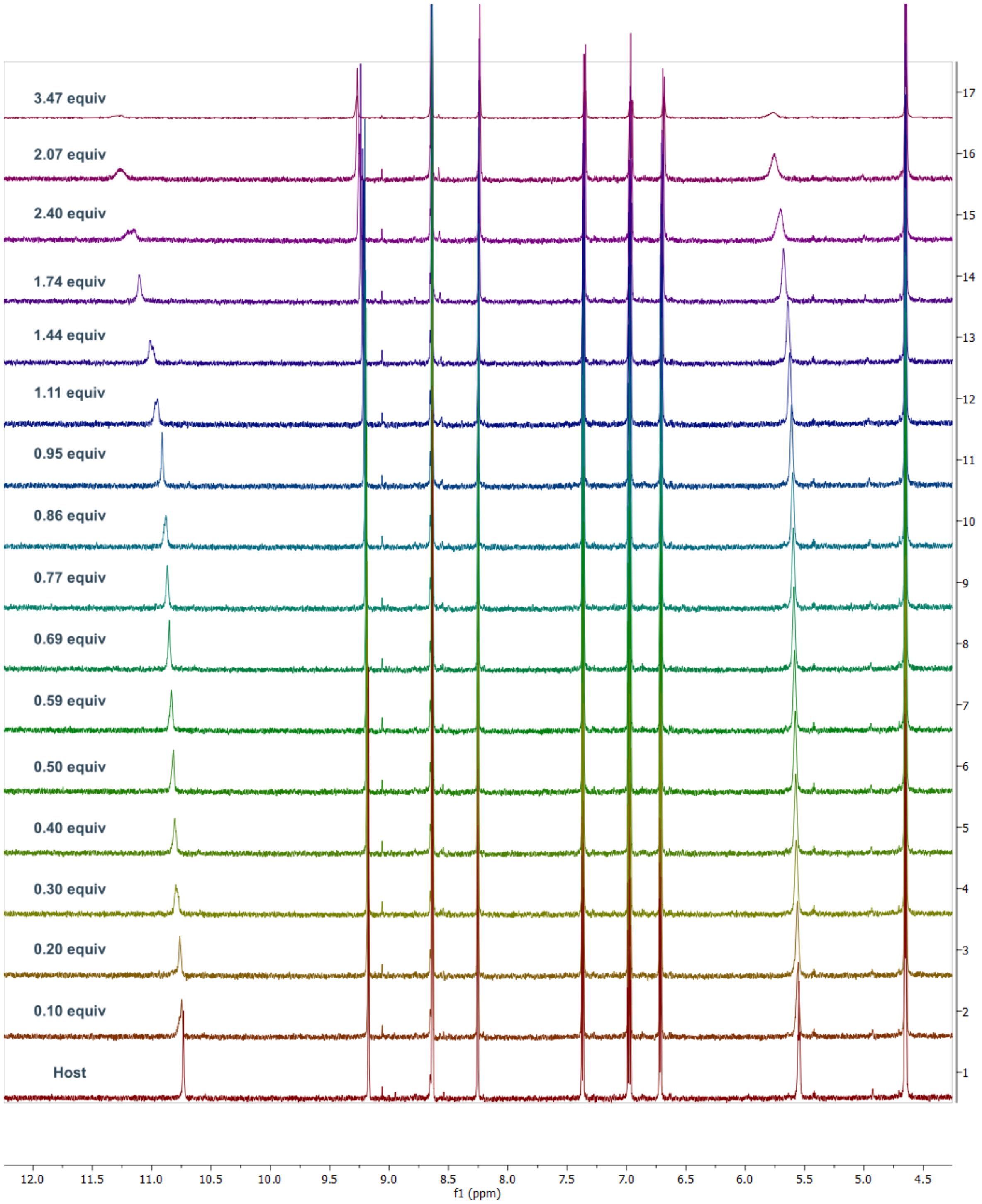

Figure 31: Stack plot for the titration of **106b** (0.001 M) with TBACl (0.015 M) in DMSO-d_6/0.5 % H2O at 298 K.

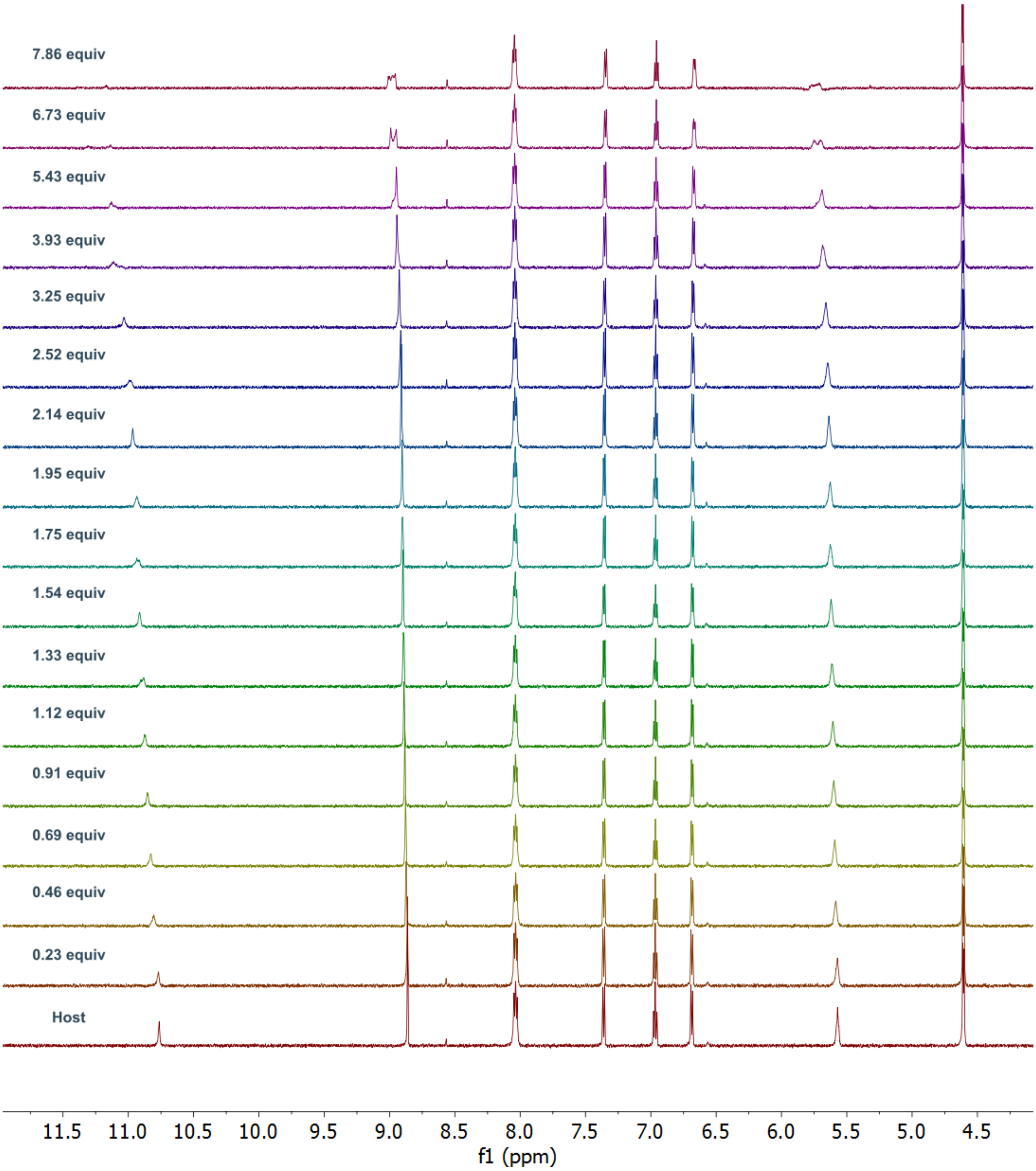

Figure 32: Stack plot for the titration of **106c** (0.001 M) with TBACl (0.015 M) in DMSO-d_6/0.5 % H2O at 298 K.

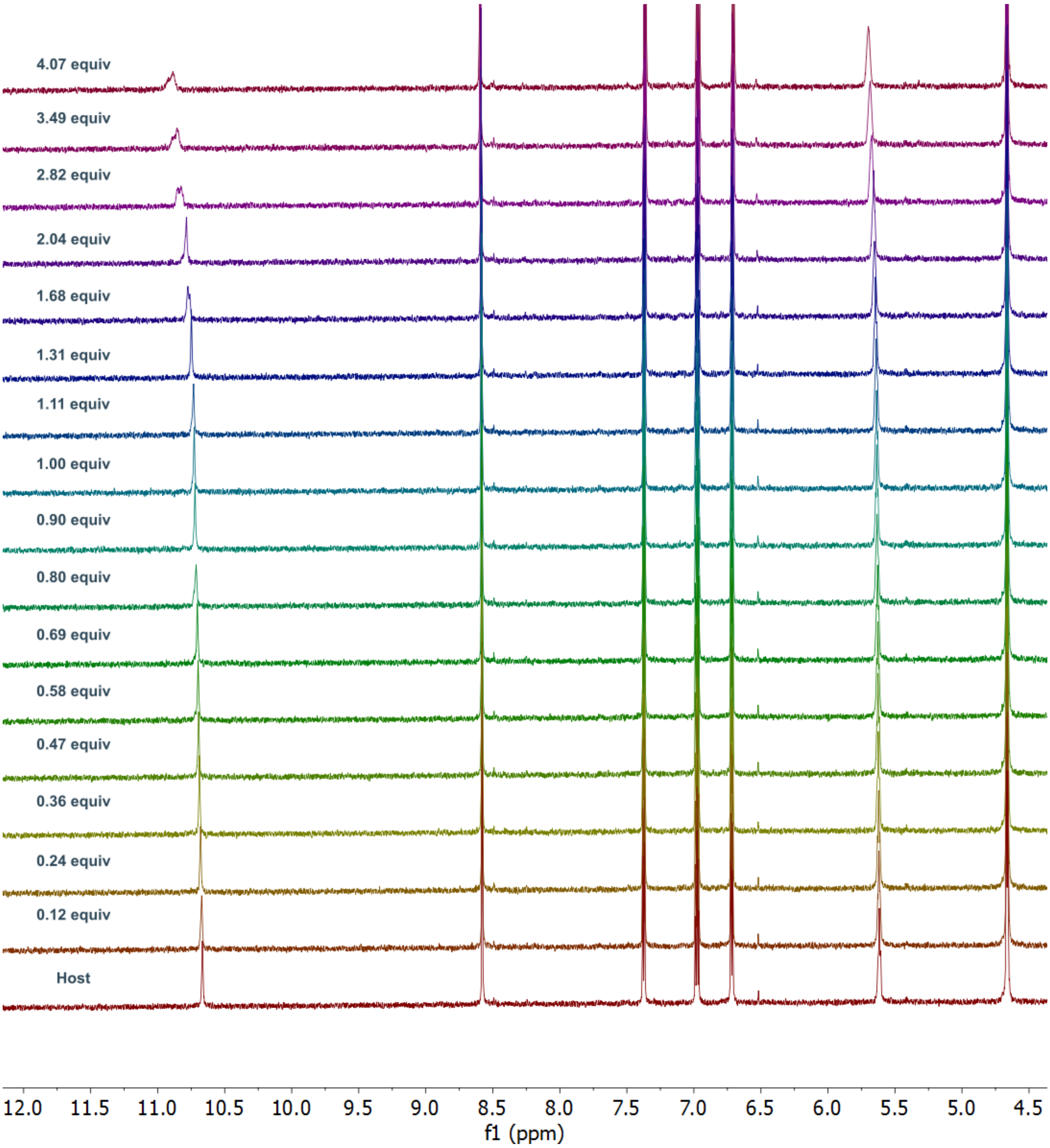

Figure 33: Stack plot for the titration of **106d** (0.001 M) with TBACl (0.015 M) in DMSO-d_6/0.5 % H_2O at 298 K.

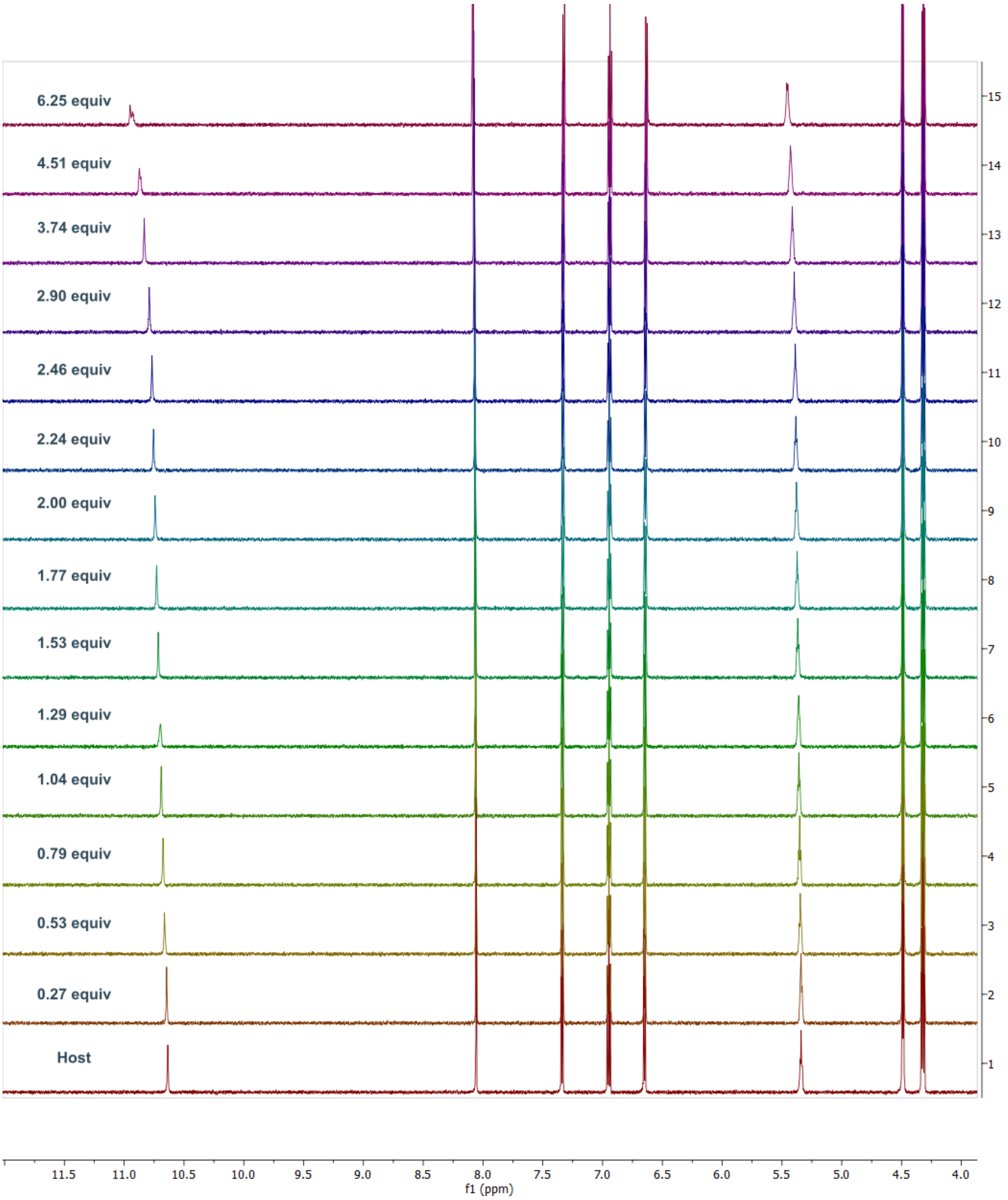

Figure 34: Stack plot for the titration of **106e** (0.001 M) with TBACl (0.015 M) in DMSO-d_6/0.5 % H_2O at 298 K.

Application in anion-binding catalysis

All the receptors were tested as anion-binding catalysts in a benchmark reaction, which is the tritylation of primary amines using an ionic tritylating agent (Figure 35).

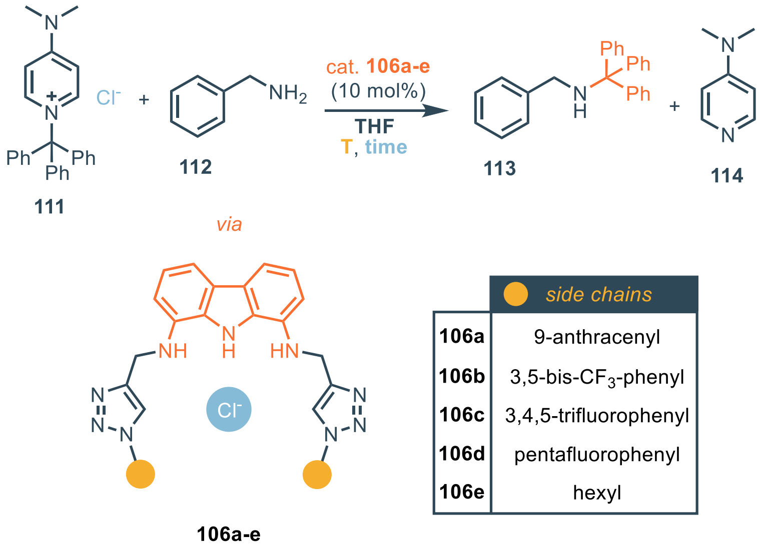

	side chains
106a	9-anthracenyl
106b	3,5-bis-CF_3-phenyl
106c	3,4,5-trifluorophenyl
106d	pentafluorophenyl
106e	hexyl

Figure 35: Model reaction to test the new catalysts **106a-e**: tritylation of benzylamine using reagent **111**.

Building on literature conditions, where a related anion-binding catalyst afforded 90% yield in THF at 45 °C after 72 h,[70] we investigated the performance of compounds **106a–e**. To this end, the reaction was carried out under the same reported conditions, and both product formation (**113**) and the release of DMAP (**114**) following the nucleophilic attack were monitored at 24 h intervals. The results are summarized in Table 10. In principle, the release of DMAP and the formation of **113** should proceed in a 1:1 ratio. However, inspection of Table 10 clearly shows that for most catalysts a discrepancy (Δ = %DMAP – %Product) develops over time, meaning that a portion of the trityl equivalents liberated is not converted into the desired product. This discrepancy is visualized in Figure 19, where Δ is plotted as a function of reaction time for each catalyst.

The comparison highlights distinct behaviors across the series:

- Catalyst **106c** clearly stands out as the most effective: the product yield steadily increases up to 76% after 72 h, while DMAP release follows the same profile and converges to the same value (Table 10, Entry 3). The discrepancy, initially ~12% at 24 h, decreases over time and vanishes at 72 h, indicating that virtually all the trityl equivalents liberated are eventually converted into the desired product. This behaviour points to a very efficient coupling between

---

[70] S. Beckendorf, S. Asmus, C. Muck-Lichtenfeld, O. G. Mancheno, *Chem. Eur. J.*, **2013**, *19*, 1581-1585

activation of **111** and productive tritylation of **112**, making **106c** the best-performing receptor in the series;

Table 10. Results of the catalysis experiments performed at 45°C [a]

		24 h		**48 h**		**72 h**	
Entry	**Catalyst**	**% DMAP (114)** [b]	**% product (113)** [b]	**% DMAP (114) b**	**% product (113)** [b]	**% DMAP (114)** [b]	**% product (113)** [b]
1	**106a**	18%	8%	26%	15%	32%	21%
2	**106b**	69%	52%	82%	66%	90%	73%
3	**106c**	61%	49%	74%	64%	76%	76%
4	**106d**	49%	34%	73%	49%	79%	54%
5	**106e**	45%	27%	68%	46%	82%	46%
6	Blank	11%	4%	12%	6%	14%	6%

[a] The reactions were performed with **111** (112 mg, 0.28 mmol, 1 equiv), catalyst **106x** (0.1 equiv) and **112** (60 mg, 0.56 mmol, 2 equiv) in THF (1.4 mL, 0.2 M) for the selected time at 45 °C; [b] Determined by ^{1}H NMR using triphenylmethane as an internal standard

- Catalyst **106b** is also highly active, delivering 73% yield of 109 after 72 h with concomitant release of 90% DMAP (Table 10, Entry 2). In this case, however, a significant discrepancy (Δ ≈ 17%) persists throughout the reaction time course. This suggests that although **106b** promotes fast activation of **111**, a notable fraction of the generated trityl cations is consistently diverted to side processes (hydrolysis, solvolysis, or recombination with DMAP), preventing full conversion into product;

- Catalyst **106d** affords intermediate activity, reaching 54% product at 72 h while releasing 79% DMAP. The discrepancy increases from 15% at 24 h to 25% at 72 h, highlighting a progressive decoupling between activation and product formation (Table 10, Entry 4). This may arise from inhibition by chloride binding, which traps the catalyst in a resting state, and/or from accumulation of side reactions that consume the trityl equivalents;

- Catalyst **106e** exhibits moderate activity, plateauing at 46% product yield after 48 h despite continued DMAP release (82% at 72 h). This results in the largest discrepancy of the series (Δ ≈ 36% at 72 h). The divergence between product and DMAP profiles points to extensive loss of trityl cations to non-productive pathways such as hydrolysis or solvent capture, and possibly to progressive catalyst deactivation (Table 10, Entry 5).

- Catalyst **106a** shows the lowest activity, providing only 21% product at 72 h with 32% DMAP released. The discrepancy (Δ ≈ 11%) is relatively modest, but the overall efficiency of the catalyst is very limited, reflecting its weak anion-binding ability (Table 10, Entry 1);
- Finally, the blank experiment (no receptor) confirms that, although slow, there is some intrinsic background reactivity of the tritylating agent, leading to 14% DMAP and 6% product after 72 h (Δ ≈ 8%).

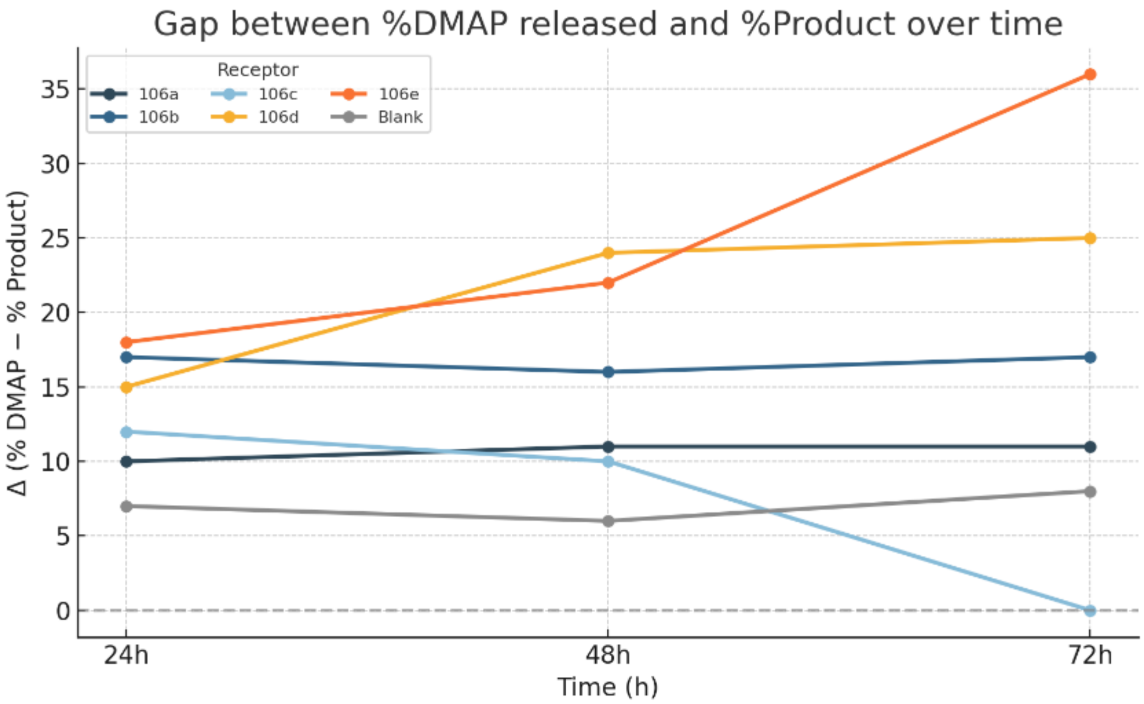

Figure 36. Difference between the % DMAP released (**110**) and % product (**109**) vs time at 45°C

In order to gain further insight into the origin of the observed discrepancies, additional experiments were performed at a lower temperature (30 °C). The rationale was that reducing the thermal energy of the system could slow down competing decomposition pathways of the trityl cation (such as hydrolysis or solvolysis), thereby allowing a clearer separation between productive and non-productive channels.

Lowering the reaction temperature from 45 to 30 °C produced significant changes in both the overall activity and the coupling efficiency between DMAP release and product formation (Table 11).

Table 11. Results of the catalysis experiments performed at 30°C [a]

		24 h		48 h		72 h	
Entry	**Catalyst**	**% DMAP (114) [b]**	**% product (113) [b]**	**% DMAP (114) [b]**	**% product (113) [b]**	**% DMAP (114) [b]**	**% product (113) [b]**
1	**106a**	<5%	<5%	8.5%	5%	12%	9%
2	**106b**	45%	45%	71%	68%	87%	83%
3	**106c**	40%	40%	68%	64%	84%	83%
4	**106d**	30%	33%	58%	52%	64%	59%
5	**106e**	31%	18%	40%	30%	55%	36%

[a] The reactions were performed with **111** (112 mg, 0.28 mmol, 1 equiv), catalyst **106x** (0.1 equiv) and **112** (60 mg, 0.56 mmol, 2 equiv) in THF (1.4 mL, 0.2 M) for the selected time at 30 °C; [b] Determined by ^{1}H NMR using triphenylmethane as an internal standard

- **106a**: At 45 °C the catalyst was only weakly active (21% product, 32% DMAP after 72 h), and this behaviour is further attenuated at 30 °C (9% product, 12% DMAP after 72 h). The discrepancy remains modest, but the overall reactivity is extremely low. Thus, reducing the temperature mainly suppresses the already limited activity of **106a** (Table 11, Entry 1);

- **106b**: At 45 °C the catalyst was highly active but displayed a persistent discrepancy of ~17% between DMAP and product. At 30 °C, both yields and discrepancies improve significantly: 83% product and 87% DMAP after 72 h, with $\Delta \approx 4\%$. This indicates that lowering the temperature reduces the weight of competing processes (e.g., hydrolysis/solvolysis of the trityl cation), thereby channeling a larger fraction of the activation events into the desired reaction (Table 11, Entry 2);

- **106c**: At 45 °C this receptor showed excellent performance, with 76% product and essentially no discrepancy after 72 h. At 30 °C, 83% product and 84% DMAP are obtained, again with $\Delta \approx 1\%$. Thus, **106c** remains the best-performing receptor under both conditions, and at lower temperature it achieves slightly higher yield while retaining near-perfect coupling between activation and product formation. This further confirms its robustness and efficiency (Table 11, Entry 3);

- **106d**: At 45 °C the catalyst reached 54% product and 79% DMAP after 72 h, with a significant discrepancy of ~25%. At 30 °C, the product yield improves to 59% and DMAP release is 64% ($\Delta \approx 5\%$). This reduction in the discrepancy again suggests that lowering the temperature suppresses non-productive consumption of the trityl cation, resulting in better alignment between DMAP release and product formation (Table 11, Entry 4);

- **106e**: Agan, the temperature lowering allows to reduce the discrepancy between DMAP and product, although this dealignment is still consistent and is actually the highest among all the catalysts tested;

The comparison shows that lowering the temperature to 30 °C generally reduces the discrepancies between DMAP and product yields, especially for **106b** and **106d**, which at 45 °C suffered from significant differences between the amount of DMAP and product. This supports the hypothesis that at higher temperature competitive side reactions (hydrolysis, solvolysis, recombination) become more pronounced, while at 30 °C these processes are suppressed, allowing the productive channel to dominate.

In terms of absolute yields, both **106b** and **106c** perform best, delivering ~83% product at 72 h, while **106d** improves modestly and **106a** remains poorly active. Importantly, the behaviour of **106c** is consistent across both temperatures, further confirming it as the most robust and efficient receptor of the series. Figure 37 illustrates the effect of temperature on the discrepancy (Δ = %DMAP – %Product), highlighting the differences between reactions performed at 45 °C and 30 °C.

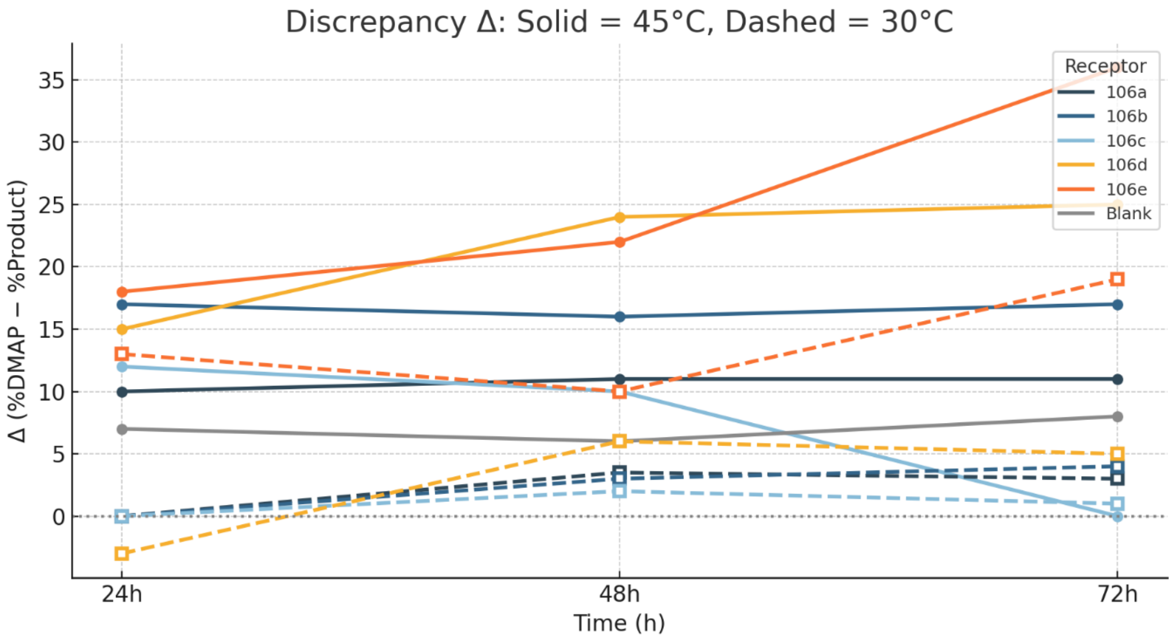

Figure 37. Discrepancy (Δ = %DMAP – %Product) as a function of time for receptors **106a–e** and the blank at 45 °C (solid lines) and 30 °C (dashed lines).

The control reaction performed in the absence of benzylamine provides important mechanistic insights. In this case, no productive pathway leading to **113** is available, and any release of DMAP must therefore originate from side reactions of the tritylating agent **111**.

Table 12 shows that all the receptors **106a-e** induce detectable release of DMAP already after 24 h, which continues to be observed at longer reaction times. This indicates that the activation of **111** by these catalysts can occur even in the absence of the nucleophile, but the resulting trityl cation is diverted towards non-productive consumption pathways, such as hydrolysis or solvolysis by the solvent. Notably, **106c**, which is the most efficient receptor under catalytic conditions, also triggers DMAP release in this test, but in the actual catalytic reaction the trityl equivalents are efficiently funnelled into product formation thanks to the presence of benzylamine. In contrast, **106a** does not seem to induce any detectable DMAP release even after 72 h, consistent with its poor catalytic activity in the presence of substrate. The blank reaction (without receptor) shows no DMAP formation up to 48 h and only a very low amount after 72 h, confirming that the tritylating agent **107** is relatively stable in THF at 30-45 °C in absence of a sufficiently strong nucleophile, and that spontaneous decomposition is minimal.

Table 12. Results of the reaction performed in absence of nucleophile [a]

Receptor	**Detection of DMAP** [b]		
	24 h	**48 h**	**72 h**
106a	No	No	No
106b	Yes	Yes	Yes
106c	Yes	Yes	Yes
106d	Yes	Yes	Yes
106e	Yes	Yes	Yes
Blank	No	No	Traces

[a] The reactions were performed with **111** (112 mg, 0.28 mmol, 1 equiv), catalyst **106x** (0.1 equiv) in THF (1.4 mL, 0.2 M) for the selected time at 45 °C; [b] Qualitative determination of DMAP content via NMR analysis

Overall, this experiment demonstrates that receptors capable of binding and activating chloride (**106b–e**) can promote the cleavage of **111** even without the nucleophile present, but in the absence of benzylamine the generated trityl equivalents are wasted into side reactions. This observation rationalizes the discrepancies observed between DMAP release and product yield in the catalytic experiments: the trityl cation can be formed catalytically but, if not captured rapidly by benzylamine, it is lost to competing processes.

Finally, the influence of moisture on the hydrolysis of **111** was investigated. No substantial differences were observed between the anhydrous and non-anhydrous conditions, which suggests that hydrolysis alone cannot fully account for the observed discrepancies. It is therefore reasonable to assume that additional processes, such as partial reversibility of the tritylation step (retro-tritylation), recombination of the trityl cation with DMAP, solvolysis by the solvent, or possible catalyst modification, also play a role in reducing the overall efficiency of the system.

Conclusions

This work successfully demonstrated the first application of the 1,8-diaminocarbazole scaffold **I** as a novel and effective platform for anion-binding catalysis. While this framework has been extensively studied for its anion recognition properties in sensing and transport, its potential to act as a supramolecular catalyst had, until now, remained unexplored. The central hypothesis of this project was that the carbazole core, possessing three strategically positioned hydrogen-bond-donor (HBD) sites, a rigid and pre-organized structure, and a complete absence of competing hydrogen-bond acceptors, represents an ideal, yet overlooked, architecture for promoting chemical reactions via non-covalent interactions.

A family of catalysts (**106a-e**) with varied terminal arms was synthesized to probe the structure-activity relationship in a benchmark N-tritylation reaction. Quantitative binding studies identified catalyst **106c** as the strongest chloride binder (K_A = 125 M^{-1}), consistent with its electron-deficient structure. The catalytic evaluation, however, revealed a complex relationship between binding affinity and efficacy.

The results suggest that binding strength, while a contributing factor, is not the sole determinant of catalytic performance. While the strongest binder, **106c**, was a top-performing catalyst (up to 83% yield), other results show a more complex picture. For instance, catalyst **106a**, the second-strongest binder, showed low activity, which may be attributed to steric hindrance from its bulky arms leading to non-productive binding. Conversely, catalyst **106b**, a weaker binder than **106a**, proved to have a similar activity compared to **106c**, therefore suggesting that an optimal binding geometry can be more critical for turnover than binding strength alone.

Current efforts are already underway to expand the utility of this catalyst family. Future work will focus on two primary directions. First, we are exploring the application of these achiral catalysts in a broader range of transformations that proceed with an anion abstraction mechanism, aiming to demonstrate the generality of the carbazole scaffold in anion-binding catalysis. Second, we are designing and constructing new chiral architectures based on this framework. The ultimate goal is to leverage the powerful binding properties and structural modularity of the carbazole core to achieve high levels of stereocontrol, thereby developing the first enantioselective catalytic systems based on this promising platform.

Experimental section

Instrumentation

Nuclear magnetic resonance analyses (^{1}H-,^{19}F- and ^{13}C-NMR spectra) were acquired using a Bruker Avance III 400 MHz spectrophotometer, a Bruker Ascend Evo 600 MHz spectrophotometer and a Magritek 60 MHz spectrophotometer. Chemical shifts (δ) are reported in ppm relative to residual solvent signals for ^{1}H- and ^{13}C-NMR (^{1}H-NMR: 7.26 ppm for $CDCl_3$; ^{13}C-NMR: 77.16 ppm for $CDCl_3$; ^{1}H-NMR: 7.26 ppm for DMSO-d_6; ^{13}C-NMR: 39.52 ppm for DMSO-d_6). Both ^{13}C-NMR and ^{19}F-NMR spectra were acquired with ^{1}H broadband decoupled mode. Coupling constants are given in Hz. ^{1}H-NMR yields were measured by analysing the reaction mixture using triphenylmethane as internal standard. Chromatographic purifications of compounds **109a-e and 110a-e** and were performed using automated Biotage® Isolera LS Systems. Fluorescence measurements were performed on a PerkinElmer LS-50 spectrofluorometer (PerkinElmer.Inc, Waltham, MA, USA). X-ray diffraction analyses were performed on a Bruker D8 Venture diffractometer at 240 or 298 K.

Material and methods

Starting material were purchased from BLDPharm, Merck and TCI and used as received unless otherwise stated. Silica Gel 60A (35-70 μm), HPLC solvents, deuterated solvent and analytical grade solvents were purchased from Merck. Compounds **I**, **108a-d** and **111** were prepared according to reported literature methods, and their characterization matches with the values reported in literature.[65-71]. Proton NMR titrations were performed by adding aliquots of the putative anionic guest (as the TBA salt, 0.015 M), dissolved in a solution of the receptor (0.001 M) in DMSOd_6/0.5% H_2O to a solution of the receptor (0.001 M).

---

[71] a) M. J. Chmielewski, *Synthesis*, **2010**, *18*, 3067-3069

Experimental procedures

Synthesis of **108e**

In a dry 50 mL round-bottom flask equipped with a magnetic stir bar and sealed with a rubber septum, the atmosphere was cycled three times under vacuum and nitrogen. Sodium azide (0.69 g, 10.6 mmol, 1.1 equiv) was dissolved in anhydrous DMSO (21 mL) to afford a 0.5 M stock solution, which was stirred at room temperature for 16 h until a clear solution was obtained. Subsequently, 1-bromohexane (1.59 g, 9.62 mmol, 1.0 equiv) was added under a nitrogen atmosphere. The reaction mixture was stirred at room temperature for 24 h. Upon completion, the mixture was diluted with diethyl ether (10 mL) and transferred to a separatory funnel. The ether phase was separated, and the DMSO washed again with Et_2O (10 mL x 3). The ether phases were collected, dried over anhydrous $MgSO_4$, filtered, and concentrated under reduced pressure, to afford 860 mg of hexyl azide **108e** (6.76 mmol, 70% yield).

^{1}H NMR (400 MHz, $CDCl_3$): δ 3.21 (t, *J* = 7.0 Hz, 2H); 1.55 (m, 2H); 1.37-1.23 (m, 6H); 0.86 (t, *J* = 7.0 Hz, 3H). The spectroscopic data matched those reported in the literature.[72]

General procedure for the synthesis of compounds **109a-e**

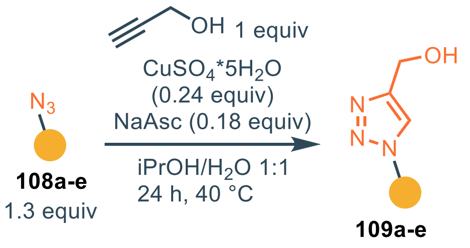

	● *ending arms*
109a	9-anthracenyl
109b	3,5-bis-CF_3-phenyl
109c	3,4,5-trifluorophenyl
109d	pentafluorophenyl
109e	hexyl

In a 100 mL round-bottom flask equipped with a magnetic stir bar, a solution of azide **108a-e** (7.0 mL, 7.0 mmol, 1.3 equiv, 1.0 M in iPrOH) was diluted with iPrOH (6 mL) and H_2O (13 mL) under ambient atmosphere. Copper(II) sulfate pentahydrate (320 mg, 1.30 mmol, 0.24 equiv), sodium ascorbate (193 mg, 0.98 mmol, 0.18 equiv), and propargyl alcohol (320 µL, 5.40 mmol, 1.0 equiv) were then sequentially added. The resulting suspension was stirred at 40 °C for 24 h using a DrySyn heating

---

[72] R. Valderrama-Calejòn, E. L. Vargas, I. Alonso, M. Tortosa, B. Cid, *Chem. Eur. J.*, **2025**, *31*, e202404081

block. After completion of the reaction, the mixture was diluted with water (30 mL) and extracted with dichloromethane (4 × 30 mL). The combined organic layers were washed with brine (4 × 20 mL), dried over anhydrous $MgSO_4$, filtered, and concentrated under reduced pressure to afford a dark red solid. Purification by flash column chromatography (DCM/MeOH 95:5) gave the desired triazoles **109a-e**.

General procedure for the synthesis of compounds **110a-e**

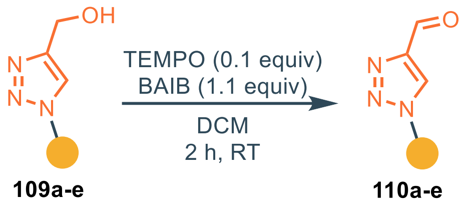

109a-e **110a-e**

	● *ending arms*
109a	9-anthracenyl
109b	3,5-bis-CF_3-phenyl
109c	3,4,5-trifluorophenyl
109d	pentafluorophenyl
109e	hexyl

In a 50 mL round-bottom flask equipped with a magnetic stir bar, TEMPO (47 mg, 0.30 mmol, 0.10 equiv) was added to a stirred solution of the corresponding alcohol **109a-e** (3.00 mmol, 1.0 equiv) and BAIB (1.20 g, 3.30 mmol, 1.1 equiv) in dichloromethane (15 mL) at room temperature. The reaction mixture was stirred at ambient temperature for 2 h. Upon completion, the mixture was diluted with DCM (15 mL) and washed with saturated aqueous sodium thiosulfate solution (2 × 20 mL). The aqueous phase was extracted with DCM (4 × 20 mL), and the combined organic layers were washed with saturated $NaHCO_3$ solution (2 × 20 mL), followed by brine (1 × 20 mL). The organic layer was dried over anhydrous Na_2SO_4, filtered, and concentrated under reduced pressure. The crude product was purified by flash column chromatography (petroleum ether/ethyl acetate, 9:1 → 8:2) to afford the desired aldehydes **110a-e**.

Synthesis of **Im-a**

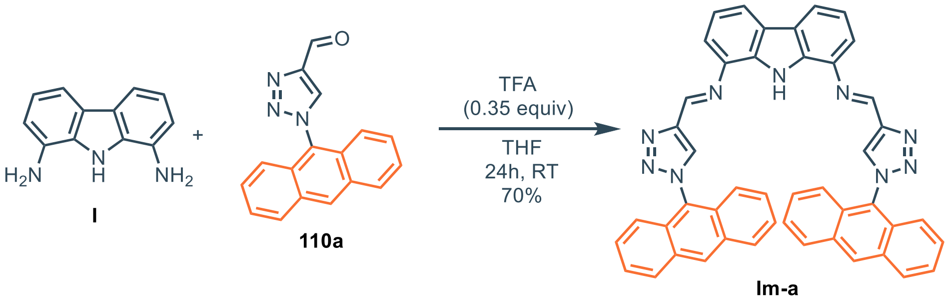

I **110a** **Im-a**

A 10 mL round-bottom flask equipped with a magnetic stir bar was flame-dried and subjected to vacuum/N_2 cycles while heating with a heat gun. Aldehyde **110a** (318 mg, 1.16 mmol, 2.2 equiv) and

1,8-diaminocarbazole **I** (104 mg, 0.529 mmol, 1.0 equiv) were added under a nitrogen atmosphere, and an additional vacuum/N_2 cycle was performed to ensure anhydrous conditions. Anhydrous THF (4 mL) was then added, followed by trifluoroacetic acid (TFA, 13.8 µL, 0.185 mmol, 0.35 equiv). The resulting suspension was stirred at room temperature for 24 h. After completion, the mixture was transferred to a centrifuge tube and centrifuged at 5000 rpm for 15 min. The supernatant was removed, and the solid residue was washed with THF (2 mL) and centrifuged again under the same conditions. The resulting solid was then dried under reduced pressure and used in the following step without further purifications.

Synthesis of **106a**

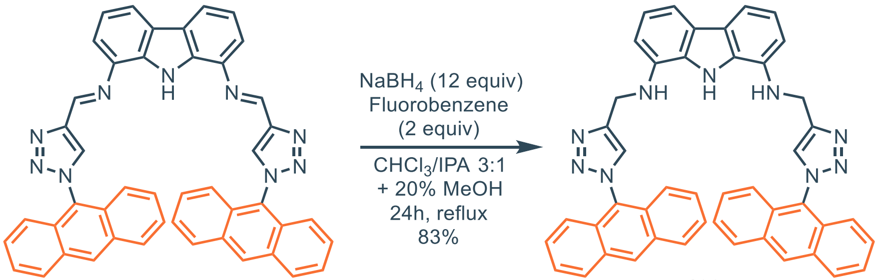

Im-a **106a**

A suspension of **Im-a** (497 mg, 0.702 mmol, 1.0 equiv) in a 3:1 mixture of chloroform/*i*PrOH (15 mL/5 mL) was placed in a 100 mL round-bottom flask equipped with a magnetic stir bar. Fluorobenzene (132 µL, 1.40 mmol, 2.0 equiv) was added, and the mixture was heated at reflux using a DrySyn heating block. Sodium borohydride (319 mg, 8.43 mmol, 12.0 equiv) dissolved in methanol (5 mL, corresponding to 20% of the total solvent volume) was then added dropwise. The resulting suspension was stirred at reflux for 24 h. After completion, the reaction mixture was cooled to room temperature and diluted with EtOAc (30 mL). The yellow solid formed was collected by Büchner filtration, washed successively with brine and EtOAc, and concentrated under reduced pressure. The crude solid was further washed three times with EtOAc, and the combined organic layers were washed with brine, dried over anhydrous Na_2SO_4, filtered, and evaporated to afford the desired product **106a** as a yellow solid (83% yield).

Synthesis of **106b**

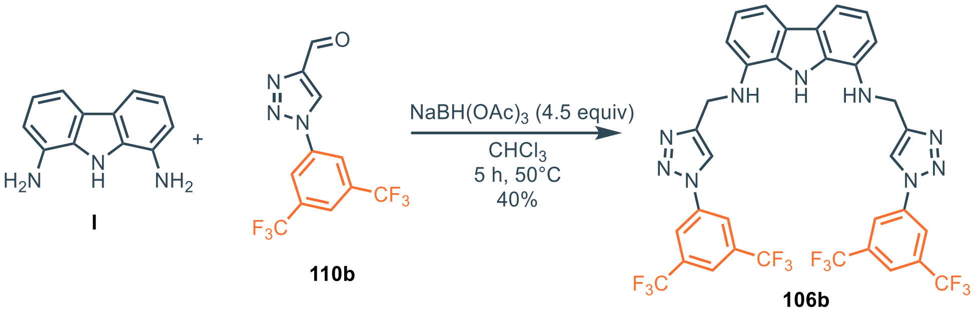

In a 50 mL round-bottom flask equipped with a magnetic stir bar, 1,8-diaminocarbazole **I** (128 mg, 0.65 mmol, 1.0 equiv), aldehyde **110b** (400 mg, 1.30 mmol, 2.0 equiv), and sodium triacetoxyborohydride ($NaB(OAc)_3H$, 617 mg, 2.90 mmol, 4.5 equiv) were combined in chloroform (8 mL). The reaction mixture was stirred at 50 °C for 5 h, during which the color changed from yellow to gray. After completion, the reaction mixture was diluted with EtOAc (40 mL) and washed with saturated aqueous NH_4Cl solution (2 × 20 mL). The combined aqueous layers were extracted with DCM (2 × 20 mL), and the combined organic extracts were dried over anhydrous $MgSO_4$, filtered, and concentrated under reduced pressure. The resulting gray solid was suspended in MeCN (10 mL), transferred to a centrifuge tube, and centrifuged (5000 rpm, 10 min). The supernatant was discarded, affording the desired product **106b** as a gray solid (40% yield).

Synthesis of **Im-c**

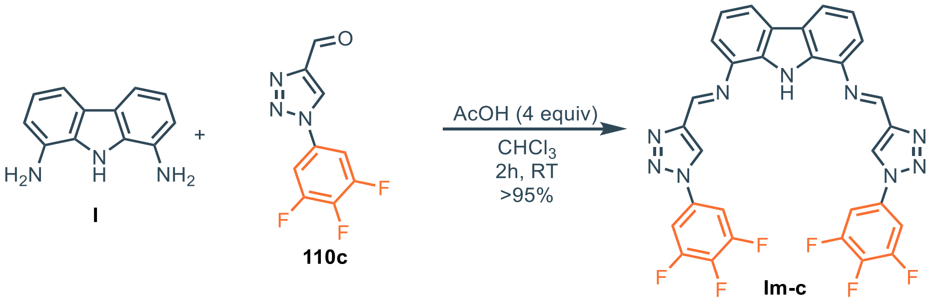

In a 12 mL vial equipped with a magnetic stir bar, 1,8-diaminocarbazole **I** (89 mg, 0.45 mmol, 1.0 equiv) and aldehyde **110c** (301 mg, 0.92 mmol, 2.0 equiv) were combined. Chloroform (6 mL) and acetic acid (103 μL, 1.8 mmol, 4.0 equiv) were then added, and the reaction mixture was stirred at room temperature for 2 h. After completion, the mixture was transferred to a centrifuge tube, and the solid product was isolated by centrifugation (5000 rpm, 10 min). The supernatant was discarded, affording a bright green solid which is used in the following step without further purifications.

Synthesis of **106c**

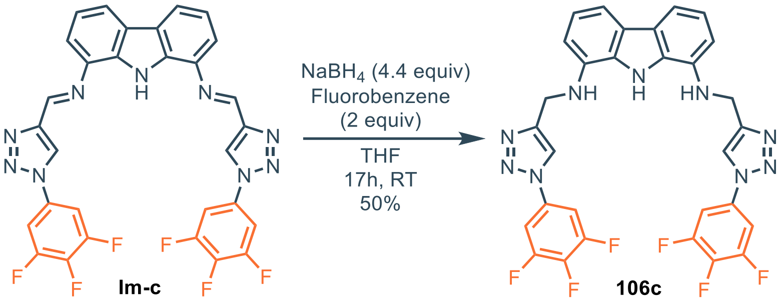

In a 100 mL round-bottom flask equipped with a magnetic stir bar, **Im-c** (286 mg, 0.47 mmol, 1.0 equiv) was dissolved in THF (34 mL) together with fluorobenzene (88 µL, 0.93 mmol, 2.0 equiv). Sodium borohydride (77 mg, 2.00 mmol, 4.4 equiv) was then added in one portion at room temperature. After a few minutes, the reaction mixture turned red and became homogeneous. The mixture was stirred at room temperature for 17 h, during which the color gradually changed to light brown. After completion, the solvent was removed under reduced pressure, and the residue was dissolved in EtOAc (20 mL). The organic phase was washed with brine (3 × 20 mL), dried over anhydrous Na_2SO_4, filtered through cotton, and concentrated under reduced pressure. The crude product was washed with acetonitrile (3 × 5 mL) to remove residual impurities, affording the desired compound **106c** as a gray solid (yield: 50%).

Synthesis of **106d**

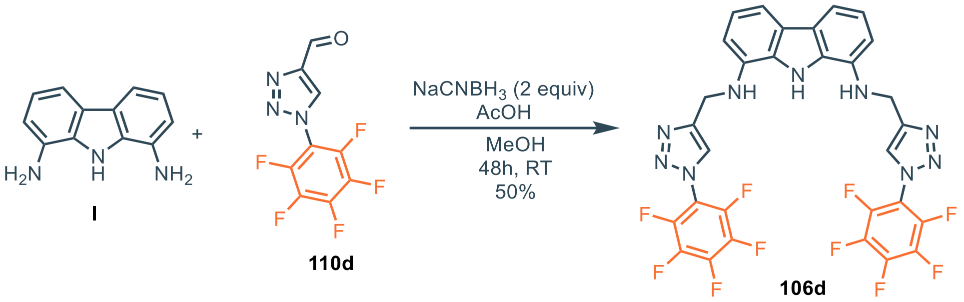

In a 4 mL vial equipped with a magnetic stir bar, **I** (41 mg, 0.21 mmol, 1.0 eq.) was dissolved in 1 mL of dry methanol. Glacial acetic acid was added (75 µL, 1.3 mmol, 6.4 eq.) along with the aldehyde **110d** (150 mg, 0.41 mmol, 2.0 eq.). The reaction was left to stir for 5 minutes and after $NaBH_3CN$ (26 mg, 0.41 mmol, 2.0 eq.) was added. The reaction mixture was left to stir at RT for 24 h. After this time, the reaction mixture was transferred to a Falcon tube, centrifuged, and the supernatant was removed. The solid was washed with methanol and centrifugated two times. The resulting solid was then dried under vacuum, affording the desired compound **106d** as a grey solid (yield 60%).

Synthesis of **106e**

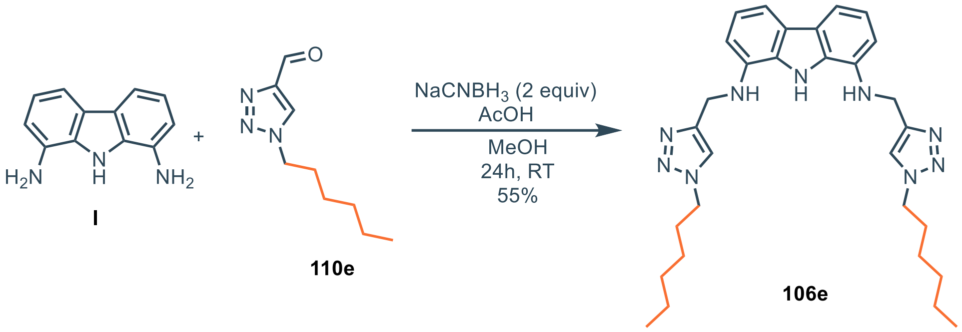

I

110e

106e

In a 4 mL vial equipped with a magnetic stir bar, **I** (41 mg, 0.21 mmol, 1.0 eq.) was dissolved in 1 mL of dry methanol. Glacial acetic acid was added (75 µL, 1.3 mmol, 6.4 eq.) along with the aldehyde **110e** (74 mg 0.41 mmol, 2.0 eq.). The reaction was left to stir for 5 minutes and after NaBH$_3$CN (26 mg, 0.41 mmol, 2.0 eq.) was added. The reaction mixture was left to stir at RT for 24 h. After this time, the reaction mixture was transferred to a Falcon tube, centrifuged, and the supernatant was removed. The solid was washed with methanol and centrifugated two times. Then, all the methanol was evaporated under vacuum to obtain a grey solid which is the desired product **106e** with 55% yield.

General procedure for the tritylation reaction

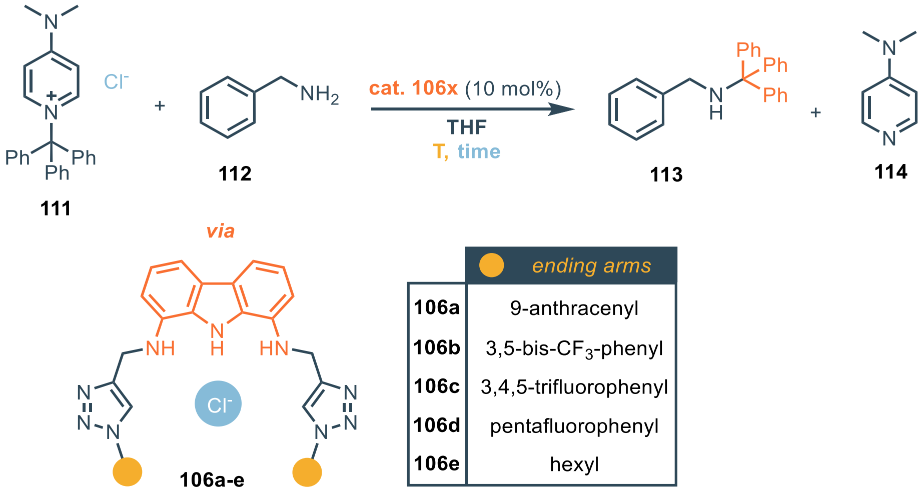

111

112

113

114

106a-e

	● *ending arms*
106a	9-anthracenyl
106b	3,5-bis-CF$_3$-phenyl
106c	3,4,5-trifluorophenyl
106d	pentafluorophenyl
106e	hexyl

In a screw-cap 4 mL vial, compound **111** (112 mg, 0.28 mmol) and catalyst **106a-e** (0.1 equiv, 0.028 mmol) were suspended in THF (1.4 mL, 0.2 M). Afterwards, compound **112** (2 equiv., 0.56 mmol, 61.2 µL) was added, and the reaction was left to stir at the selected temperature for the selected time. Conversion and yield were evaluated via NMR using triphenylmethane as internal standard. At the end of the reaction, the mixture was concentrated in vacuo and compound **113** was obtained purifying the reaction mixture with flash column chromatography (pentane/DCM 9:1).

Characterizations

Characterization of **109a**

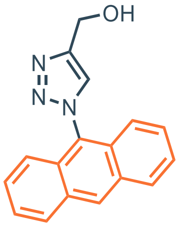

109a

Orange solid obtained with yield >95%

^{1}H NMR (400 MHz, CDCl$_3$) δ 8.66 (s, 1H), 8.09 (d, *J* = 8.3 Hz, 2H), 7.95 (s, 1H), 7.56 –7.43 (m, 4H), 7.31 (d, *J* = 8.6 Hz, 2H), 5.08 (d, *J* = 4.5 Hz, 2H), 2.77 – 2.69 (m, 1H).

^{13}C NMR (101 MHz, CDCl$_3$) δ 147.83, 131.30, 129.97, 128.51, 128.37, 128.17, 126.21, 126.12, 122.19, 56.96.

Characterization of **109b**

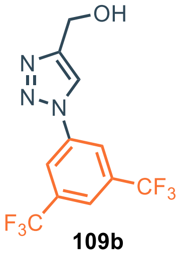

109b

Orange solid obtained with yield >95%

^{1}H NMR (400 MHz, DMSO-d$_6$) *δ* 9.06 (s, 1H), 8.65 (s, 2H), 8.22 (s, 1H), 5.44 (t, *J* = 5.5 Hz, 1H), 4.64 (d, *J* = 5.5 Hz, 2H).

^{13}C NMR (101 MHz, DMSO-d$_6$) *δ* 149.7, 138.0, 131.7 (q, *J* = 33.7 Hz), 122.8 (q, *J* = 237.4 Hz), 121.7, 121.6, 120.5, 54.9

^{19}F NMR (376 MHz, DMSO-d$_6$) *δ* -61.44 (s).

Characterization of **109c**

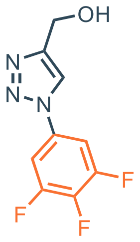

109c

Orange solid obtained with yield >95%

^{1}H NMR (400 MHz, CDCl$_3$) *δ* 7.95 (s, 1H), 7.50 – 7.43 (m, 2H), 4.91 (s, 2H).

^{13}C NMR (101 MHz, CDCl$_3$) δ 151.8 (m), 140.0 (m), 132.2, 120.0, 105.6, 105.5, 56.6

^{19}F NMR (376 MHz, CDCl$_3$) *δ* -130.13 (d, *J* = 20.6 Hz, 2F), -158.79 (t, *J* = 20.6 Hz, 1F).

Characterization of **109d**

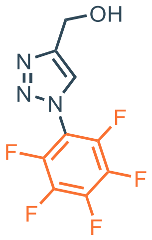

109d

Orange oil obtained with 73% yield

^{1}H NMR (400 MHz, CDCl$_3$) *δ* 7.85 (s, 1H), 4.91 (s, 2H).

^{13}C NMR (101 MHz, CDCl$_3$) *δ* 148.4, 144.1 – 140.8 (m), 143.5 – 140.5 (m), 139.9 – 136.2 (m), 124.8, 112.9 (m), 55.8.

^{19}F NMR (376 MHz, CDCl$_3$) *δ* - 145.27–146.08 (m, 2F), -149.91 (t, *J* = 21.5 Hz, 1F), - 158.87–160.06 (m, 2F).

Characterization of **109e**

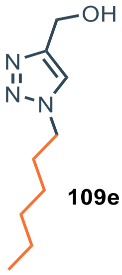

109e

Orange oil obtained with >95% yield

^{1}H NMR (600 MHz, CDCl$_3$) δ 7.52 (s, 1H), 4.76 (d, *J* = 2.0 Hz, 2H), 4.31 (td, *J* = 7.3, 1.9 Hz, 2H), 1.87 (h, *J* = 7.3 Hz, 2H), 1.29 (d, *J* = 5.3 Hz, 8H), 0.88 – 0.83 (m, 4H)

^{13}C NMR (151 MHz, CDCl$_3$) δ 147.9, 121.7, 56.3, 50.5, 31.2, 30.3, 26.2, 22.5, 14.0.

Characterization of **110a**

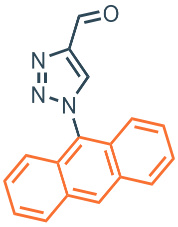

110a

Yellow solid obtained with yield >95%

^{1}H NMR (400 MHz, CDCl$_3$) δ 10.41 (s, 1H), 8.72 (s, 1H), 8.51 (s, 1H), 8.12 (d, *J* = 7.9 Hz, 2H), 7.55 (t, *J* = 6.6 Hz, 4H), 7.24 (d, *J* = 8.4 Hz, 2H).

^{13}C NMR (101 MHz, CDCl$_3$) δ 185.24, 147.89, 131.22, 130.76, 129.76, 128.81 – 128.62 (m), 128.19, 127.16, 126.30, 121.53.

Characterization of **110b**

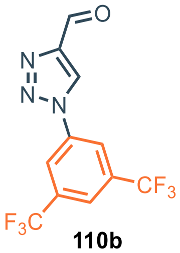

110b

White solid obtained with 77% yield

^{1}H NMR (400 MHz, CDCl$_3$) δ 10.25 (s, 1H), 8.72 (s, 1H), 8.32 (s, 2H), 8.04 (s, 1H).

^{13}C NMR (101 MHz, CDCl$_3$) δ 184.6, 148.8, 137.4, 134.2 (q, J = 34.6 Hz), 123.9, 123.5, 123.5 (dt, J = 7.4, 3.7 Hz), 121.3 – 120.9 (m).

^{19}F NMR (376 MHz, CDCl$_3$) δ -63.10 (s).

Characterization of **110c**

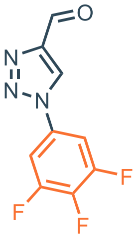

110c

Yellow solid obtained with 58% yield

^{1}H NMR (400 MHz, CDCl$_3$) δ 10.22 (s, 1H), 8.48 (s, 1H), 7.57 – 7.46 (m, 2H).

^{13}C NMR (151 MHz, CDCl$_3$) δ 184.9, 150.6 (m), 147.6, 139.3 (m), 131.6 (m), 126.5, 109.5 – 104.0 (m).

^{19}F NMR (376 MHz, CDCl$_3$) δ -129.0 (d, J = 20.6 Hz, 2F), -156.6 (t, J = 20.6 Hz, 1F)

Characterization of **110d**

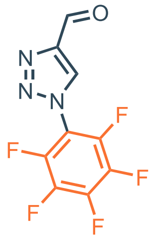

110d

White solid obtained with 75% yield

^{1}H NMR (400 MHz, CDCl$_3$) δ 10.26 (s, 1H), 8.40 (s, 1H).

^{13}C NMR (101 MHz, CDCl$_3$) δ 184.1, 147.6, 142.9 (dtt, *J* = 261.0 Hz, 26.5 Hz, 4.27 Hz), 142.4 (ddq, *J* = 258.6 Hz, 13.3 Hz, 4,12 Hz), 139.8 – 136.6 (m, J = 256.8 Hz), 128.3, 112.1 (dt, *J* = 14.2 Hz, 4.4 Hz)

^{19}F NMR (376 MHz, CDCl$_3$) δ -143.42 – -146.17 (m, 2F), -147.87 (tt, J = 21.5, 2.9 Hz, 1F), -156.55 – -160.31 (m, 2F).

Characterization of **110e**

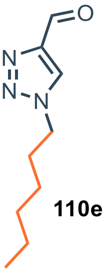

110e

Yellowish solid obtained with 80% yield

^{1}H NMR (600 MHz, CDCl$_3$) δ 10.21 (1H), 8.09 (d, *J* = 2.4 Hz, 1H), 4.42 (t, *J* = 7.1 Hz, 2H), 1.94 (p, *J* = 7.3 Hz, 2H), 1.37 – 1.26 (m, 6H), 0.87 (t, *J* = 6.1 Hz, 3H).

^{13}C NMR (151 MHz, CDCl$_3$) δ 185.19 (d, *J* = 2.9 Hz), 147.78, 125.17, 50.85, 31.07, 30.08, 26.05, 22.39, 13.92.

Characterization of **106a**

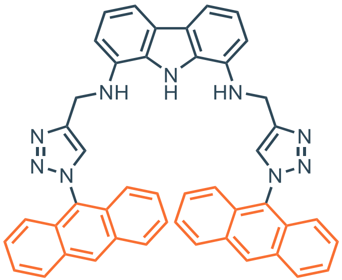

106a

^{1}H NMR (400 MHz, DMSO-d$_6$) δ 10.79 (s, 1H), 8.94 (s, 2H), 8.66 (s, 2H), 8.25 (d, *J* = 8.4 Hz, 4H), 7.64–7.50 (m, 8H), 7.43 (d, *J* = 7.8 Hz, 2H), 7.16 (d, *J* = 8.7 Hz, 4H), 7.05 (t, *J* = 7.7 Hz, 2H), 6.82 (d, *J* = 7.6 Hz, 2H), 5.72 (t, *J* = 5.8 Hz, 2H), 4.78 (d, *J* = 5.5 Hz, 4H).

^{13}C NMR (151 MHz, DMSO-d$_6$) δ 145.7, 134.0, 130.7, 129.7, 128.8, 128.5, 128.2, 128.2, 127.7, 127.6, 126.1, 123.1, 121.6, 119.6, 109.6, 106.0, 40.1.

HRMS (ESI$^+$): m/z 712.2904 [M+H]$^+$

Characterization of **106b**

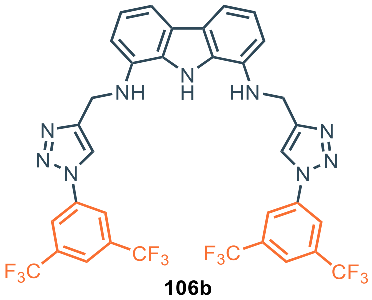

106b

^{1}H NMR (400 MHz, DMSO-d$_6$) δ 10.70 (s, 1H), 9.17 (s, 2H), 8.63 (s, 4H), 8.25 (s, 2H), 7.37 (d, *J* = 7.7 Hz, 2H), 6.98 (t, *J* = 7.7 Hz, 2H), 6.72 (d, *J* = 7.7 Hz, 2H), 5.52 (t, *J* = 5.5 Hz, 2H), 4.65 (d, *J* = 5.5 Hz, 4H).

^{13}C NMR (151 MHz, DMSO-d$_6$) δ 147.2, 137.9, 133.8, 131.9 (q, *J* = 33.7 Hz), 128.5, 123.0, 122.8 (q, *J* = 273,5 Hz) 122.1, 121.9 (hept, *J* = 3.7 Hz), 120.6 (q, *J* = 3.3 Hz), 119.6, 109.6, 105.5, 38.9

^{19}F NMR (376 MHz, DMSO-d$_6$): -61.4 Hz

HRMS (ESI$^+$): m/z 784.1763 [M+H]$^+$

Characterization of **106c**

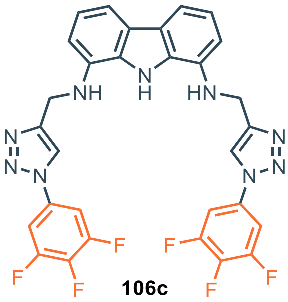

106c

^{1}H NMR (400 MHz, DMSO-d$_6$) δ 10.71 (s, 1H), 8.86 (s, 2H), 8.14–7.96 (m, 4H), 7.36 (d, *J* = 7.7 Hz, 2H), 6.97 (t, *J* = 7.7 Hz, 2H), 6.69 (d, *J* = 7.7 Hz, 2H), 5.53 (t, *J* = 5.4 Hz, 2H), 4.61 (d, *J* = 5.4 Hz, 4H). **^{13}C NMR (151 MHz, DMSO-d$_6$)** δ 151.2 (ddd, *J* = 248.2, 10.4, 4.7 Hz), 147.4, 140.2 – 137.9 (m), 134.2, 133.1 – 132.3 (m), 129.0, 123.5, 122.3, 120.1, 110.0, 106.1 (m), 105.9 (m), 39.3.

^{19}F NMR (376 MHz, DMSO-d$_6$): δ -132.3 (d, *J* = 22.0 Hz, 2F), -161.2 (t, *J* = 22.0 Hz, 1F).

HRMS (ESI$^+$): m/z 620.1715 [M+H]$^+$

Characterization of **106d**

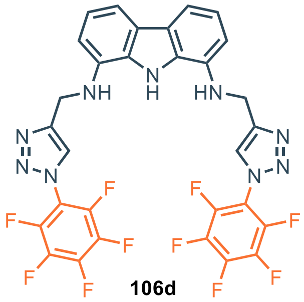

106d

^{1}H NMR (600 MHz, DMSO-d$_6$) δ 10.69 (s, 1H), 8.58 (s, 2H), 7.37 (d, *J* = 7.8 Hz, 2H), 6.98 (t, *J* = 7.7 Hz, 2H), 6.72 (d, *J* = 7.6 Hz, 2H), 5.62 (t, *J* = 5.8 Hz, 2H), 4.66 (d, *J* = 5.8 Hz, 4H).

^{13}C NMR (151 MHz, DMSO-d$_6$) δ 146.2, 142.9 – 141.2 (m), 142.5 – 140.8 (m), 138.4 – 136.7 (m), 133.7, 128.6, 126.2, 123.1, 119.6, 112.7 (m), 109.7, 105.6, 38.5

^{19}F NMR (376 MHz, DMSO-d$_6$): -147.3 (m, 2F), -151.7 (t, 1F), -161.1 (m, 2F)

HRMS (ESI$^+$): m/z 692.1336 [M+H]$^+$

Characterization of **106e**

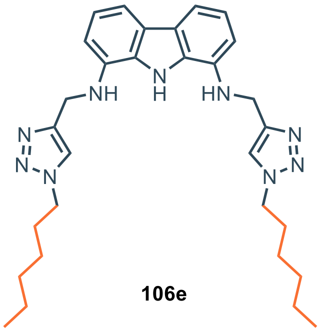

106e

^{1}H NMR (600 MHz, DMSO-d$_6$) δ 10.65 (s, 1H), 8.06 (s, 2H), 7.34 (d, *J* = 7.8 Hz, 2H), 6.95 (t, *J* = 7.7 Hz, 2H), 6.65 (d, *J* = 7.6 Hz, 2H), 5.35 (t, *J* = 5.6 Hz, 2H), 4.49 (d, *J* = 5.6 Hz, 4H), 4.32 (t, *J* = 7.1 Hz, 4H), 1.78 (p, *J* = 7.2 Hz, 4H), 1.28 – 1.17 (m, 13H), 0.86 – 0.81 (m, 6H).

^{13}C NMR (151 MHz, DMSO-d$_6$) δ 145.5, 134.4, 128.9, 123.5, 123.4, 120.0, 109.8, 105.8, 49.7, 39.4, 31.1, 30.2, 26.0, 22.4, 14.3

HRMS (ESI$^+$): m/z 528.3534 [M+H]$^+$

NMR titrations – experimental details

2 mL of a DMSO-d_6/0.5% water stock solution of the compound **106a-e** (host) were prepared ([H] = 1 mM). From this solution, 1 mL was taken to prepare the solution of the titrating agent (guest; tetrabutylammonium chloride); in this way the dilution effect is avoided. 0.5 mL of the solution of the host were put into an NMR tube, which was capped with a septum, and the 1H NMR spectrum was recorded. Subsequently, an aliquot of the solution of the guest was added with a proper microsyringe through the septum; the solution was then homogenised and the spectrum recorded. This process was repeated several times. For each ^{1}H NMR titration, the signal of the proton of the carbazole NH group was monitored for changes in chemical shift, which provided several data sets that were employed in the determination of the association constants Ka. The fitting was performed with Bindfit.[69] When possible, data were fitted satisfactorily to the 1:1 (H:G) binding model, H being the receptor and G the anion (chloride).

Fitting binding isotherms

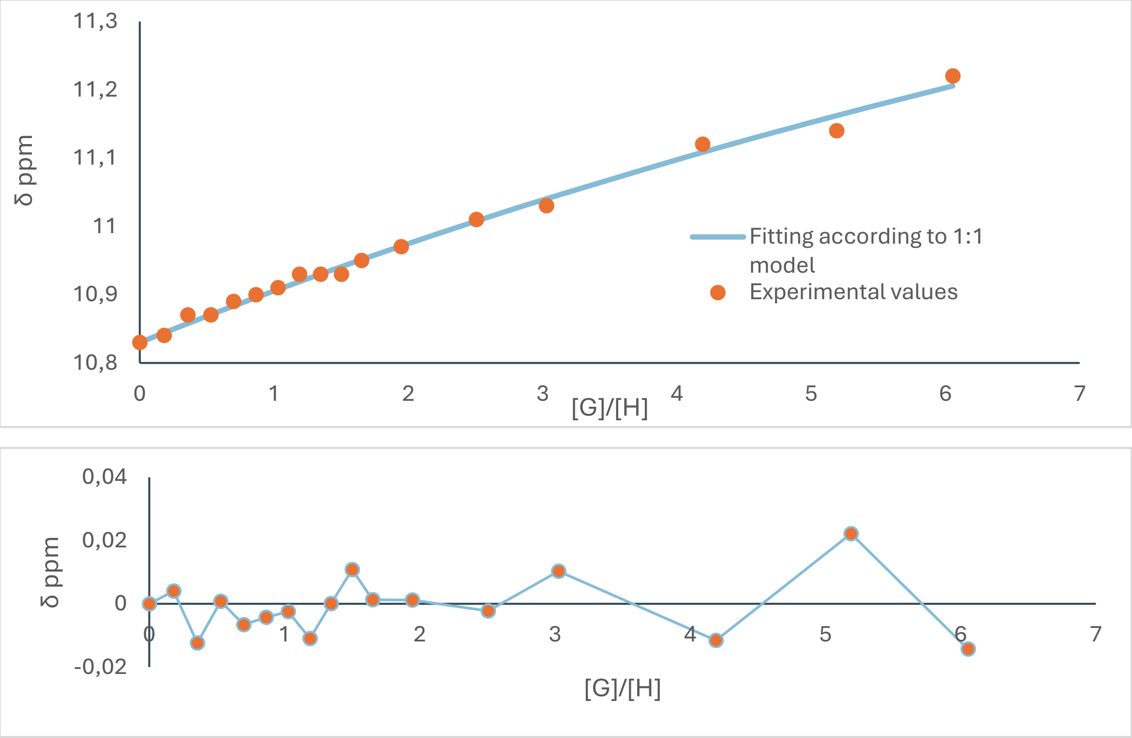

Figure S1. Binding isotherms for titration (^{1}H NMR, 298 K) of **106a** with TBACl in DMSO-d_6 + 0.5% H_2O (up) and the corresponding residual plots (down).

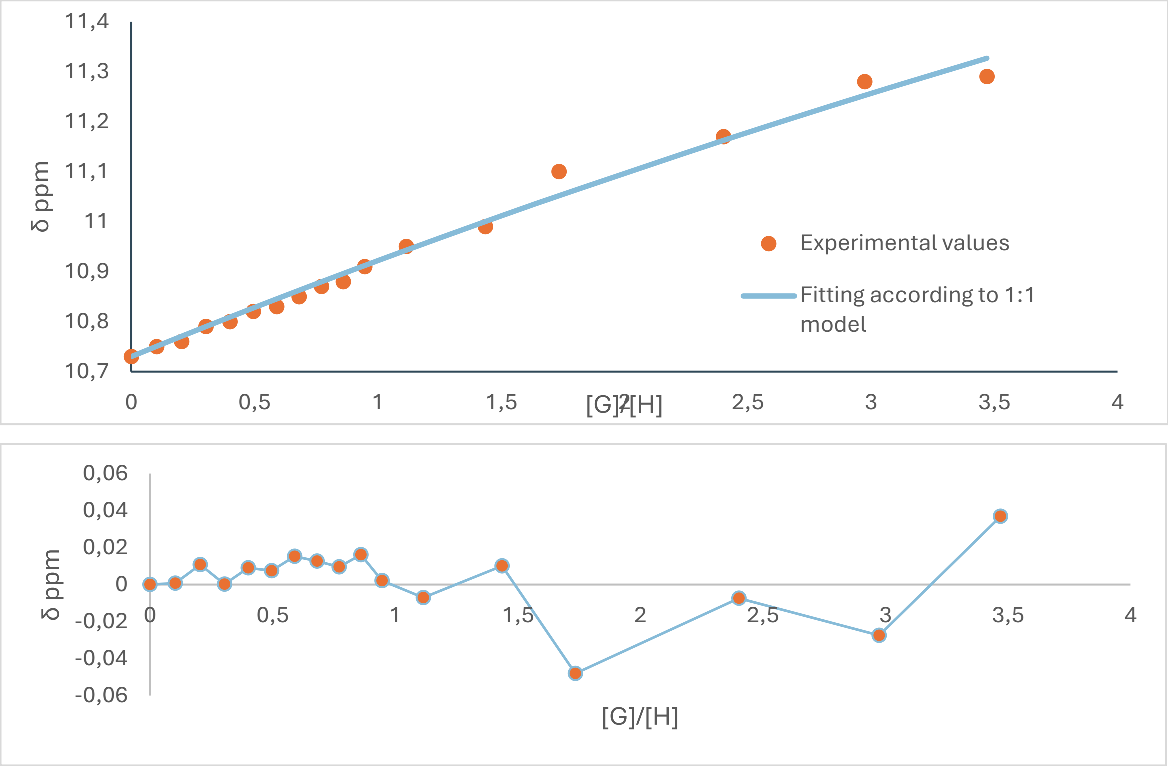

Figure S2. Binding isotherms for titration (^{1}H NMR, 298 K) of **106b** with TBACl in DMSO-d_6 + 0.5% H_2O (up) and the corresponding residual plots (down).

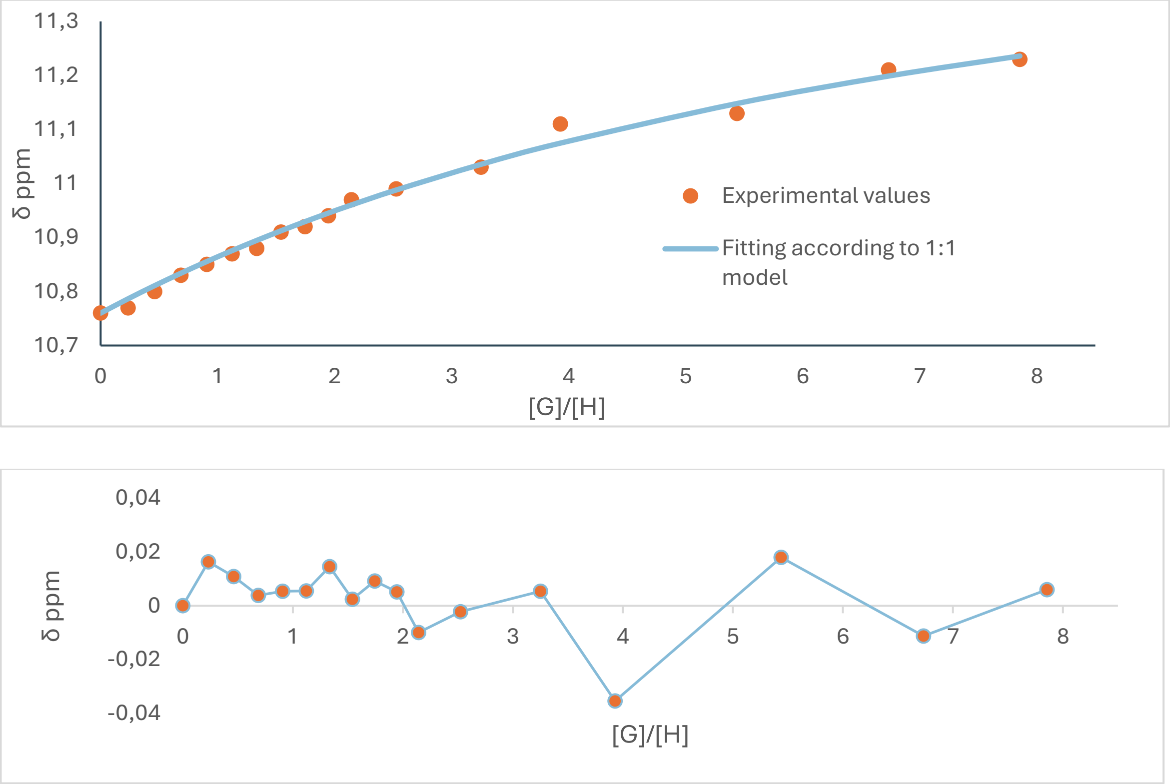

Figure S3. Binding isotherms for titration (^{1}H NMR, 298 K) of **106c** with TBACl in DMSO-d_6 + 0.5% H_2O (up) and the corresponding residual plots (down).

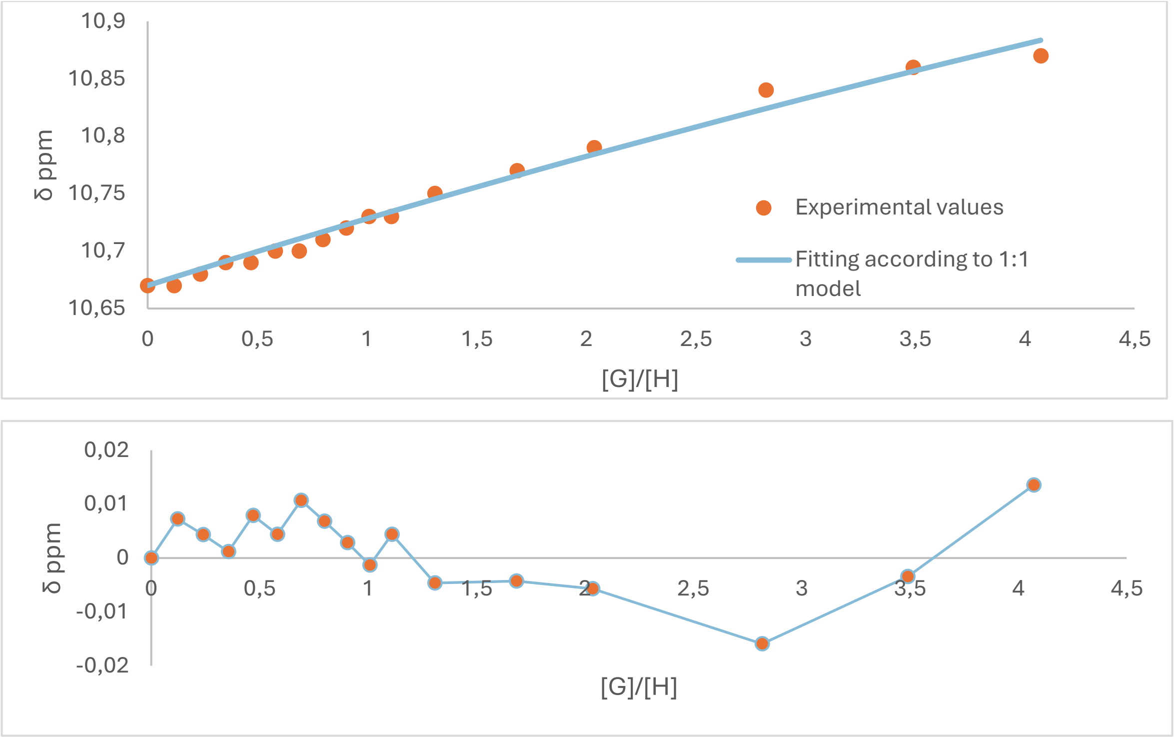

Figure S4. Binding isotherms for titration (^{1}H NMR, 298 K) of **106d** with TBACl in DMSO-d$_6$ + 0.5% H_2O (up) and the corresponding residual plots (down).

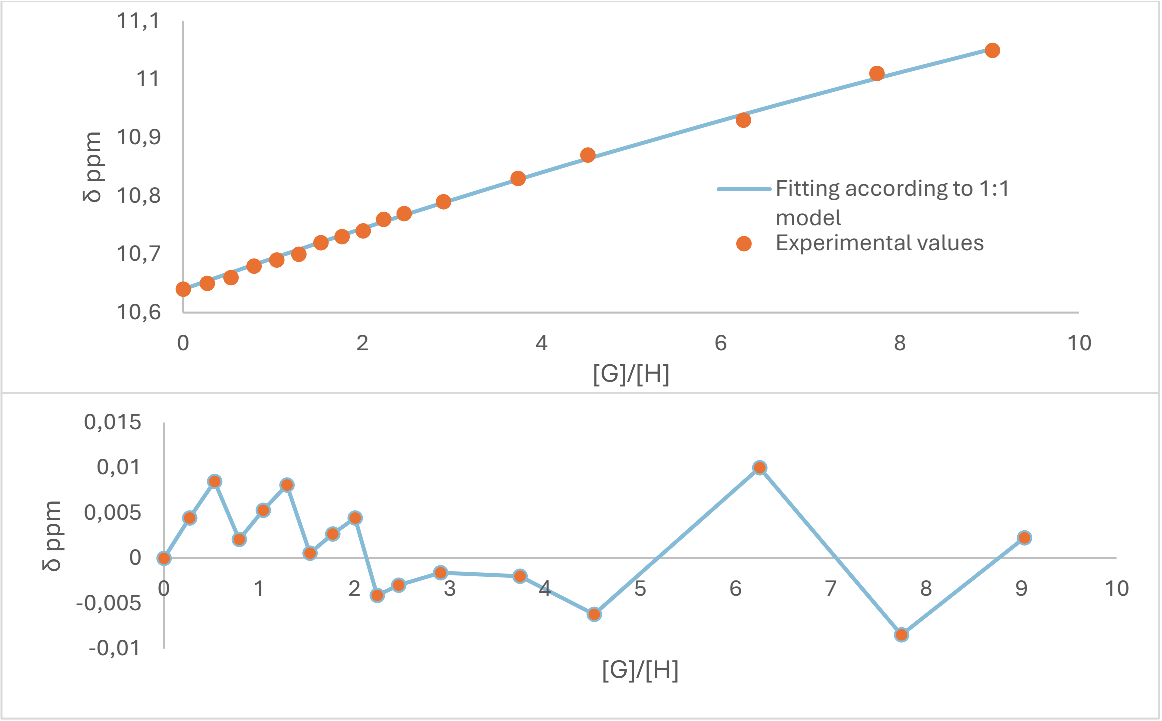

Figure S5. Binding isotherms for titration (^{1}H NMR, 298 K) of **106e** with TBACl in DMSO-d$_6$ + 0.5% H_2O (up) and the corresponding residual plots (down).

Application of all-cis-fluorinated cyclohexanes in anion-binding catalysis

Synthesis and supramolecular properties of all-cis-fluorinated cyclohexanes – an overview

All-cis hexafluorocyclohexane (**115**) has emerged as a promising platform for the noncovalent binding of electron-rich species (e.g. anions), due to its peculiar facial polarization. from the unique arrangement of all six fluorine atoms on one face of the cyclohexane ring, generating a strong dipole moment; in fact, compound **115** is regarded as the most polar organic molecule reported to date (Figure 38a). The first synthetic route to compound **115** was developed by O'Hagan and colleagues,[73] but it involved a multistep, labor-intensive process, which limited experimental investigations of its properties; for this reason, the study of the peculiar properties of this facially-polarised scaffold remained elusive for a lot of time, while most of the study focused on theoretical calculation.[74] A major breakthrough came in 2018, when Glorius and coworkers introduced a one-step, stereoselective hydrogenation of fluoroarenes using ruthenium–NHC catalysts, enabling access to a range of cis-fluorinated cyclohexanes, including bi-, tri-, tetra-, penta- and hexafluorinated derivatives (Figure 38b).[75] That same year, von Delius and co-workers provided the first experimental evidence of anion binding by compound **115**, showing that both **115** and its methoxy derivative **116** could bind chloride ions in solution and in the solid state with moderate affinity (K_a = 400 M^{-1} and 170 M^{-1} in acetone, respectively) (Figure 38c).[76]

Later, the same group repurposed this highly polar scaffold to drive living supramolecular polymerization, using the dipole moment of all-cis fluorocyclohexanes to form kinetically trapped monomers that assemble into uniform, seed-initiated nanofibers. This approach enabled precise control over fiber length and the formation of supramolecular block copolymers, expanding the utility of this motif from anion recognition to programmable materials assembly.[77]

---

[73] N. S. Keddie, A. Z. Slawin, T. Lebl, D. Philp and D. O'Hagan, *Nat. Chem.*, **2015**, *7*, 483-488

[74] (a) B. E. Ziegler, M. Lecours, R. A. Marta, J. Featherstone, E. Fillion, W. S. Hopkins, V. Steinmetz, N. S. Keddie, D. O'Hagan, T. B. McMahon, *J. Am. Chem. Soc.,* **2016**, *138*, 7460-7463; (b) S. Md Pratik, A. Nijamudheen, A. Datta, *ChemPhysChem*, **2016**, *17*, 2373-2381; (c) W.-M. Sun, B.-L. Ni, D. Wu, J.-M. Lan, C.-Y. Li, Y. Li, Z.-R. Li, *Organometallics*, **2017**, *35*, 3352-3359

[75] M. P. Wiesenfeldt, Z. Nairoukh, W. Li., F. Glorious, *Science*, **2017**, *357*, 908-912

[76] O. Shyshov, K. A. Siewerth, M. von Delius, *Chem. Commun.*, **2018**, *54*, 4353-4355

[77] O. Shyshov, S. V. Haridas, L. Pesce, H. Qi, A. Gardin, D. Bochicchio, U. Kaiser, G. M. Pavan, M. von Delius, *Nat. Commun.*, **2021**, *12*, 3134

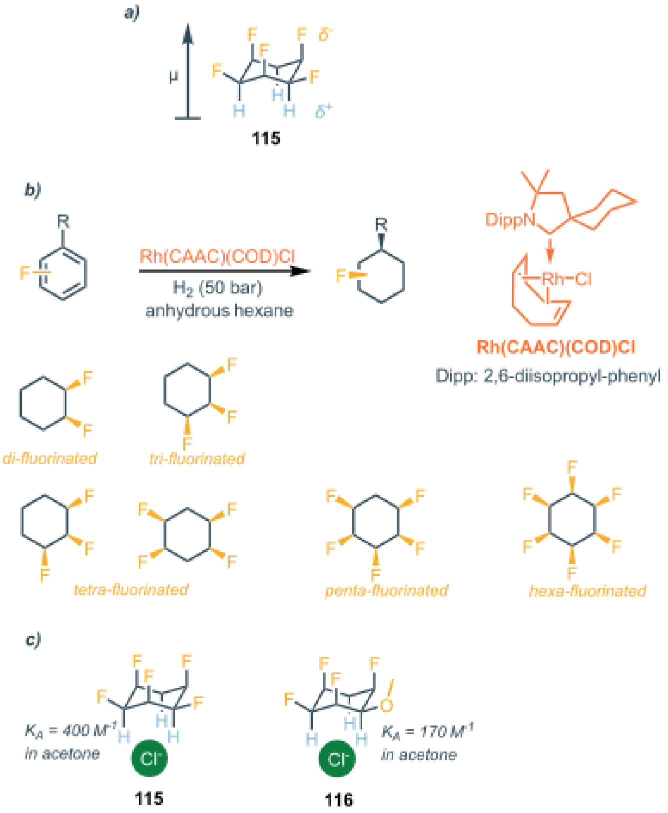

Figure 38. a) Facial polarization of x; b) One-step synthesis of x proposed by Glorious and coworkers; c) Binding properties of x and x towards Cl- in solution

Subsequent studies focused on structure–property relationships, revealing that the three axial fluorine atoms are primarily responsible for the facial polarization. Moreover, the introduction of mono-, bi-, and tri-alkyl substituents was shown to provide tunability and expanded the scope of potential applications.[78] In this regard, in 2024 von Delius and coworkers reported the synthesis and evaluation of supramolecular properties of all-cis-2,4,6-trifluorocyclohexane-1,3,5-triol.[79] Functionalization of the triol core with nonpolar alkyl chains (e.g., dodecanoyl esters) yielded gelators with fibrous morphologies. Additionally, a tripodal architecture based on this triol demonstrated halide binding via synergistic hydrogen/halogen bonding, with a binding affinity of K_A = 140 M^{-1} in dichloromethane (Figure 39).

---

[78] T. J. Poskin, B. A. Piscelli, K. Yoshida, D. B. Cordes, A. M. Z. Slawin, R. A. Cormanich, S. Yamada, D. O'Hagan, *Chem. Commun.*, **2022**, *58*, 7968-7971

[79] S. V. Haridas, M. von Delius, *Chem. Commun.*, **2024**, *60*, 606

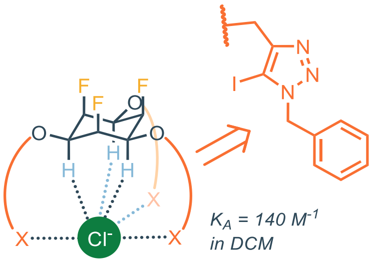

Figure 39. all-cis-2,4,6-trifluorocyclohexane-1,3,5-triol derivative and binding properties towards Cl⁻ in solution

Despite these advances, the application of fluorinated cyclohexanes in catalysis remains unexplored, representing an exciting frontier for future research.

Aim of the project

The purpose of the current project is to explore the applicability of all-cis-fluorinated frameworks in anion-binding catalysis, taking advantage of the peculiar facial polarization possessed from this motif. Nucleophilic aromatic substitution reactions (S_NAr) are a key tool in the medicinal chemist's arsenal. They enable the functionalization of electron-deficient aromatic systems, common structural motifs in many pharmaceuticals, allowing the incorporation of diverse groups critical for biological activity. They are especially valuable for the functionalization of electron-deficient aromatic systems,[80] which are frequently found in drug-like scaffolds such as pyridines, quinolines,[81] and fluorinated aromatics. These transformations are commonly used for the late-stage modification of complex molecules, allowing medicinal chemists to rapidly generate analogs and optimize biological activity through structure–activity relationship (SAR) studies.

One of the major advantages of S_NAr chemistry is that it can be performed without the use of transition-metal catalysts, which is increasingly important in pharmaceutical manufacturing due to the cost, toxicity, and regulatory concerns associated with metal residues. Moreover, these reactions are compatible with a broad range of nucleophiles (e.g., amines, alkoxides, thiols), making them particularly useful for introducing pharmacophores or modifying bioactive cores.

However, despite these strengths, S_NAr reactions also present notable limitations. First, they are generally restricted to highly activated aromatic rings,[82] typically those bearing strong electron-withdrawing groups such as nitro or trifluoromethyl substituents, limiting their applicability to more

---

[80] F. Terrier, *Chem. Rev.*, **1982**, *82*, 77-152

[81] J. Miller, *Aromatic Nucleophilic Substitution*; Elsevier, Amsterdam, **1968**, pp-140-169

[82] F. Terrier, *Nuclear Aromatic Displacement: The Influence of the Nitro Group*; VCH, New York, **1991**

diverse or electron-rich systems. Furthermore, the reactions often require elevated temperatures (≥100 °C)[83] and prolonged reaction times, especially when working with sterically hindered or poorly reactive substrates, which can compromise selectivity and increase energy costs. These harsh conditions may also lead to undesirable side reactions, such as elimination or degradation of sensitive functional groups. For these reasons, the development of new protocols which would enable S_NAr reactions with broader scope and under milder conditions is highly attractive.

In a nucleophilic aromatic substitution, a Meisenheimer intermediate (or σ intermediate) is formed upon the nucleophile's attack on the aromatic ring, which represents the rate-determining step of the reaction (Figure 40a).[84] The development of a catalyst which could noncovalently bind the Meisenheimer intermediate could be a good strategy to allow for its stabilization, thus promoting the reaction.

In particular, we speculated that the three axial pre-organized arrangement of hydrogens could be optimal for binding aromatic anions, particularly those where the negative charge is delocalized in ortho and para positions relative to a substituent, as per the Meisenheimer intermediate (Figure 40b).

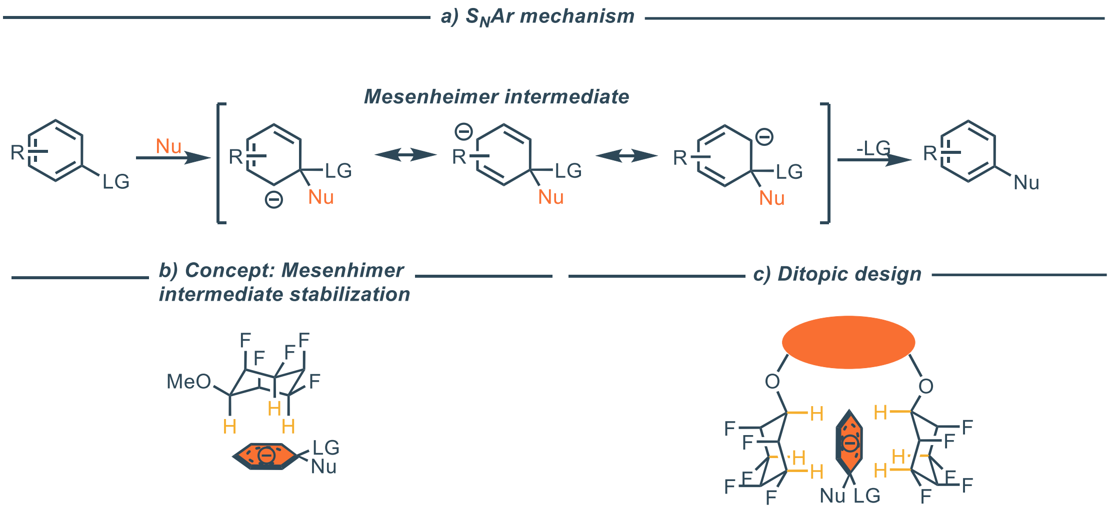

Figure40. a) General mechanism of the S_NAr reaction; b) The three axial hydrogen atoms could stabilize aromatic anions; c) Ditopic design would enable multiple presentation of the fluorinated cyclohexane moiety

We further hypothesized that presenting the fluorinated cyclohexane moiety in a divalent manner using an appropriate platform could facilitate binding of the intermediate on both of its faces, offering additional stabilization (Figure 40c). To achieve this, a terephthalate derivative of the fluorinated cyclohexane was synthesized and thoroughly characterized. Moreover, preliminary experimental

---

[83] C. F. Bernasconi, *J. Am. Chem. Soc.*, **1968**, *90*, 4982–4988

[84] G. A. Artamkina, M. P. Egorov, I. P. Beletskaya, *Chem. Rev.* **1982**, *82*, 427–459

results showed that the designed displays effective rate enhancement in a model reaction (nucleophilic aromatic substitution of morpholine on fluoropyridine).

Results and discussion

Design and synthesis and characterization of the catalyst

The catalyst was designed to present the fluorinated cylohexanes motifs in a divalent fashion. For this reason, a cleft-type structure was chosen, in order to perform binding of the anion with a sandwich-like orientation. The terephtalic acid motif was chosen, for its peculiar di substitution in para position and the possibility of fuctionalising it with the all-cis-2,3,4,5,6-trifluorocyclohexane-1-ol via ester coupling.

All-cis-2,3,4,5,6-trifluorocyclohexane-1-ol **117** was prepared according to literature procedures,[74,75] through a stereoselective hydrogenation of fluorinated anisole **118**. The fluorinated cyclohexanes-methyl ether **116** is then deprotected with BuSH and $AlCl_3$ to afford the pure fluorinated cyclohexanol (Scheme 1a). The catalyst was prepared reacting **117** with terephtaloyl chloride **119**; the pure product **120** easily crashes out of the reaction mixture and is recovered pure in almost quantitative yield upon washings with water (Scheme 1b).

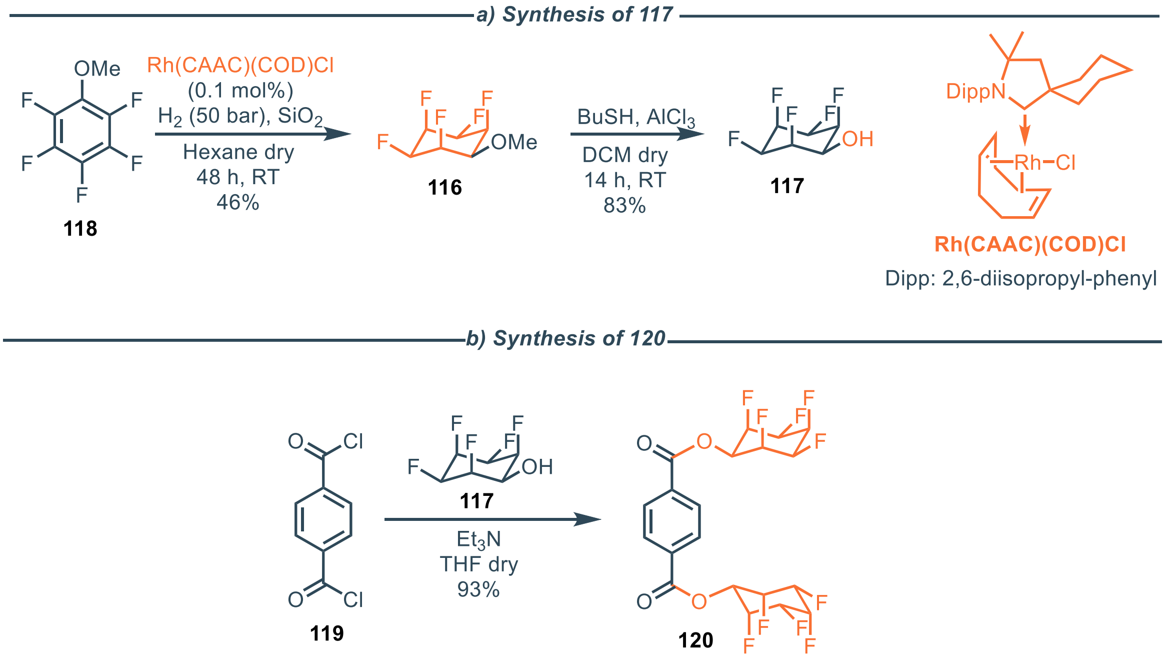

Scheme 1. Synthesis of all-cis-2,3,4,5,6-pentalfluorocyclohexan-1-ol (a) and terephthalate-based catalyst **112** (b)

Single-crystal X-ray diffraction (SCXRD) analysis of compound **120**, obtained by slow cooling of a supersaturated acetone solution, revealed noteworthy structural features. In the solid state, compound **120** adopts a planar conformation, with its two cyclohexane rings aligned in a linear arrangement and the fluorine atoms oriented on opposite faces of the molecular plane. This geometry likely reflects the guest-free conformation that minimizes electrostatic repulsion and favors self-aggregation (Figure 41a). Examination of the crystal packing shows the presence of intermolecular hydrogen-bonding interactions, specifically between electron-rich fluorine atoms of one molecule and polarized cyclohexyl C–H donors of neighboring molecules. Additionally, a co-crystallized acetone molecule engages in hydrogen bonding with C–H groups of the cyclohexane scaffold, further stabilizing the lattice (Figure 41b).

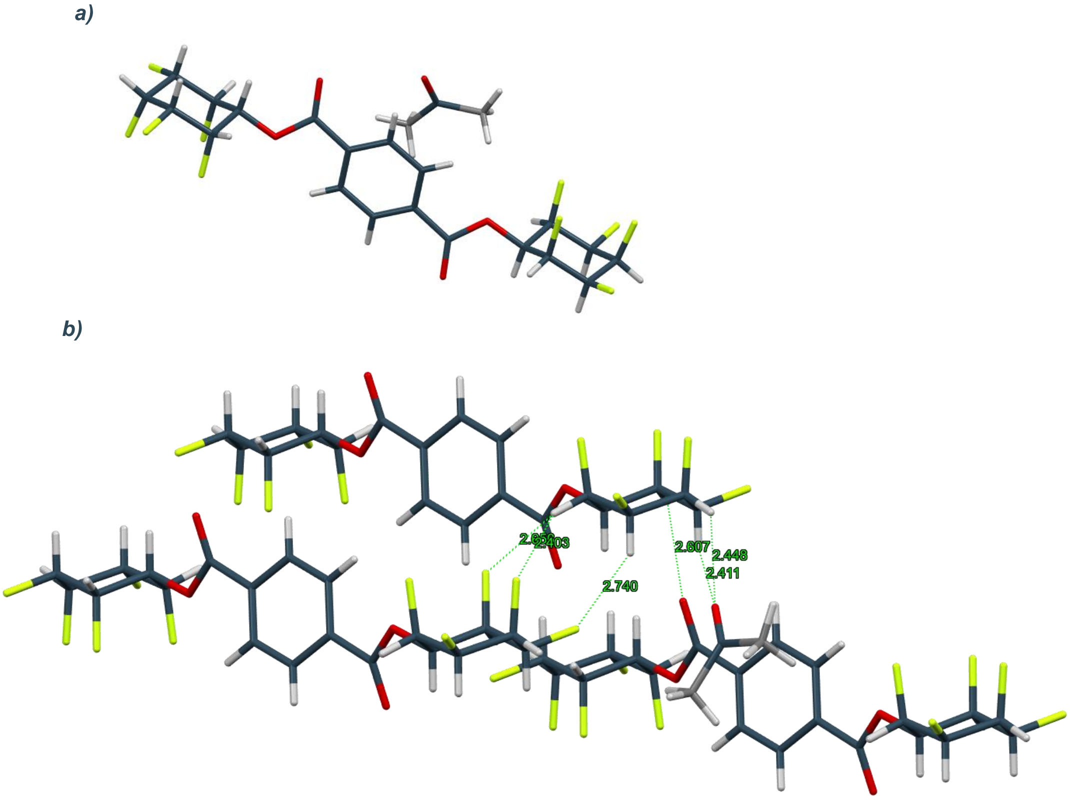

Figure 41. Crystal structure of **6** (a) and its paking mode (b)

Following the solid-state analysis, the binding properties of compound **6** toward aromatic anions in solution were investigated. To this end, NMR titration experiments were conducted using tetrabutylammonium phenolate (TBA-PhO$^-$) as a model substrate. Phenolate was selected as a representative surrogate of a Meisenheimer intermediate, due to its ability to delocalize negative charge over the ortho- and para-positions of the aromatic ring.

TBA-phenolate was synthesized by deprotonating phenol with tetrabutylammonium hydroxide in methanol, leading to precipitation of the product from the reaction mixture.[85] The resulting solid was isolated by filtration. Notably, the TBA-phenolate product retains approximately 33% methanol content, as determined by mass balance, and cannot be fully desolvated even under high vacuum and heating. In addition, the material is strongly hygroscopic and was therefore handled and stored under inert atmosphere in a glovebox.

This solid was used directly in titration experiments, accounting for its residual solvent content. In a preliminary qualitative test, the addition of 3 equivalents of TBA-phenolate to a solution of compound **120** in CD_3CN resulted in a noticeable upfield shift of the aromatic protons of compound **120**, along with changes in the multiplicity of the cyclohexane ring protons, suggesting an interaction. Simultaneously, the aromatic proton of the phenolate exhibited a downfield shift, consistent with the formation of a supramolecular complex (Figure 42).

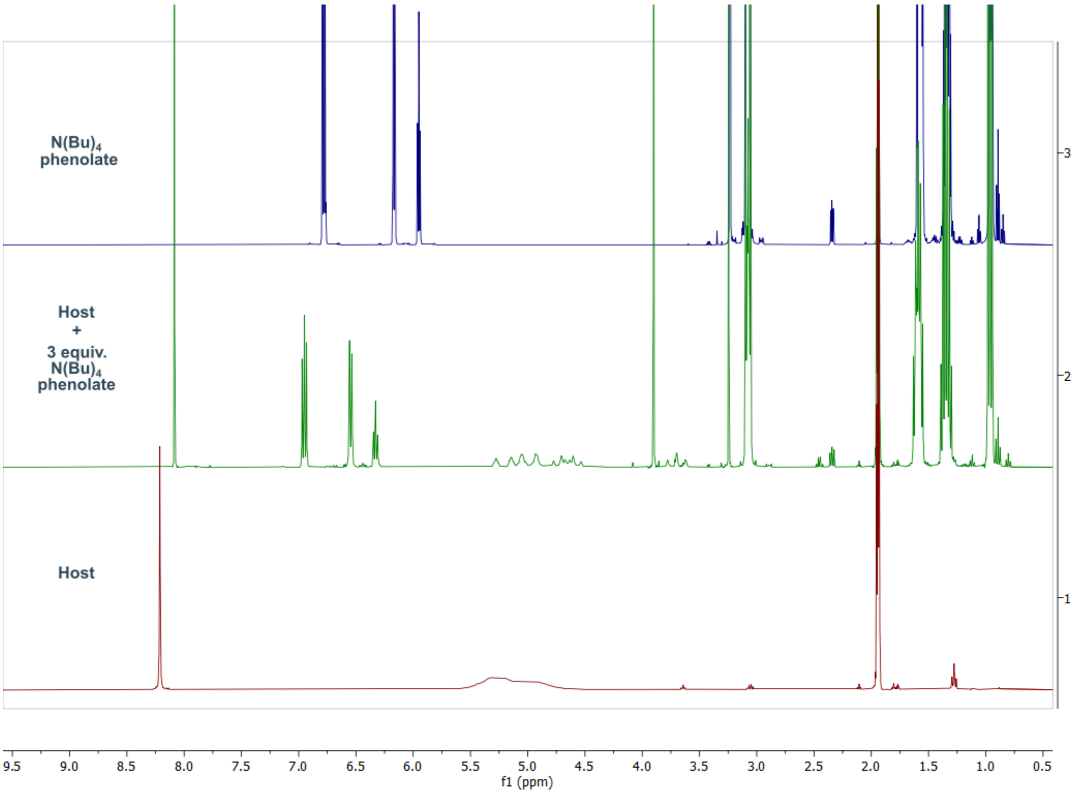

Figure 42. Stacked NMR spectra of the host **120** (low), NBu4 phenolate (up), and host + 3 equivalents of NBu_4 phenolate (middle) in CD_3CN. Final concentration 10 mM

---

[85] R. J Mayer, M. Breugst, N. Hampel, A. R. Ofial, H. Mayr, *J. Org. Chem.*, **2019**, *84*, 8837-8858

Encouraged by the preliminary findings, a full ^{1}H NMR titration was carried out in acetone-d$_6$ to quantitatively investigate the interaction between compound **120** and TBA-phenolate. The stacked NMR spectra from the titration experiment are shown in Figure 43 Upon incremental addition of the guest, the aromatic protons of the phenolate anion exhibit a slight downfield shift (from ~6.0 to 7.0 ppm), which initially suggests complex formation under a slow exchange regime on the NMR timescale. However, the aromatic proton signal of compound **120**, initially observed at 8.3 ppm, progressively disappears, while a new peak emerges at 8.0 ppm. This behavior is characteristic of fast exchange between free and complexed species. At a 1:2 host- guest ratio, the original 8.3 ppm signal is no longer detectable, and the 8.0 ppm resonance becomes dominant, suggesting full conversion. As expected, the aliphatic protons of the tetrabutylammonium (TBA) cation remain unchanged, confirming that the interaction is confined to the phenolate anion and compound **120**.

However, this spectral evolution also raised the possibility of chemical reactivity rather than mere complexation. Specifically, it was hypothesized that the phenolate anion may undergo nucleophilic attack on the pentafluorocyclohexyl ester moiety of compound **120**, forming a reactive intermediate. This intermediate could then be further attacked by residual methanol present in the sample, ultimately yielding methyl terephthalate as the final product.

This hypothesis is supported by TLC analysis performed directly on the titration NMR sample, which revealed a new spot distinct from the original host (Rf = 0.66, Figure 44 up). Furthermore, ^{1}H NMR comparison between the titration mixture (after addition of 30 equivalents of guest) and the material recovered from preparative TLC (pTLC) in Acetone-d$_6$ showed identical spectral features. The signal at 8.0 ppm was thus attributed to dimethyl terephthalate, together with the signal at 3.8 ppm from the methyl esters (Figure 44 down).

Figure 43 Stacked NMR spectra obtained by addition of TBA phenolate solution (in CD_3CN) to a solution of compound **120** in Acetone-d_6, using 1,2,4,5-tetrafluorobenzene as internal standard. Final concentration 5 mM

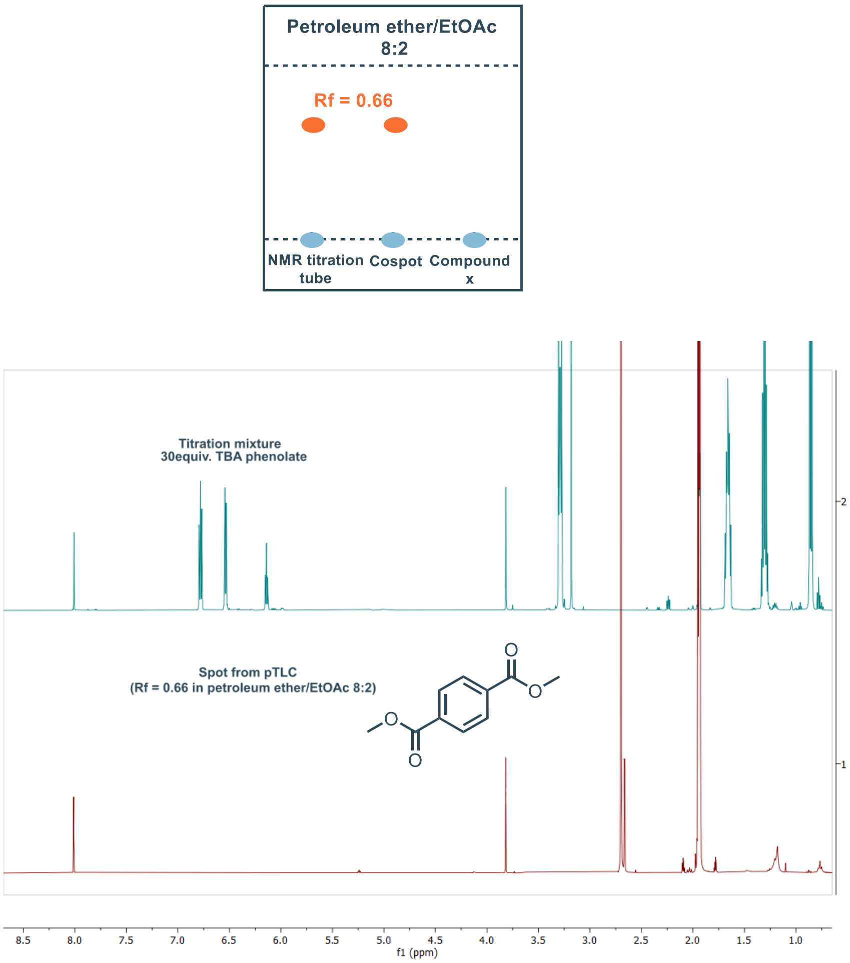

Figure 44. up: TLC analysis revealed the formation of a new spot; down: NMR stacking revealed the formation of dimethyl terephthalate (NMR spectra recorded in Acetone-d_6).

Although the attempt to determine the binding properties of compound **120** toward TBA-phenolate was unsuccessful, likely due to competing reactivity, we proceeded to investigate its potential catalytic activity in a series of nucleophilic aromatic substitution (S_NAr) reactions.

Catalysis explorative experiments

Given the high reactivity of compound **120** toward nucleophilic displacement, the selection of both substrates and reaction conditions for the targeted S_NAr reactions must be carefully considered. Several key criteria were considered:

- A weak nucleophile is required to avoid transesterification of the catalyst;
- Highly basic conditions are to be avoided, as they may promote hydrolysis of the catalyst;
- Heteroarenes are preferred as electrophilic substrates due to their enhanced susceptibility to S_NAr, stemming from their ability to stabilize the developing negative charge in the Meisenheimer intermediate;

- Where possible, commercially available starting materials are selected to ensure practicality and reproducibility;
- The chosen reaction should either fail or proceed inefficiently in the absence of the catalyst, allowing the catalytic effect to be clearly demonstrated;
- Ideally, the reaction should be carried out at room temperature (RT), where supramolecular interactions are typically stronger and more effective in modulating reactivity.

With these criteria in mind, the nucleophilic aromatic substitution on 2-fluoro-pyridine using morpholine as nucleophile was selected as a feasible transformation. 2-Fluoropyridine was selected as the aromatic core due to its higher reactivity compared to a non-heteroaromatic compound, although it still presents a significant challenge. Initially, both reactions were conducted under the conditions outlined below, in agreement with the literature.[86] The reaction conditions involve employing two different scavengers for the fluoride ions released during the re-aromatization process.

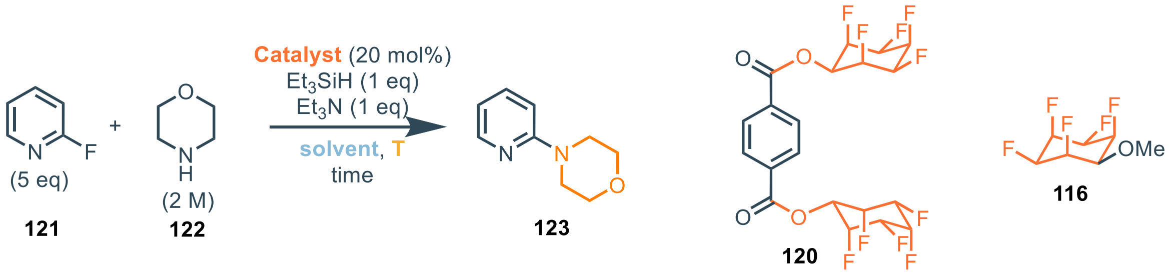

Scheme 2. Nucleophilic aromatic substitution of fluoropyridine **113** with morpholine **114**

We aimed to evaluate the reactivity at low temperatures, employing both the ditopic catalyst **120** and its monotopic analogue **116**. As summarized in Table 13, no product formation was observed at room temperature or at 30 °C with either catalyst, in both CD_3CN and benzene-d_6. Moreover, no detectable degradation of either the starting material or the catalysts was observed under these conditions.

Table 13: Optimization of the reaction conditions – experiments at RT and 30 °C

Entry	Solvent	T (°C)	Catalyst	Time	Ratio **122** : **123** [a]
1	CD_3CN	RT	112	24 h	100:0
2	CD_3CN	RT	108	24 h	100:0
3	CD_3CN	30 °C	112	24 h	100:0
4	CD_3CN	30 °C	108	24 h	100:0

---

[86] M. Otsuka, K. Endo, T. Shibata, *Chem. Commun.*, **2010**, *46*, 336-338

5	Benzene-d_6	RT	112	24 h	100:0
6	Benzene-d_6	RT	108	24 h	100:0
7	Benzene-d_6	30 °C	112	24 h	100:0
8	Benzene-d_6	30 °C	108	24 h	100:0

[a] : ratio of **122** : **123** determined via NMR analysis

To enhance reactivity, the reaction temperature in CD_3CN was increased. In an initial attempt under non-anhydrous conditions, elevating the temperature up to 70 °C resulted in minimal product formation, with no significant catalytic effect observed (Table 14, entries 1 and 2). Notably, repeating the same experiment under a nitrogen atmosphere led to a marked improvement in reaction rate, with a clear difference between the catalyzed and uncatalyzed reactions (Table 14, entries 3 and 4), reaching full conversion of the starting material after increasing the temperature to 70°C in presence of the catalyst. It is worth noting that these reactions were initially conducted at 50°C for 24 hours and analyzed by ^1H NMR. Subsequently, the temperature was increased to 60°C and analyzed after another 24 hours. The temperature was then further increased to 70°C for 24 hours and analyzed again. For this reasons, the ratios obtained from the NMR at 70°C do not represent the conversion of the starting material at that temperature within 24 hours, as some reactivity occurred at 60°C as well.

Table 14 Optimization of the reaction conditions – experiments at 50°C to 70°C

Entry	**Solvent**	**Catalyst**	**Ratio 122 : 123** [a]		
			24 h, 50°C	**+ 24 h, 60°C**	**+ 24 h, 70°C**
1	CD_3CN	---	100:0	99:1	96:4
2	CD_3CN	**112**	100:0	96:4	90:10
3	CD_3CN [b]	---	94:6	83:17	39:61
4	CD_3CN [b]	**112**	91:9	58:42	0:100
5	DMSO-d_6	---	96:4	78:22	60:40
6	DMSO-d_6	**112**	96:4	77:23	57:43

[a] : ratio of **122** : **123** determined via NMR analysis; [b] : reaction carried out with exclusion of moisture

Finally, as expected, DMSO proved to be a good solvent to perform the reaction under examination, even though no difference is noticeable between the catalysed and the blank reaction (Table 14, Entry 5 and 6). The results of the catalysis experiments are summarized in Figure 45.

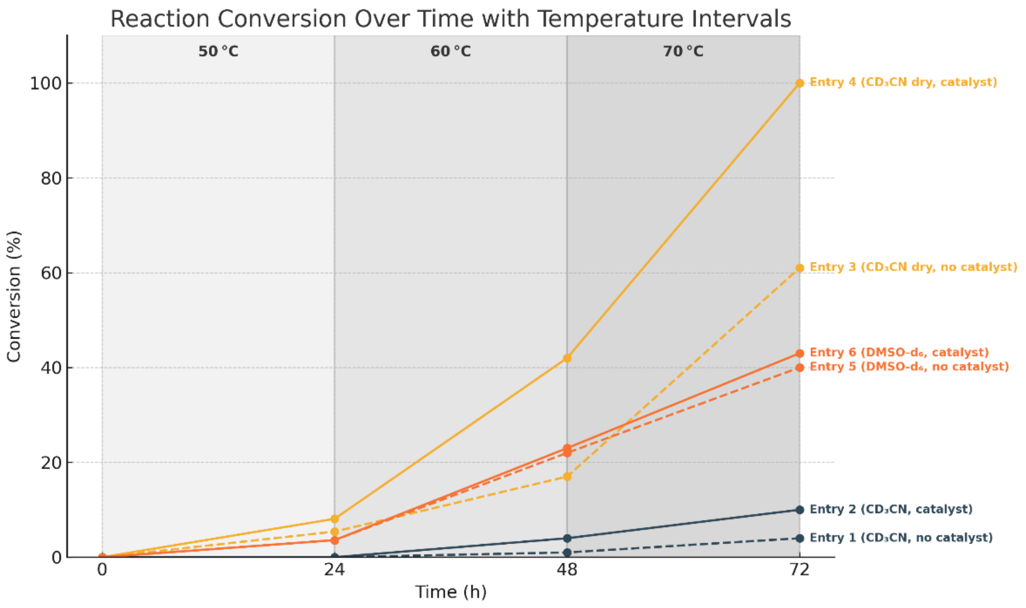

Figure 45. Time-dependent conversion profiles for various reaction conditions, highlighting the cumulative effect of stepwise temperature increase (50 °C → 60 °C → 70 °C) and the influence of catalyst and solvent on overall reactivity.

While these data offer preliminary insights, the results suggest that compound **6** may exert a genuine catalytic effect in the reaction under study. Further investigations will be necessary to elucidate the underlying mechanism of this proposed catalysis, alongside a more extensive optimization and scope evaluation of the reaction system.

Conclusions

In this work, the design, synthesis, and preliminary evaluation of the catalytic activity of compound **120**, a ditopic scaffold based on all-cis fluorinated cyclohexane motifs, were presented. The molecule was engineered to enable noncovalent binding of electron-rich aromatic anions through a facially polarized cleft-type architecture. Structural analysis via single-crystal X-ray diffraction revealed intermolecular hydrogen-bonding interactions in the solid state, while NMR studies suggested the possibility of supramolecular binding in solution. However, further analysis revealed that competing chemical reactivity may overshadow purely noncovalent interactions in some conditions, particularly in the presence of nucleophilic guests like phenolate.

Building on these findings, the potential catalytic behavior of compound **120** was investigated in a model nucleophilic aromatic substitution (S_NAr) reaction. Although no conversion was observed under mild conditions, Preliminary signs of catalytic activity were observed at elevated temperatures under strictly anhydrous conditions, suggesting a possible role for compound **120** in promoting the reaction. The results suggest a possible catalytic role for compound **120** especially when combined with solvent and moisture control.

Importantly, this chapter represents an exploratory study rather than a comprehensive mechanistic or scope-driven investigation. The main objective was to assess the feasibility of using fluorinated cyclohexane frameworks as supramolecular catalysts. The promising trends observed lay the groundwork for future research, including reaction scope exploration, catalyst fine-tuning, and detailed mechanistic studies.

Experimental section

Materials and methods

All commercially available reagents and solvents were purchased from Merck- Sigma Aldrich, ABCR, TCI Germany and were used without further purification. Hydrogenation reactions were carried out in a 150 mL Roth High pressure steel reactor. NMR spectra were recorded on a BrukerAvance 600 (^{1}H: 600 MHz; ^{13}C: 151 MHz) and BrukerAvance 400 (^{1}H: 400 MHz; ^{13}C: 126 MHz, ^{19}F: 376 MHz) spectrometers at 298 K and referenced to the residual solvent peak (^{1}H: chloroform- d, 7.26 ppm; acetone-d$_6$, 2.05 ppm; dichloromethane-d$_2$, 5.32 ppm; methanol-d$_4$, 3.31 ppm; ^{13}C: chloroform-d, 77.6 ppm; acetone-d$_6$, 206.68 ppm; methanol-d$_4$, 49 ppm; dichloromethane-d$_2$, 53.84 ppm). Coupling constants (J) are denoted in Hz and chemical shifts (δ) in ppm. Multiplicities are denoted as follows: s = singlet, d = doublet, t = triplet, m = multiplet, br = broad. High-resolution mass spectrometry (HRMS) was performed using a Fourier Transform Ion Cyclotron Resonance (FT-ICR) mass spectrometer solariX (Bruker Daltonik GmbH, Bremen, Germany) equipped with a 7.0 T superconducting magnet and interfaced to an Apollo II Dual ESI/MALDI source (using trans-2[3-(4-tert-butylphenyl)-2methyl-2propenylidene]malononitrile (DCTB) as matrix for MALDI), which can be switched from ESI/APCI to MALDI operation almost instantaneously. Analytical thin layer chromatography was used to monitor reactions on pre-coated aluminium plates and visualized by dipping in KMnO$_4$ stain followed by heating, or via UV analysis (254-366 nm).

Experimental procedures & characterization

Synthesis of compound **112**

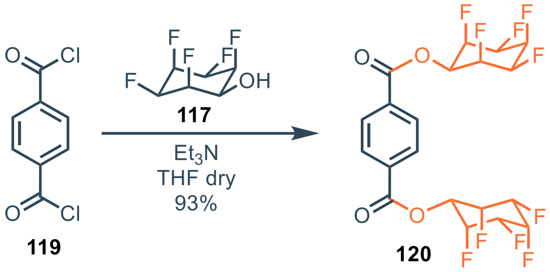

In a pre-dried schlenk flask, fluorinated cyclohexanol **117** (100 mg, 0.53 mmol, 2 equiv) was suspended in THF (7 mL) under N_2 atmosphere. The solution was cooled to 0°C with an ice bath and terephtaloyl chloride **119** (53 mg, 0.26 mmol, 1 equiv) was subsequently added. Et_3N (180 µL, 1.3 mmol, 5 equiv) was added afterwards, and a white solid fastly crashed out. The suspension was allowed to stir at RT under inert atmosphere. After 18 h, the suspension was centrifuged, the supernatant removed and the residue washed with THF (x2) and water (x2). The resulting white solid was allowed to dry under high vacuum, delivering the desired product **129** with 93% yield.

^{1}H NMR (600 MHz, DMSO-d$_6$, 373 K): δ 8.18 (s, 4 H), 5.73 (t, 2 H), 5.38-5.13 (m, 10 H)

^{13}C NMR (150 MHz, DMSO-d$_6$, 373 K): δ 163.5, 132.9, 129.3, 85.7 (m), 84.4 (m), 67.4 (m)

^{19}F NMR (377 MHz, DMSO-d$_6$, 373 K): -212.7 (bs), -213.2 (bs), -214.7 (bs)

HRMS (ESI$^-$): m/z 623.0179 $[M+CF_3COO]^-$

General procedure for the SNAr reaction

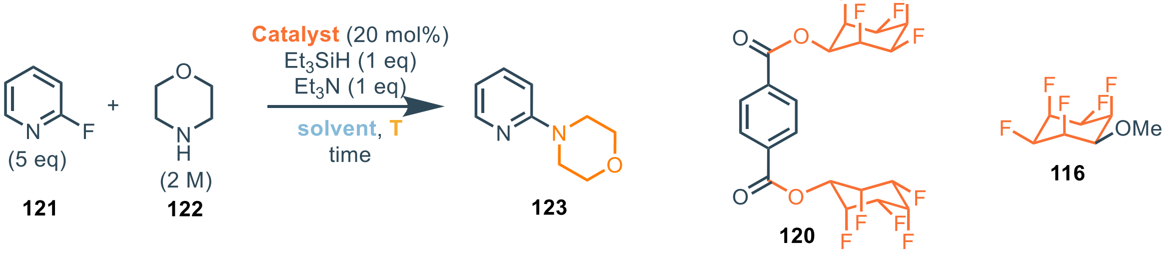

In a 10 mL pre-dried schlenk flask the catalyst (0.2 equiv) was added under N_2 flux. Then morpholine **122** (35 µL, 0.4 mmol, 1 equiv, 2 M), Et_3N (56 µL, 0.4 mmol, 1 equiv), Et_3SiH (64 µL, 0.4 mmol, 1 equiv), 2-fluoro-pyridine **121** (170 µL, 2 mmol, 5 equiv) and the selected solvent (0.2 mL) were added under N_2 atmosphere, and the reaction was allowed to stir at the selected T for 24 h. The reaction was monitored after 24 h via ^{1}H NMR integrating the CH_2 signals of the morpholine **122** *vs* the CH_2 signals of the product **123**. The reaction can be checked via TLC (petroleum ether/EtOAc 8:2, Rf = 0.22, intense fluorescent spot). The product **123** was isolated concentrating the reaction mixture in vacuo and purified via flash column chromatography (petroleum ether/EtOAc 8:2).

^{1}H NMR (400 MHz, $CDCl_3$, 298 K): δ 8.20 (dd, 1 H), 7.50 (td, 1 H), 6.70-6.61 (m, 2 H), 3.83 (t, 4 H), 3.50 (t, 4H). The data matches with the ones reported in literature.[87]

HRMS (ESI$^+$): 165.1029 $[M+H]^+$

Crystallographic data

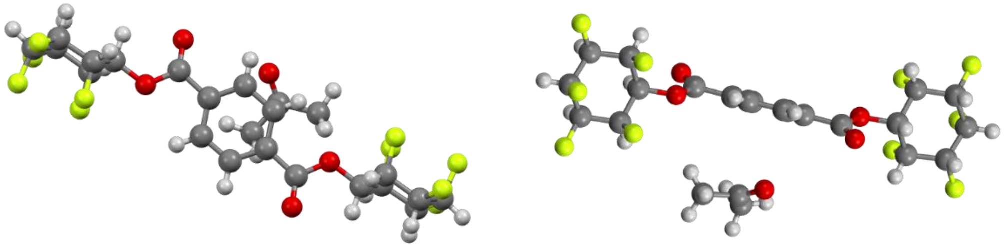

Figure S1 Front (left) and top (right) view

Single clear light colourless block-shaped crystals of **112** were obtained by cooling of a supersatured solution in acetone and measured at 150 K

Table S1 Crystal data and structure refinement for **6** [88]

Formula	$C_{26}H_{28}F_{10}O_6$
ρcalc (g/cm^3)	1.549
μ (mm^{-1})	0.153
Formula Weight	626.48
Colour	clear light colourless
Shape	block-shaped
Crystal size (mm^3)	0.31 × 0.11 × 0.06
Temperature (K)	150.05(10)
Crystal System	triclinic
Space Group	P-1

---

[87] Y. Li, Z. Lv, Y. Wang, Z. Wan, P. Knochel, Y.-H. Chen, *Org. Lett.* **2024**, *26*, 2, 503–507

[88] a) V. Dolomanov, L. J. Bourhis, R. J. Gildea, J. A. K. Howard, H. Puschmann, *J Appl Cryst*, **2009**, *42*, 339-341; b) G. M. Sheldrick, *Acta Cryst* **2015**, *A71*, 3-8; c) G. M. Sheldrick, *Acta Cryst* **2015**, *C71*, 3-8

a (Å)	5.6952(5)
b (Å)	10.3648(8)
c (Å)	11.9965(9)
α (°)	103.333(7)
β (°)	92.481(7)
γ (°)	101.742(7)
Volume (Å^3)	671.61(10)
Z	1
Z'	0.5
Wavelength (Å)	0.71073
Radiation type	MoKα
θ_{min} (°)	3.506
θ_{max} (°)	29.465
Measured reflections	9002
Independent reflections	3251
Reflections $[I > 2\sigma(I)]$	1680
R_{int}	0.0631
Parameters	192
Restraints	0
Largest Peak (e Å^{-3})	0.396
Deepest Hole (e Å^{-3})	-0.297
GooF	1.035
wR_2 (all data)	0.129
wR_2	0.1148
R_1 (all data)	0.1468
R_1	0.0638

Chapter 5 – From Lab Bench to Industry: Reinventing Tolterodine Synthesis via Prins Reaction

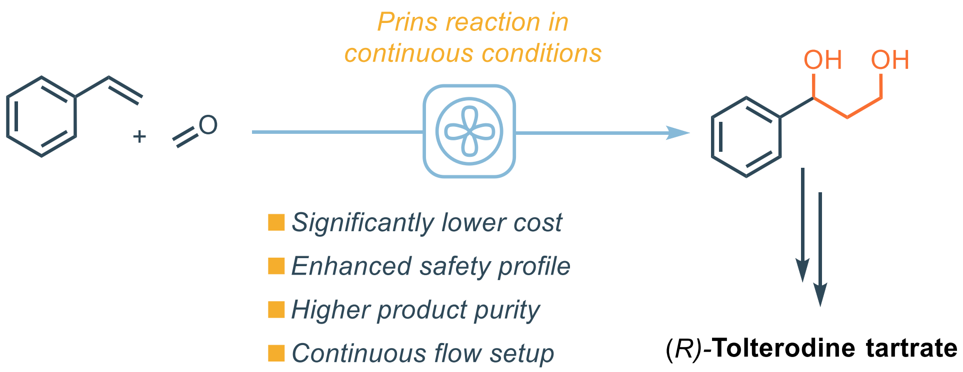

Chapter outline *– In this chapter, a cost-effective and scalable synthetic route to 1-phenyl-1,3-propanediol, an intermediate useful for the preparation of Tolterodine, is presented. The strategy is based on a Prins reaction to access a diacetate derivative, followed by hydrolysis. Batch and flow conditions were optimized, highlighting improvements in safety, cost effectiveness, and product purity. A comparison with classical methods underscores the industrial relevance of the new approach.*

Introduction

Tolterodine: Mechanism of Action and Clinical Significance

Tolterodine is a competitive muscarinic receptor antagonist clinically employed in the management of overactive bladder (OAB),[1] a prevalent urological disorder characterized by urinary urgency, with or without urge incontinence, and often accompanied by increased frequency and nocturia.[2] The impact of OAB on quality of life is substantial, driving ongoing research into pharmacological strategies that can modulate bladder contractility without eliciting unacceptable side effects. Early pharmacological treatments, such as oxybutynin, proved effective but were frequently associated with systemic anticholinergic adverse effects, most notably xerostomia and constipation, which limited patient compliance.[3]

---

[1] L. Nivebrant, B. Hallén, G. Larsson, *Life Sci*, **1997**, *60*, 1129-1136

[2] E. A. Gormley, D. J. Lightner, M. Faraday, S. P. Vasavada, *J Urol*, **2015**, *193*, 1572-1580

[3] R. A. Appell, *Urology*, **1997**, *56*, 90-96

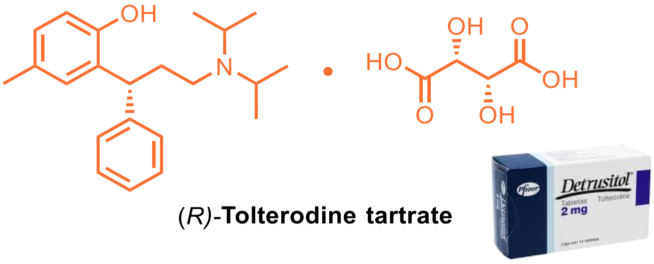

(*R*)-**Tolterodine tartrate**

Figure 1. Tolterodine tartrate marketed by Pfizer under the name Detrusitol

Tolterodine, introduced in the late 1990s as a second-generation antimuscarinic agent, was developed to overcome these limitations by achieving functional selectivity for the bladder over other peripheral tissues, particularly the salivary glands. This selectivity is not due to absolute receptor subtype specificity but rather to differences in tissue pharmacokinetics, distribution, and local metabolism.[3]

Pharmacologically, tolterodine is a competitive antagonist at muscarinic acetylcholine receptors (mAChRs), particularly the M2 and M3 subtypes expressed in the detrusor smooth muscle.[4] Inhibition of these receptors reduces parasympathetic-mediated detrusor contractions during the bladder filling phase, thereby increasing bladder storage capacity and decreasing urgency episodes. A key feature of tolterodine's pharmacological profile is its rapid hepatic metabolism via cytochrome P450 2D6 (CYP2D6) to 5-hydroxymethyl tolterodine, an active metabolite with potency comparable to the parent compound.[5] Both molecules contribute significantly to the overall therapeutic effect, ensuring sustained antimuscarinic activity while potentially mitigating peak plasma concentration–related adverse effects.

Through this dual mechanism—parent drug and equipotent metabolite—tolterodine provides effective symptom relief for OAB while maintaining a favorable tolerability profile compared with earlier antimuscarinic therapies. Its development marked a significant step forward in the pharmacological management of OAB, combining clinical efficacy with improved patient adherence.

Market analyses estimate the global tolterodine market to be worth around USD 800 million in 2025, with a steady compound annual growth rate (CAGR) of approximately 3%, driven by factors

---

[4] T. Schneider, C. Fetscher, S. Krege, M. C. Michel, *J. Pharmacol. Exp. Ther*, **2004**, *309*, 1148-1153

[5] N. Brynne, M. M. S. Stahl, B. Hallen, P. O. Edlund, L. Palmer, P. Höglund, J. Gabrielsson, *Int. J. Clin. Pharmacol. Ther.*, **1997**, *35*, 287-295

such as population aging and the increasing prevalence of overactive bladder.[6]Against this backdrop, there is a clear industrial incentive to develop cost-effective and scalable synthetic routes capable of supporting sustainable large-scale production to meet the anticipated rise in global demand.

Synthetic approaches to Tolterodine

To meet the increasing demand for tolterodine, a wide variety of synthetic strategies have been explored, ranging from early racemic approaches—often followed by resolution—to more advanced asymmetric methodologies designed to directly yield the pharmacologically active (R)-enantiomer. The following section outlines the principal racemic and asymmetric syntheses developed over the years, highlighting their key transformations, advantages, and limitations.

Racemic Syntheses

Early synthetic efforts primarily focused on obtaining racemic tolterodine, with the desired (R)-enantiomer subsequently isolated via diastereomeric salt resolution, typically using L-(+)-tartaric acid. While effective, this approach inherently limits the maximum theoretical yield to 50% for the desired enantiomer, necessitating racemization and recycling of the unwanted (S)-enantiomer.

The earliest synthetic route to tolterodine, reported in 1989, proceeds via a dihydrocoumarin intermediate formed by condensing p-cresol **1** with cinnamic acid **2**, yielding 6-methyl-4-phenyl-3,4-dihydrocoumarin **3**. This lactone serves as a versatile precursor for several synthetic strategies described later. In the original process, the lactone ring is opened, methylated, and reduced with $LiAlH_4$ to give the corresponding alcohol **5**, which is then converted into a tosyl derivative. Subsequent nucleophilic substitution with diisopropylamine produces intermediate **7**, and final cleavage of the phenolic methyl ether with a strong Lewis acid furnishes racemic tolterodine (Scheme 1).[7]

---

[6] DataInsightsMarket, *Global Tolterodine Market Report*, **2025**, https://www.datainsightsmarket.com/reports/tolterodine-1221584 (accessed August 11, 2025).

[7] N. A. Jonsson, B. A. Sparf, L. Mikiver, P. Moses, L. Nilvebrant, G. Glas, EP 325571 A1, **1989**.

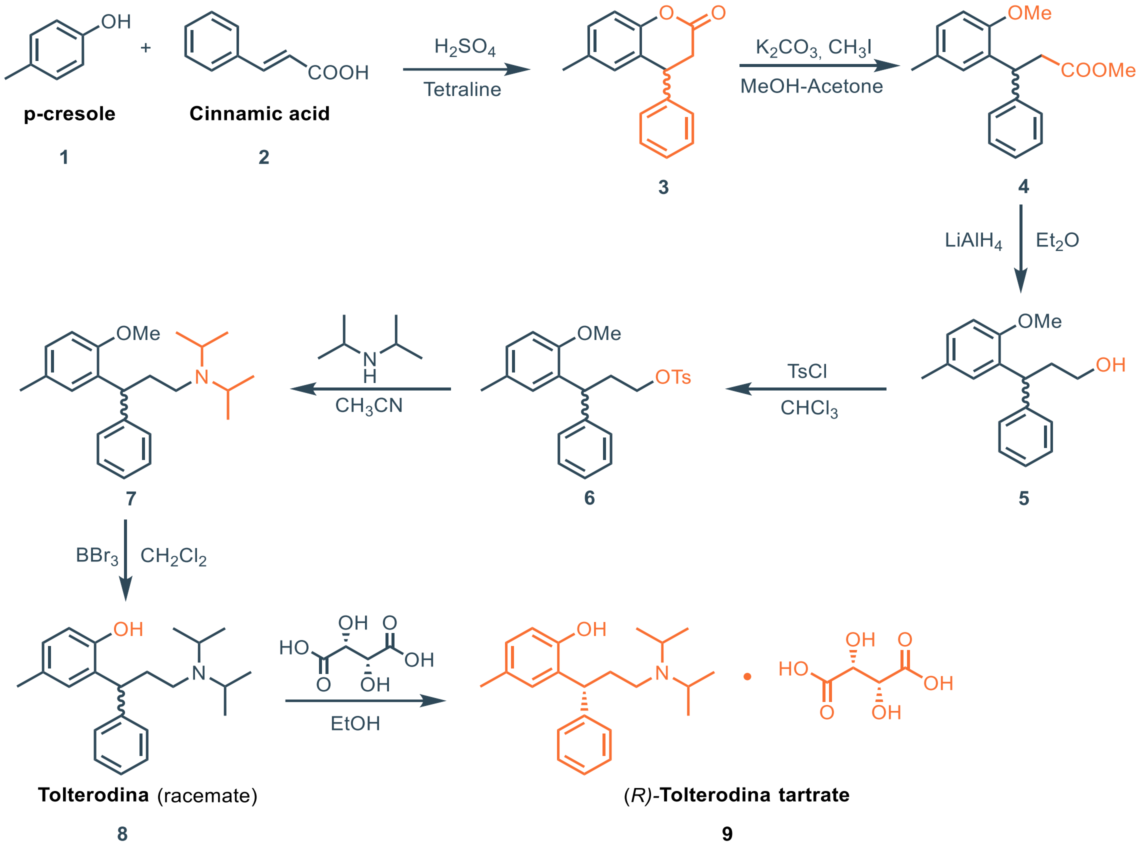

Scheme 1. First synthesis of Tolterodine as racemate and following resolution with (L)-Tartaric acid

This synthetic protocol employs inexpensive and readily available starting materials; however, it requires numerous steps, resulting in only moderate overall yields, particularly in the final two steps, with an overall yield of 5.5% yield. In addition, the use of methyl iodide, a highly toxic reagent, poses significant safety and environmental concerns, making it unsuitable for large-scale industrial applications. To improve efficiency and practicality, subsequent studies introduced modification to the original protocol. In 1991, the same group reported a variant in which intermediate **4** was hydrolyzed to the corresponding carboxylic acid, transformed into the acyl chloride, and coupled with diisopropylamine to form an amide. Reduction of this amide, followed by ether deprotection, yielded the racemic target (Scheme 2a).[8] Another modification involved reducing the lactone to hemiacetal **12** with DIBAL-H, followed by hydrolysis and reductive amination with diisopropylamine, affording tolterodine (Scheme 2b).[9]

---

[8] N. A. Jonsson, B. A. Sparf, L. Mikiver, P. Moses, L. Nilvebrant, G. Glas, US 5382600 A, **1991**.

[9] J. R. Gage, J. E. Cabaj, US 5922914 A, **1997**

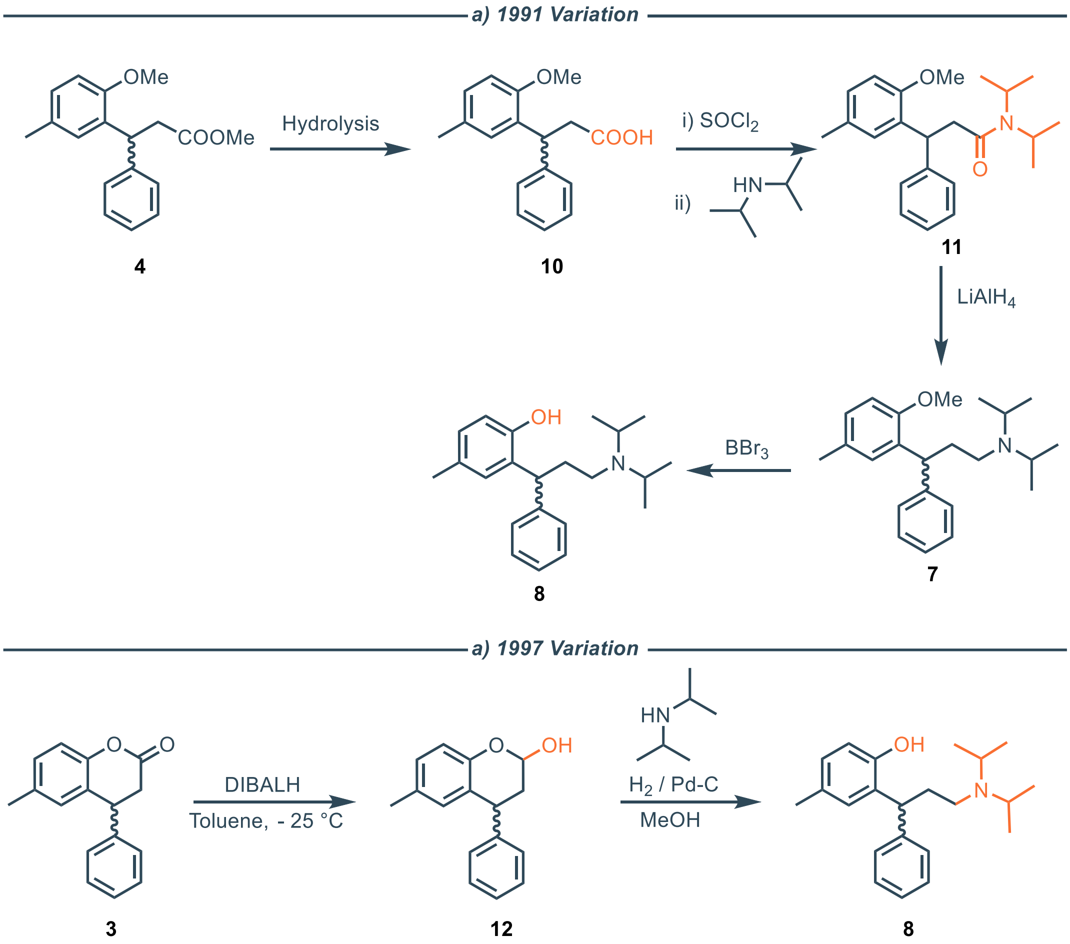

Scheme 2. Variation on the original synthesis starting from intermediates **3** and **4**

A further refinement introduced benzyl protection of the phenolic hydroxyl group. In this approach, lactone **3** is treated with benzyl bromide in methanol to afford adduct **13**, which is then reduced with Red-Al and tosylated to produce intermediate **14**. Reaction with diisopropylamine followed by hydrogenolysis yields racemic tolterodine. This method eliminates the need for BBr_3 in the deprotection step and replaces $LiAlH_4$ with the safer Red-Al (Scheme 3). Moreover, this protocol allows access to tolterodine with an overall yield of 30%, significantly higher to the previously reported methods.[10]

---

[10] K. S. Reddy, M. Ramakrishna, M. Arunagiri, R. L. Kumari, S. Venkataraman , *Org. Proc. Res. Dev.*, **2005**, *9*, 314–318

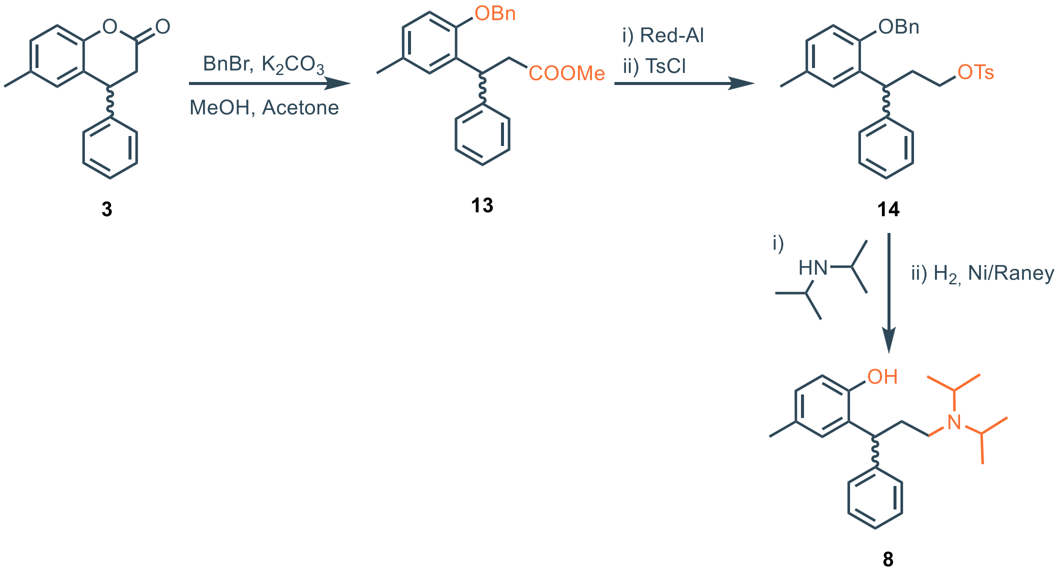

Scheme 3. Further variation to avoid strong Lewis acids and aggressive reducing agents

Intermediate **12** can also be accessed via Rh-catalyzed regioselective hydroformylation of 1-[(2-hydroxy-5-methyl)]-1-phenylethene **15**. The resulting hemiacetal undergoes reductive amination with diisopropylamine in the presence of Pd/C to deliver tolterodine directly.[11] A key advantage of this methodology is the ability to carry out the hydroformylation step in a biphasic water/toluene system, which is environmentally friendly, simplifies product separation, and enables near-quantitative recovery of the costly rhodium catalyst. Conversely, the use of syngas (CO/H_2) necessitates stringent safety measures, particularly in large-scale industrial operations.

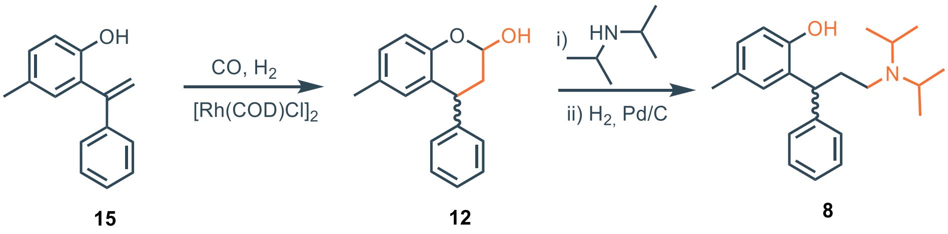

Scheme 4. Alternative route to hemiacetal **12**

Another well-established strategy relies on the reduction of lactone **3** with $LiBH_4$ to give diol **16**, which is subsequently dimesylated and subjected to nucleophilic displacement to form intermediate **17**. Hydrolysis of the phenolic mesyl group then affords racemic tolterodine (Scheme 5a).[12] Although this process avoids hazardous reagents and remains cost-effective, it still requires the use of a reducing agent (albeit in stoichiometric amounts). This reagent releases hydrogen gas,

---

[11] C. Botteghi, T. Corrias, M. Marchetti, S. Paganelli, O. Piccolo, *Org. Proc. Res. Dev.*, **2002**, *6*, 379–383

[12] J. H. Kang, J. H. Lee, Y. J. Park, K. S. Kim, J. Y. Lee, *Bull. Korean Chem. Soc.* **2008**, *29*, 519-520

the handling of which can be challenging, particularly in large-scale industrial settings. In contrast, the shortest known route is a direct one-step synthesis in which *p*-cresol reacts with 3-phenyl-prop-2-en-1-amine (**DIPCA, 18**) under strongly acidic conditions (neat or at high concentration) to give tolterodine (Scheme 5b).[13]

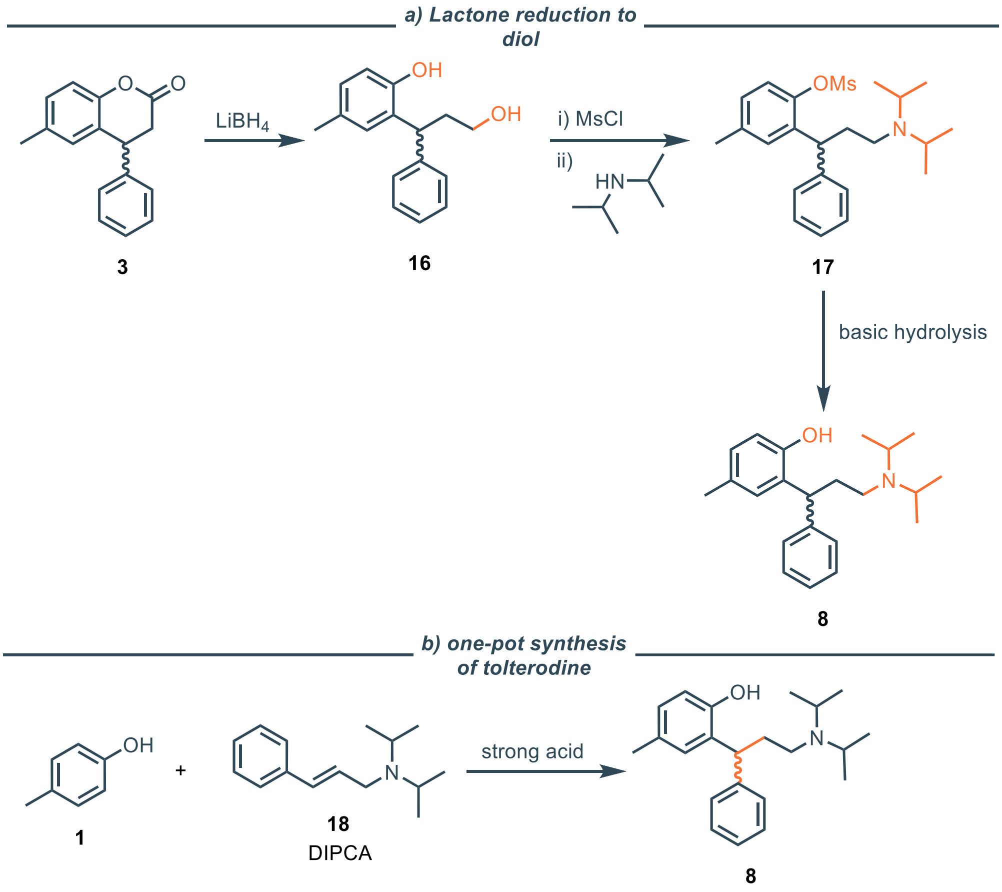

Scheme 5. a) lactone reduction to afford diol **15;** b) one-step synthesis of tolterodine

In 2006, Razzetti, Mantegazza, and co-workers reported an alternative approach starting from ether **20**, which undergoes lithiation and subsequent reaction with chloroethyl diisopropylamine to produce intermediate **21**. In acidic medium, this rearranges to yield tolterodine (Scheme 6).[14] Although effective, this synthetic protocol employs a lithiating agent, necessitating strict temperature control to prevent hazardous exothermic events. Furthermore, the yield of the final step is critical, averaging only around 50%.

---

[13] A. L. Bonde-Larsen, P. Martìn Pascual, J. Martìn Suarez, M. Armengol Montserrat, WO2007017544A2, **2003**

[14] G. Razzetti, S. Mantegazza, R. Roberto, P. Allegrini, EP1693361B1, **2006**

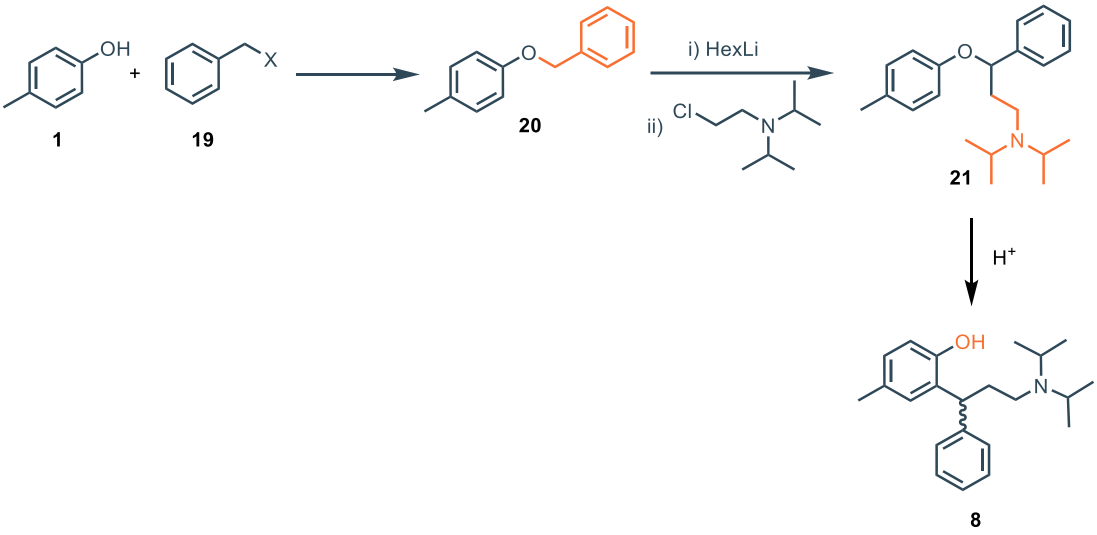

Scheme 6. Synthetic protocol proposed by Razzetti, Mantegazza and coworkers

Another notable strategy involves diol **23**, obtained by reducing benzoyl ethyl acetate. Selective activation of its primary hydroxyl as a nosylate enables nucleophilic substitution with diisopropylamine to form intermediate **24**. Under Brønsted or Lewis acidic catalysis, this compound undergoes electrophilic aromatic substitution with *p*-cresol, affording racemic tolterodine (Scheme 7).[15] However, a significant disadvantage is that the reduction of ethyl benzoylacetate to the corresponding diol is problematic for industrial application. It necessitates three equivalents of $NaBH_4$, leading to a highly exothermic and difficult-to-control process with challenging hydrogen gas management, which is deemed too costly for commercial production given the limited commercial interest in tolterodine.

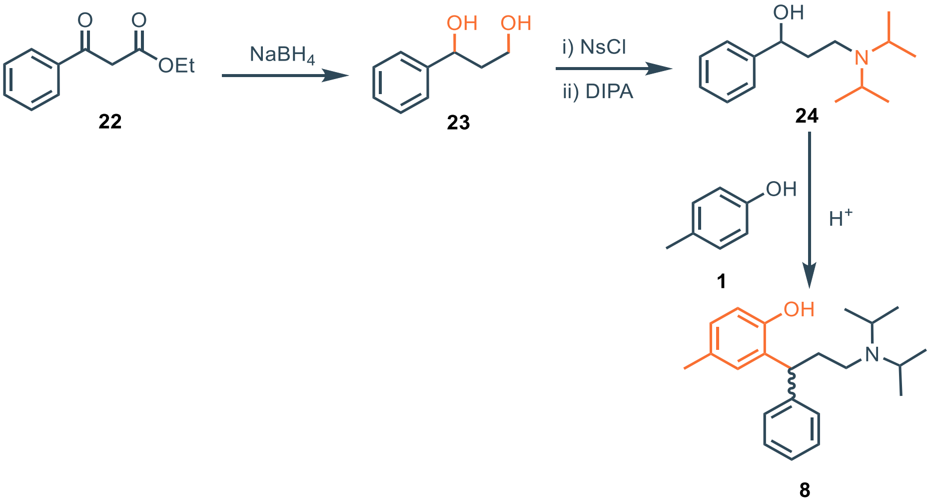

---

[15] a) K. A. De Castro, J. Ko, D. Park, S. Park, H. Rhee, *Org. Proc. Res. Dev.*, **2007**, *11*, 918–921; b) K. A. De Castro, H, Rhee, *Synthesis*, **2008**, *12*, 1841-1844

Scheme 7. Synthesis of tolterodine *via* diol **23**

Asymmetric Syntheses

The pursuit of enantiomerically pure (R)-tolterodine directly from synthesis has led to the development of numerous asymmetric methodologies, aiming to avoid the limitations and additional costs associated with racemic resolution.

One of the pioneering asymmetric synthesis of (R)-tolterodine uses oxazolidinones as chiral auxiliaries, there the asymmetric induction occurs with a Cu-assisted conjugate addition of a Grignard reagent (derived from **26**) on intermediate **25**. Removal of the chiral auxiliary allows to obtain intermediate **28**, which undergoes a similar chemistry as Scheme 2a, delivering the enantiopure tolterodine with high yield and ee (98%) (Scheme 8). Although effective, the use of chiral auxiliaries is not ideal, since these compounds are generally expensive and their use delivers poor atom economy during the synthetic protocol.[16]

Another interesting approach involves the asymmetric reduction of indenone **30** using the (S)-Me-CBS catalyst (Corey–Bakshi–Shibata catalyst). Upon basic treatment of 31 and subsequent Baeyer-Villiger oxidation, intermediate **33** is formed, which is a common precursor for most of the enantioselective approaches to tolterodine. This intermediate was then converted to (R)-tolterodine in a five-step procedure. The overall process delivers the desired compound in 10 steps with a 30% overall yield and 99% ee from commercially available starting materials. A critical aspect to achieving high enantioselectivity is the fast quenching of the reaction mixture at complete conversion, as prolonged reaction times can lead to partial racemization, making it non ideal for industrial applications (Scheme 9).[17]

---

[16] P. G. Andersson, H. K. Schink, K. Osterlund, *J. Org. Chem.*, **1998**, *63*, 8067-8070

[17] C. Hedberg, P. G. Anderson *Adv. Synth. Catal.*, **2005**, *347*, 662-666

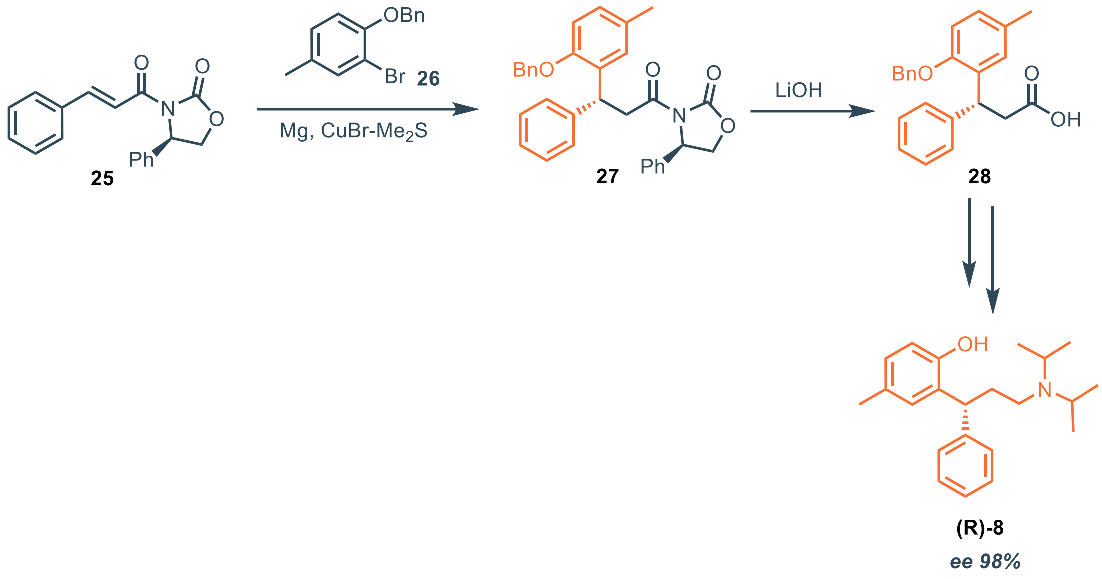

Scheme 8. Enantioselective synthesis of (*R*)-tolterodine employing chiral auxiliaries

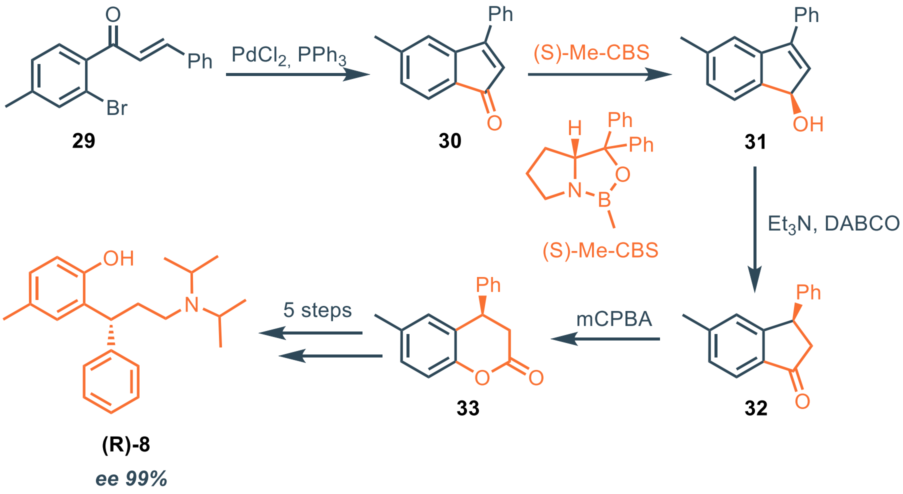

Scheme 9. Enantioselective reduction of indanone **30** with (*S*)-Me-CBS

The same intermediate **33** was prepared via asymmetric hydrogenation of a coumarin intermediate **36**, which was readily obtained via a Heck reaction from inexpensive starting materials. Using $[Rh(COD)Cl]_2$ and (S,S)-Chiraphos, 80% ee was obtained, which could be improved to >98% ee through crystallization (Scheme 10a).[18] The overall process achieves high yield and enantioselectivity and is deemed suitable for industrial scale-up; nevertheless, it was noted that the enantiomeric excess was highly sensitive to the cleanliness of the glass reaction vessel. The hydrogenation reaction also required the addition of 4 N NaOH to hydrolyze the coumarin, and an over-reduction product was observed during the lactol reduction step**.** For those reasons, the

---

[18] a) O. Piccolo, F. Ulgheri, M. Marchetti, WO 2005005356 A2, **2005;** b) F. Ulgheri, O. Piccolo, M. Marchetti, *J. Org. Chem.*, **2007**, *72*, 6056-6059

method has scarce applicability on an industrial scale. Another protocol for the asymmetric hydrogenation of **36** involves the use of $NaBH_4$ employing a cobalt catalyst with a chiral ossazoline ligand, delivering the product with 95% ee.[19] The same intermediate can be prepared through rhodium-catalyzed asymmetric 1,4-addition of arylboronic acids to 6-methylcoumarin **37**. This reaction, catalyzed by a Rh catalyst with a chiral ligand, provided the corresponding (R)-4-arylchroman-2-one **33** in over 99% ee, which was then converted to (R)-tolterodine (Scheme 10b).[20] The synthesis of intermediate **33** has also been accomplished via palladium-catalyzed asymmetric 1,4-addition of arylboronic acids to enones (e.g., *p*-methoxyphenylenone), followed by a regioselective Baeyer–Villiger oxidation.[21] In another approach, Hayashi and coworkers achieved the asymmetric construction of diaryl-methine stereogenic centers through the rhodium-catalyzed asymmetric 1,4-addition of arylboronic acids to arylmethylene cyanoacetates (**39**), employing a chiral diene-rhodium catalyst. The reaction yielded 3,3-diaryl-2-cyanopropanoates (**40**) with high enantioselectivity (up to 99% ee), which were subsequently transformed into (R)-tolterodine via nitrile reduction and reductive amination (Scheme 11).[22] The synthesis of (R)-tolterodine was completed in a five-step sequence with a good overall yield of 61%, and both benzyl and methoxymethyl protecting groups for the phenolic hydroxyl group were readily accessible and performed effectively.

---

[19] A. R. Jagdale, A. T. Sudalai, *Tetrahedron Lett.*, **2008**, *49*, 3790-3793

[20] a) G. Chen, N. Tokunaga, T. Hayashi, *Org. Lett.*, **2005**, *7*, 2285–2288; b) L. Colombo, R. Rossi, G. Castaldi, P. Allegrini, EP1584621B1, **2005**

[21] K. Kobayashi, T. Nishikata, Y. Yamamoto, N. Miyaura, *Bull. Chem. Soc. Jpn.* **2008**, *81*, 1019-1025

[22] S. Sorgel, N. Tokunaga, K. Sasaki, K. Okamoto, T. Hayashi, *Org. Lett.*, **2008**, *10*, 589-592

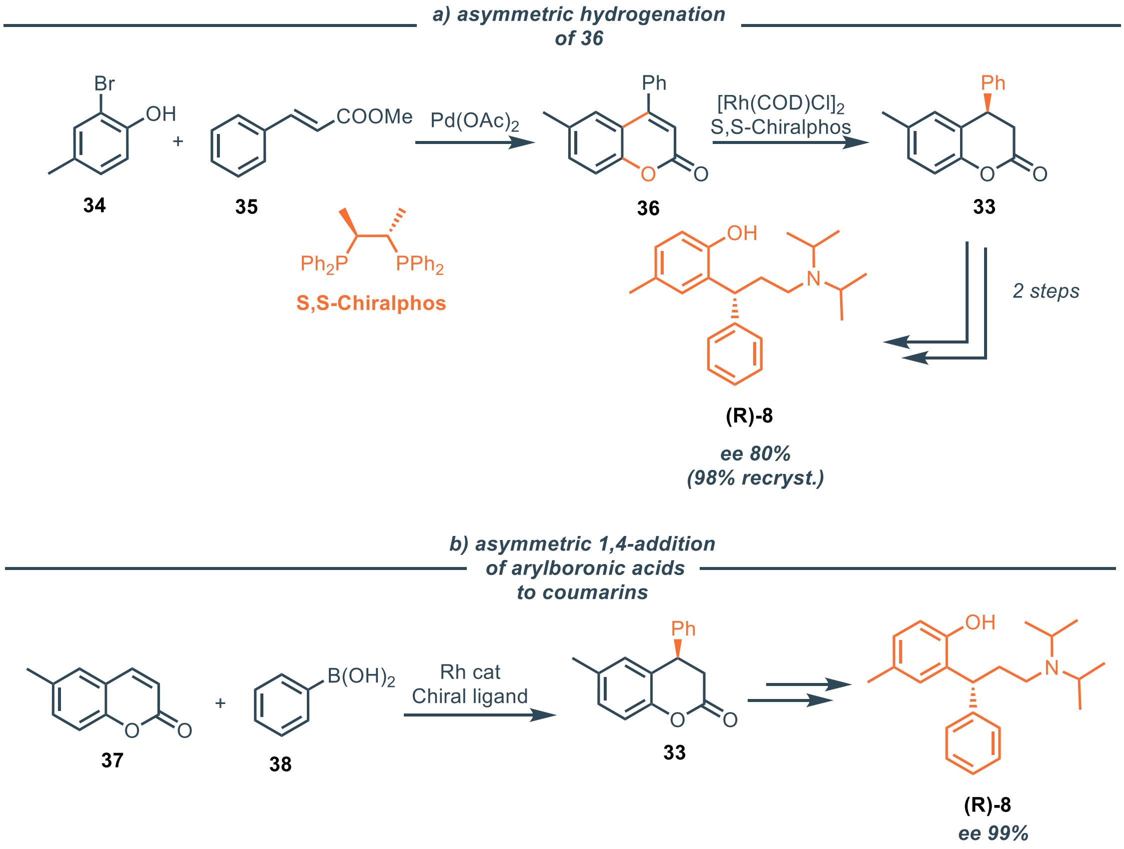

Scheme 10. Enantioselective approaches to (R)-Tolterodine employing the common intermediate **33**

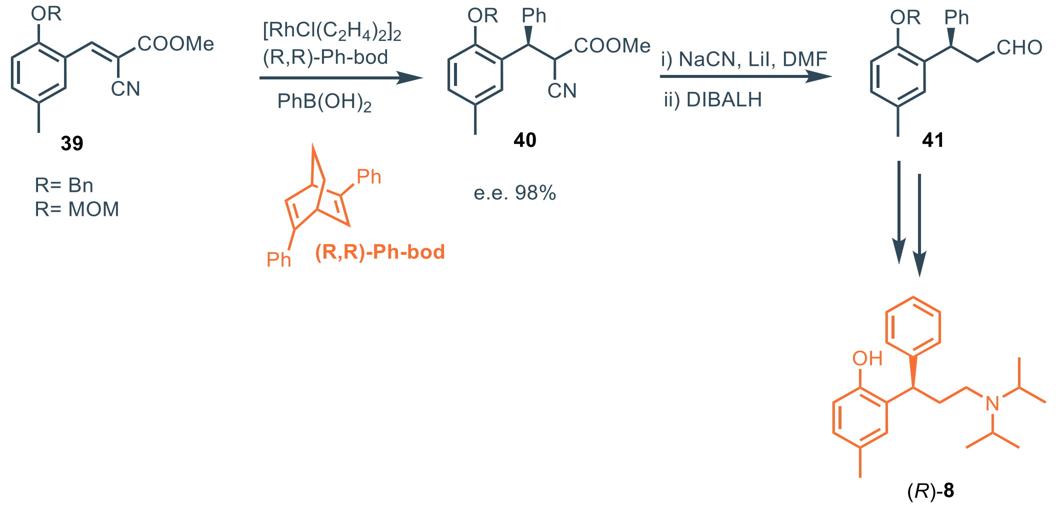

Scheme 11. Construction of 3,3-diaryl-2-cyanopropanoates **40** via rhodium-catalyzed asymmetric 1,4-addition

Stereoselective vs Non-stereoselective synthesis of Tolterodine: a cost comparison

When designing a synthetic route, particularly for industrial-scale pharmaceutical production, the economic evaluation of the process is as critical as its chemical efficiency. Beyond yield, selectivity, and step count, the choice of reagents, catalysts, and solvents directly influences production costs and ultimately determines the feasibility of scaling up. Even a highly efficient laboratory protocol may prove unsuitable for commercial manufacturing if it relies on prohibitively expensive reagents or operationally complex conditions.

In addition to the direct cost of raw materials, industrial processes must account for ancillary expenses such as the treatment and disposal of chemical waste. This is especially relevant for synthetic methodologies that employ heavy metals or precious metal catalysts, where the recovery of active species is often incomplete, generating significant waste streams. The environmental compliance costs associated with the disposal of spent catalysts and solvent residues can represent a substantial fraction of the total production budget. Therefore, a thorough cost–benefit analysis must integrate not only the price of reagents but also the downstream implications of waste management, regulatory compliance, and sustainability goals.

A cost comparison between stereoselective (Scheme 10b)[15] and racemic (resolution-based) syntheses of tolterodine (Scheme 6) exemplifies this point. The stereoselective approach avoids the 50% theoretical yield limitation inherent to resolution and minimizes by-product generation, but relies on extremely expensive chiral ligands and catalysts, such as $[Rh(COD)(MeCN)_2]BF_4$ (109200 €/kg) and (R)-(+)-BINAP (126000 €/kg), which heavily impact raw material costs. Conversely, the racemic synthesis employs more affordable reagents, such as p-cresol (24 €/kg), benzyl chloride (12 €/kg), and L-(+)-tartaric acid (30 €/kg), making it economically attractive at the procurement stage, though it requires additional operations for enantiomer resolution and potential racemization/recycling of the undesired enantiomer.

From an industrial perspective, these considerations highlight the complex interplay between reagent costs, process efficiency, and waste management in determining the most viable production strategy. A cost–benefit analysis conducted within the company where this research was carried out identified the synthetic route depicted in Scheme 7 as the most advantageous approach for the preparation of tolterodine.[15] Nonetheless, several critical issues were highlighted during its evaluation. The present work is framed within the context of this route, aiming to develop and implement an improved protocol that addresses these limitations, with particular emphasis on enhancing both safety and cost-efficiency for potential industrial application.

Aim of the project

The synthesis of intermediate **23**, a key 1,3-diol building block for the API Tolterodine, is currently hindered by significant economic, safety, and operational drawbacks (Scheme 12). The pharmaceutical company Dipharma Francis S.r.l., which has a direct commercial interest in this API, commissioned this work to design an alternative and more efficient synthetic route that overcomes these industrial-scale challenges.

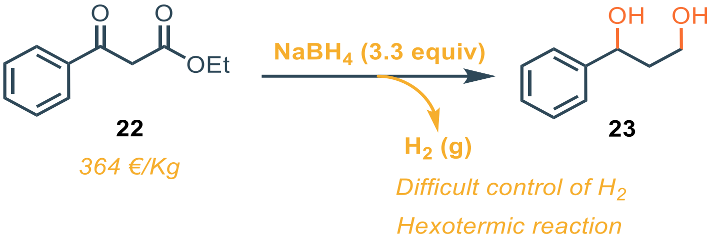

Scheme 12. First step of the synthesis proposed by Rhee and coworkers – economical and safety issues

In particular, the synthesis of **23** is currently performed via reduction of ethyl benzoylacetate **22**; to get a good conversion in a reasonable reaction time, the reaction requires three equivalents of sodium borohydride. On a large scale, the excess of reducing agent renders the process highly exothermic and difficult to control. Furthermore, managing the hydrogen gas evolved during the reaction poses significant operational challenges. Moreover, compound **22** is expensive (364€/Kg); the development of a different synthetic strategy which employs more economical starting materials is indeed highly desirable. A thorough cost analysis is indeed essential, as tolterodine is a pharmaceutical product with limited commercial appeal, making low production costs a priority. Consequently, the selected process must employ inexpensive as well as safe reagents, which rules out enantioselective routes due to the high cost of chiral catalysts, such as those described earlier. In contrast, non-stereoselective pathways that conclude with the resolution of a racemic mixture are economically more viable. The synthetic challenge we addressed is therefore of both industrial and academic interest. Our objective was to design an alternative synthetic route to the diol intermediate **23** that overcomes the economic, safety, and handling issues. The strategy we devised involves accessing the diol via a protected intermediate **42**, which could be converted into the target compound through a hydrolysis step. For the preparation of this intermediate **42**, a literature survey identified the Prins reaction[23] as a suitable method, enabling the synthesis 1,3 diols from simple and inexpensive starting materials, namely styrene **43** and formaldehyde **44** (Scheme 13). These starting materials are cheap, easily accessible and widely used in the chemical industry, making this synthetic procedure easily feasible.

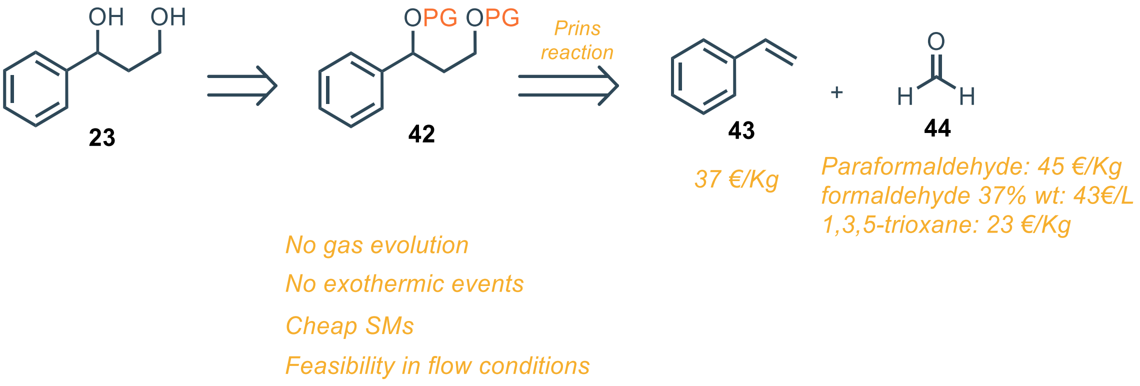

Scheme 13. Advantages of the Prins reaction for the synthesis of intermediate **23**

In this chapter, the development and implementation of this approach are described. The reaction was systematically optimized, affording the protected diol **42** in yields of up to 72%. Notably, the process was successfully scaled to multigram quantities without any reduction in efficiency, underscoring the robustness and reproducibility of the method. In addition, a dedicated optimization enabled the reaction to be performed in a flow setup, opening new possibilities to transfer this process in a continuous fashion, to minimize reagents exposure and enabling automation of all process steps.

Prins reaction

The Prins reaction, first reported by Hendrik Jacobus Prins in 1919,[24] remains a well-established transformation in synthetic organic chemistry, particularly valued for its capacity to construct 1,3-diols and six-membered cyclic acetals such as 1,3-dioxanes. The reaction involves the acid-catalyzed electrophilic addition of aldehydes or ketones to alkenes, and it finds widespread application in both academic and industrial synthetic strategies due to its simplicity, efficiency, and use of readily available starting materials.

---

[23] a) D. Adams, S. P. Bhatnagar, *Synthesis* **1977**, 661; b) E. Arundale, L. A. Mikeska, *Chem. Rev.*, **1952**, *51*, 505-555

[24] V I Isagulyants, T G Khaimova, V R Melikyan, S V Pokrovskaya, *Russ. Chem. Rev.*, **1968**, *37*, 17

At a mechanistic level, the transformation begins with the protonation of a carbonyl compound—typically an aldehyde—by a Brønsted acid, generating an activated oxocarbenium species **46**. This intermediate is then attacked by the π electrons of an alkene (**45**), resulting in the formation of a resonance-stabilized β-hydroxy carbocation (**Int1**). From this point, the reaction may evolve along different trajectories depending on the reaction environment and reagent stoichiometry. In principle, under aqueous conditions or in the presence of water as a nucleophile, the intermediate carbocation may be trapped by water to yield a 1,3-diol (**40**). Alternatively, in media containing an excess of the carbonyl compound, a second molecule of aldehyde can act as a nucleophile toward the carbocation, giving rise to an α-hydroxyalkyl intermediate (**Int2**) which then undergoes intramolecular cyclization and deprotonation to furnish a 1,3-dioxane ring (**48**) (Scheme 14).

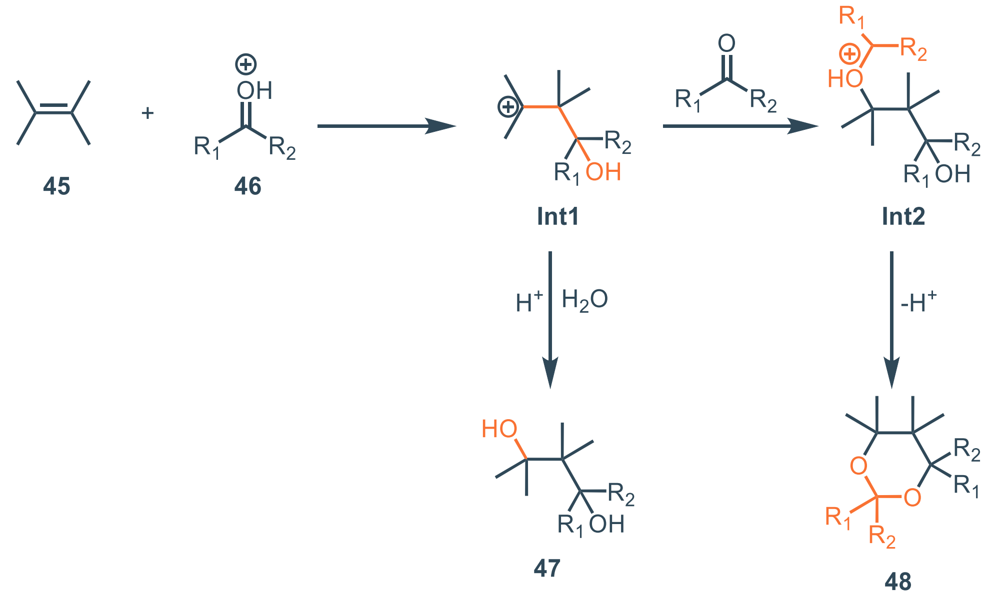

Scheme 14. Mechanism of Prins reaction

However, it is important to note that while the formation of the diol is often cited in general mechanistic descriptions, it is not always observed in practice. The selectivity of the reaction is highly substrate-dependent and strongly influenced by experimental conditions such as solvent polarity, temperature, stoichiometry, and the nature of the acid catalyst. Indeed, several studies have reported that even under conditions designed to favor water interception—such as limiting the carbonyl compound to a single equivalent and conducting the reaction in aqueous media—the formation of 1,3-diols is often low-yielding or absent. This is particularly true for aromatic alkenes such as styrene, whose reactivity tends to favor dioxane formation.[23b]

In the present study, the reaction between styrene and formaldehyde was investigated. Despite attempts to steer the reaction toward diol formation through controlled stoichiometry and aqueous conditions, the experimental outcome consistently revealed the predominance of 1,3-dioxane as the main product. These observations suggest that, in this specific system, the mechanistic pathway leading to the diol is either kinetically inaccessible or thermodynamically disfavored. As such, while the formation of a 1,3-diol remains a theoretically plausible outcome within the general Prins framework, it does not manifest under the conditions employed in this study. This reinforces the importance of detailed mechanistic and condition-specific investigations when considering the practical applicability of classic reactions in new synthetic contexts.

Results and discussion

Synthesis of 1,3-dioxane **49**

The Prins reaction represents a convenient and scalable method for the synthesis of 1,3-dioxanes from alkenes and formaldehyde. As an initial objective, efforts were directed toward the optimization of a reliable and operationally simple protocol to deliver the dioxane product **49** in high yield, using the safest and most cost-effective conditions possible. The overarching strategy involved leveraging an acid-catalyzed hydrolysis of dioxane **42** to access the target 1,3-diol **23**. To this end, we adopted literature procedure[25] involving a 1:2.8 molar ratio of styrene **43** to formaldehyde **44**, a stoichiometry known to ensure complete conversion and near-quantitative formation of the dioxane intermediate **42**. The results of this optimization study are summarized in Table 1.

Table 1. Synthesis of dioxane **49** – optimization (selected experiments)

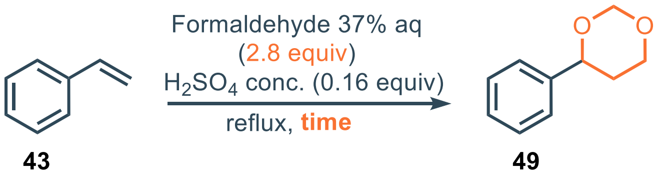

Entry	Time (h)	Yield (%)[a]
1[b]	5	30

---

[25] R. L. Shriner, P. R. Ruby, *Org. Synth.*, **1953**, *33*, 72

2^{b}	5	30
3^{b}	24	60
4^{b}	29	76
5^{c}	6	98
6^{cd}	6	50

a: isolated yield; *b*: Et$_2$O as extraction solvent; *c*: EtOAc / HCl 1M sat. with NaCl as extraction mixture; *d*: 1:1 molar ratio of styrene/formaldehyde

During the early phases of this work, it became clear that significant modifications to the work-up protocol were required. While benzene is used in prior protocols to extract the product into the organic phase, its toxicity and environmental risks render it unsuitable for modern laboratory or industrial practice. For this reason, diethyl ether was initially explored as an alternative extraction solvent, due to its low boiling point and practical handling advantages (Entries 1–4). Despite full reaction conversion under these conditions, the use of diethyl ether consistently led to problematic emulsions during aqueous work-up, which significantly impaired product recovery. This prompted the replacement of diethyl ether with the more benign and operationally robust solvent ethyl acetate (EtOAc). Furthermore, we found that employing a 1 M hydrochloric acid solution saturated with NaCl as the aqueous phase facilitated efficient phase separation and allowed for the complete isolation of product **49** in quantitative yield (Entry 5). Lowering the reaction temperature to 80 °C further improved practicality without compromising product yield, albeit at the expense of longer reaction times.

A key question in this study was whether the diol **23** could be accessed directly via aqueous Prins conditions, bypassing the need for hydrolysis of the dioxane. To investigate this, we performed the reaction using a 1:1 molar ratio of styrene and formaldehyde (Entry 6), which, according to general mechanistic considerations, should favour water as the nucleophile in place of a second formaldehyde molecule. However, under these aqueous and equimolar conditions, the desired diol was not observed at all. Instead, the reaction produced dioxane **49** in only 50% yield, with the remaining 50% corresponding to unreacted styrene. This result strongly suggests that the intramolecular cyclization to form the 1,3-dioxane **49** is kinetically and thermodynamically favoured over interception of the intermediate carbocation by water. The data therefore indicate that, at least for styrene as a substrate, direct formation of the 1,3-diol via the Prins reaction is not viable, and that the route through dioxane hydrolysis remains the only productive pathway under the conditions investigated.

Hydrolysis of dioxane **49**

In the early stages of the study of the hydrolysis of **49**, we proceeded to use standard conditions, using an highly acidic environment provided by 37% HCl in H_2O. While at RT no reactivity was present, maintaining the reaction at reflux temperature for 24 h allowed us to recover the desired product, albeit with an unsatisfactory yield (Scheme 15).

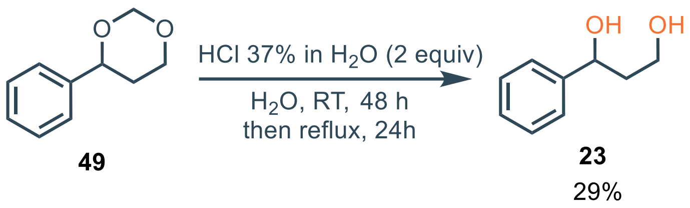

Scheme 15. Acidic hydrolysis of **49**

With the idea to study different reaction conditions, we therefore attempted to use an heterogeneous catalyst, such Amberlyst-15, an ion-exchange resin composed of a sulfonic acid-based polymer matrix acts as a strong proton exchanger, making it highly effective in the deprotection of acetals. This property has been demonstrated in previous studies conducted by the research group in which this doctoral work was carried out, particularly in the context of the deprotection of the dimethyl acetal of acetaldehyde.[26] The results of the optimization are summarized in Table 2.

---

[26] a) V. Nori, A. Sinibaldi, G. Giorgianni, F. Pesciaioli, F. Di Donato, E. Cocco, A. Biancolillo, A. Landa, A. Carlone, *Chem. Eur. J.*, **2022**, *28*, e202104524; b) A. Brusa, D. Iapadre, M. E. Casacchia, A. Carioscia, G. Giorgianni, G. Magagnano, F. Pesciaioli, A. Carlone, *Beilstein J. Org. Chem.*, **2023,** *19,* 1243–1250

Table 2. Hydrolysis of **49** mediated by Amberlyst-15 [a]

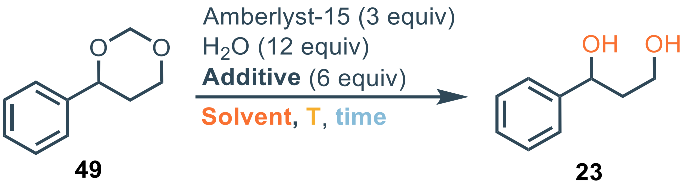

Entry	Solvent	T (°C)	time (days)	Additive	Result
1	MeOH	50	3	-	Reagent degradation, no product observed
2	iPrOH	80	8	-	Traces
3	Ethylene glycol	80	8	-	Reagent degradation, no product observed
4 [b]	iPrOH	80	6	-	Traces
5	iPrOH	80	6	Benzylamine	Traces
6	iPrOH	80	6	Ethylene glycol	Traces

a: reactions performed at 0.1 M concentration of dioxane **49**; *b*: [**49**] = 0.5 M

Several reaction conditions were explored in an effort to hydrolyze dioxane **49** to the corresponding 1,3-diol **23** using Amberlyst-15 as an acid catalyst. A variety of solvents with different polarities and boiling points were tested to facilitate high-temperature operation and promote nucleophilic attack by water on the acetal moiety. Among the solvents screened, only isopropanol showed marginal activity, while methanol and ethylene glycol resulted in either reagent degradation or no observable product formation (Entries 1-3). Attempts to improve the conversion by increasing substrate concentration (Entry 4) or by introducing additives aimed at sequestering released formaldehyde—such as benzylamine or ethylene glycol—led to, at best, trace amounts of the desired product (Entries 5-6). Overall, none of the tested conditions yielded the 1,3-diol in synthetically useful amounts, suggesting that the hydrolysis of dioxane **49** under these acidic conditions is highly inefficient, possibly due to competing side reactions or solvent interference. Conventional methods for acetal cleavage, including treatment with 2 M HCl in THF at 70 °C and p-toluenesulfonic acid (TsOH) in methanol at room temperature, proved ineffective in promoting the hydrolysis of dioxane **49**.[27] While the conversion of 1,3-dioxanes to their corresponding alcohols has been reported using trimethylsilyl triflate (TMSOTf) in combination with 2,2'-bipyridine,[28] the high cost and limited scalability of these reagents render the method impractical for industrial applications. In light of these limitations, our efforts turned toward identifying an alternative Prins-based strategy that could generate an intermediate more prone to undergo deprotection under mild and scalable conditions.

Prins reaction in acetic acid – batch conditions

Given the above limitations, we hypothesized that performing the Prins reaction in the presence of acetic acid might lead to the formation of the corresponding diacetate derivative **50**,[23b] which could subsequently undergo straightforward basic saponification to afford the target diol **23** (Scheme 16).

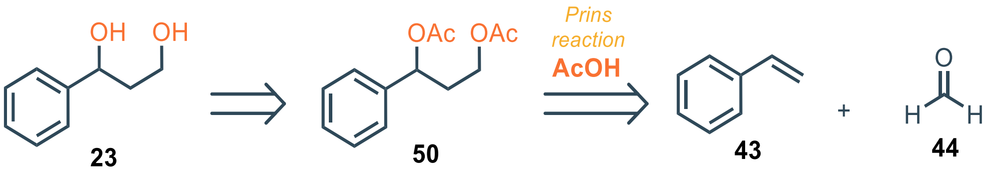

Scheme 16. Synthesis of diacetate **50** accomplished via Prins reaction in AcOH

The next stage of this study focuses on optimizing the Prins reaction conditions to access compound **50**, and on evaluating its subsequent hydrolysis to obtain the desired diol **23**.

---

[27] a) G. R. Brown, A. J. Foubister, J. A. Hudson, *J. Pharm. Pharmacol.*, **1990**, *42*, 53–55; b) B. H. Lipshutz, B. E. Huff, K. E. McCarthy, S. M. J. Mukarram, T. J. Siahaan, W. D. Vaccaro, H. Webb, A. M. Falick, T. A. Miller, *J. Am. Chem. Soc.*, **1990**, *112,* 7032-7041

[28] C. D. Dìaz-Oviedo, R. Maji, B. List, *J. Am. Chem. Soc.*, **2021**, *143*, 20598–20604

Table 3 – Prins reaction to afford diacetate **50** (selected experiments) [a]

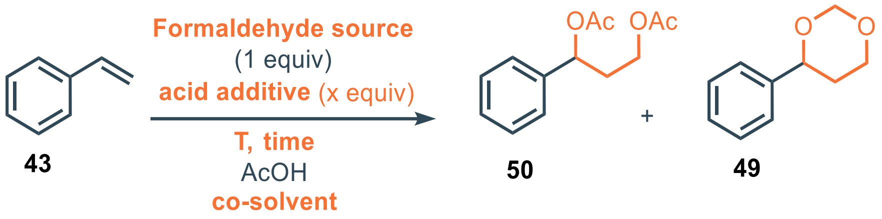

Entry	CH_2O source	Eq. AcOH	Acid	Equiv acid	T (°C)	Time	NMR yield [b]	Ratio 50:49 [a]
1[c]	CH_2O 37% in wt.	5 V	H_2SO_4	2.8	RT	3 h	62%	80:20
2[d]	CH_2O 37% in wt.	5 V	H_2SO_4	2.8	RT	3 h	76%	91:9
3[d]	CH_2O 37% in wt.	5 V	H_2SO_4	1.5	RT	3 h	58%	84:16
4[e]	$(CH_2O)_n$	10 V	H_2SO_4	1.5	15°C	3 h	73%	95:5
5[e]	1,3,5-Trioxane	10 V	H_2SO_4	1.5	15°C	3 h	66%	97:3
6[e]	1,3,5-Trioxane	10 V	H_2SO_4	0.25	50°C	4 h	68%	88:12
7[e]	1,3,5-Trioxane	10 V	H_2SO_4	0.5	50°C	3 h	68%	93:7
8[e]	1,3,5-Trioxane	10 V	H_2SO_4	0.25	80°C	1.5 h	50%	94:6
9[e]	1,3,5-Trioxane	10 V	MsOH	1.5	50°C	4 h	72%	97:3
10[f]	1,3,5-Trioxane	5 eq	MsOH	1.5	50°C	4 h	41%	95:5

a: Reaction performed on using 1 equiv. of styrene **43** (48 mmol, 5 g), 1 equiv. of formaldehyde (with trioxane, 0.33 equiv) in the selected solvent, with the selected acid additive at the selected T for the selected time; *b*: Determined via ^{1}H NMR analysis using 1,4-dimethoxybenzene as internal standard; *c*: Mixture of styrene in AcOH added dropwise on a solution of CH_2O in H_2SO_4; *d*: Mixture of H_2SO_4 and AcOH added dropwise on a solution of CH_2O and styrene in AcOH; *e*: formaldehyde solution and acid additive in AcOH added dropwise on a solution of styrene in AcOH; *f*: formaldehyde and acid additive solution in AcOH added dropwise on a solution of styrene in toluene (10 V)

A series of reaction conditions was explored to enable the synthesis of the diacetate intermediate **50** via a modified Prins reaction. Styrene **43** was reacted in glacial acetic acid, which served both as solvent and nucleophile, in the presence of Brønsted acid catalysts and various formaldehyde sources. Initial experiments using aqueous formaldehyde (37% wt.) with sulfuric acid (Entry 1) gave promising results, affording **50** in 62% yield with a selectivity of 80:20 over the competing product.

Closer analysis of the reaction profile revealed that the main byproduct was the 1,3-dioxane derivative **49**, formed via competitive Prins cyclization involving two equivalents of formaldehyde. In addition, acid-catalyzed polymerization of styrene was observed, particularly in the presence of strong acid or elevated temperatures. These two competing reactions contributed to a consistent gap between the overall conversion of styrene and the combined yields of **50** and **49**, which we attribute to styrene oligomerization and other non-productive pathways. While the formation of dioxane could be minimized under optimized conditions, styrene polymerization remained a limiting factor for overall efficiency.

To improve control over the reaction and increase selectivity, we evaluated the effect of the reagent addition order. Notably, when a solution of sulfuric acid in AcOH was added dropwise to a solution of styrene and aqueous formaldehyde in AcOH, both yield and selectivity improved significantly (Entry 2), compared to the reverse addition order (Entry 1). This modification likely minimizes local acid concentration spikes and favors better mixing, avoiding degradation of intermediates.

Building on these findings, we next investigated the effect of acid stoichiometry. Reducing the amount of sulfuric acid from 2.8 to 1.5 equivalents (Entry 3) resulted in a clear drop in yield, from 76% to 58%, despite complete conversion of styrene. This suggests that insufficient acid slows or diverts the productive reaction pathway, possibly allowing competing degradation processes of the intermediate to dominate.

Given that the addition of strong acid to aqueous formaldehyde is highly exothermic and potentially hazardous, we next turned to solid, anhydrous formaldehyde sources to improve safety and operational control. Both paraformaldehyde and 1,3,5-trioxane (Entries 4 and 5-9) showed comparable reactivity and excellent selectivity toward **50**. While paraformaldehyde required thermal activation to depolymerize, trioxane proved more manageable, undergoing smooth acid-catalyzed activation at lower temperatures. Due to its better operational profile and similar performance, 1,3,5-trioxane was selected as the preferred formaldehyde source for further development.

Optimization efforts focused on tuning the acid strength and reaction temperature. When sulfuric acid was employed as the catalyst, a clear relationship emerged between acid loading and temperature. Specifically, reducing the amount of sulfuric acid from 1.5 to 0.25 equivalents (Entries 5 and 6) required increasing the reaction temperature from 15 °C to 50 °C in order to maintain productive reactivity. Under these adjusted conditions, the yield of **50** improved from 50% to 68%, though with a slight reduction in selectivity. Furthermore, increasing the acid loading from 0.25 to 0.5 equivalents (Entry 6 vs. Entry 7) enabled the reaction to reach completion in a shorter time without compromising either yield or selectivity. Moreover, increasing the temperature up to 80 °C resulted in a diminished reaction time with a dramatic decrease of the yield, although the starting material is fully converted (Entry 8), suggesting that degradation of styrene becomes predominant at high temperatures. These results highlight the sensitivity of the reaction kinetics to the proton concentration and temperature, and suggest that fine-tuning acid strength can be an effective lever to balance efficiency and practicality.

Methanesulfonic acid (MsOH) was then investigated as a more industrially compatible alternative (Entries 9–10). In particular, Entry 9, using trioxane and MsOH at 50 °C, led to excellent selectivity (97:3) and yield (70%). Even when employing 1.5 equivalents of methanesulfonic acid, it was necessary to raise the temperature to 50 °C in order to achieve effective reactivity within practical reaction times. Lowering the temperature led to a marked decrease in reaction rate, highlighting the critical role of thermal activation in maintaining both efficiency and throughput under these acid-catalyzed conditions. MsOH was not only effective as a catalyst in this transformation but also offered strategic benefits in terms of process integration, as it is employed in downstream steps of the tolterodine synthesis. Its use facilitates raw material standardization and simplifies procurement along the supply chain. In contrast, lowering the acetic acid concentration (Entry 10) and using toluene as a solvent negatively impacted the yield (41%), reinforcing the need for a sufficiently polar and nucleophilic medium to achieve high efficiency.

Once the optimized conditions for the synthesis of compound **50** were established (Entry 10), attention was turned to the deprotection step to obtain the target diol **23**. It should be emphasize that, at this level, we were not interested in isolating compound **50** pure, since the synthetic pathway leading to tolterodine (Scheme 7) would allow us to purify the key intermediate **24**, present downstream in the process, via precipitation as fumarate salt. For this reasons, the following steps were conducted in a telescoped fashion. Initially, the hydrolysis of the diacetate was performed under basic conditions using catalytic amounts of sodium methoxide or ethoxide in methanol, relying on a transesterification mechanism. While this approach was generally effective, it occasionally suffered from incomplete conversion. This issue was traced back to residual acetic acid carried over from the previous step, which could neutralize the catalytic base and thereby inhibit the deprotection process. To overcome this limitation and ensure robustness, we adopted a more practical and scalable hydrolysis protocol using aqueous 30% sodium hydroxide under reflux conditions. This method consistently delivered high conversion to the desired diol and allowed for straightforward recovery of the product via extraction. In addition to improved reliability, the use of concentrated NaOH proved advantageous in terms of cost-efficiency and operational simplicity, making it better suited for potential scale-up (Scheme 17).

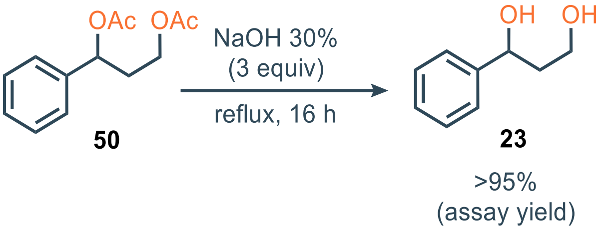

Scheme 17. Hydrolysis of diacetate **50** to afford diol **23**

Scale-Up and Final Conversion to Intermediate 24 (Fumarate Salt)

To assess the feasibility and robustness of the developed process, intermediate **23** was carried through the subsequent synthetic steps outlined in Scheme 7, leading to the formation of intermediate **24**, which was isolated and purified as its fumarate salt. The entire sequence was performed on a multigram scale, starting from 50 g of styrene, in order to evaluate the scalability of the approach. Both the overall yield and the purity of the final intermediate were compared to those obtained via the traditional synthetic route, which involves the reduction of benzoyl ethyl acetate **22** to access the 1,3-diol **23**. A side-by-side comparison of the two synthetic pathways is presented in Scheme 18.

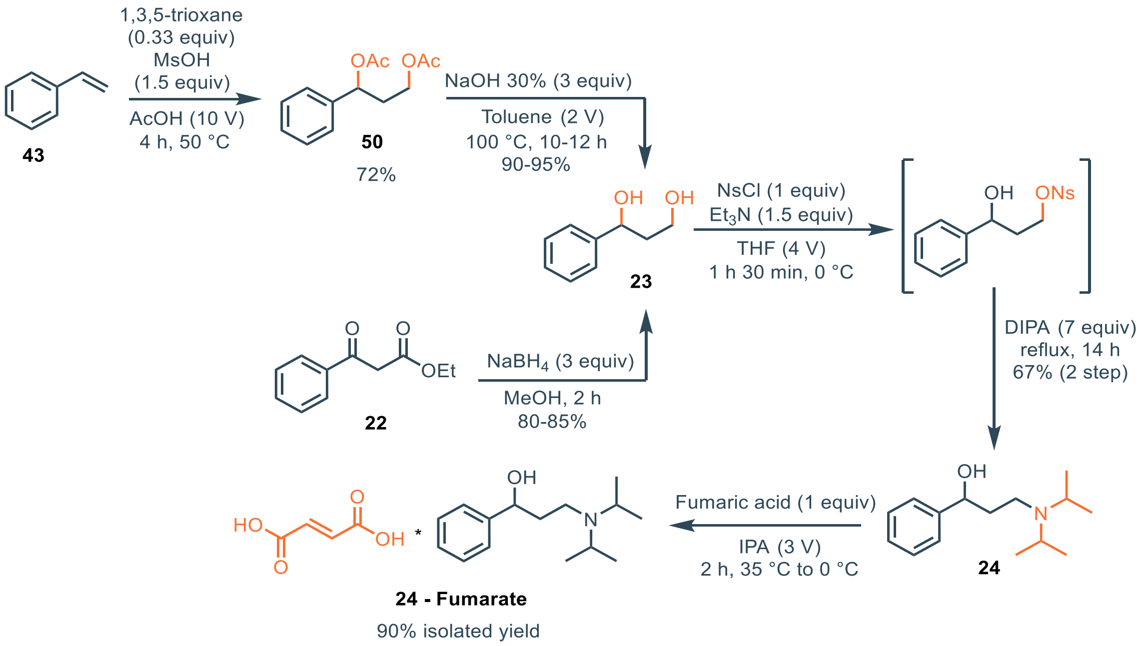

Scheme 18. Comparison of the traditional vs new synthetic pathways for the synthesis of intermediate **24** and its corresponding fumarate salt

While the traditional process delivers the fumarate intermediate **24 – Fumarate** with 51% overall yield, the new approach proposed in the present work presents a slightly lower overall yield of 40%. Nevertheless, a preliminary cost analysis reveals that the newly developed route offers significant economic advantages in terms of raw material and solvent expenses. Specifically, the cost of reagents and solvents required to produce 1 kg of the key intermediate diol **23** via the new route (starting from styrene) is estimated to be approximately €460, whereas the corresponding cost for the classical reduction route from ethyl benzoylacetate exceeds $800 per kilogram.[29] This translates to a process that is almost two times more cost-effective, despite its slightly reduced yield.

In addition to the economic benefit, the new route offers operational advantages that are particularly relevant at scale. Most notably, it avoids the use of strong reducing agents such as sodium borohydride, thereby eliminating the formation of hydrogen gas, which poses safety concerns and requires specialized containment and handling infrastructure in industrial settings. This contributes to a safer and more manageable process, especially when considering implementation at larger scale.

Moreover, GC analysis of the final intermediate **24 – Fumarate**, obtained from two independent preparations of diol **23**, revealed a meaningful difference in product quality. In one case, diol **23** was synthesized through the newly developed sequence, involving the Prins reaction followed by alkaline hydrolysis of the diacetate intermediate **50**; in the other, it was obtained via the classical reduction of ethyl benzoylacetate using sodium borohydride. Both batches were subjected to the same downstream steps to obtain intermediate **24** as the fumarate salt.

The comparison highlighted that the batch derived from the Prins-based route exhibited a superior purity, achieving 99.50% as determined by GC, compared to 97.61% for the batch prepared via the conventional approach. This observation is particularly relevant in light of the slightly lower overall yield of the Prins sequence (40% vs. 51%), suggesting that the cleaner impurity profile of the Prins-based process may compensate for the modest difference in efficiency.

---

[29] The economic evaluation is based on laboratory-scale list prices obtained from Sigma-Aldrich, TCI Chemicals, and Fluorochem as of February 12, 2026.

Taken together, these findings reinforce the advantages of the newly developed route, which combines economic competitiveness, a more favorable safety profile, due to the absence of hazardous reducing agents such as sodium borohydride and the associated evolution of hydrogen gas, and high final product quality, making it a viable and attractive alternative to the classical synthetic strategy. Current investigations are now ongoing to perform a use test employing the batch of intermediate **24 – Fumarate** obtained through the newly developed route, with the aim of completing the synthesis of Tolterodine. The goal is to verify that the final API meets the required purity specifications and that its impurity profile remains comparable to that obtained using the conventional synthetic pathway. This step will provide further confirmation of the robustness and industrial viability of the proposed route.

Prins reaction in acetic acid – continuous conditions

Having established robust conditions for the Prins reaction in batch, we then evaluated the potential benefits of performing the same transformation under continuous flow conditions. The aim was not only to improve scalability, but also to address several operational and safety challenges encountered during batch processing. One major advantage of flow chemistry lies in the possibility to limit prolonged operator exposure to corrosive acids and volatile reagents. In an optimized flow setup, reagents can be premixed and delivered in closed systems, while the acidic workup phase can be integrated in-line, significantly reducing manual handling and improving containment. Similarly, flow operation allows for a more controlled and continuous introduction of the formaldehyde source, thereby minimizing the risks associated with their toxicity and volatility. This setup avoids the accumulation of reactive intermediates and improves overall safety, particularly in the context of scale-up. Moreover, the precise control over residence time provided by flow systems represents a key asset in managing the delicate balance between full conversion and side reactivity. Unlike batch, where local concentration gradients and thermal fluctuations can promote undesired pathways, flow enables tight control over reaction parameters, potentially minimizing degradation of the starting material and the formation of undesired byproducts such as the 1,3-dioxane. The ability to maintain uniform temperature profiles and avoid hotspots is particularly valuable in this exothermic transformation. Thermal management in flow not only enhances reproducibility but also improves selectivity by maintaining optimal reactivity throughout the reactor channel. Finally, from a practical standpoint, flow chemistry offers a modular platform that can be seamlessly integrated with downstream operations such as in-line quenching, liquid-liquid separation, or purification. This enables a streamlined, telescoped process with reduced cycle times, improved safety, and lower solvent consumption, factors that are particularly attractive for industrial implementation.

To this end, we conducted the optimization of the reaction in continuous conditions employing the Asynt® fReactor™ (Figure 2), a miniaturized continuous stirred tank reactor (CSTR) specifically designed for continuous synthesis with 1.6 mL internal volume. The rationale behind this choice lies in the reactor's ability to provide sufficient mixing energy to ensure optimal mass transfer, which is essential for the efficient conversion of biphasic liquid–liquid systems and would be difficult to achieve in static or poorly mixed environments. Efficient mass transfer is a key parameter in driving such biphasic reactions to completion.

In addition to its mixing performance, the modular nature of the fReactor platform offers important advantages for process development and scale-up. Through numbering-up strategies, multiple units can be operated in parallel with minimal modifications to the setup, allowing for a straightforward and reproducible increase in throughput. Furthermore, the reactor configuration supports in-line workup operations, enabling the integration of downstream steps such as quenching, extraction, or phase separation directly within the flow system. This design flexibility not only enhances process intensification but also contributes to safer and more efficient handling of reactive or hazardous intermediates.

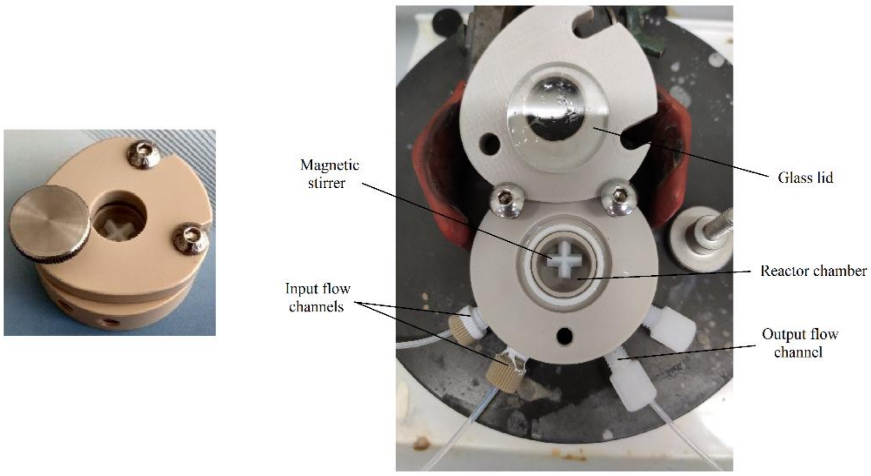

Figure 2. Asynt® fReactor™ and its components

In an initial approach, we investigated the Prins reaction under continuous flow conditions using a three-input configuration, in which styrene, 1,3,5-trioxane, and methanesulfonic acid (MsOH) were independently pumped into the Asynt® fReactor™ as separate solutions in acetic acid. The concentrations were adjusted to 1.95 M for styrene, 2.38 M for 1,3,5-trioxane (calculated relative to formaldehyde monomer), and 2.31 M for MsOH, thus maintaining a 1:1 molar ratio between styrene and formaldehyde (monomer equivalent). The flow rates were changed during the optimization to evaluate different equivalents per minute of acid pumped and different residence times, while temperature variations allowed us to monitor the kinetic of this reaction in continuous conditions. The results of this preliminary optimization using 1 equiv/min of MsOH are summarized in Table 4. It is important to note that these experiments were exploratory in nature, and therefore assay yields were not determined for each entry, but only for the most promising entries (e.g. with almost full conversion of the starting material). Product distribution was instead estimated by crude ^{1}H NMR analysis of the output streams, without isolation or purification. Despite the absence of precise quantification, valuable trends can be observed. At 25 °C, conversion was minimal even at extended residence times (Entry 4), with styrene **43** remaining the major component. Upon increasing the temperature to 50 °C, a progressive improvement in conversion was observed with increasing residence time, and formation of the desired diacetate **50** became significant after 5 to 10 minutes (Entries 7–8). Interestingly, the 1,3-dioxane byproduct **49** was only observed in appreciable amounts at longer residence times, indicating a competing secondary reaction pathway. Increasing the temperature to 80 °C did not significantly improve the overall conversion under short residence times (Entries 9–11).

Table 4. Prins reaction in flow conditions with the three-input configuration - 1:1:1 (formaldehyde/MsOH/styrene) ratio between the three components [a]

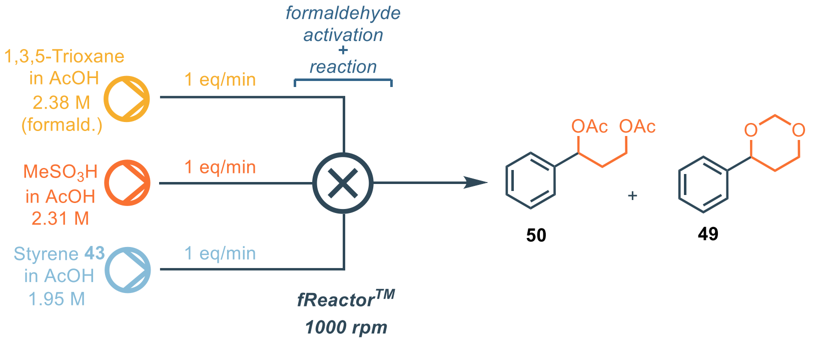

Entry	T (°C)	RT (min)	Ratio 43 : 50 : 49 [b]

1	25 °C	1	100 : 0 : 0
2		2	100 : 0 : 0
3		5	99 : 1 : 0
4		10	94 : 6 : 0
5	50 °C	1	100 : 0 : 0
6		2	96 : 4 : 0
7		5	81 : 17 : 0
8		10	64 : 32 : 3
9	80 °C	1	100 : 0 : 0
10		2	94 : 6 : 0
11		5	80 : 11 : 9
12		10	48 : 34 : 18

a: Reactions performed using 1 equiv/min of Styrene, 0.33 equiv/min of 1,3,5-trioxane (1 equiv/min of formaldehyde monomer) and 1 equiv/min of MsOH; *b*: determined *via* NMR analysis

However, when the residence time was extended to 10 minutes (Entry 12), a notable increase in conversion was observed compared to the corresponding experiment at 50 °C (Entry 8), suggesting that longer residence times can compensate for slower activation kinetics under moderate acid loading. Nonetheless, this improvement in conversion came at the expense of product selectivity, with a decrease in the ratio of diacetate **50** over the undesired dioxane **49**, indicating that higher temperatures may also promote competing side reactions under these conditions.

In several of the higher-temperature or long-residence-time experiments, the output mixtures were found to be dark in color and difficult to analyze by NMR due to baseline broadening and overlapping signals. This behavior, along with the presence of unidentifiable peaks in the spectra, strongly suggests thermal or acid-catalyzed degradation of styrene, likely via oligomerization or polymerization pathways. This phenomenon, already known from batch studies, appears to be accentuated under high-temperature flow conditions, particularly when reaction time is not strictly controlled. Thus, to increase the kinetic of the Prins reaction we decided to increase the equivalents of MsOH, with the idea that this could accelerate the reaction, avoiding oligomerization of the Styrene. The results of the optimization using 2 equiv/min of MsOH are summarized in Table 5.

The results clearly show that increasing the flow rate of methanesulfonic acid (MsOH) from 1 to 2 equivalents per minute has a significant impact on the reactivity profile of the system. At 50 °C, while comparable residence times (5–20 minutes) in the lower-acid regime resulted in limited conversion and modest formation of the diacetate **50** (with styrene **43** still largely unreacted, entries 5-8, Table 4), the increased acid flow rate led to a marked improvement in product formation (Entries 1-5, Table 5).

In particular, at 80 °C and 20 minutes residence time (Entry 6, Table 5), the proportion of **50** reaches 86%, with only 5% of styrene remaining, indicative of near-complete conversion. Among all tested conditions, Entry 6 was selected for yield determination, affording compound **50** in 64% NMR yield. While this yield is slightly lower than that obtained under optimized batch conditions, it was achieved with a significantly shorter reaction time, underscoring the efficiency and practicality of the continuous setup.

Table 5. Prins reaction in flow conditions with the three-input configuration - 1:2:1 (formaldehyde/MsOH/styrene) ratio between the three components [a]

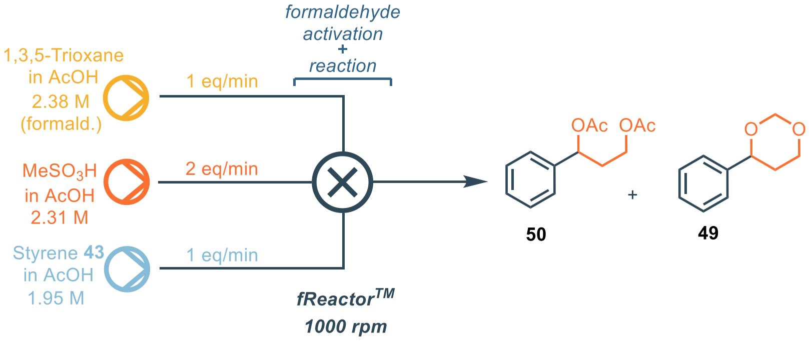

Entry	T (°C)	RT (min)	Ratio 43 : 50 : 49 [b]
1	50 °C	5	84 : 15 : 1
2		10	50 : 46 : 3
3		20	30 : 66 : 4
4	80 °C	5	53 : 43 : 4
5		10	27 : 67 : 6
6		20	5 : 86 : 9 [c]

a: Reactions performed using 1 equiv/min of Styrene, 0.33 equiv/min of 1,3,5-trioxane (1 equiv/min of formaldehyde monomer) and 2 equiv/min of MsOH; *b*: determined *via* NMR analysis; *c*: NMR yield of **50**: 64% determined via ^{1}H NMR using 1,4-dimethoxybenzene as internal standard

In order to further enhance the efficiency of the process, we chose to move away from the three-input configuration. We hypothesized that, under those conditions, 1,3,5-trioxane was not being effectively activated, leading to a sluggish reaction outcome. This kinetic imbalance likely resulted in unreacted styrene being exposed to acidic and heated conditions, promoting its degradation rather than productive transformation. To address this limitation, we opted to pre-activate the formaldehyde source by preparing a stock solution of 1,3,5-trioxane and MsOH in acetic acid. This strategy enabled a two-input configuration, in which the stock solution and a separate solution of styrene were independently pumped into the Asynt® fReactor™. The reaction outcome was monitored at different temperatures, at different residence times and with 1 and 2 equivalents per minute of MsOH. The results are summarised in Table 6.

Table 6. Prins reaction in flow conditions with the two-input configuration – temperature and acid equivalents optimization [a]

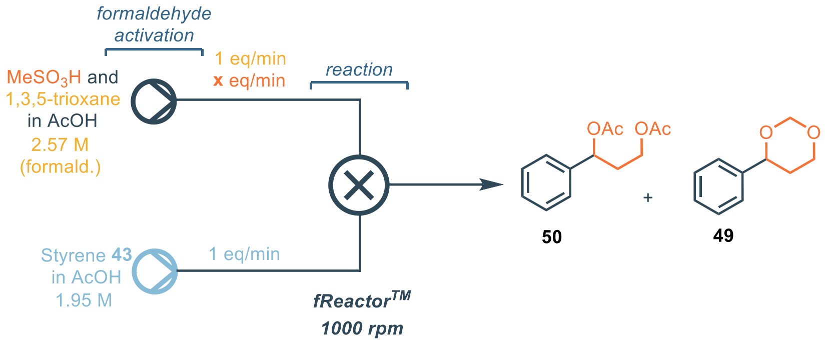

Entry	T (°C)	Equiv/min MsOH	RT (min)	Ratio 43 : 50 : 49 [b]	NMR yield of 50 (%) [c]
1	50 °C	1 equiv/min	5	74 : 19 : 7	/
2			10	48 : 41 : 12	/
3			20	29 : 57 : 14	/
4	80 °C	1 equiv/min	5	25 : 58 : 17	/
5			10	10 : 71 : 19	/
6			20	8 : 74 : 18 [c]	/
7	50 °C	2 equiv/min	5	22 : 70 : 8	/
8			10	13 : 77 : 10	/
9			20	4 : 86 : 10	53%
10	80 °C	2 equiv/min	5	0 : 87 : 13	57%
11[d]	50 °C	2 equiv/min	5	12 : 80 : 11	59%
12[d]			10	3 : 86 : 11	62%

a: Reactions performed using 1 equiv/min of Styrene, 0.33 equiv/min of 1,3,5-trioxane (1 equiv/min of formaldehyde monomer) and 1 or 2 equiv/min of MsOH; *b*: determined *via* NMR analysis; *c*: NMR yield of **50** determined via ^{1}H NMR using 1,4-dimethoxybenzene as internal standard; *d*: 2.6 bar-BPR (Back-pressure regulator) installed downstream the CSTR

In all cases, pre-activation of the formaldehyde oligomer proved to be an effective strategy to improve the reactivity. In particular, almost full conversion of styrene occurs at 50 °C with 2 equiv/min of MsOH when the 1,3,5-trioxane is pre-activated (Table 6, entry 9), delivering 53% of diacetate **50**, while 30% of residual styrene is present in the same conditions with the three-input configuration (Table 5, entry 3). Moreover, at 80 °C, full conversion of styrene is accomplished in only 5 minutes of RT (Table 6, entry 10) with 57% yield, while 20 minutes were required to accomplish a similar result when 1,3,5-trioxane was not pre-activated (Table 5, entry 6). Given the shorter residence time needed using this setup, we moved on through the optimization of the reaction conditions using this approach, even though the best yield obtained (57%, Table 6, entry 10) is slightly lower than the one observed when the three-input configuration was used (64%, Table 5, entry 6).

With the aim of improving both the reaction setup and its overall performance, we speculated that the introduction of a back-pressure regulator (BPR) downstream of the CSTR could avoid any loss of gaseous formaldehyde, released upon its activation. This modification was expected to enhance safety, reproducibility, and efficiency of the process. Gladly, the introduction of this technological solution allowed us to consistently reduce the working temperature and the residence time with a yield improvement (Table 6, entries 11-12).

Having established the optimal parameters in terms of temperature (50 °C), residence time (5 - 10 min), pressure control (BPR at 2.4 bar), and formaldehyde activation (formaldehyde monomer to MsOH ratio of 1:2), we hypothesized that further improvements in reactivity could be achieved by carefully adjusting the styrene-to-formaldehyde ratio. Specifically, we reasoned that a slight excess of aldehyde might accelerate the Prins reaction, thereby reducing the degradation of styrene under acidic and high temperature conditions, even though this could lower the selectivity of the process, facilitating the formation of the dioxane **49**, for whose formation 2 equivalents of aldehyde are required. The data of the experiments performed varying the equivalents of aldehyde are summarized in Table 7. The data obtained reveal that increasing the equivalents of formaldehyde have a general beneficial effect on the efficiency of the setup, allowing the reaction to get to completion with shorter residence times (Table 7, entry 1-3 vs Table 6, entry 7-9) without affecting the selectivity of the reaction toward the diacetate **50**. In particular, the best conditions were found in Table 7, entry 1, delivering the desired product with 69% yield, indicating that an optimal balance between the reagents used has been achieved.

Table 7. Prins reaction in flow conditions with the two-input configuration using downstream BPR – optimization of the formaldehyde equivalents [a]

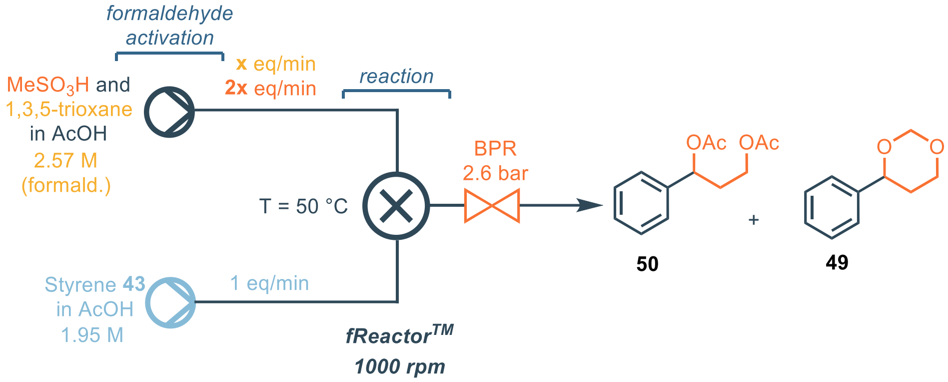

Entry	Equiv/min formaldehyde	RT (min)	Ratio 43 : 50 : 49 [b]	NMR yield of 50 (%) [c]
1	1.2 equiv/min	5	0 : 88 : 12	69%
2	1.2 equiv/min	10	0 : 85 : 15	67%
3	1.5 equiv/min	5	0 : 82 : 18	69%

a: Reactions performed using 1 equiv/min of styrene, 0.4–0.5 equiv/min of 1,3,5-trioxane (corresponding to 1.2–1.5 equiv/min of formaldehyde monomer), and MsOH in an amount equal to twice the number of formaldehyde equivalents; *b*: determined *via* NMR analysis; *c*: NMR yield of **50** determined via ^{1}H NMR using 1,4-dimethoxybenzene as internal standard;

Once the optimal reaction conditions had been identified, we sought to further refine the flow setup by carrying out the activation of 1,3,5-trioxane directly under continuous conditions, rather than relying on the preparation of a premixed stock solution with MsOH. To this end, we designed the flow system illustrated in Scheme 18, in which 1,3,5-trioxane (1.2 equiv/min, calculated as formaldehyde monomer) is activated by methanesulfonic acid (2.4 equiv/min, corresponding to a 1:2 formaldehyde/MsOH ratio) in a first Asynt® fReactor™ operated at room temperature. The resulting solution, containing the in situ activated formaldehyde, proceeds directly into a second reactor where it reacts with styrene (1 equiv/min) at 50 °C with a residence time of 5 minutes. This configuration offers several practical advantages: it reduces manual handling of corrosive reagents, improves operational safety, and ensures better reproducibility by minimizing variability associated with batchwise stock solution preparation. Moreover, the inline activation of the trioxane eliminates the need for reagent pre-mixing, making the process more streamlined and scalable.

Gladly, the redesigned setup proved to be equally effective in delivering the desired product, achieving full conversion of the starting material, a ratio of **50**:**49** (85:15, determined via ^{1}H-NMR) and a yield of **50** (67%, determined via ^{1}H-NMR using 1,4-dimethoxybenzene as internal standard) comparable to those obtained under the previously optimized conditions (Table 7, entry 1). This outcome confirms the robustness of the continuous activation strategy and enables direct access to the diacetate intermediate under fully continuous and operationally simplified conditions, without the need for pre-activation steps.

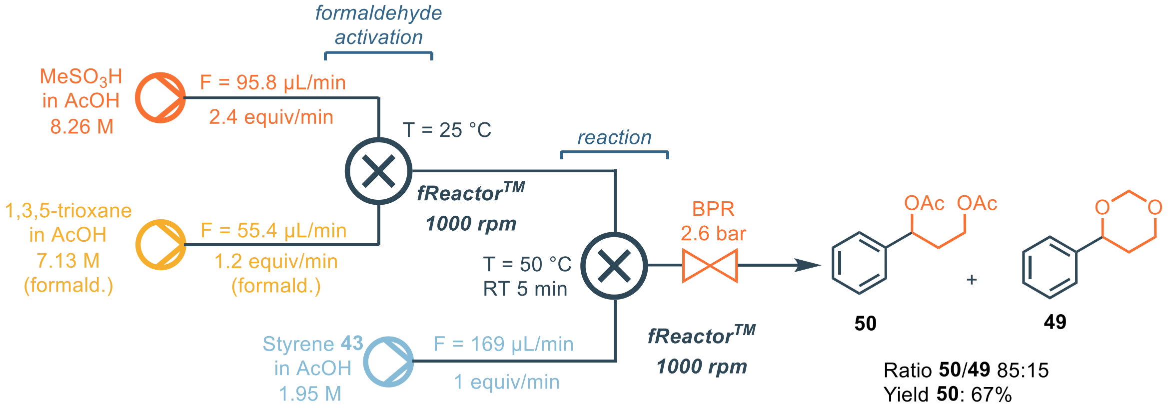

Scheme 18. Prins reaction in flow conditions with continuous activation of the 1,3,5-trioxane

Once the reaction conditions had been established, attention was turned to the optimization of the work-up procedure. As a starting point, we referred to the batch protocol (see Experimental Section), which involves extraction with 6 volumes of 1 M NaOH solution and 6 volumes of toluene. These conditions were shown to effectively quench the residual acidity without causing detectable hydrolysis of compound **50**. To adapt this to the continuous process, the initial strategy consisted of directing the reactor outflow into a stirring container pre-loaded with a biphasic mixture of 1 M NaOH and toluene (Scheme 19), which is then transferred into a separatory funnel for phase separation. Given a crude collection period of 30 minutes, it was estimated that approximately 2 g of styrene had been processed. For the quench and extraction, 13 mL of each phase (corresponding to 6 volumes) were used. After separation, the organic phase was concentrated under reduced pressure, affording the diacetate **50** in 72% yield, with a diacetate-to-dioxane ratio of 87:13, in line with the selectivity observed in the preceding flow experiments.

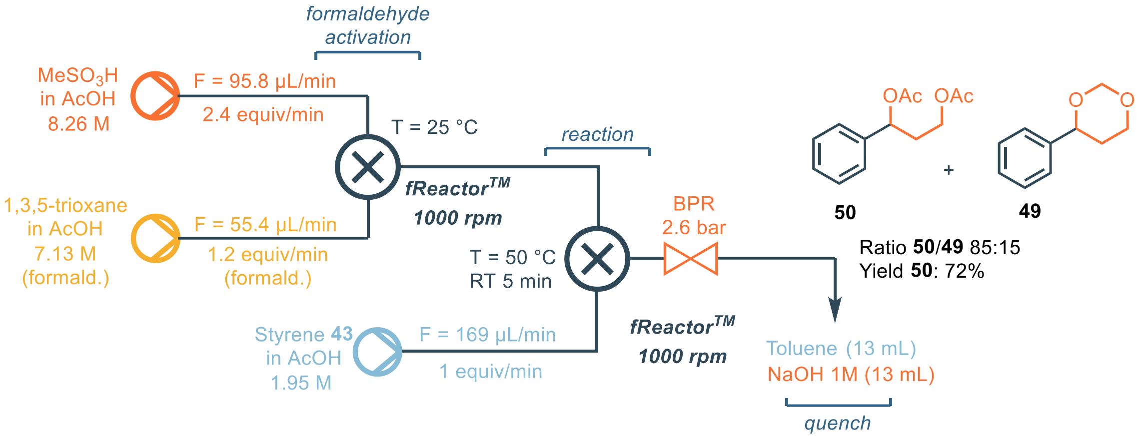

Scheme 19. Prins reaction in flow conditions with continuous activation of the 1,3,5-trioxane and offline workup

Having determined the appropriate volumes for the quenching and extraction phases, we next turned our efforts toward implementing the work-up under continuous flow conditions. For this purpose, a third Asynt® fReactor™ was integrated into the system, where 1 M NaOH and toluene were each introduced at a flow rate of 6 V/min, together with the reaction stream exiting the second CSTR, as shown in Scheme 20. To enable continuous and reliable phase separation, the setup was coupled with a Zaiput SEP-10 liquid–liquid membrane separator, equipped with a 0.5 μm porous PTFE membrane, resulting in a fully automated quench and extraction system. The organic phase containing product **50** was directly collected and made available for the subsequent hydrolysis step, minimizing handling and streamlining the process. This fully integrated setup enabled straightforward isolation of the crude product simply by concentrating the organic phase exiting the Zaiput membrane separator. Under these conditions, a yield of 74% (determined by NMR) was achieved with excellent selectivity. Notably, using only a single Asynt® fReactor™ module (1.6 mL internal volume), it was possible to produce 2.28 g of crude material in 30 minutes, corresponding to 1.71 g of compound **50**. These promising results highlight the potential scalability of the system through a numbering-up approach, whereby multiple reactor units can be operated in parallel to significantly boost productivity without altering the reaction parameters. This proof-of-concept demonstrates the feasibility of a fully continuous workflow encompassing reagent premixing, reaction, quenching, extraction, and phase separation in a closed and modular system. Such a design not only improves operational efficiency but also minimizes exposure to corrosive acids and toxic reagents, offering a safer and more sustainable alternative for the synthesis of intermediate **50** on an industrially relevant scale.

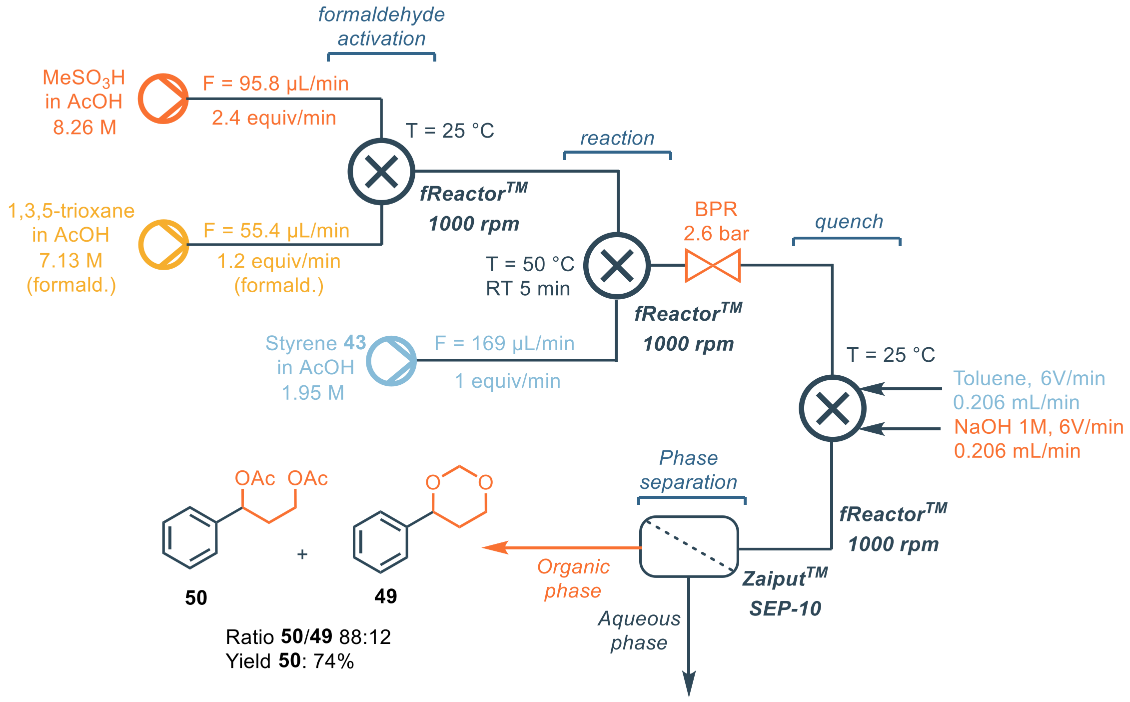

Scheme 20. Prins reaction in flow conditions with continuous workup and automatic phase separation

Conclusions

In this study, a novel synthetic route was developed for the preparation of the diol intermediate **23**, a key precursor in the industrial synthesis of Tolterodine, based on the Prins reaction between styrene and formaldehyde. This strategy was designed to overcome the limitations of classical ester reduction methods involving borohydride reagents, which pose significant safety concerns due to hydrogen gas evolution, and entail high raw material costs and operational complexity at scale.

The proposed route, employing inexpensive and widely available starting materials, led to the formation of the diacetate intermediate **50** in good yields and with high reproducibility. Subsequent mild alkaline hydrolysis provided the target diol **23**. Process optimization was successfully carried out both in batch and continuous flow conditions, resulting in a scalable and industrially viable synthetic protocol. Although the overall yield of the newly developed route (40%) was slightly lower than that of the traditional process (51%), a detailed cost analysis revealed a more than twofold reduction in production costs per kilogram of intermediate. In addition, this approach eliminated the use of hazardous reducing agents and generated a higher purity product (99.5% vs. 97.6% by GC), thereby offering a compelling balance between efficiency, safety, and economic feasibility.

Importantly, the continuous flow implementation further enhanced the process by improving heat and mass transfer, reducing reaction times, and minimizing operator exposure to corrosive and volatile reagents. The robustness, reproducibility, and scalability of the process were confirmed on multigram scale, highlighting the practical potential of this approach in pharmaceutical manufacturing. Overall, the developed methodology represents a viable alternative for Tolterodine intermediate production, particularly in scenarios where cost-efficiency, safety, and process intensification are critical. The results also open the door to broader application of Prins-based strategies to access complex molecular architectures in a sustainable and scalable manner.

Experimental section

Instrumentations

Nuclear magnetic resonance analyses (1H- and 13C-NMR spectra) were acquired using a Bruker Advance III 400 MHz spectrophotometer and a Varian-Oxford-500 spectrophotometer at 500 MHz. Chemical shifts (δ) are reported in ppm relative to residual solvent signals for ^{1}H- and ^{13}C-NMR (^{1}H-NMR: 7.26 ppm for $CDCl_3$; ^{13}C-NMR: 77.16 ppm for $CDCl_3$). ^{13}C-NMR spectra were acquired with ^{1}H broadband decoupled mode. Coupling constants are given in Hz. ^{1}H-NMR yields were measured by analysing the reaction mixture using triphenylmethane and 1,4-dimethoxybenzene as internal standard. Chromatographic purifications of compounds **23** and **49** were performed using automated Biotage® Isolera LS Systems. Reaction mixtures were stirred and heated with the support of the magnetic stirrer Heidolph® MR Hei-Standard or Heidolph® MR 3001 K, each equipped with Heidolph® EKT Hei-Con. The flow reactor was equipped with Asynt® fReactor™ as the main mixing unit. The chemicals and solutions were pumped in the flow reactor with Chemyx Fusion 4000 syringe pump, Chemyx Fusion 6000 syringe pump, KF Technology NE-1000 syringe pump, KF Technology NE-4000 double syringe pump or Hitec Zang SyrDos™-syringe pump. The inline liquid-liquid separation was performed with Zaiput SEP-10™. The back-pressure regulator used is Biotech P-761 Cartridge. For the reactor coil and the connecting tubes of the flow reactors SepaChrom PTFE tubing 1.59 mm I.D. 1/8” O.D. are used.

Materials and methods

The solvents and chemicals are commercial products, purchased from BLDPharm, Merck and TCI, and they were used as received without further purification unless stated otherwise.

Experimental procedures

Synthesis of 4-phenyl-1,3-dioxane 49

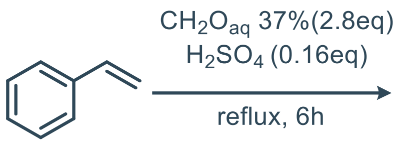

43 **49**

A 37% aqueous solution of formaldehyde (6.25 mL, 84 mmol, 2.8 eq) was placed in a 50 mL round-bottom flask, followed by the addition of a 96% concentrated sulfuric acid (267 µL, 4.8 mmol, 0.16 eq). Styrene (3.45 mL, 30 mmol, 1.0 eq) was then added, and the biphasic mixture was stirred vigorously under reflux to promote efficient contact between the immiscible phases. The progress of the reaction was monitored by periodic analysis of aliquots via ^{1}H-NMR spectroscopy. After 6 h, the reaction mixture was cooled to room temperature and extracted with ethyl acetate (3 × 10 mL). The combined organic layers were washed with 1 M HCl saturated with NaCl (3 × 10 mL), dried over anhydrous Na_2SO_4, filtered through cotton, and concentrated under reduced pressure. The crude product was obtained as a yellow oil (4.82 g, 29.4 mmol, 98% yield).

^{1}H-NMR (400 MHz, $CDCl_3$): δ 7.43 – 7.27 (m, 5H), 5.23 (d, J = 6.4 Hz, 1H), 4.91 (d, J = 6.3 Hz, 1H), 4.66 (dd, J = 11.3, 2.6 Hz, 1H), 4.21 (m, 1H), 3.89 (m, 1H), 2.19 – 2.03 (m, 1H), 1.78 – 1.68 (m, 1H).

The chemical shifts are consistent with those reported in the literature.[28]

Synthesis of 1-Phenyl-1,3-propanediol (23) via acetal hydrolysis

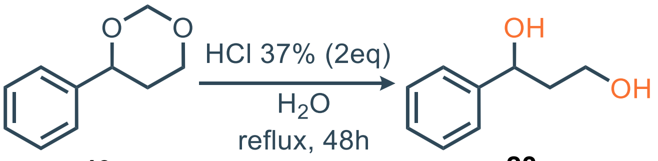

49 **23**

4-Phenyl-1,3-dioxane (250 mg, 1.52 mmol, 1.0 eq) was placed in a 50 mL round-bottom flask sealed with a rubber septum, which was pierced with a needle connected to a balloon in order to monitor the evolution of formaldehyde. Water (15 mL) and HCl (286 μL, 3.05 mmol, 2.0 eq) were then added, and the reaction mixture was stirred vigorously and heated to reflux for 48 h, with progress monitored by TLC. After 48 h the reaction mixture was extracted with EtOAc (3 × 10 mL), and the combined organic layers were washed with saturated $NaHCO_3$ solution (2 × 10 mL) followed by brine (1 × 10 mL). The organic phase was dried over anhydrous Na_2SO_4, filtered through cotton, and concentrated under reduced pressure. The crude residue was purified by flash column chromatography using an isocratic elution with petroleum ether/ethyl acetate (6:4), affording 1-phenyl-1,3-propanediol as a highly viscous oil (67.8 mg, 0.45 mmol, 29% yield).

^{1}H-NMR (400 MHz, DMSO-d$_6$): δ 7.34–7.29 (m, 4H), 7.24–7.18 (m, 1H), 5.13 (d, J = 4.48 Hz, 1H), 4.68–4.62 (m, 1H), 4.42 (t, J = 5.07 Hz, 1H), 3.55–3.37 (m, 2H), 1.81–1.62 (m, 2H).

^{13}C-NMR (100 MHz, DMSO-d$_6$): δ 146.5, 128.0, 126.6, 125.7, 69.5, 58.0, 42.6.

The chemical shifts are consistent with those reported in the literature.[30]

Synthesis of 1,3-diacetoxy-1-phenylpropane (50) in batch conditions

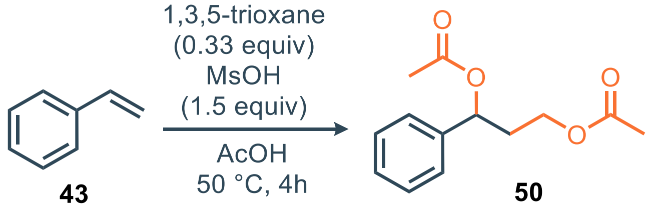

A 1 L jacketed glass stirred tank reactor equipped with a mechanical agitator and maintained under an inert atmosphere were charged with styrene (50.0 g, 55.19 mL, 0.48 mol, 1.0 eq), 1,3,5-trioxane (14.42 g, 0.48 mol of formaldehyde monomer, 1.0 eq), and acetic acid (262.5 g, 250 mL, 5 vol) and the mixture was heated to 50 °C under stirring. A solution of acetic acid (262.5 g, 250 mL, 5 vol) and methanesulfonic acid (69.29 g, 46.75 mL, 0.72 mol, 1.5 eq) was then added dropwise to the reaction mixture over 30 min via an addition funnel. The reaction was maintained at 50 °C under agitation for 4 h, during which the progress was monitored by ^{1}H-NMR spectroscopy. After completion, the mixture was cooled to 25 °C, diluted with toluene (300 mL), and the organic phase was washed with aqueous 1 M NaOH (2 × 200 mL) until the aqueous layer reached pH ≈ 5. The organic layer was concentrated under reduced pressure to afford the crude product without further

---

[30] E. Ascic, R. G. Ohm, R. Petersen, M. R. Hansen, C. L. Hansen, D. Madsen, D. Tanner, T. E. Nielsen, *Chem. Eur. J.*, **2014**, *20*, 3297-3300

purification. This provided 105.5 g of crude, which contains 71.25% m/m of 1,3-diacetoxy-1-phenylpropane **50** (77 g) with 72% NMR yield. The crude was used in the following step without further purifications.

^{1}H-NMR (500 MHz, CDCl$_3$): δ 7.38-7.27 (m, 5H), 5.86 (dd, *J* = 8.0, 5.6 Hz, 1H), 4.15 (m, 1H), 4.02 (m, 1H), 2.24 (m, 1H), 2.12 (m, 1H), 2.08 (s, 3H), 2.03 (s, 3H).

The chemical shifts are consistent with those reported in the literature.[31]

Synthesis of 1-phenyl-1,3-propanediol (23) via hydrolysis of 1,3-diacetoxy-1-phenylpropane 50

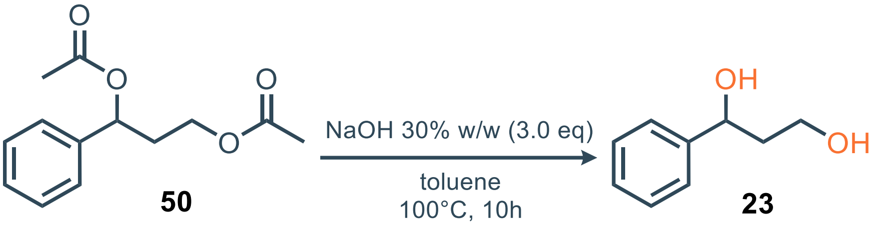

In a 1 L jacketed glass stirred tank reactor equipped with a mechanical agitator, 1,3-diacetoxy-1-phenylpropane **50** (71.25 g, 0.302 mol, 1.0 equiv.) and toluene (200 mL) were charged at 50 °C. A 30% w/w aqueous solution of NaOH (118.51 g, 0.904 mol, 3.0 equiv.) was then added dropwise. The reaction mixture was subsequently heated to 100 °C and stirred for 10 h. The progress of the reaction was monitored by ^{1}H-NMR spectroscopy. After 10 h, the aqueous phase was separated, and the organic layer was extracted with toluene (100 mL). The combined organic extracts were washed with saturated NaCl solution (50 mL) and concentrated under reduced pressure, affording 73.75 g of crude material which contains 56.15% m/m of 11-phenyl-1,3-propanediol **23** (41.41 g) with 90% NMR yield. The crude was used in the following step without further purifications.

^{1}H-NMR (500 MHz, DMSO-d$_6$): δ 7.34–7.29 (m, 4H), 7.24–7.18 (m, 1H), 5.13 (d, J = 4.48 Hz, 1H), 4.68–4.62 (m, 1H), 4.42 (t, J = 5.07 Hz, 1H), 3.55–3.37 (m, 2H), 1.81–1.62 (m, 2H).

^{13}C-NMR (125 MHz, DMSO-d$_6$): δ 146.5, 128.0, 126.6, 125.7, 69.5, 58.0, 42.6.

The chemical shifts are consistent with those reported in the literature.[29]

---

[31] A. D. Satterfield, A. Kubota, M. S. Sanford, *Org. Lett.*, **2011**, *13*, 1076–1079

Synthesis of 3-(diisopropylamino)-1-phenylpropan-1-ol (24)

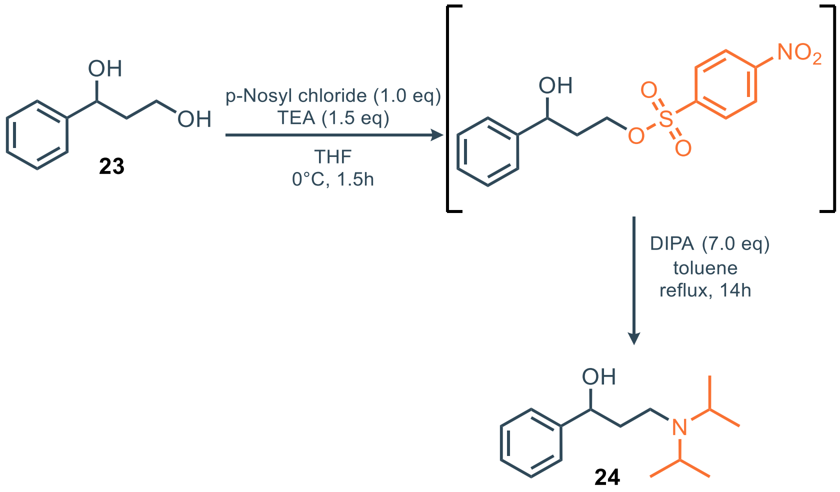

In a 1 L jacketed glass stirred tank reactor equipped with a mechanical agitator, 1-phenyl-1,3-propanediol **23** (71.3 g of crude, content of **23**: 56.15% m/m, 40.08 g, 0.263 mol, 1.0 eq), THF (160 mL), and p-nitrobenzenesulfonyl chloride (58.28 g, 0.263 mol, 1.0 eq) were charged. The mixture was cooled to 0 °C, and triethylamine (39.97 g, 55.05 mL, 0.395 mol, 1.5 eq) was added dropwise while maintaining the temperature between 0 and 5 °C. The reaction mixture was stirred for 1.5 h, and the progress was monitored by ^{1}H-NMR spectroscopy. After 1.5 h, water (140 mL) was added, and the organic phase was extracted with toluene (140 mL), washed with saturated NaCl solution (50 mL), and concentrated under reduced pressure. The resulting toluene solution of 3-hydroxy-3-phenylpropyl 4-nitrobenzenesulfonate was used directly in the subsequent step without further purification.

In a 500 mL jacketed glass stirred tank reactor equipped with a mechanical agitator, the toluene solution of 3-hydroxy-3-phenylpropyl 4-nitrobenzenesulfonate (320 mL, 0.263 mol, 1.0 eq) and diisopropylamine (186.3 g, 258.75 mL, 1.84 mol, 7.0 eq) were charged. The reaction mixture was heated to reflux and stirred for 14 h. The progress of the reaction was monitored by ^{1}H-NMR spectroscopy. After 14 h, the mixture was cooled to room temperature, and the volume was reduced to approximately 200 mL. Water (150 mL) was then added, and the organic layer was extracted with EtOAc (200 mL). The aqueous phase was separated and extracted with EtOAc (200 mL). The combined organic extracts were washed with saturated NaCl solution (200 mL) and concentrated under reduced pressure to afford 63.9 g of a yellowish crude material which contains 64.60% m/m of 3-(diisopropylamino)-1-phenylpropan-1-ol **24** (41.27 g) with 66.7% NMR yield over two steps. The crude was used in the following step without further purifications.

^{1}H-NMR (500 MHz, CDCl$_3$): δ 7.39-7.19 (m, 5H), 4.90 (dd, J = 9.9, 2.5 Hz, 1H), 3.20 (hept, J = 6.8 Hz, 2H), 2.87-2.73 (m, 2H), 1.84 (m, 1H), 1.66 (m, 1H), 1.14 (d, J = 6.8 Hz, 6H), 1.02 (d, J = 6.8 Hz, 6H).

^{13}C-NMR (125 MHz, CDCl$_3$): δ 145.5, 128.4, 127.0, 125.8, 76.3, 47.5, 44.2, 35.3, 21.9, 18.8.

The chemical shifts are consistent with those reported in the literature.[15]

Synthesis of 3-(diisopropylamino)-1-phenylpropan-1-ol Fumarate (24-Fumarate)

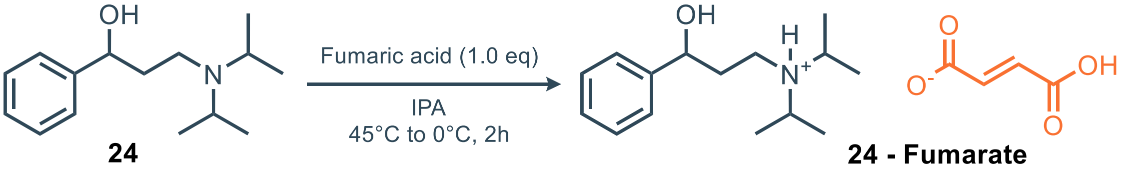

A 500 mL jacketed glass stirred tank reactor equipped with a mechanical agitator was charged with 3-(diisopropylamino)-1-phenylpropan-1-ol **24** (60 g of crude, content of **24**: 64.60% m/m, 38.76 g, 0.165 mol, 1.0 eq) and isopropanol (220 mL). The reaction mixture was heated to 45 °C, and fumaric acid (19.15 g, 0.165 mol, 1.0 eq) was added portionwise. Seeding was introduced to the solution until the onset of precipitation was observed. The temperature was then gradually decreased from 45°C to 0°C over 2 h to complete the crystallization. The resulting solid was collected by Büchner filtration under reduced pressure to afford 3-(diisopropylamino)-1-phenylpropan-1-ol fumarate **24-Fumarate** pure as a crystalline white solid (52.06 g, 0.148 mol, 90% yield).

^{1}H-NMR (500 MHz, DMSO-d$_6$): δ 7.38-7.29 (m, 4H), 7.26-7.19 (m, 1H), 4.68-4.64 (m, 1H) , 3.39 (hept, J = 6.6 Hz, 2H), 2.99-2.84 (m, 2H), 1.92-1.86 (m, 2H), 1.66 (m, 1H), 1.14 (d, J = 6.6 Hz, 12H).

^{13}C NMR (126 MHz, DMSO-d$_6$) δ 167.62, 145.48, 135.06, 128.07, 126.86, 125.61, 70.41, 51.98, 43.42, 36.92, 18.24, 18.09

ESI-MS (+): 236.20 $[M+H]^+$

General Flow procedure for the synthesis of 1,3-diacetoxy-1-phenylpropane (50)

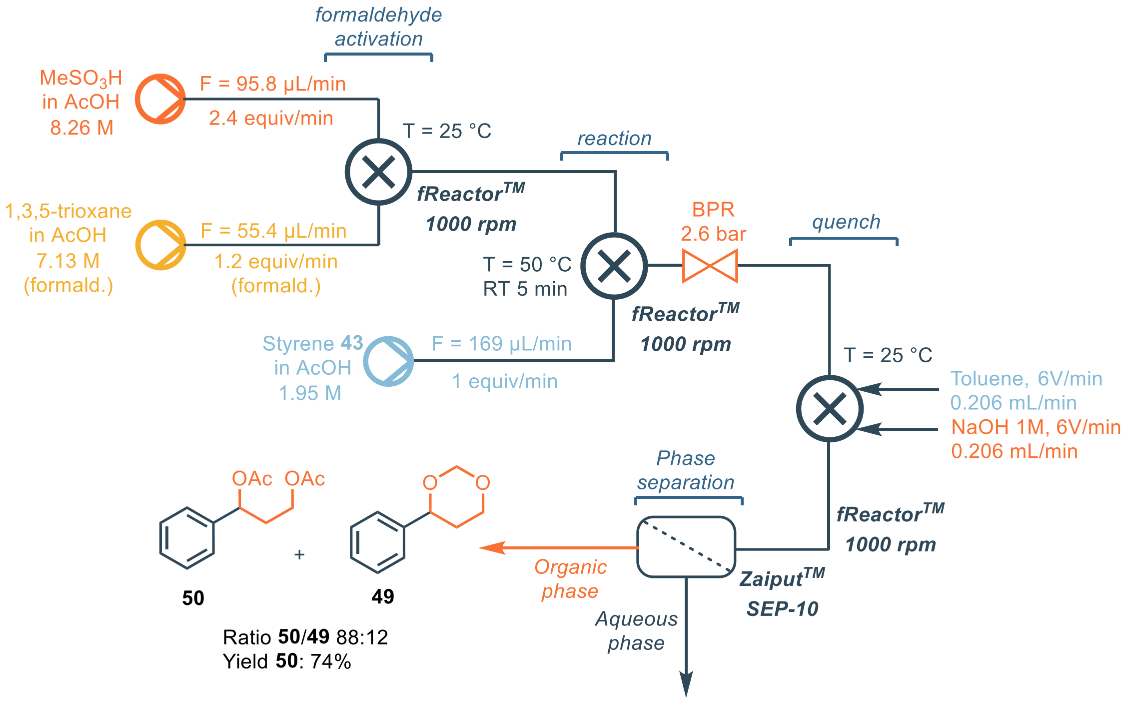

Preparation of stock solutions: In two separate round-bottom flasks, a 7.14 M solution of 1,3,5-trioxane in acetic acid was prepared by dissolving 1,3,5-trioxane (8 g, 0.089 mol, corresponding to 0.266 mol of monomeric formaldehyde) in acetic acid (32 g, 30.47 mL, 0.51 mol), and an 8.26 M solution of methanesulfonic acid in acetic acid was prepared by dissolving methanesulfonic acid (24.8 g, 6.84 mL, 0.26 mol) in acetic acid (15.2 g, 14.47 mL, 0.25 mol). The 1,3,5-trioxane solution was loaded into a Hitec Zang® syringe pump, while the methanesulfonic acid solution was transferred into a 20 mL NORM-JECT® syringe fitted to a Chemyx® syringe pump. A third solution, consisting of styrene (6 g, 6.62 mL, 0.058 mol) in acetic acid (24 g, 22.85 mL, 0.49 mol, 1.95 M), was also loaded into a 20 mL NORM-JECT® syringe and fitted to a Chemyx® syringe pump. A fourth syringe (20 mL, NORM-JECT®) was filled with toluene, while a fifth syringe of the same type was charged with 1M NaOH solution (0.8 g, 0.02 mol). These latter two syringes were mounted on an NE-4000® two channel programmable syringe pump and connected to a Zaiput liquid–liquid membrane separator (SEP-10) equipped with a PTFE membrane (0.5 µm pore size).

Flow setup: All syringes were connected via PTFE capillary tubing (1.59 mm I.D.) to miniaturized CSTR reactors (Asynt fReactor™, 1.6 mL), placed on a heating plate at RT (reactor 1 and 3) 50 °C (reactor 2) and magnetically stirred. Once the stock solutions had been loaded into the syringe pumps, the feeds were started as follows: 1,3,5-trioxane 20% w/w (3.89 g, 0.026 mol, 0.055

mL/min, 1.2 equiv relative to formaldehyde monomer), methanesulfonic acid 62% w/w (8.04 g, 0.052 mol, 0.096 mL/min, 2.4 equiv), styrene 20% w/w (11.45 g, 0.022 mol, 0.169 mL/min, 1.0 equiv), toluene (6 V/min, 0.204 mL/min), and NaOH 1 M (6 V/min, 0.204 mL/min).

Reaction and work-up: After 30 minutes of equilibration, the organic and aqueous phases were continuously separated and collected in distinct Erlenmeyer flasks for 30,55 minutes of reaction. The organic fraction was concentrated in vacuo, affording 2.28 g of a yellowish crude material, which contains 75,30% w/w of 1,3-diacetoxy-1-phenylpropane **50** (1.72 g) with 75.30% NMR yield.

Conclusions

In **Chapter 1**, a comprehensive introduction to the field of organocatalysis has been provided. The chapter covers the fundamental principles and diverse activation modes of both covalent and non-covalent organocatalysis. Key historical milestones are discussed alongside recent cutting-edge examples from the literature, offering a broad overview of the state-of-the-art and the evolution of this powerful synthetic discipline.

In **Chapter 2**, the first application of **NCDs** in asymmetric iminium ion catalysis via Asymmetric Counteranion-Directed Catalysis has been shown. The study focuses on the 1,4-reduction of α,β-unsaturated aldehydes, where easily prepared, achiral CDs are paired with a chiral phosphoric acid (**CPA**) as the stereoinducing element. An extensive optimization identified that **CDs** with a higher density of accessible surface amines outperform simple molecular catalysts. This nano-organocatalytic system, using a non-symmetrical Hantzsch ester, provides access to a range of saturated aldehydes with good yields and high enantioselectivities (up to 84% ee). The formation of the key iminium ion on the CD surface was confirmed via ^{19}F NMR spectroscopy.

In **Chapter 3**, a unique case of enantiodivergence in asymmetric organocatalysis, driven by minimal modifications to an achiral reagent, has been discussed. The study focuses on the transfer hydrogenation of α,β-unsaturated aldehydes using a system of **NCDs** and a **CPA**. It was discovered that simply switching the Hantzsch ester's alkyl substituents from dimethyl to diethyl completely reverses the product's stereochemistry from the (R)- to the (S)-enantiomer. This counterintuitive phenomenon is rationalized through a synergistic experimental and computational investigation, which reveals that the stereochemical switch is governed by weak London dispersion forces controlling the enthalpic stability of the pre-reactive supramolecular assembly.

In **Chapter 4**, two distinct yet conceptually related strategies in anion-binding catalysis have been presented, both centered on the development of novel non-covalent catalysts. The first part describes the rational design, synthesis, and application of a new family of catalysts based on the 1,8-diaminocarbazole scaffold, a rigid framework featuring three hydrogen-bond-donor (HBD) sites. The second, more exploratory part introduces the first-ever catalytic application of all-cis-fluorinated cyclohexanes, leveraging their exceptionally strong molecular dipole moment to achieve anion stabilization. The aim of this chapter is twofold: first, to establish the previously unexplored 1,8-diaminocarbazole framework as an effective platform for anion-binding catalysis in a benchmark N-tritylation reaction; second, to provide a proof-of-concept for the catalytic activity of facially polarized fluorinated cyclohexanes by designing a ditopic receptor to promote a challenging nucleophilic aromatic substitution (S_nAr) reaction. A clear structure-activity relationship was established for the carbazole-based catalysts, where binding affinities, quantified by NMR and fluorescence titrations, directly correlated with catalytic performance, identifying an electron-deficient derivative (**106c**) as the most efficient catalyst (83% yield). For the fluorinated cyclohexanes, the synthesized ditopic catalyst successfully accelerated the S_nAr reaction at elevated temperatures, demonstrating a significant rate enhancement compared to the uncatalyzed background reaction and confirming its catalytic potential.

In **Chapter 5**, a novel, safer, and more cost-effective synthetic route to a key intermediate of the drug Tolterodine has been presented. The currently employed industrial process relies on the hazardous reducing agent sodium borohydride ($NaBH_4$), which poses significant safety risks due to its exothermic nature and the evolution of flammable hydrogen gas. The new strategy completely avoids this reagent by employing a Prins reaction between styrene and formaldehyde in acetic acid to form a diacetate intermediate, followed by a straightforward hydrolysis. The process was successfully optimized in both batch and continuous flow, resulting in a protocol that is almost twice as cost-effective, eliminates severe safety hazards, and yields a product of higher purity than the traditional method.

List of publications

- D. Iapadre, **A. Carioscia**, F. Pesciaioli, A. Carlone, *Paper submitted*
- E. Cocco, **A. Carioscia,** F. Pesciaioli, M. Prato, G. Filippini, M. Aschi, A. Carlone, *Paper submitted*
- A. Vetrano, N. Di Fonte, O. Monasson, F. Perrella, M. Porco, F. Mercuri, G. Dell'Orletta, F. Petragnano, **A. Carioscia**, D. Deodato, D. Calcagno, G. Salvitti, S. Reale, F. Pesciaioli, C. Ferrante, D. Tedeschi, G. Grasso, P. Benassi, E. Peroni, A. Carlone, I. Daidone, C. Iacobucci, *Small,* **2026,** 0:e14872
- **A. Carioscia**, D. Iapadre, E. Incerto, J. Di Pietro, L. Giansanti, F. Pesciaioli, A. Carlone, *Chem Eur J*, **2025**, *31*, e20250012
- **Carioscia,** E. Cocco, M. E. Casacchia, G. Gentile, M. Mamone, G. Giorgianni, E. Incerto, M. Prato, F. Pesciaioli, G. Filippini, A. Carlone, *ACS Catal.*, **2024**, *14*, 13429–13438
- Brusa, D. Iapadre, M. E. Casacchia, **A. Carioscia**, G. Giorgianni, G. Magagnano, F. Pesciaioli, A. Carlone, *Beilstein J Org Chem*, **2023**, *19*, 1243–1250.

Conferences & Seminars attended

Seminars

- Dott. Luca Capaldo, Photochemistry and photocatalysis: how to?
- Prof. Giovanni Pitari, Physical and Chemical Processes responsible for climate change
- Prof. Armando Carlone, Sustainable Development of industrial Processes in Pharma
- Prof. Armando Carlone, Asymmetric Organocatalysis
- Prof. Laura Palombi, Excursus on synthesis, functionalization and structural investigation of nitrogen-containing small organic molecules: isoindolinones, 13th March 2024
- Dott. Antonio Del Vecchio, (Radio)Isotopic Chemistry for the Labeling of Pharmaceuticals, 18th-20th June 2024;

- Prof. Marta Fiorenza, English Course B2 Level, September 2024;
- Prof. Mattia Silvi, Organic photoredox catalysis, 24th-25th September 2024;
- Prof. Luisa Giansanti, Supramolecular Chemistry Course

Conferences & Contributions

- CDCO 2025 – Cagliari (September 2025) Oral presentation "Nitrogen-Rich Carbon Dots as Effective Catalysts in the 1,4-Reduction of α,β-Unsaturated Aldehydes via Ion Pair Asymmetric Nano-Organocatalysis"
- ISOS 2025 – Corbella Summer School, Gargnano (May 2025) Oral presentation "Nitrogen-Rich Carbon Dots as Effective Catalysts in the 1,4-Reduction of α,β-Unsaturated Aldehydes via Ion Pair Asymmetric Nano-Organocatalysis" (Fully funded fellowship)
- MYCS 2024, November 2024 (Rimini). Oral presentation "Nitrogen-Rich Carbon Dots as Effective Catalysts in the 1,4-Reduction of α,β-Unsaturated Aldehydes via Ion Pair Asymmetric Nano-Organocatalysis" (Fully funded fellowship and Award for Best Oral Presentation)
- SCI2024 – Elements of Future, September 2024 (Milano). Oral presentation "New Hydrogen Bonding Motifs for Anion Binding Catalysis" (Fully funded fellowship)
- C3 Day, June 2024 (Bologna). Oral presentation "New Hydrogen Bonding Motifs for Anion Binding Catalysis"
- International Supramolecular Chemistry Summer School 2nd edition, May 2024 (S. Margherita di Pula). Poster presentation "New Hydrogen Bonding Motifs for Anion Binding Catalysis"
- Seminar, March 2024 (L'Aquila), "New Hydrogen Bonding Motifs for Anion Binding Catalysis"
- SupraChem 2024, February 2024 (Ulm). Poster presentation "New Hydrogen Bonding Motifs for Anion Binding Catalysis"
- ISPROCHEM 2023, May 2023 (Gargnano). No contribution (Fully funded fellowship)

- CINMPIS DAYS 2023, February 2023 (Pisa). Flash oral presentation “CDs in Asymmetric Organocatalysis via ACDC” (Fully funded fellowship)

Aknowledgments

Without a doubt, these three PhD years have been the most intense of my life so far. This is mainly because I learned so much, on both a scientific and a personal level. Of course, I definitely learned a lot of chemistry (when I started, I didn't even know what an *iminium ion* was!) and, above all, I learned how to *do* research and how to *be* a researcher. But this experience certainly taught me so much about myself as a person, about my limits, my demons, and also how to face them. Being confronted with the *me of yesterday* every single day taught me how to tackle my overwhelming pessimism and my impostor syndrome, and not to dwell on moments of sadness and frustration, by trying to put events into perspective. I learned that the *process* is often more important than the *content*, and that it's important to enjoy the small daily joys.

It is clear that I would have never reached this level of self-awareness (on which I'm still working, of course) without some crucial people who have accompanied me throughout this intense journey. That's the beauty of a PhD: you share a journey with many people — some who, like you, are going through the same path and can fully understand and support you; and others who silently watch from the outside, but who are safe harbors where you can always find comfort.

First of all, I would like to thank my supervisor, Prof. Armando Carlone. Thank you for believing in me (more than I believed in myself) and for always giving me trust and autonomy in my work. You were a kind and understanding guide, and always available for a word of comfort during my low moments. I also want to thank my co-supervisor, Dr. Fabio Pesciaioli: you were an important guide and taught me a lot (always sharpen the Pasteurs before a PTLC!!). Thank you both for everything.

I also want to thank Dr. Simone Mantegazza and Dr. Gabriele Razzetti for their impeccable supervision throughout the PhD, but especially in the last year. Thank you for your valuable advice and for the kind words you shared about me. I also thank the entire Dipharma team, for welcoming me, helping me, and making me feel at home. I'm looking forward to the next *OLLONE* concert.

I also extend my heartfelt thanks to Prof. Max von Delius and all the members of the Delius Group, for welcoming me during my period abroad. I will forever remember the Pizza SCHPETZIALE and I still dream at night about Andreas's desserts. Thank you, you were a great added value to my time in your research group.

It wouldn't have been the same journey without my lab mates: Emanuele, Alessandro, Edith, Debora, Elena, Matteo, Martina. Your presence lightened the weight of the lab work, and running columns shoulder to shoulder with you (especially in the summer) to the rhythm of *questo è il lato A e questo è il lato B* and *MEOW MEOW MEOW MEOW* was (*almost*) enjoyable. Thanks for everything, *monelli.*

Even outside the lab, the University of L'Aquila brought plenty of joys: Caterina, Valerio, Giulia S., Sara, Francesco, Nicola, Daniel, Matteo, and all my already mentioned group fellows: you were the added value of these years. Despite your unfair accusations of me being a *wolf*, I love you all dearly. One day we will return to sing *Country Road* (badly) all together, while we order our fifteenth beer (in addition to *du mangiarini* kindly offered) from All Beers, spending 6€ each (L'Aquila is a wonderful city!!!).

I also want to thank all my friends who were close to me outside of the academic context: Giona, Gioele, Giulia B., Irene, Marco, Matilde, Giulia G., Federico. Despite the distance, it was always wonderful to spend time together. I love you all very much.

I want to thank my entire family, from my loving aunts to my welcoming grandparents, and also those who are now watching us from above. Your support over these years has been fundamental; thank you for always making me feel so loved and adored.

I also want to thank my parents, Anna and Santino, and my sister, Sofia, from the bottom of my heart. You are, without a doubt, the most important people in my life. I am sure that without you, I would never have been able to face these 3 years. With your emotional (and logistical) support, you made me feel at home even when I was 3000 km away. I have always felt understood, welcomed, and loved, and for that, I consider myself very lucky. I could never have wished for anything better. I hope I have made you proud of me. Sofia: always believe in yourself and in your potential. You are a wonderful, sensitive, and intelligent girl. Know that I will always be there for you.

I also want to thank my two landlords, Lola and Freddie. Thank you for granting me the honour of cuddling you whenever YOU want. You are the joy of my life.

Lastly, I want to thank Lorenzo. I know how much it would embarrass you if I put into writing everything I'd like to say to you (you would definitely find it *CRINGE*), so I'll avoid doing so; some things, let's just keep them between us. I simply thank you for everything you have wanted to build with me over these years. You were, and are, fundamental.

Senza alcun dubbio, questi tre anni di dottorato sono stati i più intensi della mia vita fin ora. Questo deriva principalmente dal fatto che ho imparato tanto, sia scientificamente che personalmente. Certo, ho sicuramente imparato tanta chimica (quando ho iniziato, neanche sapevo cosa fosse uno ione imminio!) e, soprattutto, ho imparato a fare ricerca e ad essere un ricercatore. Ma sicuramente questa esperienza mi ha insegnato tanto su di me come persona, su quali sono i miei limiti, i miei demoni, e anche come affrontarli. Essere ogni giorno a confronto con il "me stesso di ieri" mi ha insegnato come affrontare il mio pessimismo imperante e la mia sindrome dell'impostore, e a non soffermarmi su momenti di tristezza e frustrazione, cercando di mettere in prospettiva gli eventi. Ho imparato che il "processo" è spesso più importante del "contenuto", e che è importante godere delle piccole gioie quotidiane.

È evidente che non sarei mai riuscito a raggiungere una consapevolezza del genere (sulla quale sto ovviamente ancora lavorando) senza alcune figure cruciali che mi hanno accompagnato durante questo intenso percorso. Il bello del dottorato è anche questo: si condivide un viaggio con tante persone: alcune che, come te, stanno facendo lo stesso percorso, e che quindi possono capirti perfettamente e dare conforto. Altre che, invece, silenziosamente ti osservano da fuori, ma che sono porti sicuri nei quali trovare conforto.

È opportuno che, per primo, ringrazi il mio supervisor, Prof. Armando Carlone. Grazie per aver creduto in me (più di quanto lo facessi io) e per avermi sempre dato fiducia e autonomia nel lavoro. Sei stato una guida gentile e comprensiva, e sempre disponibile per una parola di conforto nei miei momenti di down. Voglio anche ringraziare il mio co-supervisor, Dott Fabio Pesciaioli: sei stato una guida importante e mi hai insegnato molto (sempre fare la punta alle Pasteur prima di una PTLC!!). Grazie di tutto a entrambi.

Voglio anche ringraziare il Dott. Simone Mantegazza e il Dott. Gabriele Razzetti per la loro impeccabile supervisione durante tutto il PhD, ma specialmente nell'ultimo anno. Grazie per i preziosi consigli e per le belle parole spese nei miei confronti. Ringrazio anche tutta la squadra di Dipharma, per avermi accolto, aiutato e fatto sentire a casa. Non vedo l'ora che ci sia il prossimo concerto di *OLLONE*.

Ringrazio sentitamente anche il Prof. Max von Delius e tutti i membri del Delius Group, per avermi accolto durante il mio periodo all'estero. Mi ricorderò per sempre della Pizza SCHPETZIALE e ancora mi sogno la notte i dolci di Andreas. Grazie, siete stati un grande valore aggiunto per il mio periodo nel vostro gruppo di ricerca.

Non sarebbe stato lo stesso percorso senza i miei compagni di laboratorio Emanuele, Alessandro, Edith, Debora, Elena, Matteo D. S., Martina. La vostra presenza ha alleggerito il peso del lavoro, e scolonnare spalla a spalla con voi (specialmente d'estate) al ritmo di "questo è il lato A, e questo è il lato B" e "MIAO MIAO MIAO MIAO" è stato quasi piacevole. Grazie di tutto, monelli.

Anche fuori dal laboratorio, l'Università degli Studi dell'Aquila ha regalato non poche gioie: Caterina, Valerio, Giulia S., Sara, Francesco, Nicola, Daniel, Matteo T., e tutti i miei compagni di gruppo già menzionati: siete stati il valore aggiunto di questi anni. Nonostante le vostre ingiuste accuse sul mio essere un lupo, vi voglio un mondo di bene. Un giorno torneremo a cantare (male) Country Road tutti assieme, mentre chiediamo la quindicesima birra (oltre a "du mangiarini" gentilmente offerti) dal All Beers spendendo 6€ a testa (L'Aquila è una città meravigliosa!!!).

Voglio ringraziare anche tutti gli amici che mi sono stati vicini al di fuori del contesto accademico: Giona, Gioele, Giulia B., Irene, Marco, Matilde, Giulia G., Federico. Nonostante la distanza, è sempre stato bello passare del tempo assieme. Vi voglio tanto bene.

Ringrazio tutta la mia famiglia, dalle amorevoli zie agli accoglienti nonni, e anche a chi ormai ci guarda da lassù. Il vostro supporto in questi anni è stato fondamentale; grazie per avermi fatto sempre sentire un nipote amato e adorato.

Ci tengo anche a ringraziare dal profondo del mio cuore i miei genitori Anna e Santino, e mia sorella Sofia. Siete senza alcun dubbio le persone più importanti della mia vita. Sono sicuro che, senza di voi, non sarei mai riuscito ad affrontare questi 3 anni. Con il vostro supporto emotivo (e logistico) mi avete fatto sentire a casa anche quando ero a 3000 Km di distanza. Mi sono sempre sentito capito, accolto, amato, e per questo mi ritengo molto fortunato. Non avrei mai potuto desiderare niente di meglio. Spero di avervi resi fieri di me. Sofia: credi sempre in te stessa e nelle tue potenzialità. Sei una ragazza meravigliosa, sensibile ed intelligente. Sappi che per te ci sarò sempre.

Voglio anche ringraziare sentitamente i miei due padroni di casa, Lola e Freddie. Grazie per concedermi l’onore di coccolarvi quando VOI volete. Siete la gioia della mia vita.

Per ultimo, voglio ringraziare Lorenzo. So quanto ti imbarazzerebbe se mettessi per iscritto tutto ciò che vorrei dirti (so che lo troveresti cringe), quindi eviterò di farlo; certe cose, teniamocele per noi soltanto. Semplicemente ti ringrazio per tutto ciò che hai voluto costruire con me in questi anni. Sei stato, e sei, fondamentale.

Tesi redatta con il cofinanziamento dell'Unione europea-NextGeneration EU - Piano Nazionale di Ripresa e Resilienza Missione 4, Componente 2 – Investimento 3.3. del PNRR – "Dottorati innovativi che rispondono ai fabbisogni di innovazione delle imprese" – CUP E11I22000250001

Finanziato dall'Unione europea
NextGenerationEU

Ministero dell'Università e della Ricerca

Italiadomani
PIANO NAZIONALE DI RIPRESA E RESILIENZA

UNIVERSITÀ DEGLI STUDI DELL'AQUILA